Signals and Communication Technology

Mohammad Abdul Matin *Editor*

Wideband, Multiband, and Smart Antenna Systems

Springer

Signals and Communication Technology

This series is devoted to fundamentals and applications of modern methods of signal processing and cutting-edge communication technologies. The main topics are information and signal theory, acoustical signal processing, image processing and multimedia systems, mobile and wireless communications, and computer and communication networks. Volumes in the series address researchers in academia and industrial R&D departments. The series is application-oriented. The level of presentation of each individual volume, however, depends on the subject and can range from practical to scientific.

Indexing: All books in "Signals and Communication Technology" are indexed by Scopus and zbMATH

For general information about this book series, comments or suggestions, please contact Mary James at mary.james@springer.com or Ramesh Nath Premnath at ramesh.premnath@springer.com.

More information about this series at http://www.springer.com/series/4748

Mohammad Abdul Matin
Editor

Wideband, Multiband, and Smart Antenna Systems

Springer

Editor
Mohammad Abdul Matin
Department of Electrical and Computer
Engineering (ECE)
North South University
Dhaka, Bangladesh

ISSN 1860-4862 ISSN 1860-4870 (electronic)
Signals and Communication Technology
ISBN 978-3-030-74310-9 ISBN 978-3-030-74311-6 (eBook)
https://doi.org/10.1007/978-3-030-74311-6

This Springer imprint is published by the registered company Springer Nature Switzerland AG
The registered company address is: Gewerbestrasse 11, 6330 Cham, Switzerland

Acknowledgements

First of all, I am grateful to my Lord Almighty ALLAH who helped and guided me throughout my life. My sincere thanks to the authors of different chapters whose invaluable contributions help me in completing this book, also thanks to the authors whose manuscript was not included due to rigorous review process. The editor is indebted to numerous reviewers for valuable suggestions and comments during the review process. The authors are so cooperative during different stages of book development process. I am also beholden to the Springer team, in particular Mary James for her cordial assistance throughout this project. I wish to include here a word of appreciation to them including Pradheepa Vijay for smoothly and efficiently handling the project during production stage and keeping it in line with the publisher's policies. I would also like to thank my wife Momtaz Begum and my children Zabeer Ahmed and Zawad Ahmed for their patience and support. My special thanks to Mrs. Sufia Khaton (dearest mother) for the motivation that has encouraged me to keep going.

Best Regards,

North South University, Bangladesh Mohammad Abdul Matin

Contents

Chapter 1
Advances in Wideband, Multiband, and Smart Antenna Systems for Wireless Communication

Mohammad Abdul Matin

1.1 Introduction

Today, people like to enjoy their life in a fast lifestyle, and therefore, high speed wireless communication has become essential for delivering content and knowledge in the information age. This leads to a large demand for compact multiband or wideband antennas to prop up wireless communication devices such as cell phones, tablets, laptops, computers, and other related devices [1]. Compact design permits more space to integrate other electronic components. In addition, a number of other requirements exist such as antenna packaging, antennas on chip without compromising its performance while integrating in wireless devices. Therefore, designers propose different innovative approaches to reduce the complexities and difficulties in the design of wireless device. The aim of this book is to showcase latest R&D trends and novel methods in designing and analyzing broadband, multiband, and reconfigurable antennas for 5G and B5G mobile and wireless applications, as well as integrating in small volume wireless devices. This book provides theoretical and experimental approaches to some extent which would be useful to the researchers, scientist, engineers, and senior students in the field of antenna engineering. This book also highlights unique design issues to help the reader as well to understand more advanced research.

M. A. Matin (✉)
Department of Electrical and Computer Engineering (ECE), North South University, Dhaka, Bangladesh
e-mail: mohammad.matin@northsouth.edu

M. A. Matin (ed.), *Wideband, Multiband, and Smart Antenna Systems*, Signals and Communication Technology, https://doi.org/10.1007/978-3-030-74311-6_1

1.2 Research Contribution

This book attempts to explore the cutting edge research developments in wideband, multiband, and smart antenna systems and is organized into 13 chapters.

- Chapter " Wideband Antennas" provides a brief overview of wideband antenna techniques and the key aspects of the operating principles and design requirements associated with some of the most familiar wideband antennas. This chapter includes discussion on some of the core fabrication and measurement challenges associated with such antennas.
- Chapter "Printed UWB Antennas: Design and Principle" presents the recent developments of printed UWB antennas. Different types of printed antennas with UWB performances have been investigated. The results show that the printed UWB antennas have a simple structure, a low fabrication cost, and a compact size with high portability and mobility.
- Chapter "MIMO Antennas for 5G Enabled Devices" provides an overview of 5G MIMO technology and its significance followed by the evolution of MIMO antennas—from 4G to 5G. As 5G poses several challenges from antenna design point of view for both sub-6 GHz and mm-wave bands, it is crucial to investigate the limitations and design considerations for such systems. This chapter features MIMO antenna designs for base station (BS) as well as handheld devices for both sub-6GHz and mm-wave bands.
- Chapter "High-Isolation Compact Wideband MIMO Antennas for 5G Wireless Communication" focuses on mutual coupling reduction technique for wideband multiple-input-multiple-output (MIMO) antennas in a parallel configuration and presents a novel approach which is based on ground plane alterations. Rigorous numerical optimization of all geometry parameters is carried out to ensure the minimum size of the structures while satisfying two performance constraints. The results are verified experimentally. The effects of the user's hand on the antenna performance are also investigated through full-wave EM analysis using the standard human phantom.
- Chapter "Fixed and Scanned-Beam Antenna Arrays for 5G applications" highlights a variety of low profile and high gain antenna array designs, both for fixed-beam as well as scan beam for 5G applications. This chapter also includes two other topics, namely arrays with polarization diversity, and MIMO antennas that are likely to play important roles in 5G applications, both in sub-six and millimeter-wave designs.
- Chapter "Co-design of 4G LTE and Millimeter-Wave 5G Antennas for Future Mobile Devices" delves the desired specifications for co-design of 4G and 5G antenna modules along with design examples as Co-designing 4G LTE and mmWave 5G antennas with optimal characteristics is the appropriate method to achieve backward compatibility.
- Chapter "Application of the Whale Optimization Algorithm to Antenna Design for mm-wave 5G Communications Systems" describes a new nature inspired algorithm the Whale Optimization Algorithm (WOA) for antenna design and

investigates the applicability and validity of the proposed design framework using numerical analysis.
- Chapter "Reconfigurable Antenna: Analysis and Applications" provides a brief history of reconfigurable antenna along with the techniques and properties for the reconfiguration of an antenna. Some existing proposed reconfigurable antenna designs, methods, and their constraints are also discussed. In addition, the applications and the benefits of reconfigurable antennas are highlighted.
- Chapter "Smart antenna design: radiation pattern agility by Branch-Line Coupler" presents a new approach for agility in the radiation pattern by using simple transmission lines that make up a quadrupole called a Branch-Line Coupler (BLC). The principle of this new approach modifies the configuration of the antenna system radiation pattern by a simple or a combination of excitations allowing to have good performances.
- Chapter "Time-Domain Approach Towards Smart Antenna Design" deals with the feasibility of time-modulated linear arrays (TMLAs) for different applications by optimizing several parameters of the array. Pattern synthesis with or without suppressing the Sideband Radiations (SRs) as well as exploiting the sidebands are briefly described with several examples. Throughout this chapter, 16-element TMLAs are considered and a wavelet mutation-based differential evolution (DEWM) is used for optimal solution. Few other well-known optimization techniques for electromagnetic problems such as PSO and real-coded GA (RGA) based results are also presented for comparison.
- Chapter "Wireless Power Transfer for Implantable and Wearable Medical Devices" concentrates on common wireless power transfer (WPT) techniques for implantable and wearable medical devices. WPT through Implantable antennas can suffer from misalignment issues due to the curved surface of the anatomical system and body movement during daily life. The main types of misalignment due to patient movements were analyzed and provided solution for two case studies.

1.3 Conclusion

This book covers current and emerging trends in research and development of wideband, multiband, and smart antenna systems for modern wireless communications featuring a structured approach. Features include:

- Reviews existing designs as well as offers an in-depth treatment of wideband, multiband, and smart antennas for modern wireless communications.
- Focuses on advanced design, synthesis, and computational methods for wideband, multiband, and smart antennas and attempts to make everything real world.
- Presents simulation and experimental results to illustrate concepts and develops knowledge both in theory and practical skills.

This book will help lot of research scholars, practicing engineers, and beginners to understand principles applicable in designing wideband, multiband, and smart antenna systems for modern wireless communications.

References

1. M.A. Matin (Ed.), *Wideband, Multiband, and Smart Reconfigurable Antennas for Modern Wireless Communications* (IGI Global, Pennsylvania, 2015)

Dr. Mohammad A Matin is a Professor of the Department of Electrical and Computer Engineering at North South University (NSU), where he has been since 2008. He was first appointed as Assistant Professor and then promoted to Associate Professor in 2011 and later on Professor at North South University. While in that post, he was also the coordinator of the EEE program. During 2012-2017, he was an Associate Professor at Universiti Teknologi Brunei (UTB), Brunei Darussalam. He received his B.Sc. degree in Electrical and Electronic Engineering from BUET (Bangladesh), M.Sc. degree in Digital Communication from Loughborough University, UK and PhD in Wireless Communication from Newcastle University, UK. Dr. Matin has been a visiting academic staff at the National University of Malaysia (UKM), University of Malaya (UM), etc. He has published over 100 peer-reviewed journal and conference papers. He is the author/editor of 16 (sixteen) academic books and 17 (seventeen) book chapters. Dr. Matin serves as a referee or member of the editorial board for several international journals including IEEE Communications Magazine. He is the Senior member of IEEE. He has received a number of Prizes and Scholarships including the Best Student Prize (Loughborough University), Commonwealth Scholarship, and Overseas Research Scholarship (ORS) conferred by the Committee of Vice Chancellors and Principals (CVCP) in the UK.

Chapter 2
Wideband Antennas

Umair Naeem and Vincent Fusco

2.1 Introduction

In recent years the topic of wideband antennas or wideband antenna arrays has gained significant attention with the advent of next-generation wireless technologies. In wireless communications, there is an unprecedented and ever-increasing demand for higher and higher data rates. These requirements can be catered by designing multiband and wideband systems. The antenna remains a critical and highly challenging part of any wideband "high data rate" communications system. Some of the driving factors for future generation wireless systems are; high data rates, coexistence of multiple standards, and availability of wide bandwidth data acquisition solutions.

Examples include: (1) Connected autonomous vehicles [1–4] (CAV) is one of the future generation technologies that requires high-resolution sensors for the purpose of gaining awareness of the operating environment, as well as high data rate and low latency wireless connection among vehicles. (2) High-resolution microwave imaging requires extremely wideband antennas [5] and is desired for medical, space, security, and surveillance applications.

The chapter starts with a contextual background of the topic, this will be followed by a review of some of the theoretical concepts used in the design of wideband antennas that are necessary in order to provide a foundation for the design of ultrawideband antennas. First, traveling wave theory will be explained in the context of broadband antennas. The theory behind frequency independent antennas will then be explained with the help of self-scaling and self-complementarity principles. Wideband characteristics of large flat arrays comprising of closely spaced antennas

U. Naeem (✉) · V. Fusco
The Institute of Electronics, Communications and Information Technology (ECIT), Queen's University of Belfast, Belfast, UK
e-mail: u.naeem@qub.ac.uk; v.fusco@ecit.qub.ac.uk

M. A. Matin (ed.), *Wideband, Multiband, and Smart Antenna Systems*, Signals and Communication Technology, https://doi.org/10.1007/978-3-030-74311-6_2

are then described through the theory of the current sheet array extended for the analysis of tightly coupled antennas.

Following that, a section on different wideband antenna types are discussed with the emphasis on highlighting their performance metrics and geometrical features. Frequently encountered structures are described and include traveling wave antennas such as the Yagi-Uda Antenna, the Tapered Slot Antenna, and the Helical Antenna. The family of frequency independent antennas such as Archimedean Spiral, Equiangular Spiral Antennas, Log-Periodic Antennas, Sinuous Antenna, and Tightly Coupled Antennas (TCA) are also discussed. Finally, Fractal and Dielectric Resonator Antennas are briefly touched upon.

In the final sections of this chapter, some of the fabrication and measurement challenges associated with wideband antennas will be discussed. Some key applications of wideband antennas will also be discussed. These will include communications, imaging, and material characterization. Lastly, a brief indication of the future direction for research in the field of wideband antennas will be presented and followed by concluding remarks.

2.2 Theoretical Concepts

In order to better understand the operating principles for wideband antennas, it is important to become familiar with the key concepts essential for their design and analysis. Although the relevant theory is touched upon in this section, readers are encouraged to study the suggested references should they need a deeper understanding of the topics introduced here.

2.2.1 Traveling Wave Theory

Consider the case where a long straight wire antenna is excited from one end, current or voltage distributions will appear on the wire. Voltage and current waves at the open ends of the antenna will be reflected. If we consider a case where the wire is terminated at the end opposite to the driven end by a matched load (in order to minimize the reflections), the standing waves associated with a resonant antenna can be avoided making this type of antenna inherently wider in operation than its resonant counterpart. If a length of straight wire terminated as above is placed parallel to the ground at height h, since the antenna is nonresonant a broadband behavior is observed. This configuration of the antenna is called the Beverage antenna [6], Fig. 2.1. Other examples of traveling wave antennas [7] are Helical antennas, dielectric rod antennas, aperture antennas, Yagi-Uda, log-periodic, and slotted waveguides [8].

Traveling wave antennas can be classified either as slow wave or fast wave structures based on the phase velocity of the propagating wave within the structure.

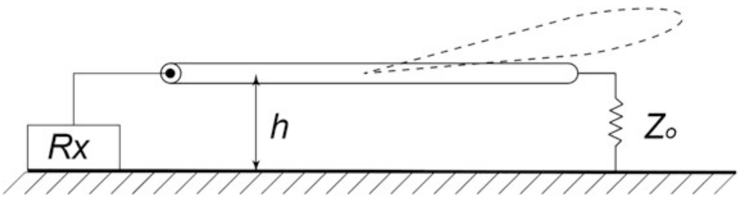

Fig. 2.1 A long wire traveling wave antenna

2.2.1.1 Slow Wave: Surface Wave ($v_p \leq c$)

A slow wave antenna is defined when the phase velocity v_p of the structure is equal to or lower than the speed of light [7, 9]. By carefully exploiting the radiation from discontinuities inside the antenna structure one can achieve a slow wave structure which is also called as **surface wave antenna** [7, 9]. A surface wave antenna interrupts the bound wave on the antenna surface through discontinuities designed into the structure thereby allowing radiation, and hence achieving a net outflow of radiated power.

2.2.1.2 Fast Wave: Leaky Wave ($v_p > c$)

A traveling wave antenna is classified as fast wave structure when the phase velocity of the traveling wave is greater than the speed of light [7, 9].

An example of fast wave structure is the leaky wave antenna which loses energy progressively by radiation as the wave propagates through the structure becoming less bound to it as it progresses. A useful account of leaky wave antennas is presented in [9]. Some specific examples of leaky wave antennas are now given.

2.2.2 Frequency Independent Antennas Theory

Antennas whose radiation and impedance characteristics, above a certain frequency, are both independent of frequency are classified as frequency independent antennas [10]. The frequency independent antenna theory is explained in the literature by two concepts: structures that can be specified by angles alone and structures that exhibit self-complementary property.

2.2.2.1 Antennas Specified by Angles Alone

The radiation and impedance behavior of an antenna will remain the same with respect to frequency of operation if its dimensions, expressed in terms of wave-

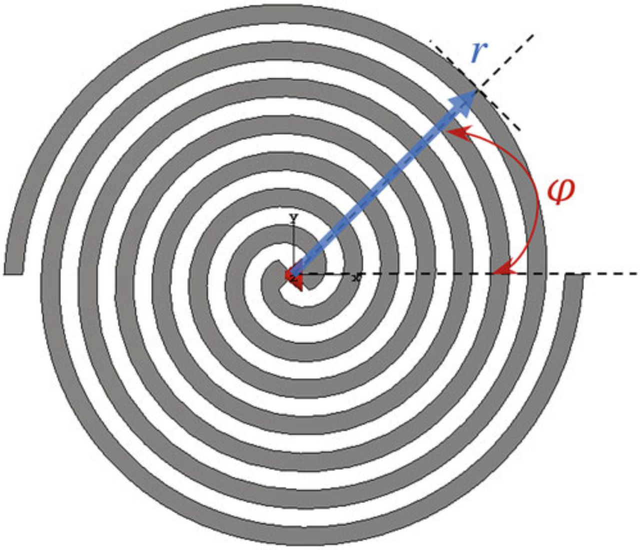

Fig. 2.2 Example of an antenna defined by angle $r = a\varphi$, where a determines the rate of wrapping of the arms

length, are constrained to remain constant. Frequency independent antennas are therefore based on the idea of self-scaling, wherein the physical size of the structure is reduced in equal proportion to wavelength of operation and consequently they exhibit broadband characteristics. One way to realize a self-scaling antenna is to specify the entire structure only in terms of angle thereby removing the need for length specification (Fig. 2.2).

The general formula defining an antenna specified by an angle is given by Eq. (2.1),

$$r = \mathrm{e}^{a(\varphi+\varphi_o)} F(\theta) \tag{2.1}$$

where a and φ_o are constants, $F(\theta)$ is function of θ in spherical coordinate system defined by r, θ, and φ. A logarithmic scaling ensures smooth structure geometry growth and consequently extension in impedance bandwidth.

An example of such a system is the equiangular spiral which can be defined by only two parameters: the rate of expansion a, and the orientation φ_o in a spherical coordinate system, the structure can be represented by Eq. (2.2),

$$\varphi + \varphi_o = \ln r^{\frac{1}{a}} \tag{2.2}$$

Following the design approach based on angle method, one can achieve nearly constant input impedance with frequency. However, radiation characteristics do not always remain constant since as frequency changes there is an equivalent "electrical" rotation of the structure. This can be mitigated by noting that the radiation pattern at the new frequency f_2 will be the same as at the previous frequency f_1 if the coordinate system is rotated about $\theta = 0°$ correspondingly. Therefore, the pattern rotates about $\theta = 0°$ axis as the frequency is swept, this rotation rate depends upon a, and the angle of rotation is given by Eq. (2.3).

$$\text{Angle of rotation} = \frac{1}{a} \ln \frac{f_1}{f_2} \tag{2.3}$$

2.2.2.2 Self-Complementary Structures

A breakthrough concept for wideband antenna design was introduced by Mushiake in 1948 [11], who established the foundation of several useful antenna designs that are still extremely popular in wideband applications. The input impedance of any self-complementary antenna will always remain constant and it does not depend on source frequency nor on its shape; consequently, there can be an infinite number of shapes that can meet self-complementary criteria, see [11–13] for a more detailed discussion and different self-complementary antenna examples.

Consider two structures that are mutually dual or "complementary" to one another, as shown in Fig. 2.3. One of the structures consists of two conducting strips

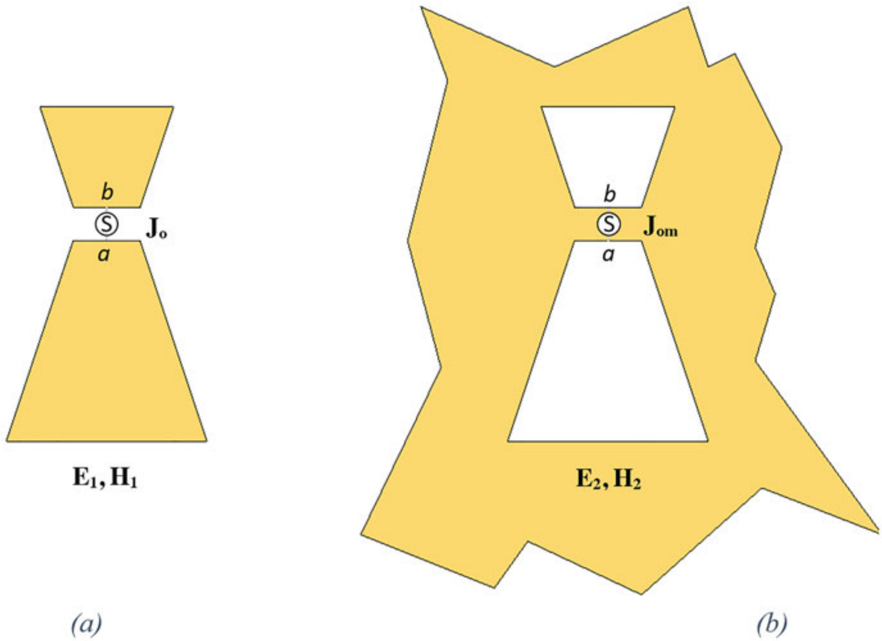

Fig. 2.3 A planar strip antenna and its complementary slot antenna (the shaded part is metal)

of an arbitrary shape and size while its dual consists of holes in a conducting sheet which are of same shape and size as its dual counterpart. The conducting strips are excited by an electric current J_o whereas its dual is excited by magnetic current J_{om}. The electromagnetic fields are defined as E_1 and H_1 for the structure consisting of conducting strips and as E_2 and H_2 for its dual. The two structures are thus said to be complementary with respect to each other and their electromagnetic characteristics are also dual of each other. The impedances of the two structures are related as,

$$Z_1 Z_2 = \left(\frac{Z_o}{2}\right)^2 \tag{2.4}$$

where Z_o is the intrinsic impedance of free space, $Z_o = 120\pi$.

Since both structures are represented as two-sided planar sheets, the electric and magnetic currents are defined on both sides of the sheets. The electric current source J_o can be represented as two symmetric current sources defined on each side of the sheet. Similarly, J_{om} can be viewed as two asymmetrical magnetic current sources. Since the two structures are dual of each other, and by the extension of Babinet's Principle, [14], their associated electromagnetic fields can be defined by Eq. (2.5).

$$\begin{aligned} E_2 &= \mp H_1 \\ H_2 &= \pm\left(\frac{1}{Z_o}\right)^2 E_1 \end{aligned} \tag{2.5}$$

where Z_o is the free space impedance.

$$\begin{aligned} Z_1 &= \frac{\int_b^a E_1 \cdot dl}{2\int_c^d H_1 \cdot dl} \\ Z_2 &= \frac{\int_c^d E_2 \cdot dl}{2\int_a^b H_2 \cdot dl} \end{aligned} \tag{2.6}$$

The input impedances for the two structures (Z_1 and Z_2) can be represented as the ratios of the integrals as shown in Eq. (2.6). The product of these impedances is given by Eq. (2.4).

For the case of a two terminal self-complementary antenna structure radiating in free space (see Fig. 2.4), the input impedance is around 188 Ω as calculated using Eq. (2.7).

$$Z = Z_1 = Z_2 = \frac{Z_o}{2} = \frac{1}{2}\sqrt{\frac{j\omega\mu}{(j\omega\varepsilon + \sigma)}} \cong 60\pi \cong 188.5\ \Omega \tag{2.7}$$

The input impedance of a four terminal self-complementary antenna structure such as that shown in Fig. 2.5 is given by Eq. (2.8). From Eq. (2.8) a general-

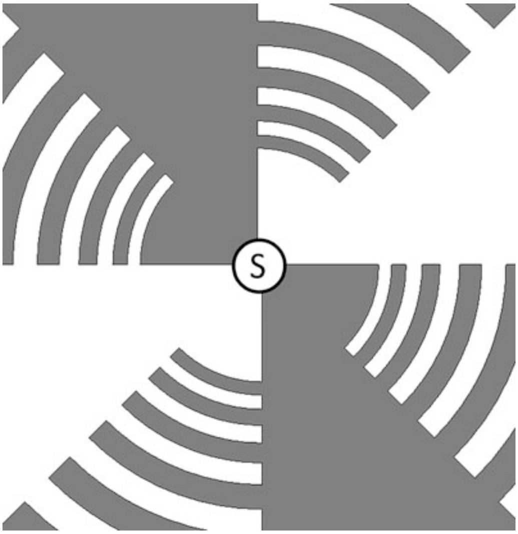

Fig. 2.4 Example of two terminal self-complementary antenna

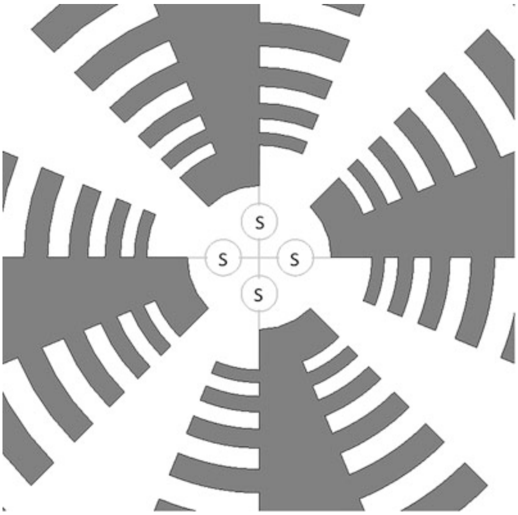

Fig. 2.5 Example of four terminal self-complementary antenna

ized expression for input impedance Z_{mn} can be derived. The generalized input impedance is given by Eq. (2.9), where, n-terminal self-complementary antennae are excited through an electric source with n-phases connected in star configuration and m is the order of rotation when the opposite terminal sources are 180° out of phase. References [11–13], give a more detailed discussion as well as some different example antenna structures.

$$Z_1 = \frac{Z_o}{2\sqrt{2}} \cong 30\pi\sqrt{2}\,\Omega \tag{2.8}$$

$$Z_{mn} = \frac{Z_o}{4\sin(m\pi/n)}\ \Omega \tag{2.9}$$

2.2.3 Current Sheet Array

Mutual coupling is generally considered to be an undesirable phenomenon in resonant antenna arrays as it is associated as being a major cause of degradation in their radiation pattern characteristics. Munk [15, 16] proposed the idea of exploiting the mutual coupling in tightly coupled arrays. The strong coupling among the antenna elements enables the realization of extremely large bandwidths. This phenomenon can be understood by the concept of current sheet array (CSA) first proposed by Wheeler in 1948 [17, 18]. Wheeler explained that a uniform current (J) flowing on an infinite and planar sheet will produce radiation which will have identical characteristics at all frequencies. Wheeler visualized the current sheet as an array of closely spaced short dipole radiating elements, as shown in Fig. 2.6. He proposed a theory where he subdivided infinite flat array of antennas into wave channels. Each channel includes one element and extends in the direction perpendicular to the plane containing the elements. These channels can then be analyzed as hypothetical waveguides capable of supporting TEM wave propagation where the wavefront of the propagating radiated wave is parallel to the plane containing the flat array. If we consider the radiating element to be a dipole then its radiation resistance is given with reference to Fig. 2.7, [17], as,

$$R = R_s\frac{h^2}{ab} = 377\frac{h^2}{ab}\ \Omega \tag{2.10}$$

where,

$R =$ radiation resistance of the radiating element
$R_s =$ wave resistance in free space
$h =$ height of antenna in meters
$a =$ rectangular cross-sectional width in meters
$b =$ rectangular cross-sectional height in meters
$l =$ radian length in free space $= \lambda/2\pi$ in meters

The radiation impedance of each element in the array is primarily influenced by the proximity of its neighboring elements. Consider a flat array where each short dipole is allocated a half-wavelength square area, Fig. 2.8. In this case, each dipole can be characterized by the radiation resistance given by Eq. (2.11). This expression is very similar to the radiation resistance of small dipole in free space except for a modification in the coefficient values. In this configuration, the antenna will radiate in both directions perpendicular to the plane of a flat array of dipoles. When $a = b = \lambda/2$, the radiation resistance of individual elements is given by,

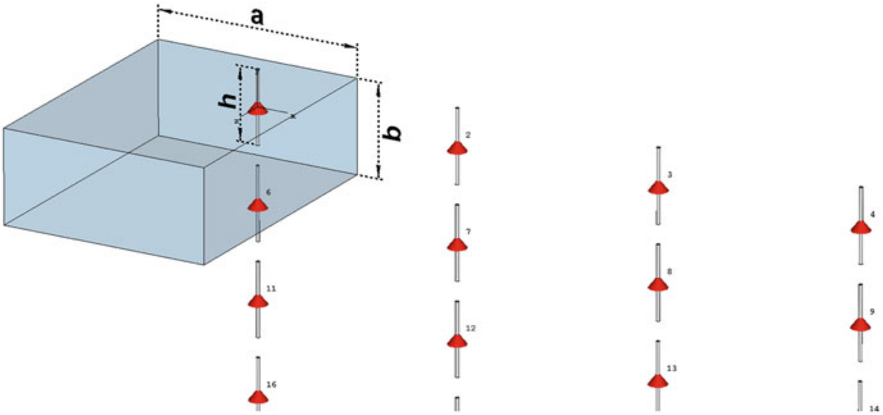

Fig. 2.6 Flat array of closely spaced dipoles with imaging waveguide unit cell shown in the top right-hand corner

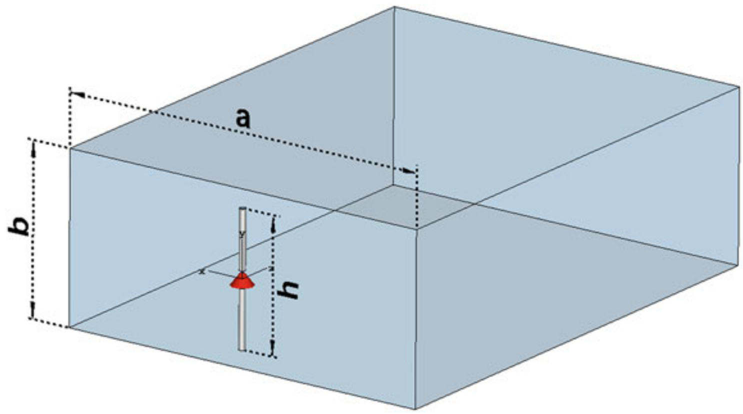

Fig. 2.7 Unit cell representing a dipole at the end of a hypothetical waveguide

$$R = \frac{60}{\pi}\left(\frac{h}{l}\right)^2 = 19.1\left(\frac{h}{l}\right)^2 \Omega \tag{2.11}$$

In the abovementioned case, the antenna can radiate power anywhere into lower and upper half-spaces. This is not desired in some cases and for such cases the antenna array can be made more preferentially directive by placing a reflector on one side of the array, Fig. 2.9, which forces the antenna to radiate in only one direction. Consider now a case where half-wave dipoles are placed in a flat array configuration and in front of a reflector. In this case, the radiation resistance of each antenna element is around 153 Ω.

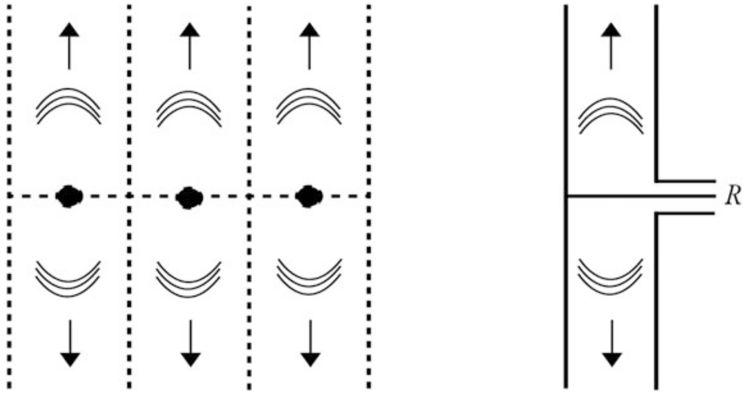

Fig. 2.8 Flat array of dipoles radiating into both lower and upper half spaces

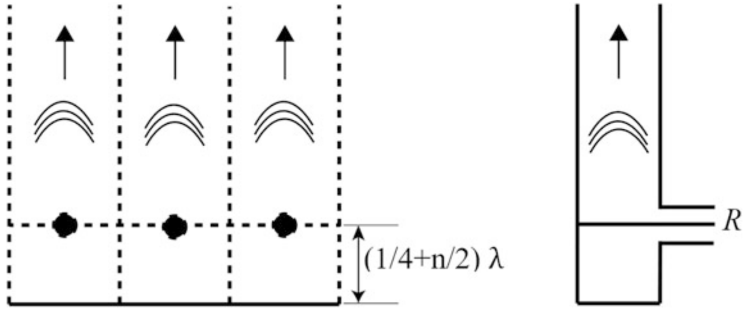

Fig. 2.9 Waveguide model for a planar array of dipoles backed by a perfect reflector

$$R = \frac{480}{\pi} = 152.8\ \Omega \tag{2.12}$$

Flat wideband antenna arrays of closely spaced radiating elements can be analyzed with good approximation with the help of this theory.

2.3 Wideband Antenna Types

Some different types of popular wideband antennas are summarized in this section. These can be designed based on the theoretical concepts as discussed in the previous section. Their geometrical and radiation characteristics will help the reader to understand their dimensional constraints and critical performance metrics.

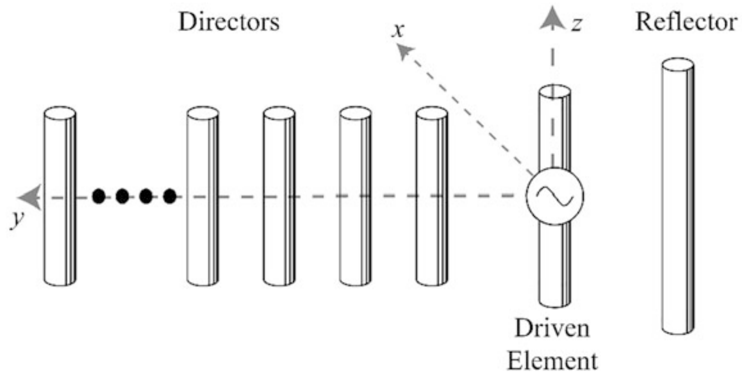

Fig. 2.10 Yagi-Uda array

2.3.1 Traveling Wave Antennas

2.3.1.1 Yagi-Uda Array

The Yagi-Uda antenna [19] is a highly popular antenna for use in the HF, VHF, and UHF frequency ranges. The basic construction of the Yagi-Uda array of linear dipoles is illustrated in Fig. 2.10. The arrangement consists of several linear dipoles, one of which called driven element is excited with the signal whereas the others behave as parasitic elements with induced currents due to mutual coupling between radiating elements. The parasitic elements placed in the main beam direction behave as directors and that on the opposite side serves as a reflector. The lengths of the directors are slightly smaller than the driven element which is smaller than the reflector and the length of the driven element is slightly less than $\lambda/2$. The spacing and length of the directors are not necessarily uniform.

The Yagi-Uda antenna has typically low input impedance which can be optimized by varying the dimensions of the antenna. Typical values of input impedance range from 12 to 62 Ω for a 15 element Yagi-Uda array for different values of reflector spacing [7]. A typical six element antenna can have directivity from 10 to 14 dBi [20] and a planar quasi-Yagi antenna can easily achieve impedance bandwidths of up to 48% [21].

2.3.1.2 Tapered Slot Antennas/Vivaldi Antennas

The tapered slot antenna is another type of traveling wave antenna in which surface waves are set up on a flared slotline on a conducting sheet [22]. A tapered slot antenna is capable of radiating an end-fire pattern over a wide bandwidth. A simple linear tapered slot antenna is shown in Fig. 2.11a. The antenna is excited from the bottom narrow slotline region, and radiation is observed as the wave propagates

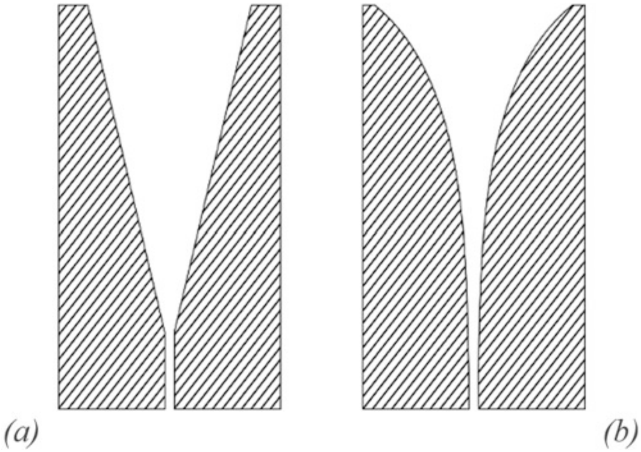

Fig. 2.11 (**a**) A linear tapered slot antenna and (**b**) Vivaldi antenna

across the tapered slot region towards the top of the structure. The antenna can be fed through a microstrip or coaxial transmission line. For waveguide applications, the tapered slot structure can be embedded inside the waveguide structure as a fin-line [23, 24].

Different variations of the tapered slot antenna can be used, such as *continuous width slot antenna* and exponentially tapered slot antenna, also called *Vivaldi antenna,* which was first proposed by Gibson in 1979 [22]. The energy is coupled to the narrow slot opening, where it is tightly bound to the surface. As the waves travel along the curved path length and the separation increases the wave becomes more coupled to the radiation fields and less to the surface. Theoretically, this type of structure can achieve infinite bandwidth, but in practice is limited by the feed at the narrow side, the slot opening at the wider side of the structure, maximum scan angle, and cross-polarization ratio in the planes other than the principal planes [23]. The radiated field has end-fire pattern and is almost the same for both the E and H planes.

2.3.1.3 Helical Antennas

Helical antennas are a type of traveling wave antennas and are realized by winding a conducting wire in the form of helix. A ground plane, that typically has a minimum diameter of ¾ wavelengths, is often used in most applications. In order to feed the Helical antenna, the conducting wire of the antenna is connected directly to the center conductor of the coaxial line while its outer conductor is connected to the ground plane of the antenna, as illustrated in Fig. 2.12. The pitch angle α of the antenna is defined by,

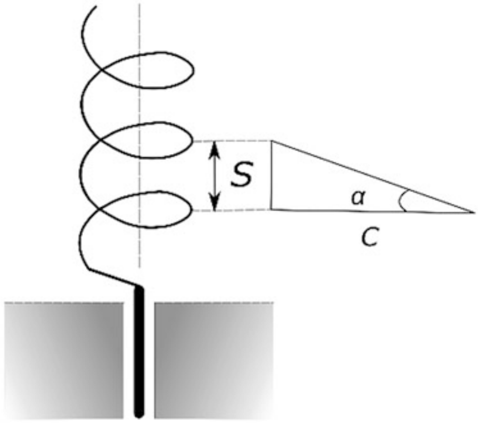

Fig. 2.12 Structure of a helical antenna with coaxial feeding

$$\alpha = \tan^{-1}\left(\frac{S}{C}\right) \tag{2.13}$$

where S is the spacing between adjacent turns and C is the circumference of the helix.

It can be observed that when $\alpha = 0°$ (and $S = 0$), the helix becomes a planar multi-loop antenna, polarization will become linear and will be oriented along the plane containing the loops. For $\alpha = 90°$ (and $C = 0$), the helix becomes a straight wire and the polarization will be linear and oriented along the length of the wire, which will be orthogonal to the previous case. The helical antenna formed when $0° < \alpha < 90°$ will in general radiate with elliptical polarization but can be tuned for circular or linear polarization as well. Other types of Helical antennas are Bifilar, Quadrifilar, and Multifilar helix antennas [25].

Helical antennas exhibit two basic modes of operation, the *Normal mode* and the *Axial mode*.

Normal Mode When the dimensions of the helix are small as compared to the wavelength, the antenna radiates similarly as a linear dipole with a maximum of its radiated field at the plane perpendicular to the axis of the helical structure, as shown in Fig. 2.13a. When the length of the helix is $\ll\lambda$ the helix can be analyzed as a combination of series connected short dipoles and small loops as shown in Fig. 2.13b. The current is therefore assumed to be uniform over the length of the structure. The radiation pattern will not depend on the number of turns therefore the radiation pattern can be derived by analyzing just a single turn. Polarization is dependent on the diameter of the helix and spacing between the turns. The bandwidth of operation in normal mode is very narrow and radiation efficiency is low, which limits its use in practical applications.

Axial Mode When the circumference of the helix is comparable to a wavelength first order transmission mode becomes significant, and if the dimensions of the

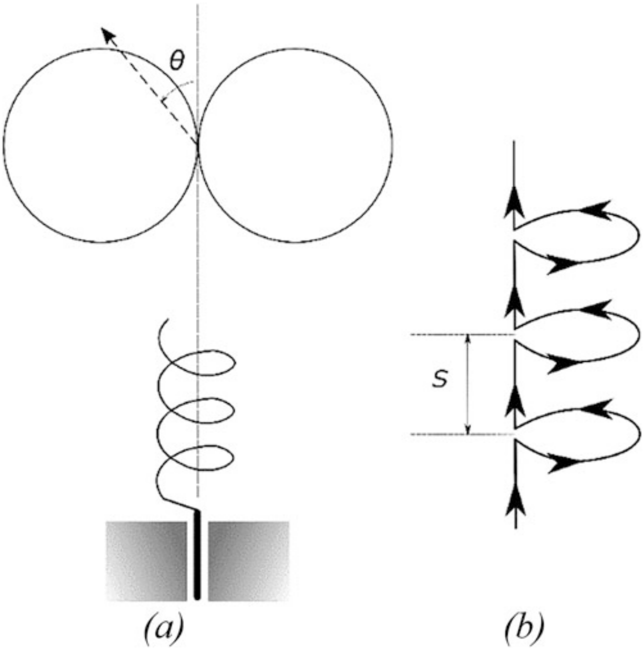

Fig. 2.13 (**a**) Radiation in normal mode and (**b**) its equivalent of connected short dipoles and small loops

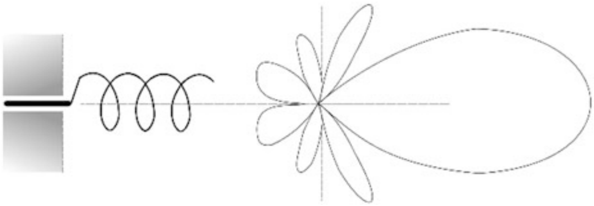

Fig. 2.14 Radiation in axial mode

helix are chosen properly the antenna will radiate in axial mode, as described in Fig. 2.14. This mode has the maximum radiation intensity along the axis of the helix. The antenna can be operated in circular polarization for a range of dimensions: $3\lambda/4 < C < 4\lambda/3$, $S \approx \lambda/4$, and $12° \leq \alpha \leq 14°$ [7] and the ground plane should be at least $\lambda/2$. In this mode of operation, the antenna has wider impedance bandwidth and greater efficiency. The input impedance of the helical antenna is given by,

$$R \simeq 140\left(\frac{C}{\lambda}\right) \tag{2.14}$$

2.3.2 *Frequency Independent Antennas*

Frequency independent antennas can be realized by exploiting the idea of self-scaling. These could be discrete, continuous, or log-periodically scaled structures. Ideally, these structures should extend infinitely to realize ideal frequency independent behavior; however, for practical applications a frequency independent structure must be truncated thereby limiting its bandwidth. It is commonly reported in the literature that it is possible to truncate the antenna with little impact on the radiation pattern. Some often used examples are now discussed.

2.3.2.1 Archimedean Spiral

The Archimedean spiral antenna consists of even number of arms wrapped around each other, as shown in Fig. 2.2. The structure is fed from the center which is the high-frequency region. The wrap rate is high at the center and decreases as the structure progresses outwards. The geometric structure of an Archimedean spiral antenna can be defined by a general formula,

$$r = r_{\mathrm{o}} + a\varphi \tag{2.15}$$

where r is the radial distance defined for angle φ, r_{o} is the initial radius, and a is the rate of wrapping of the arms. The structure can be analyzed by the principle of self-complementarity as explained in Sect. 2.2.2.2; therefore, theoretically a two arm spiral antenna will have an input impedance of around 188.5 Ω. The structure supports circular polarized radiation and the sense of polarization is decided by the direction of rotation of the arms. The structure is fed from the center with a balanced feed. The truncation or outer diameter decides the lower frequency limit whereas the inner spacing or the initial radius decides the upper frequency limit.

2.3.2.2 Equiangular Spiral Antennas

Equiangular spiral antenna is another type of self-scaling antenna which is completely defined by angles. Its structure is defined by (Fig. 2.15),

$$r = r_{\mathrm{o}} \mathrm{e}^{a\varphi} \tag{2.16}$$

This antenna can have two different realizations. One with arms of conducting sheets and the other with spiral slots. Theoretically, this structure will exhibit an impedance of 188.5 Ω, but practical implementation which requires spacing for feed and truncation at the outer extent will alter input impedance to around 164 Ω.

The antenna can be fed through a balanced transmission line and thus requires a balun. The design of the balun structures for this class of antenna can be challenging

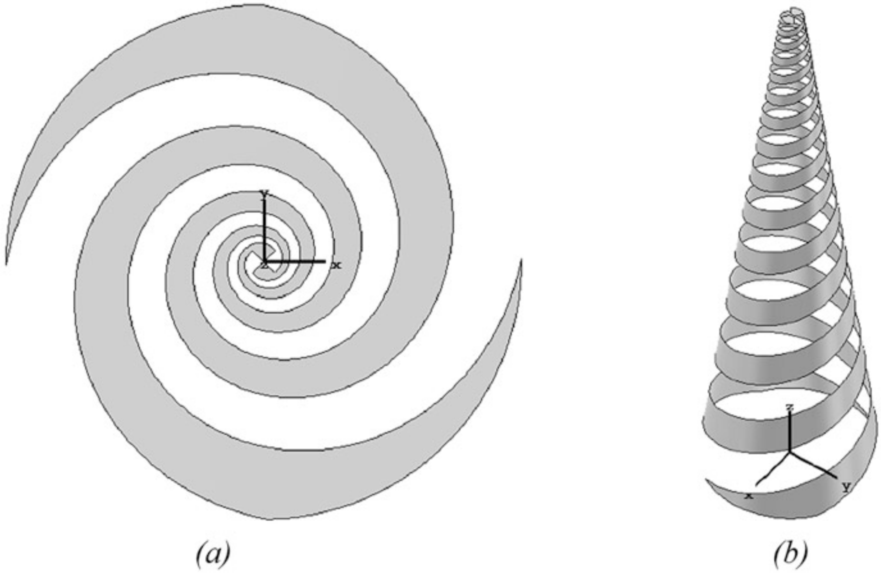

Fig. 2.15 (**a**) Equiangular spiral antenna and (**b**) conical spiral antenna

due to size and bandwidth requirements, see, for example, [26]. The slot spiral is more practical since it can be fed by an infinite balun which is implemented by an unbalanced transmission line and shielded by the ground plane of the slot antenna, as illustrated in Fig. 2.16. This is possible because of the rapid attenuation of the near fields on the arms. The need for a wider ground plane near the center of the antenna structure limits upper frequency limit. A dummy cable is often used on the opposite arm of the spiral to counter the asymmetry caused by smaller ground plane at the center, which if not used will cause a tilt in the radiation pattern. The outer radius defines the lower frequency limit whereas the upper frequency limit is governed by the feed spacing. The radiation patterns for planar spiral antennas are bidirectional. Where half-space operation is required a reflector or absorber is placed on one side of the structure [27]. The absorber preserves the wideband bandwidth operation with stable radiation patterns but will compromise the radiation efficiency, whereas the reflector ensures good radiation efficiency but a trade-off must be made on bandwidth and stable radiation characteristics. However, with the use of a reflector one can still achieve decent wideband performance by placing the radiating antenna at a ramping distance from the ground plane, this can be achieved either by tilting the antenna or the ground plane or by using stepped ground plane as proposed in [28].

Conical Spiral The spiral antenna can also be realized on a nonplanar surface to achieve unidirectional patterns without the constraint of using an absorber or reflector. An equiangular spiral can be placed on a conical surface as shown in Fig. 2.15b, in this case the maximum radiation occurs towards the vertex of the

Fig. 2.16 Infinite balun

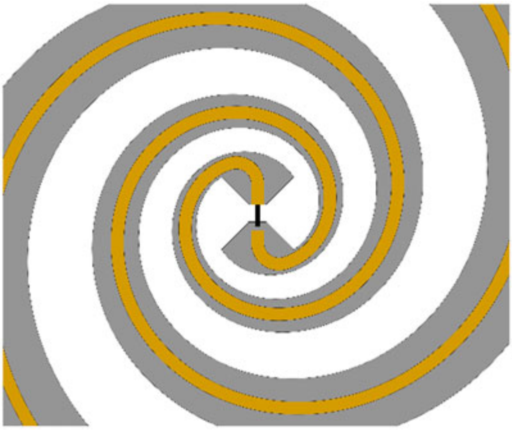

cone and along the axis of symmetry. Beamwidth can be optimized by varying the wrap angle of the spiral arms. The theoretical input impedance of the conical spiral antenna is lower than the planar spiral antennas. The input impedance decreases slowly with the decreasing cone angle [29] and typically varies from 120 to 164 Ω for cone angles from 10° to 90°. The input impedance can also be controlled by the arm width [30]. Self-scaling spiral antennas radiate circular polarization.

2.3.2.3 Log-Periodic Antennas

Planar Log-Periodic Antennas Log-periodic antennas are a class of self-scaling antennas suitable for linearly polarized radiation that scales at discrete intervals of wavelength [31]. The ripples in radiation characteristics and impedance caused by these discrete intervals can be smoothed out, over a useable frequency band, by using closely spaced scaling. A planar two arm log-periodic antenna is illustrated in Fig. 2.4. The logarithmically periodic antenna can be considered as a modification of an angular antenna. Logarithmically periodic structures can be obtained by using the following transformation [31],

$$z = \ln w \tag{2.17}$$

if, $w = \rho e^{j\theta}$, and $z = x + jy$, then,
$\rho = e^x$ or $x = \ln \rho, \theta = y$.

With the help of this transformation, circles and radial lines are transformed into vertical and horizontal lines, respectively from w to z plane.

Their radiation pattern is unidirectional and polarization is linear.

Log-periodic dipole antenna (LPDA) is an arrangement of dipoles connected by a crisscross feeding line [32]. It is a sequence of side-by-side connected dipoles, each oriented parallel to each other and logarithmically scaled in all dimensions.

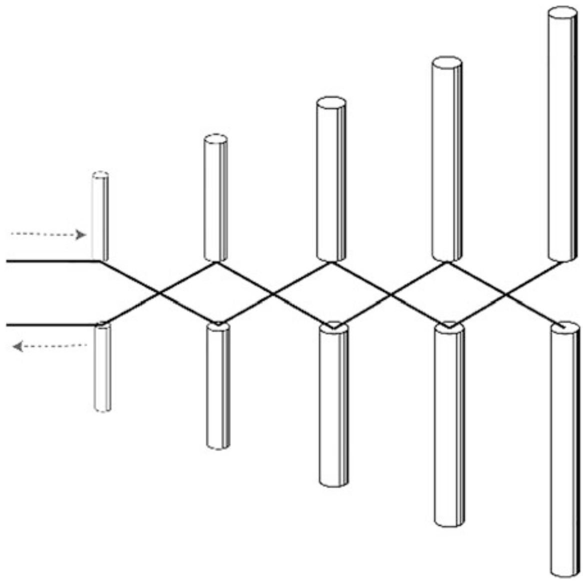

Fig. 2.17 Log-periodic dipole antenna

The scaling factor is defined in terms of geometric ratio τ. Due to the crisscross feeding arrangement, the antenna will radiate end-fire in the direction of the shorter elements. The truncation at both ends will limit the true frequency independent behavior however the LPDA can achieve significant large bandwidths.

The number of elements N is determined by,

$$N = 1 + \frac{\ln(B_S)}{\ln(1/\tau)} \tag{2.18}$$

where B_S is the designed bandwidth and τ is the geometric ratio. The average characteristic impedance Z_a of the nth element is given by,

$$Z_a = 120\left[\ln\left(\frac{l_n}{d_n}\right) - 2.25\right] \tag{2.19}$$

where l_n/d_n is the length to diameter ratio of the nth element. The center to center spacing between the feed is given by (Fig. 2.17),

$$s = d\cos h\left(\frac{Z_o}{120}\right) \tag{2.20}$$

The Eleven Antenna The Eleven Antenna can realize decade-wide bandwidths [33]. The antenna produces almost constant beamwidth and directivity over its frequency band of operation. However, the reported return loss is around 5 dB over the band. This antenna was proposed to be used as a feed for a large reflector antenna. It consists of two parallel dipoles half a wavelength apart, Fig. 2.18, yielding a directivity of 11 dB over decade bandwidth, and hence its name. The structure is log-periodic with backfire radiation pattern, as opposed to the LPDA which has end-fire pattern as previously discussed. The structure is differentially fed and capable of radiating in both orthogonal polarizations.

2.3.2.4 Sinuous Antenna

Dual polarized sinuous antenna was first proposed by Du Hamel in 1987 [34]. The sinuous antenna can be classified as a type of log-periodic antenna. The structure of the sinuous antenna is defined only by angles, as illustrated in Fig. 2.19. The antenna can be used for linear or circular polarized applications. The structure of the sinuous antenna is self-scaling which means it has theoretically infinite bandwidth. Truncation and feed spacing limit the bandwidth. The inner radius defines the upper frequency limit whereas the outer radius defines the lower frequency limit. The radiation pattern is bidirectional, in order to get a unidirectional pattern, the antenna is backed by a reflector or an absorber [34, 35]. The beam width and phase center

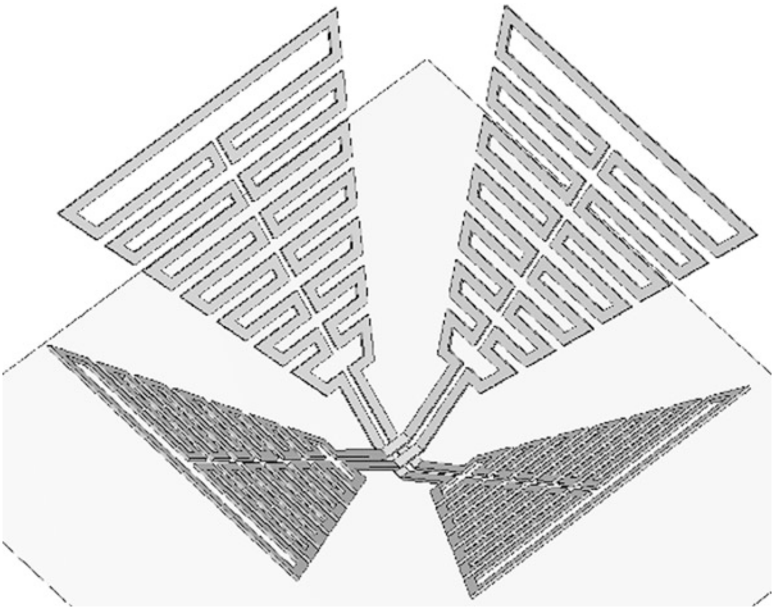

Fig. 2.18 An illustration of the Eleven Antenna

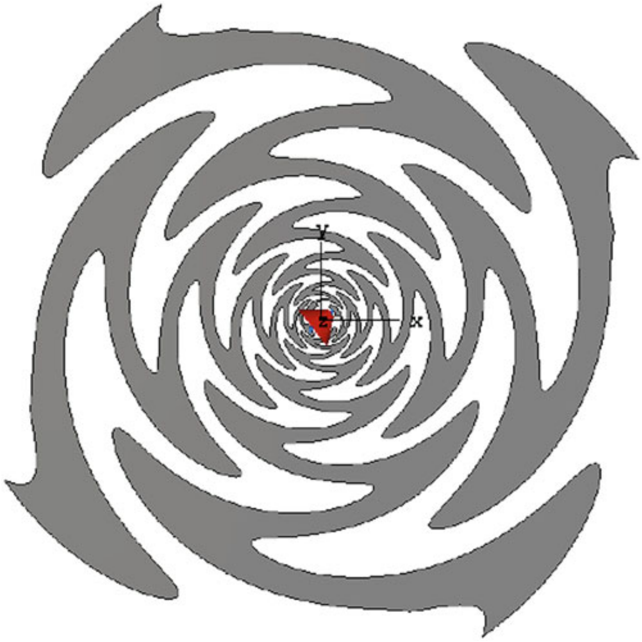

Fig. 2.19 A four arm sinuous antenna

remain constant over a wide frequency band. The input impedance of the sinuous structure in free space is given by,

$$Z_{\mathrm{m}} = \frac{60\pi}{\sin\frac{M\pi}{N}}\Omega \tag{2.21}$$

where M is the mode number and N is the number of arms

2.3.2.5 Tightly Coupled Antennas (TCA)

Tightly Coupled Array of Dipoles The concept of connected linear arrays of collinear radiating elements was first proposed by Baum [36] in 1970 and later studied in detail by Hansen [37]. It was demonstrated that this arrangement improves the wideband performance of the antenna system. The arrangement consists of a long wire with multiple feeds, making linear connected dipoles. It was observed that when the length of the dipoles are reduced from half-wavelength to about 0.1 wavelength the current along the array will become almost constant, thereby approximating Wheeler's current sheet [17]. With this arrangement, the impedance mismatch is more acceptable as compared to an array of dipoles that are not connected [38]. This type of antenna array requires differential feeding closely packed inside the unit cell. A tightly coupled dipole array with integrated balun was proposed in [39]. The antenna system achieved a bandwidth of 7.35:1 and was capable of radiating with dual polarization (Fig. 2.20).

Checkerboard Arrays Arrays of planar coupled elements can also be used in the form of checkerboard arrays. The structure proposed in [40, 41] consists of three layers sandwiched together. The top layer is a circuit board printed with pattern of square patches on a thin dielectric sheet, the middle layer is foam and the bottom layer is the ground plane. In Fig. 2.21, top view of a prototype of 5 × 4 element checkerboard array is shown, impedance bandwidths of 3:1 can be achieved [40].

The Planar Ultrawideband Modular Antenna (PUMA) Another type of antenna based on Munk's current sheet principle is the Planar Ultrawideband Antenna (PUMA) [42, 43]. The antenna offers possibility of scanning at wide scan angles and exhibiting low cross-polarization. This antenna has a unique feeding for tightly coupled dipole antennas. This antenna array can be implemented as modular tiles and does not require any external baluns, Fig. 2.22. The antenna can achieve dual polarization with a bandwidth of operation of up to 5:1.

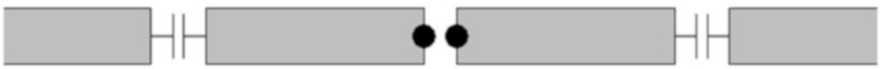

Fig. 2.20 Unit cell of a tightly coupled array of dipoles

Fig. 2.21 Checkerboard array

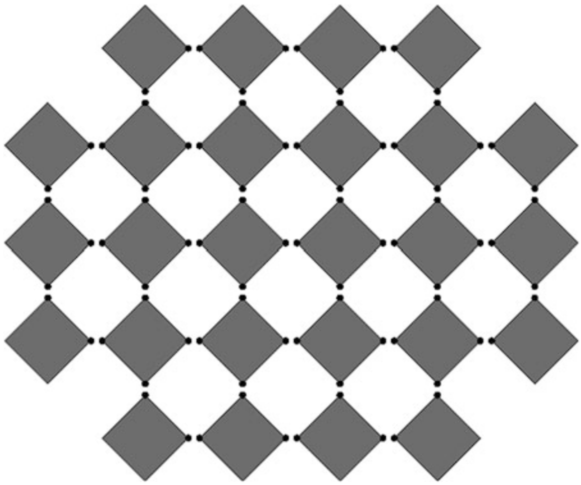

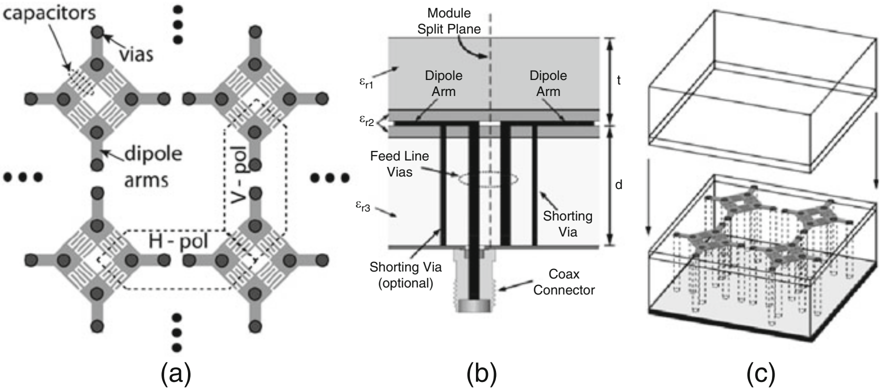

Fig. 2.22 The PUMA antenna [44]. (Source: S. S. Holland and M. N. Vouvakis, "The Planar Ultrawideband Modular Antenna (PUMA) Array," IEEE Transactions on Antennas and Propagation, vol. 60, no. 1, pp. 130–140, Jan. 2012)

2.3.3 Fractal Antennas

The geometry of the fractal antenna consists of multiple copies of its own unit structure with scaled dimensions and growing in a recursive manner. These antennas have advantage of achieving compact design and can address multiband or wideband applications [45]. The Fractal structure has inspired numerous antenna studies was introduced by Mandelbrot [46] and describes a family of shapes based on self-similarity of their geometrical features.

An example fractal antenna structure can be designed by starting with an equilateral triangle. Next a smaller rotated triangle, with its vertices on the midpoints of the side of the original triangle, is removed from the structure. This process can be continued as many times as desired. This resulting fractal structure is called Sierpinski gasket fractal, as shown in Fig. 2.23. In [47] a detailed account of the theory and design of fractal antennas has been presented.

2.3.4 Dielectric Resonator Antennas

By overlap tuning the resonant modes of the dielectric resonator antenna (DRA) one can achieve wideband operation [48, 49]. Single mode DRAs do not exhibit wide impedance bandwidth however they can be made wideband by employing different techniques such as optimizing their shape, placing conducting strips, combining with different radiators, and stacking multiple DRs of different shapes. Wide bandwidths of up to 1.94:1 are reported in the literature [50, 51]. Bandwidth as wide as 3:1 was achieved by using the hybrid DRA in [52].

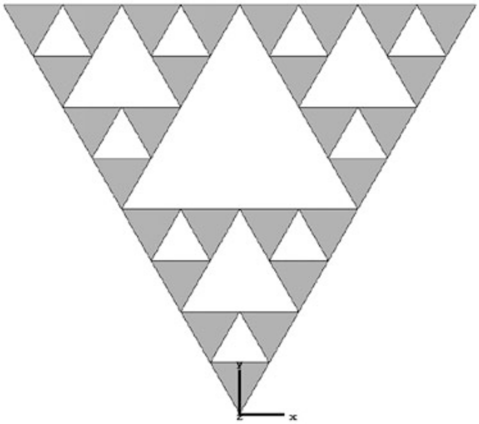

Fig. 2.23 Structure of Sierpinski gasket fractal

2.3.5 Summary of Antenna Types

The performance metrics of different wideband antennas are summarized in Table 2.1. This provides a brief overview of different aspects of antenna performance, which can help antenna designers to choose the best antenna type for their specific applications.

2.4 Fabrication Issues

The choice of fabrication technique used to realize any given of the antenna structures discussed has major implications for their practical performance characteristics. With increase in frequency, wavelength decreases and so does the dimensions of the structure. Antenna designs for frequencies up to microwave band can be implemented using standard PCB techniques on low loss substrates, for millimeter-wave antenna designs, thick film techniques using high-quality ceramic substrates are suitable, [57, 58], and for THz and beyond applications, thin film fabrication techniques [59, 60] are more reliable, fabrication of antennas based on carbon nanotubes are also being researched [44].

The choice of materials is critical in the design of wideband antennas. The intrinsic electrical material parameters from which they are constructed should not vary over the required bandwidth of operation. Consequently, high-performance dielectrics should be used as substrate materials, i.e., those with low loss tangent and low dielectric dispersion. This usually leads to an increase in cost, particularly if higher frequency operation is desired. Low temperature co-fired ceramics (LTCC) are often used for multilayer structures for antennas operating at millimeter-wave frequencies [61–63]. Glass substrates are also used especially for THz applications [64, 65].

Table 2.1 Summary of different antenna types

Antenna type	Input impedance (Ω)	Bandwidth	Form factor (typical values)	Modular design	Manufacturing effort
Yagi-Uda	~30–70	1.5:1 [53]2.18:1 [54]	$0.5\lambda \times 6\lambda$	Yes	Moderate
Tapered slot	~85 (slotline)	6:1, 10:1	$1.5\lambda_{low} \times 2\lambda_{low}$	Yes	Low
Helical	141 × Circumference/λ 105–186 (axial mode)	1.7:1	$0.5\lambda \times 0.5\lambda \times 2\lambda$	Yes	High
Spiral	~100	9:1 [35]>20:1 [26]	$0.3\lambda_{low} \times 0.3\lambda_{low}$	No	Low
Log periodic	Variable	3:1	$0.5\lambda_{low} \times 0.4\lambda_{low}$	Yes	Moderate
Sinuous	~133 (four arm)	9:1 [35]	$\sim 0.6\lambda_{low} \times 0.6\lambda_{low}$	No	Low
TCA	~100	7.35:1 [39]	$\sim 0.65\lambda_{low} \times 0.65\lambda_{low} \times 0.15\lambda_{low}$	Yes	Low
Fractal	50	1.22:1 (multiband over 16:1) [55]	$\sim 2\lambda_{low} \times 2\lambda_{low} \times 0.2\lambda_{low}$	No	Low
DRA	50 (slot coupled)	1.35:1 [51]	$\sim 0.38\lambda_{low} \times 0.33\lambda_{low} \times 0.1\lambda_{low}$	Yes	High

λ_{low} = lowest operating frequency
All the antennas reported here have bandwidth higher than 1.22:1. Fractional bandwidth for UWB systems is defined as 20% [56] or 1.22:1.

Most of the frequency independent antennas have bidirectional radiation characteristics, which are often not desired in practical applications. Conventional wideband antenna designs suggest bulky and nonplanar structures, this limits their use in certain environments particularly in volume critical applications. Wideband antennas often require a reflector on one side of the radiating structure, or they must be placed above a ground plane at some defined spacing. Different techniques are suggested to address this problem [26, 34, 42, 66]. However, this comes with a compromise in respect of the realizable impedance bandwidth and radiation characteristics of the wideband antenna. Reducing the dimensions and making a wideband antenna low profile is therefore a challenging task. Some antenna designs include a cavity backing the main radiator. This cavity can either be reflective or can be filled with absorbing material. Metamaterials can be used to reduce the profile of wideband antennas, as an example, a wideband antenna is proposed in [67] which is backed by a thin metamaterial absorber.

Differential feeding is another aspect, which is very common in wideband antennas, that introduces integration problems for antenna designers. Usually, a wideband balun is desired to connect antenna with the front-end electronics. The performance of the balun can critically limit the performance of the antenna [39]. Also, the integration of the balun may make the antenna nonplanar and often requires including the functionality of impedance transformation. Examples where the balun is directly incorporated within the antenna design are given in [42, 43].

2.5 Measurement Issues

Wideband antennas can be characterized for their performance by using either far-field or near-field techniques. Since the antenna is required to be measured over a very wide range of frequencies, the electrical dimensions of the antenna under test (AUT) can become impractical to be used in the same setup for all frequencies. The minimum far-field distance is related by the dimensions of the AUT and frequency of operation, as given by Eq. (2.22).

$$r_o \geq \frac{2D^2}{\lambda} \tag{2.22}$$

where D is the maximum dimension of the antenna aperture and λ is the free space wavelength. Compact antenna test ranges (CATR) may address the requirement of very large antenna test range [68]. Far-field (FF) characteristics can also be obtained by acquiring near-field (NF) data from planar, cylindrical, or spherical scanning and then performing NF to FF transformation [68, 69]. In this case, measurement parameters over the wide frequency range are critical for data accuracy. The instrumentation requires calibration of wideband transmitters and receivers over a wide frequency of operation. A comprehensive account of antenna test procedures is given in [68].

Measuring gain over wide frequency is also very critical in analyzing the performance of wideband antenna. This may require the availability of different standard gain antennas. Measurement of polarization is also important as this may not remain the same over the whole frequency band of operation. It is to be noted that the wideband antennas show useful performance up to certain scan angles [39]. However, for some wideband antennas, with the change in frequency the main beam rotates which can lead to a change in beamwidth about the azimuth axis. Having knowledge of these effects prior to measurement activity and proper planning can save precious time, sometimes this can often be acquired during the computer simulation design phase for the antenna.

2.6 Applications

2.6.1 Communications

The exponential growth of interest in the Internet of Things (IoT) [70–75] and associated systems infrastructure suggests that multiband and wideband wireless systems will need to come to the fore. Such systems are likely only be possible with efficient wideband antennas. Novel future generation communication technologies require multi-standard Device to Device communications through wireless channels for emerging applications such as Connected Autonomous Vehicles (CAV), Smart Homes, Smart Cities, Industry 4.0, Virtual Reality (VR), and Augmented Reality (AR). One candidate for such applications is ultrawideband (UWB) technology [76–80] for short distance communications and precision location. UWB technology is now being widely adopted by wireless industry as it provides precision ranging or localization for portable indoor devices, and naturally requires wideband antenna radiating elements.

2.6.2 Imaging

Microwave, Millimeter-wave, and Terahertz frequencies are used for electromagnetic imaging applications [5, 81–83]. These can broadly be characterized into (1) Passive and (2) Active imaging. In passive imaging, the detection process, by means of a radiometer, relies on natural external illumination of the target, e.g., microwave radiation scattered by the earth. Passive microwave imaging finds its applications in remote sensing and security and surveillance. Radio telescopes are used for passive imaging of celestial objects. Extremely wideband antennas are used to study Cosmic Microwave Background [60, 84].

Active microwave imaging uses the principle of radar by transmitting the radio signal and measuring the characteristics of the echo signal with respect to the transmitter reference. Coherent detection processes mean that aperture synthesis techniques can be used to increase image resolution [85, 86]. Automotive radars, synthetic aperture radars (SAR), ground penetrating radar (GPR), non-destructive testing (NDT), and medical imaging devices use active imaging techniques and tend to work best when multispectral imaging, using wideband antennas, is deployed [83].

2.6.3 Electromagnetic Characterization of Materials

Microwaves can be used to measure the electrical properties of materials [87–89]. These include solids, liquids, metals, composite materials, and engineered metamaterials [90, 91]. Further applications include characterization of biological tissue samples, analysis of food quality, and quality control [88, 89]. In all of these applications, the ability to characterize over a wide frequency band is extremely useful.

2.7 Future Directions

New generation wireless technologies such as 5G promises data rates in Gbps range which is only possible with a sufficient wideband system [57]. For systems applications deploying the IoT (Internet of Things) the use of smart and intelligent sensors at scale which can operate across multiple standards will most likely require wideband antennas within the broader system infrastructure [70–75]. Wideband antenna arrays can be used within Large Intelligent Surfaces, [92–94], which is an emergent enabling technology for 6G communications systems [92].

The fabrication of complex nonplanar wideband antennas will become more practical with additive manufacturing technologies such as 3D printing [95]. Here antennas can be directly formed through a 3D printing process using metal, dielectric, or combination of both. Additive manufacturing will reduce the cost significantly for low- and medium-volume production as compared to the conventional fabrication processes. For higher frequency applications, Millimeter-wave through Terahertz, the use of novel semiconductor materials and glass substrates provide feasible substrate materials that can be directly printed using high precision lithography [57].

2.8 Conclusion

This chapter provides a brief overview of the theoretical concepts required for understanding some of the most common types of wideband antennas. Different types of traveling wave and frequency independent antennas were discussed and key reference information provided to allow the reader to further determine their feasibility for specific applications. This chapter also provided a short account of fabrication and measurement challenges associated with wideband antenna systems.

With the introduction of new bandwidth intensive technologies, wideband antenna systems will undoubtedly be in greater demand finding new applications and requiring new form factors. Here technologies such as 3D printing will enable antenna designers to realize complex antenna structure which was once unthinkable to fabricate.

References

1. W.D. Jones, Keeping cars from crashing. IEEE Spectrum **38**(9), 40–45 (2001). https://doi.org/10.1109/6.946636
2. W. Menzel, A. Moebius, Antenna concepts for millimeter-wave automotive radar sensors. Proc. IEEE **100**(7), 2372–2379 (2012). https://doi.org/10.1109/JPROC.2012.2184729
3. K. Abboud, H.A. Omar, W. Zhuang, Interworking of DSRC and cellular network technologies for V2X communications: A survey. IEEE Trans. Vehic. Technol. **65**(12), 9457–9470 (2016). https://doi.org/10.1109/TVT.2016.2591558
4. S. Chen et al., Vehicle-to-everything (v2x) services supported by LTE-based systems and 5G. IEEE Commun. Stand. Mag. **1**(2), 70–76 (2017). https://doi.org/10.1109/MCOMSTD.2017.1700015
5. D.M. Sheen, D.L. McMakin, T.E. Hall, Three-dimensional millimeter-wave imaging for concealed weapon detection. IEEE Trans. Microw. Theory Tech. **49**(9), 1581–1592 (2001). https://doi.org/10.1109/22.942570
6. H.H. Beverage, C.W. Rice, E.W. Kellogg, The wave antenna a new type of highly directive antenna. Trans. Am. Inst. Electric. Eng. **XLII**, 215–266 (1923). https://doi.org/10.1109/T-AIEE.1923.5060870
7. C.A. Balanis, *Antenna Theory: Analysis and Design* (John Wiley & Sons, Hoboken, NJ, 2012)
8. R.C. Johnson, H. Jasik, *Antenna Engineering Handbook* (McGraw-Hill Book Company, New York, 1984)
9. D.R. Jackson, C. Caloz, T. Itoh, Leaky-wave antennas. Proc. IEEE **100**(7), 2194–2206 (2012). https://doi.org/10.1109/JPROC.2012.2187410
10. V. Rumsey, Frequency independent antennas, in *1958 IRE International Convention Record*, (IEEE, New York, 1957), pp. 114–118. https://doi.org/10.1109/IRECON.1957.1150565
11. Y. Mushiake, Self-complementary antennas. IEEE Antennas Propag. Mag. **34**(6), 23–29 (1992). https://doi.org/10.1109/74.180638
12. Y. Mushiake, A report on Japanese development of antennas: From the Yagi-Uda antenna to self-complementary antennas. IEEE Antennas Propag. Mag. **46**(4), 47–60 (2004). https://doi.org/10.1109/MAP.2004.1373999
13. G.A. Deschamps, Impedance properties of complementary multiterminal planar structures. IRE Trans. Antennas Propag. **AP-7**(Special Supplement), S371 (1959)
14. M. Born, E. Wolf, A. Bhatia, *Principles of Optics: Electromagnetic Theory of Propagation, Interference and Diffraction of Light* (Cambridge University Press, Cambridge, 1999)
15. B.A. Munk, Broadband wire arrays, in *Finite Antenna Arrays and FSS*, ed. by B. A. Munk, (Wiley, New York, 2005). https://doi.org/10.1002/0471457531.ch6
16. B. Munk et al., A low-profile broadband phased array antenna, in *IEEE Antennas and Propagation Society International Symposium*. Digest. Held in conjunction with: USNC/CNC/URSI North American Radio Sci. Meeting (Cat. No.03CH37450), Columbus, OH, vol. 2, (2003), pp. 448–451. https://doi.org/10.1109/APS.2003.1219272

17. H.A. Wheeler, The radiation resistance of an antenna in an infinite array or waveguide. Proc. IRE **36**(4), 478–487 (1948). https://doi.org/10.1109/JRPROC.1948.229650
18. H. Wheeler, Simple relations derived from a phased-array antenna made of an infinite current sheet. IEEE Trans. Antennas Propag. **13**(4), 506–514 (1965)
19. H. Yagi, Beam transmission of ultra short waves. Proc. Inst. Radio Eng. **16**(6), 715–740 (1928). https://doi.org/10.1109/JRPROC.1928.221464
20. D. Cheng, C. Chen, Optimum element spacings for Yagi-Uda arrays. IEEE Trans. Antennas Propag. **21**(5), 615–623 (1973). https://doi.org/10.1109/TAP.1973.1140551
21. Q. Yongxi, W.R. Deal, N. Kaneda, T. Itoh, A uniplanar quasi-Yagi antenna with wide bandwidth and low mutual coupling characteristics, in *IEEE Antennas and Propagation Society International Symposium. 1999 Digest*. Held in conjunction with: USNC/URSI National Radio Science Meeting (Cat. No.99CH37010), Orlando, FL, vol. 2, (1999), pp. 924–927. https://doi.org/10.1109/APS.1999.789463
22. P.J. Gibson, The Vivaldi Aerial, in *1979 9th European Microwave Conference, Brighton, UK*, (1979), pp. 101–105. https://doi.org/10.1109/EUMA.1979.332681
23. J. Shin, D.H. Schaubert, A parameter study of stripline-fed Vivaldi notch-antenna arrays. IEEE Trans. Antennas Propag. **47**(5), 879–886 (1999). https://doi.org/10.1109/8.774151
24. A. Beyer, B. Roth, Development of millimeter wave antennas in slotline technique for integrated communication systems, in *International Symposium on Antennas and Propagation Society, Merging Technologies for the 90's, Dallas, TX, USA*, vol. 4, (1990), pp. 1918–1921. https://doi.org/10.1109/APS.1990.115510
25. A. Adams, R. Greenough, R. Wallenberg, A. Mendelovicz, C. Lumjiak, The quadrifilar helix antenna. IEEE Trans. Antennas Propag. **22**(2), 173–178 (1974). https://doi.org/10.1109/TAP.1974.1140755
26. J. Dyson, The equiangular spiral antenna. IRE Trans. Antennas Propag. **7**(2), 181–187 (1959). https://doi.org/10.1109/TAP.1959.1144653
27. J.L. Volakis, M.W. Nurnberger, D.S. Filipovic, Slot spiral antenna. IEEE Antennas Propag. Mag. **43**(6), 15–26 (2001). https://doi.org/10.1109/74.979491
28. P.H. Rao, M. Sreenivasan, L. Naragani, Dual band planar spiral feed backed by a stepped ground plane cavity for satellite boresight reference antenna applications. IEEE Trans. Antennas Propag. **57**(12), 3752–3756 (2009). https://doi.org/10.1109/TAP.2009.2023880
29. J. Dyson, The unidirectional equiangular spiral antenna. IRE Trans. Antennas Propag. **7**(4), 329–334 (1959). https://doi.org/10.1109/TAP.1959.1144707
30. J. Dyson, The characteristics and design of the conical log-spiral antenna. IEEE Trans. Antennas Propag. **13**(4), 488–499 (1965). https://doi.org/10.1109/TAP.1965.1138471
31. R. DuHamel, D. Isbell, Broadband logarithmically periodic antenna structures, in *1958 IRE International Convention Record*, (IEEE, New York, 1957), pp. 119–128. https://doi.org/10.1109/IRECON.1957.1150566
32. D. Isbell, Log periodic dipole arrays. IRE Trans. Antennas Propag. **8**(3), 260–267 (1960). https://doi.org/10.1109/TAP.1960.1144848
33. R. Olsson, P. Kildal, S. Weinreb, The eleven antenna: A compact low-profile decade bandwidth dual polarized feed for reflector antennas. IEEE Trans. Antennas Propag. **54**(2), 368–375 (2006). https://doi.org/10.1109/TAP.2005.863392
34. R.H. DuHamel, Dual polarized sinuous antennas, US4658262A, 1987
35. V.K. Tripp, J.J.H. Wang, The sinuous microstrip antenna, in *Antennas and Propagation Society Symposium 1991 Digest, London, Ontario, Canada*, vol. 1, (1991), pp. 52–55. https://doi.org/10.1109/APS.1991.174771
36. C.E. Baum et al., Transient arrays, in *Ultra-Wideband, Short-Pulse Electromagnetics*, ed. by C. E. Baum et al., vol. 3, (Plenum, New York, 1997), pp. 129–138
37. R. Hansen, Linear connected arrays [coupled dipole arrays]. IEEE Antennas Wireless Propag. Lett. **3**, 154–156 (2004). https://doi.org/10.1109/LAWP.2004.832125
38. I. Tzanidis, Ultrawideband Low-Profile Arrays of Tightly Coupled Antenna Elements: Excitation, Termination and Feeding Methods, Ph.D. Dissertation, The Ohio State University, 2011, http://rave.ohiolink.edu/etdc/view?acc_num=osu1316439948

39. J.P. Doane, K. Sertel, J.L. Volakis, A wideband, wide scanning tightly coupled dipole array with integrated Balun (TCDA-IB). IEEE Trans. Antennas Propag. **61**(9), 4538–4548 (2013). https://doi.org/10.1109/TAP.2013.2267199
40. D.R. DeBoer et al., Australian SKA Pathfinder: A high-dynamic range wide-field of view survey telescope. Proc. IEEE **97**(8), 1507–1521 (2009). https://doi.org/10.1109/JPROC.2009.2016516
41. S.G. Hay et al., Focal plane array development for ASKAP (Australian SKA Pathfinder), in *The Second European Conference on Antennas and Propagation, EuCAP 2007, Edinburgh*, (2007), pp. 1–5. https://doi.org/10.1049/ic.2007.0899
42. S.S. Holland, M.N. Vouvakis, The planar ultrawideband modular antenna (PUMA) array. IEEE Trans. Antennas Propag. **60**(1), 130–140 (2012). https://doi.org/10.1109/TAP.2011.2167916
43. S.S. Holland, D.H. Schaubert, M.N. Vouvakis, A 7–21 GHz dual-polarized planar ultrawideband modular antenna (PUMA) array. IEEE Trans. Antennas Propag. **60**(10), 4589–4600 (2012). https://doi.org/10.1109/TAP.2012.2207321
44. Y. He, Y. Chen, L. Zhang, S. Wong, Z.N. Chen, An overview of terahertz antennas. China Commun. **17**(7), 124–165 (2020). https://doi.org/10.23919/J.CC.2020.07.011
45. D.H. Werner, S. Ganguly, An overview of fractal antenna engineering research. IEEE Antennas Propag. Mag. **45**(1), 38–57 (2003). https://doi.org/10.1109/MAP.2003.1189650
46. B.B. Mandelbrot, *The Fractal Geometry of Nature* (W. H. Freeman, New York, 1983)
47. D.H. Werner, R.L. Haupt, P.L. Werner, Fractal antenna engineering: The theory and design of fractal antenna arrays. IEEE Antennas Propag. Mag. **41**(5), 37–58 (1999). https://doi.org/10.1109/74.801513
48. A.A. Kishk, Y. Yin, A.W. Glisson, Conical dielectric resonator antennas for wide-band applications. IEEE Trans. Antennas Propag. **50**(4), 469–474 (2002). https://doi.org/10.1109/TAP.2002.1003382
49. T. Chang, J. Kiang, Bandwidth broadening of dielectric resonator antenna by merging adjacent bands. IEEE Trans. Antennas Propag. **57**(10), 3316–3320 (2009). https://doi.org/10.1109/TAP.2009.2029372
50. A. Rashidian, L. Shafai, D.M. Klymyshyn, Compact wideband multimode dielectric resonator antennas fed with parallel standing strips. IEEE Trans. Antennas Propag. **60**(11), 5021–5031 (2012). https://doi.org/10.1109/TAP.2012.2210018
51. S. Dhar, R. Ghatak, B. Gupta, D.R. Poddar, A wideband Minkowski fractal dielectric resonator antenna. IEEE Trans. Antennas Propag. **61**(6), 2895–2903 (2013). https://doi.org/10.1109/TAP.2013.2251596
52. M. Lapierre, Y.M.M. Antar, A. Ittipiboon, A. Petosa, Ultra wideband monopole/dielectric resonator antenna. IEEE Microw. Wireless Compon. Lett. **15**(1), 7–9 (2005). https://doi.org/10.1109/LMWC.2004.840952
53. L.C. Kretly, A.S. Ribeiro, A novel tilted dipole quasi-Yagi antenna designed for 3G and Bluetooth applications, in *Proceedings of the 2003 SBMO/IEEE MTT-S International Microwave and Optoelectronics Conference - IMOC 2003. (Cat. No.03TH8678)*, vol. 1, (2003), pp. 303–306. https://doi.org/10.1109/IMOC.2003.1244875
54. H. Chu, Y.-X. Guo, H. Wong, X. Shi, Wideband self-complementary Quasi-Yagi antenna for millimeter-wave systems. IEEE Antennas Wirel. Propag. Lett. **10**, 322–325 (2011). https://doi.org/10.1109/LAWP.2011.2142171
55. C. Puente-Baliarda, J. Romeu, R. Pous, A. Cardama, On the behavior of the Sierpinski multiband fractal antenna. IEEE Trans. Antennas Propag. **46**(4), 517–524 (Apr. 1998). https://doi.org/10.1109/8.664115
56. ETSI technical report on short range devices using ultra-wide band, Part 3: Worldwide UWB regulations between 3.1 and 10.6 GHz, ETSI TR 103 181-3 V2.1.1 (2019-01). [Online]
57. W. Hong, Solving the 5G mobile antenna puzzle: Assessing future directions for the 5G mobile antenna paradigm shift. IEEE Microw. Mag. **18**(7), 86–102 (2017). https://doi.org/10.1109/MMM.2017.2740538
58. A.C. Bunea, D. Neculoiu, Experimental characterization of a 94 GHz LTCC 1×4 microstrip patch antenna array, in *2015 Asia-Pacific Microwave Conference (APMC), Nanjing*, (2015), pp. 1–3. https://doi.org/10.1109/APMC.2015.7413209

59. S. Pan, L. Gilreath, P. Heydari, F. Capolino, Investigation of a wideband BiCMOS fully on-chip W-band bowtie slot antenna. IEEE Antennas Wirel. Propag. Lett. **12**, 706–709 (2013). https://doi.org/10.1109/LAWP.2013.2264538
60. A. Suzuki et al., Commercialization of micro-fabrication of antenna-coupled transition edge sensor bolometer detectors for studies of the cosmic microwave background. J. Low Temp. Phys. **193**(5–6), 744–751 (2018). https://doi.org/10.1007/s10909-018-1903-6
61. C. Liu, Y. Guo, X. Bao, S. Xiao, 60-GHz LTCC integrated circularly polarized helical antenna array. IEEE Trans. Antennas Propag. **60**(3), 1329–1335 (2012). https://doi.org/10.1109/TAP.2011.2180351
62. W. Liu, Z.N. Chen, X. Qing, 60-GHz thin broadband high-gain LTCC metamaterial-mushroom antenna array. IEEE Trans. Antennas Propag. **62**(9), 4592–4601 (2014). https://doi.org/10.1109/TAP.2014.2333052
63. I.K. Kim et al., Linear tapered cavity-backed slot antenna for millimeter-wave LTCC modules. IEEE Antennas Wirel. Propag. Lett. **5**, 175–178 (2006). https://doi.org/10.1109/LAWP.2006.874069
64. N. Ranjkesh, A. Taeb, N. Ghafarian, S. Gigoyan, M.A. Basha, S. Safavi-Naeini, Millimeter-wave suspended silicon-on-glass tapered antenna with dual-mode operation. IEEE Trans. Antennas Propag. **63**(12), 5363–5371 (2015). https://doi.org/10.1109/TAP.2015.2493164
65. A. Taeb, N. Ranjkesh, S. Gigoyan, G. Rafi, S. Safavi-Naeini, A millimeter-wave dielectric resonator antenna based on Silicon-On-Glass (SOG) technology, in *2016 17th International Symposium on Antenna Technology and Applied Electromagnetics (ANTEM), Montreal, QC*, (2016), pp. 1–2. https://doi.org/10.1109/ANTEM.2016.7550193
66. A. Chippendale, J. O'Sullivan, J. Reynolds, R. Gough, D. Hayman, S. Hay, Phased array feed testing for astronomy with ASKAP, in *2010 IEEE International Symposium on Phased Array Systems and Technology, Waltham, MA*, (2010), pp. 648–652. https://doi.org/10.1109/ARRAY.2010.5613298
67. U. Naeem, V. Fusco, D. Zelenchuk, R. Cahill, Low profile absorber backed extremely wideband antennas, in *2020 14th European Conference on Antennas and Propagation (EuCAP), Copenhagen, Denmark*, (2020), pp. 1–4. https://doi.org/10.23919/EuCAP48036.2020.9136050
68. IEEE Standard Test Procedures for Antennas, in *ANSI/IEEE Std 149-1979* (1979), pp. 0_1. https://doi.org/10.1109/IEEESTD.1979.120310
69. Y. Rahmat-Samii, V. Galindo-Israel, R. Mittra, A plane-polar approach for far-field construction from near-field measurements. IEEE Trans. Antennas Propag. **28**(2), 216–230 (1980). https://doi.org/10.1109/TAP.1980.1142316
70. L. Chettri, R. Bera, A comprehensive survey on Internet of things (IoT) toward 5G wireless systems. IEEE Internet Things J. **7**(1), 16–32 (2020). https://doi.org/10.1109/JIOT.2019.2948888
71. A. Al-Fuqaha, M. Guizani, M. Mohammadi, M. Aledhari, M. Ayyash, Internet of things: A survey on enabling technologies, protocols, and applications. IEEE Commun. Surv. Tutorials **17**(4), 2347–2376 (2015). https://doi.org/10.1109/COMST.2015.2444095
72. A. Zanella, N. Bui, A. Castellani, L. Vangelista, M. Zorzi, Internet of things for smart cities. IEEE Internet Things J. **1**(1), 22–32 (Feb. 2014). https://doi.org/10.1109/JIOT.2014.2306328
73. L.D. Xu, W. He, S. Li, Internet of things in industries: A survey. IEEE Trans. Ind. Informatics **10**(4), 2233–2243 (2014). https://doi.org/10.1109/TII.2014.2300753
74. S.M.R. Islam, D. Kwak, M.H. Kabir, M. Hossain, K. Kwak, The internet of things for health care: A comprehensive survey. IEEE Access **3**, 678–708 (2015). https://doi.org/10.1109/ACCESS.2015.2437951
75. M.R. Palattella et al., Internet of things in the 5G era: Enablers, architecture, and business models. IEEE J. Selected Areas Commun. **34**(3), 510–527 (2016). https://doi.org/10.1109/JSAC.2016.2525418
76. N. Patwari, J.N. Ash, S. Kyperountas, A.O. Hero, R.L. Moses, N.S. Correal, Locating the nodes: Cooperative localization in wireless sensor networks. IEEE Signal Process. Mag. **22**(4), 54–69 (2005). https://doi.org/10.1109/MSP.2005.1458287
77. M.Z. Win, R.A. Scholtz, Ultra-wide bandwidth time-hopping spread-spectrum impulse radio for wireless multiple-access communications. IEEE Trans. Commun. **48**(4), 679–689 (2000). https://doi.org/10.1109/26.843135

78. D. Porcino, W. Hirt, Ultra-wideband radio technology: Potential and challenges ahead. IEEE Commun. Mag. **41**(7), 66–74 (2003). https://doi.org/10.1109/MCOM.2003.1215641
79. G.R. Aiello, G.D. Rogerson, Ultra-wideband wireless systems. IEEE Microw. Mag. **4**(2), 36–47 (2003). https://doi.org/10.1109/MMW.2003.1201597
80. F. Zafari, A. Gkelias, K.K. Leung, A survey of indoor localization systems and technologies. IEEE Commun. Surv. Tutorials **21**(3), 2568–2599 (2019). https://doi.org/10.1109/COMST.2019.2911558
81. G. Tricoles, N.H. Farhat, Microwave holography: Applications and techniques. Proc. IEEE **65**(1), 108–121 (1977). https://doi.org/10.1109/PROC.1977.10435
82. P.M. Meaney, K.D. Paulsen, J.T. Chang, M.W. Fanning, A. Hartov, Nonactive antenna compensation for fixed-array microwave imaging. II. Imaging results. IEEE Trans. Med. Imaging **18**(6), 508–518 (1999). https://doi.org/10.1109/42.781016
83. Q.H. Liu et al., Active microwave imaging. I. 2-D forward and inverse scattering methods. IEEE Trans. Microw. Theory Tech. **50**(1), 123–133 (2002). https://doi.org/10.1109/22.981256
84. S. Walker et al., Demonstration of 220/280 GHz multichroic feedhorn-coupled TES polarimeter. J. Low Temp. Phys. **199**(3–4), 891–897 (2020). https://doi.org/10.1007/s10909-019-02316-1
85. P.A. Rosen et al., Synthetic aperture radar interferometry. Proc. IEEE **88**(3), 333–382 (2000). https://doi.org/10.1109/5.838084
86. N.H. Farhat, Principles of broad-band coherent imaging. J. Opt. Soc. Am. **67**, 1015–1021 (1977)
87. D.C. Thompson, O. Tantot, H. Jallageas, G.E. Ponchak, M.M. Tentzeris, J. Papapolymerou, Characterization of liquid crystal polymer (LCP) material and transmission lines on LCP substrates from 30 to 110 GHz. IEEE Trans. Microw. Theory Tech. **52**(4), 1343–1352 (2004). https://doi.org/10.1109/TMTT.2004.825738
88. H. Choi et al., Design and in vitro interference test of microwave noninvasive blood glucose monitoring sensor. IEEE Trans. Microw. Theory Tech. **63**(10), 3016–3025 (2015). https://doi.org/10.1109/TMTT.2015.2472019
89. P.I. Deffenbaugh, R.C. Rumpf, K.H. Church, Broadband microwave frequency characterization of 3-D printed materials. IEEE Trans. Compon. Packag. Manuf. Technol. **3**(12), 2147–2155 (2013). https://doi.org/10.1109/TCPMT.2013.2273306
90. W.E. Courtney, Analysis and evaluation of a method of measuring the complex permittivity and permeability microwave insulators. IEEE Trans. Microw. Theory Tech. **18**(8), 476–485 (1970). https://doi.org/10.1109/TMTT.1970.1127271
91. J. Baker-Jarvis, M.D. Janezic, B.F. Riddle, R.T. Johnk, P. Kabos, C.L. Holloway, et al., *Measuring the Permittivity and Permeability of Lossy Materials: Solids Liquids Metals Building Materials and Negative-Index Materials* (NIST Tech, Boulder, 2005)
92. W. Saad, M. Bennis, M. Chen, A vision of 6G wireless systems: Applications, trends, technologies, and open research problems. IEEE Netw. **34**(3), 134–142 (2020). https://doi.org/10.1109/MNET.001.1900287
93. Q. Wu, R. Zhang, Intelligent reflecting surface enhanced wireless network via joint active and passive beamforming. IEEE Trans. Wirel. Commun. **18**(11), 5394–5409 (2019). https://doi.org/10.1109/TWC.2019.2936025
94. E. Basar, M. Di Renzo, J. De Rosny, M. Debbah, M. Alouini, R. Zhang, Wireless communications through reconfigurable intelligent surfaces. IEEE Access **7**, 116753–116773 (2019). https://doi.org/10.1109/ACCESS.2019.2935192
95. B. Zhang, Y. Guo, H. Zirath, Y.P. Zhang, Investigation on 3-D-printing technologies for millimeter-wave and terahertz applications. Proc. IEEE **105**(4), 723–736 (2017). https://doi.org/10.1109/JPROC.2016.2639520

Umair Naeem received the B.E. degree in electrical engineering from the NED University of Engineering and Technology, Karachi, Pakistan, in 2005. He received Master's and Ph.D. degrees both in high-frequency electronics and optoelectronics from the University of Limoges, Limoges, France, in 2007 and 2010, respectively.

He is currently working as Principal Engineer at Centre for Wireless Innovation, ECIT Institute, Queen's University Belfast, Belfast, UK. Prior to that, he has served both in industry and in academia. He was head of the Transceivers (LEO satellites) division at SUPARCO, the space agency of Pakistan. He also worked as Assistant Professor at COMSATS University, Islamabad, Pakistan.

He has authored and coauthored over 40 articles in top-tier scientific journals and conferences. He is providing editorial service and serving as a reviewer for several scientific journals. His research interests include; synthesis of microwave and millimeter-wave components and circuits, multifunctional RF front ends, antennas, and electromagnetic bandgap structures.

Vincent Fusco established, at scale, internationally recognized research in microwave and millimeter-wave circuits and antenna systems. He holds the Queen's University of Belfast personal chair in High Frequency Electronics and is director of research for EEECS. He is an influential microwave engineer recognized by academe and industry across the world.

He is internationally recognized for his pioneering work in the area of active antennas used in mobile wireless systems. Fusco's 650 peer-reviewed publications are the bedrock of much of the microwave technology that is an integral part of today's wireless communications systems. He has published two well-regarded textbooks, translated into three languages, and has a strong patent portfolio, and has obtained grant research income from EPSRC, EU, and Industry.

He is a Fellow of the Royal Academy of Engineering, Member of the Royal Irish Academy, Fellow of the IEEE, Fellow of the IET, and Fellow of the Irish Academy of Engineers. In 2012, he was awarded the IET Mountbatten Medal and in 2019 the Royal Irish Academy medal for Engineering Science.

He was a founding member, and currently CTO, of the Institute for Electronics, Communications and Information Technology ECIT at Queen's University which now employs 235 people.

Chapter 3
Printed UWB Antennas: Design and Principle

Javad Nourinia, Changiz Ghobadi, and Bahman Mohammadi

3.1 Introduction

Ultra-wideband (UWB) communications are characterized by a bandwidth of 7.5 GHz from 3.1 to 10.6 GHz with a low emission power level under −41.3 dBm/MHz for propagation short pulse with minimum distortion [1]. Consequently, a suitable printed antenna with wide impedance bandwidth, compact size, and desired radiation characteristics over the entire operating band plays a critical role in UWB systems [2]. Various shapes of radiating printed elements, such as elliptical, circular, hexagonal, square, and rectangular, have been developed to provide wide impedance bandwidth [3]. Figure 3.1 shows four typical printed UWB antennas with simple geometry, reasonable bandwidths, and compact size. One of the conventional printed UWB antennas, shown in Fig. 3.1a, is a monopole antenna with a microstrip feed line which yields good omnidirectional radiation patterns. Printed antennas with coplanar waveguide (CPW) feed lines are more preferred because of their easier integration with surface components, lower radiation loss, and less sensitivity to thickness of substrate [4]. Recently, printed UWB slot antennas include a wide aperture radiator and a feeding line within the slot with very wide impedance bandwidth, low profile, stable omnidirectional pattern, and low near-field coupling with nearby objects have been investigated [5].

J. Nourinia (✉) · C. Ghobadi · B. Mohammadi
Northwest Antenna and Microwave Research Laboratory (NAMRL) and Department of Electrical Engineering, Urmia University, Urmia, Iran
e-mail: j.nourinia@urmia.ac.ir; ch.ghobadi@urmia.ac.ir; b.mohammadi@urmia.ac.ir

M. A. Matin (ed.), *Wideband, Multiband, and Smart Antenna Systems*, Signals and Communication Technology, https://doi.org/10.1007/978-3-030-74311-6_3

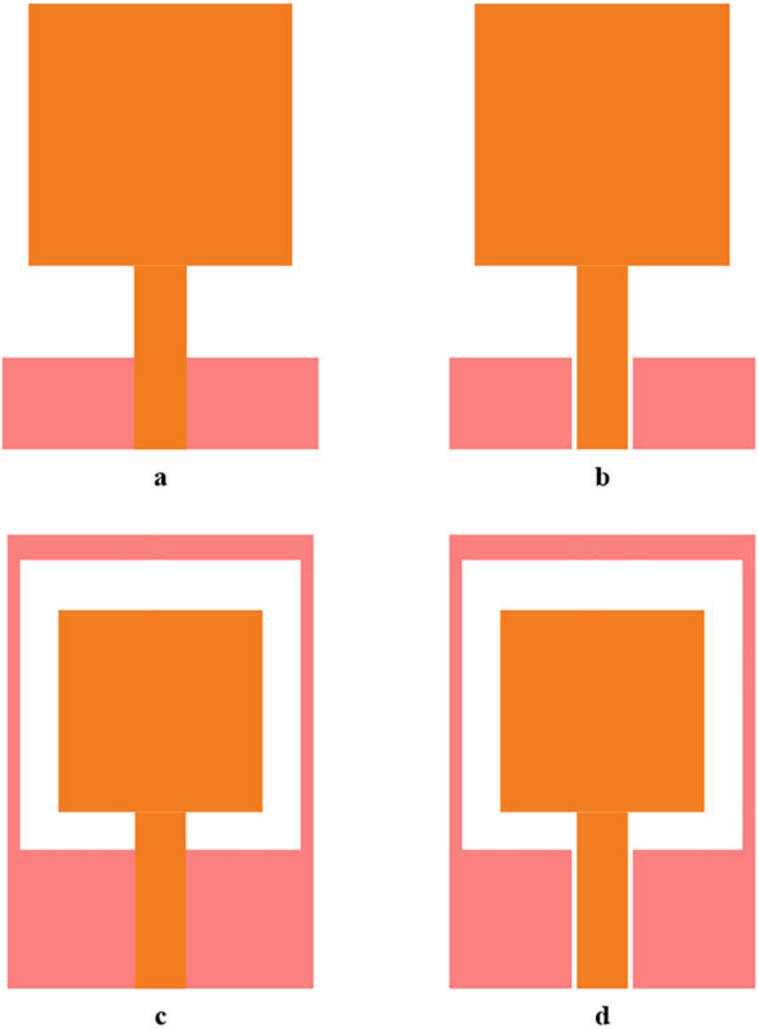

Fig. 3.1 Monopole antenna with (**a**) microstrip-fed, (**b**) CPW-fed; Slot antenna with (**c**) microstrip-fed, (**d**) CPW-fed

3.2 Bandwidth Enhancement of UWB Antennas

To improve the impedance bandwidth of printed antennas, different geometries of stubs, slits, or slots in the feed line, ground plane, and radiating patch have been introduced, significantly enhances the antenna performance [6]. In [7], a printed UWB monopole antenna is presented consists of a simple step-shaped radiation patch and truncated ground plane structure. The total antenna area is

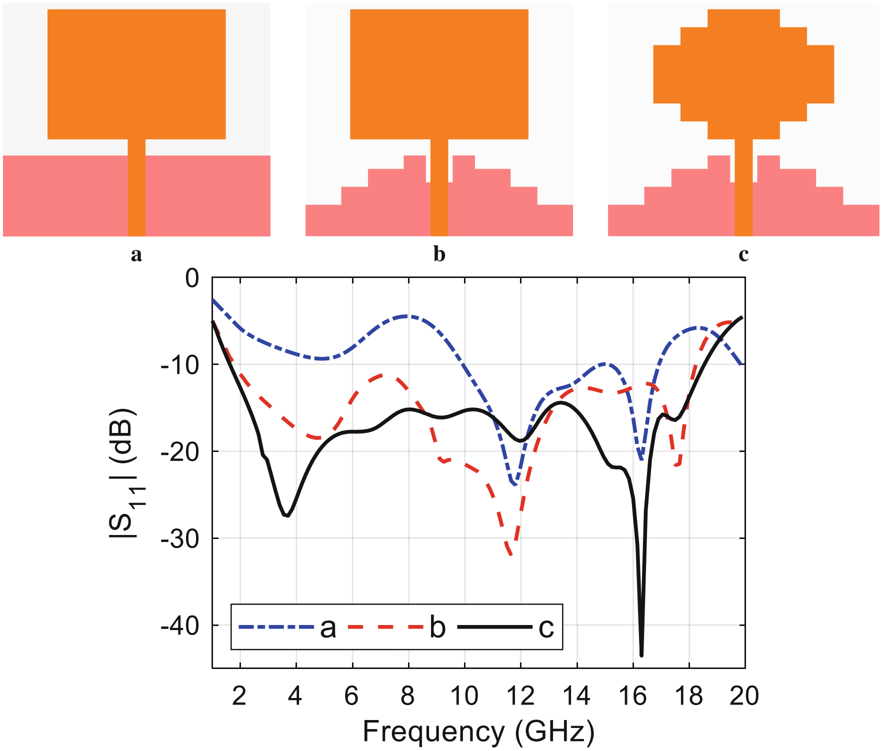

Fig. 3.2 Antenna design procedure and simulated $|S_{11}|$ [7]

30 mm × 26 mm that is etched on a low-cost FR4 substrate with a height of 1.6 mm, $\varepsilon_r = 4.4$, and $\tan\delta = 0.02$. The antenna is excited with a 50 Ω microstrip feeding line with a width of 2 mm and a length of 10.5 mm. All simulation data are achieved by HFSS. The final values of the antenna parameters are obtained by a parametric study so that each time a parameter changes and the other parameters are fixed.

Figure 3.2 illustrates the design procedure and simulated $|S_{11}|$. The basic antenna design (*a* in Fig. 3.2) consists of a 50 Ω microstrip feeding line, a truncated rectangular ground plane, and a rectangular radiating patch. Case *a* has a −10 dB $|S_{11}|$ bandwidth for 10–16.9 GHz. By inserting steps on the ground plane proportionately, *b* in Fig. 3.2, the bandwidth is broadened and enhanced from 1.6 to 18.25 GHz. This is because the stepped ground plane increases the electrical length, acts as a matching transforms, and leads to a capacitive loading, which negates the inductive reactance of the radiating patch to approach an approximately real resistive input impedance. The steps in the ground plane improve the impedance matching and effects on the lower edge frequency. Finally, by forming the radiating patch, *c* in Fig. 3.2, impedance matching extended from 1.6 to 18.55 GHz. This is because adding the steps at the radiating patch perturb the current distributions, smooth changing from one resonance to another, create additional surface paths, and excite more resonances. Therefore, broader impedance matching is obtained, especially at the upper frequency edge.

Figure 3.3 shows the simulated current distributions at 4, 12, and 16 GHz. In Fig. 3.3a at 4 GHz, the current is intensified on the edges of the ground plane. This distribution indicates that forming the edges of the ground plane affects the lower frequency band. With the frequency increasing at 12 GHz in Fig. 3.3b, the currents are concentrated on the stepped rectangular patch, and hence the antenna matching changes at this band due to the patch resonances. Figure 3.3c shows the current surface is more robust on the sides of the radiating patch at 16 GHz. It is concluded the embedding of steps on the radiating patch extends the upper frequency band. Figure 3.4 shows the simulated normalized radiation patterns at 4 and 8 GHz. It is observed which the antenna presents an acceptable omnidirectional radiation characteristic received singles from all directions.

In [8], a multi-resonance compact printed CPW-fed UWB slot antenna with an excellent omnidirectional radiation pattern at the whole operating band is presented. This antenna is composed of a ground plane with a T-shaped slit and a radiating patch with an inverted T-shaped slot that gives a wide bandwidth from 2.55 to 15 GHz. This compact slot antenna is fed with a 50 Ω CPW feeding line with a width of 2 mm and a gap of 0.15 mm. The total antenna size is 30 mm $\times$ 30 mm which is printed on a low-cost FR4 substrate with a thickness of 1.6 mm, $\varepsilon_r = 4.4$, and tan$\delta = 0.02$. Figure 3.5 shows the antenna design steps and simulated $|S_{11}|$. The basic antenna design, *a* in Fig. 3.5, consists of a rectangular slot and a square radiating patch that can give the fundamental and third resonance frequencies at 2.86 and 9.23 GHz, respectively. By etching a T-shaped slit matching element in the ground plane, *b* in Fig. 3.5, the second resonance frequency is excited at 6.63 GHz and the lower frequency matching is improved. Finally, by embedding an inverted T-shaped slot on the radiating patch, *c* in Fig. 3.5, an additional fourth resonance at 13.7 GHz is excited and improves the impedance matching and bandwidth, especially at the upper frequencies.

This antenna has stable good omnidirectional radiation patterns even at upper frequency band. This is because this antenna has a modified fork-shaped feeding configuration which restricts the excitation of horizontal current components and assures that only the dominant uniform vertical current components are presented in the structure. Therefore, an enhancement in the impedance matching and polarization properties are observed. Figure 3.6 shows the simulated radiation pattern at 3 and 10 GHz. It can be observed that the radiation characteristics are nearly omnidirectional for both frequencies. Figure 3.7 shows the simulated current surfaces at 3, 7, and 10 GHz. This distribution indicated that at 3, 7, and 10 GHz the current surface is stronger in the rectangular slot, T-shaped slit in the ground plane, and edges of the square radiating patch, respectively. Hence, the antenna impedance matching varies at these frequencies.

Figure 3.8 illustrates examples of antenna bandwidth enhancement with different commonly defected structures. In [9], Fig. 3.8a, a monopole antenna with a bandwidth from 3.12 to 12.73 GHz includes a truncated rectangular ground plane, a square radiating patch with a modified T-shaped slit in the ground plane, and

Fig. 3.3 Simulated current distributions at: (**a**) 4 GHz, (**b**) 12 GHz, (**c**) 16 GHz

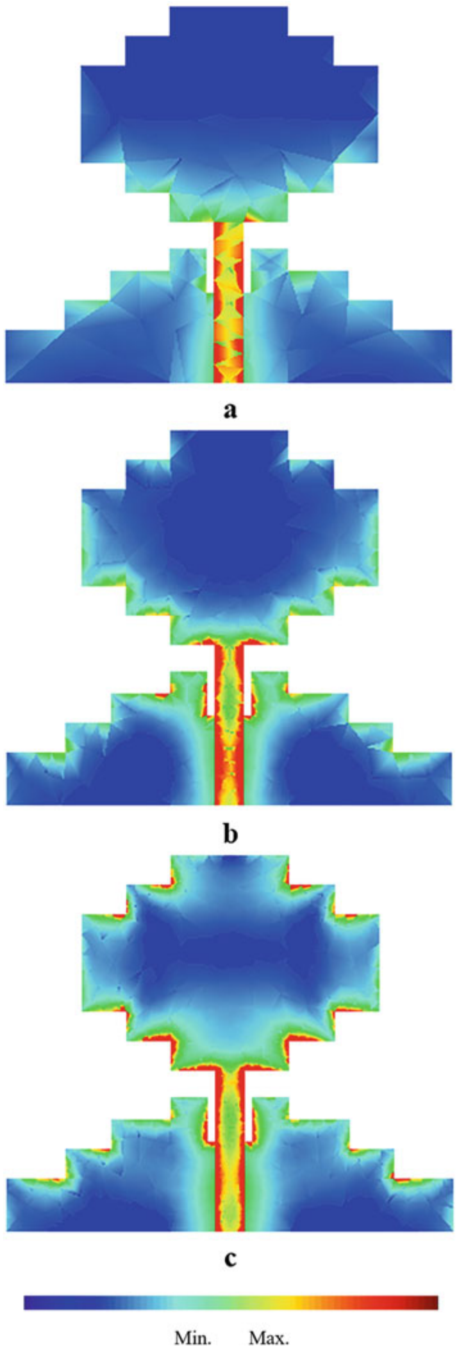

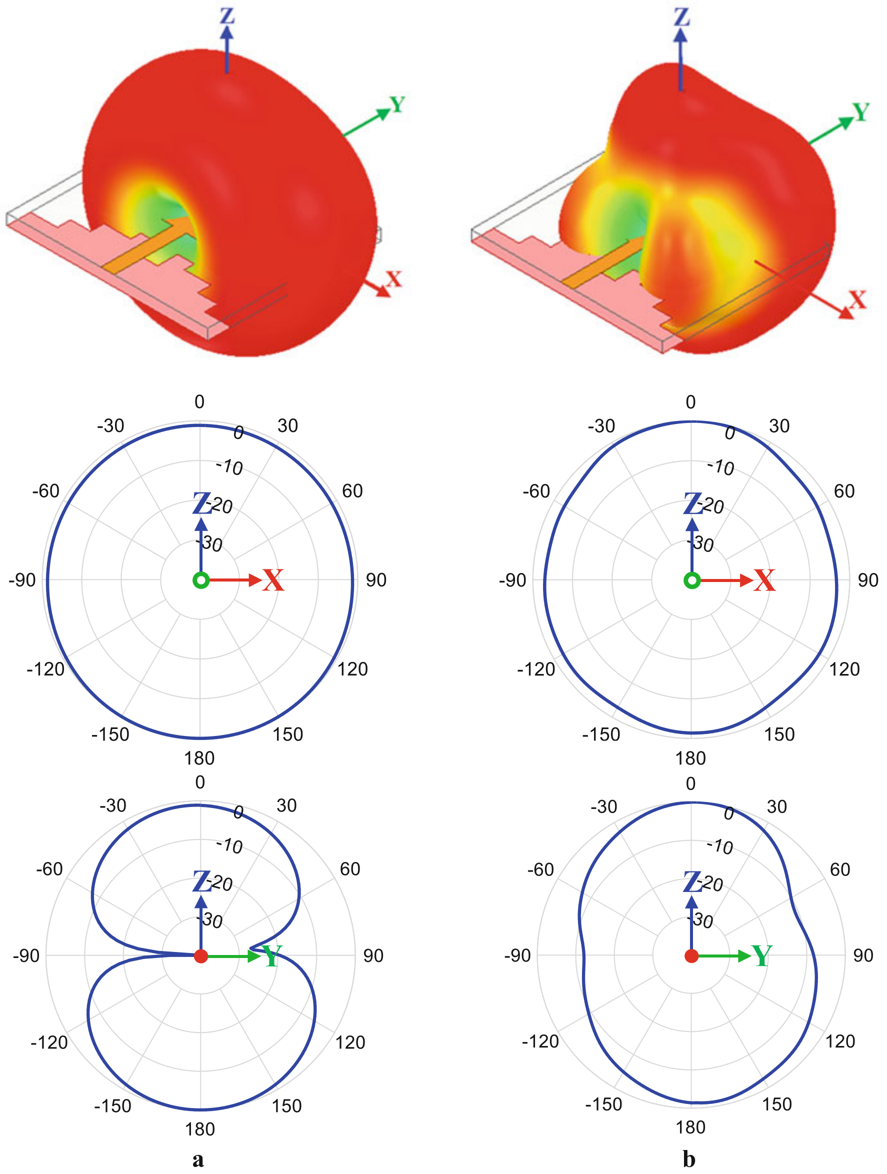

Fig. 3.4 Simulated radiation patterns at: (**a**) 4 GHz, (**b**) 8 GHz

two rectangular slots in the radiating patch are presented. In [10], Fig. 3.8b, a UWB monopole antenna with a small size of 12 mm × 18 mm and a fractional bandwidth of more than 133% consists of a checkered-shaped semi-fractal defect on the square radiating patch and two mirror L-shaped defects in the rectangular

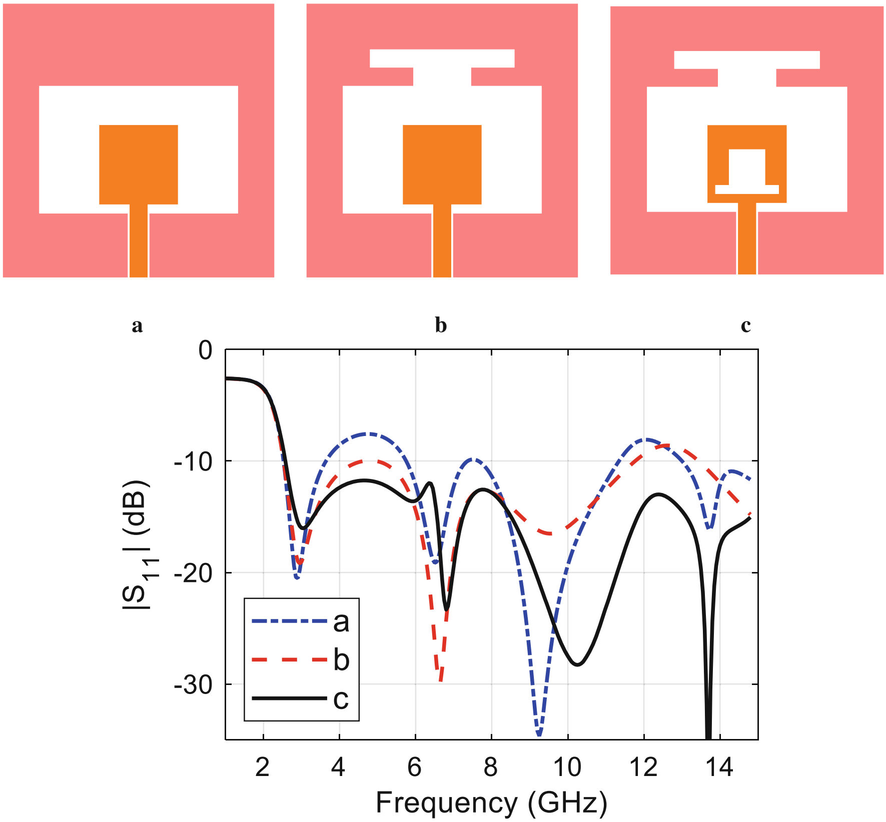

Fig. 3.5 Antenna design steps and simulated $|S_{11}|$ [8]

ground plane are introduced. In [11], Fig. 3.8c, using self-complementary structures and Babinet's equivalence principle, a small UWB monopole antenna includes a radiating patch and a ground plane with a sleeve and a slot structure in the stepped form is designed. In [12], Fig. 3.8d, a UWB monopole antenna with an inverted trapezoid radiation patch with smooth taper transition between the patch and the feedline and a truncated ground plane with two-step staircase defects for impedance matching and bandwidth enhancement is proposed.

To enhance the characteristics of printed antennas, another method is based on the use of parasitic elements that have been proposed [14]. These parasitic elements can be embedded in the radiating patch or ground plane to improve the antenna performance. However, some of these parasitic elements increase the antenna size. In other designs, the parasitic element is embedded on the opposite side of the substrate, increasing the fabrication cost and complexity. In [13], a UWB circle-like slot antenna with stable omnidirectional patterns and a very wideband from 2.7 to 19.5 GHz (151%) is presented. The antenna is composed of a circle-like slot and

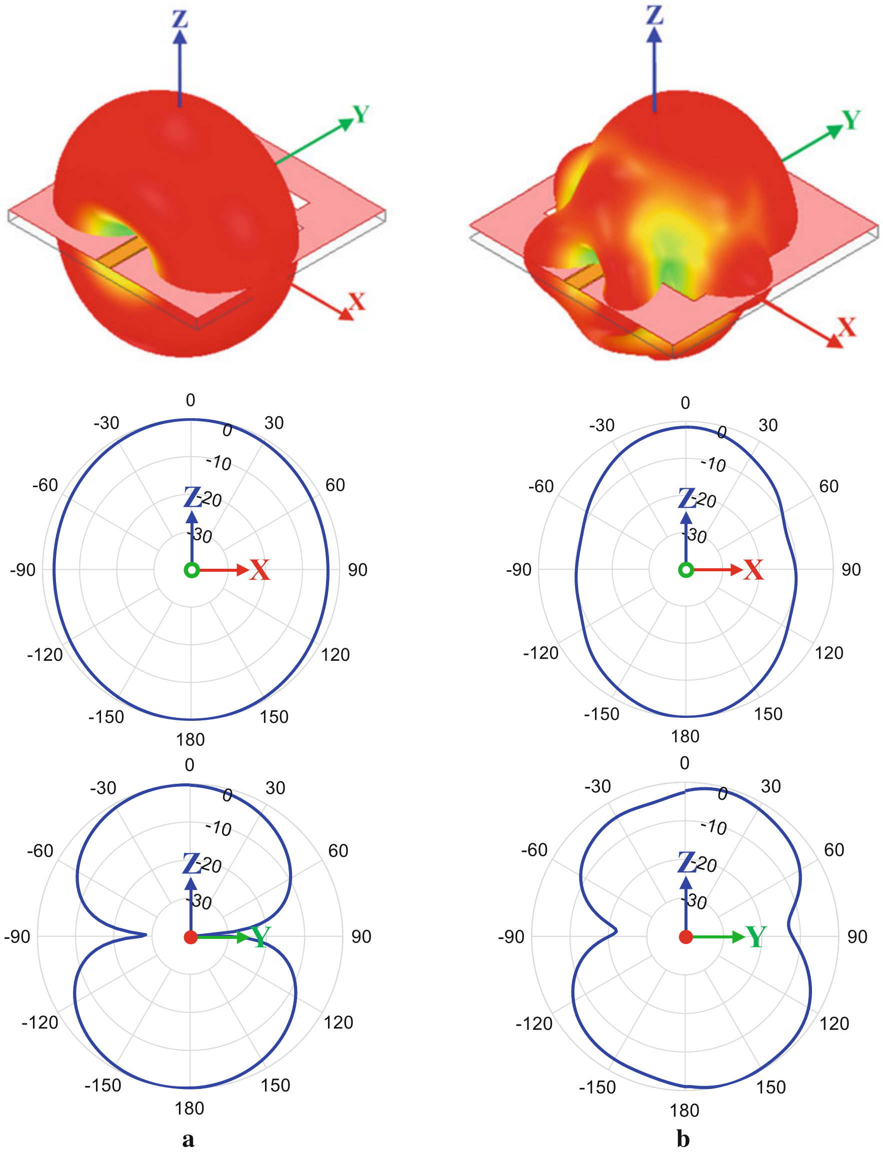

Fig. 3.6 Simulated radiation patterns at: (**a**) 3 GHz and (**b**) 10 GHz

a rectangular radiating patch. The antenna size is 26 mm × 30 mm printed on a low-cost FR4 substrate with a height of 1.6 mm, $\varepsilon_r = 4.4$, and tan$\delta = 0.0.2$. This compact antenna is fed with a 50 Ω CPW feeding line with a width of 2.6 mm and a gap of 0.3 mm. The circle-like aperture with a radius of 12.5 mm reduces the slot area and satisfies the impedance matching, especially at lower frequencies. As illustrated in

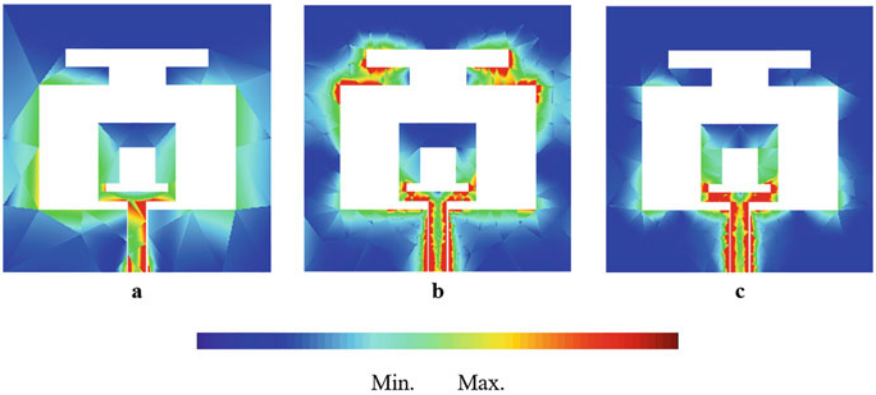

Fig. 3.7 Simulated current distributions at: (**a**) 3 GHz, (**b**) 7 GHz, (**c**) 10 GHz

Fig. 3.9, embedding a pair of L-shaped tuning stubs on the back layer of the substrate connected to the radiating patch by four via connections, enhances the impedance bandwidth. This due to the increase of vertical current flows in the radiating patch and much uniform distribution of magnetic currents in the slot through the L-shaped tuning stubs.

Figure 3.10 shows examples of antenna bandwidth enhancement with different parasitic elements. In [15], Fig. 3.10a, bandwidth enhancement is achieved by new additional resonant modes of two embedded shorted rectangular quarter-wavelength resonators near the feed line at the top edge of the ground plane. In [16], Fig. 3.10b, a UWB monopole antenna with a small size of 23 mm $\times$ 26.5 mm, a relatively good impedance matching, and a wideband response consists of a two-tapered radiating patch with different slopes separated by a gap of length 16.8 mm and width of 0.2 mm is presented. In [17], Fig. 3.10c, a compact modified CPW-fed antenna with multioctave bandwidth over the frequency range from 3.06 to 35 GHz consists of a truncated ground plane with symmetrically slits at its center and sides, an inverted triangular patch with two rectangular defects, and a narrow rectangular parasitic element is introduced. In [18], Fig. 3.10d, a multi-resonance UWB slot-like CPW-fed sleeve-monopole antenna with a wide bandwidth from 3.09 to 12.86 GHz consists of a coupled U-shaped strip and a pair of embedded folded strips is designed. In this antenna, wide impedance bandwidth is obtained with additional resonances of coupled parasitic strips, especially at the upper frequency band.

It has been demonstrated that the incorporation of a fork-like feeding structure in printed antennas can efficiently improve the excitation and uniformity of the vertical current components and greatly eliminate the horizontal current distribution that results in extending the impedance matching bandwidth, stable omnidirectional radiation patterns, and a cross-polarization suppression even at higher frequencies [23]. Figure 3.11 shows examples of antenna bandwidth enhancement with different fork-like feeding structures. In [19], Fig. 3.11a, a UWB slot antenna with bandwidth

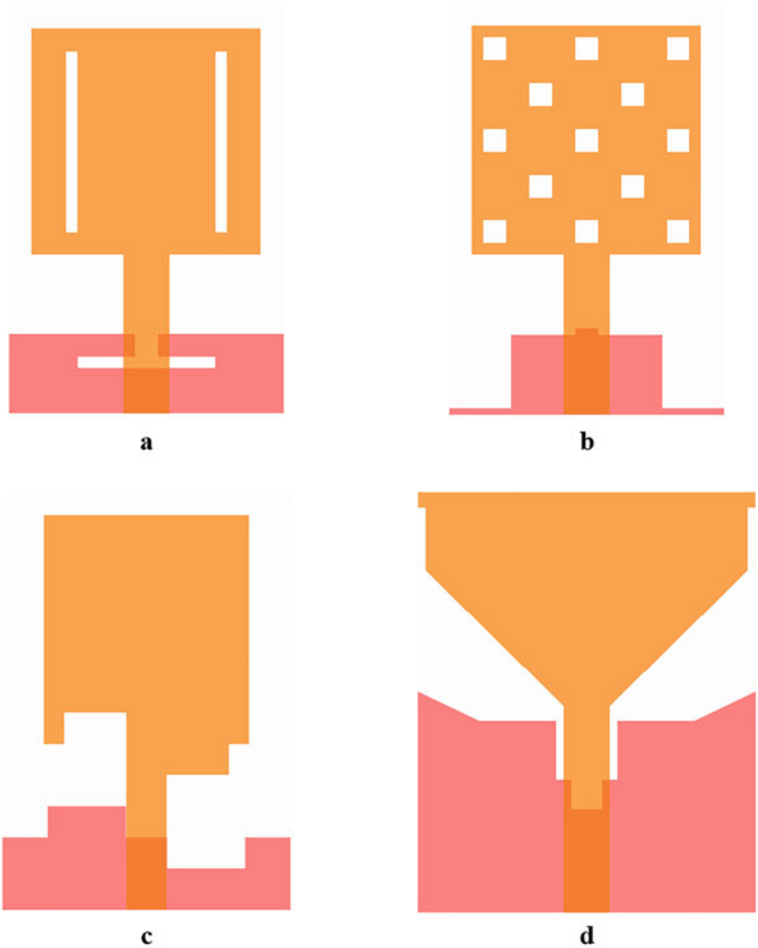

Fig. 3.8 Bandwidth enhancement with different defected structures: (**a**) [9], (**b**) [10], (**c**) [11], (**d**) [12]

from 3 to 11 GHz includes a quasi-isosceles triangle slot, and a microstrip feed line with fork-like tuning arms is designed. In this antenna, tuning stubs increase the number of resonances and present a current continuity in the entire slot. Therefore, the impedance matching and radiation purity are improved. Similarly, in Fig. 3.11b [20], a modified semi-circle-like slot antenna with a fork-shaped feeding microstrip line is proposed. This antenna operated over 2.2–18 GHz. In [21], Fig. 3.11c, a small UWB double-fed monopole antenna with a size of 14 mm $\times$ 20 mm consists of a two-step tapered radiating patch loaded with a modified trapezoid-shaped slot is introduced. This feeding configuration improves the matching operating bandwidth. In [22], Fig. 3.11d, a compact CPW-fed monopole antenna with a size

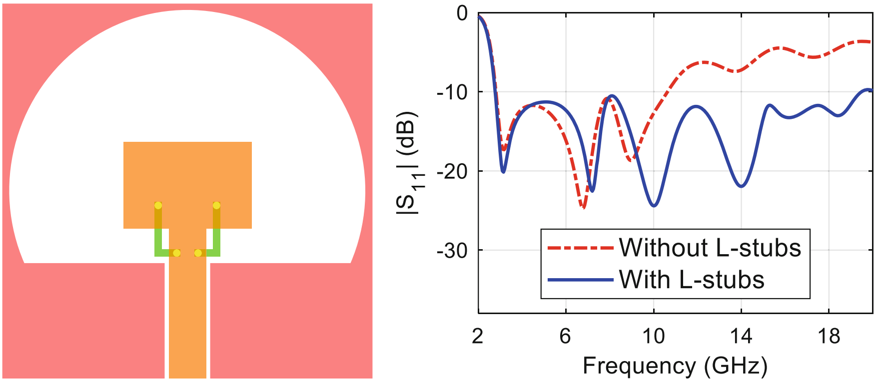

Fig. 3.9 Bandwidth enhancement of circle-like slot antenna with embedding two shorting L-shaped tuning stubs [13]

of 24 mm × 24 mm and bandwidth from 2.76 to 40 GHz includes a hexagonal patch radiator and the tapered ground plane is presented. In this antenna, super-wideband operating bandwidth is obtained by using a trident-shaped feeding line results in a smooth transition from one resonance frequency to another.

Nowadays, fractal geometries have been implemented to enhance printed antenna characteristics like size miniaturization and wideband performance [27]. Fractal structures are usually defined with an infinite number of times a repeating process in various iteration and fractal dimensions. The size reduction can be obtained by the space-filling property and the multiband or UWB operation can be achieved using the self-complementary feature. The space-filling feature leads to an increase of the total electrical length which presents a large surface area in a limited space and as the fractal iteration increase with self-similarity property, more impedance bandwidth will be obtained. Figure 3.12 shows examples of antenna bandwidth enhancement with different fractal geometries. In [24], Fig. 3.12a, a UWB circular multifractal monopole antenna with a small size of 22 mm × 30 mm and a broad impedance matching from 3 to 12 GHz is proposed. In this antenna, fractal geometry includes three arched sections of equal 120° with a difference in the radios that can adjust the resonant frequency ratios and the lower band-edge frequency. In [25], Fig. 3.12b, a UWB microstrip-fed modified Pythagorean tree fractal monopole antenna with a compact size of 25 mm × 25 mm and an operating band over 2.6–11.12 GHz is introduced. In this antenna, the fractal structure is designed by removing the first iterations large side square of a conventional Pythagorean tree fractal and isosceles triangles with steep angles of 10°. Additional resonances and much wider matching bandwidth will be achieved by only increasing the iterations of tree fractal. In [26], Fig. 3.12c, a super-wideband microstrip-fed star-triangular fractal monopole antenna with a small area of 20 mm × 20 mm and bandwidth between 1 and 30 GHz is designed. By increasing the iterations of the modified star-triangular fractal, the antenna bandwidth will be extended.

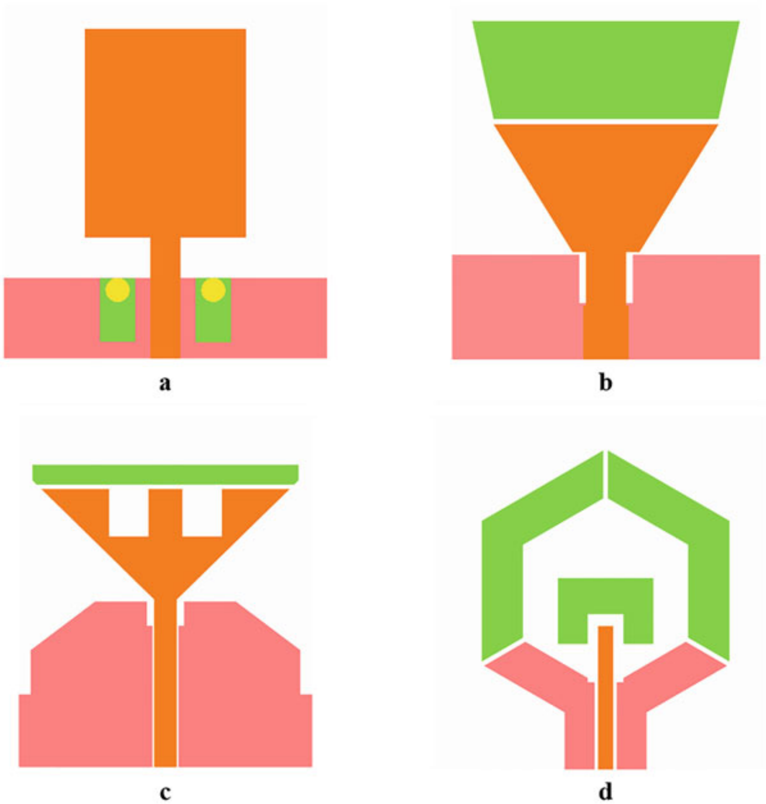

Fig. 3.10 Bandwidth enhancement with different parasitic elements: (**a**) [15], (**b**) [16], (**c**) [17], (**d**) [18]

3.3 Size Miniaturization of UWB Antennas

Recently, many novel techniques have introduced towards size miniaturization of printed UWB antennas and serval structures have developed to present reducing the antenna size while maintaining desired bandwidth, matching and radiation performances [28]. The typical method to size miniaturization can be obtained using substrates with high dielectric constants at the expense of excitation undesired surface waves, in the following, fractal structures with space-filling and self-similarity features present compact antennas. Further size miniaturization can be achieved using slowing the wave propagation property with reactive loading structures, such as imposing slot or slit in the patch radiator or ground plane, lumped component, and metamaterial composite materials that increase the propagation constant, bring down the lowest operating frequency, and increase the electrical length. Compact low-profile printed UWB antennas are highly favorable to integrate with RF systems in portable, mobile, and medical applications. The most straightforward technique

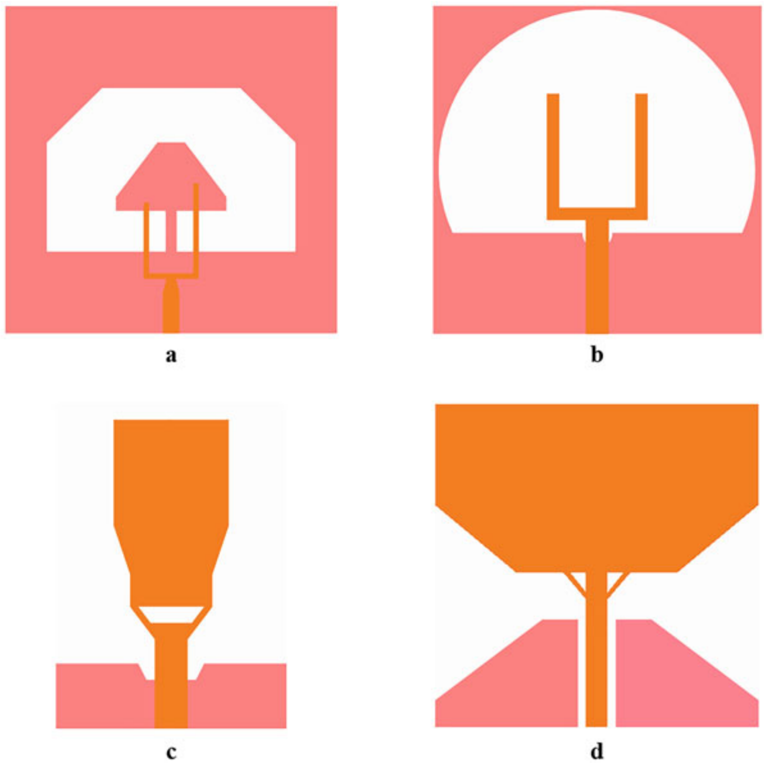

Fig. 3.11 Bandwidth enhancement with fork-like feeding structure: (**a**) [19], (**b**) [20], (**c**) [21], (**d**) [22]

to present size reduction is by halving the reference antenna relative to the axis of symmetry and adjusting the feeding line's width. The minimized antenna compared to the original full-size reference antenna has similar characteristics and an almost 45% area reduction.

As an example, a miniaturization process with a halving technique is demonstrated in [29]. The reference full-size UWB antenna is shown in Fig. 3.13, case *a*, which includes a circular patch and an incomplete semi-circular ground plane with a wide square slit below the tapered feed line. The low-cost dielectric used is FR4 with $\varepsilon_r = 4.4$, $\tan\delta = 0.02$, and a thickness of 1.6 mm. All simulations are performed with ANSYS HFSS. Figure 3.13 shows the miniaturization process of the proposed UWB antenna. By halving the reference antenna (*a*) along the axis of symmetry, the width of the feed line is also halved, which almost doubles the feed line impedance. This mismatch of impedance in antenna *b* increases the level of $|S_{11}|$. In antenna *b*, instead of halving the feed line, it can use a full-width feed line. In the minimized antenna (*c*), the impedance matching is not disturbed and the resulting $|S_{11}|$ is similar to the reference antenna (*a*). Since the electrical lengths of

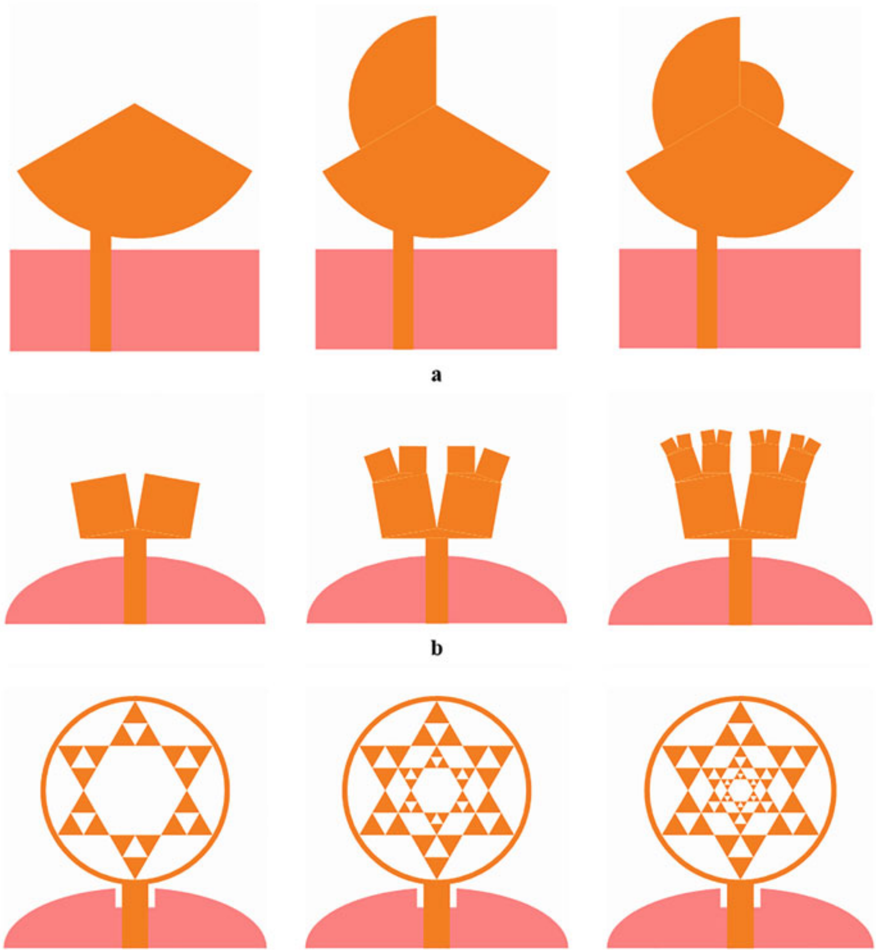

a

b

c

Fig. 3.12 First three iterations of different fractal antennas: (**a**) [24], (**b**) [25], (**c**) [26]

antenna *a* and *c* are equal. Therefore, the lower edge of the working band and the location of resonances in the three antennas are approximately identical. In antenna *c*, by halving and modifying the reference antenna, a 40% reduction in the antenna area is achieved.

Figure 3.14 shows the fabricated prototypes under test inside the anechoic chamber and the measured results of the reference and minimized antennas. The $|S_{11}|$ is measured using a PNA model of E8363C. The measured results show an -10 dB $|S_{11}|$ bandwidth extends from 2.5 up to 13 GHz (135.5%) for reference antenna and from 2.23 up to 13 GHz (144.5%) for a minimized antenna. As can be observed from measured $|S_{11}|$ results, the first resonance frequency of the

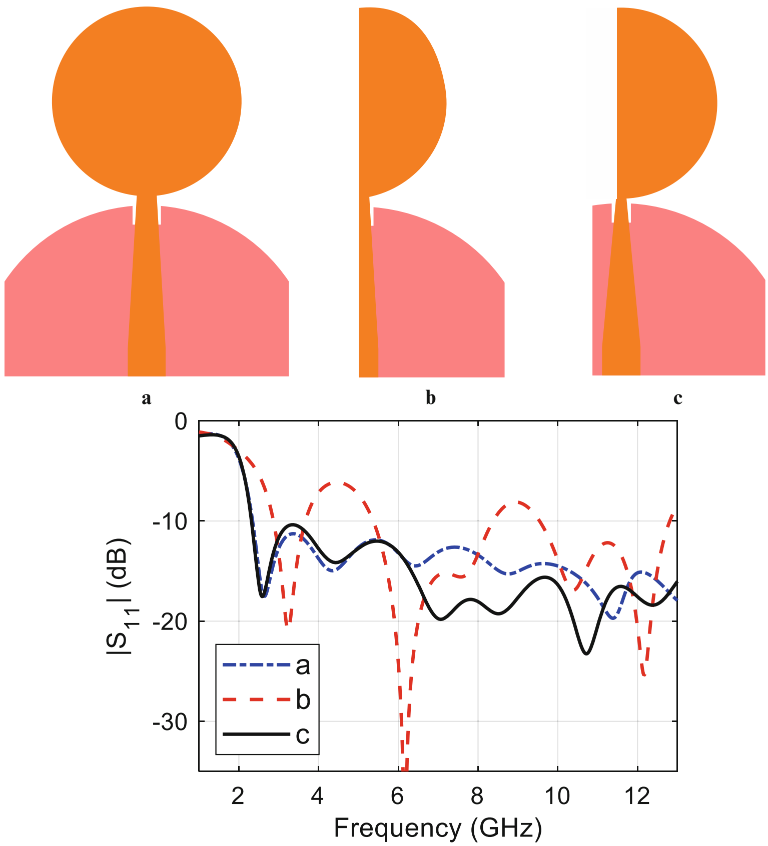

Fig. 3.13 Size miniaturization process and simulated $|S_{11}|$ [29]

minimized antenna is shifted down compared to that of the reference antenna. The displacement of the first resonance frequency is due to creating an additional effective current path along the left edges of the feed line and semi-circular patch radiator of the minimized antenna while for a full-size reference antenna, the currents are mainly distributed along the edges of circular patch radiator. Figure 3.14 shows the measured peak and average gains are 3.3 and 2.7 dBi for reference antenna, respectively, and 2.9 and 2.3 dBi for the minimized antenna, respectively. Compared to the reference antenna, the minimized antenna's gain is lower due to the reduction of the antenna dimensions. Besides, at higher frequencies, the gains of antennas are similar, owing to the minimized antenna pattern is more directional. Gain measured is obtained by a comparison method in a pyramidal chamber with ETS 3117 dual-ridged horn as reference and transmitter antennas.

The proposed halving technique can be applied for the miniaturization of various printed antennas with symmetrical structures. Figure 3.15 shows the size miniaturization of different antennas presented in Fig. 3.1. The aforementioned

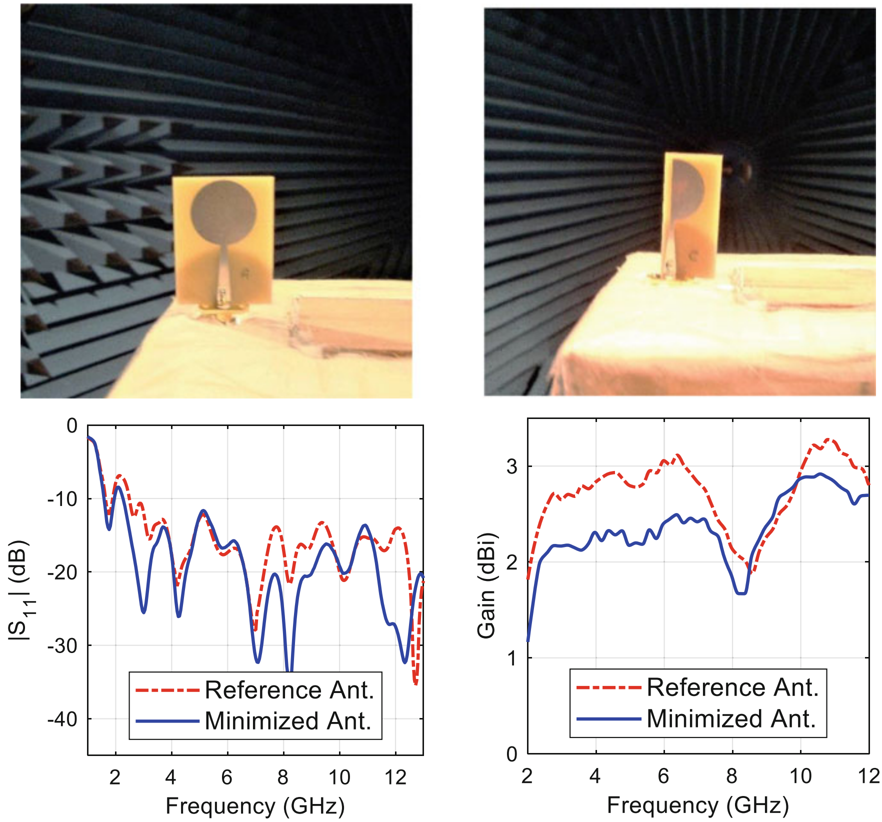

Fig. 3.14 Prototypes and measured results of reference and minimized UWB antennas [29]

CPW feed lines in Fig. 3.1b, d are converted to asymmetric coplanar strip (ACS) feed lines. Also, the slot antennas in Fig. 3.1c, d are converted to monopole-like antennas. These minimized antennas are suitable for compact MIMO and diversity systems. The cross-polarization level of the minimized antenna compared to the reference antenna increases with the increase of frequency. This is due to the asymmetry of the minimized antenna. In reference antenna due to the symmetry and out-of-phase of the currents on the ground plane along the horizontal direction, cancel each other out. By shrinking the reference antenna, one side of these currents on the ground plane is removed and the other side increases cross-polarization. To reduce the cross-polarization at high frequency in the minimized antenna, it is recommended to reduce the ground plane's width. In [30], the characteristic mode analysis (CMA) is applied to the printed UWB antenna to clear the physical operating principle behind its wideband performance.

Recently, monopole-like slot antennas include an open aperture that has been introduced to reduce the antenna size. In [31], Fig. 3.16, a printed UWB open-slot

Fig. 3.15 Size miniaturization of different antennas with halving technique

antenna consists of a trapezoid patch radiator with a bandwidth of over 2.6–13.8 GHz is presented. The total antenna size is 40 mm × 40 mm that is printed on a low-cost FR4 substrate with $\varepsilon_r = 4.4$, $\tan\delta = 0.02$, and a thickness of 1.6 mm. The antenna is excited with a 50 Ω microstrip feeding line with a width of 1.86 mm and a length of 12.8 mm. In this antenna, a rectangular defect with dimensions of 2 mm × 4 mm is etched from the upper side of the polygon-like aperture for further miniaturization. Tapers at the ground plane and radiating patch are used to matching enhancement, especially at the lower end.

3.4 Single and Multi-notched Band(s) UWB Antennas

UWB communications need to eliminate the existing narrowband interferences within the UWB frequency range [32]. Generally, notched bands with a simple structure and a sharp selectivity are realized by embedding different shapes of slits, slots, stubs, and parasitic elements on the feeding line, ground plane, or radiating patch [33]. A printed UWB monopole antenna with dual band-notch performance is introduced in [34]. The antenna includes a square patch radiator, an E-shaped slot, a pair of L-shaped slits, and a truncated ground plane with a V-shaped protruded strip. The additional resonances of a modified 45° V-shaped protruded strip can enhance the impedance bandwidth, especially at the upper end. The antenna size is 10 mm × 16 mm that is printed on a low-cost FR4 substrate of permittivity 4.4, loss tangent 0.02, and thickness 1.6 mm. The proposed antenna is connected to a 50 Ω microstrip feed line with a width of 2 mm and a length of 6 mm.

Figure 3.17 shows the dual band-notch design process and simulated $|S_{11}|$. The basic structure (*a* in Fig. 3.17) consists of an ordinary square radiating patch with a V-shaped protruded strip that operates from 3.55 to 17.7 GHz. In antenna *b*, to create

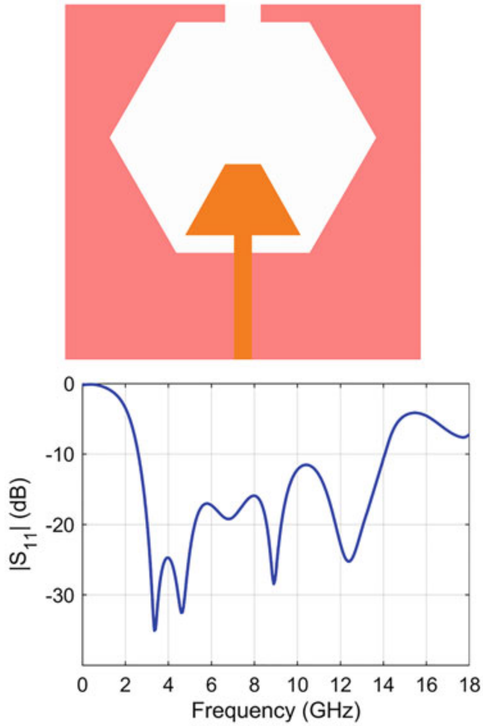

Fig. 3.16 Size miniaturization with monopole-like slot structure [31]

a single band-notch property from 4.15 to 5.9 GHz, two L-shaped slits are embedded in the patch radiator's sides. In antenna *c*, etching an E-shaped slot on the center of the square radiating patch, dual band-notch characteristics in the 3.45–4.15 GHz and 4.85–5.9 GHz is achieved. The electrical lengths of the L-shaped slits and the E-shaped slot are respectively about a quarter-guide-wavelength and a half-guide-wavelength at the center frequency of notched bands. The proposed antenna operates from 3.1 to 17.7 GHz and has a simple structure and notched bands with a sharp skirt. Figure 3.18 shows the simulated current distributions on the radiating patch at first and second notch frequencies. It can be cleared that at the notch frequencies, the current flows are more dominant on the interior and exterior edges of the defective structures. They have oppositely directed and neutralized the effects of each other. Hence, at these frequencies, the radiation fields cancel out, the antenna impedance changes and produces a high attenuation. Therefore, the antenna does not radiate effectively.

Figure 3.19 shows examples of different defected geometries for single- or dual-notch characteristics. In [35], Fig. 3.19a, by employing two L-shaped slits inserted on the ground plane, a stopband from 5 to 5.9 GHz is achieved. In this antenna with a bandwidth from 3.1 to 10.6 GHz, a much wider bandwidth is produced by using a pair of folded strips on the truncated ground plane. In [36], Fig. 3.19b, to prevent interference with WLAN systems, two symmetrically connected arch-shaped slots

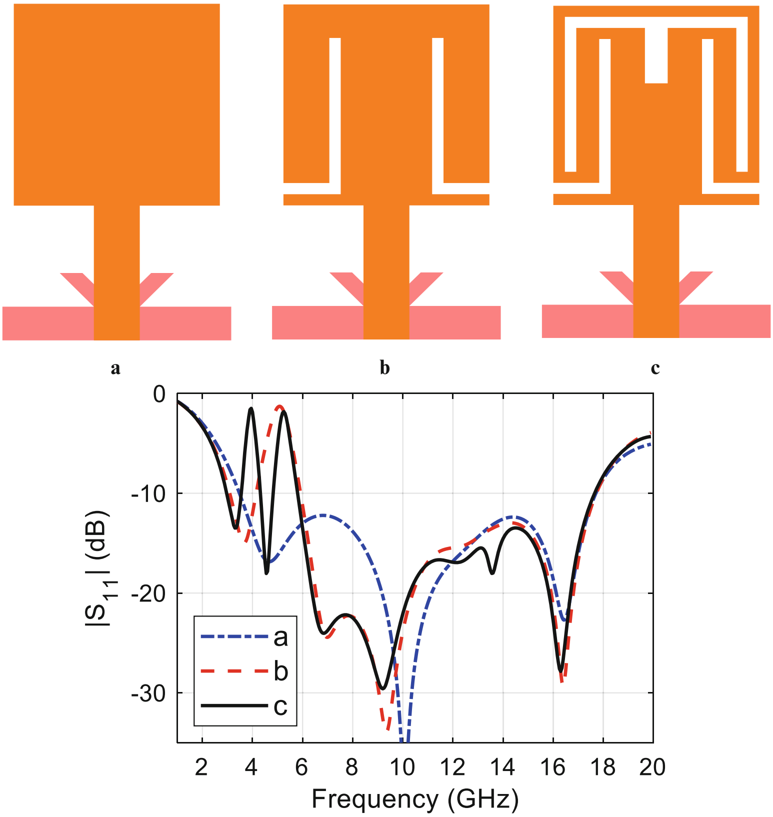

Fig. 3.17 Dual band-notch design process and simulated $|S_{11}|$ [34]

with a variable separated angle etched on the patch are presented. The proposed antenna has a compact size of 26 mm × 26 mm and covers the frequency range between 2.5 and 15 GHz. The embedded slot acts as a resonant structure. The notch frequency can be controlled with the total lengths of the slot.

Moreover, by changing the slot's position, the bandwidth and the performance of the rejection band can be adjusted. Also, the slot increases the electrical length of the patch radiator due to its inductive loading effect and results in a reduction of the lower end frequency. In [37], Fig. 3.19c, by removing an inverted V-shaped slot with folded ends from the patch radiator, a single band-notched function in the frequency band of 5–6 GHz is obtained. This CPW-fed slot antenna has a compact size of 20 mm × 18 mm and a wide bandwidth of 3.04–20.22 GHz. In [38], Fig. 3.19d, dual band-rejection performances at 3.75 and 5.5 GHz are introduced using two rectangular slits. The proposed microstrip-fed antenna has a small size of 12 mm × 18 mm and a wide bandwidth from 2.5 to 11 GHz. By varying the position and the dimensions of the slits, frequencies and bandwidths of notched bands with lower edge frequency can be adjusted. In [39], Fig. 3.19e, a compact UWB circle-

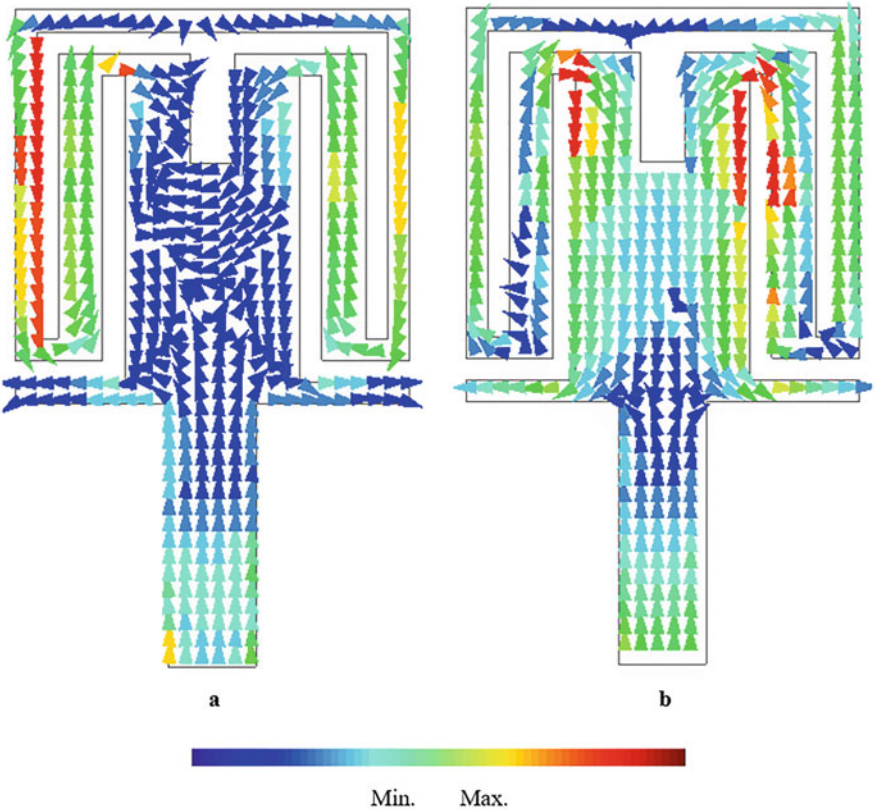

Fig. 3.18 Simulated current distributions of the proposed UWB dual-notched antenna at: (**a**) 4 GHz, (**b**) 5.3 GHz

like CPW-fed slot antenna with two notched bands at 3.8 and 5.4 GHz is proposed. The antenna has a small size of 26 mm × 26 mm and a wide bandwidth from 2.75 to 14.2 GHz. By cutting an L-shaped slit from the ground plane and a U-shaped slot from the radiating patch, the dual-frequency band stops performance is achieved. The bandwidths of rejection bands can be controlled by changing the width of the L-shaped slit and adjusting the position of the U-shaped slot. The L-shaped slit acts as a quarter-wavelength resonator at the center of the lower notched frequency band. Likewise, the U-shaped slot behaves like a half-wavelength resonator in the higher notch resonance frequency. In [40], Fig. 3.10f, etching a narrow rectangular slot on the patch radiator can stop the 5.13–5.87 GHz band for WLAN applications, and removing two symmetrically C-shaped slots on the ground plane can reject the frequency range of 7.59–9.03 GHz for satellite communications. The proposed dual band-notched antenna has a small size of 20 mm × 20 mm and operates in the frequency range of 2.6–13.3 GHz.

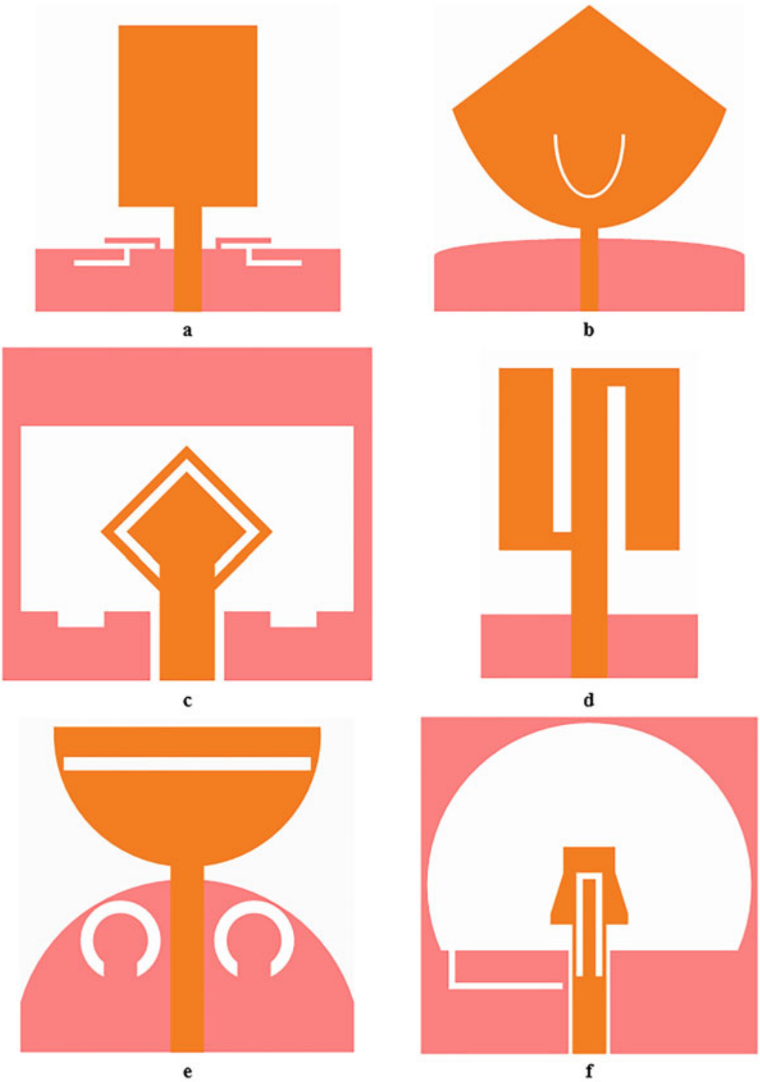

Fig. 3.19 Different defected geometries for: single notch: (a) [35], (b) [36], (c) [37]; dual notch: (d) [38], (e) [39], (f) [40]

Electromagnetic bandgap (EBG) structures have widely developed to mutual coupling reduction, gain enhancement, and spurious response removal [41]. Currently, mushroom-type EBG cells in different shapes: triangular, square, hexagonal, circular, sinusoidal, and so on are widely used to create band-notch characteristics with the advantages of accurate predicting of rejection frequencies by dispersion diagram and without distortion effects on antenna radiation patterns. In most of

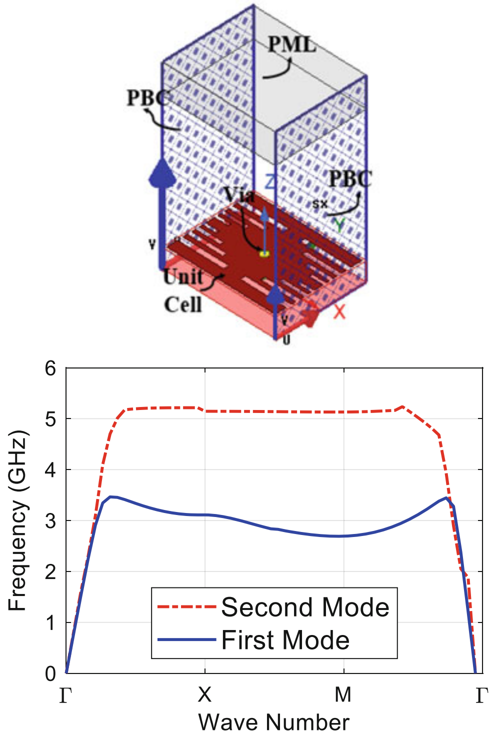

Fig. 3.20 Proposed slitted EBG unit cell and dispersion diagram [29]

the EBG rejection structures, two or more EBG cells in different sizes are used to produce one or two-notch bands. In [29], Fig. 3.20, a slitted mushroom-type EBG cell is presented to independently filter undesired WLAN and WiMAX bands in the UWB range. The antenna is then integrated with a pair of similar slitted EBG structures beside the feeding line to enhance filtering ability. The presented EBG structure has many benefits, like independent control over the notch-bands, little effects on antenna performance, and reduction of the required number of EBG cells. The proposed printed UWB dual-notched antenna is shown in case *c* of Fig. 3.21, consisting of a circular patch radiator, a tapered microstrip feed line, a truncated semi-circle ground plane, and a couple of similar EBG structure in the besides of the feed line. The proposed antenna is printed on a low-cost FR4 substrate with $\varepsilon_r = 4.4$, $\tan\delta = 0.02$, and a height of 1.6 mm. All full-wave simulation results are achieved by ANSYS HFSS. Figure 3.20 presents the boundary condition for the Eigen-mode analysis and dispersion diagram of the proposed slitted EBG unit cell. As observed, there are two frequency band stops wherein these regions no modes propagate.

Figure 3.21 illustrates the dual-notched design steps. Antenna *a* is the reference UWB antenna with a −10 dB bandwidth from 2.11 up to 13 GHz. In antenna *b*, to obtain a single notch-band at 3.5 GHz with a bandwidth of 2.7–4.1 GHz, a pair of square mushroom-type EBG cells are coupled to the antenna feeding line. The

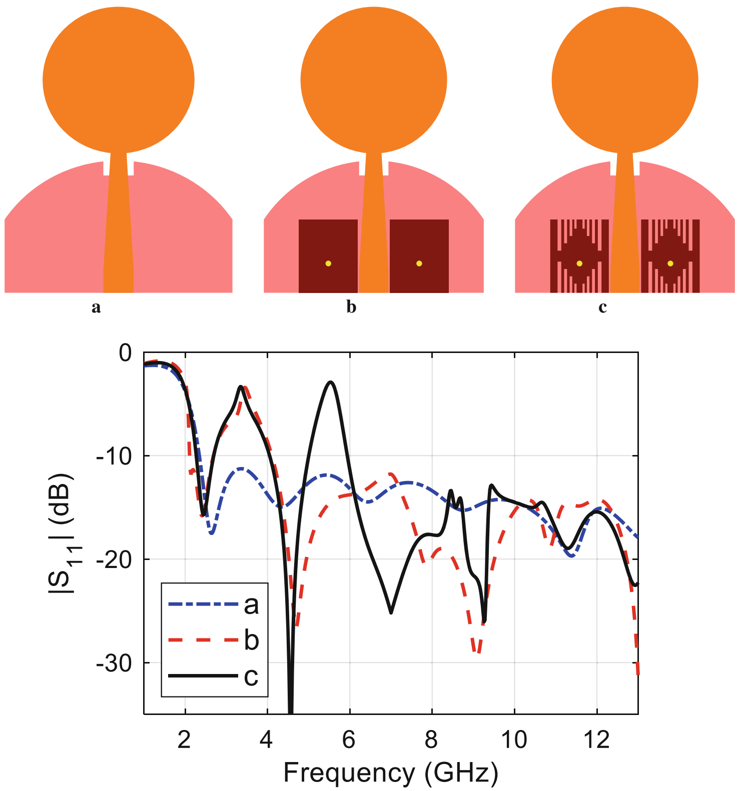

Fig. 3.21 Dual-notched design steps and simulated $|S_{11}|$ [29]

patch size of the EBG cell is set for the first resonance frequency located at 3.5 GHz. In antenna *c*, to produce a higher frequency notched band at 55 GHz, open slits are placed at the EBG patch's sides. The proposed printed dual-notched printed antenna exhibits $|S_{11}|$ with -10 dB bandwidth from 2.28 up to 13 GHz with notched bands of 2.7–4.1 GHz and 5–5.95 GHz. It can be observed that the change in the width of the gap between the feed line and the EBG structure does not affect the resonance locations, but adjusts the amount of filtered bandwidths. The coupling increases by decreasing the gap's width, resulting in increased bandwidth and severity of the notch. Figure 3.22 presents the simulated current distributions of the proposed dual-notch planar antenna at different frequencies. In Fig. 3.22a at 3.5 GHz, the maximum current is concentrated through the central area of slitted EBG around via connection, and thus leaving minimum current to the patch radiator for radiation. In Fig. 3.22b at 5.5 GHz, the maximum current mostly conducting along the edges of the slits, and therefore the antenna matching varies at this frequency and creating a large reflection at the upper notch frequency. In Fig. 3.22c at 4 GHz, current distributions at EBG cells are minimum and nearly symmetrical distributed on the

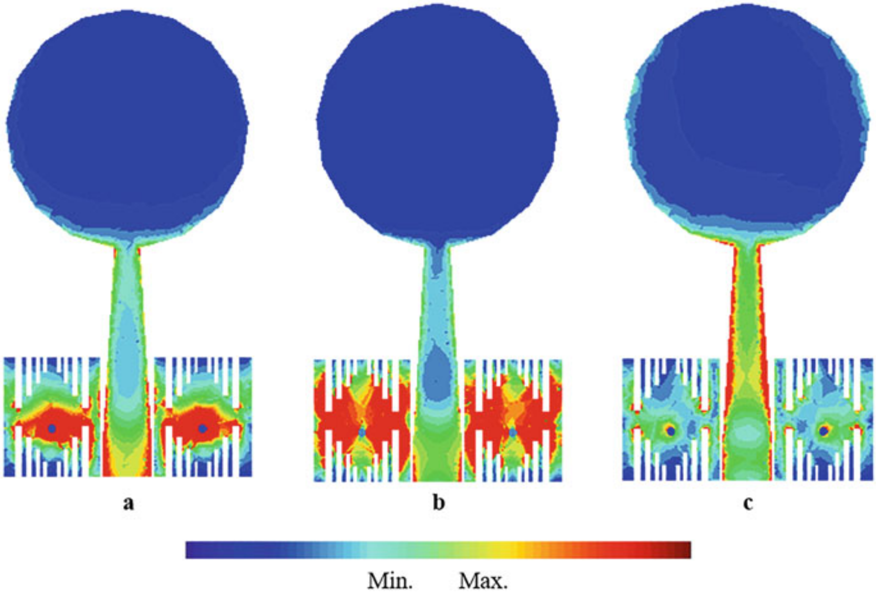

Fig. 3.22 Simulated current distributions of proposed UWB dual-notched at: (**a**) 3.5 GHz, (**b**) 5.5 GHz, (**c**) 4.5 GHz

radiating patch. It means at the passband frequency, the EBG structure has a small effect on the UWB antenna performance.

According to Fig. 3.13, due to the structural symmetry of the proposed dual-notched antenna, by halving the reference antenna relative to the symmetry axis and modifying the feed line width, a minimize antenna with dual-notched can be obtained. Figure 3.23 shows the prototypes, simulated and measured $|S_{11}|$ of the reference and minimized dual-notched antennas. The measured $|S_{11}|$ shows -10 dB bandwidth extends from 2.5 up to 13 GHz with dual-notched bands of 510 MHz (3.17–3.68 GHz, 14.9%) and 680 MHz (5.09–5.78 GHz, 12.7%) for reference antenna and from 2.23 up to 13 GHz for the minimized antenna with a dual rejection of 430 MHz (3.17–3.60 GHz, 12.7%) and 640 MHz (4.92–5.56 GHz, 12.2%). A little discrepancy between measurement and simulation data is observed during our tests, which can be a result of soldering inaccuracy of the SMA connector, the accuracy of PCB etching, quality of the substrate, broadband range of simulation, and other environmental factors like measurement in free space. It can be seen that though one EBG cell can be used to obtain dual-notched performance, the bandwidth and rejection magnitude are higher when two EBG cells are placed in the vicinity of the transmission line. This is due to the reduction of capacitance coupling between the feeding line and EBG structure in the case of a single EBG cell. Producing dual-notched performance with a single EBG cell has the benefit of a more compact antenna and the disadvantage of asymmetric structure.

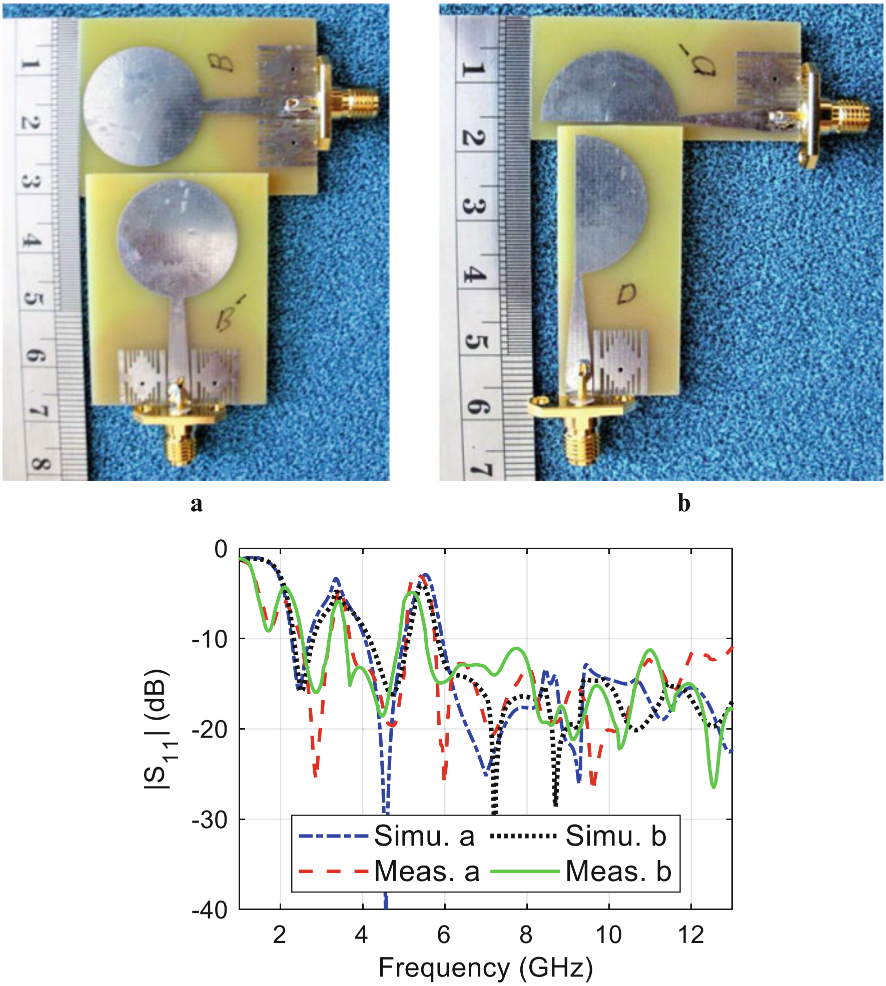

Fig. 3.23 Prototypes and results of the reference and minimized UWB dual-notched antenna [29]

Figure 3.24 shows the S_{21} measurement setup of the proposed UWB dual-notch antenna. The S_{21} measurement is carried out in a typical environmental condition, i.e., free space, with an E8363C PNA. The antenna prototypes were connected by a 1.5 m low loss cable to the ports of PNA. At the ports of antennas, the PNA is calibrated. The free space effects are reduced with an absorber with a thickness of 5 cm. Antenna distance is 60 cm that is around six times the lowest working frequency wavelength. Both the transmitting and receiving antennas are identical. The measurement is performed in face to face (F.F.) and side by side (S.S.) states. Figures 3.25 and 3.26 show the measured transfer characteristics of the full-size reference and minimized antennas, with or without the notch-bands in F.F. and S.S., respectively. Obviously, the $|S_{21}|$ has a sharp reduction in the notched bands and a

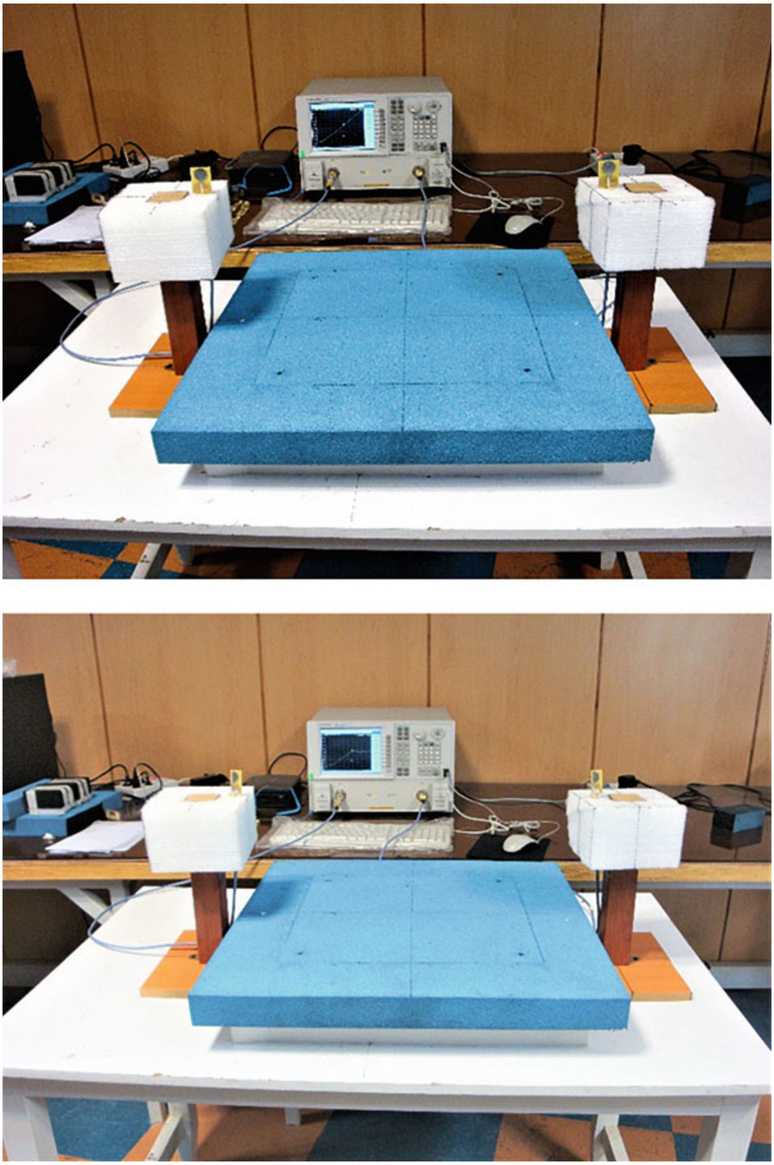

Fig. 3.24 Measurement setups of transfer characteristics [29]

smooth variation in the operating bands. Also, the group delay is nearly flat across operating bands except at the notched bands. Finally, the minimized antenna has a similar behavior to that of the full-size reference antenna. Hence, the proposed antennas have the capability of transmitting and receiving short pulses without deformation.

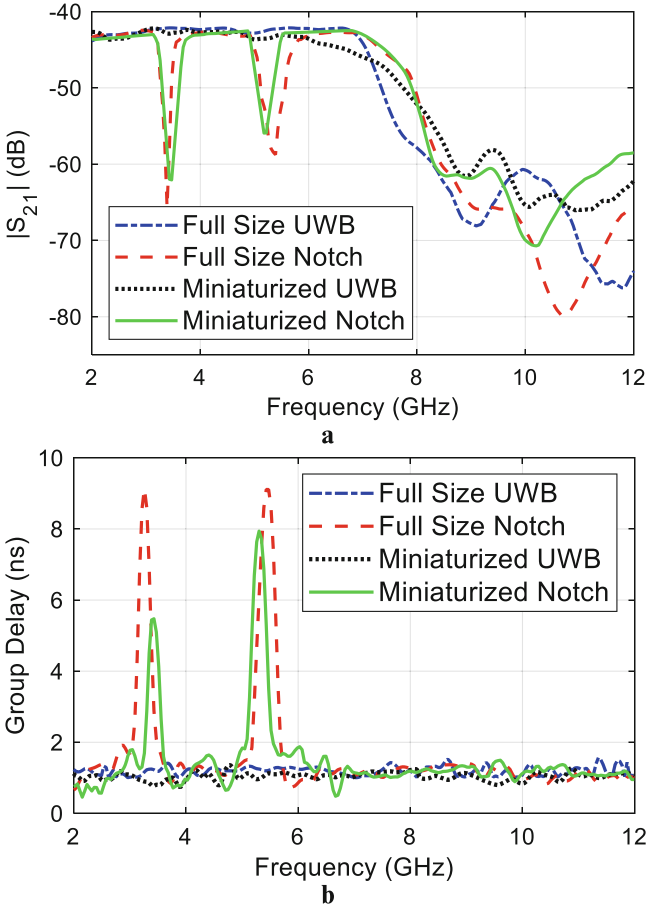

Fig. 3.25 Measured F.F. transfer characteristics: (**a**) $|S_{21}|$, (**b**) group delay [29]

In [42], Fig. 3.27, a UWB CPW-fed slot antenna with triple band-notched characteristics is presented. Bandwidth enhancement and triple band-notched function are obtained with a parasitic element at the back layer of the substrate. The proposed antenna includes a quasi-circle-like slot and a rectangular patch radiator. The antenna size is 27 mm $\times$ 27 mm that is printed on a low-cost FR4 substrate with $\varepsilon_r = 4.4$, tan$\delta = 0.02$, and a thickness of 1.6 mm. This compact slot antenna is excited with a 50 Ω CPW-fed line with a width of 3 mm and a gap of 0.3 mm. As observed from the $|S_{11}|$ results, the fork-shaped parasitic element in Fig. 3.27c is connected to the radiation patch through four via connections with radii of 0.25 mm and 0.5 mm enhances the impedance bandwidth at the upper frequency band. This is due to the increase of the uniformity and vertical surface currents in the patch with the fork-shaped parasitic element. As observed in Fig. 3.27b, the fork-shaped parasitic element has different stubs to provide triple notched bands.

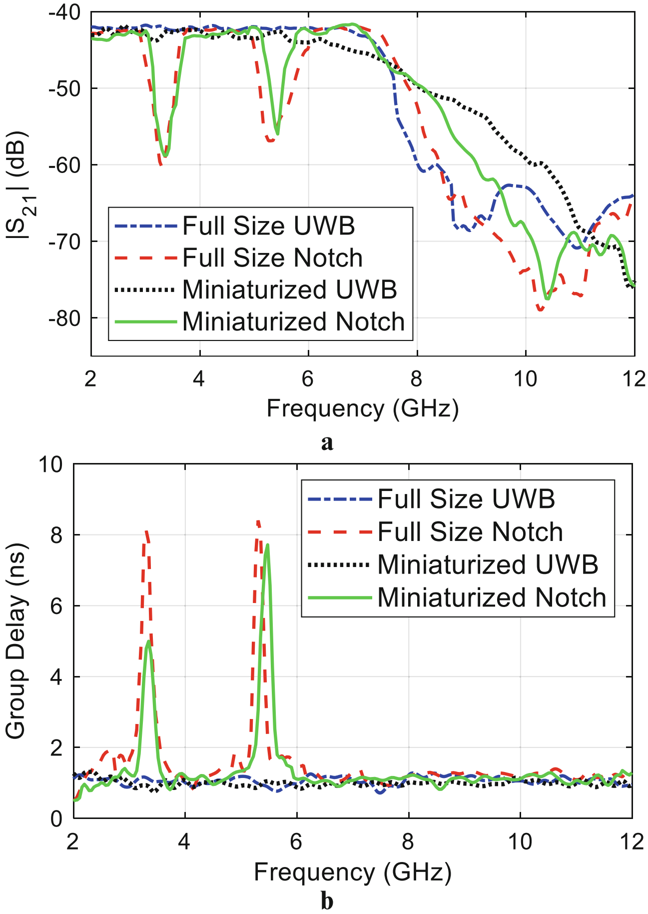

Fig. 3.26 Measured S.S. transfer characteristics: (**a**) $|S_{21}|$, (**b**) group delay [29]

The T-shaped stub in Fig. 3.27d is composed of two quarter-guide-wavelength inverse L-shaped resonators at 3.3 GHz. The C-shaped stubs in Fig. 3.27e are the quarter-guide-wavelength resonators at 5.5 GHz, and the Z-shaped stubs are the quarter-guide-wavelength resonators at 7.8 GHz. The center frequencies of the rejection bands can be adjusted by tuning the length of quarter-wavelength resonators. The proposed antenna operates from 2.5 to 20 GHz (155%) with triple notch-bands at 3.3–3.7 GHz, 5.1–6.2 GHz, and 7.1–8 GHz to filter the WiMAX, WLAN, and X-band, respectively.

Figure 3.28 shows examples of printed UWB antennas with single notch performance by different parasitic elements. In [43], Fig. 3.28a, a modified symmetrical H-shaped parasitic element on the ground plane is used to generate a single band-stop performance. The proposed antenna operates over the frequency range from

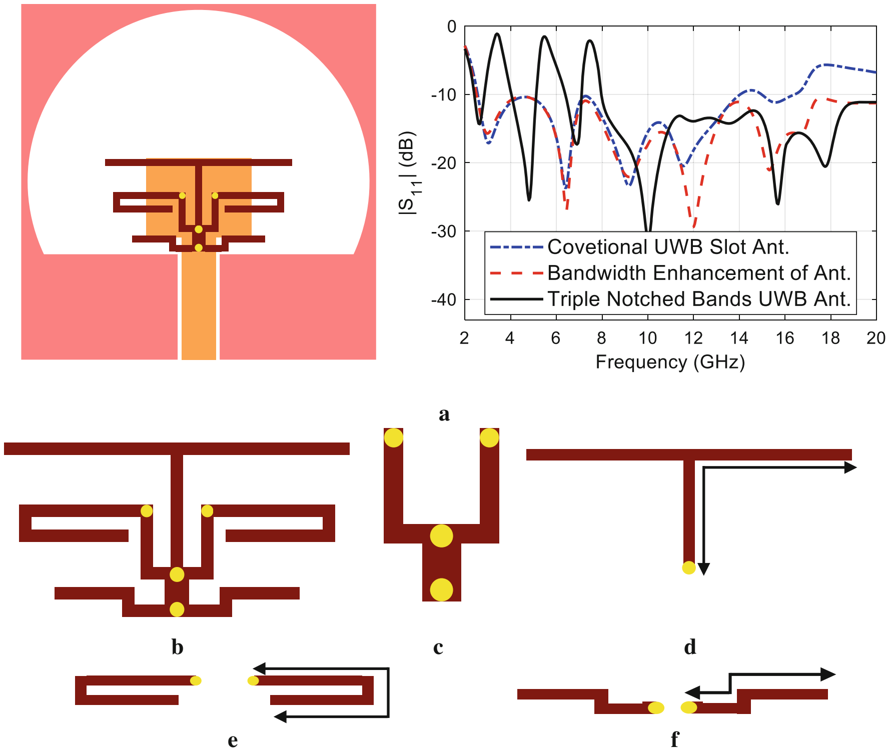

Fig. 3.27 (**a**) UWB CPW-fed quasi-circle like slot antenna and simulated $|S_{11}|$, (**b**) proposed parasitic element, (**c**) fork-shaped parasitic element, (**d**) T-shaped stub, (**e**) C-shaped stubs, (**f**) Z-shaped stub [42]

3.1 to 14 GHz with a band-rejection in the frequency band of 5.1–5.9 GHz. In [44], Fig. 3.28b, an inverted semi-ellipse-shaped parasitic element on the backside of the main radiator is used to omit the undesired frequency band of 5.1–5.9 GHz. In the notch frequency, the current flows are more dominant on the parasitic element and are in a reversed direction with the current on the main patch. Therefore, the desired high attenuation at the rejection frequency can be obtained and the radiation fields cancel out. In [45], Fig. 3.28c, two rod-shaped parasitic elements on the back of the substrate are implemented to generate a rejection function in the frequency range of 5.1–5.9 GHz. The proposed antenna has a small size of 12 mm $\times$ 12 mm and a usable bandwidth of 3–22.5 GHz (153%). In [46], Fig. 3.28d, using a modified T-shaped parasitic element on the backplane of the substrate, a band-notch performance at 5.07–5.92 GHz is provided. This antenna has a compact size of 12 mm $\times$ 18 mm and covers the frequency range of 2.6–19.3 GHz (150%).

Figure 3.29 shows multiple notches performances by different parasitic elements. In [47], Fig. 3.29a, two inverted L-shaped parasitic elements on the bottom of the substrate connected to the patch radiator by two via connections are used to present

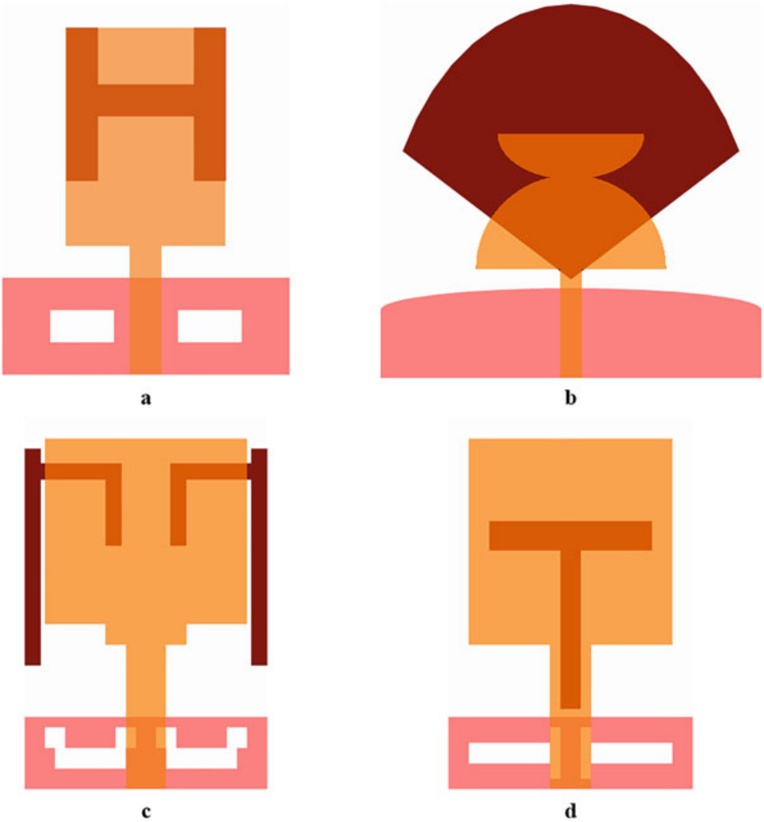

Fig. 3.28 Different parasitic elements for single notch performances: (**a**) [43], (**b**) [44], (**c**) [45], (**d**) [46]

a dual filtering function. The proposed antenna operates from 2.5 up to 12 GHz with dual filtering characteristics at 3.1–3.9 GHz and 5.2–5.9 GHz. By changing the width and length of the two shorted stubs, the bandwidth and position of rejection bands can be adjusted. Likewise, in Fig. 3.29b [48], two nested C-shaped parasitic elements on the back layer of the substrate are inserted to produce two frequency band-notches at 3–3.8 GHz and 5.1–6.2 GHz. The C-shaped parasitic elements are connected to the patch by two via connections. The proposed CPW-fed slot antenna has a compact size of 26 mm $\times$ 30 mm and operates over the frequency range of 2.5 up to 25 GHz. Much wider impedance bandwidth is obtained by using a fork-like feed line. The bandwidth and position of the rejected bands can be controlled by adjusting the position and length of C-shaped parasitic elements, respectively. In [49], Fig. 3.29c, dual-notched performances at 3.5 and 5.5 GHz are generated using a parasitic E-shaped element on the backside of the substrate that is electromagnetically coupled to the patch radiator. The lower edge of operating

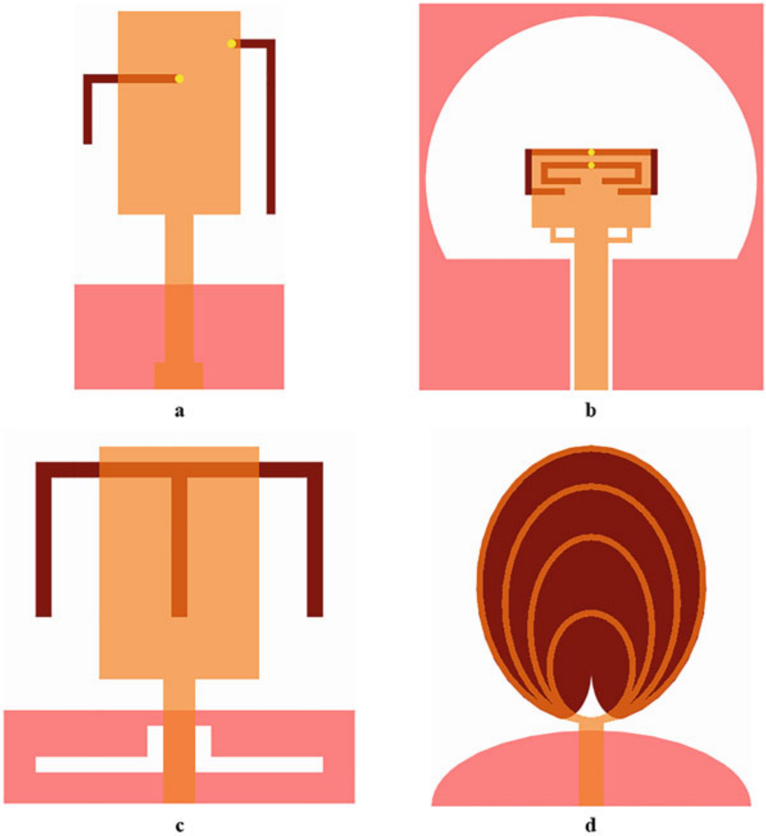

Fig. 3.29 Multiple notches by different parasitic elements: (**a**) [47], (**b**) [48], (**c**) [49], (**d**) [50]

frequency and the position of band-rejections can be adjusted by properly tuning the dimensions of the E-shaped capacitive-couple parasitic element. In [50], Fig. 3.29d, multiple notch performance is obtained by the coupling of multiple rings radiating fractal patch with a heart-shaped backplane parasitic element. With the increasing fractal iteration on the fractal patch, multiple band-rejections are obtained. The proposed antenna has a compact size of 25 mm × 25 mm and an operating bandwidth from 2.4 to 12 GHz with triple notched bands at 3–3.3 GHz, 4.25–5.1 GHz, and 7.2–8.1 GHz.

Figure 3.30 shows examples of single notch characteristics by different tuning stubs. In [51], Fig. 3.30a, a band-stop frequency property is obtained by loading two L-shaped and a T-shaped stubs on an E-shaped patch radiator. The proposed antenna has a small size of 10 mm × 17 mm and operates from 2.9 to 14 GHz with a rejection function in the frequency range of 5.01–5.98 GHz. In [52], Fig. 3.30b, by embedding two rectangular stubs in the square radiating patch, frequency band-notched characteristic is obtained. The proposed antenna has a compact size

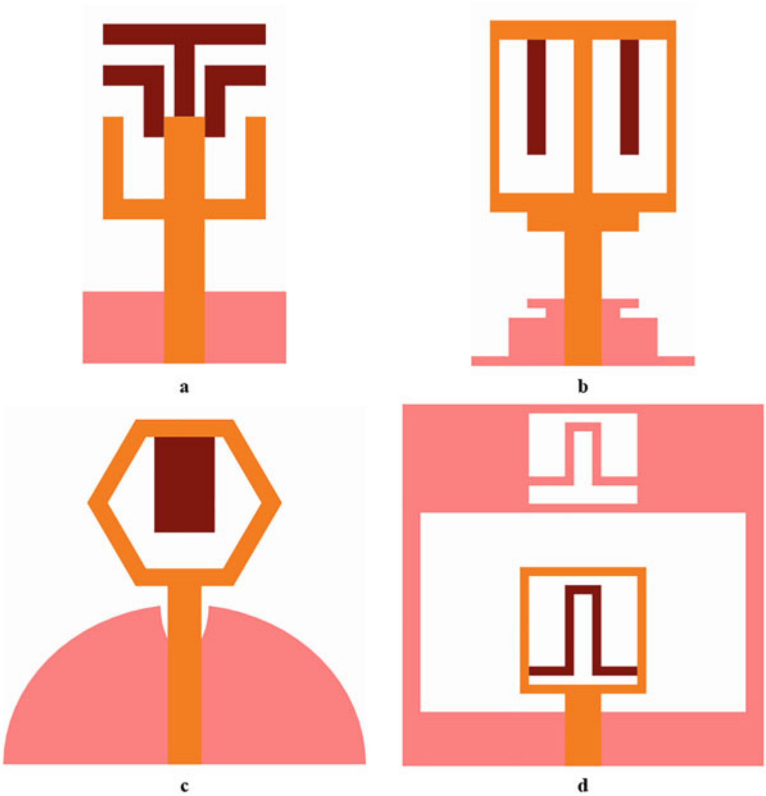

Fig. 3.30 Different tuning stubs for single notch operation: (**a**) [51], (**b**) [52], (**c**) [53], (**d**) [54]

of 12 mm × 19 mm, a wide bandwidth of 2.85–16.73 GHz, and shows the band-stop performance in the frequency range of 5.02–5.97 GHz. At the rejection frequency, the currents are concentrated on the rectangular stubs, which may cause the attenuation and canceling of the radiation fields in the far zone. Likewise, in Fig. 3.30c at [53], by embedding a rectangular stub in an octagonal-shaped ring patch, band-notch performance in the frequency band of 5.15–5.825 GHz is achieved. The proposed antenna has a compact size of 30 mm × 30 mm and exhibits a super-wideband operating range from 2.39 to 40 GHz. The strip's length determines the center frequency of the notch-band. In [54], Fig. 3.30d, by protruding a folded-stub within a square-ring patch radiator, a band-notch characteristics in the frequency range of 5.02–5.97 GHz is obtained. The presented microstrip-fed slot antenna has a small size of 20 mm × 20 mm and bandwidth from 3.07 to 14.03 GHz. Much wider impedance bandwidth is achieved by inserting a folded-stub inside a rectangular slot in the ground plane's top section. At the notch frequency, the folded-stub in the radiation ring patch behaves as a half-wavelength resonator. The current flows

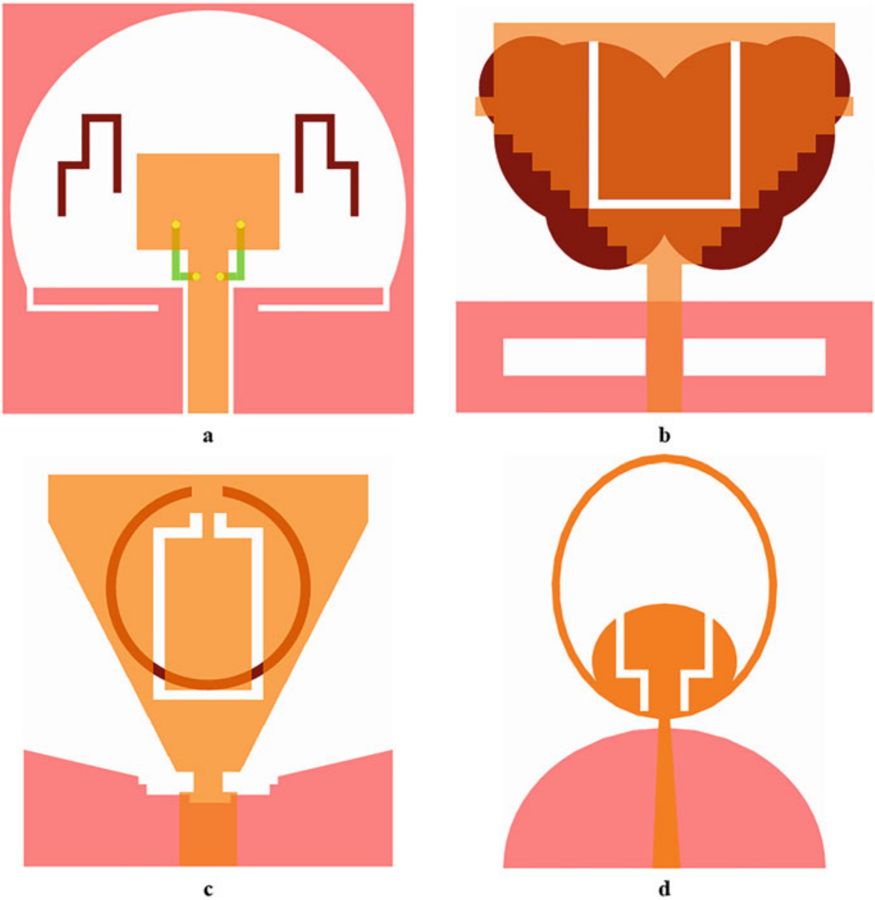

Fig. 3.31 Different combinational techniques for dual-notch characteristics: (**a**) [55], (**b**) [56], (**c**) [57], (**d**) [58]

are more concentrated along the edges of the folded-stub in opposite directions. Therefore, a high attenuation near the rejection frequency can be achieved.

Figure 3.31 illustrates examples of dual-notch performance by different combinational techniques. In [55], Fig. 3.31a, by etching a pair of L-shaped slits in the ground plane and embedding two parasitic elements inside the radiation circle-like slot, dual-notched characteristics can be obtained. By embedding a couple of L-shaped tuning stubs on the back layer of the substrate, bandwidth enhancement at the upper frequency band is realized. The effective length of each open L-shaped slit is around a quarter-guide-wavelength at 3.7 GHz and each L-shaped parasitic element is a half-guide-wavelength at 5.5 GHz. By adjusting the width of the L-shaped slit and changing the horizontal section length of the parasitic elements, the bandwidths of band-rejection filtering performances can be controlled. The proposed antenna has a wideband bandwidth from 2.1 to 20 GHz with dual-rejection bands of 3.1–4 GHz and 5.1–6.1 GHz. In [56], Fig. 3.31b, dual band-notch function at 3.25–3.85 GHz and 4.9–6.2 GHz is presented by etching a U-shaped slot at the stepped patch radiator and a butterfly-shaped parasitic element on the substrate back layer, respectively. Likewise, in Fig. 3.31c at [57], dual band-rejection performance is obtained by printing a split ring-shaped back-layer parasitic element for filter the range of 5.24–6.22 GHz and by etching a C-shaped slot on the tapered patch radiator to stop the band of 3.49–3.81 GHz. In [58], Fig. 3.31d, the dual band-notched characteristic is obtained by an arch-shaped slot and a pair of step-shape slits to notch the frequency ranges of 3.7–4.2 GHz and 5–6 GHz, respectively. The antenna has a small size of 20 mm × 25 mm and a multi-resonance super-wideband bandwidth of 2.2–20.4 GHz.

3.5 Broadband Circularly Polarized UWB Antennas

Circularly polarized (CP) antennas have become more prevalent in many applications like portable devices, radars, satellite systems, and mobile communications owing to their ability the reduction multipath fading, more flexibility in the orientation angle of the transmitter and receiver antennas against rotation effect and polarization mismatch, better weather penetration and mobility. Due to the rapid development of multifunctional communication services with high data rate and distance enhancement, the demand for broadband CP antennas has been increased. Recently, different printed CP antennas have been introduced to achieve the broad impedance and axial ratio (AR) bandwidths [59].

In [60], Fig. 3.32, an asymmetric broadband CP open-slot UWB antenna is introduced. The presented antenna includes an offset microstrip feedline with a tuning stub and a ground plane with an open wide circular slot and a horizontal slit. The proposed antenna with a simple structure, compact size, flat gain, and stable radiation characteristics is attractive for ISM, WiMAX, WLAN, and C-band applications. Antennas with open-slot property can be arranged on the corner of a circuit board and present size miniaturization since the length of an open-slot is equivalent to half of a conventional half-wavelength closed slot resonator. The antenna has a compact area of 25 mm × 25 mm and is etched on a low-cost FR4 substrate with $\varepsilon_r = 4.4$, $\tan\delta = 0.02$, and a height of 1.6 mm. The feedline position relative to the open-slot can enhance the impedance matching and AR bandwidths. The tuning stub on the feedline can improve the impedance matching at the lower edge of the operating band by adjusting the coupled energy to the radiating slot. The measured results indicate 3.2–14 GHz (125%) impedance bandwidth, 3.2–6 GHz (61%) AR bandwidth, and an average peak gain of 4 dBic within the AR bandwidth.

Figure 3.33 illustrates the simulated current distributions at 4.5 GHz. It can be observed the surface currents at 0° and 90° are equal and opposite in phase to 180° and 270° that shows the presented CP antenna propagates right circular polarization (RCP) in back-direction and left circular polarization (LCP) in the top direction.

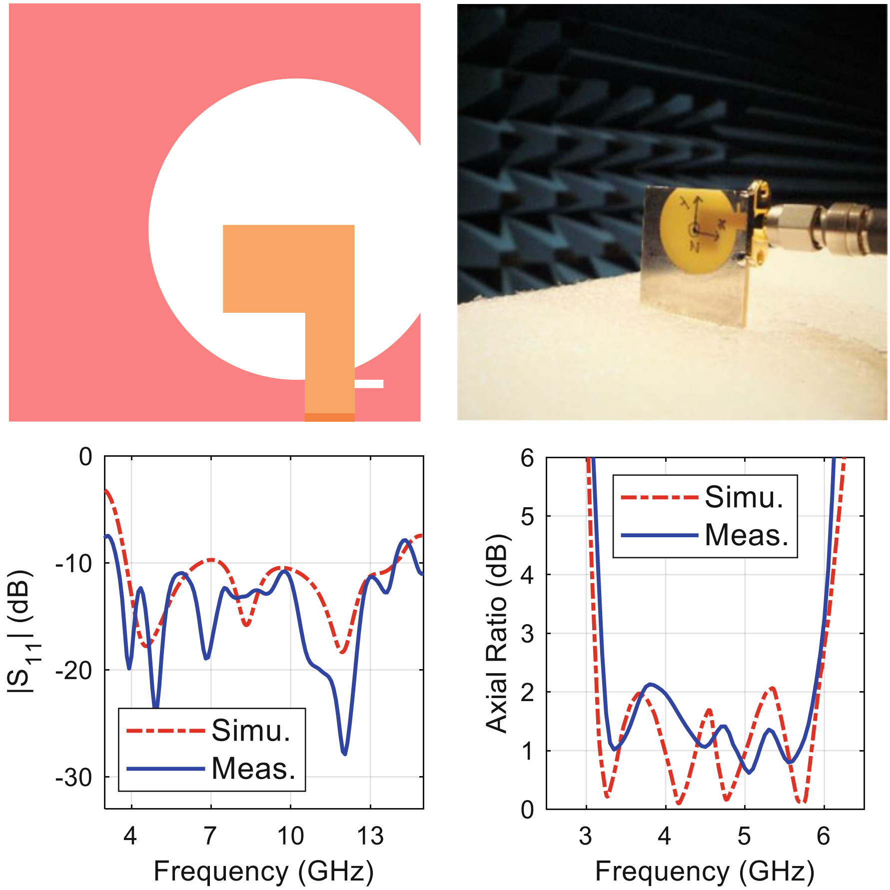

Fig. 3.32 The asymmetric broadband CP open-slot UWB antenna [60]

Circular polarization is realized by generating two perpendicular electric fields with the same amplitude and phase difference of 90°. With the proper positioning of the feedline at the around middle of the open-slot and etching a horizontal slit, the CP conditions are available for several frequencies. Therefore, a broadband CP characteristic is obtained.

In [61], Fig. 3.34, a compact broadband CP shifted monopole UWB antenna is presented. The proposed antenna includes a shifted monopole on the side of an FR4 dielectric, a modified ground plane with shorted width, and a vertical stub at the shorted end. The designed CP antenna has a simple fabrication, small size and broad impedance, and AR bandwidths without using parasitic elements or multiple slots and stubs. The proposed antenna is compact with an area of 19.5 mm × 36 mm and printed on an FR4 substrate with a height of 1.6 mm, $\varepsilon_r = 4.4$, and tan$\delta = 0.02$. By modifying the ground plane the impedance matching is enhanced, especially

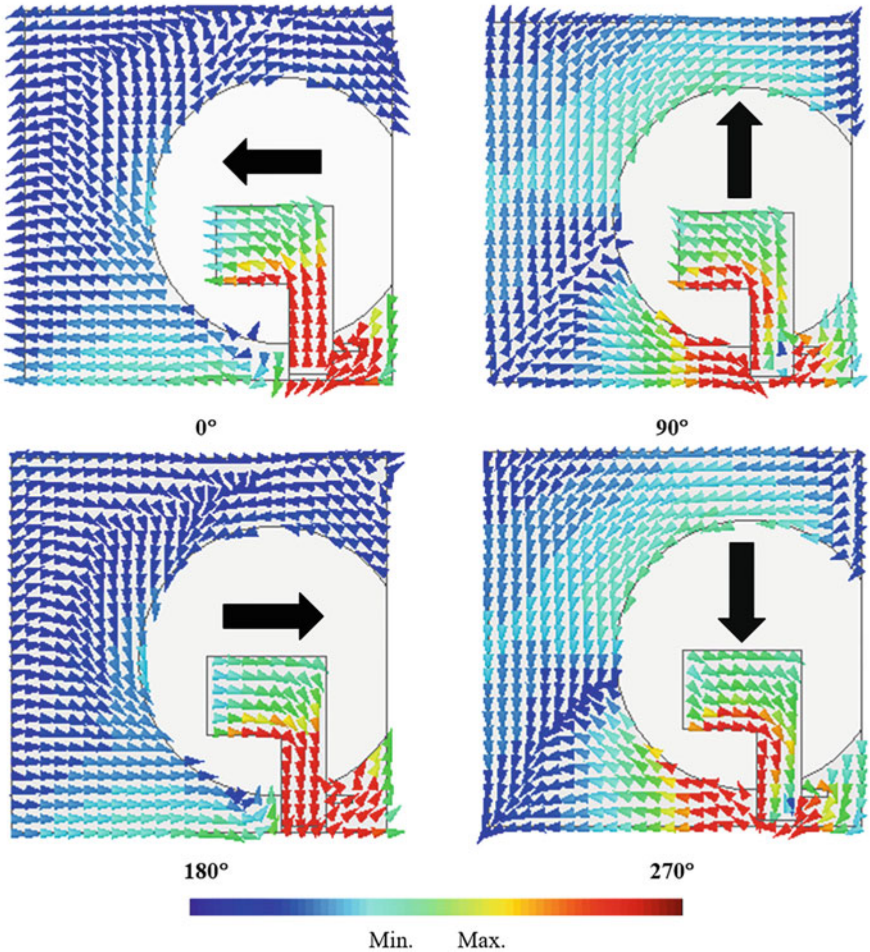

Fig. 3.33 Simulated current distributions showing LCP at 4.5 GHz [60]

at the lower end. This is because the extended ground plane has an increased electrical length and reduces the coupling between the ground plane and rectangular radiator. Also, modification in the ground plane enhances the AR bandwidth owing to increases of horizontal currents at the shorted ground plane and vertical currents at the vertical edge.

Generally, the printed CP wide slot antennas with wide intrinsic impedance bandwidth and lower sensitivity to fabrication accuracy have been particularly attractive for broad impedance and AR bandwidths [63]. In [62], Fig. 3.35, a CPW-fed broadband CP square slot UWB antenna is presented. The proposed CP antenna includes two embedded inverted L-shaped strips at the two opposite corners of the wide square slot, a pair of etched spiral slits in the ground plane, and a rectangular

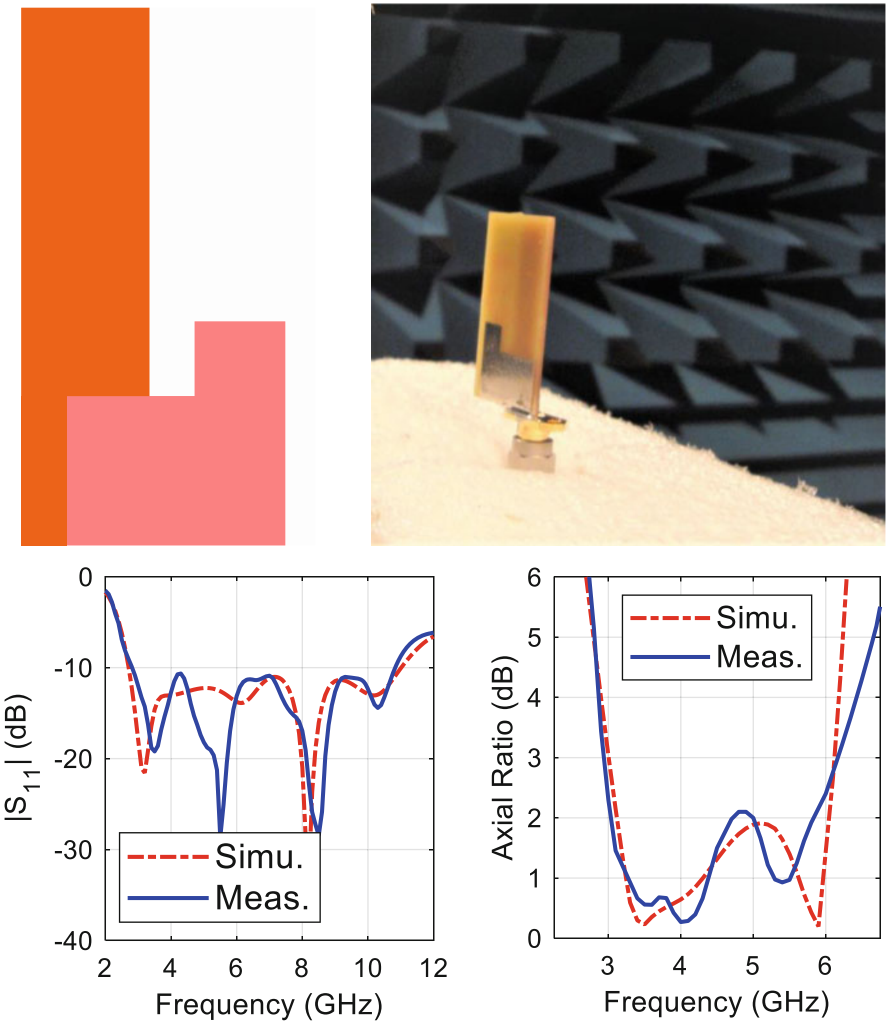

Fig. 3.34 The compact broadband CP shifted monopole UWB antenna [61]

radiator with a vertical tuning stub and a wide slit. The antenna has a low fabrication cost, a simple structure, and a total size of 20 mm × 20 mm which is printed on an FR4 dielectric with $\varepsilon_r = 4.4$, $\tan\delta = 0.02$, and a thickness of 0.8 mm. This slot antenna is excited with a 50 Ω CPW feedline with a gap of 0.2 mm and a signal line with a width of 3 mm. The proposed CP antenna exhibits a UWB impedance bandwidth from 3.45 to 12.30 GHz (112%) and a broadband AR bandwidth from 5.45 to 10.32 GHz (62%). The inverted L-shaped strips on the ground plane generate two perpendicular resonant modes with a 90° phase difference leading to a CP performance. In the following, by etching two spiral slits on the ground plane,

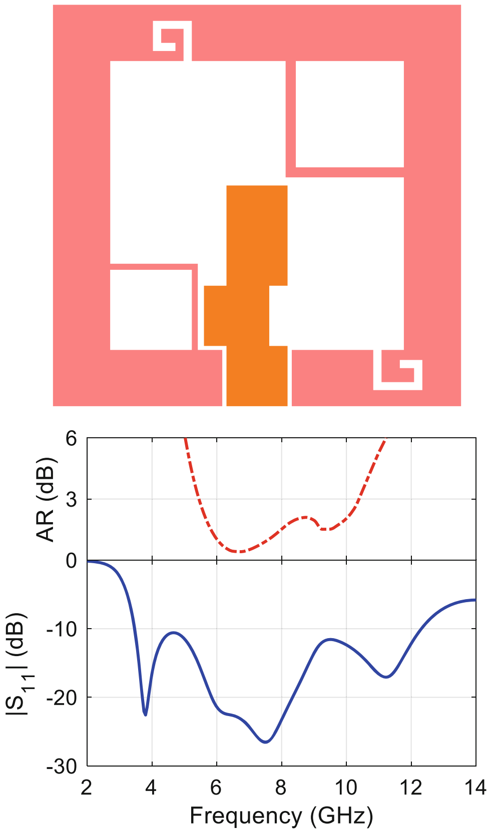

Fig. 3.35 The CPW-fed broadband CP square slot UWB antenna [62]

new paths for currents rotation are provided that significantly improve the AR bandwidth. Finally, embedding a wide slit and a marrow vertical tuning stub in the feeding line enhances the coupling between the inverted-L strip and the feedline, expanding the impedance matching, especially at the upper frequency end.

Figure 3.36 shows examples of different UWB CPW-fed slot antennas with broadband CP characteristics. In [64], Fig. 3.36a, a broadband CPW-fed CP square slot antenna for UWB applications is presented. The proposed antenna consists of a rectangular patch radiator, a pair of unequal-size inverted L-strips around two opposite corners, and a feeding line with a tuning slit and a vertical tuning stub. This antenna has a total area of 60 mm × 60 mm and is printed on low-cost FR4 dielectric with permittivity of 4.4, loss tangent of 0.02, and a thickness of 0.8 mm. The proposed broadband CP antenna operates over the impedance bandwidth of 2.67–13 GHz (132%) and AR bandwidth of 4.9–6.9 GHz (32.2%). Likewise, in Fig. 3.36b at [65], a broadband CPW-fed CP square slot antenna with three inverted-L strips around the corners of the slot is introduced. The proposed antenna has dimensions of 60 mm × 60 mm that is etched on an FR4 substrate with $\varepsilon_r = 4.4$, $\tan\delta = 0.02$, and a thickness of 0.8 mm. The results show an impedance bandwidth

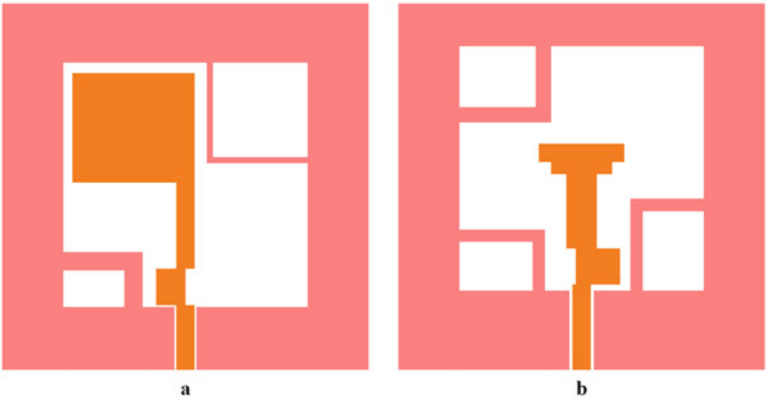

Fig. 3.36 Broadband CP characteristic with different UWB CPW-fed slot antennas: (**a**) [64], (**b**) [65]

of 2–7 GHz (110%) and an AR bandwidth of 2.03–5.12 GHz (86%). Broadband CP performance is mainly related to the three embedded inverted-L strips in the corners of the square slot.

3.6 Reconfigurable UWB Antennas

Nowadays, increasing demand for spectrum utilization of adaptive and smart wireless products in different regions of the world have led to the significant development of printed reconfigurable antennas with efficient power consumption, system versatility and flexibility in different standards, and reduces antenna size with high potential for a software-defined radio, cognitive radio (CR), and MIMO applications [66]. Typically, a reconfigurable antenna can realize the desired performances with various types of switches like p-i-n or varactor diodes or microelectromechanical systems (MEMS). Reconfigurable antennas, according to their functionalities can be classified as a combination of the reconfigurable frequency with rejection or selecting multiple bands to interference elimination or multiband applications, reconfigurable patterns with altering the shape of the pattern to the desired radiation directions, and reconfigurable polarization with polarization switching to multipath fading reduction. Reconfigurable techniques have been widely implemented in printed UWB antennas to realize switchable notch-bands and cognitive radio communications. UWB antenna with reconfigurable rejection frequency bands can switch between a conventional full UWB spectrum and a band-notched UWB antenna to enhance the UWB system's performances and effectively utilize the UWB spectrum. In the CR-UWB communications, a sensing UWB antenna is used to identify the free channels and a reconfigurable narrowband antenna is used for communicating.

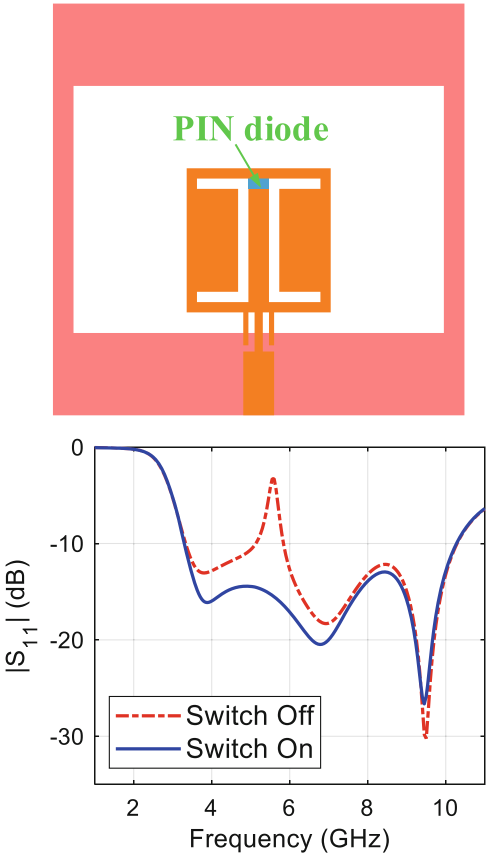

Fig. 3.37 The reconfigurable UWB slot antenna with the switchable band-notch performance [67]

A rectangular printed UWB slot antenna with switchable band-notched performance is presented in [67]. The proposed reconfigurable UWB slot antenna is illustrated in Fig. 3.37. This symmetrical antenna includes a square slot, a square radiating patch, two modified L-shaped slits on the feedline to broaden impedance bandwidth at the upper frequency band and a pi-shaped slot integrated with a p-in diode to switch of rejection band electronically. In the proposed antenna, to obtain a switchable rejection band, a p-i-n diode is used along with the slot. In the forward bias of the p-i-n diode, the pi-shaped slot is changed to two C-shaped slots which are created additional resonances, results in enhanced impedance bandwidth, especially at the upper end, and therefore full coverage of the UWB spectrum in the frequency band of 3.3 to over 10.25 GHz. When the p-i-n diode is OFF, this slot antenna operates as a band-notched antenna to eliminate narrowband signals' interferences in the range of 5.15–5.85 GHz. In the simulation, to implement the OFF state of the switch, a lumped capacitor with 0.17 pF and to simulate the ON state, a lumped resistor with 2.1 Ω is used. The proposed reconfigurable antenna has a symmetrical structure, stable omnidirectional pattern, and fast switching. The

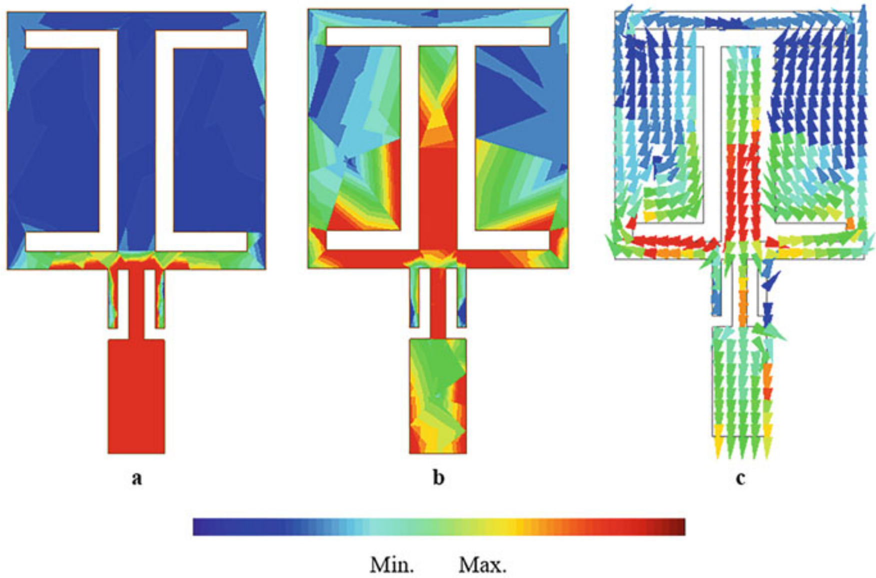

Fig. 3.38 Simulated current distributions on the patch radiator at 5.5 GHz: (**a**) switch-ON, (**b**) and (**c**) switch-OFF

designed slot antenna has a compact area of 20 mm × 20 mm which is etched on an FR4 dielectric with $\varepsilon_r = 4.4$, $\tan\delta = 0.02$, and a thickness of 0.8 mm.

Figure 3.38 shows the simulated current distributions on the patch radiator at 5.5 GHz in On and Off states. As observed in Fig. 3.38a, at ON state, the current density is mostly intensified on the lower edges of the square radiating patch, and therefore the antenna matching changes at this frequency since the patch resonances. In Fig. 3.38b, c, at the rejection frequency band, at the OFF state, the maximum current density mainly conducting along the edges of the slot and they have oppositely directed between the slot edges. Therefore, at this frequency, the antenna impedance changes and radiation fields cancel out with high attenuation.

Figure 3.39 illustrates examples of different UWB antennas with reconfigurable performances. In [68], Fig. 3.39a, an incorporated dual port single substrate UWB and a reconfigurable narrowband antenna are presented for cognitive radio applications. The proposed CR antenna includes a UWB antenna for sensing and a tunable narrowband slot resonator for communicating that is printed on a unique dielectric. The designed CR antenna includes an elliptical disc monopole, a partial ellipse ground plane, a stepped feedline, and a narrow H-shaped slot resonator with a symmetric tub inside the slot to reduce the electrical length of the slot and isolation enhancement between two antennas. The embedded slot is loaded by a varactor diode to tune the communication band. The H-shaped slot is excited by a shifted microstrip line with a reconfigurable frequency band in the range of 5–6 GHz. The presented antenna is etched on a 40 mm × 36 mm RO4350B substrate

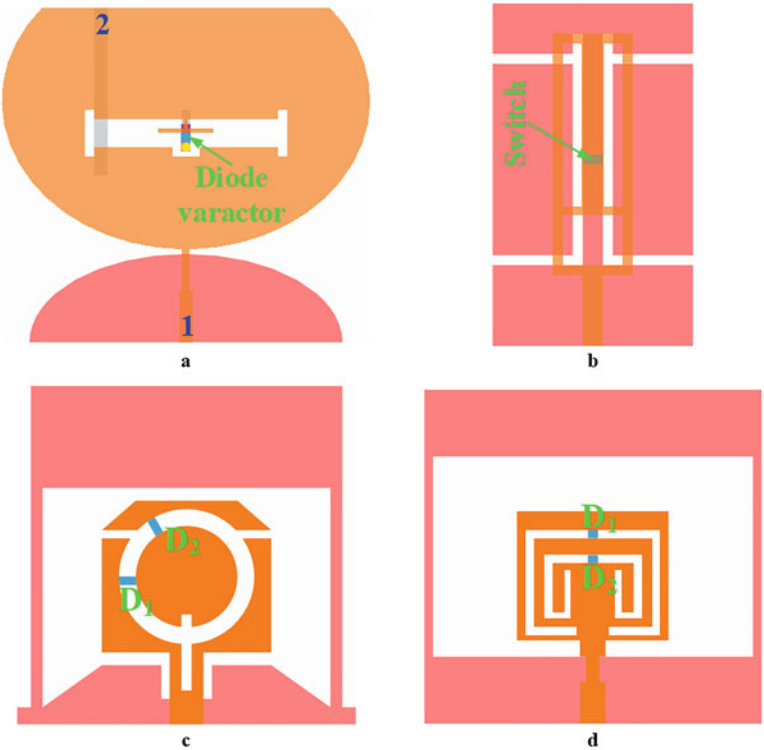

Fig. 3.39 Different UWB antennas with reconfigurable performances: (**a**) [68], (**b**) [69], (**c**) [70], (**d**) [71]

with $\varepsilon_r = 3.48$, tan$\delta = 0.0037$, and a thickness of 0.662 mm. The results show a UWB sensing band from 3.3 to 11 GHz, a tunable communication band from 5 to 6 GHz with around 220 MHz bandwidth at each biasing voltage and isolation of more than 20 dB in most of the band. In [69], Fig. 3.39b, a reconfigurable antenna with simultaneously single and dual-band performances is presented. The proposed antenna consists of a simple rectangular ring patch with an embedded T-shaped stub, two modified open U-shaped slots in the two opposite sides of the ground plane, and a narrow slot as a switch into the current path on the ground plane. The designed antenna has a total size of 20 mm $\times$ 34 mm $\times$ 1 mm on an FR4 dielectric with $\varepsilon_r = 4.4$ and tan$\delta = 0.02$. The measured results indicate dual-band characteristics of 1.38–3.98 GHz (97%) and 5.15–6.2 GHz (18.5%) for ON state, and a single wide bandwidth of 3.55–6.15 GHz (53%) for OFF state.

In [70], Fig. 3.39c, with two p-i-n diodes, a printed UWB slot antenna with reconfigurable single and dual band-notch performances is proposed. The proposed microstrip-fed slot antenna includes a modified rectangular patch radiator etched with a circular and two narrow rectangular slots, a fork-shape feeding line, a ground plane with a wide rectangular slot, two symmetrical triangular slits, and a rectangular slit under the feedline. To produce reconfigurable single and dual band-rejection characteristics, two p-i-n diodes are integrated across the circular slot. The proposed antenna has a small size of 20 mm $\times$ 20 mm, simple structure, sharp functionality in notched band, a possibility to adjust the bandwidth and frequency position of notch-bands, and a low-cost FR4 dielectric with $\varepsilon_r = 4.4$ and a thickness of 0.8 mm. the results show a UWB bandwidth from 3.12 to 12.51 GHz (12%) and a switchable single rejection band of 3.12–3.84 GHz (21%) and 5–6.07 GHz (19%) when diodes D_1 and D_2 are respectively on. Besides, dual-rejection bands of 3.12–3.82 GHz (20%) and 4.9–6.06 (21%) are presented when both diodes D_1 and D_2 are simultaneously on. In [71], Fig. 3.39d, a compact UWB slot antenna with reconfigurable single and dual-notch performances is presented. The introduced antenna includes a square patch radiator, a stepped microstrip feedline, and a ground plane etched with a wide rectangular slot. By cutting two folded narrow slots on the radiating patch and then integrated two p-i-n diodes D_1 and D_2 across these slots, reconfigurable single and dual band-rejection functions are obtained. The proposed antenna has a compact area of 20 mm $\times$ 20 mm that is etched on an FR4 dielectric with $\varepsilon_r = 4.4$, $\tan\delta = 0.02$, and a thickness of 0.8 mm. The results show a UWB bandwidth from 3.7 to 10.7 GHz, when both diodes D_1 and D_2 are concurrently OFF, a single band-rejection performance at 3.15–3.85 GHz when D_1 is OFF and D_2 is ON, and a single band-notch function at 5.43–6.16 GHz when D_1 is OFF and D_2 is ON, and a dual band-notch characteristics at 3.2–4.2 GHz and 5.5–6.15 GHz when both diodes of D_1 and D_2 are simultaneously ON.

3.7 UWB MIMO Diversity Antennas

MIMO antennas with compact size and different types of directivity like frequency, pattern, spatial, and polarization are used to mitigate the effects of multipath fading due to reflection, diffraction, scattering, and variable frequency shifts of propagation signals in dynamic and dense environments with a dynamically increasing number of application and users which results in improved the signal-noise-ratio, accuracy, data rate, power level, energy-saving and reliability of wireless communications [72]. In MIMO communications, a combination of several antennas are used in the transmitter-receiver system. In contrast, in the conventional ones, there is only one antenna at a time. By intelligently combining-selecting the received signals from various independent antenna elements with different fading properties, the strength of the signal at the receiver can be improved. Using MIMO techniques in UWB systems with minimal transmission power, the communication range coverage can be extended. Recently, various designs have been introduced to meet the necessary criteria in MIMO systems, like field correlation, isolation, and compactness. The distance between antenna elements in the MIMO system is still challenging due to the minimal area inside a compact closely packed portable device. The near wavelength degrades the field correlation and isolation by the large surface waves and space radiations. Hence, various methods like slots or parasitic elements have been developed to design miniaturized MIMO antennas with a wideband frequency range. The most common way to create polarization diversity in MIMO antennas is to use identical elements perpendicular to each other.

To evaluate the performances of a MIMO system, some additional parameters must be cleared, such as isolation and envelope correlation coefficient (ECC) between different antenna elements [73]. The ECC indicates how much the receive signals in different elements are isolate or independent from each other. The ECC between two antenna element of a MIMO diversity system, based on far-field radiations, is calculated as

$$\rho_{r12} = \frac{\left| \iint\limits_{4\pi} \overrightarrow{F}_1(\theta,\varphi) \times \overrightarrow{F}_2\left(\theta,\varphi\right) d\Omega \right|^2}{\iint\limits_{4\pi} \left| \overrightarrow{F}_1(\theta,\varphi) \right|^2 d\Omega \iint\limits_{4\pi} \left| \overrightarrow{F}_2(\theta,\varphi) \right|^2 d\Omega} \tag{3.1}$$

In Eq. (3.1), θ and φ show the spherical elevation and azimuth angles, respectively. The $\overrightarrow{F}_1(\theta,\varphi)$ or $\overrightarrow{F}_2(\theta,\varphi)$ is a vector function for electric far-field in spherical coordinates that includes the shape, polarization, and relative phase information of full spherical radiation pattern. For an ideal MIMO system, if the radiation patterns of two different antennas are the same, the ECC would be $\rho_r = 1$. Conversely, if they are completely independent, the ECC would be zero, such as when one antenna is perfectly vertical-polarized, and the other one is perfectly horizontal-polarized, or when one antenna completely radiates to the top direction and the other one completely radiates to the bottom direction. Typically, a practical MIMO antenna with pretty good directivity performance requires an ECC lower than 0.5. Due to the reciprocity theory, the ECC of a MIMO diversity system can be obtained from the calibrated S-parameters by using the following formula

$$\rho_{i12} = \frac{\left|S_{11}^* S_{12} + S_{21}^* S_{22}\right|^2}{\left(1 - |S_{11}|^2 - |S_{21}|^2\right)\left(1 - |S_{22}|^2 - |S_{12}|^2\right)} \tag{3.2}$$

The S_{21} indicates the isolation between two antenna elements that typically should be more than 15 dB. In practice, Eq. (3.2) is a simple, inexpensive, fast, easy, and wideband method to obtain the ECC that relies on the isolation and input impedances of the antennas. Nevertheless, it is assumed that the MIMO antenna works with 100% radiation efficiency, radiates in a uniform multipath environment, and has significant low dielectric and conductor losses [74]. Therefore, the ECC calculation using Eq. (3.1) with far-field patterns is more reliable and advised by most designers.

In [75], Fig. 3.40, a double band-notched UWB MIMO antenna with a small size of 22 mm × 42 mm is presented for polarization diversity applications. The MIMO

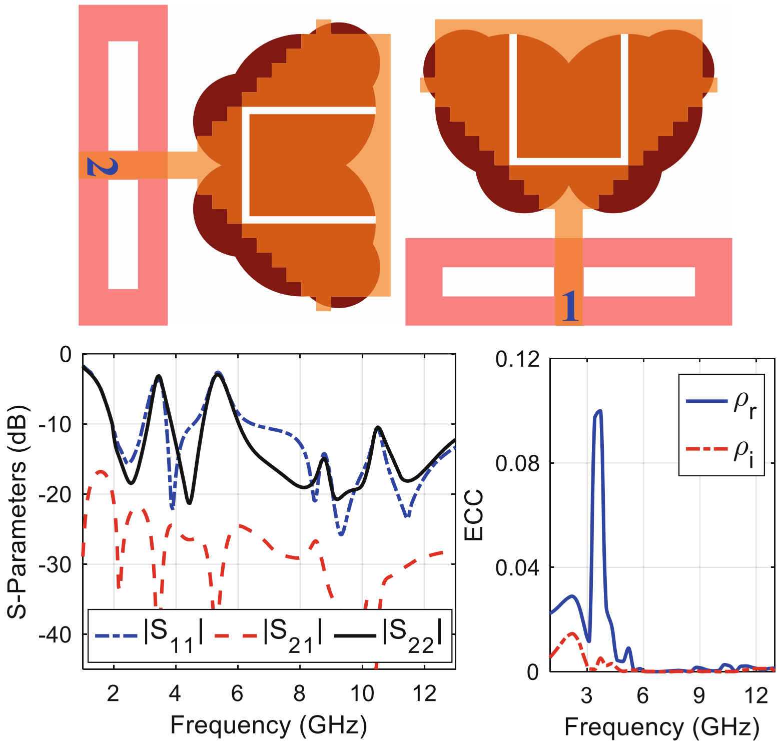

Fig. 3.40 The double band-notched UWB MIMO antenna with polarization diversity performance [75]

antenna includes two identical elements that are placed orthogonally to attain polarization diversity and good isolation between the two input ports. The proposed double band-notched UWB MIMO antenna is designed on an FR4 substrate with $\varepsilon_r = 4.4$, tanδ of 0.02, and a thickness of 1 mm. The basic antenna element is presented in [56], consisting of a triangular staircase radiation patch, a 50 Ω microstrip feedline, and a ground plane with two rectangular slots. To create only one band-rejection function at 4.9–6 GHz, a butterfly-shaped parasitic element is embedded on the substrate's backside. An additional notch-band is obtained at 3.1–3.8 GHz by etching a U-shaped slot in the patch radiator. It can be observed that the proposed UWB MIMO antenna with polarization diversity has an isolation of more than 20 dB. Furthermore, the antenna's ECC is below 0.04 over the full operating bandwidth that shows a good diversity performance. The proposed MIMO antenna has an omnidirectional radiation pattern, stable gain, low-profile, and orthogonal polarization that is practically suitable for antenna diversity.

Figure 3.41 proposes a high isolation UWB MIMO antenna with spatial diversity. The presented MIMO antenna includes two simple conventional circular monopole antennas with a truncated rectangular ground plane. It shows isolation of more than

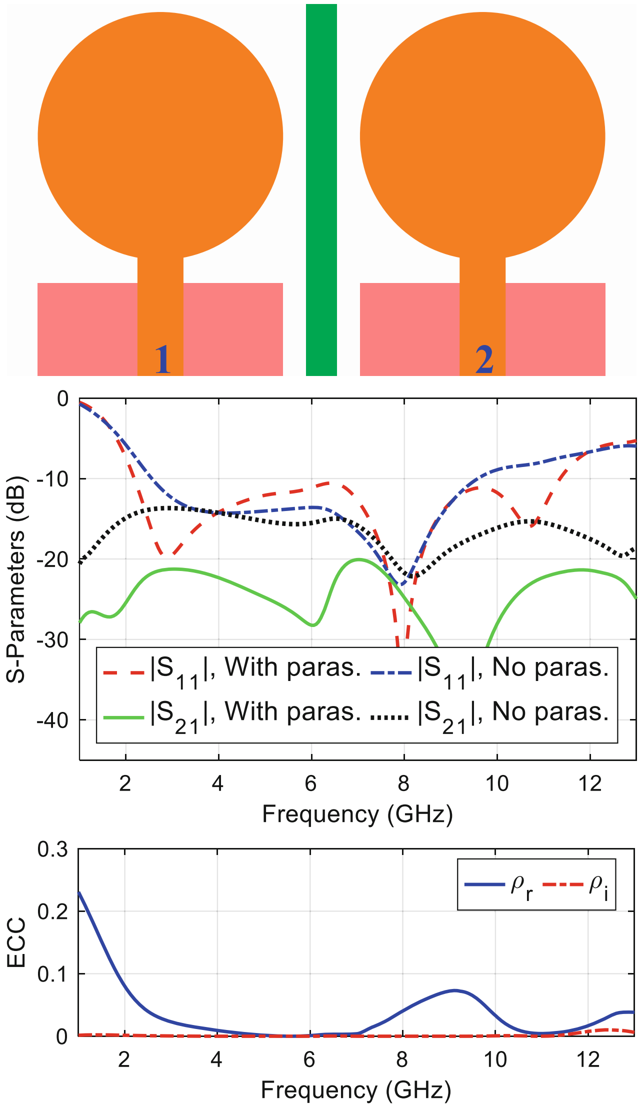

Fig. 3.41 High isolation UWB MIMO antenna with spatial diversity performance

20 dB and an impedance bandwidth over the frequency range of 2.13–11.36 GHz. The MIMO antenna has a compact area of 24 mm × 41 mm. A narrow rectangular parasitic strip with a width of 2 mm is embedded on the substrate back layer to improve the wideband isolation between antenna elements. The low-cost substrate used is FR4 with $\varepsilon_r = 4.4$, $\tan\delta = 0.02$, and a thickness of 1.6 mm.

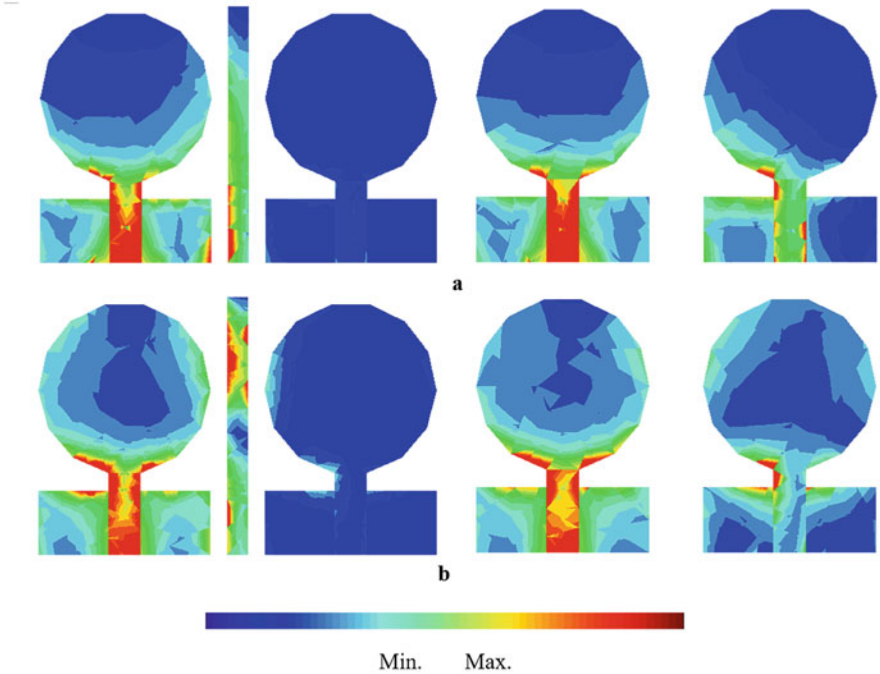

Fig. 3.42 Simulated current distributions with excitation of port 1 at: (**a**) 4 GHz, (**b**) 8 GHz

Figure 3.41 shows when the rectangular isolator is present, a UWB high isolation performance with more than 20 dB over the full UWB bandwidth is obtained. The parasitic strip between two antennas acted as a reflector and separated the circular monopoles' radiation patterns and hence reduces the mutual coupling [76]. Also, it can be observed that the embedded rectangular strip increases the impedance matching and operating bandwidth. The parasitic element introduces more resonances and lengthens the surface waves patch. Therefore, the matching will be enhanced and the operating bandwidth will be extended, especially at the lower end. The calculated ECC in Fig. 3.41 is lower than 0.08 which confirms that the presented UWB MIMO antenna is the right choice for diversity systems. Figure 3.42 illustrates the simulated currents distributions with and without narrow rectangular strip at different frequencies when only port 1 is excited and port 2 is terminated with a 50 Ω wideband matching. The distributions show how the parasitic element reduces the coupling between two monopole antennas. In Fig. 3.42a at 4 GHz, it can be observed the flow of current from port 1 to port 2 is blocked by the rectangular strip and there is a very negligible current on the right antenna. Therefore it increases the isolation. In Fig. 3.42b, at 8 GHz, most of the radiation pattern of antenna 1 is coupled to the parasitic strip and trapped in it indicating the presented isolator structure can effectively reduce mutual coupling between the patch radiators.

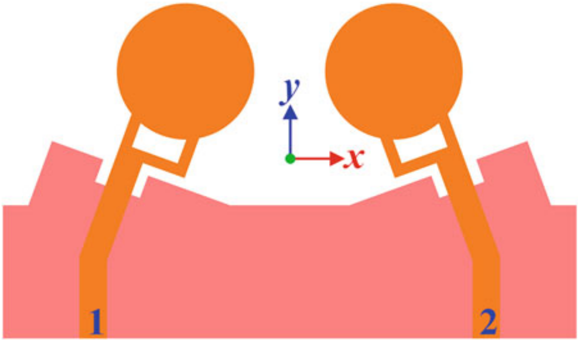

Fig. 3.43 The UWB MIMO antenna with pattern diversity performance [77]

In [77], Fig. 3.43, a UWB MIMO antenna with pattern diversity performance is presented. The pattern diversity with broad space coverage, multipath fading, and interference alleviation, required less area and antenna elements, the directive antennas with various independent beam patterns connected to channels with different strengths. The antenna is printed on a low cost 1.6 mm FR4 substrate with $\varepsilon_r = 4.4$, tan$\delta = 0.02$, and a size of 50 mm $\times$ 60 mm. The elements are excited by 3 mm width microstrip lines with an impedance of 50 Ω. The proposed UWB MIMO antenna includes two wrench-shaped feeding monopole antennas with a unidirectional pattern that are situated with a 20° rotation angle to adjust the radiation of the main beam. The wrench-shaped feedline unidirectional radiation UWB monopole antenna was presented in [78] which can significantly increase the directivity of pattern diversity antenna compared to a conventional monopole antenna with Omni or quasi-Omni radiations. Wrench-shaped feeding structure introduced vertical currents and reduced horizontal currents which were derived from the study of characteristics modes theory [78]. In the proposed diversity antenna, modification and shaping of the ground plane suppresses the back-lobe radiation, improving the impedance matching, antenna bandwidth, and port isolation. The proposed pattern diversity antenna can radiate waves on the two sides with in-phase excitation and on the forward side with 180° out-of-phase excitation.

Figure 3.44 shows the working principle of the proposed UWB pattern diversity antenna. The terms $E_{1/2}$ and $k_{1/2}$ represent the electric field and wave propagation direction, respectively. As shown in Fig. 3.44a, when port 1 and port 2 are excited with equal magnitude and in-phase signals, the diversity antenna will radiate in two sides of $\pm x$ directions with nulls in the $\pm y$ axes. It is due to the cancelation of the x-component of the total electric field. Therefore, the total electric field will be y-polarized. On the other hand, with equal amplitude and 180° out-of-phase signals on ports 1 and 2, the y-component of the total electric field will be canceled. Hence, the proposed pattern diversity antenna will radiate the x-polarized electric field with a maximum along the y-axis. Figure 3.45 shows the simulated radiation pattern of the proposed UWB pattern diversity antenna in XY-plane at different frequencies. It shows the proposed antenna presents a stable pattern diversity performance

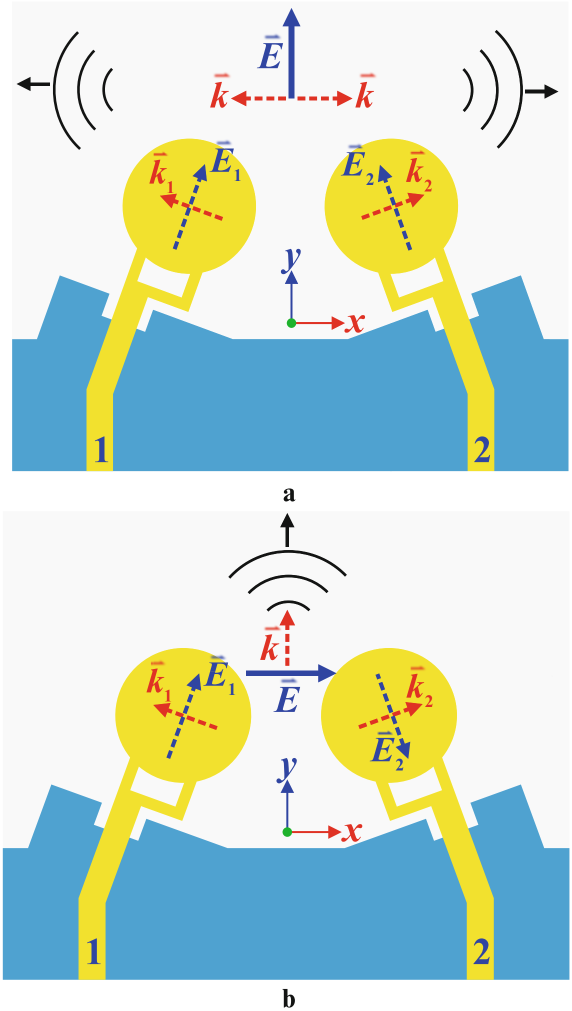

Fig. 3.44 Principle of the proposed UWB pattern diversity antenna: (**a**) in-phase excitation, (**b**) 180° out-of-phase excitation [77]

across the frequency band. Finally, the presented pattern diversity antenna with printed structure, wide bandwidth, compact size, simple design, lightweight, stable main beam, and low levels of side-lobe, back-lobe, and cross-polarization can widely use in cognitive radio, radar transceivers, smart arrays, base-station, satellite communications, and monopulse targeting-tracking systems.

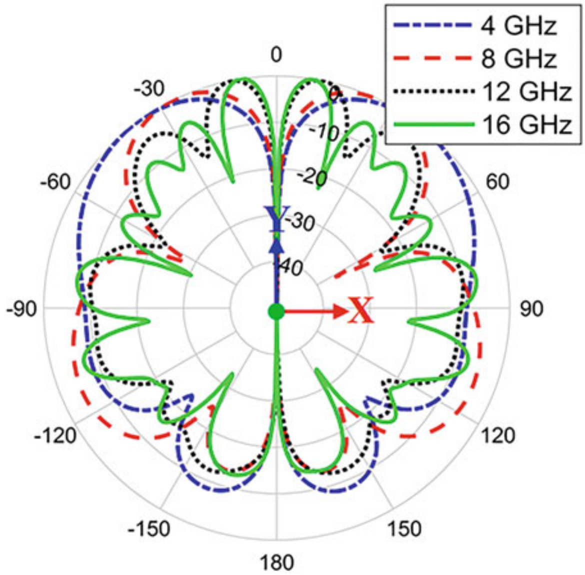

a

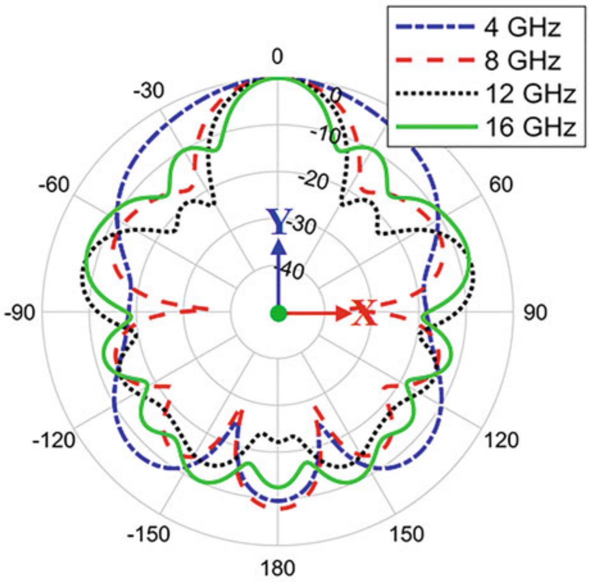

b

Fig. 3.45 Simulated radiation patterns of the proposed UWB pattern diversity antenna with: (**a**) in-phase and (**b**) 180° out-of-phase feeding cases [77]

3.8 Conclusion and Future Directions

In this chapter, recent developments of printed UWB antennas have been studied. Different types of printed antennas with UWB performances have been investigated. The results show that the printed UWB antennas have a simple structure, a low fabrication cost, and a compact size with high portability and mobility. Several directions can be developed in the future progress of UWB antennas, such as compact UWB directional antennas for interferences sources detection, UWB antenna arrays with high directional radiation patterns, UWB pattern diversity to alleviate the multipath fading effects, and wearable antennas with flexible and textile structures for wireless body area networks.

References

1. M. A. Matin (ed.), *Ultra Wideband Communications: Novel Trends-Antennas and Propagation* (BoD–Books on Demand, Norderstedt, Germany, 2011)
2. H.G. Schantz, *The Art and Science of Ultrawideband Antennas* (Artech House, Norwood, MA, 2015)
3. B. Lembrikov (ed.), *Ultra Wideband* (BoD–Books on Demand, Norderstedt, Germany, 2010)
4. G.M. Galvan-Tejada, M.A. Peyrot-Solis, H.J. Aguilar, *Ultra Wideband Antennas: Design, Methodologies, and Performance* (CRC Press, Boca Raton, FL, 2017)
5. Z.N. Chen, X. Qing, S.P. See, Printed UWB antennas. *Microstrip and Printed Antennas*, p. 305 (2011)
6. Y. Li, W. Li, Q. Ye, R. Mittra, A survey of planar ultra-wideband antenna designs and their applications, in *Forum for Electromagnetic Research Methods and Application Technologies (FERMAT)*, vol. 1, (2014), pp. 1–16
7. M. Akbari, M. Koohestani, C. Ghobadi, J. Nourinia, A new compact planar UWB monopole antenna. Int. J. RF Microw. Comput. Aided Eng. **21**(2), 216–220 (2011)
8. A. Kamalvand, C. Ghobadi, J. Nourinia, M. Ojaroudi, N. Ojaroudi, Omni-directional/multi-resonance CPW-fed small slot antenna for UWB applications. Appl. Comput. Electromagn. Soc. J. **28**(9) (2013)
9. M. Ojaroudi, C. Ghobadi, J. Nourinia, Small square monopole antenna with inverted T-shaped notch in the ground plane for UWB application. IEEE Antennas Wirel. Propag. Lett. **8**, 728–731 (2009)
10. M. Moosazadeh, C. Ghobadi, M. Dousti, Small monopole antenna with checkered-shaped patch for UWB application. IEEE Antennas Wirel. Propag. Lett. **9**, 1014–1017 (2010)
11. M. Ojaroudi, H. Ebrahimian, C. Ghobadi, J. Nourinia, Small microstrip-fed printed monopole antenna for UWB application. Microw. Opt. Technol. Lett. **52**(8), 1756–1761 (2010)
12. H.J. Lak, C. Ghobadi, J. Nourinia, A novel ultra-wideband monopole antenna with band-stop characteristic. Wirel. Eng. Technol. **2**, 235–239 (2011)
13. R. Emadian, M. Mirmozafari, C. Ghobadi, J. Nourinia, Bandwidth enhancement of dual band-notched circle-like slot antenna. Electron. Lett. **48**(7), 356–357 (2012)
14. T. Saeidi, I. Ismail, W.P. Wen, A.R. Alhawari, A. Mohammadi, Ultra-wideband antennas for wireless communication applications. Int. J. Antennas Propag. **2019** (2019)
15. A. Ghobadi, C. Ghobadi, J. Nourinia, A novel band-notched planar monopole antenna for ultrawideband applications. IEEE Antennas Wirel. Propag. Lett. **9**, 608–611 (2010)
16. R. Zaker, C. Ghobadi, J. Nourinia, A modified microstrip-fed two-step tapered monopole antenna for UWB and WLAN applications. Prog. Electromagn. Res. **77**, 137–148 (2007)

17. A. Siahcheshm, J. Nourinia, Y. Zehforoosh, B. Mohammadi, A compact modified triangular CPW-fed antenna with multioctave bandwidth. Microw. Opt. Technol. Lett. **57**(1), 69–72 (2015)
18. S. Bashiri, C. Ghobadi, J. Nourinia, M. Ojaroudi, CPW-fed slot-like sleeve-monopole antenna with bandwidth enhancement for UWB wireless communications. Appl. Comput. Electromagn. Soc. J. **28**(9) (2013)
19. A. Siahcheshm, C. Ghobadi, J. Nourinia, Design of a quasi-isosceles triangle slot antenna for UWB applications. J. Electromagn. Waves Appl. **22**(5–6), 749–757 (2008)
20. V. Sadeghi, C. Ghobadi, J. Nourinia, Design of UWB semi-circle-like slot antenna with controllable band-notch function. Electron. Lett. **45**(25), 1282–1283 (2009)
21. M. Ojaroudi, G. Kohneshahri, J. Noory, Small modified monopole antenna for UWB application. IET Microw. Antennas Propag. **3**(5), 863–869 (2009)
22. M. Akbari, M. Koohestani, C. Ghobadi, J. Nourinia, Compact CPW-fed printed monopole antenna with super-wideband performance. Microw. Opt. Technol. Lett. **53**(7), 1481–1483 (2011)
23. R. Cicchetti, E. Miozzi, O. Testa, Wideband and UWB antennas for wireless applications: A comprehensive review. Int. J. Antennas Propag. **2017** (2017)
24. H.E. Zadeh, C. Ghobadi, J. Nourinia, Circular multifractal UWB monopole antenna. IEICE Electron. Express **7**(10), 717–721 (2010)
25. J. Pourahmadazar, C. Ghobadi, J. Nourinia, Novel modified pythagorean tree fractal monopole antennas for UWB applications. IEEE Antennas Wirel. Propag. Lett. **10**, 484–487 (2011)
26. V. Waladi, N. Mohammadi, Y. Zehforoosh, A. Habashi, J. Nourinia, A novel modified star-triangular fractal (MSTF) monopole antenna for super-wideband applications. IEEE Antennas Wirel. Propag. Lett. **12**, 651–654 (2013)
27. A. Karmakar, Fractal antennas and arrays: A review and recent developments. Int. J. Microw. Wirel. Technol. **13**, 1–25 (2020)
28. M. Fallahpour, R. Zoughi, Antenna miniaturization techniques: A review of topology- and material-based methods. IEEE Antennas Propag. Mag. **60**(1), 38–50 (2017)
29. M. Ghahremani, C. Ghobadi, J. Nourinia, M.S. Ellis, F. Alizadeh, B. Mohammadi, Miniaturised UWB antenna with dual-band rejection of WLAN/WiMAX using slitted EBG structure. IET Microw. Antennas Propag. **13**(3), 360–366 (2018)
30. A.T. Mobashsher, A. Abbosh, Utilizing symmetry of planar ultra-wideband antennas for size reduction and enhanced performance. IEEE Antennas Propag. Mag. **57**(2), 153–166 (2015)
31. N. Farrokh-Heshmat, J. Nourinia, C. Ghobadi, Band-notched ultra-wideband printed open-slot antenna using variable on-ground slits. Electron. Lett. **45**(21), 1060–1061 (2009)
32. P.P. Shome, T. Khan, R.H. Laskar, A state-of-art review on band-notch characteristics in UWB antennas. Int. J. RF Microw. Comput. Aided Eng. **29**(2), e21518 (2019)
33. G. Kumar, R. Kumar, A survey on planar ultra-wideband antennas with band notch characteristics: Principle, design, and applications. AEU-Int. J. Electron. Commun. **109**, 76–98 (2019)
34. M. Mehranpour, J. Nourinia, C. Ghobadi, M. Ojaroudi, Dual band-notched square monopole antenna for ultrawideband applications. IEEE Antennas Wirel. Propag. Lett. **11**, 172–175 (2012)
35. M. Mirmozafari, C. Ghobadi, H. Mirhedayati, A. Rezaee, A planar UWB monopole antenna with on-ground slot band-notch performance. Appl. Comput. Electromagn. Soc. J. **28**(8) (2013)
36. R. Eshtiaghi, R. Zaker, J. Nouronia, C. Ghobadi, UWB semi-elliptical printed monopole antenna with subband rejection filter. AEU-Int. J. Electron. Commun. **64**(2), 133–141 (2010)
37. S. Mohammadi, J. Nourinia, C. Ghobadi, M. Majidzadeh, Compact CPW-fed rotated square-shaped patch slot antenna with band-notched function for UWB applications. Electron. Lett. **47**(24), 1307–1308 (2011)
38. M. Ojaroudi, C. Ghobadi, J. Nourinia, N. Ojaroudi, Ultra-wideband small square monopole antenna with dual band-notched function. Microw. Opt. Technol. Lett. **54**(2), 372–374 (2012)
39. S.R. Emadian, C. Ghobadi, J. Nourinia, A novel compact dual band-notched slot antenna for ultrawideband applications. Microw. Opt. Technol. Lett. **54**(6), 1365–1368 (2012)

40. M. Najafpur, J. Nourinia, F.A. Jazi, Design of a novel ultra-wideband semicircular printed antenna with dual-band notched characteristic. Appl. Comput. Electromagn. Soc. J. **30**(3) (2015)
41. S. Peddakrishna, T. Khan, A. De, Electromagnetic band-gap structured printed antennas: A feature-oriented survey. Int. J. RF Microw. Comput. Aided Eng. **27**(7), e21110 (2017)
42. S.R. Emadian, J. Ahmadi-Shokouh, C. Ghobadi, J. Nourinia, Study on frequency and impulse response of novel triple band notched UWB antenna in indoor environments. AEU-Int. J. Electron. Commun. **96**, 93–106 (2018)
43. R. Zaker, C. Ghobadi, J. Nourinia, Novel modified UWB planar monopole antenna with variable frequency band-notch function. IEEE Antennas Wirel. Propag. Lett. **7**, 112–114 (2008)
44. R. Eshtiaghi, J. Nourinia, C. Ghobadi, Electromagnetically coupled band-notched elliptical monopole antenna for UWB applications. IEEE Trans. Antennas Propag. **58**(4), 1397–1402 (2010)
45. M. Rostamzadeh, S. Mohamadi, J. Nourinia, C. Ghobadi, M. Ojaroudi, Square monopole antenna for UWB applications with novel rod-shaped parasitic structures and novel V-shaped slots in the ground plane. IEEE Antennas Wirel. Propag. Lett. **11**, 446–449 (2012)
46. R. Rouhi, C. Ghobadi, J. Nourinia, M. Ojaroudi, Microstrip-fed small square monopole antenna for UWB application with variable band-notched function. Microw. Opt. Technol. Lett. **52**(9), 2065–2069 (2010)
47. H. Mardani, C. Ghobadi, J. Nourinia, A simple compact monopole antenna with variable single- and double-filtering function for UWB applications. IEEE Antennas Wirel. Propag. Lett. **9**, 1076–1079 (2010)
48. S.R. Emadian, C. Ghobadi, J. Nourinia, M.H. Mirmozafari, J. Pourahmadazar, Bandwidth enhancement of CPW-fed circle-like slot antenna with dual band-notched characteristic. IEEE Antennas Wirel. Propag. Lett. **11**, 543–546 (2012)
49. R. Zaker, C. Ghobadi, J. Nourinia, Bandwidth enhancement of novel compact single and dual band-notched printed monopole antenna with a pair of L-shaped slots. IEEE Trans. Antennas Propag. **57**(12), 3978–3983 (2009)
50. J. Pourahmadazar, C. Ghobadi, J. Nourinia, H. Shirzad, Multiband ring fractal monopole antenna for mobile devices. IEEE Antennas Wirel. Propag. Lett. **9**, 863–866 (2010)
51. H. Karimi, C. Ghobadi, J. Nourinia, M. Ojaroudi, Enhanced bandwidth small E-shaped monopole antenna for UWB applications with variable frequency band-notch function. Microw. Opt. Technol. Lett. **54**(1), 267–271 (2012)
52. M. Ojaroudi, G. Ghanbari, N. Ojaroudi, C. Ghobadi, Small square monopole antenna for UWB applications with variable frequency band-notch function. IEEE Antennas Wirel. Propag. Lett. **8**, 1061–1064 (2009)
53. H. Shahsavari, J. Nourinia, H. Shirzad, M. Shokri, S. Asiaban, Z. Amiri, B. Virdee, Compact planar super-wideband antenna with band-notched function. Appl. Comput. Electromagn. Soc. J. **28**(7) (2013)
54. A. Valizade, C. Ghobadi, J. Nourinia, N. Ojaroudi, M. Ojaroudi, Band-notch slot antenna with enhanced bandwidth by using ω-shaped strips protruded inside rectangular slots for UWB applications. Appl. Comput. Electromagn. Soc. J. **27**(10) (2012)
55. S.R. Emadian, J. Ahmadi-Shokouh, A. Raisi, C. Ghobadi, J. Nourinia, Time-domain properties of dual-band-notched circle-like slot antenna in indoor environments. Electron. Lett. **55**(1), 10–12 (2018)
56. P. Beigi, J. Nourinia, B. Mohammadi, A. Valizade, Bandwidth enhancement of small square monopole antenna with dual band notch characteristics using u-shaped slot and butterfly shape parasitic element on backplane for UWB applications. Appl. Comput. Electromagn. Soc. J. **30**(1) (2015)
57. S. Hoseyni, J. Nourinia, C. Ghobadi, S. Masumina, B. Mohammadi, A compact design and new structure of monopole antenna with dual band notch characteristic for UWB applications. Appl. Comput. Electromagn. Soc. J. **31**(7) (2016)

58. S.R. Ebadzadeh, J. Nourinia, C. Ghobadi, Extremely UWB/multiresonance monopole antenna with dual band-notched function. Microw. Opt. Technol. Lett. **56**(11), 2628–2630 (2014)
59. U. Banerjee, A. Karmakar, A. Saha, A review on circularly polarized antennas, trends and advances. Int. J. Microw. Wirel. Technol. **12**(9), 922–943 (2020)
60. M.S. Ellis, F.B. Effah, A.R. Ahmed, J.J. Kponyo, J. Nourinia, C. Ghobadi, B. Mohammadi, Asymmetric circularly polarized open-slot antenna. Int. J. RF Microw. Comput. Aided Eng. **30**(5), e22141 (2020)
61. M.S. Ellis, A.R. Ahmed, J.J. Kponyo, F.B. Effah, J. Nourinia, C. Ghobadi, B. Mohammadi, Compact broadband circularly polarized printed antenna with a shifted monopole and modified ground plane. J. Instrum. **14**(11), P11026 (2019)
62. P. Sadeghi, J. Nourinia, C. Ghobadi, Square slot antenna with two spiral slots loaded for broadband circular polarisation. Electron. Lett. **52**(10), 787–788 (2016)
63. P. Sadeghi, J. Nourinia, C. Ghobadi, Slotting into place. Electron. Lett. **52**(10) (2016)
64. J. Pourahmadazar, C. Ghobadi, J. Nourinia, N. Felegari, H. Shirzad, Broadband CPW-fed circularly polarized square slot antenna with inverted-L strips for UWB applications. IEEE Antennas Wirel. Propag. Lett. **10**, 369–372 (2011)
65. N. Felegari, J. Nourinia, C. Ghobadi, J. Pourahmadazar, Broadband CPW-fed circularly polarized square slot antenna with three inverted-L-shape grounded strips. IEEE Antennas Wirel. Propag. Lett. **10**, 274–277 (2011)
66. C. Saha, J.Y. Siddiqui, Y.M.M. Antar, *Multifunctional Ultrawideband Antennas: Trends, Techniques and Applications* (CRC Press, Boca Raton, FL, 2019)
67. A. Valizade, C. Ghobadi, J. Nourinia, M. Ojaroudi, A novel design of reconfigurable slot antenna with switchable band notch and multiresonance functions for UWB applications. IEEE Antennas Wirel. Propag. Lett. **11**, 1166–1169 (2012)
68. E. Erfani, J. Nourinia, C. Ghobadi, M. Niroo-Jazi, T.A. Denidni, Design and implementation of an integrated UWB/reconfigurable-slot antenna for cognitive radio applications. IEEE Antennas Wirel. Propag. Lett. **11**, 77–80 (2012)
69. F. Mirzamohammadi, J. Nourinia, C. Ghobadi, A novel dual-wideband monopole-like microstrip antenna with controllable frequency response. IEEE Antennas Wirel. Propag. Lett. **11**, 289–292 (2012)
70. N. Tasouji, J. Nourinia, C. Ghobadi, F. Tofigh, A novel printed UWB slot antenna with reconfigurable band-notch characteristics. IEEE Antennas Wirel. Propag. Lett. **12**, 922–925 (2013)
71. B. Badamchi, J. Nourinia, C. Ghobadi, A.V. Shahmirzadi, Design of compact reconfigurable ultra-wideband slot antenna with switchable single/dual band notch functions. IET Microw. Antennas Propag. **8**(8), 541–548 (2014)
72. R. Yadav, L. Malviya, UWB antenna and MIMO antennas with bandwidth, band-notched, and isolation properties for high-speed data rate wireless communication: A review. Int. J. RF Microw. Comput. Aided Eng. **30**(2), e22033 (2020)
73. I. Nadeem, D.Y. Choi, Study on mutual coupling reduction technique for MIMO antennas. IEEE Access **7**, 563–586 (2018)
74. H. Li, B.K. Lau, MIMO systems and antennas for terminals, in *Handbook of Antenna Technologies*, (Springer, Singapore, 2016), pp. 2347–2388
75. V. Najari, J. Nourinia, C. Ghobadi, B. Mohammadi, A double band-notched UWB MIMO antenna, in *2017 4th Conference on Knowledge Based Engineering and Innovation (KBEI)*, (IEEE, New York, 2017), pp. 891–892
76. B. Azarm, J. Nourinia, C. Ghobadi, M. Majidzadeh, N. Hatami, On development of a MIMO antenna for coupling reduction and WiMAX suppression purposes. AEU-Int. J. Electron. Commun. **99**, 226–235 (2019)
77. S.M. Mubarak, J. Nourinia, C. Ghobadi, B. Mohammadi, Novel ultra-wideband pattern diversity antenna, in *2021 6th Conference on Knowledge Based Engineering and Innovation (KBEI)*, (IEEE, New York, 2021), pp. 131–132
78. M.S. Ellis, Z. Zhao, J. Wu, Z. Nie, Q.H. Liu, Unidirectional planar monopole ultra-wideband antenna using wrench-shaped feeding structure. Electron. Lett. **50**(9), 654–655 (2014)

Javad Nourinia received his BSc in Electrical and Electronic Engineering from Shiraz University, MSc degree in Electrical and Telecommunication Engineering from Iran University of Science and Technology, and PhD degree in Electrical and Telecommunication from University of Science and Technology, Tehran, Iran, in 2000. He was in the Faculty of the Department of Electrical Engineering as an Assistant Professor from 2002 to 2006 and an Associate Professor from 2007 to 2012, and has been a Full Professor since 2013. He has been the Head of the Faculty Engineering Department from 2013 to 2017 and a Distinguished Professor at Urmia University. His publications have been cited over 4600 times. He has been included in the Top One Percent of the World's Scientists and Academics according to Thomson Reuters' list since 2016. His research interests include small antennas, filters, MIMO antennas, periodic structures, wave propagation, and measurements.

Changiz Ghobadi received his BSc in Electrical Engineering and MSc degrees in Electrical Engineering Telecommunication from Isfahan University of Technology, Isfahan, Iran, and PhD degree in Electrical Telecommunication from the University of Bath, Bath, UK, in 1998. He is currently a Professor in the Department of Electrical Engineering of Urmia University, Urmia, Iran. He established Northwest Antenna and Microwave Research Laboratory (NAMRL) at the University of Urmia, focusing on microwave, antennas, and propagation devices characterization, design, and fabrication. He has supervised and administered more than 130 MSc and 32 PhD students and their thesis. He has authored and coauthored over 320 scientific publications, including accredited journals and conferences. His papers have been cited over 4500 times. He has been included in the Top One Percent of the World's Scientists and Academics according to Thomson Reuters' list in 2017 and 2020. His primary research interests are antenna design, radar, and adaptive filters.

Bahman Mohammadi received his BSc in electrical engineering-telecommunication from Tabriz University, Tabriz, Iran, in 2011 and MSc and PhD degrees (both with honor) in electrical engineering-microwave, antenna and propagation from Urmia University, Urmia, Iran, respectively in 2013 and 2018. He has coauthored more than 80 journal and conference papers. His research interests include periodic structures, filters, MIMO antennas, metamaterial, and optimization. He is a member of the IEEE APS and IEEE MTT-S. He was the chair of the IEEE student branch at Urmia University from 2015 to 2018. He was the recipient of the best paper award in IST2018 at antenna track, one of the best reviewer of AEUE journal in 2018, and premier researcher of West Azerbaijan province in 2019.

Chapter 4
MIMO Antennas for 5G-Enabled Devices

Rifaqat Hussain, Muhammad Umar Khan, Mohamed A. Abou-Khousa, and Mohammad S. Sharawi

4.1 Introduction

In recent years, wireless devices connected to the internet exponentially increased along with continuous demand for high-speed connectivity. Technologies such as augmented reality, cloud-based computing, and enhanced connectivity have evolved and been a significant part of the young generation's lifestyle. Soon, cars, street lighting, electronic appliances, sensors, actuators, and all other wireless devices will be communicating with one another in the Internet of Things (IoT). Moreover, ultra-reliable and low-latency communications are required for automated driving, airborne vehicles, and industry automation for the dawn of the Fourth Industrial Revolution (IR), remote robotics management in extreme dangerous circumstances, smart grid implementations, and remote surgery. To cope with these technological advancements in the field, wireless standards are continuously being enhanced. This

R. Hussain (✉)
Electrical Engineering Department, King Fahd University of Petroleum and Minerals (KFUPM), Dhahran, Saudi Arabia
e-mail: rifaqat@kfupm.edu.sa

M. U. Khan
Electrical Engineering Department, RIMMS, National University of Sciences and Technology, Islamabad, Pakistan
e-mail: umar.khan@seecs.edu.pk

M. A. Abou-Khousa
Department of Electrical and Computer Engineering, Khalifa University of Science and Technology, Abu Dhabi, UAE
e-mail: mohammed.aboukhousa@ku.ac.ae

M. S. Sharawi
Electrical Engineering Department, Polytechnique Montréal, Montréal, QC, Canada
e-mail: mohammad.sharawi@polymtl.ca

M. A. Matin (ed.), *Wideband, Multiband, and Smart Antenna Systems*, Signals and Communication Technology, https://doi.org/10.1007/978-3-030-74311-6_4

is accomplished through the realization of next generation 5G technologies. With the current research pace and the consent of regulatory authorities, the widespread commercialization and adoption of 5G technology are expected by 2025 [1].

Future 5G technology is expected to support higher capacities (100–1000) more than the current 4G Long-Term Evolution (LTE) system, faster data speeds, lower latency, higher reliability communication, and a large number of connected devices. More specifically, the users and application trends as reported in [1] are as follows:

1. Supporting low latency and high reliability human-centric communication
2. Supporting low latency and high reliability machine-centric communication
3. Supporting high user density
4. Maintaining high quality at high mobility
5. Enhanced multimedia services
6. Internet of Things
7. Convergence of applications
8. Ultra-accurate positioning applications.

To achieve the 5G design targets as mentioned above, information theory suggests the three key approaches to achieve several-fold increase in system capacity as [2] follows:

1. Ultra-dense networks: The ultra-dense network (UDN) is an emerging technique to meet the high data traffic requirements in 5G mobile communications. It is also known as small cell technology that can be utilized to enhance the network capacity. Low-power, dense, and small cells can be utilized to off-load the wireless data traffic from macrocells, having more than 80% of the wireless data. The network densification has already been adopted in LTE and LTE-Advanced (LTE-A) cellular networks with minimum data rates of 10–20 Mbps with monthly data usage of 20–50 GB data. However, it is envisioned that LTE will no longer be sufficient for 5G mm-wave mobile applications [3].
2. Large bandwidth: A large bandwidth is highly desirable for 5G mm-wave applications. Fortunately, higher frequency bands offer larger bandwidth to achieve higher capacity. Licensed 5G bands above 6 GHz are 27.5–29.5 GHz that will be available in Americas, while 24.25–27.5 GHz range is considered to be implemented in Europe. The higher frequency bands of operation offer larger bandwidth and hence effectively address the higher system capacity requirements [1].
3. High spectrum efficiency: The most viable approach to increase the spectral efficiency is by using multiple antennas or to use the multiple-input–multiple-output (MIMO) technology. Massive multiple-input–multiple-output (m-MIMO) is an emerging technology that utilizes a large number of antennas probably 100 or more as compared to current existing wireless MIMO systems. This would lead to a significant improvement in the spectrum efficiency. A large number of antennas help in focusing energy in smaller areas and hence provide huge improvements in throughput and radiated energy efficiency. Moreover, MIMO

systems perform better in scattering non-line-of-sight (NLOS) environments, which is more practical for the future 5G networks [4].

Each of these approaches is expected to increase the system capacity to an order of magnitude as compared to current 4G systems. Fortunately, mm-wave frequencies with a very small wavelength are a feasible/optimal solution to provide larger bandwidths where small cell sizes are attractive solutions for short-range mm-wave and to design large antenna arrays/massive MIMO to be accommodated in a very small area. A judicious solution to optimize all parameters together would result in 1000-fold increase in capacity for 5G [5].

4.2 Evolution of MIMO Technology: From 4G to 5G

Initially, MIMO technology was developed to focus on the spatial diversity to mitigate the impacts of multipath fading. The pioneering work on MIMO implementation was reported in [6, 7], while new technologies have been developed over the years to form the basis of modern MIMO communication systems for fourth-generation (4G) LTE system as released in the Generation Partnership Project (3GPP) report release 8 (Rel-8). In 4G wireless communication systems, three major technologies were used to enhance the data rate: (1) adaptive modulation coding (AMC), (2) orthogonal frequency division multiple access (OFDMA), and (3) MIMO technology. The first two technologies are mainly concerned about the modulation and coding schemes, while the MIMO dealt with the physical layer of communication system to combat multipath fading. In MIMO systems, the data is transmitted through multiple antennas, and thus the chances of getting good representation of data in a multipath fading environment increase along with an increase in data rate [8]. The evolution of MIMO technology can be classified into three different categories. Each one of them was developed roughly during distinct epochs. These are

1. Point-to-Point MIMO
2. Multiuser MIMO
3. m-MIMO.

A quick overview and an evolution of each MIMO technology are given in this section, while the details of MIMO Antenna systems for 4G and 5G with comprehensive literature review will be presented in the subsequent sections.

4.2.1 Point-to-Point MIMO

Point-to-Point (P2P) MIMO technology is the basis for modern MIMO communications. The concept of antenna diversity as demonstrated in [6, 7] in the late 1990s represented the simplest form of a MIMO system. This implied that the data being transmitted from a single user was intended to be received by another individual. P2P MIMO consisted of a base station (BS) equipped with an antenna array serves a terminal equipped with an antenna array. Various terminals are orthogonally multiplexed through time and frequency division multiplexing. In [9], multiple transmitting and receiving antennas were used for a single user over an additive Gaussian channel. The multipath fading was observed with conclusions to find the potential gains of such multi-antenna systems over single-antenna systems. Other interesting findings were reported in [10], where multiple antennas were used in P2P MIMO configurations with unknown channel parameters. The studies concluded that the capacity approaches the capacity obtained as the prior information about propagation coefficients was known. The main advantage of P2P MIMO is being the simplest form of MIMO for both uplink and downlink, which is an attractive choice by virtue of its optimality and simplicity.

4.2.2 Multiuser MIMO

In Multiuser MIMO, multiple streams of data, at the same frequency bands, are simultaneously allocated to different users. A single BS serves a multiplicity of terminals by using same time and frequency. The concept of the Multiuser MIMO is derived from P2P MIMO setup by breaking up the K-antenna terminal into multiple autonomous terminals. A comprehensive study on the transition from P2P MIMO to Multiuser MIMO system was conducted in [11]. This work discussed the spatial degrees of freedom offered by multiple antennas to enhance the system capacity. This could be achieved by scheduling multiple users to simultaneously share the spatial channel. Thus, this was the fundamental paradigm shift from single-user communication to multiuser communication.

The 4G LTE was officially introduced in 3GPP Rel-8 standardization for the first time. All the subsequent releases only enhanced the LTE technology. The main advantages of the standardization include the use of multiple MIMO antenna scheme, high peak data rates up to 300 Mbps in downlink and 75 Mbps in uplink when using 2×2 MIMO antenna with 20 MHz bandwidth. Moreover, it was envisioned to obtain high spectral efficiency and low latency of 5 ms for IP packets in ideal radio conditions using MIMO system.

There are two important distinctions between P2P MIMO and Multiuser MIMO. First, in Multiuser MIMO, each terminal performs coding and decoding independently, and hence various terminals do not cooperate. Second, in multiple-access channel, each terminal is subject to an individual power constraint, while in P2P channel, the total radiated power is averaged out to find each antenna power limit constraint.

4.2.3 m-MIMO

m-MIMO is a useful and scalable version of Multiuser MIMO to enhance the gain of traditional MIMO. The concept of m-MIMO was originally conceived in [12]. The solution provided was to use large number of antenna arrays (hundreds of antennas) at the BS to simultaneously serve dozens of user terminals. The propagation channel of each terminal is characterized by smart processing at the BS to achieve enhanced system capacity. Two main advantages of m-MIMO are as follows:

1. Excellent Spectral Efficiency: An excellent spectral efficiency is envisioned using m-MIMO as spatial multiplexing of several terminals is performed using the same time–frequency resource. Efficient multiplexing can be achieved for various channels with diverse propagation environment.
2. Superior Energy Efficiency: In m-MIMO, high gain values of the antennas allow to reduce the radiated power as the main beam can be directed toward the target with less power. Also, the use of lower power-rated electronics for large number of elements reduces the high power requirements on BS power amplifier.

Each BS contained a large number of antenna elements (typically hundreds of antenna elements), M, that serves a cell with dozens of user terminals/equipments, K. Each terminal may have a single antenna element or may be equipped with several antenna elements in MIMO configuration. In m-MIMO technology, all the user equipments and terminals occupy the full-time frequency resources simultaneously in both uplink and downlink transmissions. The multiplexing and demultiplexing of signal processing are achieved by utilizing a large number of antennas and channel state information at every BS [12].

m-MIMO can provide 3D MIMO targeting the control and propagation of signals in three-dimensional space [13]. The 3D propagation of m-MIMO antennas was studied by the 3GPP. Each BS is equipped with an antenna array to adjust both azimuth and elevation angles and thus ensure the propagation in 3D space. The large number of antennas also increases capacity and larger multiplexing gains. Thus, 3D MIMO with massive antennas can be practical deployment in 5G mm-wave communication. All of this may be enabled through the LTE-Advanced and 5G specifications created by hundreds of contributing scientists and engineers at the Third Generation Partnership Project (3GPP). The transformation to 5G will also transform our lives, our economy, our jobs, and our industries.

4.3 5G Challenges: An Antenna Design Perspective

The motivation to utilize 5G broadband mobile communication is also accompanied with a plethora of challenges and issues to be addressed for the successful deployment. In this section, various challenges in 5G from an antenna implementation perspective are highlighted. It includes both user equipment (UE) and BS MIMO

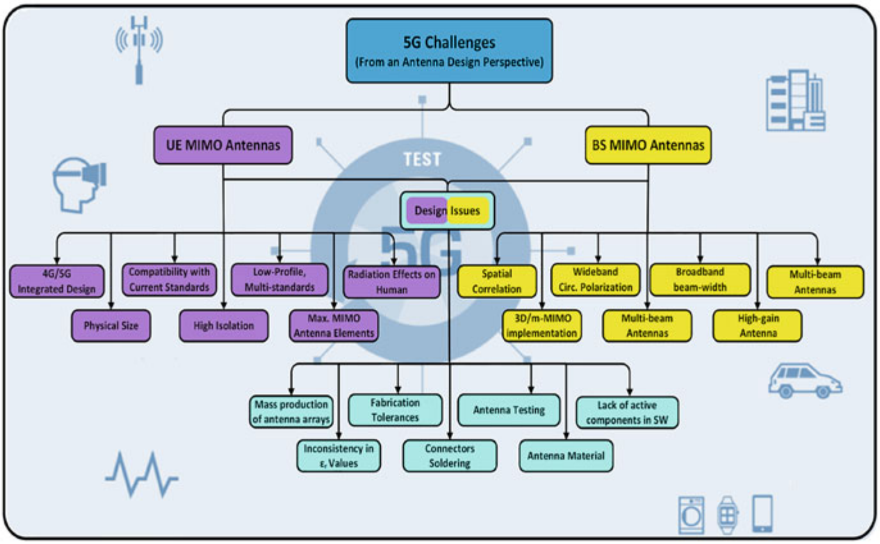

Fig. 4.1 5G challenges—an antenna perspective

antenna design. Moreover, antenna design issues in both UE and BS are also discussed. The various 5G MIMO antenna design challenges and their classification are shown in Fig. 4.1 and are briefly summarized below.

4.3.1 UE MIMO Antenna Design Challenges

Despite numerous advantages of 5G technology, the implementation of UE MIMO antennas poses certain challenges that need to be addressed. These challenges are related to both mm-wave bands and sub-6 GHz bands. A number of key challenges of UE MIMO antenna design are shown in Fig. 4.1 and are briefly discussed in this section.

5G sub-6 GHz wireless standards are becoming popular to ensure the smooth transition from existing 4G networks to upcoming 5G standards. The key idea is to utilize the existing 4G infrastructure for future 5G systems. During the transitional phase, integrated 4G/5G UE MIMO antenna solutions are highly desirable. It is quite challenging to design low-profile multi-standard antenna systems with the strict constraints of the physical size of UE devices. Also, such solutions are required to be compatible with existing technologies. For MIMO implementation, the UE should be equipped with a maximum number of antenna elements with high isolation values between closely spaced antenna elements. Furthermore, it is of utmost importance to characterize the antennas for MIMO performance metrics.

With the advent of the 5G technologies with high data rate and fast internet, an exponential increase in the number of mobile phones and other wireless handheld devices is expected. The radio frequency radiation emitted from such devices near the head and other parts of the body can be absorbed and converted to heat which might affect human health. Hence, it is critical to characterize the UE devices with many MIMO antenna elements for specific absorption rate (SAR). SAR is a measure of radio frequency (RF) energy exposure and absorption by the body. Hence, it is important to ensure radiated power levels that are within the regulatory limits, i.e., SAR levels less than 1.6 W/Kg. As SAR values are highly dependent on the conductivity and the operating frequency bands, it is a challenging requirement to optimize the UE to operate within the safe limit as per FCC policy [14]. Similarly for BS, the FCC permits an effective radiated power of up to 500 watts per channel, but the majority of cell sites in urban and suburban areas operate at effective radiated power levels of 100 watts per channel or less [15].

4.3.2 BS Antennas: m-MIMO

m-MIMO is one of the key technologies of the 5G cellular system where the BS will be equipped with several orders of magnitude more antennas as compared to 4G LTE systems. The advantages of using m-MIMO include enhanced spectral efficiency, increased system capacity, energy efficiency, low-power cost-effective components, and simpler signal processing algorithms [16]. However, implementations of such antenna systems are associated with certain challenges that have to be addressed for successful deployment. The suggested sub-6 GHz and mm-wave bands for 5G communication are 3.4–3.8 GHz, 4.4–4.9 GHz, 24–29 GHz, 37–40 GHz, and 66–76 GHz. Some of the challenges that are related to both of these bands are presented next.

4.3.2.1 Spatial Correlation

For massive MIMO BS antennas, it is required that the transmitting and receiving antennas form independent channels with identical characteristics to enhance the system capacity and reliability. However, for m-MIMO antenna elements, the correlation among various channels increases, and they start behaving more like ordinary channels. This is due to fact that antenna elements are connected close to each other for 5G BS applications. This would result in highly correlated channels with deterioration in 5G m-MIMO BS performance with spatial diversity loss [17]. Various BS antennas with configuration and structure are reported in the literature to reduce the spatial correlation to enhance the MIMO system performance [16].

4.3.2.2 3D/m-MIMO Implementation

3D or m-MIMO is the extension of MIMO with a large number of antenna elements on the BS to achieve the basic requirements of 5G technology and beam steering capabilities in azimuth and elevation. It is highly desirable to design and implement 3D or m-MIMO for BS applications. However, the increased number of antenna elements adds more complexity to design and operating algorithms for 5G communications.

4.3.2.3 Wideband Circularly Polarized MIMO

Wideband circularly polarized MIMO antennas are generally required for many 5G applications. However, it is quite challenging to achieve the desired characteristics of circular polarization over a wideband. This is due to the difficulty in maintaining the phase shift between the axes of the radiating antenna structure over a wideband [18].

4.3.2.4 Multi-beam Antennas

Multi-beam antennas are key to 5G wireless communication systems. Multi-beam antennas are helpful to enhance signal-to-noise ratio and improve spectral and energy efficiencies and are crucial for enabling beamforming in massive-MIMO antenna system. Multi-beam antenna systems are capable of generating and propagating several independent and simultaneous beams with high gain. This requirement is the basis of beamforming in 5G [19]. Various multi-beam antenna designs are comprehensively studied in [20], which include both passive multi-beam antennas and digital multi-beam antennas.

4.3.2.5 Broadband Beamwidth

For m-MIMO BS antennas, it is required to have a consistent beamwidth and flat gain across the bands of operation. It is a quite challenging requirement to control both parameters simultaneously, which may limit the antenna operating bandwidth and performance [21].

4.3.2.6 High-Gain Antennas

For 5G applications, it is essential to design a high-gain MIMO antenna system. This is to overcome the losses in signal quality and strength due to atmospheric attenuations at mm-wave bands. Hence, high directive high-gain antennas are critical for 5G BS applications and antenna arrays at UE [22].

4.3.2.7 Multi-standard Antennas

5G wireless systems require a smooth transition from 3G/4G to 5G. During the early stage of deployment, integrated solutions would be required that are compatible with the current standards and the future 5G technology. Therefore, it is necessary to integrate 3G and 4G antennas with m-MIMO antenna system on BS or use multi-band solutions. Thus, it is technically challenging to come up with such novel solutions. In addition, user terminals will also require to be equipped with 4G/5G integrated solution to operate at different operating bands simultaneously [19].

4.3.3 Design Issues: Challenges for UE and BS

5G antenna design faces several challenges from both UE and BS type. These can be categorized as follows [18, 19, 23]:

(a) Mass production of antenna arrays: consistency in the production of both UE and BS antennas is highly desirable.
(b) Different ϵ_r values: any difference in the ϵ_r values of the same substrate might result in large deviation in antenna geometry especially in mm-wave bands.
(c) Fabrication tolerances: any difference in the dimensions of antenna due to fabrication may affect the results severely.
(d) Connectors soldering: variations in soldering precision and not accounting for connectors in the modeling stage may change the antenna characteristics.
(e) Antenna testing: for m-MIMO, both circuit parts and antennas are closely located, and hence it is quite challenging to separate them for testing purpose. Furthermore, over the air (OTA) methods to test RF specifications are a big challenge for m-MIMO BS antennas.
(f) Selecting antennas material: to achieve high performance of m-MIMO antennas implementation, it is desirable to enhance the radiation efficiency and robustness of the board. This reduces the flexibility of selecting any particular material for the antenna design.
(g) Lack of active component models in SW: several high-frequency software (SW), including HFSS, Feko, etc., lack the modeling flexibility of active components. On the other hand, SW like ADS is very efficient for modeling active circuits. These are some of the challenges that an antenna designer is currently facing.
(h) Integration issues: the frequency bands of 4G and 5G overlap mainly due to the mobile communications cellular services. Two different frequency ranges are defined for 5G communication: FR1 (410 MHz–7.125 GHz) and FR2 (24.250–52.6 GHz). 5G and LTE networks share some common frequency bands due to the fact that 5G will be compatible with LTE during the early stage of deployment [24]. Integration of 4G and 5G antenna design is one of the challenges that antenna designers are currently facing.

4.4 Sub-6 GHz 5G MIMO Antenna Systems

The early stage of 5G commercialization will include 5G communication standards for both mm-wave and sub-6 GHz bands to ensure smooth transition to 5G by utilizing the existing BS sites for 3.5/4.5 GHz. The frequency bands of 4G and 5G overlap mainly due to the mobile communication cellular services. Two different frequency ranges are defined for 5G communication: FR1 (410 MHz–7.125 GHz) and FR2 (24.250–52.6 GHz). 5G and LTE networks share some common frequency bands due to the fact that 5G will be compatible with LTE during the early stage of deployment [24].The 3.5/4.5 GHz bands are suitable for dense urban coverage and support enhanced mobile broadband along with existing 2 GHz sites that can be reused for 5G communication. The sub-1 GHz bands are mostly suitable in scenario for wide coverage with indoor penetration, to reuse 800/900 MHz sites, massive IoT, and ultra-reliable low-latency communication [25].

4.4.1 UE MIMO Antenna Systems

Most common challenges for sub-6 GHz MIMO implementations for UE include multi-band antenna design with larger bandwidth, to accommodate the maximum number of antenna elements within the given space, high mutual coupling between closely spaced antenna elements, highly correlated MIMO channels, metal frame and liquid crystal display (LCD) screen blockage that might severely affect the MIMO antenna performance. UE and mobile terminals are required to accommodate the maximum number of antenna elements for sub-6 GHz 5G applications to be able to overcome hand blockage. 12-port MIMO antennas were reported in [25, 26], as shown in Fig. 4.2a and b. An interesting 12-element compact antenna design with high isolation values was reported in [25]. The compact antenna structure was realized using an orthogonal polarization methodology. A quarter-mode substrate integrated waveguide (SIW) antenna was combined with two open-ended slots that resulted in a compact 3-antenna block operating at a frequency band of 3.4–3.6 GHz. Good impedance matching and isolation were obtained due to orthogonal polarization. Another 12-port MIMO antenna array for 5G smartphone applications using 5G technology was reported in [26]. The dual bands obtained were from 3.4 to 3.8 GHz and 5.150 to 5.925 GHz that are compatible with existing 4G and future 5G MIMO applications in UE.

Several 8-antenna element designs for smartphone 5G applications in sub-6 GHz bands were reported in the literature as shown in Fig. 4.3. The solutions provided mainly focused on and were coming up with a compact antenna design to accommodate the maximum number of antenna elements on a smartphone backplane size, with enhanced isolation and polarization diversity as well as multi-band antenna's operation. In [27, 28], 8-element antennas were presented with dual polarization, operating at 2.6 GHz and 3.7 GHz, respectively. The antenna radiated

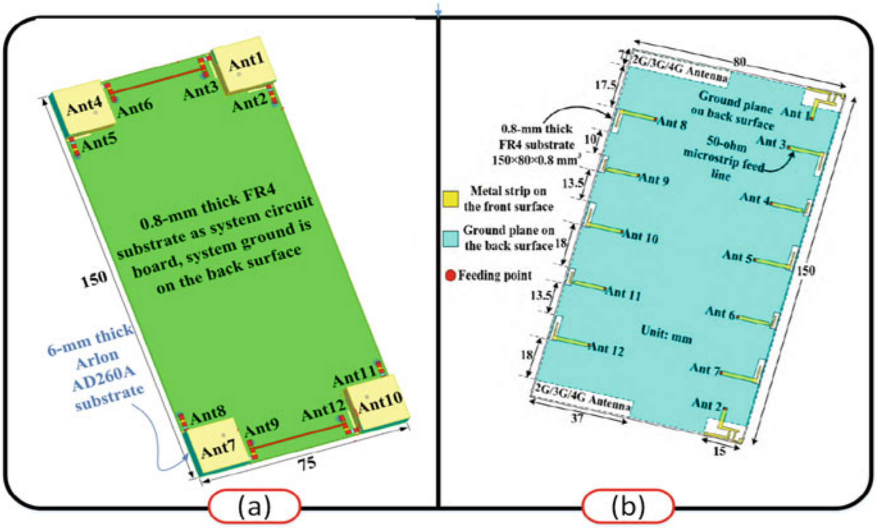

Fig. 4.2 Sub-6 GHz 5G user terminal MIMO: (**a**) 12-element MIMO [25] and (**b**) 12-element MIMO [26]

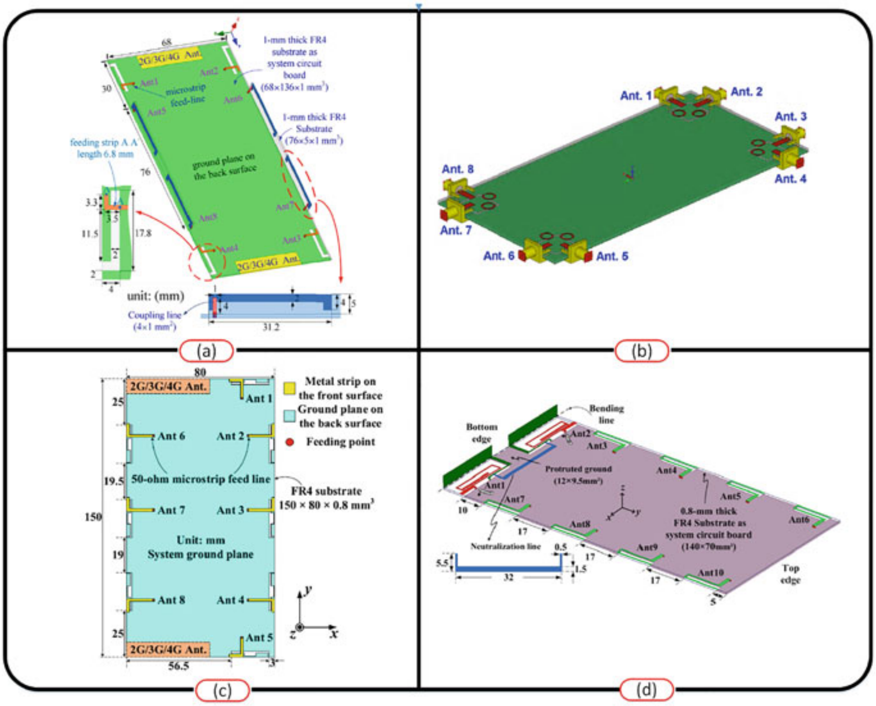

Fig. 4.3 Sub-6 GHz 8-element 5G MIMO antenna design: (**a**) MIMO antenna with dual polarization [27], (**b**) 8-element MIMO with dual polarization [28], (**c**) 8-element MIMO [29], and (**d**) 8-element MIMO [30]

in different directions, which helped in reducing the mutual coupling between closely spaced antenna elements. The polarization diversity in each antenna design made them suitable to be utilized for 5G MIMO applications. An attempt was also made to integrate multi-functional antenna elements on the same substrate [29, 30] by covering 3G/4G/5G standards. Such antenna designs with a large number of antenna elements (8 elements in this case) are highly desirable for the smooth transition from 4G to 5G communication standards supporting 8 × 8 MIMO that is standardized in 5G 802.11ac, for example.

Another important aspect and highly desirable feature of 5G MIMO mobile antennas are their very compact structure with a maximum number of antenna elements. A highly compact antenna design with four antenna pairs operating at 3.4–3.6 GHz was presented in [31], for 5G mobile phone applications. Orthogonal modes were used to place antenna pairs close to each other, having different current distribution at the same operating band. A high isolation performance, better than 17 dB, was obtained without any additional decoupling structures across the desired band of operation. Similarly, an attempt was made to reduce the envelope correlation coefficient (ECC) based on the theory of characteristic modes (TCM) [32]. The analysis was performed on an 8-port MIMO array for 5G mobile applications. The methodology used was useful to get physical insights on how to reduce the ECC values for multi-antenna designs with an arbitrary antenna structure. Moreover, several multi-band/wideband metal rim-based 5G MIMO antenna designs were reported in [33–35]. The antenna elements used were slot radiators on the outer periphery of the metal rim in a MIMO configuration. Table 4.1 shows the various characteristics of sub-6 GHz 5G antenna design for handheld devices including antenna type, single-element dimensions, bands covered, and a number of antenna elements. This helps in comparing the main features of current antenna designs in this category. Another rational behind large antenna elements is the fact that based on the hand grip position of a handheld device, a large number of antenna are still not blocked and can provide high-order MIMO connection, i.e., 4 × 4 if half are blocked.

Table 4.1 Comparison of sub-6 GHz antenna designs

Ref.	Ant. type	Ant. size (mm^2)	Bands (GHz)	Elements
[25]	SIW and slot	17 × 17	3.4∼3.6	12
[26]	Slot	10 × 14	3.4∼3.8, 5.15∼5.925	12
[27]	Monopole and slot	5 × 31.2, 4 × 17.8	2.55∼2.65	8
[33]	Metal rim slots	2 mm rim width	0.82∼0.96, 1.71∼2.69,	5
[34]	IFA and slot	7 × 12.4	3.3∼7.1	8
[35]	Monopole and slot	7.5 × 20	3.3∼5	8

4.4.2 BS MIMO Antenna Systems

Among several challenges of 5G deployment, the major one is the transition from 4G LTE to 5G with m-MIMO antenna design for BS applications. During the transitional phase, both sub-6 GHz and mm-wave frequency bands will be provided with integrated solutions. The existing base station sites are being utilized to accommodate the 5G deployment in sub-6 GHz bands as well. For sub-6 GHz 5G BS, m-MIMO antenna configurations have been reported in the literature.

Very few m-MIMO BS antennas are reported in the literature for sub-6 GHz bands for 5G communication standards [36–43]. In [36], 72-port triangular-shaped m-MIMO antenna system was presented to accommodate 288 antenna elements, operating at a frequency band from 3.45 to 3.55 GHz. The complete antenna system consisted of 3 layers, each with dimensions of $44.4 \times 29.6 \times 0.1524\,\mathrm{cm}^3$ as shown in Fig. 4.4a. Each port consisted of 2×2 on the top side with feeding network on the backplane of PCB board. The antenna was operating in dual mode: in the first mode, it was working as an individual MIMO antenna design with low field coupling because of tilted beam patterns, while in the second mode, it was operating as a beam switching array for m-MIMO applications and suitable for potential 5G BS. In [37], 64 RF channels with 256 antenna elements were implemented with an active multi-beam antenna system for m-MIMO applications at 5.8 GHz for 5G communication systems. The design is suitable for digital beamforming and m-MIMO channel estimation for 5G wireless communications. The proposed 64-channel multi-beam antenna system consists of 8 PCB boards forming a 6-layer antenna structure. Each PCB board included 8-channel RF front-ends with an array of 32 elements, fabricated on both sides of the board. The dimensions of each board were $32 \times 21.5\,\mathrm{cm}$ as shown in Fig. 4.4b.

In [38], a dual-polarized indoor BS antenna was presented as shown in Fig. 4.4c. The proposed antenna covered several sub-6 GHz 5G bands. Two orthogonal dipole antennas were utilized to achieve dual polarization. The proposed antenna covered 3 frequency bands: 0.7–0.96 GHz, 1.7–3 GHz, and 3.3–3.8 GHz with independent tuning structure. The compact low-profile antenna design, stable radiation patterns, high polarization purity, and simple feeding structure are suitable for indoor mobile BS applications for sub-6 GHz 5G communication standards. In [39], a 3D circular conformal MIMO antenna system was presented as shown in Fig. 4.4d. The given antenna design consisted of three magnetoelectric dipole (MED) antennas. The dual-band antenna design covered frequency bands of 1.68–2.93 GHz (impedance bandwidth of 54.2%) and 3.32–3.64 GHz (impedance bandwidth of 9.2%). The antenna presented is well suited to be deployed in future sub-6 GHz 5G MIMO mobile BS applications.

In [40], a dual-polarized antenna array was presented for sub-6 GHz BS applications. It covered frequency bands of 2.5–2.69 GHz and 3.3–3.6 GHz. The proposed antenna array is suitable to be utilized in sub-6 GHz BS applications. Similarly in [41], a compact 2-element MIMO BS antenna was presented with a metasurface superstrate. A double-layer short wire unit cell was utilized to optimize the

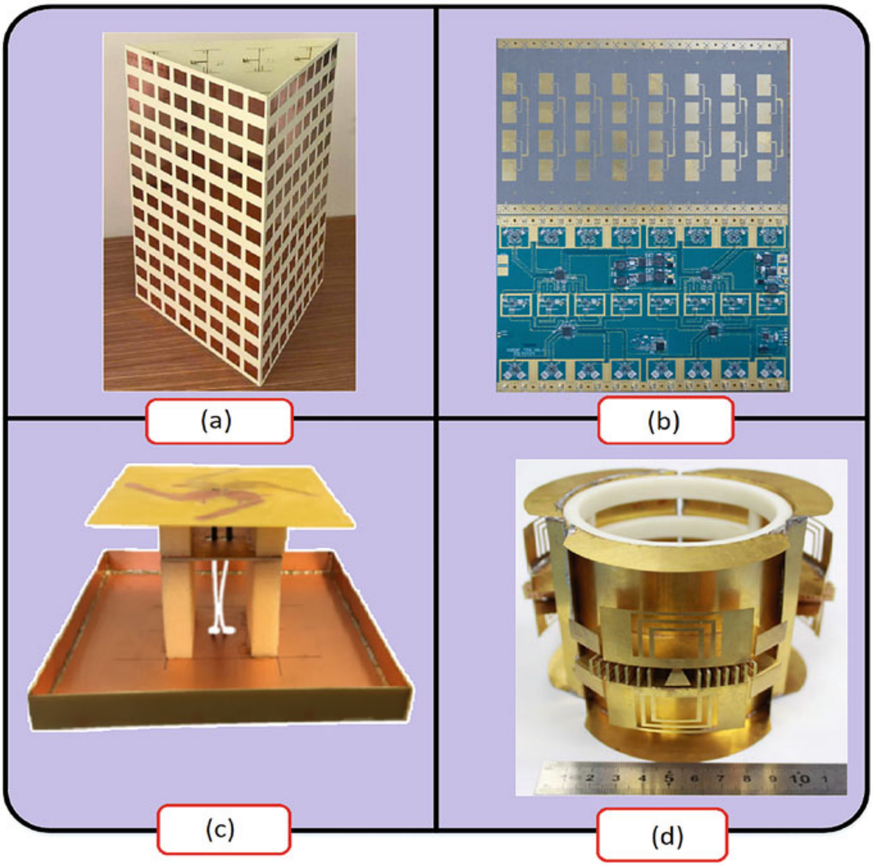

Fig. 4.4 sub-6 GHz BS antenna: (**a**) triangular 72-port m-MIMO BS system [36], (**b**) 8-channel RF front-ends and antenna arrays integrated on individual PCB [36], (**c**) dual-polarized BS antenna [38], and (**d**) circular conformal MIMO antenna [39]

superstrate dimensions. Thus, it helped in decoupling two nearby spaced, 0.27λ, Bowtie antennas in the H-plane. An isolation improvement of at least 15 dB was observed for frequency bands from 2.3 to 2.690 GHz. In [42], a novel Vivaldi antenna was presented that is suitable for bases station applications. The antenna is suitable for both 4G and 5G applications. The given antenna is working well in the frequency bands from 1.8 to 2.5 GHz. The single-antenna element had dimensions of 13.1 × 14.1 cm^3. Similarly, sub-6 GHz multi-beam BS antenna for 5G applications was presented in [43]. The antenna covered frequency bands from 3.3 to 7.0 GHz with an arbitrary number of beams with arbitrary vertical and horizontal beamwidths. The beam can be switched electronically, and hence it can be used as a good configuration for switched beam smart BS antennas.

In [44], the first real-time m-MIMO test bed—LuMaMi by Lund University—was presented. It was capable of handling 100 coherent radio frequency transceiver chains with high-throughput processing of 384 Gbps of real-time baseband data in both the transmit and the receive directions and up to 128 antenna elements operating at a center frequency of 3.7 GHz. The LuMaMi test bed is shown in Fig. 4.5a. In 2017, Huawei launched its first 5G BS active antenna unit, BBU5900, as shown in Fig. 4.5b. This unit features baseband unit box 6 in 1, with 6 modes of operation (GSM, UMTS, LTE FDD, LTE TDD, NB-IoT, and 5G NR); transmission capacity of 50 Gbps to meet the requirements of multi-band, multi-mode, and m-MIMO co-site deployment; and with a series of multi-antenna RF modules supporting 4T4R/8T8R/64T64R, extreme user experience in the 4.5G/5G era [45]. At Mobile World Congress (MWC) 2018, Samsung showcased the first m-MIMO products supporting the new 5G New Radio 3GPP specifications for sub-6 GHz operation. The various products of m-MIMO access units (AUs), as shown in Fig. 4.5c, were provided for diverse deployment scenarios including normal, wide, and high rise buildings to increase gigabit speeds and capacity and build a 5G mobile network using its 2.5 GHz Time Division Duplex-LTE spectrum. Samsung's m-MIMO solutions support 32T32R and 64T64R configurations and also provide simple transition from LTE to 5G [46].

4.5 Integrated Sub-6 GHz and mm-Wave 5G MIMO Antennas

For the upcoming 5G, a smooth transition from 4G standards is highly desirable to adopt with 5G technology. The early stage deployment of 5G technology is mainly focused on the sub-6 GHz communication standards that are compatible with existing 4G standards along with the mm-wave 5G bands. This leads to the implementation of multi-functional antenna designs and wireless communication devices. Hence, an integrated antenna solution for mobile terminals and other wireless handheld devices is highly desirable. Several works have been reported in the literature with interesting integrated solutions. One of the pioneering 4G/5G integrated works was presented in [47]. The proposed antenna design targeted wireless handheld devices compatible with the existing 4G standards along with upcoming 5G systems operating at mm-wave band. The sub-6 GHz antenna consisted of modified monopole-based antenna design integrated with mm-wave slot antenna array. The antenna covered frequency bands from 1.870 to 2.53 MHz and mm-wave band at 28 GHz. In the proposed integrated antenna design, 4G MIMO antenna design was integrated with 5G mm-wave antenna system as shown in Fig. 4.6. The multilayer design had a backplane dimensions of $60 \times 100 \times 0.965\,\text{mm}^3$. Both types of antennas were carefully placed to obtain mm-wave antenna array operation along with good MIMO operation of 4G antenna design.

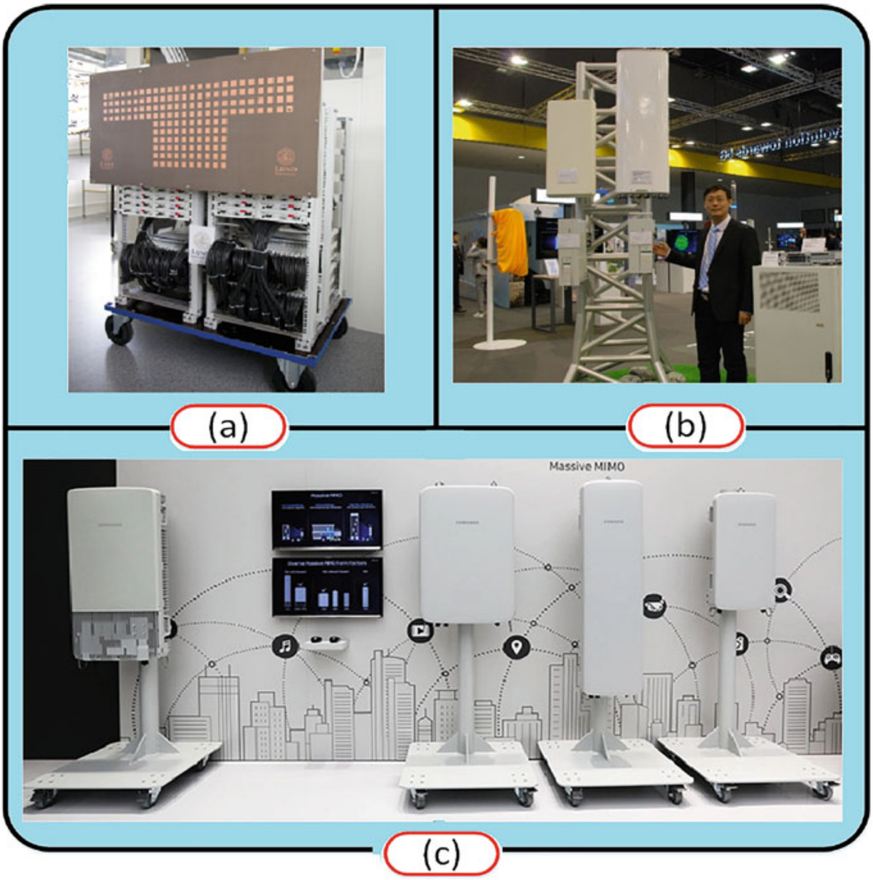

Fig. 4.5 Sub-6 GHz BS antenna: (**a**) m-MIMO test bed—LuMaMi [44], (**b**) Huawei 5G BS active antenna—BBU5900 [45], and (**c**) Samsung various products of m-MIMO AU [46]

The design is best suited for upcoming 5G antenna design along with existing 4G MIMO antenna operation.

A 4G/5G antenna design consisting of 2-element slot-based 4G MIMO antenna integrated with 2-element connected antenna array (CAA) was presented in [48]. The integrated antenna system covered multiple frequency bands: 1.975–2.08, 2.16–2.23, 2.35–262, 3.06–314, and 3.48–3.54 GHz for 4G standards while 16.5–17.8 GHz band for 5G applications. The proposed antenna geometry is shown in Fig. 4.7a. Similarly, an integrated 4G/5G antenna design was presented in [49], as shown in Fig. 4.7b. The 4G dual-band modified monopole antenna design covered a wide frequency band from 1.9 to 3.3212 GHz and 3.517 to 3.712 GHz, respectively. The 5G antenna was a linear connected array (LCA) design that covered a frequency band from 25.7 to 30.50 GHz. In [50], a 4G/5G antenna design consisted of modified monopole MIMO antenna integrated with a planar connected array (PCA) was

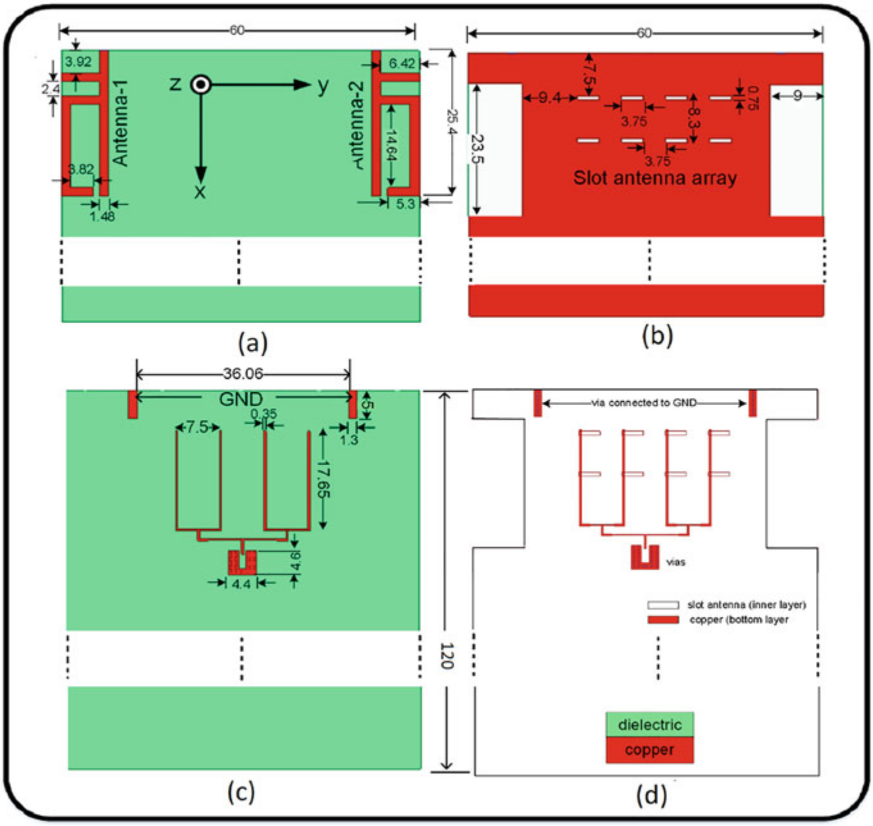

Fig. 4.6 4G/5G antenna system: (**a**) 4G MIMO antennas, (**b**) mm-wave antenna array, (**c**) mm-wave feed network, and (**d**) mm-wave 5G slot antenna array with feeding network [47]

presented. The antenna covered frequency bands of 2.1 and 12.5 GHz for 4G and 5G applications, respectively.

Similarly, a dual-function 4G/5G slot antenna at microwave and mm-wave was presented in [51]. A wide slot on the edge of the antenna board is utilized as a dual-purpose frequency reconfigurable 4G antenna and mm-wave antenna design. The frequency reconfigurable antenna design was operating from 2.05 to 2.7 GHz, while connected slot antenna array (CSAA) covered the 5G frequency band from 23 to 29 GHz. The antenna geometry is given in Fig. 4.8a. In [52], an integrated antenna system was presented for 4G as well as 5G wireless handheld device applications. The dual-band 4G antenna was operating at 3.8 and 5.5 GHz, while the 5G array was operating from 24.4 to 29.3 GHz. Moreover, the proposed antenna design also exhibited beam steering capability from the mm-wave 5G antenna array. The proposed antenna claimed several advantages including compact antenna structure, high gain, and planar configuration antenna design. Hence, the antenna design is

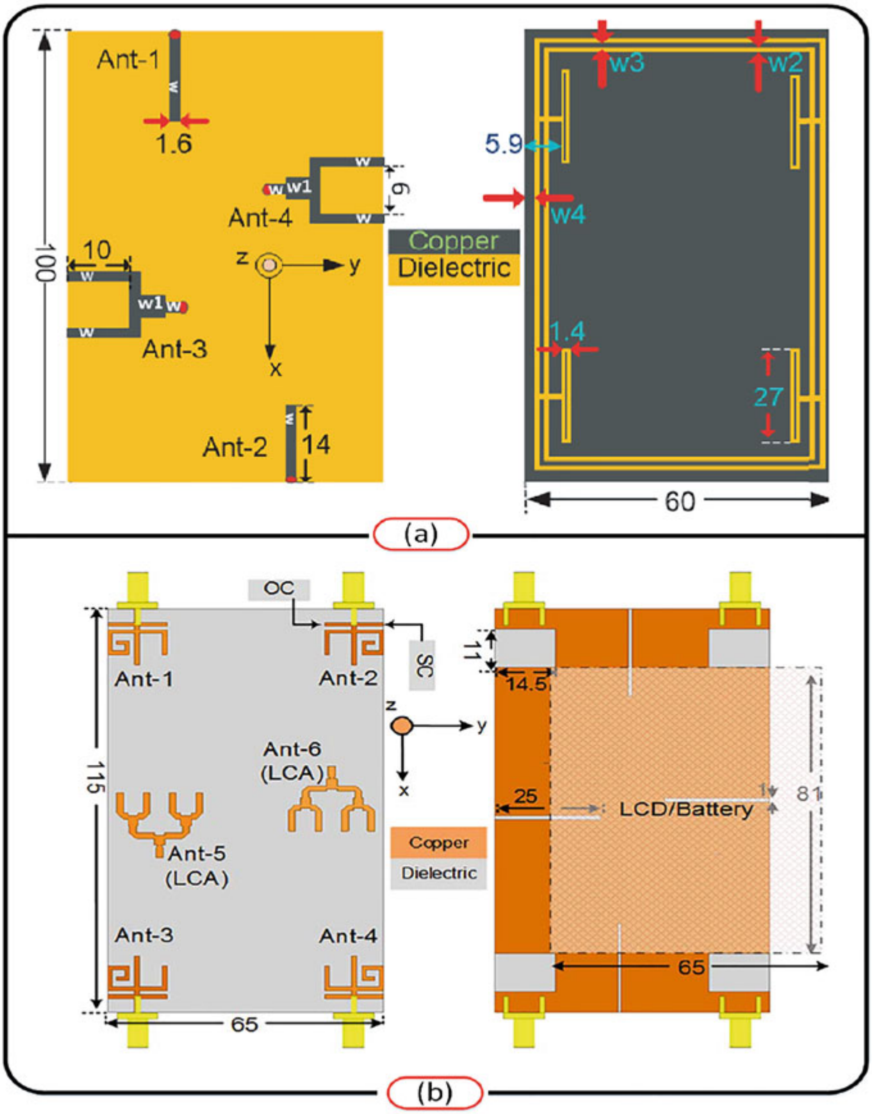

Fig. 4.7 Integrated 4G/5G MIMO antenna: (**a**) 2-element 4G and 5G MIMO antenna [48] and (**b**) 4G and 5G LCA MIMO [49]

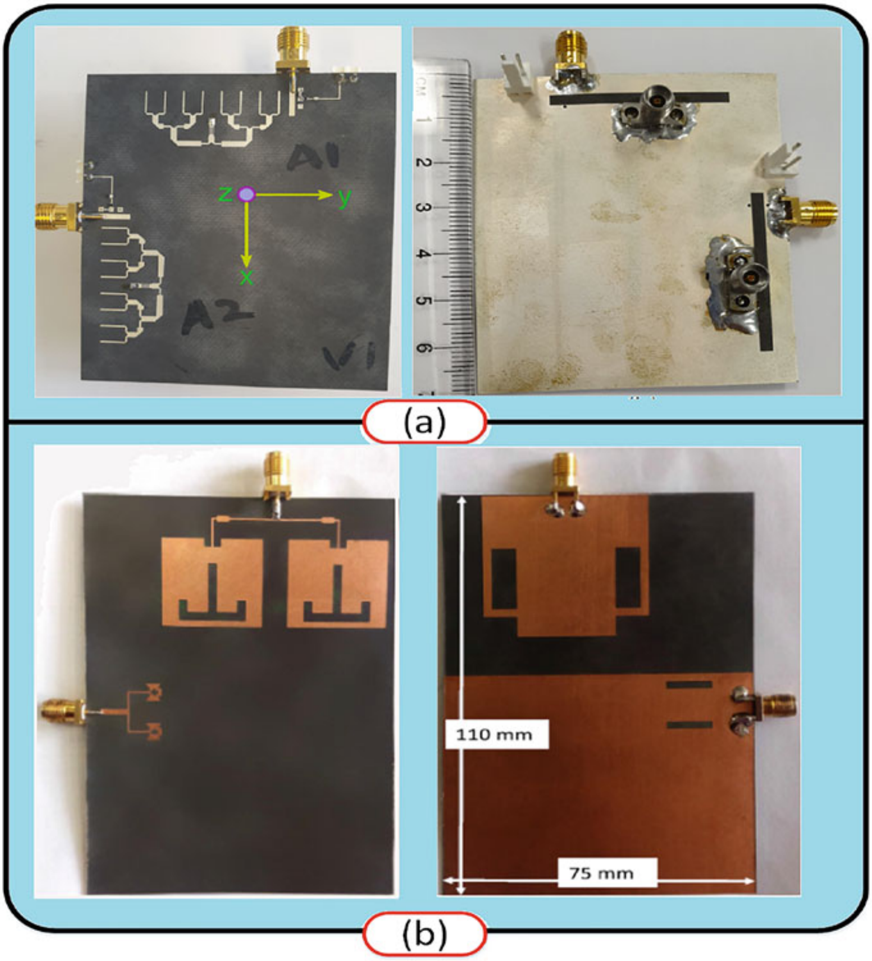

Fig. 4.8 (**a**) The geometry of 2-element MIMO antenna system [51] and (**b**) The geometry of 2-element MIMO antenna system [52]

suitable to be used for current and future wireless handheld devices. In [53], an integrated single antenna element solution for both mm-wave and LTE antenna design was presented in a metal-rimmed handset. Both the antenna elements share the same structure and volume. The LTE bands covered were from 0.7 to 0.96 GHz and 1.71 to 2.69 GHz, while the mm-wave band covered was 25–30 GHz. The volume occupied by this design was $150 \times 75 \times 7\,\text{mm}^3$. Table 4.2 compares various 4G/5G antenna integrated solutions. The analysis included various antenna types, their sizes, both mm-wave and micro-wave bands covered, and peak gain values. It is clear from the given table that monopole and slot antennas are widely used for

Table 4.2 Comparison of integrated 4G/5G antennas

Ref.	Ant. type {4G, 5G}	Ant. size (mm^2)	Bands (GHz) {4G, 5G}	Ant. elements {4G, 5G}
[47]	{Monopole, Slot}	100 × 60	{1.872–2.53, 28}	{2, 1(Array)}
[50]	{Monopole, Slot}	100 × 60	{2.01–2.257, 12.5}	{2, 1(Array)}
[48]	{Slot, Slot}	100 × 60	{(2.1, 2.75, 2.8), 17}	{2, 2}
[49]	{Monopole, Slot}	115 × 65	{1.9–3.712, 28}	{4, 2(Array)}
[51]	{Slot, Slot}	70 × 60	{2.05–2.7, 28}	{2, 2 (Array)}
[52]	{Patch, Slot}	110 × 75	{(3.8, 5.5), 28}	{2, 2(Array)}
[54]	{Monopole, Slot}	104 × 104	{(2.4–2.8, 5.1–5.6), 28}	{4, 4}

such integrated solutions because of their compact sizes, easy fabrication, and the wideband operation.

On the other hand, the sub-6 GHz miniaturized antenna design is approached recently from active component integration perspectives especially by co-designing transmitting and receiving amplifiers with the antenna. The design methodologies are comprehensively presented in [55–58]. The co-designing approach offers flexibility in antenna design and its miniaturization which is later demonstrated in sub-6 GHz MIMO antenna applications [59, 60] for broadband operation covering multi-octave bandwidth. The integrated antenna shows minimum realized gain and efficiency of 14.1 dBi and 60%, respectively, over the 1.8–5.5 GHz band.

4.6 mm-Wave 5G MIMO Antenna Systems

mm-wave 5G communication systems will provide exponentially increasing wireless data traffic and yield high spatial resolutions with compact antenna size. This motivated the researchers to use mm-wave for 5G communication systems at 28 GHz and 38 GHz. The two main advantages of mm-wave antennas are small antenna apertures with high gains along with wide bandwidth. In this section, a comprehensive overview is presented for mm-wave 5G UE and BS antennas along with commercially available antenna solutions for mm-wave 5G applications.

4.6.1 mm-Wave UE Antenna Systems

A mm-wave MIMO antenna is highly instrumental to meet high speed requirements in 5G communication systems. A large number of antenna elements could be utilized to maximize the spectral and energy efficiencies in mm-wave communications. Several works have been reported in the literature using mm-wave 5G antenna arrays or single-element designs for mobile terminals and small wireless handheld devices.

Very few mm-wave-based MIMO antennas have been found in the literature. A mm-wave multi-beam tapered slot-based MIMO antenna was presented in [61]. The antenna element is fed by a substrate integrated waveguide which is compatible with mm-wave integrated circuits. The proposed antenna exhibited good beamforming performance in the frequency band from 22.5 to 32 GHz with a gain varies from 8.2 to 9.6 dBi. The antenna is suitable to be utilized for 5G beamforming applications. A 1×4 H-plane array integrated with the multi-channel mm-wave transceivers. Several other types of 5G mm-wave MIMO antennas were reported in the literature. This included a quasi Yagi–Uda antenna [62], electromagnetic bandgap backed antenna [63], printed inverted F-shaped (PIFA) [64], and 3D printed magnetoelectric dipole antennas [65] as shown in Fig. 4.9a–d, respectively.

For mm-wave UE antenna applications, various types of monopoles, dipoles, and patch antennas have been reported in the literature; they are compact in size, low weight, and low cost. These antennas can be easily integrated with circuit elements. However, such antennas are typically with low radiation efficiency, low gain, and narrow impedance bandwidth. On the other hand, dielectric resonator antennas (DRAs) are known for their good radiation characteristics and high gain and do not suffer from conduction losses. Several DRA-based MIMO antennas are reported in the literature [66–69] as shown in Fig. 4.10a–d. All the DRA MIMO antenna designs presented in [66–68] focused on mm-wave frequency bands with decoupling structures to reduce the mutual coupling between closely spaced antenna elements. In [66], a metamaterial-based polarization-rotator (MPR) wall was investigated to minimize the mutual coupling between mm-wave DRAs as shown in Fig. 4.10a. The MPR wall resulted in the orthogonal TE modes, which reduces the mutual coupling between closely spaced DRAs. The MPR helped in reducing the mutual coupling more than 16 dB on an average. The MPR wall has no effect on the antenna characteristics including input impedance and radiation pattern. In [67], a simple decoupling structure was proposed to reduce mutual coupling between MIMO DRA antenna. The decoupling structure consisted of vias that effectively change the field distributions that helped in reducing the coupled fields. The isolation of the H-plane coupled MIMO DRA array was enhanced from 15.2 to 34.2 dB, while E-plane array was improved from 13.1 to 43 dB at 26 GHz. The DRA-based two-element MIMO antenna is shown in Fig. 4.10b.

SIW-based MIMO antenna designs are highly desirable for mm-wave bands because of their compact size and light-weight structure. Most of the MIMO based-SIW antennas reported were targeting sub-6 GHz bands [72, 73], while very few were in mm-wave band [74]. Single-element and antenna array-based SIWs were reported in [71, 75, 76]. In [71], a SIW-fed monopole antenna was presented for 5G mobile handsets. The antenna array consisted of an array of 8-element printed monopoles with beam scanning capabilities. A peak gain of 12.3 dBi was observed at 30 GHz. The antenna structure and scattering curves are shown in Fig. 4.10d. In [75], a linearly polarized dual-band SIW antenna array of four elements was presented operating at 28 and 38 GHz. The maximum gain values obtained were 11.9 dBi and 11.2 dBi at 28 GHz and 38 GHz, respectively. Similarly, a wideband SIW horn antenna with beam steerable arrays was presented in [76]. To improve

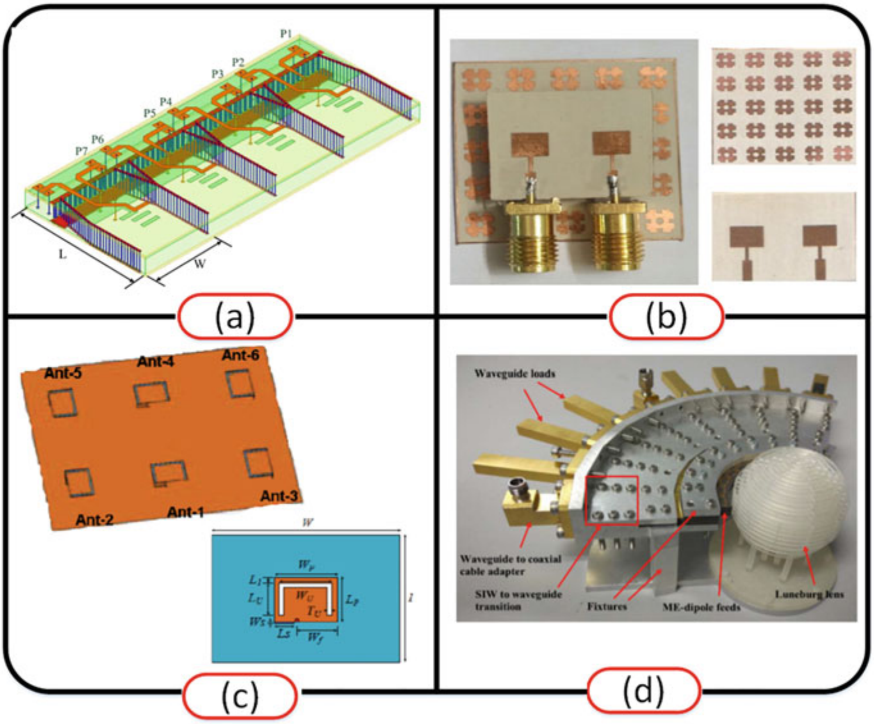

Fig. 4.9 5G mm-wave MIMO antennas: (**a**) quasi Yagi–Uda antenna [62], (**b**) electromagnetic bandgap backed antenna [63], (**c**) printed inverted F-shaped (PIFA) [64], and (**d**) 3D printed magnetoelectric dipole antennas [65]

the impedance matching and to enhance the radiation performance, a tapered ladder transition was placed at the horn aperture. Moreover, air-via technology was utilized to achieve the beam tilting in specific directions. A stable radiation performance was achieved over a wide bandwidth. The antenna realized gain values obtained were 6.4, 8.5, and 8.7 dBi at frequency bands of 28, 38, and 60 GHz, respectively.

System-on-chip (SoC) is being utilized to integrate the complete RF front-end along with antenna elements directly on the same silicon die in a so-called antenna-on-chip (AoC). This provides attractive solutions such as the miniaturization of antenna size, low power consumption, low cost, and flexibility. Several antenna solutions based on AoC were reported in the literature [77–80]. In [77], a 28 GHz RF IC-based CMOS direct conversion transceiver with 2×4 patch antenna array for 5G communication was presented. Beamforming and reconfigurable transceiver architecture were utilized for high effective isotropic radiated power at 28 GHz for 5G smartphone application. Low efficiency is one major issue of on-chip antennas.

The work presented in [78] was designed and optimized at nanoscale technology. It demonstrated a 28–33 GHz receiver front-end with a compact integrated on-

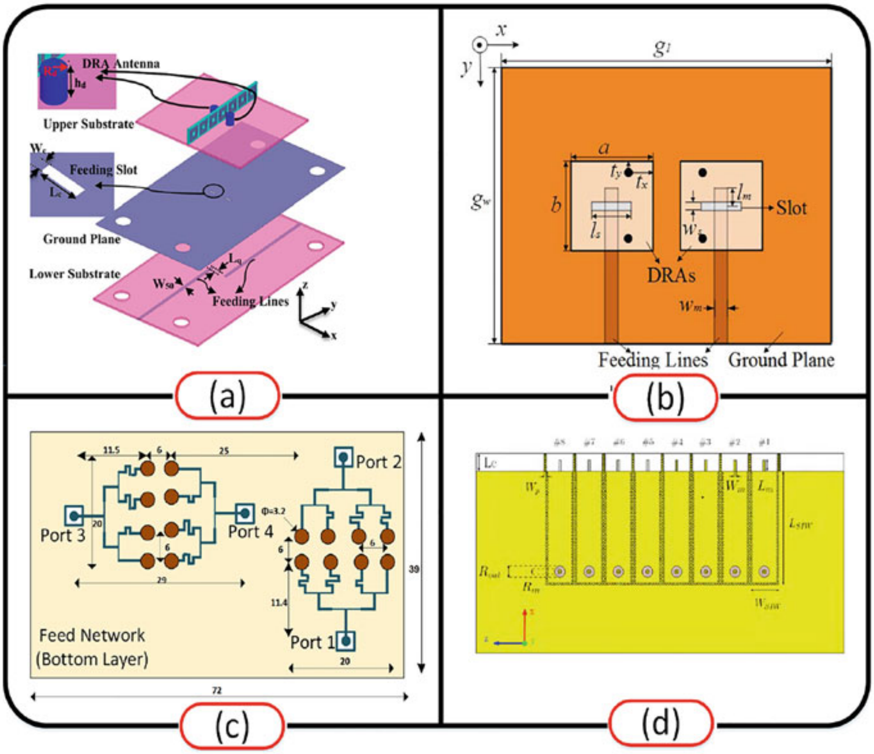

Fig. 4.10 DRA MIMO antenna: (**a**) layout of the 2-element DRA MIMO antenna with the MPR wall [66], (**b**) DRA MIMO decoupled antenna [67], (**c**) 4-element DRA MIMO antenna [70], and (**d**) 8-element SIW monopole antenna [71]

chip antenna that was realized in a digital 28-nm CMOS technology for 5G communication systems. Figure 4.11a shows the chip micrograph that highlights the receiver components. The active integrated antenna occupied a core area of 0.73 mm^2 and mounted on Rogers 4003 assembly in an antenna-in-package (AiP) form. Similarly, 64-element, 2 $\times$ 2 transmit/receive (TRX) beamformer chips operating in 28–32 GHz were presented in [79] for 5G communication. Sixteen modules of the 2 $\times$ 2 MIMO TRX chips were assembled on a 12-layer PCB together along stacked-patch antennas. The 64-element phased array could scan to $\pm 50°$ in azimuth (H-plane) and $\pm 25°$ in elevation (E-plane) with low side-lobe level. The top and bottom views of the 64-element array, PCB integrated stacked-patch antennas and beamformer ICs are shown in Fig. 4.11b. 5G AoC/AiP phased arrays are suitable candidates for 5G MIMO applications.

In [64], mm-wave 5G UE antenna characterization, design considerations, and associated challenges were discussed. Moreover, phased array antenna modules with horizontal and vertical polarization were demonstrated at the mm-wave band of 60 GHz as shown in Fig. 4.12. However, the first commercially available 5G mm

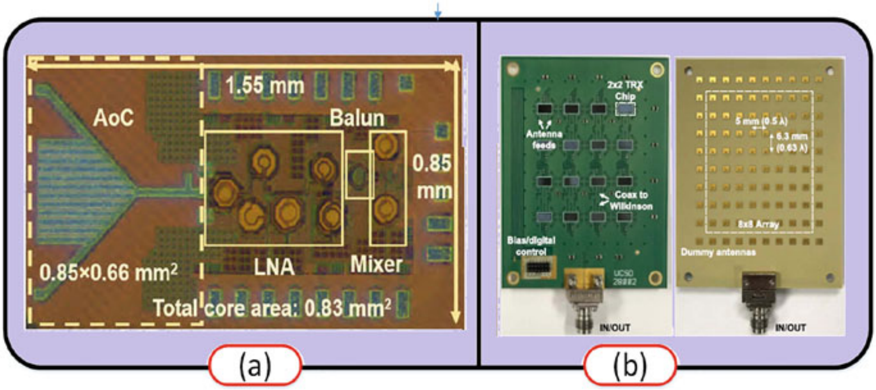

Fig. 4.11 SoC: (**a**) AiP integrated antenna at 33 GHz [78] and (**b**) beamformer ICs along with stacked-patch antennas [79]

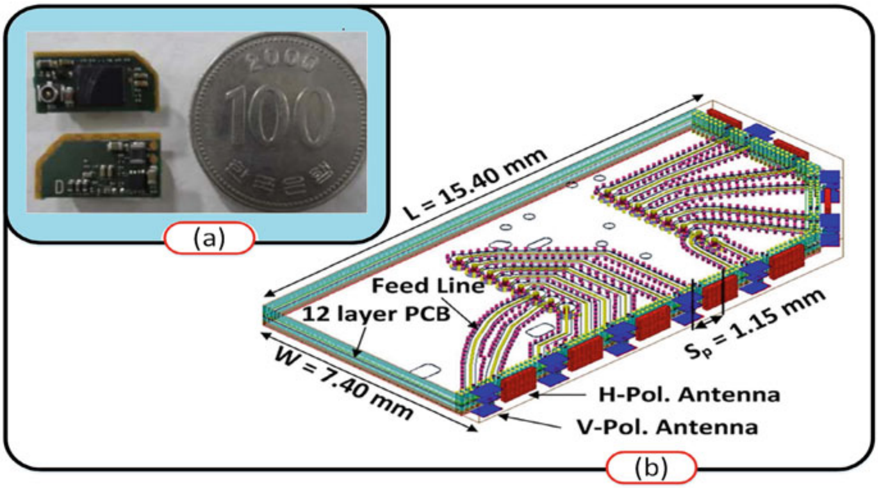

Fig. 4.12 (**a**) Phased array antenna module at 60 GHz and (**b**) dual-polarized antenna module [64]

wave antenna module (QTM052) for smartphones was introduced by Qualcomm Technologies in July 2018. The modules were integrated with the Snapdragon X50 5G modem that met the 5G New Radio (NR) specification. It covered three 5G bands: 26.5∼29.5 GHz (n257), 27.5∼28.35 GHz (n261), and 37∼40 GHz (n260). Further optimization and size reduction of QTM052 module enabled the use of up to 4 modules to be mounted along the edge of smartphones. The QTM052 consisted of three main modules: a phased array antenna with Qualcomm's X50 5G modem that was being utilized to control the beamforming and beam steering, radio transceiver, and power management. Figure 4.13 shows Qualcomm QTM052 family of fully integrated 5G mm wave modules for smartphones and other mobile devices [65].

Table 4.3 summarizes various mm-wave-based MIMO antenna solutions for user equipment terminals.

4.6.2 mm-Wave BS Antenna System

For upcoming 5G technology, mm-wave-based MIMO and m-MIMO antenna system with pattern reconfigurable and beamforming capabilities at 28/38 GHz are highly desirable for base station applications. Pattern reconfigurable antennas that dynamically change the radiation characteristics are attractive solutions for 5G

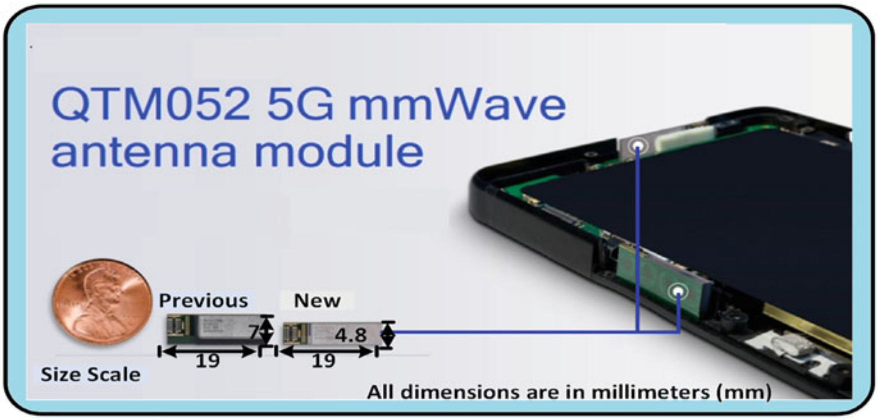

Fig. 4.13 Qualcomm QTM052 module for mm-wave antenna for smartphones [65]

Table 4.3 Comparison of mm-wave UE MIMO antennas

Ref.	Ant. type –	Ant. size mm^2	Band(s) (GHz)	# of ant. elements?	Peak gain (dBi)	BF ?
[61]	Slot	12.2 × 11	24–32	1 × Array	8.2–9.6	No
[62]	Quasi YU	12.2 × 11	34–38	1 × Array	11	Yes
[63]	Patch	19 × 15	23.6–24.4	2	6	No
[66]	DRA	–	57–64	2	–	No
[67]	DRA	21.77 × 11	25.1–27	2	6.2–6.7	No
[68]	DRA	20 × 20	27.5–28.35	2	8–10	No
[69]	Antipodal Vivaldi	$\pi \times 9.51^2$	76–77	4	6.2–7.5	Yes
[70]	DRA	39 × 72	29.5–32.5	2	6	No
[74]	SIW-based DRA	8.7 × 17.4	27.5–28.4	2	4.2	No
[81]	Aperture and dipole	–	43.3–52.3	2	5	No

BS antennas. For m-MIMO mm-wave 5G communication cellular networks, a BS would be equipped with a very large number of antenna elements. Very few mm-wave m-MIMO BS antennas with beamforming capabilities have been reported in the literature at mm-wave band of 28/38 GHz [82–86]. Some of the interesting works containing antenna arrays for mm-wave BS applications are provided in [87–91]. In [82], a multi-beam folded reflectarray antenna was presented, while in [83], a two-stage Rotman lens beamformer antenna was reported for mm-wave m-MIMO application. In [84], a mm-wave beamformer with smart antennas for 5G application was presented. Several prototypes of 5G beamforming architectures were developed and tested. This included 2 × 2 (16 antennas) and 4 × 4 (64 antennas) arrays. The solution is suitable for m-MIMO phased array systems in both frequency and time domains for next generation mm-wave 5G applications.

In [85], a 64-channel m-MIMO transceiver with a fully digital beamforming (DBF) architecture operating at 28 GHz was presented for 5G mm-wave communications. In the given design, the antenna elements were arranged as a 2D array of 16 columns and 4 rows to enable for good beamforming resolution. The half-wavelength inter-element spacing was achieved with a bend SIW feeding network as shown in Fig. 4.14a, while Fig. 4.14b shows the fully integrated digital beamforming hardware. According to the paper claims, the performance of the DBF-based m-MIMO transceiver was fully tested and validated. Moreover, a data rate of 5.3-Gb/s throughput was achieved for a single user in mobile, while 50.73 Gb/s was achieved for multiuser MIMO scenario. The results achieved verified the feasibility of using 64-channel DBF-based mm-wave m-MIMO transceiver in 5G cellular communication systems. In [86], a digital multi-beam 1D planar lens array with wide scanning angle was presented for mm-wave m-MIMO applications. The antenna array consisted of 16 dual tapered slot antenna elements as shown in Fig. 4.15a, while Fig. 4.15b shows the developed prototype of the proposed design. The proposed antenna covered the frequency bands from 25.25 to 28 GHz. The wide radiation pattern in H-plane enabled the beam scanning in the azimuth plane. Furthermore, a multilayered planar lens has been optimized to enhance the beam gain in E-plane to ensure the wide beam scanning with fewer antenna elements. For the proposed work, the results showed that a beam scanning coverage of ±40° in the horizontal plan with peak gain value of 24.8 dBi was observed. The proposed architecture of the multi-beam antenna array is suitable to be utilized in 5G mm-wave wireless communication systems.

In [87], a modified Yagi–Uda mm-wave BS antenna was presented operating at 29–31 GHz with pattern reconfigurable characteristics. The given antenna was designed on flexible RO3003 substrate and was integrated with an artificial magnetic conductor (AMC) surface. The Yagi–Uda and AMC used director loop diamond shapes with a flexible bending structure operating at high frequencies as shown in Fig. 4.16a. The use of a flexible substrate helped in tilting the beam in different directions, and thus multiple beam configurations were studied. Similarly in [88], a multi-polarized dual-band mm-wave BS was designed operating at 28/38 GHz. The

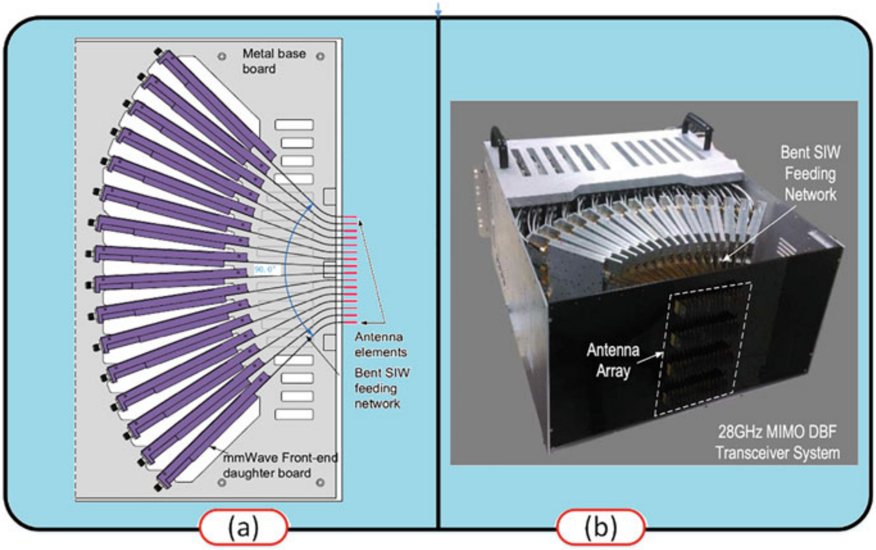

Fig. 4.14 Digital beamforming m-MIMO: (**a**) top view of array with bent SIW feeding network and (**b**) 64-channel DBF-based mm-wave m-MIMO transceiver system [85]

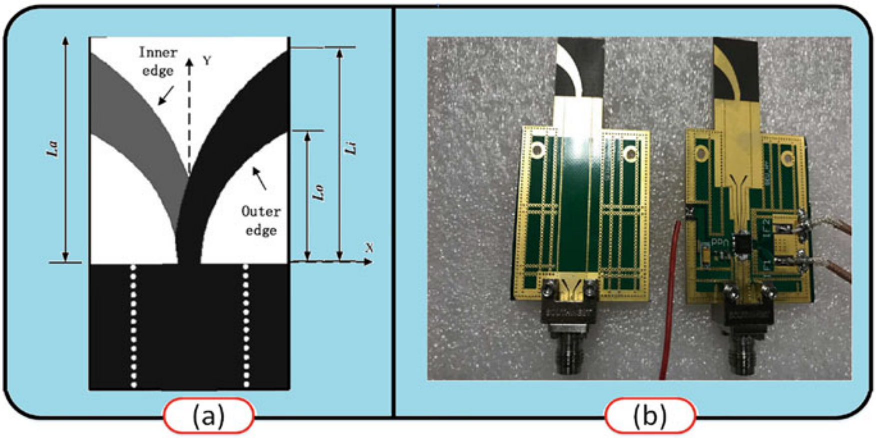

Fig. 4.15 Digital beamforming 1D planar array (**a**) Top view of array with bent SIW feeding network (**b**) Beamformer prototype [86]

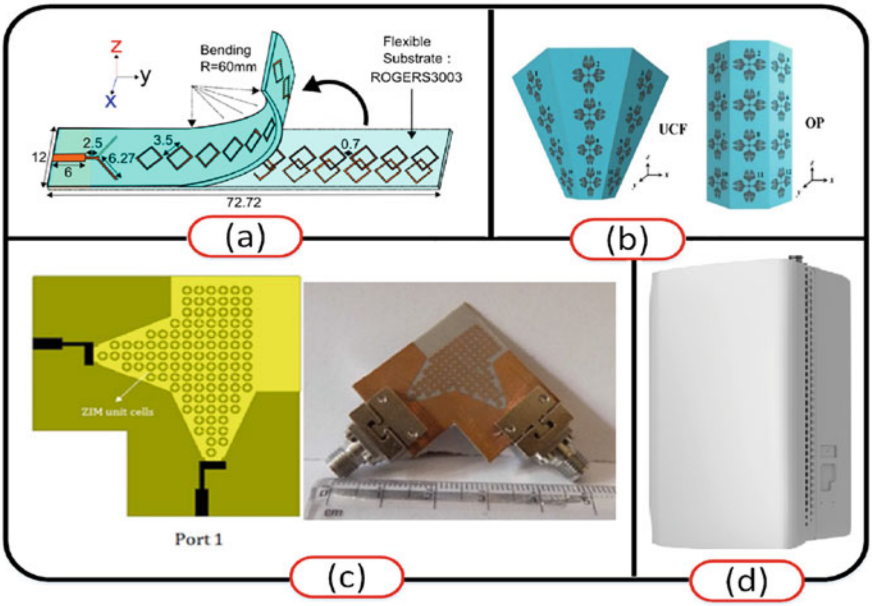

Fig. 4.16 mm-wave BS antennas: (**a**) AMC antenna configuration [87], (**b**) dual-band UCF and OP structure antennas [88], (**c**) shared-aperture antenna [89], and (**d**) Samsung 5G NR AU operating at 28 GHz [92]

proposed design is a good candidate for 5G BS antennas for future 5G networks. Two versions of the proposed antenna were designed and presented as shown in Fig. 4.16b. In the first configuration, an upside conical frustum (UCF) configuration contained 32-element circularly polarized antenna array to synthesize multi-beam operation. In the second configuration, an array of 32 elements was structured in an octagonal prism (OP). A modified version of the gravitational search algorithm (GSA) and particle swarm optimization (PSO) were implemented to form an algorithm for simultaneously controlling the multiple V/H beam polarization and directivity. The results obtained for both configurations were compared in terms of reflection coefficient, realized gain, radiation efficiency, and coverage efficiency. Better results were obtained in UCF configuration than the OP configuration. A unique shared-aperture antenna for mm-wave 5G BS applications was presented in [89], as shown in Fig. 4.16c. The proposed antenna design was operating in the mm-wave 5G frequency band from 27 to 30 GHz. The proposed antenna exhibited orthogonal pattern diversity with high gain value in the desired band of interest. For simultaneous gain enhancement for both ports, the shared-aperture antenna was loaded with a dual-polarized zero-index metamaterial structure. The end-fire gains for the orthogonal ports were in the range of 9.2–9.6 dBi. The access unit (AU) contained 1000 antenna elements along with a digital unit as one compact box. Samsung demonstrated that the AU using two test mobile devices had achieved approximately 4.3 Gbps speed on each with a peak speed of 8.5 Gbps across both devices [92].

Moreover, in [90], a dual-polarized 2 × 2 antenna subarray structure was proposed for mm-wave 5G BS applications. The antenna subarray design consisted of four radiating structures and is shown in Fig. 4.16d. The antenna was fabricated using a multilayer LTCC process, thus provided full integration with acceptable precision. The maximum gain value of the proposed design was 10.8 dBi and was achieved with an impedance bandwidth of 530 MHz operating with a center frequency of around 37 GHz. The antenna presented was compact and suitable to be deployed at the front-end of the beam steering mm-wave BS. Similarly, several mm-wave 5G BS antennas have been presented including magnetoelectric dipole wideband antenna [91] and antipodal tapered slot antenna array [93].

4.7 Conclusions

Next generation 5G MIMO wireless communication systems are required to meet the high data rate, greater transmission speed, low latency, high reliability, and enhanced spectral efficiencies. In the near future, 5G wireless devices will proliferate in all aspects of our lives. Therefore, researchers are attracted toward the research and development of 5G technologies. As MIMO antennas are an integral part of 5G standards, an attempt is made to provide a comprehensive overview of the state-of-the-art 5G MIMO antenna designs for both sub-6 GHz and mm-wave spectra. The evolution of MIMO wireless technology from 4G to 5G and various types of MIMO implementation are briefly outlined for wireless communication systems. Apart from certain advantages, 5G implementations posed several challenges from an antenna design perspective for both sub-6 GHz and mm-wave bands; hence, it is crucial to investigate the limitations and design consideration for MIMO antenna implementations. This chapter features MIMO antenna designs for BS as well as handheld devices for both sub-6 GHz and mm-wave bands. Moreover, the recent developments in sub-6 GHz 5G MIMO, integrated 4G and mm-wave 5G MIMO, mm-wave 5G MIMO antennas, and mm-wave m-MIMO for both user equipment (UE) and BS antenna designs are reported in a comprehensive manner. Furthermore, an attempt is made to include state of the art, available commercial 5G antennas for BS, AU, and UE to give an insight about their capabilities and recent trends in the domain.

References

1. M. Series, IMT vision–framework and overall objectives of the future development of IMT for 2020 and beyond. Recommendation ITU **2083** (2015)
2. F. Boccardi, R.W. Heath, A. Lozano, T.L. Marzetta, P. Popovski, Five disruptive technology directions for 5G. IEEE Commun. Mag. **52**(2), 74–80 (2014)
3. T.E. Bogale, L.B. Le, Massive MIMO and mmWave for 5G wireless HetNet: potential benefits and challenges. IEEE Veh. Technol. Mag. **11**(1), 64–75 (2016)
4. E.G. Larsson, O. Edfors, F. Tufvesson, T.L. Marzetta, Massive MIMO for next generation wireless systems. IEEE Commun. Mag. **52**(2), 186–195 (2014)
5. S. Mumtaz, J. Rodriguez, L. Dai, *MmWave Massive MIMO: A Paradigm for 5G* (Academic, Cambridge, 2016)
6. G.J. Foschini, Layered space-time architecture for wireless communication in a fading environment when using multi-element antennas. Bell Labs Tech. J. **1**(2), 41–59 (1996)
7. G.J. Foschini, M.J. Gans, On limits of wireless communications in a fading environment when using multiple antennas. Wirel. Personal Commun. **6**(3), 311–335 (1998)
8. M.S. Sharawi, *Printed MIMO Antenna Engineering* (Artech House, Norwood, 2014)
9. E. Telatar, Capacity of multi-antenna Gaussian channels. Eur. Trans. Telecommun. **10**(6), 585–595 (1999)
10. B.M. Hochwald, S. Ten Brink, Achieving near-capacity on a multiple-antenna channel. IEEE Trans. Commun. **51**(3), 389–399 (2003)
11. D. Gesbert, M. Kountouris, R. Heath, C. Chae, T. Salzer, From single user to multiuser communications: shifting the MIMO paradigm. IEEE Signal Processing Magazine. **129** (2008)
12. T.L. Marzetta, Noncooperative cellular wireless with unlimited numbers of base station antennas. IEEE Trans. Wireless Commun. **9**(11), 3590–3600 (2010)
13. M.S. Sharawi, 3D MIMO antenna designs, in *Wiley 5G Ref: The Essential 5G Reference Online* (Wiley, New York, 2020), pp. 1–16
14. X. Liu, H.-J. Chen, Y. Alfadhl, X. Chen, C. Parini, D. Wen, Conductivity and frequency dependent specific absorption rate. J. Appl. Phys. **113**(7), 074902 (2013)
15. F.C. Commission, et al., Human exposure to radio frequency fields: Guidelines for cellular and PCS sites (2014). http://transition.fcc.gov/cgb/guides/human-exposure-rf-fields-guidelines-cellular-and-pcs-sites
16. A. Doll, J.-P. Harel, Technology challenges in massive-MIMO radiating platforms, in *2017 Sixth Asia-Pacific Conference on Antennas and Propagation (APCAP)* (IEEE, Piscataway, 2017), pp. 1–2
17. L. Sanguinetti, E. Björnson, J. Hoydis, Toward massive MIMO 2.0: understanding spatial correlation, interference suppression, and pilot contamination. IEEE Trans. Commun. **68**(1), 232–257 (2019)
18. R. Mittra, Some challenges in millimeter wave antenna designs for 5G, in *2018 International Symposium on Antennas and Propagation (ISAP)* (IEEE, Piscataway, 2018), pp. 1–2
19. Z. Wu, B. Wu, Z. Su, X. Zhang, Development challenges for 5G base station antennas, in *2018 International Workshop on Antenna Technology (iWAT)* (IEEE, Piscataway, 2018), pp. 1–3
20. W. Hong, Z.H. Jiang, C. Yu, J. Zhou, P. Chen, Z. Yu, H. Zhang, B. Yang, X. Pang, M. Jiang, et al., Multibeam antenna technologies for 5G wireless communications. IEEE Trans. Antennas Propag. **65**(12), 6231–6249 (2017)
21. W. Hong, Solving the 5G mobile antenna puzzle: assessing future directions for the 5G mobile antenna paradigm shift. IEEE Microw. Mag. **18**(7), 86–102 (2017)

22. D.A. Sehrai, M. Abdullah, A. Altaf, S.H. Kiani, F. Muhammad, M. Tufail, M. Irfan, A. Glowacz, S. Rahman, A novel high gain wideband MIMO antenna for 5G millimeter wave applications. Electronics **9**(6), 1031 (2020)
23. D.A. Outerelo, A.V. Alejos, M.G. Sanchez, M.V. Isasa, Microstrip antenna for 5G broadband communications: Overview of design issues, in *2015 IEEE International Symposium on Antennas and Propagation & USNC/URSI National Radio Science Meeting* (IEEE, Piscataway, 2015), pp. 2443–2444
24. T.-K. Le, U. Salim, F. Kaltenberger, An overview of physical layer design for ultra-reliable low-latency communications in 3GPP release 15 and release 16 (2020). Preprint arXiv:2002.03713
25. M.-Y. Li, Y.-L. Ban, Z.-Q. Xu, J. Guo, Z.-F. Yu, Tri-polarized 12-antenna MIMO array for future 5G smartphone applications. IEEE Access **6**, 6160–6170 (2017)
26. Y. Li, Y. Luo, G. Yang, et al., 12-port 5G massive MIMO antenna array in sub-6GHz mobile handset for LTE bands 42/43/46 applications. IEEE Access **6**, 344–354 (2017)
27. M.-Y. Li, Y.-L. Ban, Z.-Q. Xu, G. Wu, K. Kang, Z.-F. Yu, et al., Eight-port orthogonally dual-polarized antenna array for 5G smartphone applications. IEEE Trans. Antennas Propag. **64**(9), 3820–3830 (2016)
28. N.O. Parchin, Y.I.A. Al-Yasir, A.H. Ali, I. Elfergani, J.M. Noras, J. Rodriguez, R.A. Abd-Alhameed, Eight-element dual-polarized MIMO slot antenna system for 5G smartphone applications. IEEE Access **7**, 15612–15622 (2019)
29. Y. Li, Y. Luo, G. Yang, et al., High-isolation 3.5 GHz eight-antenna MIMO array using balanced open-slot antenna element for 5G smartphones. IEEE Trans. Antennas Propag. **67**(6), 3820–3830 (2019)
30. Y.-L. Ban, C. Li, G. Wu, K.-L. Wong, et al., 4G/5G multiple antennas for future multi-mode smartphone applications. IEEE Access **4**, 2981–2988 (2016)
31. L. Sun, H. Feng, Y. Li, Z. Zhang, Compact 5G MIMO mobile phone antennas with tightly arranged orthogonal-mode pairs. IEEE Trans. Antennas Propag. **66**(11), 6364–6369 (2018)
32. Y. Liu, A. Ren, H. Liu, H. Wang, et al., Eight-port MIMO array using characteristic mode theory for 5G smartphone applications. IEEE Access **7**, 45679–45692 (2019)
33. Q. Chen, H. Lin, J. Wang, L. Ge, Y. Li, T. Pei, et al., Single ring slot-based antennas for metal-rimmed 4G/5G smartphones. IEEE Trans. Antennas Propag. **67**(3), 1476–1487 (2018)
34. Q. Cai, Y. Li, X. Zhang, W. Shen, Wideband MIMO antenna array covering 3.3–7.1 GHz for 5G metal-rimmed smartphone applications. IEEE Access **7**, 142070–142084 (2019)
35. L. Sun, Y. Li, Z. Zhang, Z. Feng, Wideband 5G MIMO antenna with integrated orthogonal-mode dual-antenna pairs for metal-rimmed smartphones. IEEE Trans. Antennas Propag. **68**(4), 2494–2503 (2019)
36. M.A. Al-Tarifi, M.S. Sharawi, A. Shamim, Massive MIMO antenna system for 5G base stations with directive ports and switched beamsteering capabilities. IET Microw. Antennas Propag. **12**(10), 1709–1718 (2018)
37. P. Xingdong, H. Wei, Y. Tianyang, L. Linsheng, Design and implementation of an active multibeam antenna system with 64 RF channels and 256 antenna elements for massive MIMO application in 5G wireless communications. China Commun. **11**(11), 16–23 (2014)
38. A. Alieldin, Y. Huang, S.J. Boyes, M. Stanley, S.D. Joseph, Q. Hua, D. Lei, A triple-band dual-polarized indoor base station antenna for 2G, 3G, 4G and sub-6 GHz 5G applications. IEEE Access **6**, 49209–49216 (2018)
39. B. Feng, K.L. Chung, J. Lai, Q. Zeng, A conformal magneto-electric dipole antenna with wide h-plane and band-notch radiation characteristics for sub-6-GHz 5G base-station. IEEE Access **7**, 17469–17479 (2019)

40. Y. Liu, S. Wang, N. Li, J.-B. Wang, J. Zhao, A compact dual-band dual-polarized antenna with filtering structures for sub-6 GHz base station applications. IEEE Antennas Wireless Propag. Lett. **17**(10), 1764–1768 (2018)
41. F. Liu, J. Guo, L. Zhao, X. Shen, Y. Yin, A meta-surface decoupling method for two linear polarized antenna array in sub-6 GHz base station applications. IEEE Access **7**, 2759–2768 (2018)
42. A. El-Bacha, R. Sarkis, Design of tilted taper slot antenna for 5G base station antenna circular array, in *2016 IEEE Middle East Conference on Antennas and Propagation (MECAP)* (IEEE, Piscataway, 2016), pp. 1–4
43. M. Sanad, N. Hassan, A sub-6 GHz multi-beam base station antenna for 5G with an arbitrary beam-tilting for each beam, in *2019 IEEE Radio and Wireless Symposium (RWS)* (IEEE, Piscataway, 2019), pp. 1–4
44. J. Vieira, S. Malkowsky, K. Nieman, Z. Miers, N. Kundargi, L. Liu, I. Wong, V. Öwall, O. Edfors, F. Tufvesson, A flexible 100-antenna testbed for massive MIMO, in *2014 IEEE Globecom Workshops (GC Wkshps)* (IEEE, Piscataway, 2014), pp. 287–293
45. Huawei, Huawei launches golden 5G-ready base station, massive MIMO antenna unit (2017)
46. D. Schoolar, Massive MIMO comes of age (2017)
47. R. Hussain, A.T. Alreshaid, S.K. Podilchak, M.S. Sharawi, Compact 4G MIMO antenna integrated with a 5G array for current and future mobile handsets. IET Microw. Antennas Propag. **11**(2), 271–279 (2017)
48. M.S. Sharawi, M. Ikram, A. Shamim, A two concentric slot loop based connected array MIMO antenna system for 4G/5G terminals. IEEE Trans. Antennas Propag. **65**(12), 6679–6686 (2017)
49. M. Ikram, M. Sharawi, A. Shamim, A. Sebak, A multiband dual-standard MIMO antenna system based on monopoles (4G) and connected slots (5G) for future smart phones. Microw. Opt. Technol. Lett. **60**(6), 1468–1476 (2018)
50. M. Ikram, R. Hussain, M.S. Sharawi, 4G/5G antenna system with dual function planar connected array. IET Microw. Antennas Propag. **11**(12), 1760–1764 (2017)
51. M. Ikram, E. Al Abbas, N. Nguyen-Trong, K.H. Sayidmarie, A. Abbosh, Integrated frequency-reconfigurable slot antenna and connected slot antenna array for 4G and 5G mobile handsets. IEEE Trans. Antennas Propag. **67**(12), 7225–7233 (2019)
52. S.I. Naqvi, A.H. Naqvi, F. Arshad, M.A. Riaz, M.A. Azam, M.S. Khan, Y. Amin, J. Loo, H. Tenhunen, An integrated antenna system for 4G and millimeter-wave 5G future handheld devices. IEEE Access **7**, 116555–116566 (2019)
53. J. Kurvinen, H. Kähkönen, A. Lehtovuori, J. Ala-Laurinaho, V. Viikari, Co-designed mm-wave and LTE handset antennas. IEEE Trans. Antennas Propag. **67**(3), 1545–1553 (2018)
54. M. Ikram, N. Nguyen-Trong, A. Abbosh, Multiband MIMO microwave and millimeter antenna system employing dual-function tapered slot structure. IEEE Trans. Antennas Propag. **67**(8), 5705–5710 (2019)
55. S.K. Dhar, M.S. Sharawi, F.M. Ghannouchi, Microwave connector de-embedding and antenna characterization [education corner]. IEEE Antennas Propag. Mag. **60**(3), 110–117 (2018)
56. S.K. Dhar, O. Hammi, M.S. Sharawi, F.M. Ghannouchi, Power amplifier based integrated and miniaturized active antenna, in *2015 9th European Conference on Antennas and Propagation (EuCAP)* (IEEE, Piscataway, 2015), pp. 1–4
57. S.K. Dhar, T. Sharma, F.M. Ghannouchi, M.S. Sharawi, Miniaturized antenna integrated receiving front-end, in *2017 IEEE International Conference on Antenna Innovations & Modern Technologies for Ground, Aircraft and Satellite Applications (iAIM)* (IEEE, Piscataway, 2017), pp. 1–5
58. M.S. Sharawi, S.K. Dhar, O. Hammi, F.M. Ghannouchi, Miniaturised active integrated antennas: a co-design approach. IET Microw. Antennas Propag. **10**(8), 871–879 (2016)

59. S. Dhar, M. Sharawi, O. Hammi, F. Ghannouchi, An active integrated ultra-wideband MIMO antenna. IEEE Trans. Antennas Propag. **64**(4), 1573–1578 (2016)
60. S.K. Dhar, M.S. Sharawi, A UWB semi-ring MIMO antenna with isolation enhancement. Microw. Opt. Technol. Lett. **57**(8), 1941–1946 (2015)
61. B. Yang, Z. Yu, Y. Dong, J. Zhou, W. Hong, Compact tapered slot antenna array for 5G millimeter-wave massive MIMO systems. IEEE Trans. Antennas Propag. **65**(12), 6721–6727 (2017)
62. Y.-W. Hsu, T.-C. Huang, H.-S. Lin, Y.-C. Lin, Dual-polarized quasi Yagi–Uda antennas with endfire radiation for millimeter-wave MIMO terminals. IEEE Trans. Antennas Propag. **65**(12), 6282–6289 (2017)
63. A. Iqbal, A. Basir, A. Smida, N.K. Mallat, I. Elfergani, J. Rodriguez, S. Kim, Electromagnetic bandgap backed millimeter-wave MIMO antenna for wearable applications. IEEE Access **7**, 111135–111144 (2019)
64. W. Hong, K.-H. Baek, S. Ko, Millimeter-wave 5G antennas for smartphones: Overview and experimental demonstration. IEEE Trans. Antennas Propag. **65**(12), 6250–6261 (2017)
65. Q.T. Inc., First 5G mmwave antenna module for smartphone. Microw. J. (2018)
66. M. Farahani, J. Pourahmadazar, M. Akbari, M. Nedil, A.R. Sebak, T.A. Denidni, Mutual coupling reduction in millimeter-wave MIMO antenna array using a metamaterial polarization-rotator wall. IEEE Antennas Wirel. Propag. Lett. **16**, 2324–2327 (2017)
67. Y.M. Pan, X. Qin, Y.X. Sun, S.Y. Zheng, A simple decoupling method for 5G millimeter-wave MIMO dielectric resonator antennas. IEEE Trans. Antennas Propag. **67**(4), 2224–2234 (2019)
68. Y. Zhang, J.-Y. Deng, M.-J. Li, D. Sun, L.-X. Guo, A MIMO dielectric resonator antenna with improved isolation for 5G mm-wave applications. IEEE Antennas Wirel. Propag. Lett. **18**(4), 747–751 (2019)
69. C. Di Paola, K. Zhao, S. Zhang, G.F. Pedersen, SIW multibeam antenna array at 30 GHz for 5G mobile devices. IEEE Access **7**, 73157–73164 (2019)
70. M.T. Hussain, M.S. Sharawi, S. Podilchack, Y.M. Antar, Closely packed millimeter-wave MIMO antenna arrays with dielectric resonator elements, in *2016 10th European Conference on Antennas and Propagation (EuCAP)* (IEEE, Piscataway, 2016), pp. 1–4
71. C. Di Paola, K. Zhao, S. Zhang, G.F. Pedersen, SIW multibeam antenna array at 30 GHz for 5G mobile devices. IEEE Access **7**, 73157–73164 (2019)
72. C. Di Paola, K. Zhao, S. Zhang, G.F. Pedersen, Wideband SIW horn antenna with phase correction for new generation beam steerable arrays, in *2019 IEEE 90th Vehicular Technology Conference (VTC2019-Fall)* (IEEE, Piscataway, 2019), pp. 1–4
73. M. Mantash, A. Kesavan, T.A. Denidni, Millimetre-wave antenna with tilted beam for future base station applications. IET Microw. Antennas Propag. **13**(2), 223–230 (2018)
74. K.R. Mahmoud, A.M. Montaser, Synthesis of multi-polarised upside conical frustum array antenna for 5G mm-wave base station at 28/38 GHz. IET Microw. Antennas Propag. **12**(9), 1559–1569 (2018)
75. N. Ashraf, O. Haraz, M.A. Ashraf, S. Alshebeili, 28/38-GHz dual-band millimeter wave SIW array antenna with EBG structures for 5G applications, in *2015 International Conference on Information and Communication Technology Research (ICTRC)* (IEEE, Piscataway, 2015), pp. 5–8
76. C. Di Paola, K. Zhao, S. Zhang, G.F. Pedersen, Wideband SIW horn antenna with phase correction for new generation beam steerable arrays, in *2019 IEEE 90th Vehicular Technology Conference (VTC2019-Fall)* (IEEE, Piscataway, 2019), pp. 1–4
77. H.-T. Kim, B.-S. Park, S.-S. Song, T.-S. Moon, S.-H. Kim, J.-M. Kim, J.-Y. Chang, Y.-C. Ho, A 28-GHz CMOS direct conversion transceiver with packaged 2×4 antenna array for 5G cellular system. IEEE J. Solid-State Circ. **53**(5), 1245–1259 (2018)

78. M.K. Hedayati, A. Abdipour, R.S. Shirazi, M.J. Ammann, M. John, C. Cetintepe, R.B. Staszewski, Challenges in on-chip antenna design and integration with RF receiver front-end circuitry in nanoscale CMOS for 5G communication systems. IEEE Access **7**, 43190–43204 (2019)
79. K. Kibaroglu, M. Sayginer, T. Phelps, G.M. Rebeiz, A 64-element 28-GHz phased-array transceiver with 52-dBm EIRP and 8–12-Gb/s 5G link at 300 meters without any calibration. IEEE Trans. Microw. Theory Tech. **66**(12), 5796–5811 (2018)
80. L. Aluigi, G. Orecchini, L. Larcher, A 28 GHz scalable beamforming system for 5G automotive connectivity: An integrated patch antenna and power amplifier solution, in *2018 IEEE MTT-S International Microwave Workshop Series on 5G Hardware and System Technologies (IMWS-5G)* (IEEE, Piscataway, 2018), pp. 1–3
81. N. Ashraf, O. Haraz, M.A. Ashraf, S. Alshebeili, 28/38-GHz dual-band millimeter wave SIW array antenna with EBG structures for 5G applications, in *2015 international Conference on Information and Communication Technology Research (ICTRC)* (IEEE, Piscataway, 2015), pp. 5–8
82. Y. Hu, W. Hong, Z.H. Jiang, A multibeam folded reflectarray antenna with wide coverage and integrated primary sources for millimeter-wave massive MIMO applications. IEEE Trans. Antennas Propag. **66**(12), 6875–6882 (2018)
83. M.A.B. Abbasi, H. Tataria, V.F. Fusco, M. Matthaiou, Performance of a 28 GHz two–stage Rotman lens beamformer for millimeter wave cellular systems, in *2019 13th European Conference on Antennas and Propagation (EuCAP)* (IEEE, Piscataway, 2019), pp. 1–4
84. S. Wane, P. Corrales, T.V. Dinh, M. Haider, J. Russer, Q.-H. Tran, C.-J. Lin, S.-W. Chang, W.-T. Tsai, R. Giacometti, et al., Millimeter-wave beamformer chips with smart-antennas for 5G: Toward holistic RFSOI technology solutions including RF-ADCs, in *2019 IEEE Texas Symposium on Wireless and Microwave Circuits and Systems (WMCS)* (IEEE, Piscataway, 2019), pp. 1–4
85. B. Yang, Z. Yu, J. Lan, R. Zhang, J. Zhou, W. Hong, Digital beamforming-based massive MIMO transceiver for 5G millimeter-wave communications. IEEE Trans. Microw. Theory Techn. **66**(7), 3403–3418 (2018)
86. Y. Hu, W. Hong, C. Yu, Y. Yu, H. Zhang, Z. Yu, N. Zhang, A digital multibeam array with wide scanning angle and enhanced beam gain for millimeter-wave massive MIMO applications. IEEE Trans. Antennas Propag. **66**(11), 5827–5837 (2018)
87. M. Mantash, A. Kesavan, T.A. Denidni, Millimetre-wave antenna with tilted beam for future base station applications. IET Microw. Antennas Propag. **13**(2), 223–230 (2018)
88. K.R. Mahmoud, A.M. Montaser, Synthesis of multi-polarised upside conical frustum array antenna for 5G mm-wave base station at 28/38 GHz. IET Microw. Antennas Propag. **12**(9), 1559–1569 (2018)
89. K.G. Sadananda, M.P. Abegaonkar, S.K. Koul, Gain equalized shared-aperture antenna using dual-polarized ZIM for mmWave 5G base stations. IEEE Antennas Wirel. Propag. Lett. **18**(6), 1100–1104 (2019).
90. K.-M. Luk, B. Wu, The magnetoelectric dipole—a wideband antenna for base stations in mobile communications. Proc. IEEE **100**(7), 2297–2307 (2012)
91. H. Chu, Y.-X. Guo, A filtering dual-polarized antenna subarray targeting for base stations in millimeter-wave 5G wireless communications. IEEE Trans. Comp. Pack. Manufact. Technol. **7**(6), 964–973 (2017)
92. S. Electronics, Samsung unveils new 5G NR integrated radio supporting 28GHz
93. R. Ma, Y. Gao, L. Cuthbert, Q. Zeng, Antipodal linearly tapered slot antenna array for millimeter-wave base station in massive MIMO systems, in *2014 IEEE Antennas and Propagation Society International Symposium* (IEEE, Piscataway, 2014), pp. 1121–1122

Rifaqat Hussain is currently a Faculty Member and associated with Antenna and Microwave Structure Design Lab (MASDL) at King Fahd University of Petroleum & Minerals, Saudi Arabia. Dr. Hussain received his B.Sc Electrical engineering degree from University of Engineering and Technology, Peshawar Pakistan in 2003 with distinction and M.S. degree in Systems Engineering from PIEAS, Pakistan in 2005. Prior to joining KFUPM, he served as Senior Engineer at Public Sector R&D organization in Pakistan from 2005 to 2011. He obtained his Ph.D degree in Electrical Engineering in Jan. 2015, from King Fahd University of Petroleum and Minerals (KFUPM), Dhahran, Saudi Arabia. His current research areas are reconfigurable antennas, 4G/5G integrated antenna designs, CubeSat antenna, IoT and 5G-enabled antenna design.

Muhammad Umar Khan is currently an assistant professor at the Research Institute for Microwave and Millimeter Wave Studies (RIMMS), National University of Sciences and Technology (NUST). He obtained his Bachelors in Electrical Engineering degree from Pakistan Navy Engineering College (PNEC), NUST, Karachi, Pakistan in 2006. He received his M.S. degree in Electrical Engineering from GIK Instittue of Engineering Sciences and Technology (GIKI), Topi, Pakistan in 2008. He received Ph.D. in Electrical Engineering from King Fahd University of Petroleum and Minerals (KFUPM), Dhahran, Saudi Arabia in 2015. His research focus duing his doctorate studies was on Microwave and Antenna Systems Design. As part of the Antennas and Microwave Structure Design (AMSD) laboratory at KFUPM, he worked on Electrically Small Antennas and MIMO Antenna Systems. His current research interests include Printed Antennas and Antenna Arrays, MIMO Antenna Systems, Millimeter-Wave antennas, Reconfigurable Antennas, Applied Electromagnetics, Microwave Electronics and Microwave System Design. He has published more than 50 refereed journal and conference papers and has one issued patent with the USPO.

Mohamed A. Abou-Khousa (IEEE Senior Member) is an Associate Professor in the Electrical Engineering and Computer Science Department at Khalifa University of Science and Technology, Abu-Dhabi, UAE. His area of expertise is focused on applied electromagnetics and antennas. He has co-authored many technical publications in his area of expertise, and has to his credit many patents. He is an Associate Editor for the IEEE Transactions on Instrumentation and Measurement (TIM). He was recognized as a TIM Outstanding Reviewer for the years 2008–2013, and TIM Outstanding Associate Editor in 2018 and 2019. He is currently serving as the Chair of the IEEE UAE Instrumentation and Measurement, Antennas and Propagation, and Microwave Theory and Techniques Joint Chapter (2018–2021). He is the recipient of many awards including IEEE IMS 2017 Outstanding Young Engineer Award, and IEEE APS 2013 H. A. Wheeler Prize Paper Award.

Mohammad S. Sharawi is a Professor of Electrical Engineering at Polytechnique Montréal, Montréal, Québec, Canada. He is also a member of the Poly-Grames Research Center at Polytechnique. He was with King Fahd University of Petroleum and Minerals (KFUPM), Saudi Arabia, between 2009-2018. He founded and directed the Antennas and Microwave Structure Design Laboratory (AMSDL) at KFUPM. He was a visiting Professor at the Intelligent Radio (iRadio) Laboratory, Electrical Engineering Department, University of Calgary, Alberta, Canada, during the Summer-Fall of 2014. He was a visiting research Professor at Oakland University during the summer of 2013. He received his PhD degree from Oakland University, Michigan, USA in 2006.

Prof. Sharawi's areas of research include Multiband Printed Multiple-Input-Multiple-Output (MIMO) Antenna systems, Reconfigurable and Active integrated Antennas, Applied Electromagnetics, Millimeter-wave MIMO antennas and Integrated 4G/5G antennas for wireless handsets and access points. He has more than 300 papers published in refereed journals and international conferences, 10 book chapters, one single authored book entitled "Printed MIMO Antenna Engineering," Artech House, 2014, and the lead author of the recent book "Design and Applications of Active Integrated Antennas," Artech house, 2018. He has 22 issued and 15 pending patents in the US Patent Office. He is serving as the Associate Editor for the IEEE Antennas and Wireless Propagation Letters (AWPL), IET Microwaves, Antennas and Propagation (MAP), and an Area Editor for Wiley Microwave and Optical Technology Letters (MOP). He is the Specialty editor of the newly launched Frontiers Journal on Communications and Networking, the System and Test-Bed design section. He served on the Technical and organizational program committees of several international conferences such as EuCAP, APS, IMWS-5G, APCAP, iWAT among many others.

Chapter 5
High-Isolation Compact Wideband MIMO Antennas for 5G Wireless Communication

Muhammad Aziz ul Haq, Slawomir Koziel, and M. Arif Khan

5.1 Introduction

Multiple-input–multiple-output (MIMO) antenna systems have significantly enhanced reliability and data capacity of communication channels over single-antenna systems without using extra bandwidth or power consumption [1]. Multiple-antenna installation (at the receiving or transmitting end) featuring low mutual coupling is essential for reliable communication [2] in new wireless technologies such as 5G and beyond. The size has always been an important issue for designers in the context of mounting antennas in physically small devices. On the other hand, densely arranged MIMO antenna elements lead to a coupling issue that degrades the MIMO system performance. The design of compact MIMO antennas with high isolation for space-limited communication devices remains a challenge for the researchers [3–5]. In some applications, such as imaging and radar systems [6], where transmitting and receiving antenna elements are placed close to each other, a high level of isolation is required to ensure adequate operation and performance.

There have been significant research efforts observed over the last few years to address the aforementioned issues. One of the simplest methods to reduce the mutual coupling effect is to place the antenna elements orthogonal to each other [7, 8]. However, for certain applications such as imaging and radar systems where a large number of antenna elements are required to enhance the system resolution,

M. A. u. Haq (✉) · S. Koziel
Engineering Optimization & Modeling Center, School of Science and Engineering, Reykjavik University, Reykjavík, Iceland
e-mail: aziz@ru.is; koziel@ru.is

M. A. Khan
School of Computing and Mathematics, Charles Sturt University, Bathurst, NSW, Australia
e-mail: mkhan@csu.edu.au

M. A. Matin (ed.), *Wideband, Multiband, and Smart Antenna Systems*, Signals and Communication Technology, https://doi.org/10.1007/978-3-030-74311-6_5

practical issues arise related to the complexity of the feeding structure (problematic for compact communication devices). Other approaches include introduction of a rectangular strip between the antenna elements [9], a parasitic coupling element [10, 11], a neutralization line [12, 13], a coupled-resonator decoupling network (CRDN) [14], electromagnetic band gap (EBG) structures [15], and metamaterial-inspired antennas [16]. These techniques have been successfully applied to reduce the mutual coupling phenomenon, but at the cost of their own limitations. In particular, they are typically applied to narrowband structures, whereas their implementation for compact wideband and ultra-wideband systems is much more complicated. Some geometry modification-based techniques intended to achieve improved isolation for wideband applications have been reported in [17–25].

It should be emphasized that the development of a particular antenna topology, including appropriate alterations such as those discussed in the previous paragraph, is not sufficient to achieve the satisfactory design. Another, often-overlooked, stage is a proper adjustment of antenna geometry parameters concerning all performance figures involved. A conventional approach here is parameter sweeping, which is laborious and does not lead to optimum results due to complex interactions between various parameters. Rigorous numerical optimization ensures superior results and should be carried out not only to achieve the best possible antenna performance but also to validate the relevance of particular topological changes introduced into the antenna structure [26].

In this chapter, a technique for isolation improvement in the context of wideband MIMO antennas in a parallel configuration is proposed. Our approach is based on appropriate ground plane modifications, primarily multi-section slits below the feed lines. These allow us to improve the antenna matching without enlarging the footprint. The "safety" margin between the maximum in-band reflection and the -10 dB acceptance limit obtained this way permits—along with rigorous optimization of antenna parameters—for enhancing isolation. The technique is generic as demonstrated using four UWB structures of various radiator shapes. Isolation at the level of -20 dB is obtained in all cases, along with satisfactory values of other performance figures (ECC, DG, and radiation pattern). An experimental validation is provided.

5.2 Ground Plane Technique for Isolation Improvement

This section discusses the proposed systematic approach to isolation enhancement for wideband MIMO antenna design. The procedure has been conceptually explained in Fig. 5.1, where subsequent stages of ground plane development have been illustrated. For the sake of clarity, only the ground plane (but not the radiators) has been shown. The starting point is a plain ground (Fig. 5.1a), with a possibly good antenna performance achieved through parameter sweeping and/or numerical optimization. In the next stage, the L-shaped stubs are inserted (Fig. 5.1b). The primary purpose of these is an improvement of the reflection

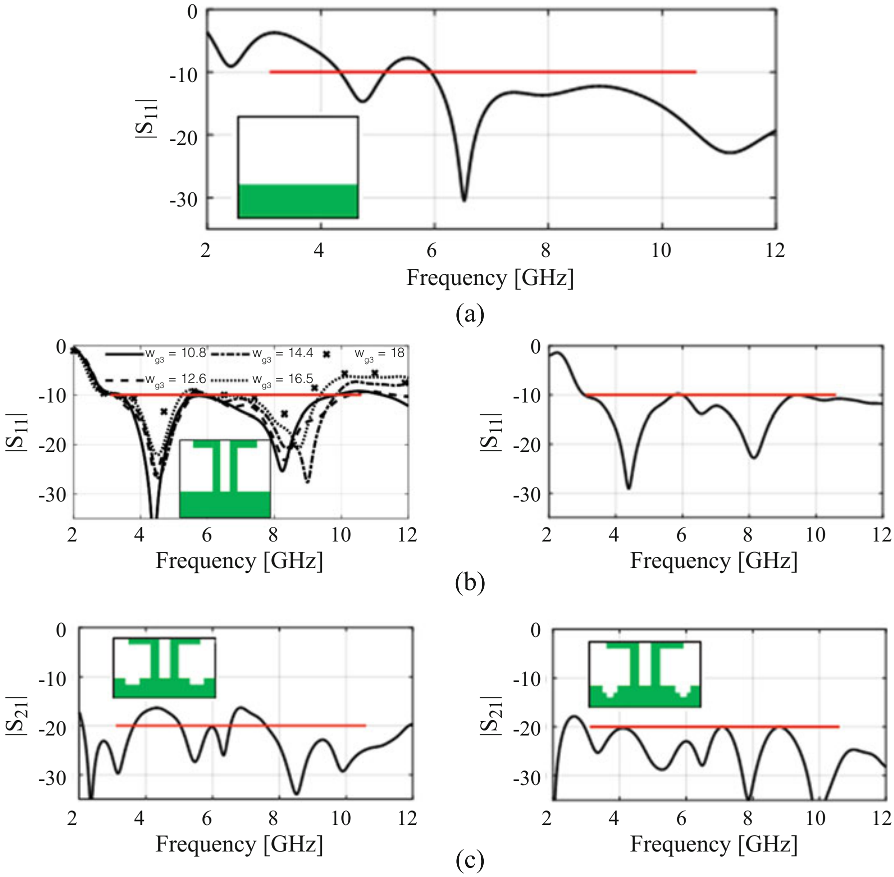

Fig. 5.1 Proposed isolation enhancement technique for wideband MIMO antennas: (**a**) Stage 0: plain ground and the pre-optimized antenna reflection response, (**b**) Stage 1: L-shaped stubs inserted and geometry parameters pre-adjusted using parameter sweeping followed by numerical optimization of the reflection response, and (**c**) Stage 2: multi-stage slits below the feed lines inserted and geometry parameters optimized for best isolation with reflection constraint ($|S_{11}| \leq -10$ dB)

response. The geometry parameter adjustment at this stage is first realized using a parameter sweeping and then (upon producing a reasonable initial design) through numerical optimization (cf. Fig. 5.1b). The second stage provides a good initial design for the last stage, which consists of inserting multi-section slits below the radiator feed lines, followed by rigorous constrained optimization of the antenna parameters. The optimization algorithm of choice is a trust-region gradient search with numerical derivatives [27] and implicit constraint handling by means of a penalty function approach [28]. Figure 5.2 shows a flowchart of the procedure. At particular stages of the process, the optimizer switches between a parameter

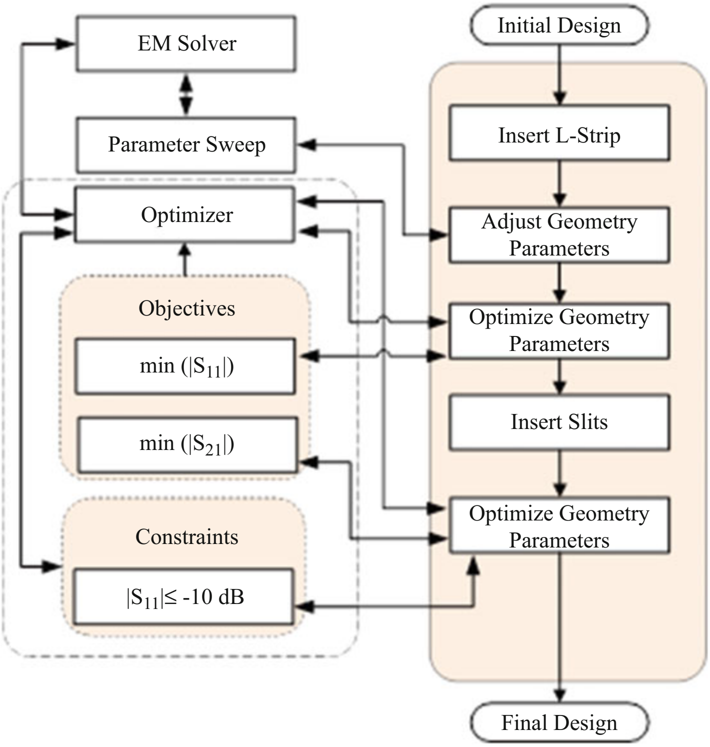

Fig. 5.2 Operation of the proposed isolation enhancement technique

sweeping routine and the gradient-based algorithm and appropriately selects the design objectives and constraints. Note that the last stage involves a constraint on the reflection response with the primary objective being isolation improvement. As demonstrated in the remaining parts of the letter, the proposed decomposition of the design preferences and constraints, as well as sequential introduction of ground plane modifications interleaved by parameter optimization, allows us to obtain consistent and competitive results. Here, the constraints are introduced to limit physical antenna size within a certain value. A custom-designed socket is used to interface the optimizer and the EM solver. The presented framework allows for switching between various numerical optimization setups where necessary, eventually leading to the optimum results in terms of both the antenna impedance matching and isolation. Furthermore, comprehensive verification carried out for a variety of radiators indicates the versatility of the techniques.

5.3 Verification Case Studies

The proposed optimization-based isolation enhancement procedure has been applied to four wideband MIMO antennas in a parallel configuration as shown in Fig. 5.3. The antennas differ in the radiator shapes, yet, in order to demonstrate the versatility of our approach, the same ground plane technique of Section 5.2 has been used to improve isolation while maintaining small footprints. All antennas are realized on a 1.55-mm thick FR-4 substrate $\epsilon_r = 4.4$. Computational models are implemented in CST Microwave Studio [30]. The models are equipped with SMA connectors to improve further agreement between the simulation and measurement data. The design variable vectors of Antennas I through IV are

$$x^{\mathrm{I}} = [l_g\ l_0\ r_1\ r_2\ d\ d_l\ d_w\ l_{g1}\ w_{g2}\ l_{g3}\ w_{g3}\ w_{01}]^T\ , \tag{5.1}$$

$$x^{\mathrm{II}} = [l_g\ l_0\ l_{01}\ w_{01}\ l_{02}\ w_{02}\ l_p\ w_p\ d\ d_l\ d_w\ l_{g1}\ w_{g2}\ l_{g3}\ w_{g3}\ u\ v]^T\ , \tag{5.2}$$

$$x^{\mathrm{III}} = [l_g\ l0\ l_{01}\ w_{01}\ l_{02}\ w_{02}\ l_p\ w_p\ r\ d\ d_l\ d_w\ l_{g1}\ w_{g2}\ l_{g3}\ w_{g3}\ u\ v]^T\ , \tag{5.3}$$

$$x^{\mathrm{IV}} = [l_g\ l_0\ l_{01}\ w_{01}\ l_{02}\ w_{02}\ l_p\ w_p\ d\ d_l\ d_w\ l_{g1}\ w_{g2}\ l_{g3}\ w_{g3}\ u\ v]^T\ ; \tag{5.4}$$

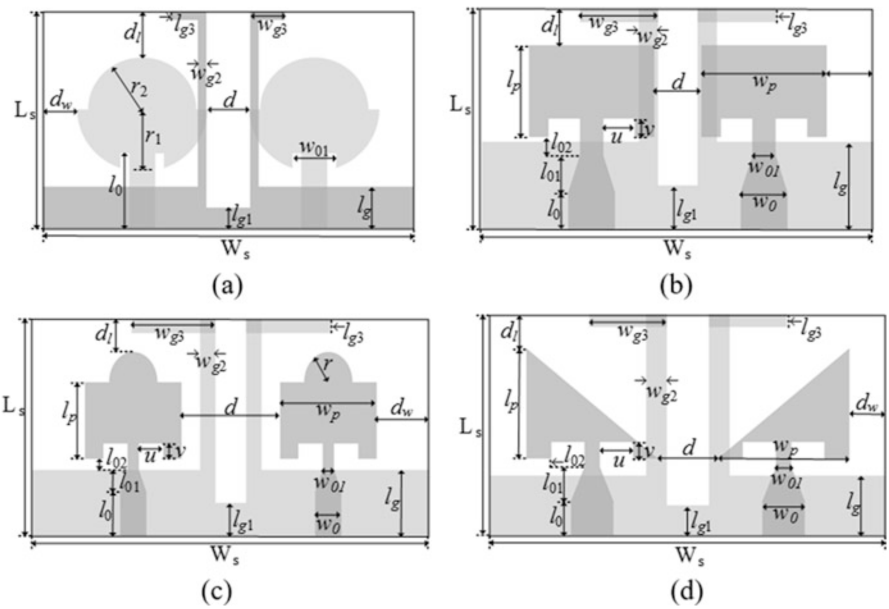

Fig. 5.3 Geometries of compact UWB-MIMO antennas utilized to validate the proposed isolation enhancement technique. (**a**) Antenna I [29], (**b**) Antenna II, (**c**) Antenna III, and (**d**) Antenna IV. The ground plane is shown using the light gray shade

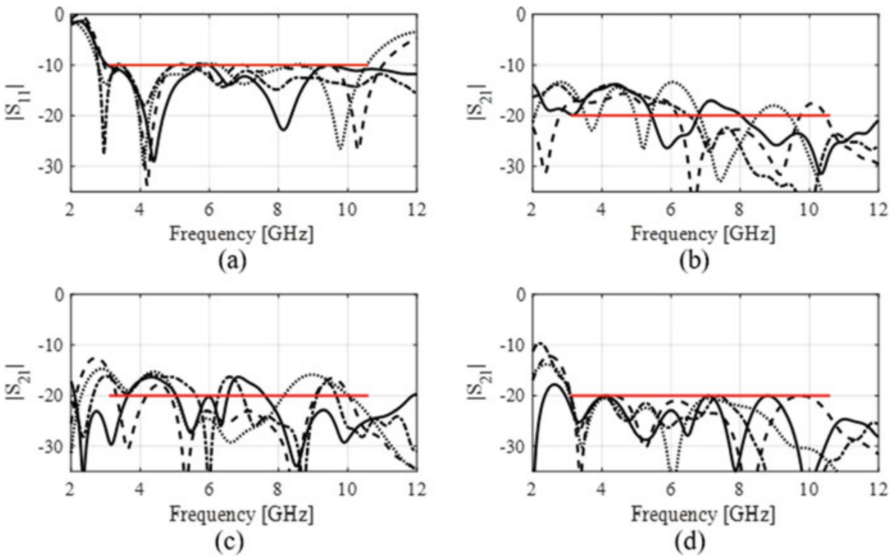

Fig. 5.4 Simulated S-parameters of the optimized benchmark antennas: Antenna I (solid line), Antenna II (dashed line), Antenna III (solid–long dashed line), and Antenna IV (dotted line); (**a**) $|S_{11}|$ response w.r.t. the initial design, (**b**) $|S_{21}|$ response w.r.t. the initial design, (**c**) $|S_{21}|$ with one-section slit, and (**d**) $|S_{21}|$ with two-section slit below the feed line

all dimensions are in millimeters (mm).

In the first stage, following the design methodology of Sect. 5.2, rigorous numerical optimization is applied to achieve the best possible matching. The results are shown in Fig. 5.4a. The numerical values corresponding to ach antenna are as follows:

$$x_1^{\mathrm{I}} = [4.05.86.70.92.95.63.30.51.51.21.03.5]^T,$$

$$x_1^{\mathrm{II}} = [73.41.82.72.67.48.3851.81.41.90.98.40.62.2]^T,$$

$$x_1^{\mathrm{III}} = [5.63.91.511.64.390.97.65.511.90.90.35.30.30.5]^T, \textit{and}$$

$$x_1^{\mathrm{IV}} = [93.73.42.83.811.67.57.64.83.8931.3130.32]^T.$$

Figure 5.4b shows the isolation characteristics of the antennas with a plain ground. In the next stage, the slits below the feed lines are added and the antenna parameters are re-optimized. Here, for illustration purposes, the results corresponding to both one- (Fig. 5.4c) and two-section slits (Fig. 5.4d) are shown. Isolation achieved for two-section slits is below −20 dB for the entire operating band. The numerical values are as follows:

$$x_3^{\mathrm{I}} = [5.77.07.40.81.35.40.71.03.04.21.84.23.80.20.90.8]^T$$

$$x_3^{\mathrm{II}} = [8.21.64.52.13.687.81053.96.14.42.913.40.31.610.30.90.3]^T$$

$$x_3^{\mathrm{III}} = [85.81.22.42.37.27.30.512.62.83.56.4315.50.30.60.43.80.40.2]^T \, and$$

$$x_3^{\mathrm{IV}} = [102.55.81.54.510.78.7153.71.93.63.9315.40.41.55.50.70.40.2]^T.$$

The effect of the slit can be further analyzed using surface current distributions, here shown at 5 GHz (cf. Fig. 5.5). For the sake of brevity, only Antenna II is considered. It can be observed that when Port 1 is excited and Port 2 is terminated with a 50 Ω impedance load, a significant amount of current is not only flowing on the ground plane but also coupled along Port 2 as shown in Fig. 5.5a. This effect is reduced to some extent by introducing a one-section slit below the feed line as shown in Fig. 5.5b. The introduction of two-section slits improves the situation significantly, and negligible amount of current is observed along Port 2 as shown in Fig. 5.5c. This does demonstrate that the introduction of the two-section slits reduces the mutual coupling to the point where both ports are almost independent of each other. In order to further validate the capability and performance of the considered MIMO antennas, envelop correlation coefficient (ECC), and diversity gain (DG), is investigated. ECC $\leq$ 0.5 is considered a requirement for an uncorrelated MIMO system. ECC can be calculated using the following expression [31]:

$$ECC = \frac{\left| \iint_{4\pi} \left[\overrightarrow{F_1}(\theta, \phi) . \overrightarrow{F_2}(\theta, \phi) \right] d\Omega \right|^2}{\iint_{4\pi} |\overrightarrow{F_1}(\theta, \phi)|^2 d\Omega \iint_{4\pi} |\overrightarrow{F_2}(\theta, \phi)|^2 d\Omega}, \quad (5.5)$$

where $\overrightarrow{F_1}(\theta, \phi)$ is the field radiation pattern of the MIMO antenna element when port i is excited (here, $i = 1, 2$) and the other port is terminated with the 50Ω load. Here, ECC has been evaluated through numerical integration of the simulated far-field data. It is clear from Fig. 5.6 that the ECC values of the benchmark antennas are lower than 0.005, which confirms the capability of the antennas for reliable communication, achieved due to the proposed decoupling structure. The differential gain, evaluated using the formula

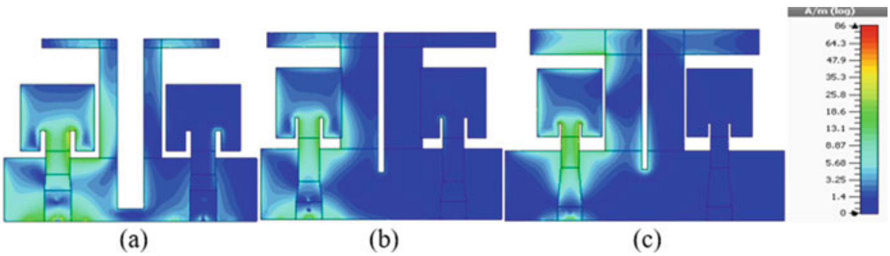

Fig. 5.5 Surface current distributions over Antenna II at 5 GHz. (**a**) Flat ground plane, (**b**) one-section slit, and (**c**) two-section slit below the feed line

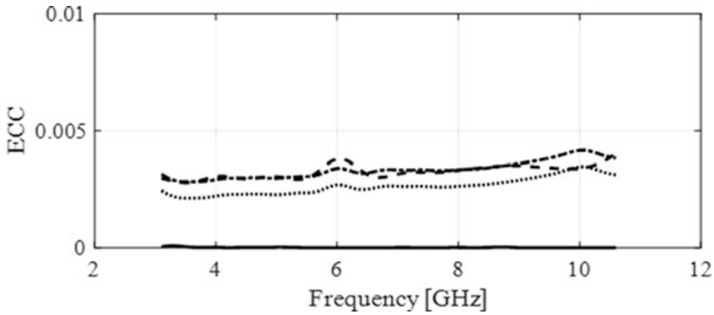

Fig. 5.6 Simulated ECC characteristics of the optimized antennas: Antenna I (solid line), Antenna II (dashed line), Antenna III (solid–long dashed line), and Antenna IV (dotted line)

$$DG = \sqrt{1 - ECC^2}\,, \tag{5.6}$$

is higher than 9.99 for the entire UWB frequency range.

5.4 Experimental Results

Experimental validation of the simulation results has been carried out for two selected structures, Antenna I and Antenna III. Due to the parallel orientation of the MIMO antennas, the results of the Port 2 are not shown as they are identical to those for Port 1. It can be observed from Fig. 5.7a that the simulated and measured $|S_{11}|$ response is below -10 dB, which is the basic requirement for any antenna operating for the UWB frequency band. Also, Fig. 5.7b illustrates the simulated and measured isolation $|S_{21}|$ for both antennas, which is under -20 dB. This demonstrates that the proposed isolation enhancement technique leads to adequate results in terms of reducing the mutual coupling between the antenna elements. Figure 5.8 illustrates the measured and simulated efficiencies of Antennas I and III. A good agreement is observed for the entire operating frequency range. Figure 5.9 shows the measured and simulated MIMO antenna performance in terms of ECC and DG corresponding to Antennas I and III. It is observed that the measured ECC and DG (here, obtained from the S-parameters) are confirming our simulations. Figure 5.10 shows the radiation patterns at 6 and 8 GHz. The radiation characteristics are nearly omnidirectional over the operating band.

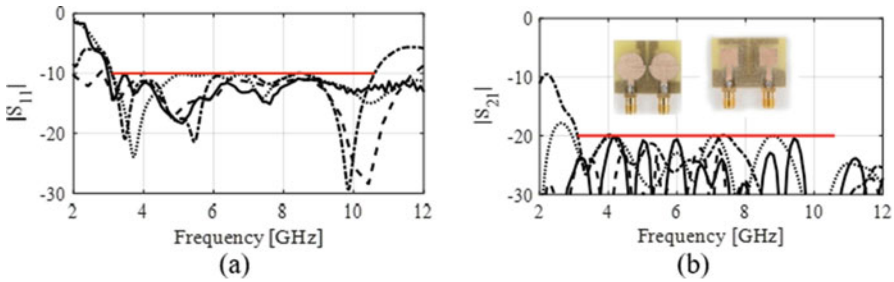

Fig. 5.7 Simulated and measured S-parameters of the optimized UWB-MIMO antennas with the two-section slit below the feed line: Antenna I measured (solid line) and simulated (dotted line) and Antenna III measured (dashed line) and simulated (long–short dashed line). (**a**) $|S_{11}|$ and (**b**) $|S_{21}|$

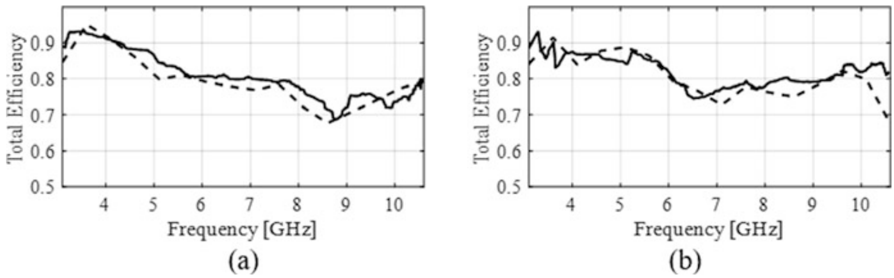

Fig. 5.8 Measured (solid line) and simulated (dashed line) efficiencies of the optimized MIMO antennas: (**a**) Antenna I and (**b**) Antenna III

5.5 Effects of Extended Ground Plane and User's Hand on Antenna Performance

In practical mobile devices, the full length of the circuit board normally acts as the ground plane for the antenna. The size of the circuit board device is decided by the design team. Therefore, this ground plane extension may affect the antenna performance. In this work, the performance of our benchmark antenna set is also investigated by integrating the antennas on the circuit board as shown in Fig. 5.11. The extended ground plane size is 123.8 $\text{mm}^2 \times$ 58.6 mm^2 (according to the available size of the iPhone 5). Figure 5.12 illustrates the simulated S-parameters of Antennas II and IV. It is clear from the figure that the reflection response is below -10 dB for the entire operating frequency band. A slight degradation in the isolation at lower frequencies is observed. However, the isolation level is still acceptable. Another investigation within the vicinity of the user's hand is also carried out and shown in Fig. 5.13. Here, the simulations indicate that the reflection response and the isolation level are not affected by the hand. From these, we can

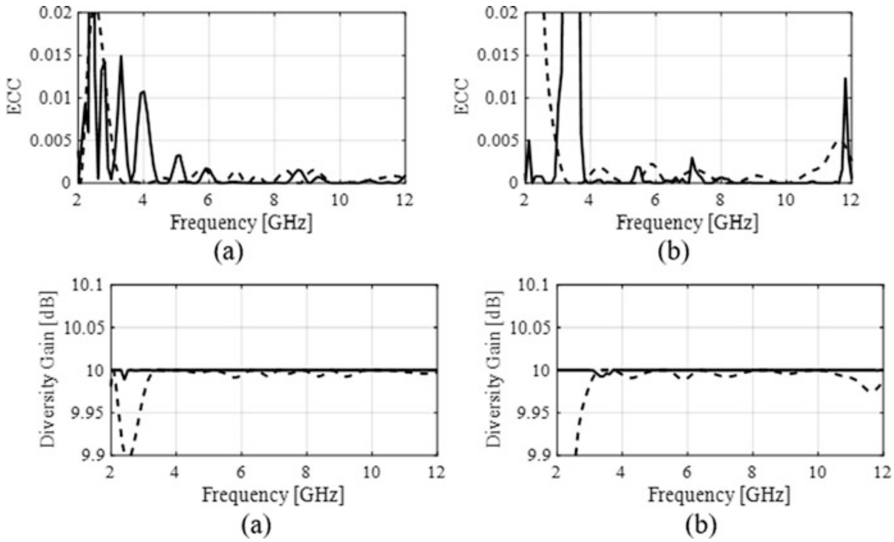

Fig. 5.9 Measured (solid line) and simulated (dashed line) ECC and DG response of the optimized antennas: (**a**) Antenna I and (**b**) Antenna III

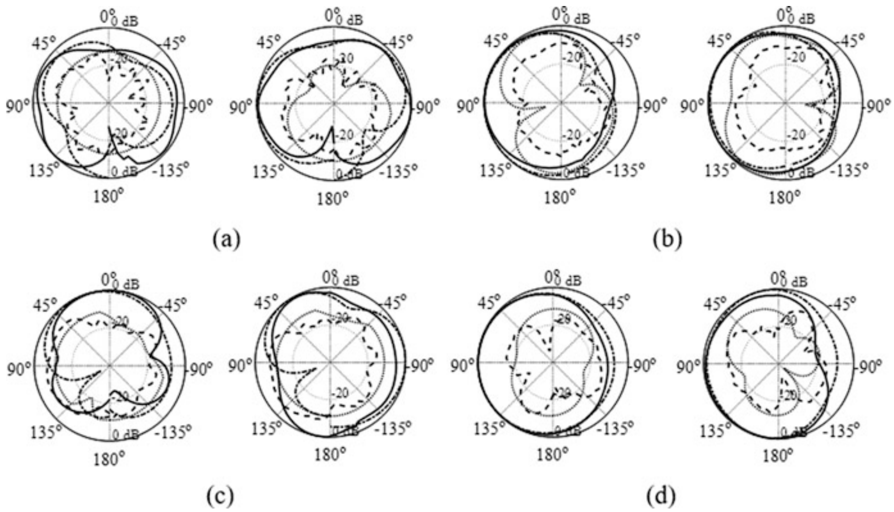

Fig. 5.10 Simulated and measured radiation pattern of the optimized UWB-MIMO antennas with the two-section slit below the feed line: Simulated co-pol (dashed line), measured co-pol (solid line), simulated cross-pol (dotted line), and measured cross-pol (long–short dashed line). The plots from left- to right-hand side are for the frequencies 6 and 8 GHz: (**a**) Antenna I E-plane, (**b**) Antenna I H-plane, (**c**) Antenna III E-plane, and (**d**) Antenna III H-plane

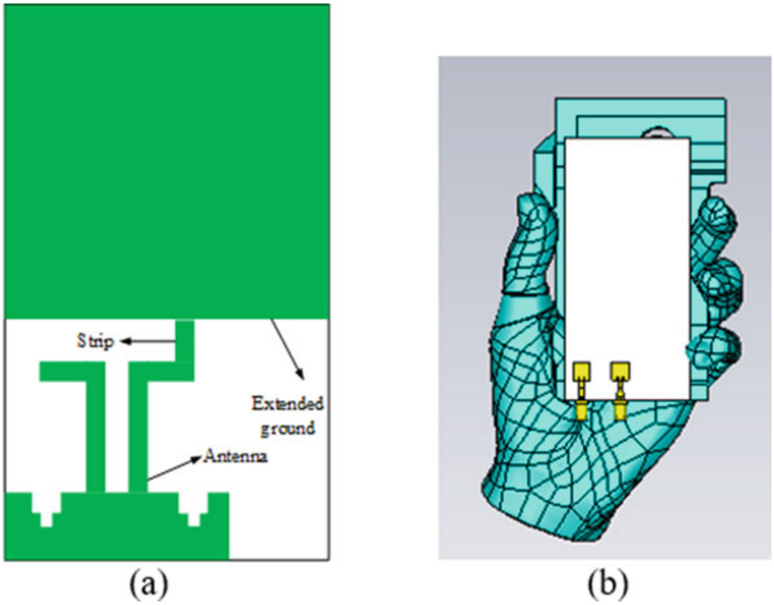

Fig. 5.11 The geometry of compact MIMO antenna with (**a**) extended ground plane and (**b**) human hand

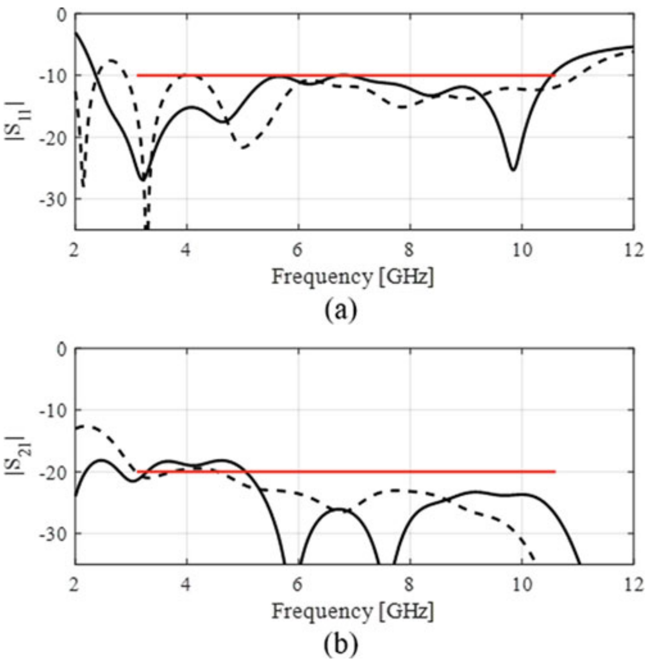

Fig. 5.12 Simulated S-parameters of the optimized benchmark antennas with extended ground plane: Antenna II (solid line) and Antenna IV (dashed line); (**a**) $|S_{11}|$ and (**b**) $|S_{21}|$

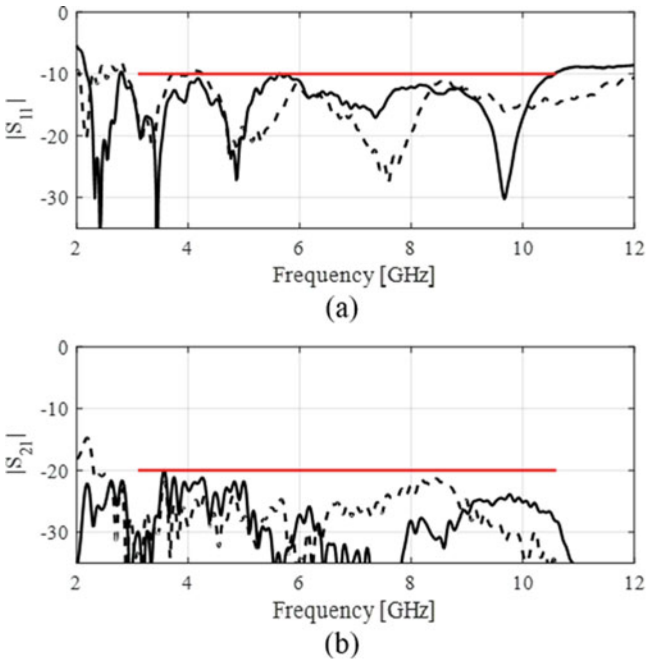

Fig. 5.13 Simulated S-parameters of the optimized benchmark antennas with the user's hand effect: Antenna II (solid line) and Antenna IV (dashed line); (**a**) $|S_{11}|$ and (**b**) $|S_{21}|$

conclude that the proposed optimized MIMO antennas can be a good candidate for the modern communication devices even when integrated with an extensive ground plane configuration.

5.6 Conclusion

In this chapter, a simple technique for enhancing element isolation in wideband MIMO antennas in a parallel configuration is carried out. Our approach combined topological modification of the ground plane with rigorous, multi-stage constrained optimization of antenna parameters. This does not only allow for achieving excellent performance in terms of electrical and field characteristics but also maintain compact size of the structures. The technique has been validated using four UWB MIMO antennas exploiting various radiators. The obtained results are consistent for all cases (in particular, isolation $|S_{21}| \leq -20\,\text{dB}$ for the entire UWB frequency range has been achieved), which demonstrates versatility of the approach. The proposed methodology can be used as a convenient tool for design automation and performance improvement of miniaturized MIMO antennas and combined with different types of ground plane and/or radiator (or feed line) modifications.

Acknowledgments This chapter is a part of a PhD thesis and was supported in part by the Icelandic Centre for Research (RANNIS) Grant 163299051, National Science Centre of Poland Grant 2015/17/B/ST6/01857, and the National Natural Science Foundation of China Grant 61471258.

References

1. S. Tripathi, A. Mohan, S. Yadav, A compact Koch fractal UWB MIMO antenna with WLAN band-rejection. IEEE Ant. Wireless Prop. Lett. **14**, 1565–1568 (2015)
2. S. Koziel, A. Bekasiewicz, Electromagnetic-simulation-driven design of compact ultra-wideband multiple-input–multiple-output antenna. IET Microwaves Ant. Prop. **10**(15), 1721–1724 (2016)
3. R. Chandel, A.K. Gautam, K. Rambabu, Design and packaging of an eye-shaped multiple-input–multiple-output antenna with high isolation for wireless UWB applications. IEEE Trans. Comp. Packaging Manuf. Techn. **8**(4), 635–642 (2018)
4. M.A.U. Haq, Geometry Modification Assessment and Design Optimization of Miniaturized Wideband Antennas. PhD Dissertation, Reykjavík University, Reykjavík, Iceland, 2019
5. R. Chandel, A.K. Gautam, K. Rambabu, Tapered fed compact UWB MIMO-diversity antenna with dual band-notched characteristics. IEEE Trans. Antennas Prop **66**(4), 1677–1684 (2018)
6. M.J. Hasan, T.A. Denidni, A.R. Sebak, Millimetre wave compact EBG structure for mutual coupling reduction applications. IEEE Trans. Antennas Prop. **63**(2), 823–828 (2015)
7. S. Koziel, A. Bekasiewicz, Q.S. Cheng, Conceptual design and automated optimisation of a novel compact UWB MIMO slot antenna. IET Microwaves Ant. Prop. **3**(8), 1162–1168 (2017)
8. L. Li, S.W. Cheung, T.I. Yuk, Compact MIMO antenna for portable devices in UWB applications. IEEE Trans. Antennas Prop. **61**(8), 4257–4264 (2013)
9. K.J. Babu, R.W. Aldhaheri, M.Y. Talha, I.S. Alruhaili, Design of a compact two element MIMO antenna system with improved isolation. Progr. Electromagn. Res. **48**, 27–32 (2014)
10. Z. Li, Z. Du, M. Takahashi, K. Saito, K. Ito, Reducing mutual coupling of MIMO antennas with parasitic elements for mobile terminals. IEEE Trans. Antennas Propag. **60**(2), 473–481 (2012)
11. J.F. Li, Q.-X. Chu, T.G. Huang, A compact wideband MIMO antenna with two novel bent slits. IEEE Trans. Antennas Propag. **60**(2), 482–489 (2012)
12. S. Su, C. Lee, F. Chang, Printed MIMO-antenna system using neutralization-line technique for wireless USB-dongle applications. IEEE Trans. Antennas Propag. **60**(2), 456–463 (2012)
13. Y. Wang, Z. Du, A wideband printed dual-antenna with three neutralization lines for mobile terminals. IEEE Trans. Antennas Propag. **62**(3), 1495–1500 (2014)
14. L. Zhao, K.L. Wu, A dual-band coupled resonator decoupling network for two coupled antenna. IEEE Trans. Antennas Propag. **63**(7), 2843–2850 (2015)
15. Q. Li, A.P. Feresidis, M. Mavridou, P.S. Hall, Miniaturized double-layer EBG structures for broadband mutual coupling reduction between UWB monopoles. IEEE Trans. Antennas Prop. **63**(3), 1168–1171 (2015)
16. C.G.M. Ryan, G.V. Eleftheriades, Two compact, wideband, and decoupled meander-line antennas based on metamaterial concepts. IEEE Antennas Wirel. Propag. Lett. **11**, 1277–1280 (2012)
17. A. Iqbal, O.A. Saraereh, A.W. Ahmad, S, Bashir, Mutual coupling reduction using F-shaped stubs in UWB-MIMO antennas. IEEE Access. **6**, 2755–2759 (2018)
18. S.S. Jehangir, M.S. Sharawi, A miniaturized UWB biplanar Yagi-like MIMO antenna system. IEEE Ant. Wireless Prop. Lett. **16**, 2320–2323 (2017)
19. J.Y. Deng, L. Guo, X. Liu, An ultrawideband MIMO antenna with a high isolation. IEEE Ant. Wireless Prop. Lett. **15**, 182–185 (2016)

20. G. Lin, C. Sung, J. Chen, L. Chen, M. Houng, Isolation improvement in UWB MIMO antenna system using carbon black film. IEEE Ant. Wireless Prop. Lett. **16**, 222–225 (2017)
21. C. Mao, Q.X. Chu, Y.T. Wu, Y.H. Qian, Design and investigation of closely-packed diversity UWB slot-antenna with high isolation. Prog. Electromagn. Res. C **41**, 13–25 (2013)
22. S. Kharche, G.S. Reddy, B. Mukherjee, R. Gupta, J. Mukherjee, MIMO antenna for Bluetooth, Wi-Fi, Wi-MAX and UWB applications. Prog. Electromagn. Res. C **52**, 53–62 (2014)
23. Y. Yang, Q. Chu, C. Mao, Multiband MIMO antenna for GSM, DCS, and LTE indoor applications. IEEE Antennas Wireless Propag. Lett. **15**, 1573–1576 (2016)
24. G. Zhai, Z.N. Chen, X. Qing, Enhanced isolation of a closely spaced four-element MIMO antenna system using metamaterial mushroom. IEEE Trans. Antennas Propag. **63**(8), 3362–3370 (2015)
25. S. Soltani, P. Lotfi, R.D. Murch, A dual-band multiport MIMO slot antenna for WLAN applications. IEEE Antennas Wireless Propag. Lett. **16**, 529–532 (2017)
26. M.A. Haq, S. Koziel, On topology modifications for wideband antenna miniaturization. AEU Int. J. Electron. Commun. **94**, 215–220 (2018)
27. A.R. Conn, N.I.M. Gould, P.L. Toint, *Trust Region Methods, MPS-SIAM Series on Optimization* (Society for Industrial and Applied Mathematics, Philadelphia, 2000)
28. A. Bekasiewicz, S. Koziel, Structure and computationally-efficient simulation-driven design of compact UWB monopole antenna. IEEE Ant. Wireless Prop. Lett. **14**, 1282–1285 (2015)
29. M.A. Haq, S. Koziel, Ground plane alterations for design of high-isolation compact wideband MIMO antenna. IEEE Access **6**, 48978–48983 (2018)
30. CST Microwave Studio, ver. 2015. CST AG, Bad Nauheimer Str. 19, D-64289 Darmstadt, Germany (2015)
31. S. Blanch, J. Romeu, I. Corbella, Exact representation of antenna system diversity performance from input parameter description. Electron. Lett. **39**(9), 705–707 (2003)

Chapter 6
Fixed- and Scanned-Beam Antenna Arrays for 5G Applications

Raj Mittra, Donia Oueslati, Abdelkhalek Nasri, Ravi Kumar Arya, and Asim Ghalib

6.1 Introduction

Aperture array antennas have emerged as popular candidates for a variety of applications, such as radar, remote sensing, navigation [1, 2], and the fifth generation (5G) Network communication [3–5] operating in the Ka-band. This millimeter-wave band for 5G communication is expected to provide a much higher data rate than heretofore, in the gigabit range, which is not possible to achieve by using current wireless services [3]. The mm-wave phased array antenna is certain to play an important role in 5G applications, thanks to its many desirable attributes such as high gain [5, 6], higher transmission rate, and shorter latency. Recently, several studies of mm-wave phased array designs for 5G applications have been

R. Mittra (✉)
Electrical and Computer Engineering, University of Central Florida, Orlando, FL, USA

Electrical and Computer Engineering Department, Faculty of Engineering, King Abdulaziz University, Jeddah, Saudi Arabia

D. Oueslati
Electrical and Computer Engineering Department, Faculty of Engineering, King Abdulaziz University, Jeddah, Saudi Arabia

ICTEAM Institute, Université Catholique de Louvain, Louvain la Neuve, Belgium

A. Nasri
Research Laboratory Smart Electricity & ICT, SEICT, LR18ES44, National Engineering School of Carthage, University of Carthage, Carthage, Tunisia

R. K. Arya
Department of Electronics & Communication Engineering, National Institute of Technology Delhi, Delhi, India

A. Ghalib
Electrical and Computer Engineering, University of Central Florida, Orlando, FL, USA

M. A. Matin (ed.), *Wideband, Multiband, and Smart Antenna Systems*, Signals and Communication Technology, https://doi.org/10.1007/978-3-030-74311-6_6

carried out in [7–9]. The phased array configuration has been proposed to serve the user in crowded areas by reducing the interference and thereby realizing a high communication rate between the base station and mobile devices. In addition, it has been argued that beam switching is essential to addressing the challenges of the future 5G applications [10–12] at millimeter-waves since it offers high-power efficiency and large channel capacity with wide-angle scan coverage. The low-profile antenna array (LPAA) design presented in [13–16] provides good performance at high frequencies, but it can only scan the beam in one plane (see Fig. 6.4), by using mechanical means [13], for instance. Recently, beam switching networks using structures, such as substrate integrated waveguide [17]; Butler matrix [18]; printed-ridge gap waveguide [19]; and magneto-electric dipole antenna array fed by RGW Butler matrix [20], have been proposed by the research community. A 1D-beam scanning technique (see Fig. 6.5) has been proposed in [12], which utilizes mechanical rotation and whose performance in terms of gain, sidelobe level, etc., varies with different orientation angles.

In this chapter, we present several different array designs that show potential for 5G applications and include both fixed- and scan-beam configurations. In addition to these, we also briefly mention MIMO designs that are likely to play important roles in 5G applications, both in sub-6 GHz and millimeter-wave designs. We begin with aperture antennas with slotted waveguide arrays that are widely used for high frequency applications, because they provide high gain, wide bandwidth, low-profile [2, 21–24], and relatively simple configurations [25]. Although several different configurations have been proposed as candidates in [26, 27] for low-profile aperture antennas with the desirable properties mentioned above, there still exists a need for improved designs of these antennas operating in the millimeter-wave regime [27].

Recently, several researchers [13–16] have proposed a variety of different design approaches to generate low-profile antenna arrays (LPAAs). In [13, 14], the authors have proposed LPAAs based on a Metasurface (MTS) design (see Fig. 6.1c) comprising of subwavelength cells printed on a grounded dielectric slab. Figure 6.1a, b shows that such an LPAA is an RHCP design, which provides good performance in one plane and realizes a gain and an efficiency around 37 dBi and 70%, respectively, at the center frequency of 29.75 GHz, though with a narrow bandwidth. Other LPAAs have also been proposed in [15, 16], with good performance in terms of gain, efficiency, and bandwidth at high frequencies. In [15], a spherical dielectric resonator, excited by a microstrip patch covered by a dielectric superstrate (see Fig. 6.2) has been proposed to achieve good gain and aperture efficiency though with a narrow bandwidth, and only with linear polarization (see Table 6.1).

The LPAA designs presented in [13–16] exhibit a narrow bandwidth, which can be improved by adding a dielectric superstrate above the array (see Fig. 6.3, for example). This technique has been proposed in [16] and it helps to achieve an enhanced frequency operating bandwidth, as shown in Table 6.1, although the design is only for linear polarization. Additionally, neither of the designs presented in Table 6.1 are very well suited for scanning. Given this backdrop, an alternative design of low-profile antenna array will be presented in this chapter, which provides

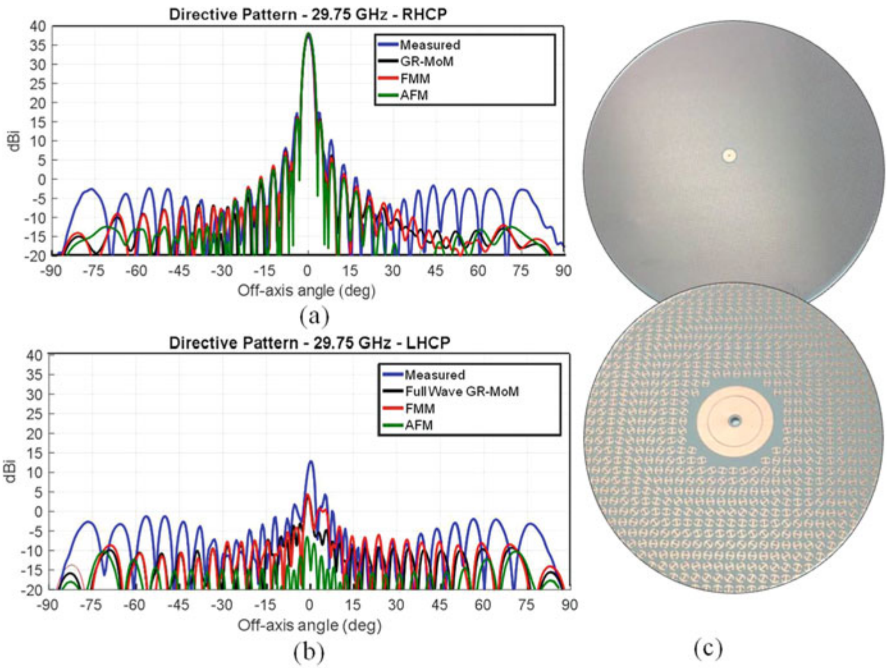

Fig. 6.1 Layout and performances of the high-efficiency MTS antenna [13]; (**a**) Co-polar and (**b**) Cross-polar 37 dB directive gain patterns by a MTS antenna at 29.75 GHz designed with product tapering spill-over efficiency of 85%. (**c**) MTS antenna layout and detail of the feeding region before the insertion of the monopole

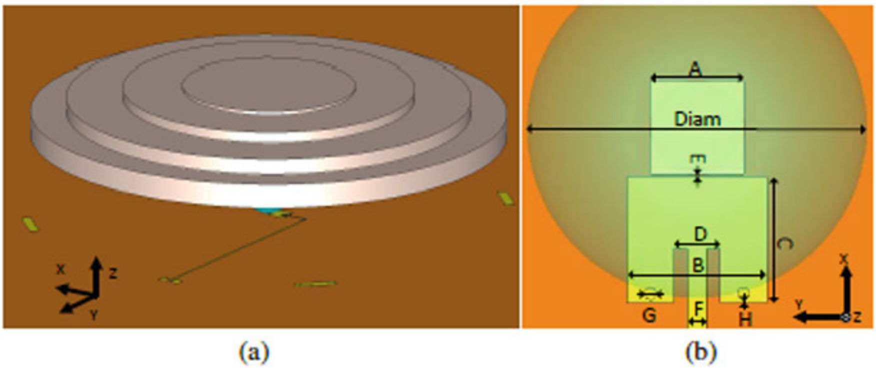

Fig. 6.2 Configuration of the spherical dielectric resonator-fed resonant cavity antenna [15]: (**a**) General view of the antenna, (**b**) top view of the microstrip resonator

Table 6.1 Electromagnetic performance characteristics provided by some recent low-profile antenna array proposed in [13–16]

	[13]	[14]	[15]	[16]
Area (λ^2)	572.5 λ^2	314 λ^2	10.8 λ^2	5.3 λ^2
Radius (λ)	13.5 λ	10 λ	1.85 λ–1.85 λ	1.3 λ
Height (λ)	0.05 λ		1.03 λ/1.05 λ	0.9 λ
Frequency (GHz)	29.75	20	72–103	10
Bandwidth ($S_{11} < -10$ dB)	–	–	5.6–9.6%	56%
3 dB bandwidth (%)	4.7	3.25	–	57
Gain (dBi)	37	33	17.8–18.4	20.7
CP	Yes	Yes	No	No
Efficiency	70%	58%	45%/51%	78.3%
Scan angle	No	No	No	No

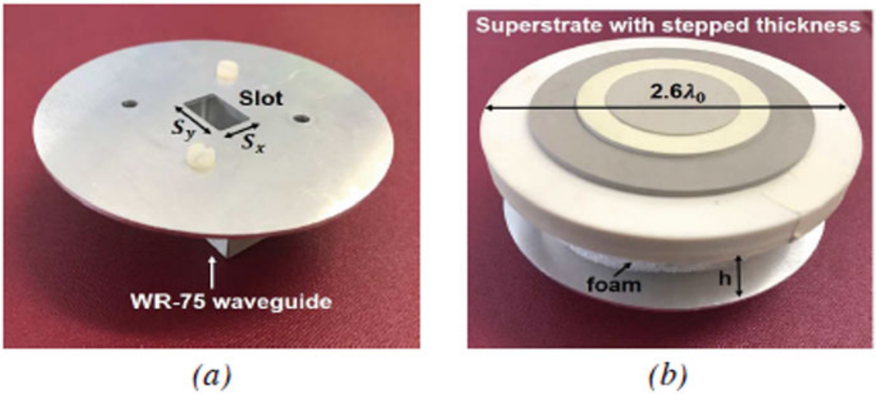

Fig. 6.3 Fabricated prototype and parts [16]: (**a**) ground plane and slot coupled WR-75 waveguide feed, (**b**) Superstrate II placed above the ground plane to form the new antenna

desirable electromagnetic performance in terms of gain, efficiency, and bandwidth in the high frequency band, with potential applications in the millimeter-wave (mm-wave) band. Furthermore, the fixed-beam designs presented herein have the potential for limited scanning, without the use of conventional phase shifters that are very lossy as well as expensive at millimeter-waves (Figs. 6.4, 6.5, and 6.6).

In this chapter, we begin by presenting an alternative design for a low-profile aperture antenna array, which is based on a different design philosophy than those mentioned above (see Maci et al. [13, 14] and Esselle et al. [12]). The proposed design achieves a wide operating bandwidth, good aperture efficency, and a stable radiation pattern at millimeter wavelengths. Next, we further enhance the performance of the array by adding a superstrate, which adds to its gain—albeit only slightly—despite being entirely passive. Our next step is to add the beam scanning capability to the array, by using a phase shifting device at millimeter-waves, which is both low-cost as well as relatively low-loss. Following this, in Sect. 6.3, we modify

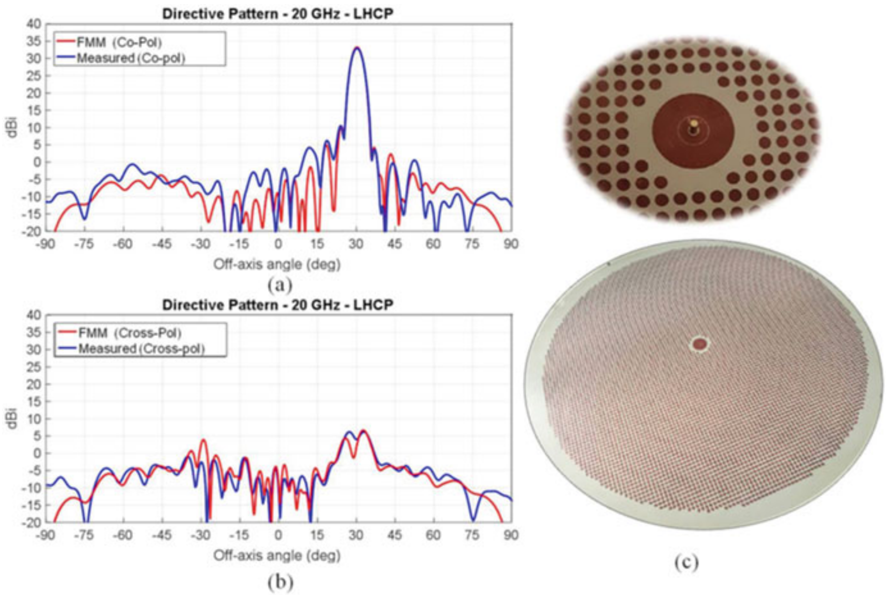

Fig. 6.4 The antenna has been designed to radiate an RHCP beam tilted 30° from broadside at 20 GHz. (**a**) Co-polar component; (**b**) cross-polar component: comparison between simulated and experimental results; (**c**) Details relevant to the aperture implementation and the feeder structure [13]

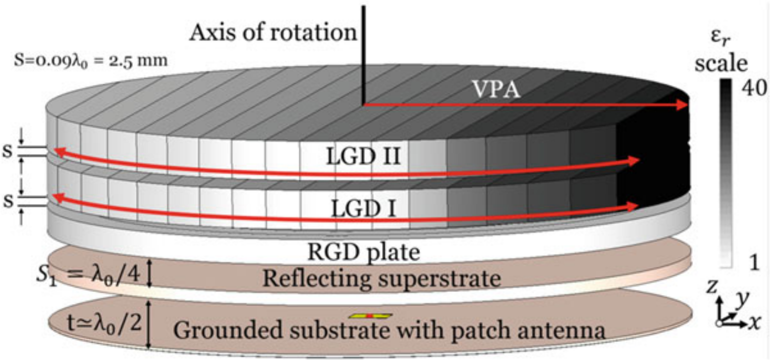

Fig. 6.5 Configuration of the beam scanning antenna system: 3D models of the RCA, RGD, and a pair of LGDs [12]

the design by adding the capability of 2D scanning, by using different techniques for realizing low-cost and low-loss phase shifters.

The design of antennas capable of wide-angle scanning and offering polarization diversity are addressed next in this chapter. The Luneburg lens, fed by an array and backed by switching circuits, is presented in some detail, followed by a discussion

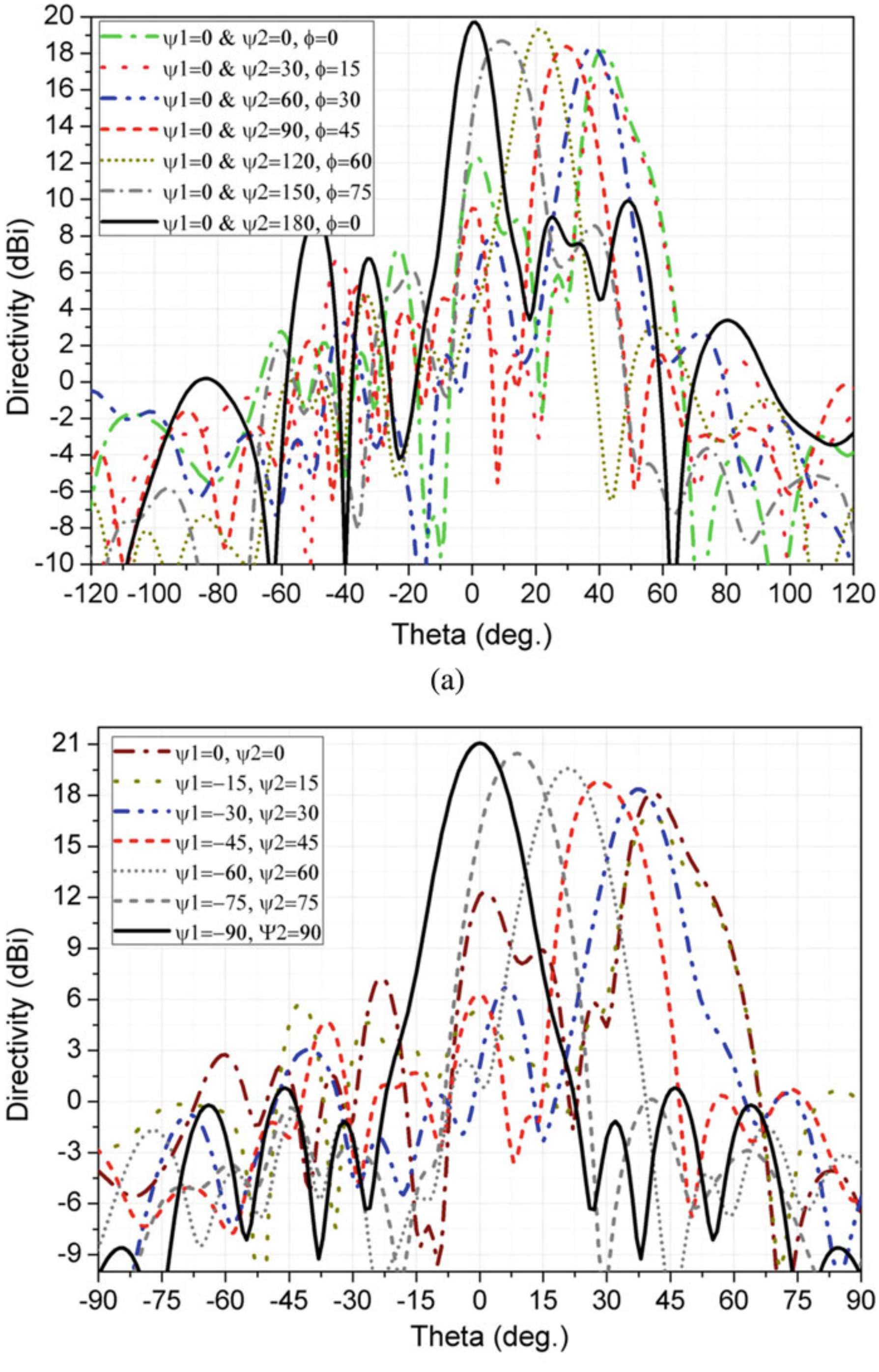

Fig. 6.6 Elevation cuts taken at (**a**) azimuth angles containing the beam peak. For each pattern cut, the azimuth angle and the orientation angles of LGD I and LGD II are given in the inset, (**b**) $\varphi = 0°$ for the different orientation angles of LGD I and LGD II [12]

of array designs that achieve polarization diversity. Finally, the topic of MIMO arrays—that are certain to play an important role both in sub-6 GHz and millimeter-wave designs—is discussed briefly and a design example of such an array is included in this chapter for the sake of illustration.

6.2 Array Beam Scanning Approach

6.2.1 Design of Low-Profile Aperture Antennas (LPAA)

In this section, we present two novel designs for a planar aperture antenna array which operates in the Ka-band, has a low-profile, simple configuration, low-cost, and improved performance compared with conventional phased array designs. The first design integrates a wideband power divider with a planar slotted waveguide array (SWA). The power divider is used to excite four waveguide arrays. Each SWA is comprised of ten slots in their top walls (see Fig. 6.7a), with the slots off-centered left and right of the center of the guide to realize an extra 180° phase shift between the adjacent slots. Unlike the case of a leaky-wave antenna, the proposed design enables us to space the slots half-a-guide wavelength apart to realize radiation along broadside without any difficulty. A standard waveguide (WR-28) is used, whose cross-section is 0.7 × 1.11 cm, and which supports the dominant mode propagating

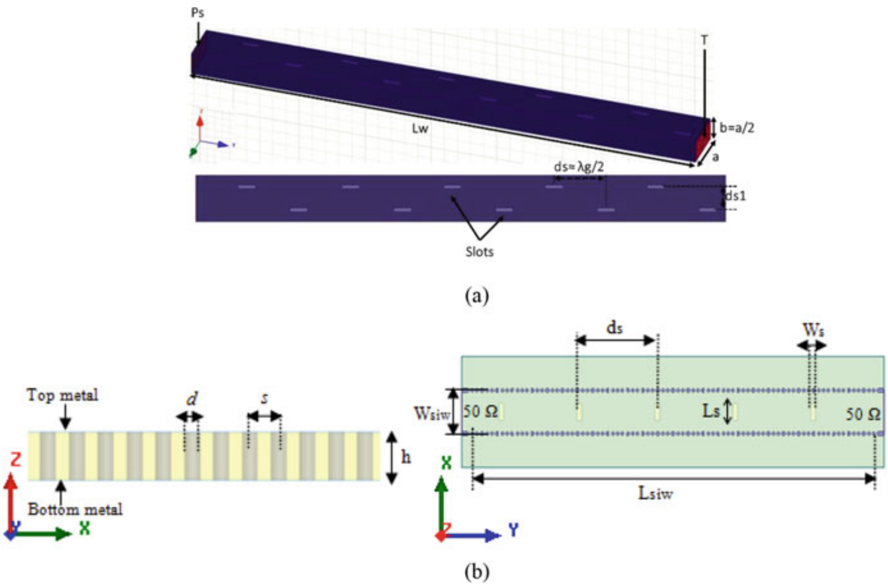

Fig. 6.7 Waveguide antenna: (**a**) rectangular waveguide and the top view of the linear array (schematic), (**b**) Side and top view of the proposed SIW slotted antenna array

in the Ka-band. The second design of the transversal waveguide slot array antenna is based on substrate integrated waveguide (SIW) technology, which helps to improve the performance of the array antenna, including its gain. The SIW transversal slot antenna array, designed to operate at the center frequency of 30 GHz, is displayed in Fig. 6.7b. The proposed SIW is fabricated by inserting metal-filled via-hole arrays in the substrate and the grounded plane. The upper and lower surfaces are metalized layers that are placed in the air medium. The width of the SIW guide, the period s of the via holes, and the diameter d are appropriately chosen to support the TE_{10} dominant mode as explained in [28].

One of the main goals of this chapter is to design a low-profile aperture array (LPAA) so that its performance characteristics are competitive, if not better, than the legacy designs. The proposed design for the array has been simulated by using the commercially available 3D-electromagnetic solver "HFSS" [29]. Both designs have achieved a 70.75% impedance bandwidth ($S_{11} < -10$ dB) in the Ka-band, good gain and efficiency, as well as a low sidelobe level. The performance is further enhanced by adding a superstrate layer above the array to improve its gain without compromising its S_{11} bandwidth. The details of the array antenna designs are presented in the following sections.

6.2.1.1 Slotted Waveguide Antenna Arrays

In this section, we descry, which be the slotted waveguide antenna array, shown in Fig. 6.7b, which is based on Substrate Integrated Waveguide (SIW) technology. We introduce the slots in the upper metal layer of the SIW, which is terminated by a 50 Ω load. We maintain the distance between each successive slot to be λ_g, the guide wavelength at 30 GHz. The slot locations are chosen such that they have the same phase at the center frequency of operation; hence, the main beam points along broadside. The slot dimensions are optimized for the best performance, and the detailed dimensions of the design are given in Table 6.2. The effects of increasing the number of slots on the S_{11} characteristics and gain parameters are investigated. Figure 6.8b shows the variation of the reflection coefficient S_{11} of the SIW slot antenna as we increase the number of slots. Note that the wideband (27–34 GHz) -10 dB characteristic of the S_{11} is maintained even as we increase the number of slots from 1 to 5. As expected, the gain of the antenna increases from -2 to 9 dB at 30 GHz as we increase the number of slots from 1 to 5 slots. Next, we design two SIW slotted antenna arrays having different sizes, namely 2 × 5 and 4 × 5, and study their S_{11} and gain performances.

Table 6.2 Geometrical parameters of the SIW waveguide antenna

λ free space	Lsiw	Wsiw	*d*	*S*	Ls	Ws	ds	*h*
1 cm	75	6.8	0.5	0.9	2.5	0.4	14	1.6

Fig. 6.8 *S*-parameters of: (**a**) The rectangular waveguide antenna with ten elements, (**b**) SIW slot antenna with increased number of slots

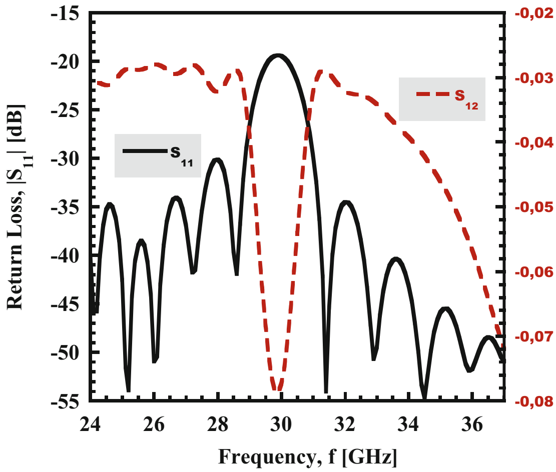

(a)

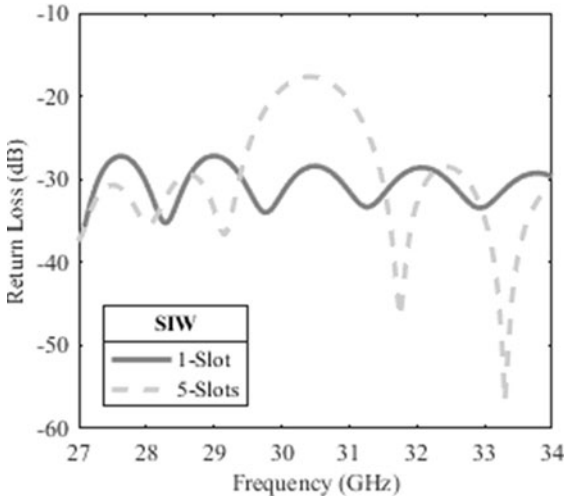

(b)

An alternative design for a linear SIW slot array, with a simple configuration, is presented below. Figure 6.7a shows a linear slot array designed for the Ka-band, with the array located in the top wall of a standard WR-28 waveguide. The slot dimensions (width and length) are 0.05 × 0.25 cm. The position and the number of slots on the linear waveguide have a significant effect on the bandwidth of the antenna [24]. The slots used in the present design are longitudinal and they are offset from the centerline of the waveguide, as shown in Fig. 6.7a, to realize the 180° phase shift we need to point the beam at boresight when the spacing between

Table 6.3 Geometrical parameters of the rectangular waveguide

λ free space	1 cm
Lw	7.65 cm
A	0.68 cm
Ds	0.75 cm
ds1	0.34 cm
λ_g	1.48 cm

the adjacent slots is one-half the guide wavelength λ_g. The design parameters of the waveguide, the slot sizes, and their positions are presented in Table 6.3.

The proposed linear array antenna is excited from the input port (Ps) and is terminated by 50 Ω (T) at the output port. The simulated results of the proposed slotted narrow waveguide antenna, obtained by using the HFSS, are shown in Fig. 6.8a. The array achieves an S_{11}, which is better than −10 dB over the frequency range of 24–37 GHz, and its insertion loss is approximately 0.06 dB across the desired band (see Fig. 6.8a). The proposed antenna also achieves a simulated gain of 16.8 dB at 30 GHz.

6.2.1.2 Power Divider Design

Wideband (WB) Power Divider

The aperture array proposed in this work was designed to account for the mutual coupling between the elements. To analyze the performance of the array we simulate a prototype version the of 4 × 10 slotted array antenna, fed by a 4:1 wideband (WB) power divider. In this section, we present the design procedure of an equiphase 4:1 WB power divider (see Fig. 6.9). Initially, a 2:1 power divider was designed and optimized for the 25.8–37.2 GHz range and was later modified to derive the 4:1 design.

The 4:1 power divider was realized by cascading three sets of 2:1 power dividers. Figure 6.9 presents the detailed dimensions and shape parameters of the power dividers. The structure includes a single input port and four 50 Ω output ports. Figure 6.10 presents the simulated results, which show that good performance of insertion loss and impedance matching has been achieved over a broadband of frequencies, ranging from 25.8 to 36 GHz. The proposed power divider is subsequently used for the 4 × 10 antenna array.

E- and *H*-Plane Power Dividers

Before closing this section, we briefly describe some designs for *E*- and *H*-plane power dividers for use in slot arrays involving multiple waveguide feeds (see Figs. 6.11 and 6.13). The main challenge we encounter in designing these power dividers is the undesired reflection from the interfaces as we subdivide the power in a

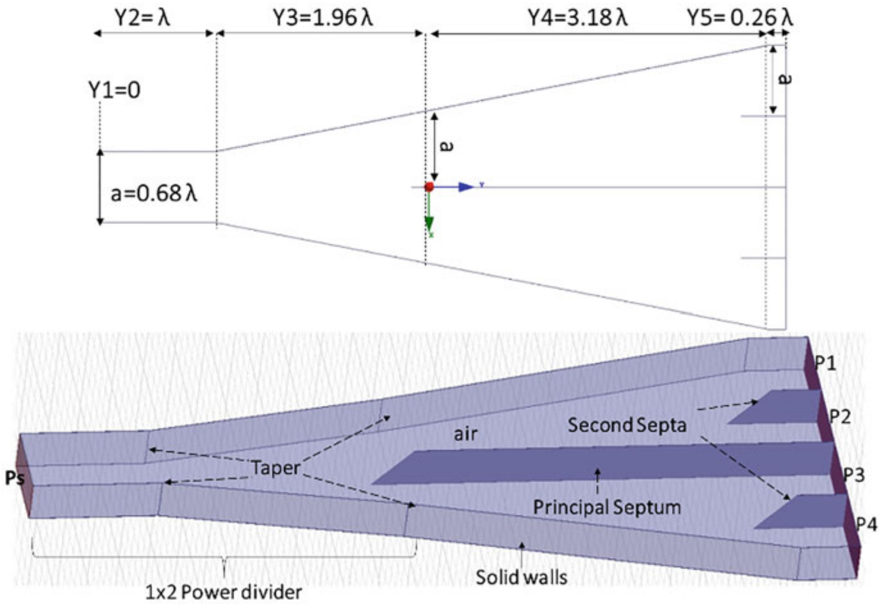

Fig. 6.9 Schematic representing the cross-section of 4:1 power divider

cascaded manner—from one waveguide to multiple ones—for a slot array with multiple waveguide feeds, as shown in Fig. 6.12. To meet this challenge, we need to optimize several of the parameters through simulation, as presented in Figs. 6.11b and 6.13. The key to minimizing the interface reflection is to avoid abrupt changes in the geometry at the interfaces, where the power division occurs. Some representative results are presented in Figs. 6.12 and 6.14, which show that both *E*- and *H*-plane power dividers can be designed by following this strategy, albeit at the cost of increasing the length of the array. However, this problem of length increase may be resolved by folding in the power divider below the feed waveguides of the array. The details are omitted here for the sake of brevity.

In the next section, we combine the 4:1 WB power divider together with four slotted waveguide arrays (Figs. 6.15 and 6.17) to construct a low-profile aperture antenna array (LPAA).

6.2.1.3 Aperture Antenna Array with a Single Feed

The proposed array (see Fig. 6.15) works in the frequency range of 24.9–36.1 GHz covering 70.75% of the Ka-band and 23.33% of the K-band. Figure 6.16 shows the effect of the radiating slots on the simulated S_{11} characteristics of the proposed array (Fig. 6.17). Figure 6.18a demonstrates that the input S_{11} is better than -10 dB over a bandwidth of 10.2 GHz. The simulated *S*-parameters, plotted in Fig. 6.16, exhibit

Fig. 6.10 *S*-Parameters of 2:1 and 4:1 power dividers: (**a**) S_{11} and (**b**) simulated coupled power

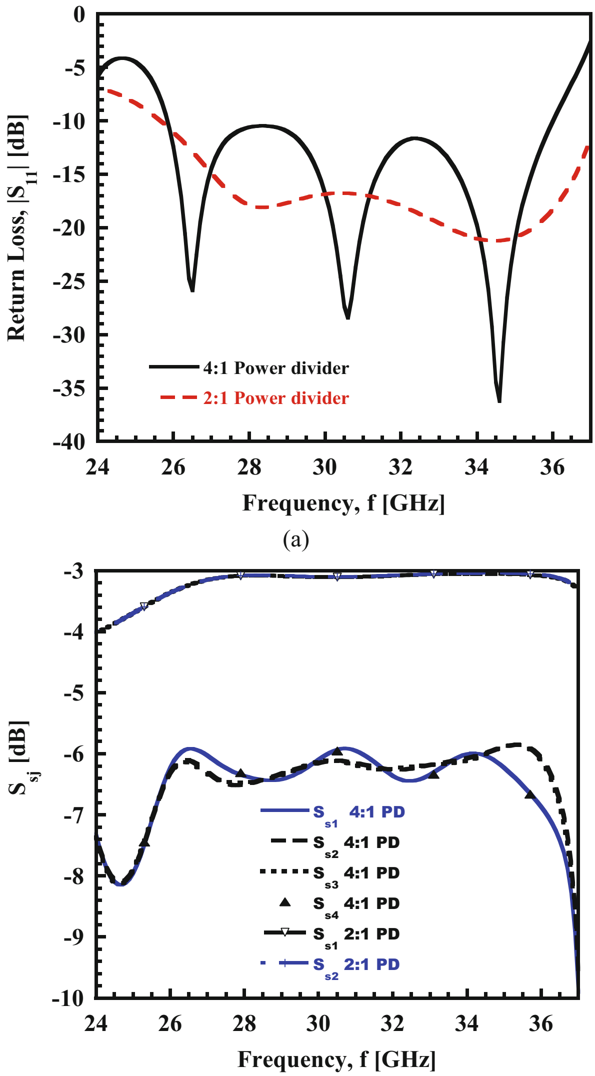

(b)

good performance in terms of the power division, which is achieved over a wide bandwidth.

The maximum simulated gain for the LPAA is presented in Fig. 6.19a, which shows that the proposed array achieves a simulated gain of 23.55 dB at 30 GHz, and 24.3 dB at the resonance frequency of 34.5 GHz. Figure 6.20 plots the radiation patterns of the proposed array antenna in the elevation plane. The simulated HPBW is 19.6° in the transverse plane (TP) and 6.9° in the longitudinal plane (LP), confirming that the directivity of the antenna is very good.

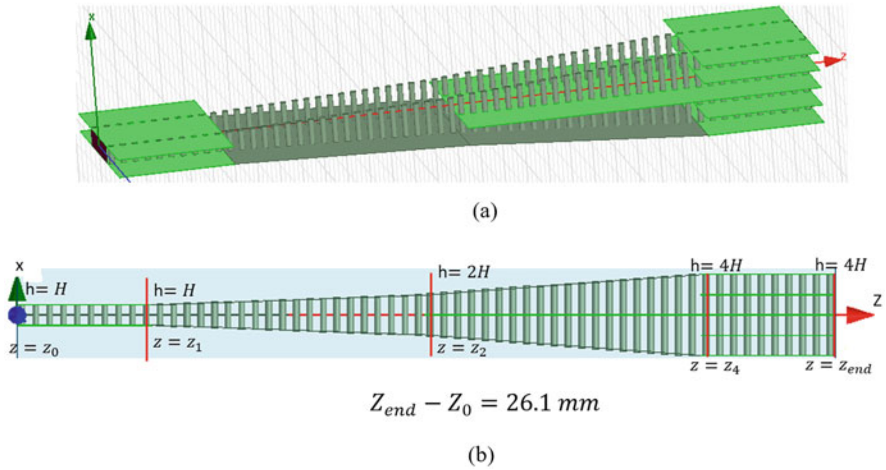

Fig. 6.11 Schematic representing the side and front views of 4:1 *E*-Plane power divider. (**a**) Side view, (**b**) Front view

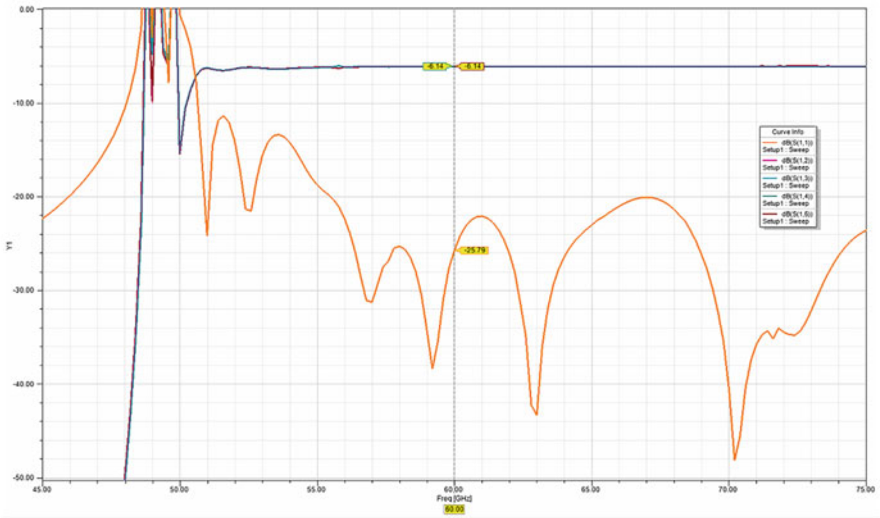

Fig. 6.12 Simulated *S*-parameters of the 4:1 *E*-plane power divider

We also combine an SIW power divider and four slotted SIW waveguide arrays to develop an alternative design for low-profile aperture array antennas. As shown in Fig. 6.17, the arrays are configured by placing the linear arrays side-by-side and exciting them with an SIW power divider. The separation distance 'da' between the array elements is chosen to be 8 mm. The array is connected to a 50 Ω input source and is terminated at the other ends with a 50 Ω matched load. The parameters of the SIW power divider have been optimized for best gain and S_{11} performances. Figure

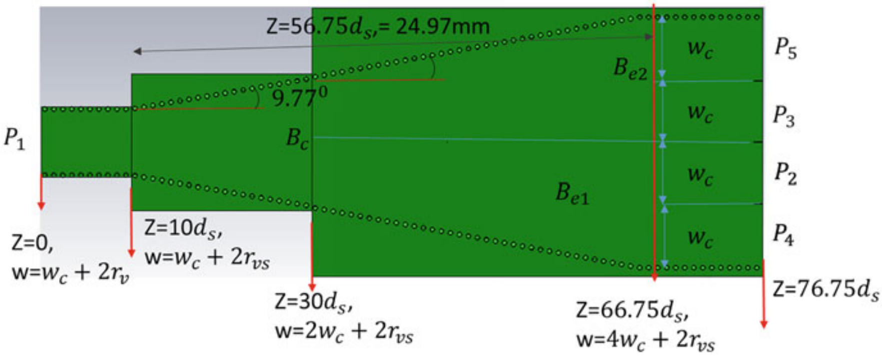

Fig. 6.13 Schematic representing the side and front views of 4:1 *H*-Plane power divider

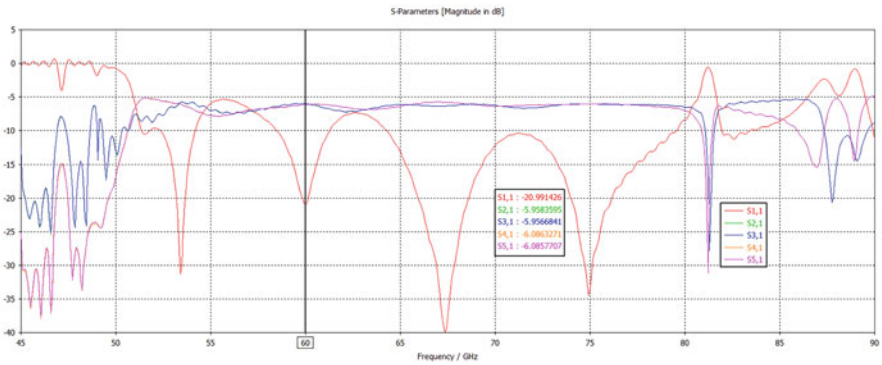

Fig. 6.14 Simulated *S*-parameters of the 4:1 *H*-plane power divider

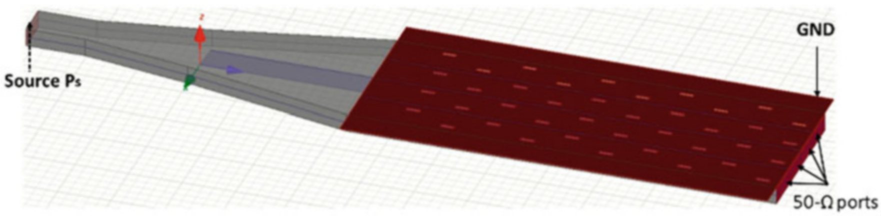

Fig. 6.15 Cross-sectional view of the combined structure, comprising of both the linear arrays and the power divider, to form a planar aperture array

6.18b plots the S_{11} performance as we increase the number of arrays and shows that the various designs exhibit S_{11} levels better than -10 dB in the frequency range of 27–32 GHz. The gain behavior of the array as a function of frequency is presented in Fig. 6.19b as the number of elements is increased. We note that the gain increases from 9 dB for the 1×5 array to 11 dB for 2×5 array and it reaches a peak of 14.34 dB for the largest array which is comprised of 4×5 elements.

Fig. 6.16 Simulated *S*-parameters of the LPAA

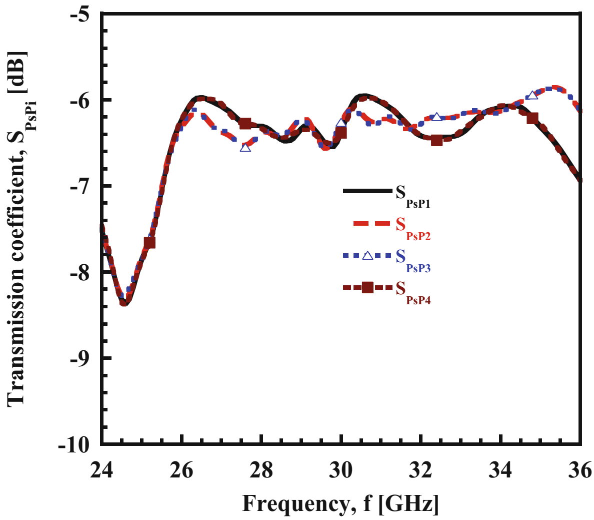

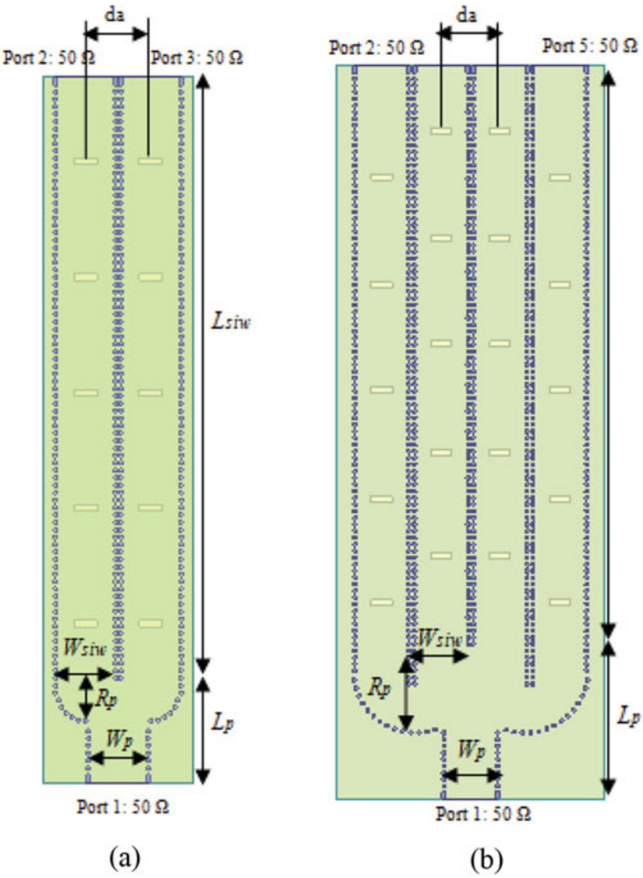

Fig. 6.17 Geometry of the proposed designs of SIW: (**a**) 2 × 5 slotted array: lp = λ_g; Lsiw = 75 mm; Wp = Wsiw = 6.8 mm; Rp = Wsiw/2; da = 8 mm; (**b**) 4 × 5 slotted array: lp = 2 × λ_g; Lsiw = 75 mm; Wp = Wsiw = Rp = 6.8 mm; da = 8 mm

Fig. 6.18 Simulated S_{11} of: (**a**) LPAA in presence of ground plane (spaced dashed line), or by adding a dielectric superstrate above the array (dashed line), (**b**) Aperture array by using $N \times 5$ SIW linear array

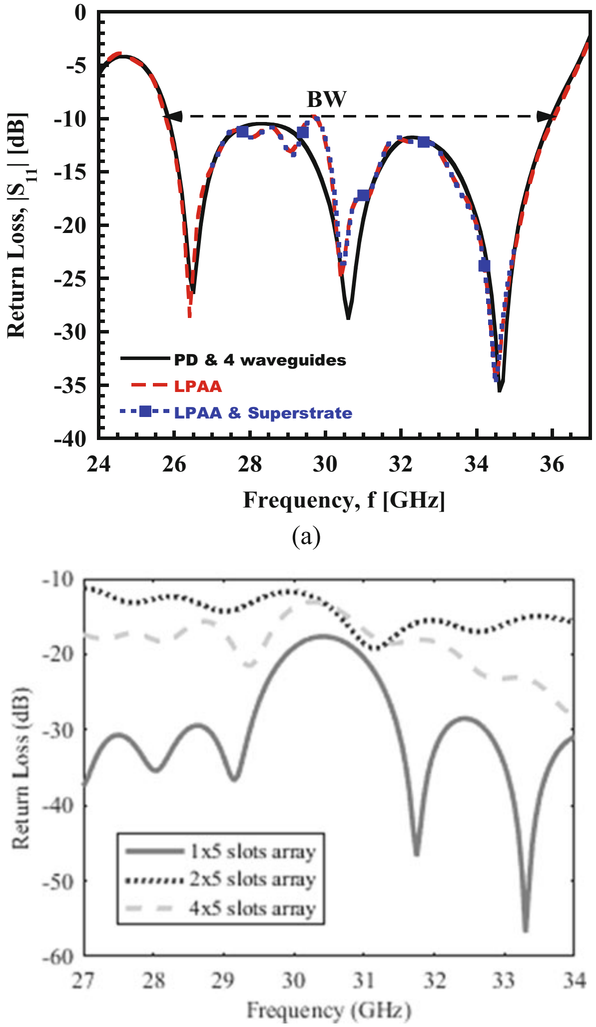

(a)

(b)

6.2.1.4 Enhancing the Maximum Gain of Aperture Arrays

To improve the level of the back radiation, the gain, and the SLL, we add a dielectric superstrate layer at a distance (h_s) above the ground plane. The superstrate (see Fig. 6.22) has the same dimensions as the ground plane $(L + \lambda/4) \times (4a + \lambda)$ and its thickness is t_s. Next, we optimized the superstrate position, thickness, and the type of the dielectric (see Table 6.4) placed above the array which has been proposed and described in the previous section.

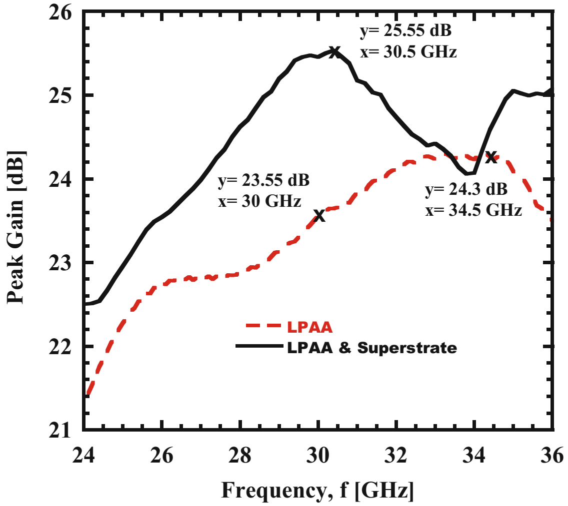

(a)

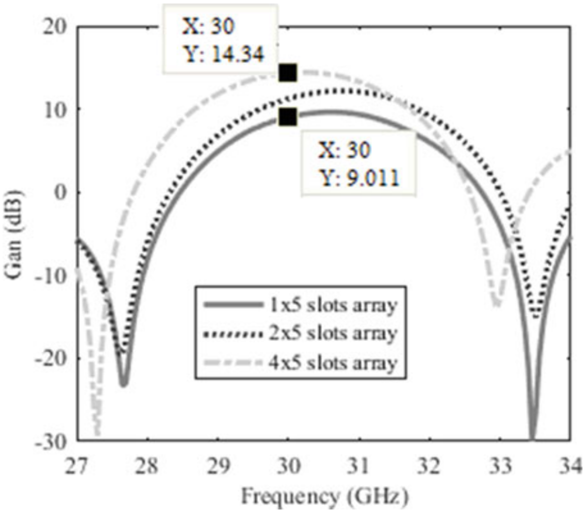

(b)

Fig. 6.19 Simulated peak gain of the LPAA vs. frequency with (dashed line) and without (spaced dashed line) superstrate. (**a**) Waveguide array. (**b**) SIW array

Next, we observe that the pattern in the transverse plane (see Figs. 6.20 and 6.21) is wide and this, in turn, causes a significant back radiation.

We now present a brief summary of the simulated results for some of the superstrate configurations, whose performance is superior to others. The HPBW, the SLL, the gain, and the superstrate dimensions are given in Table 6.5. The SLL and the back-radiation level are improved in the transverse plane (see Fig. 6.23, transverse pattern). Figure 6.19a and 6.23a, and Table 6.5 show that the peak gain

Table 6.4 Optimization of the superstrate size, material, and the position

Superstrate material	λ_m (cm)	ε_r	$\Delta\delta$	Max Gain (dB)	h	t_s	H_t (mm)
FR4	0.47	4.4	0.02	25	$0.5 \times \lambda$	$0.12 \times \lambda = 0.25 \times \lambda_m$	6.2
Glass	0.42	5.5	0	25.37	$0.5 \times \lambda$	$1.02 \times \lambda = 2.43 \times \lambda_m$	15.2
Duroid	0.67	2.2	0.0009	25.45	$0.5 \times \lambda$	$0.92\text{ cm} = 1.37 \times \lambda_m$	14.2
Rogers RT	0.4	6.15	0.0019	25.2	$0.5 \times \lambda$	$0.32\text{ cm} = 0.8 \times \lambda_m$	8.2

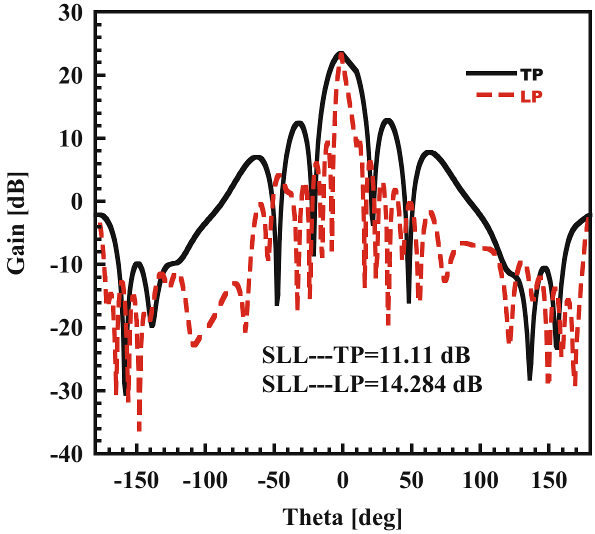

Fig. 6.20 Simulated radiation pattern of the LPAA at 30 GHz

increases by 3 dB at 30 GHz and the first resonance frequency shifts to 30.5 GHz when the superstrate is added above the array.

The technique for improving the gain of the LPAA array by using a dielectric superstrate can also be used to increase the gain of the slotted SIW antenna array. Figure 6.22b shows the 4 × 5 SIW slotted antenna array covered with a dielectric superstrate. We carry out a parametric study of the superstrate layer to increase the gain when using Roger/Duroid 5880 with $\varepsilon_r = 2.2$, and a loss tangent of 0.0009 for the superstrate of the SIW array. We find that an optimized thickness $t_s = 0.44\ \lambda_0$, where λ_0 is the free space wavelength at the frequency of 30 GHz. As shown in Fig. 6.22b, the superstrate is placed at an optimized distance d, which is 1.1 λ_0 above the upper plane of the 4 × 5 SIW antenna array. Figure 6.23b shows that the gain is increased by approximately 3 dBi at the operating frequency of 30 GHz. However, the array bandwidth is not adversely affected by the presence of the superstrate and the S_{11} remains less than −10 dB in the frequency range of 27–34 GHz (see Fig. 6.24). These results demonstrate that adding an optimally designed superstrate layer above an LPAA or SIW array can help to improve its gain performance without

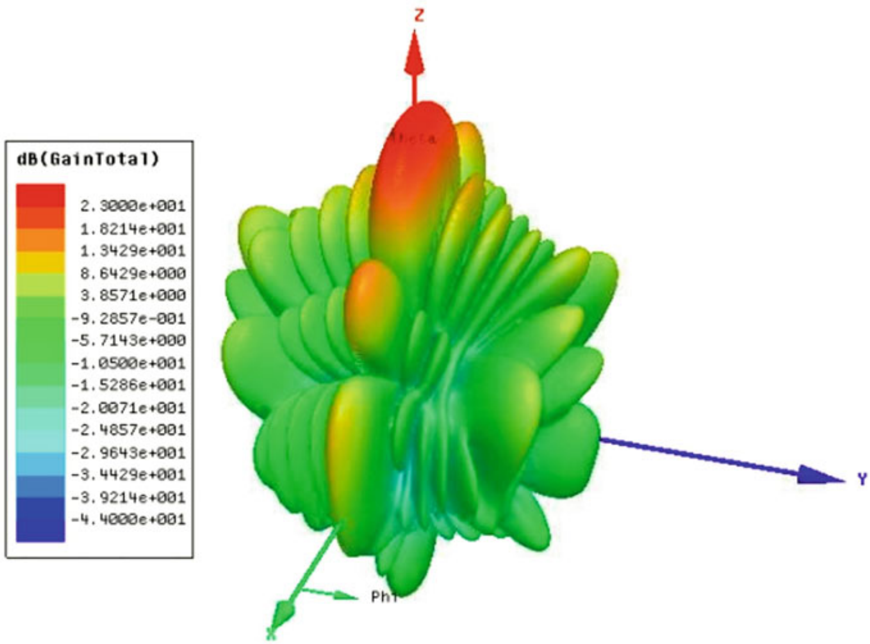

Fig. 6.21 3D-radiation pattern of the aperture array at 30.5 GHz

Table 6.5 Superstare geometry parameters and the simulated results of the array design at 30 GHz

t_s	0.92 cm
H_s	0.5 cm
E_r	2.2
$\Delta\delta$	0.0009
SLL with superstrate (LP)	12.09 dB
SLL with superstrate (TP)	20 dB
HPBW (LP)	6.9°
HPBW (TP)	14.45°
Max gain	25.55 dB

compromising its wideband nature. Table 6.6 presents a comparison between the proposed SIW slotted array with some other SIW aperture arrays that have appeared in the literature in recent years [30, 32]. A comparison between their performances in terms of bandwidth and peak gain shows that the proposed array exhibits a comparable gain and a wider impedance bandwidth characteristic than the legacy designs.

Beam scanning arrays that have high gain, low-profile, wide bandwidth, good efficiency, and wide-angle scan capability with low scan loss are desired for several applications, such as satellite communication, radar, weather sensing, marine navigation, and tracking of fast rescue craft and person-in-water [33, 34]. The design

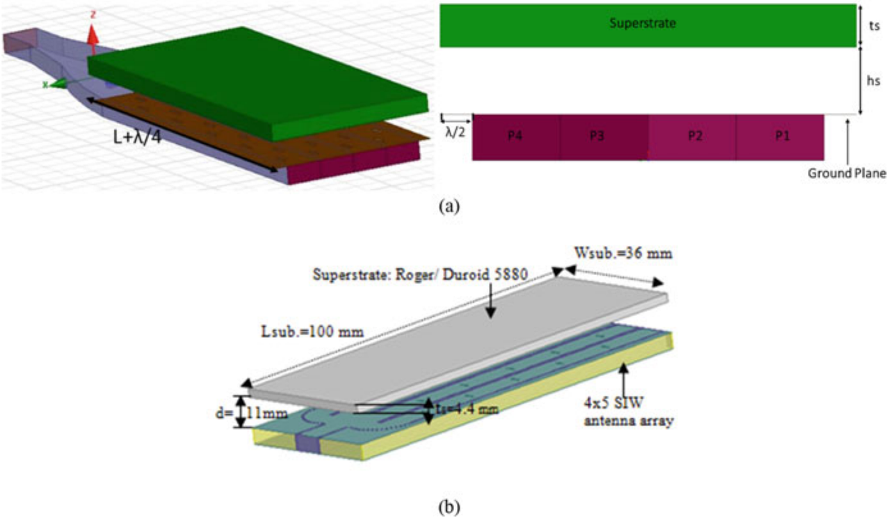

Fig. 6.22 Design of aperture array antenna with a dielectric superstrate above the rectangular waveguide array and the SIW array

of scanning arrays is a challenging task, to say the least, and it is not always possible to make minor changes to fixed-beam array designs presented in the two examples given above [13, 14], and [12], for instance, to add the scan capability except by using mechanical scanning with limited scanning speeds, which is not acceptable for many applications. This was one of the motivations for developing the two LPAA designs presented in the previous section, and we will now discuss some ways by which we can add the scan capability to the fixed-beam version of the LPAA that we have presented above. Both 1D and 2D scanning systems are discussed in Sect. 6.2.2, with the scanning achieved electronically to realize a rapid scan desired in many applications, and at a fixed frequency rather than by using a frequency scan, as in the case of leaky-wave antennas.

6.2.2 Beam Scanning Techniques

In this section, we discuss some strategies for adding scan capability to the LPAA array designs presented in Sect. 6.2.1. Phase shifting can be achieved in a waveguide array by changing the guide wavelength, which in turn changes the phase shift between the elements and causes the array to scan. A straightforward approach to doing this is to scan the frequency, as is done in a leaky-wave antenna. Below we first show the performance of the array when we scan the frequency to realize the beam scan; however, since most applications of scanning arrays call for a fixed

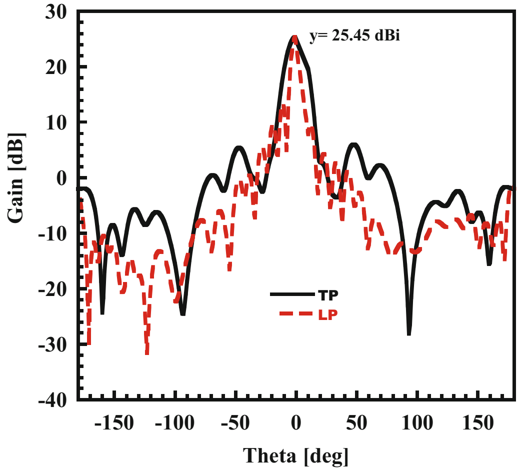

(a) Rectangular waveguide array

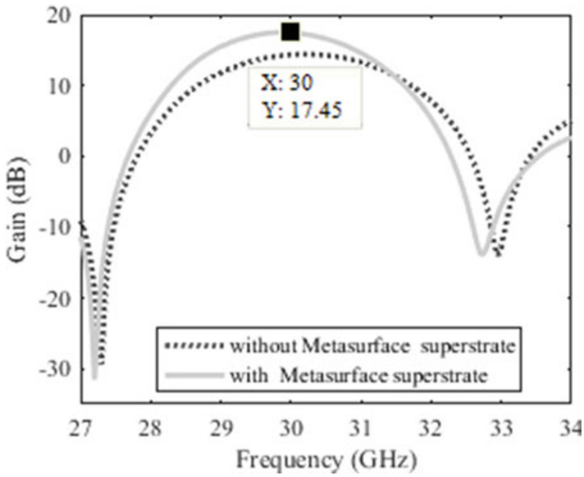

(b) SIW array

Fig. 6.23 (**a**) Simulated radiation pattern of the LPAA in the presence of a dielectric Duroîd superstrate at 30 GHz and (**b**) the Simulated Gain of the SIW array with Metasurface superstrate

frequency scan, we move on next to investigate ways we can achieve the required phase change in the guide at a fixed frequency.

6.2.3 1D Frequency Scanning LPAA Array

For the frequency-scanned antenna, we propose a 4 × 1 power divider, which excites either four planar slotted waveguide array antennas, or the Substrate Integrated Waveguide (SIW) slot array. The main beam is steered in the longitudinal plane

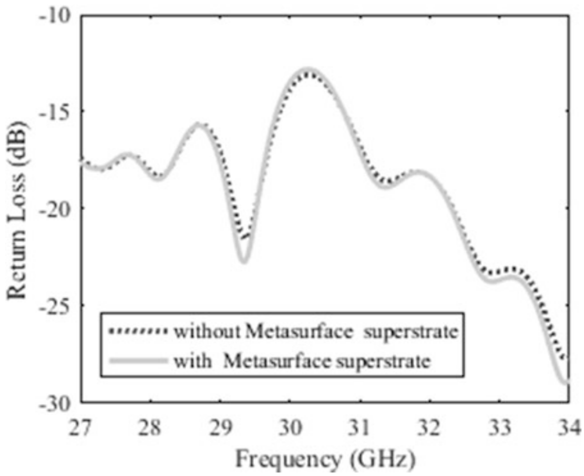

Fig. 6.24 S_{11} vs. frequency with and without metamaterial superstrate for 4×5 SIW antenna array

Table 6.6 Comparison between proposed and reported SIW slot antenna arrays

Structures	Performance			
Ref	f (GHz)	No. of element	BW (GHz)	Peak gain (dB)
[30]	32.65	1×4	[26–38]	13.8
[31]	30	1×4	[24–32]	9
[32]	30	4×8	[29–31]	18.7
SIW array without superstrate	30	4×5	[27–34]	14.43
SIW array with superstrate	30	4×5	[27–34]	17.45

by changing the frequency, as shown in Fig. 6.25. The realized scan range is from −23° to 16° and the antenna gain varies from 22 to 24.5 dB as we vary the frequency from 30 GHz, in the range of 26 to 34 GHz.

6.2.3.1 2D-Beam Scanning at a Fixed Frequency

We now turn to the problem of beam scanning at a fixed frequency. We can introduce phase shifts between the antenna elements, either by varying the guide widths to realize the beam scan in the longitudinal plane (see Fig. 6.26) or by changing the electrical lengths of the guides to scan the beam in the transverse plane, as shown in Fig. 6.27. Changing the width of the waveguide can be accomplished by moving the side walls in and out, which can be done electronically by first using vias to replace the solid walls, and then partially switching the vias on and off to change the guide wavelength and thereby scanning the beam in the longitudinal plane. Liquid metal [35–38] can also be used for the same purpose for the electronic scan moving the sidewalls out scans the beam to the right. The farthest we can shift it to is determined by the onset of the next higher order mode, which can be excited if the width of the guide is sufficiently large so that the higher order mode begins to propagate.

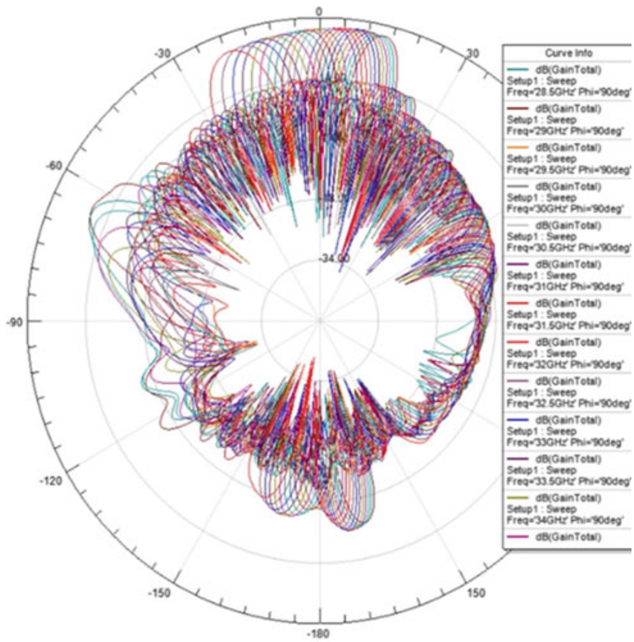

Longitudinal plane

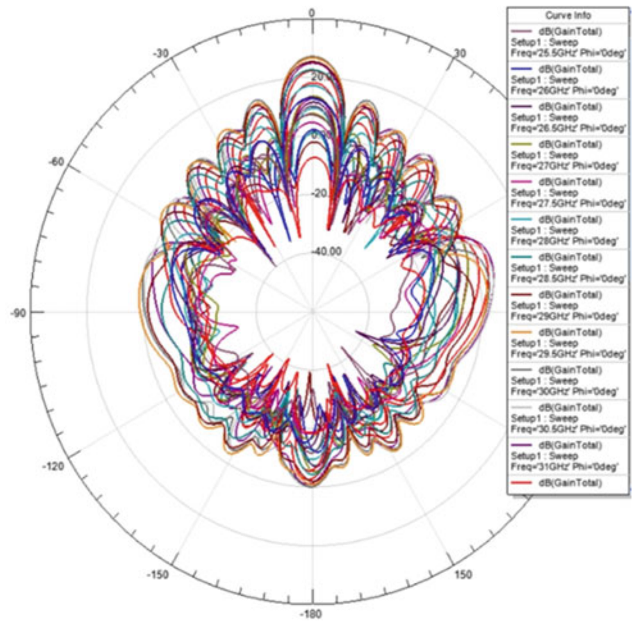

Transverse plane

Fig. 6.25 Simulated radiation patterns of the scanning proposed LPAA antenna in the longitudinal plane

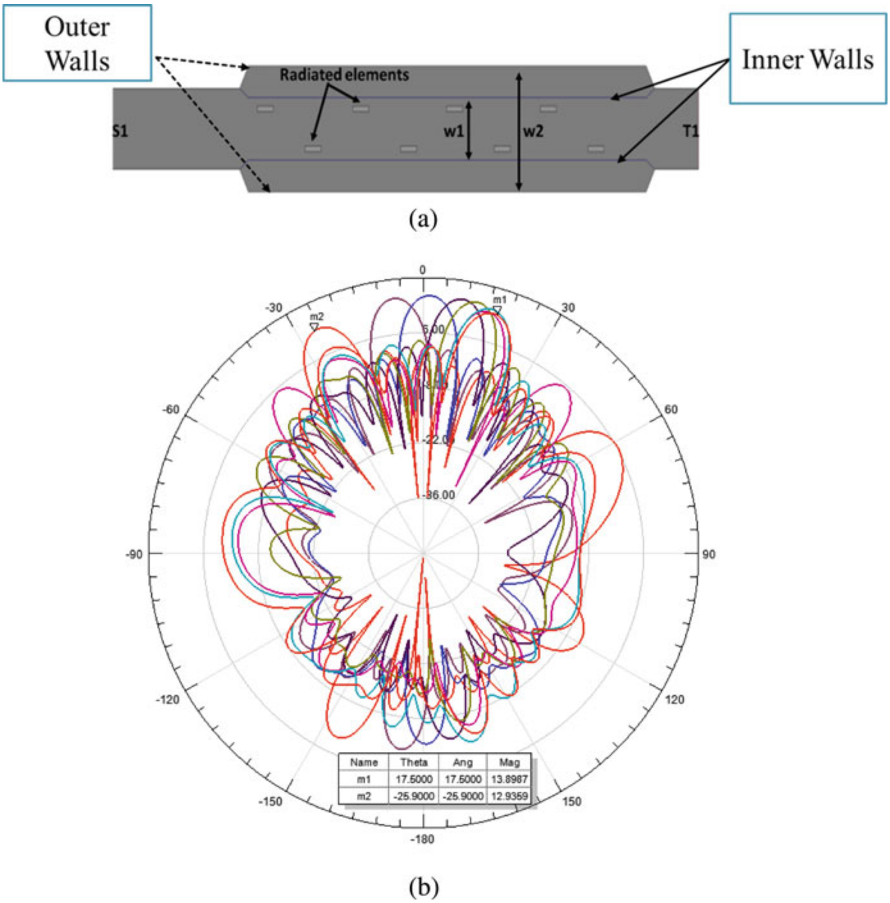

Fig. 6.26 Beam scanning LPAA antenna technique in the longitudinal plane at 30 GHz: (**a**) shematic of the mechanical beam scan technique, (**b**) simulated 2D radiation pattern at different position of the inner walls

Hence, the maximum allowable width of the guide is determined by the criterion that the waveguide must only support the dominant mode and suppress all higher order modes.

Next, let us consider the lower limit for the width of the guide. It is obvious that we cannot decrease the width below that required to ensure that the waveguide is above the cut-off for the dominant mode. Imposing these two limits on the width of the guide determines the scan range, which is 43°. Also, this approach might, in future, enable beam scan in milliseconds, which is desirable. However, further developments in liquid metal actuation technology will be needed to bring this about.

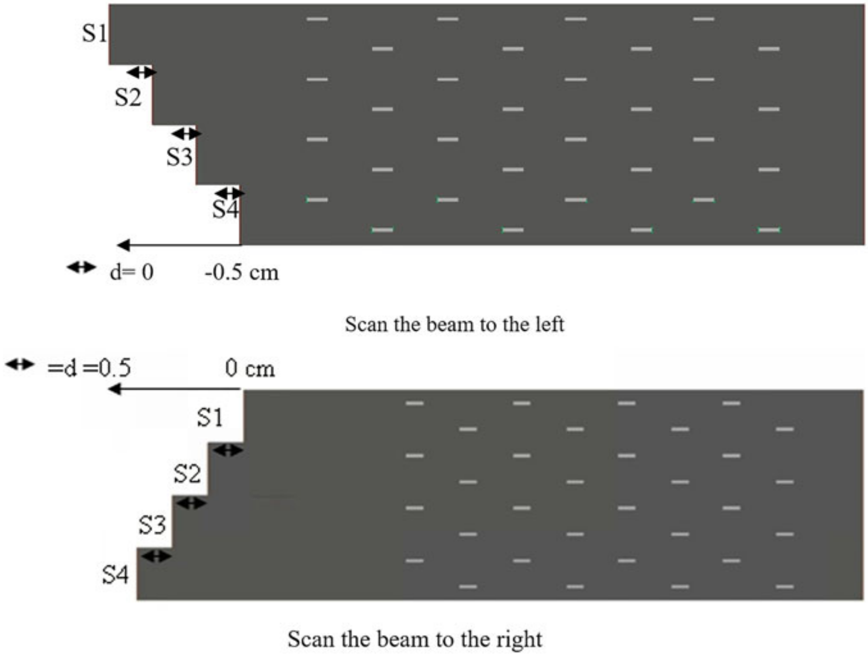

(a)

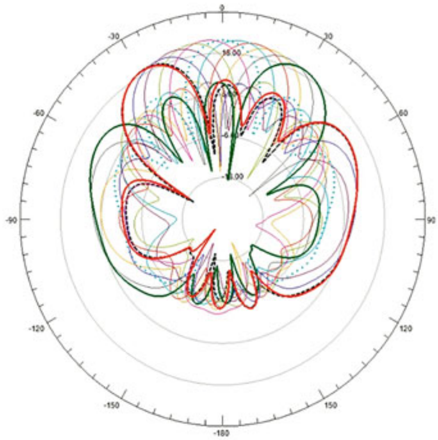

(b)

Fig. 6.27 Beam scanning LPAA antenna technique in the transverse plane at 30 GHz: (**a**) schematic of the mechanical beam scan method, (**b**) simulated 2D radiation pattern at different position of each waveguide fed position

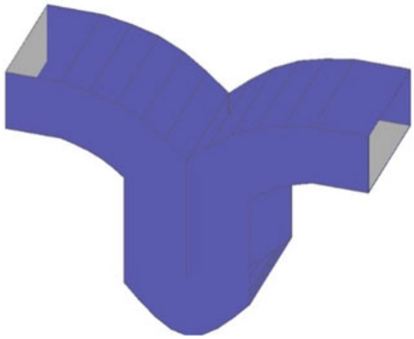

Fig. 6.28 Phase shifter using a curved waveguide

Next, let us consider the problem of scanning the beam in the transverse plane. We can accomplish this by effectively changing the lengths of the waveguides feeding the array, depending upon the desired scan angle, in a manner shown in Fig. 6.27a. This method achieves a beam scanning range of approximately 60° (see Fig. 6.27b), and it can accomplish this in milliseconds if electronic switching is employed to implement the changes in the lengths of the waveguides.

Several approaches to the practical realization of the longitudinal scans can be suggested. We can use liquid metal to vary the width of the waveguide; by replacing the inner and outer walls in Fig. 6.26a with closely spaced vias. Possible ways to alter the effective lengths of the waveguides include microfluidics, telescoping walls, and curved waveguide (Fig. 6.28) inserts with switches. In this way, it is possible to achieve beam scan in the transverse plane. Additional research is needed to develop ways to realize these types of phase shifters in practice, to replace the legacy designs originally developed for applications at microwave frequencies, using ferrites, whose counterparts become very lossy and expensive at millimeter-waves and which renders them all but impractical to use in commercial applications.

For certain applications, such as base station antenna designs for 5G, it is necessary to scan over a much wider angular range, say $-50°$ to $+50°$, than is possible by simply modifying the low-profile array designs that we have discussed above. With this in mind, we will now describe a design strategy which departs significantly from the LPAA concept. The primary reason for doing this is to come up with a design which can scan very wide angles with virtually no scan loss, which is a very desirable attribute indeed in some 5G applications. We show that the Luneburg lens is very well suited for our purpose, and then go on to discuss the details of the design, also addressing the fabrication issues in the process.

6.2.3.2 Arrays with Wide-Angle Scan Capability

In this section, we present two designs of wide-angle scanning arrays, both exciting a Luneburg lens, using feed structures to realize a scan range of $-\varphi$ to $+\varphi$ in azimuth and $+\theta$ to $-\theta$ in elevation (El), both of which are wide, on the order of 40 (EL) to

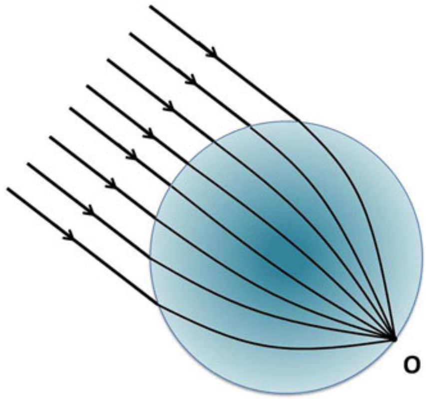

Fig. 6.29 Luneburg Lens Principle

50 (AZ) degrees. The first design utilizes a flat-base waveguide array feed with a pigeon-hole configuration, which has been reported in [39]. The second design employs a patch-array for the feed, together with switching circuits, to achieve a signal coverage over a wide area by switching a narrow beam of the patch-fed lens in a raster-scan fashion. The basic working principle of Luneburg lens antenna is shown in Fig. 6.29, when it is operating in the receive mode. The lens has a radially varying permittivity profile ε_{r}, given below in Eq. (6.1), to focus an incident plane wave at a point diametrically opposite to that of the incident side when the lens operates in the receive mode. The profile is given by:

$$\varepsilon_{\mathrm{r}} = 2 - \left(\frac{r}{R}\right)^2 \tag{6.1}$$

where r is the distance from the center of the lens, and R is the radius of the lens.

An 11-layer Luneburg lens has been presented in [39], in which the lens was fed at its base by a 6×6 array of waveguides, as shown in Fig. 6.30. Beam scanning was accomplished by switching the feeds on and off located at the bottom of the guides—one at a time—to point the beam in the desired direction. It was shown in [39] that this Luneburg lens design was able to scan up to 72° from boresight in both azimuth and elevation with little degradation of the pattern and with little scan loss. A typical radiation pattern realized by exciting one waveguide is shown in Fig. 6.31. Figure 6.32 shows the directivity of the Luneburg Lens Antenna as a function of φ for different scan angles, for $\theta = 12°$, 41°, and 64° cuts.

It is evident from Fig. 6.32 that the designed lens antenna has wide-angle scan capability. However, it is also evident that the pattern changes as we scan, which may not be desirable for some applications.

For ease of fabrication, it is desirable to reduce the number of layers of the Luneburg, without compromising its performance. It is necessary to optimize the permittivity profile in order to achieve this reduction, rather than just sampling the

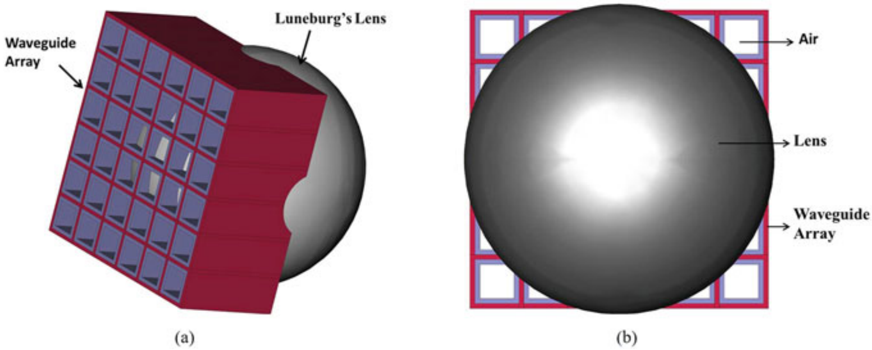

Fig. 6.30 Designed Luneburg Lens. (**a**) Isometric view. (**b**) Top view

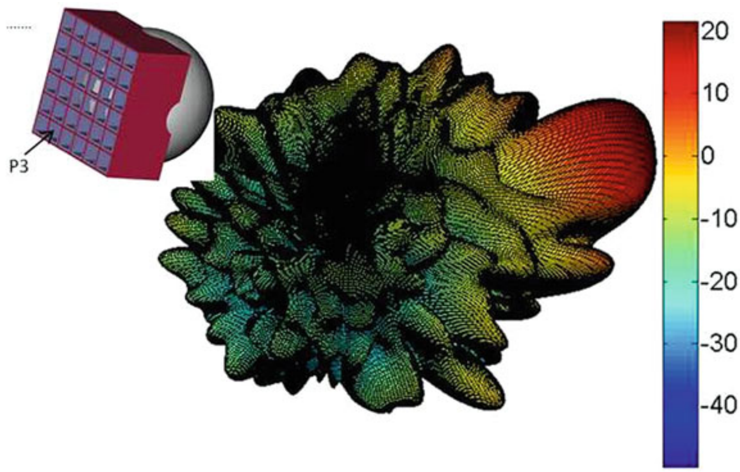

Fig. 6.31 Radiation Pattern of the Luneburg Lens Antenna when one of the waveguides is excited

continuous profile, as was done in the original 11-layer case. The optimized profile [40, 41] is presented in Table 6.7 (see column-1).

It is not difficult to understand that the required materials, listed in Table 6.7, are not commercially available off-the-shelf. To address this problem, an obvious approach is to employ artificially synthesized dielectrics to fabricate the lens, and two different techniques which can be used for this purpose are described below. First of these employs the process of laser- or machine-drilling, while the second relies upon additive manufacturing or 3D printing.

(a) *Laser cutting holes in dielectric for lens design:* For laser cutting, or machine-drilling, we use readily available dielectric boards and drill holes in the dielectric sheet to synthesize the permittivity values of the spherical shells specified in Table 6.7. Either laser- or CNC-drilling may be used for this purpose,

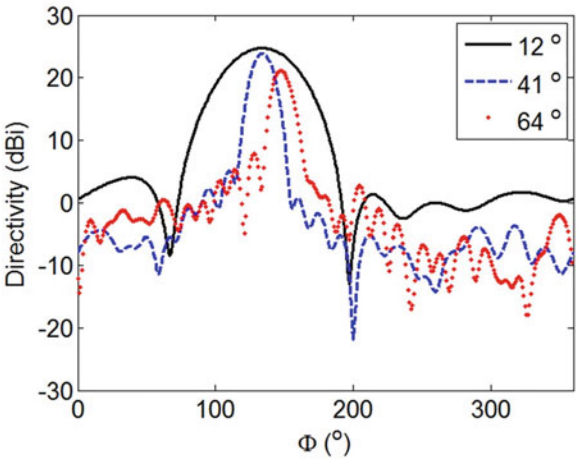

Fig. 6.32 Directivity of the Luneburg Lens Antenna as a function of φ for different scan angles for $\theta = 12°, 41°$, and 64° cut

Table 6.7 Unit cell size properties for different lens layers

Material dielectric values	S_{21} (dB)	Width (W) (mm)	$2 \times l$ (mm)
1.1538	−0.009	1.58	0.42
1.3077	−0.041	1.39	0.61
1.4615	−0.09	1.24	0.76
1.6154	−0.16	1.11	0.89
1.7692	−0.24	0.99	1.01
1.9231	−0.33	0.88	1.12

and both are well-established techniques. The Luneburg lens fabricated by using the holey-sheet approach is comprised of many layers, with the number of layers determined by the thickness of the dielectric sheet material and the diameter of the lens. Considerable care must be exercised to determine the hole pattern, which changes from sheet-to-sheet, as we go up the sphere to its pole, starting from its equator. It is necessary to numerically simulate the holey discs to ensure that the perforated discs indeed accurately mimic the artificial dielectric rings that we are attempting to synthesize.

(b) *3D printing of lens*: An alternative scheme for synthesizing artificial dielectrics is to use 3D printing. The theoretical basis for designing artificial dielectrics may be found in [42] and is omitted here.

Thermoplastic Polylactic Acid (PLA), which has a permittivity (ε_r) of 2.72, is a very common material used for 3D printing and is also the material in the present design. In this approach, we modify the permittivities of a COTS material by inserting air-voids in it to realize the required permittivity, listed in Table 6.7. To illustrate the lens design, we choose a unit cell with a periodicity 2×2 mm,

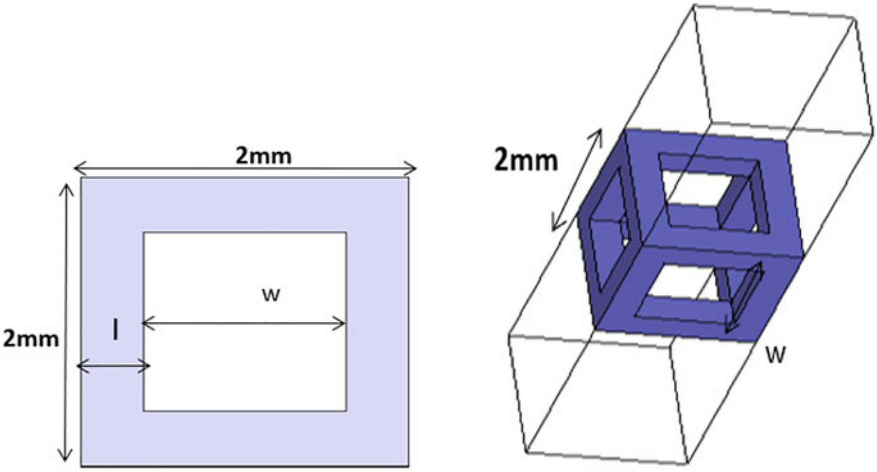

Fig. 6.33 Unit cell for Luneberg lens (different views of unit cell)

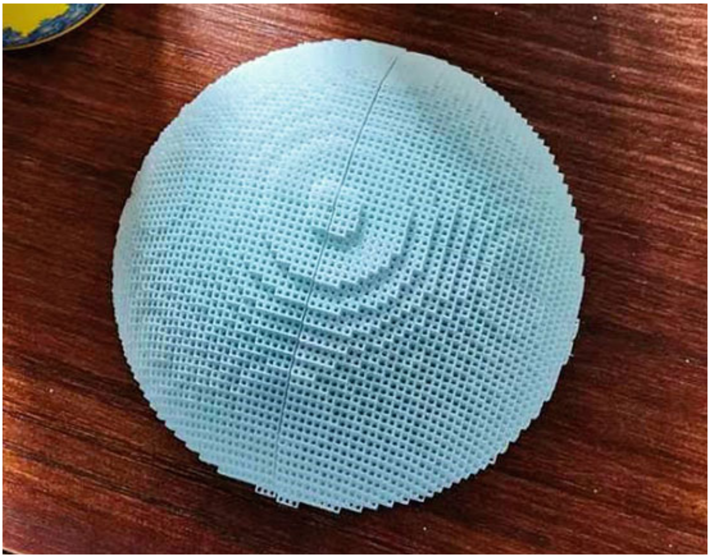

Fig. 6.34 Fabricated Luneberg Lens

and use unit cells comprising of air-voids and dielectrics, as shown in Fig. 6.33. The designed unit cells together with their required dimensions are also presented in Table 6.7. The designed cells have better than 0.4 dB insertion loss.

The PLA infill method was used to design the entire lens with a diameter of 14.5 cm, which realized a gain of 31 dB at 26 GHz, attaining good aperture efficiency. The 3D printed lens is shown in Fig. 6.34.

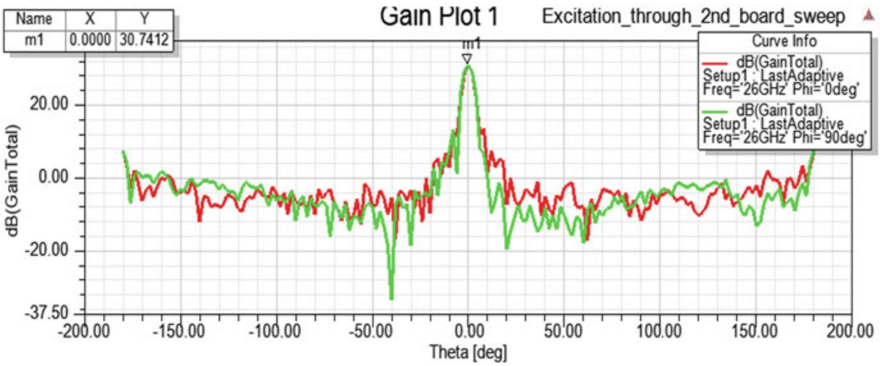

Fig. 6.35 Radiation pattern of 14.5 cm, 6 layer Luneburg lens antenna. The red curve represents the $\phi = 0°$ cut while the green represents the $\phi = 90°$ cut

Figure 6.35 shows the radiation pattern for the lens at 26 GHz. We can observe that the lens provides a gain of 30.74 dB along the broadside and the gain is maintained at this level even for wide scan angles.

Beam scanning is accomplished by switching the feed elements for the lens, one at a time, to point the beam in the desired direction. A possible feed system design is shown in Fig. 6.36. In this design, the first switching action is accomplished by PCB1, which determines which PCB2 is to be activated. Once a particular PCB2 is selected, switches located on this PCB excite a particular patch antenna, one at a time, and scans the beam to cover a service area by sequentially switching in other patches. The main advantage of this beam scanning approach is that it permits wide-angle scanning with little pattern degradation, whereas conventional array designs are prone to scan loss as well as pattern degradation beyond 30° of scan angle, which is not acceptable for many applications.

A 5 × 5 conformal patch-array (see Fig. 6.37) was designed as shown in Fig. 6.39 to feed the Luneburg Lens to verify its scan performance. The edge-to-edge separation distance between the adjacent elements of the array was chosen to be 1 mm. The conformal array (see Fig. 6.38) was placed on the surface of the Luneburg lens for excitation as shown in Fig. 6.39. The reflection and isolation coefficients were found to be better than 10 dB throughout the frequency band. The 2D radiation pattern for the $\phi = 90^{\circ}$ cut is shown in Fig. 6.40. A similar behavior was observed for the 2D radiation pattern for the $\phi = 90^{\circ}$ cut is shown in Fig. 6.41.

While the 3D printing method is very versatile, it is very challenging to maintain the accuracy of the building blocks of the lens, shown in Fig. 6.34, because of the need to control the fabrication tolerances to within fractions of a millimeter. This prompted us to revisit Method ***a***, described above, and fabricate the lens by stacking sheets of PureBlue material with permittivity (ε_r) = 2.47, in which holes are drilled to artificially synthesize the desired dielectric materials for the lens, presented earlier in Table 6.7. Figure 6.42a shows the spherical lens without the outermost layer, for which we use a "real" material, specifically a foam type, with permittivity close to

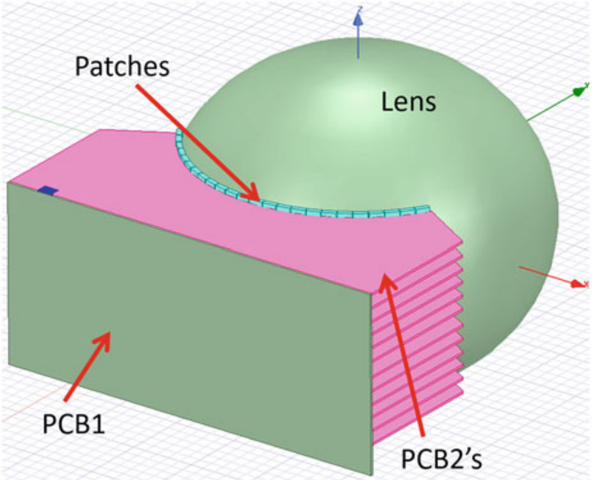

Fig. 6.36 Full lens system with switches

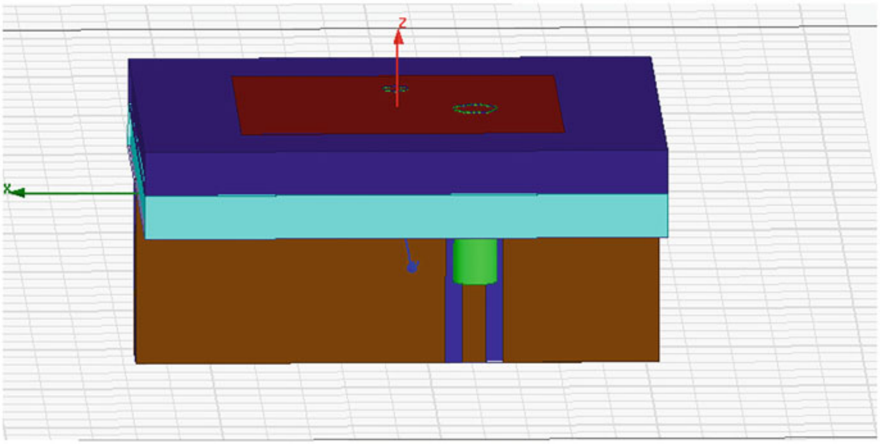

Fig. 6.37 Single patch antenna element with dual feed

1.15. Figure 6.42b, c show two different discs, together with their hole patterns, the first of which is at the equator and the second closer to the pole. Altogether, 90 of these "holey" discs are required to form the sphere, without the outermost shell.

The 2D-scanning beam of an aperture array at the desired operating frequency is not the last design challenge of aperture arrays for 5G, for which polarization diversity may also be required. Most of the antenna array based on waveguides have a linear polarization along the desired frequency range, and as the circular polarization of an antenna array is so important for the network communication

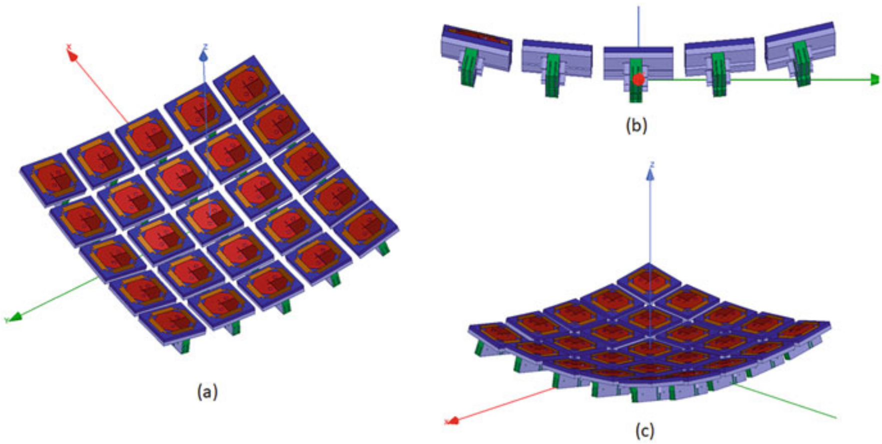

Fig. 6.38 5 × 5 conformal array: (**a**) trimetric view; (**b**) and (**c**) side view

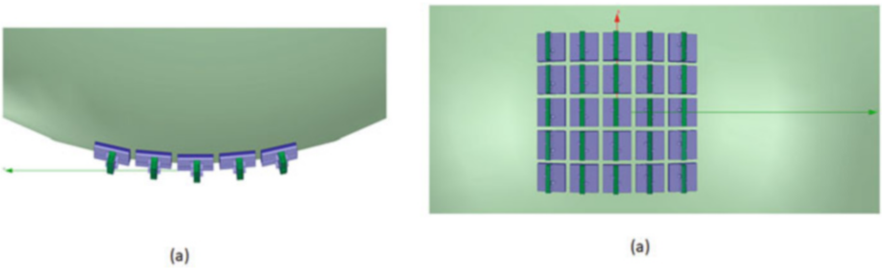

Fig. 6.39 5 × 5 conformal array exciting Luneburg lens (**a**) side view (**b**) bottom view

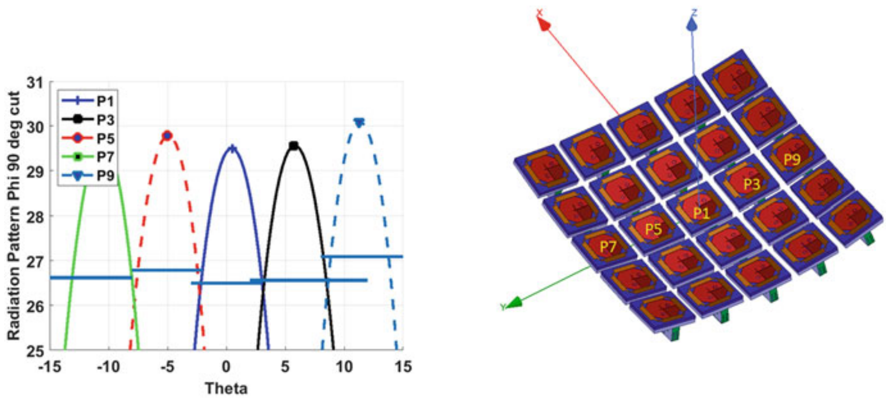

Fig. 6.40 2D radiation pattern at phi = 90°

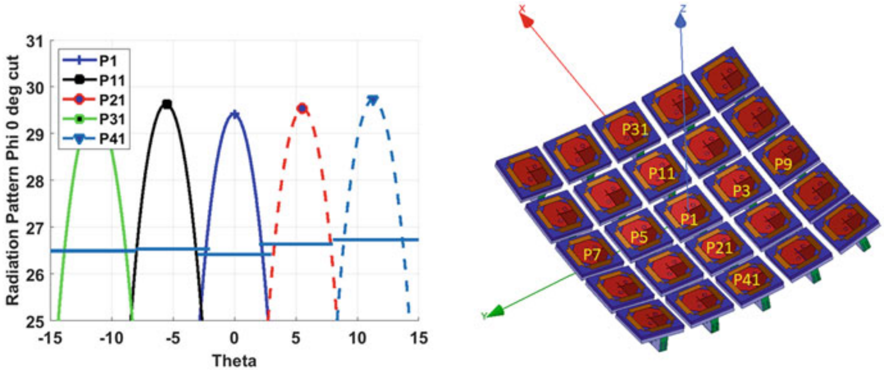

Fig. 6.41 2D radiation pattern at phi = 0°

applications, the steps to achieve a circular polarization from the linear and dual linear polarization of electromagnetic waves is presented in next section.

6.2.3.3 Beam Scanning of an SIW Array Using Electronically Switched SIW Phase Shifters

In this section, we present the design of an electronically switched phase shifter introduced in a slotted SIW array for the purpose of scanning its beam. Phase shifting is accomplished by electronically switching one or more vias located within the curved SIW sections that are introduced between two adjacent slots of the array, as shown in Fig. 6.43b.

For the sake of illustration, we begin by designing six curved sections of SIW, introduced between two straight sections which serve as the input and output ports (port-1 and -2 in Fig. 6.43) of the array. Next, we introduce five semicircular slots between consecutive curved sections, as shown in Fig. 6.43, such that the separation distance between the slots is close to one-half wavelength in freespace. The semicircular shape of the slots was chosen because its performance was better than that of the conventional rectangular-shaped slot, whether oriented vertically or horizontally. The spacing between the slots was chosen to avoid the introduction of grating lobes.

Our next step was to introduce switchable vias in the six curved sections, which could be turned "on" or "off" electronically. The realized phase taper in the slotted array can be controlled by choosing different combinations of "on" and "off" vias, which in turn determine the scan angle of the beam. As an example, to generate the seven beams presented in Fig. 6.44, we use combinations of switches represented by different colors in Fig. 6.43 for switching, we have the option to either use PIN diodes or dielectric tubes with thin walls filled with liquid metal [38].

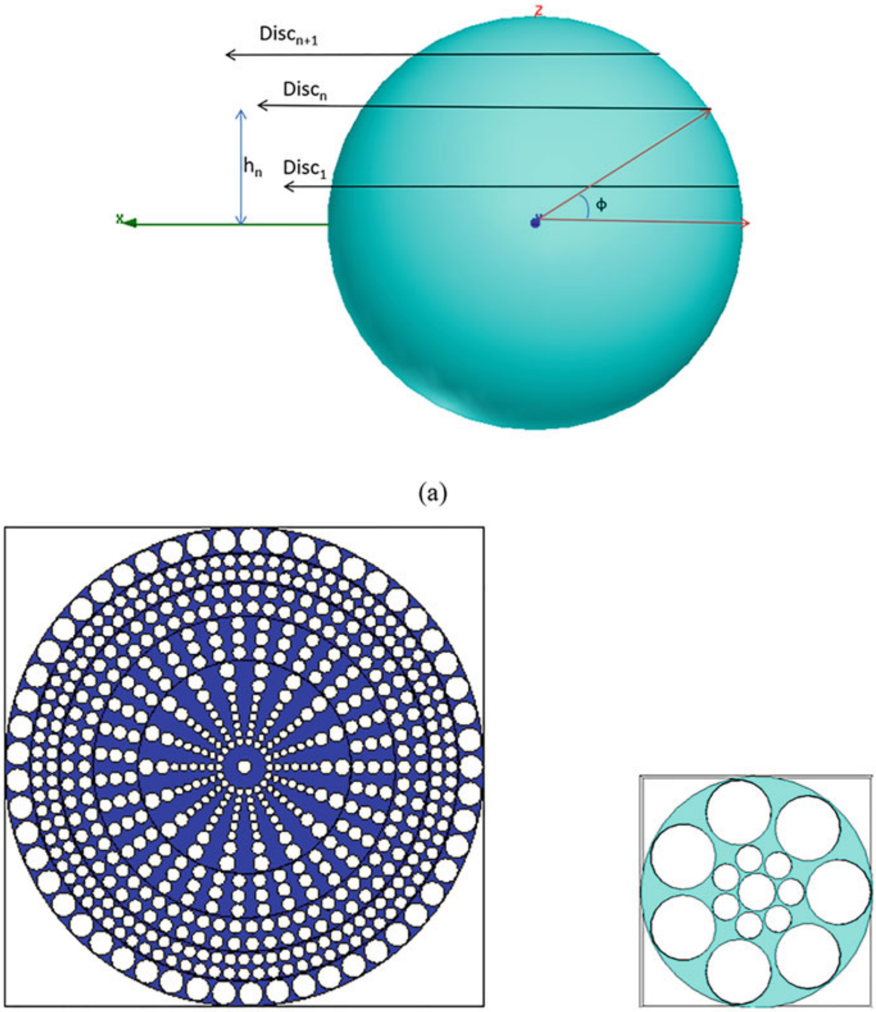

(a)

(b)

(c)

Fig. 6.42 Alternate lens design (**a**) location of upper surface of disc (**b**) disc cut near the center of the lens (**c**) lens at the extreme end of lens

High Gain Antennas with a Single Excitation

We now present the design of a high gain antenna with a "single" feed excitation, as opposed to an array configuration, which we have discussed above. For the sake of illustration, we choose a dielectric resonator antenna (DRA) as the exciter, although an alternate feed excitation using a microstrip patch or a slot antenna could also be employed in place of the DRA. The DRA design, shown in Fig. 6.45, has an overall

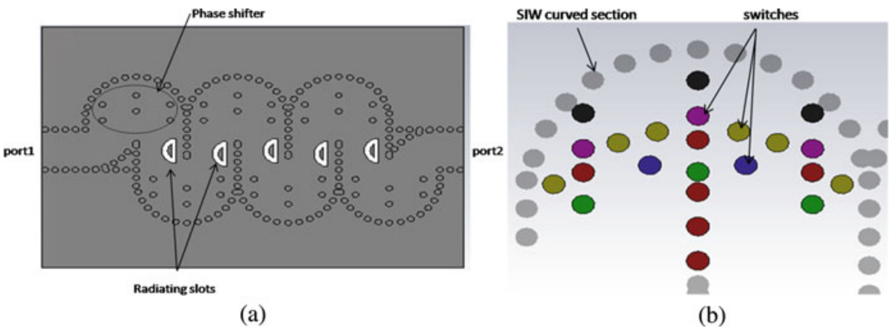

Fig. 6.43 The proposed slotted SIW curved array (**a**) an example of phase shifter, (**b**) One SIW curved section contains all switches

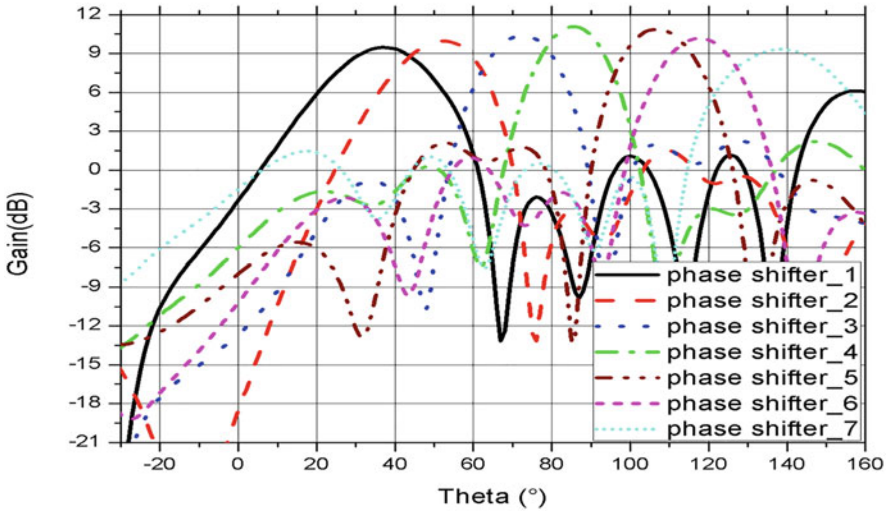

Fig. 6.44 Scan capability using SIW curved phase shifter above shows the scan performance of the array and demonstrates that the performance is good over a wide angular range

size of 7 × 7 mm backed by ground plane. The radiating element is an Alumina cylinder with $\varepsilon_r = 9.9$ and loss tangent (tanδ) of 0.0001 and with radius r equal to 2 mm. Figure 6.46 shows that the simulated gain of the proposed DRA is 6.29 dB at 26 GHz. Next, we use four metallic wings (see Fig. 6.47) to enhance the gain from 6.29 dB for the DRA to 23.2 dB for the winged configuration. The taper angle of the wing, as well as its length, was optimized to realize the best performance.

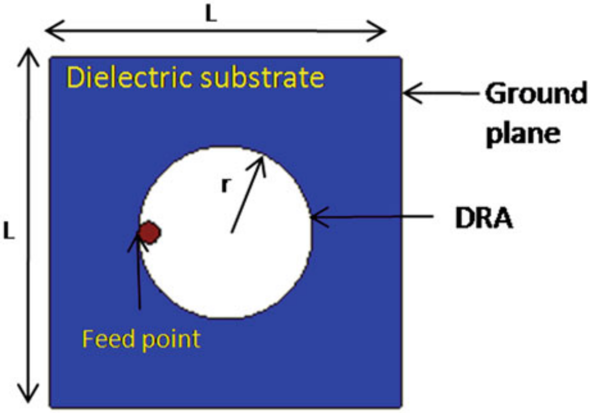

Fig. 6.45 Proposed DRA design

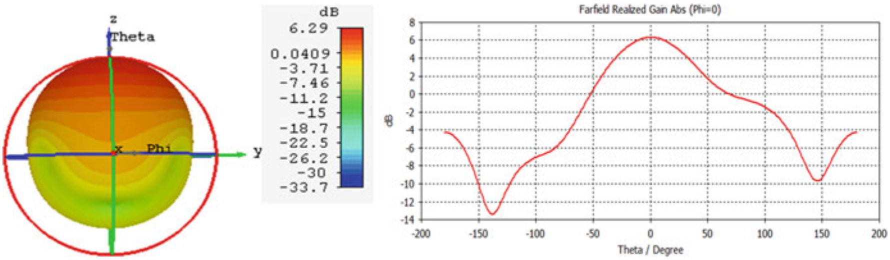

Fig. 6.46 The simulated 3D and 2D gain of the DRA at 26 GHz

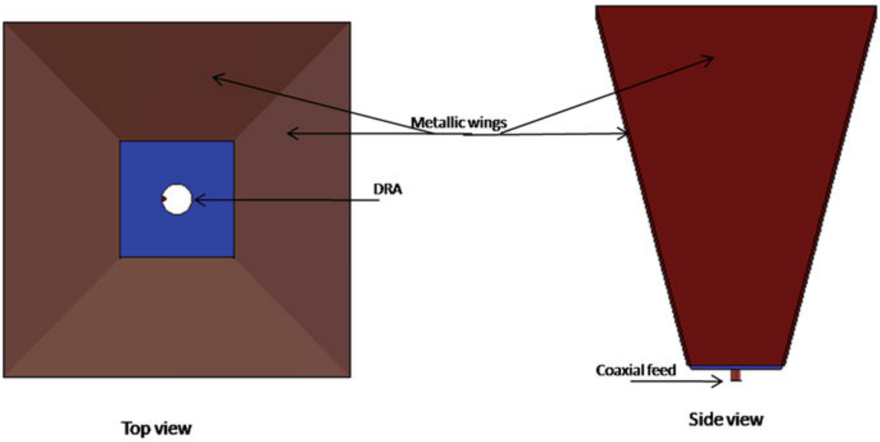

Fig. 6.47 Proposed DRA design with wings

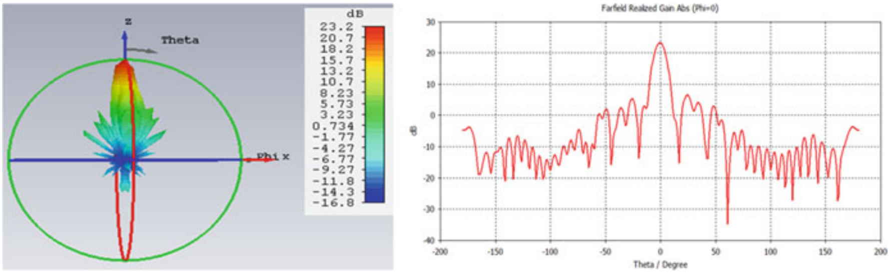

Fig. 6.48 Simulated 2D and gain 3D plots of the DRA with four wings at 26 GHz

Gain Enhancement Using Metallic Wings

We now turn to the problem of enhancing the gain of the DRA antenna by increasing its effective aperture, and the geometry we propose is shown in Fig. 6.47. It is comprised of four metallic wings added to the DRA to realize a horn-like configuration, with a tilt angle of 75° from the horizontal. Both the tilt angle and the length of the wings were chosen by optimization.

The simulated 3D and 2D radiation patterns of the DRA with wings are presented in Fig. 6.48. This gain realized by using the proposed metallic wings technique is approximately 23.2 dB at 26 GHz, whereas the gain of the DRA itself was 6.29 dB.

6.2.3.4 Wide-Angle Beam Scanning Using a Tilted Panel

We now present a novel design, shown in Fig. 6.49, for scanning the beam of the high gain DRA antenna configuration by using a reflecting panel located above the antenna whose tilt angle is changed depending upon the desired scan angle of the winged DRA antenna. The concept is relatively straightforward, and it relies upon the mechanism of specular reflection of the radiating beam emanating from the antenna located below the panel, as shown in Fig. 6.49. The panel can be realized either by using switches such as PIN diodes or using dielectric tubes filled with a liquid metal [43]. The tilting can be achieved by changing the angle of the panel by electronic means, for instance.

Figure 6.50 presents the simulated results, obtained by using the commercial software CST, for four different tilt angles of the panel, viz., 0°, 15°, 30°, and 45°, to achieve beam scan angles of 0°, 30°, 60°, and 90°, with no scan loss or pattern degradation. Additionally, the scan range can easily be extended from minus −90° to +90°. Furthermore, the panel dimensions could be optimized to improve the sidelobe level, if desired.

Finally, the proposed technique can be easily extended to achieve a two-dimensional scanning, in both longitudinal and transversal planes, by using switchable panels with tilt angles in both θ- and ϕ-planes, if desired.

Fig. 6.49 DRA design with wings and panel

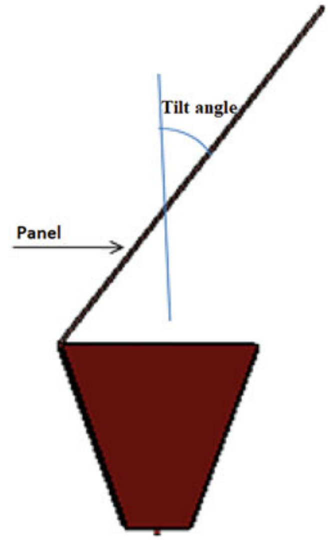

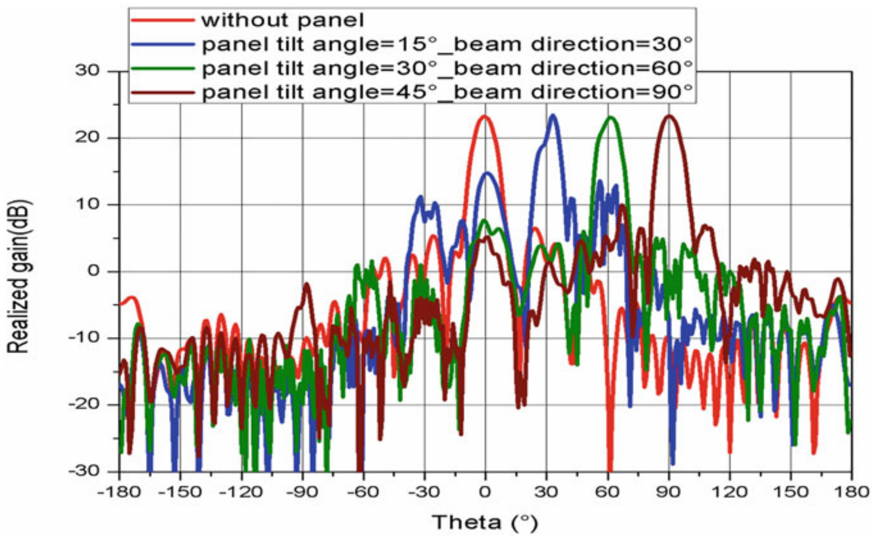

Fig. 6.50 Scan capability of the winged DRA using panels

Before closing, we add that we also have the option of using a hybrid approach in which the longitudinal scan is achieved by using phase shifters, while the transverse scan is obtained by using the panel approach. The scheme is illustrated in Fig. 6.51, which shows a slotted SIW array antenna with phase shifter and a panel placed atop the antenna for the purpose of scanning.

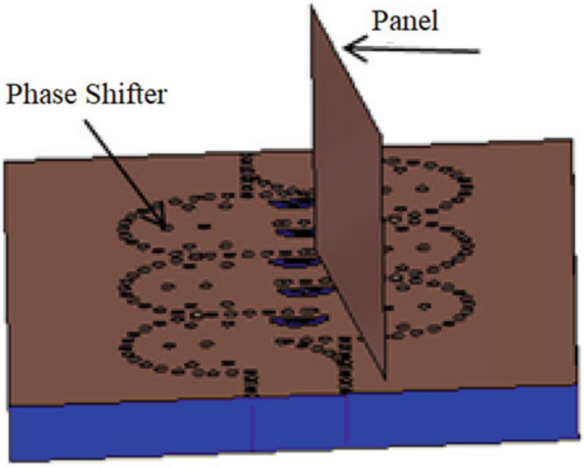

Fig. 6.51 Slotted SIW array antenna with phase shifter and a panel

6.3 Polarization Diversity Requirement for Fixed- and Scanned-Beam Antenna

The polarization of electromagnetic waves which can be transmitted or received by an antenna is one of the essential antenna parameters in the communication system. Most of the antennas are characterized by a single received polarization component with linear polarization. The LPAA structures and SIW array presented in Sect. 6.2. Are characterized with linear polarization in transverse and longitudinal plane.

In this section, we present another low-profile antenna array design of microstrip mm-wave antenna array based on a magneto-electric (ME) dipole antenna which is deployed and designed as a radiating element, where wide operating bandwidth and stable radiation pattern can be achieved over the entire frequency band centered at 26 GHz. The feed line of the dipole is connected to one/or twin microstrip lines (see Figs. 6.52 and 6.53). The design procedures of mm-wave antenna array are presented below. The proposed design for the array provides a low-cost solution which has a high gain and a relatively wide bandwidth.

We start with the design of a single wideband $\lambda/2$ dipole antenna, which has an $|S_{11}| < -10$ dB over the frequency band 23–30 GHz, as shown in Fig. 6.54. The antenna is excited from a microstrip line (ML) printed on a dielectric (duroid) substrate backed up by a ground plane. The single element is used to build a block of an array by using one ML (see Fig. 6.53) or twin lines to balance the excitation in the antenna (see Fig. 6.52). The gain of the 8×1 antenna array is presented in Fig. 6.55, where we can conclude that the gain is increased by around 10.2 dB at 26 GHz with low back lobe for both arrays, by using a single dipole elements whose gain equal to 5.5 dB and 7.2 dB at 26 GHz with one ML and twin lines, respectively. The

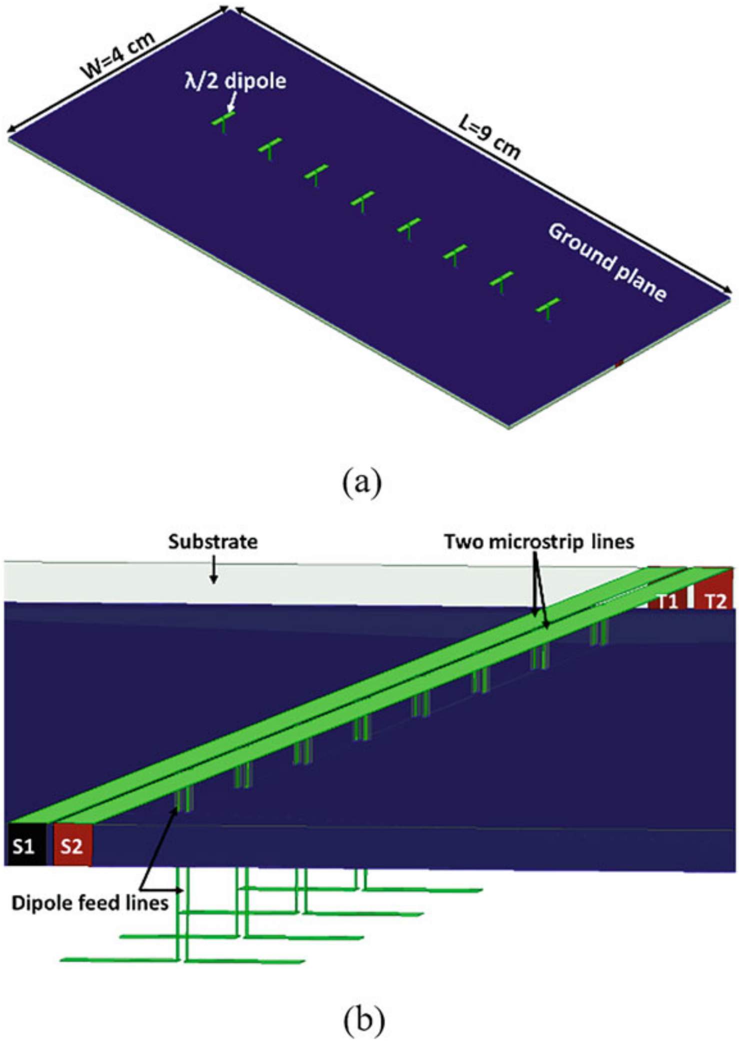

Fig. 6.52 Dipole antenna array feeding through two microstrip lines (A1). (**a**) Top view, (**b**) Bottom view

wideband behavior is maintained for the 8 × 1 array, fed by either a single line or twin lines.

Both 8 × 1 dipole antenna arrays are linearly polarized over the frequency range of 10 GHz with a center frequency of 26 GHz. Our goal is to design a dual linear or circularly polarized array which achieves both high gain and efficiency. However, as we increase the number of dipoles in the array fed by a single microstrip line, we not only lose the wide bandwidth behavior but also see an increase in the sidelobe

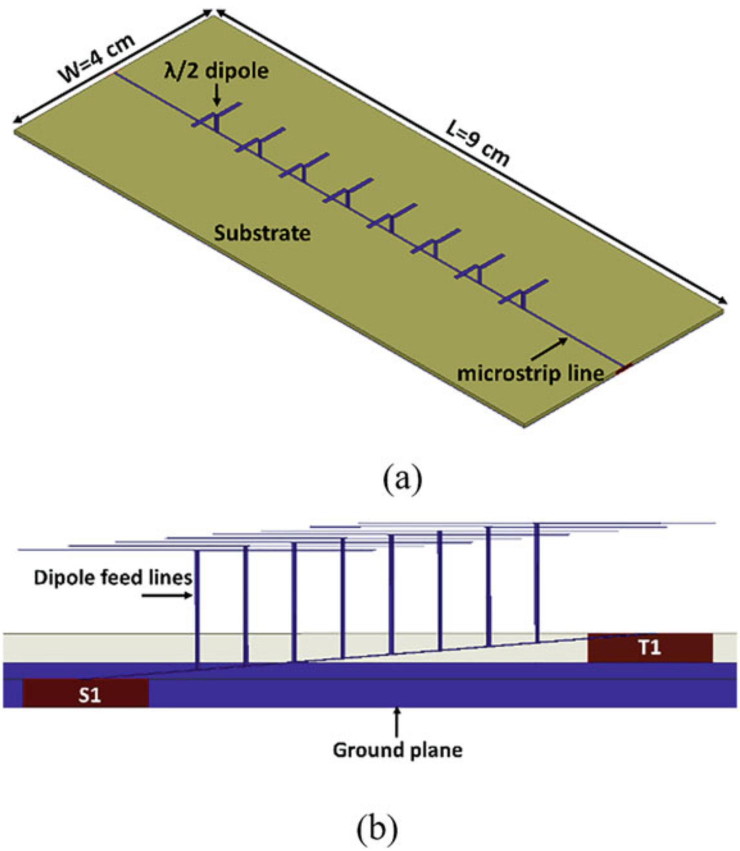

Fig. 6.53 Dipole antenna array feeding through one microstrip lines (A2). (**a**) Top view, (**b**) Bottom view

level in both planes. To avoid this problem, we choose to feed the dipole antenna array with twin microstrip lines to extend to the cases of dual linear or circular polarization, and to achieve these we combine the longitudinal and transverse dipole arrays, as detailed below.

6.3.1 Linear Polarization

We design and optimize the parameters of two separate dipole arrays (A1), one transversal and the other longitudinal, shown in Figs. 6.56a and 6.56b, respectively, both of which operate in the frequency range of 24–32 GHz. Each dipole array row is excited with sources that have a differential phase of 180° between the

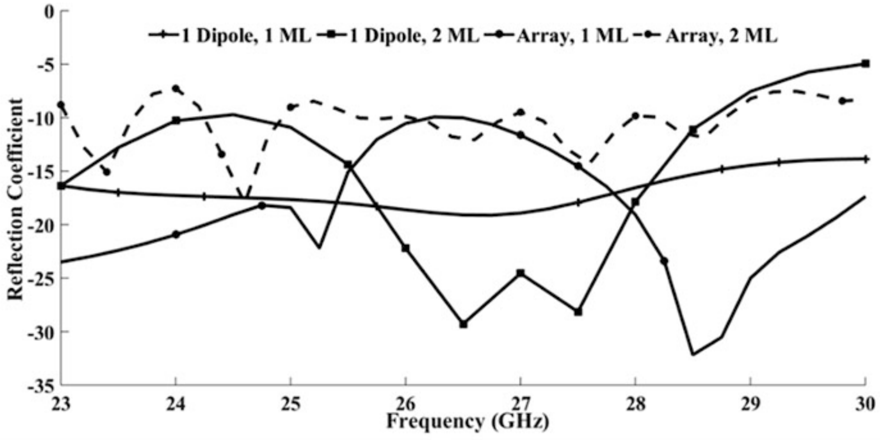

Fig. 6.54 Simulated S_{11} of one dipole antenna fed by using one or two microstrip lines (ML)

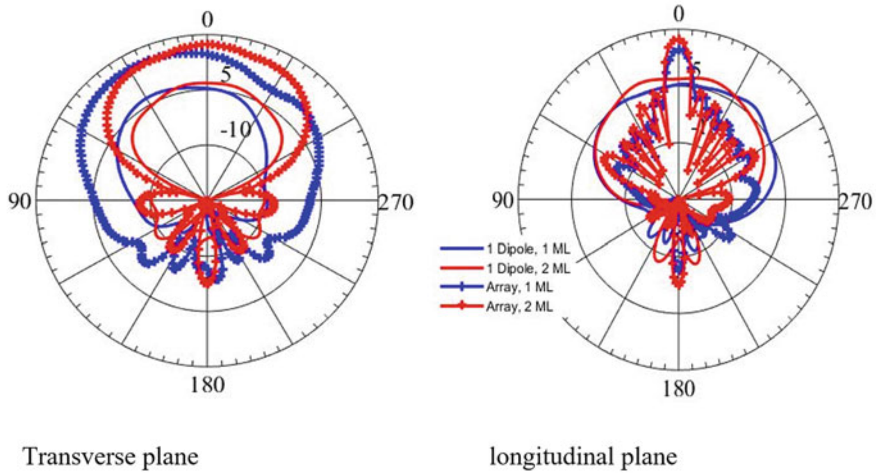

Fig. 6.55 2D-Radiation pattern for one dipole antenna and the array feeding by one or two microstrip lines at 26 GHz

coupled lines. As may be seen from Fig. 6.56c, the axial ratios of the longitudinal and transverse dipole arrays are individually greater than 15 dB over the frequency band of 24–32 GHz; hence, they are both (Fig. 6.56) linearly polarized, though their polarizations are orthogonal to each other.

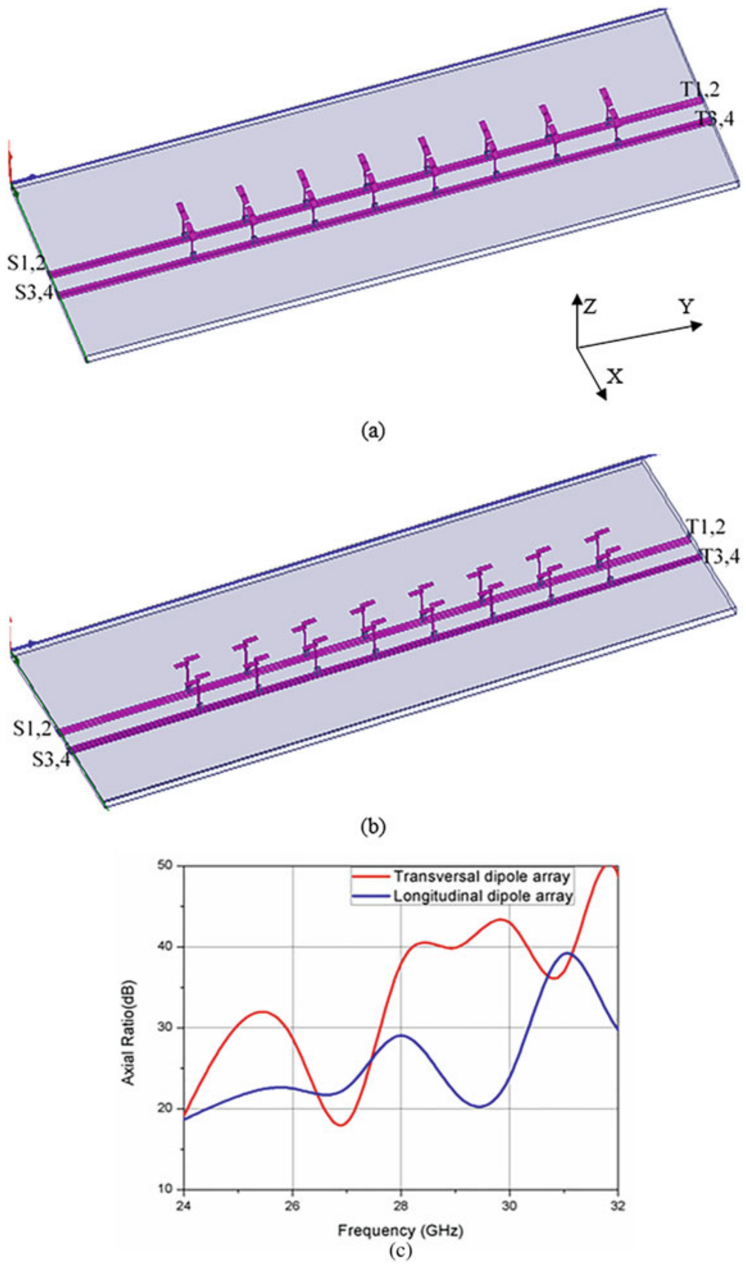

Fig. 6.56 8 × 2 dipole antenna array: (**a**) transversal dipole array, (**b**) longitudinal dipole array, and (**c**) axial ratio vs. frequency

6.3.2 Dual Linear Polarization

To achieve dual linear polarization, we simply combine the transversal and longitudinal array designs, exciting one array at a time to realize the dual linear polarization characteristic that we desire. Figure 6.57a shows an example of such a combination. The axial ratio plots presented in Fig. 6.57b show the polarization of the array when either the transverse or the longitudinal dipole array is excited.

Before closing this section, we should add that for the Luneburg lens we simply chose a microstrip patch antenna for the array element and use appropriately positioned dual probe feeds to realize the dual linear polarization. Although, it was relatively straightforward to realize the dual linear polarization characteristic. The challenging part was to reduce the coupling between the two feeds to a level below −10 dB over the entire frequency band by modifying the patch design (see Fig. 6.37).

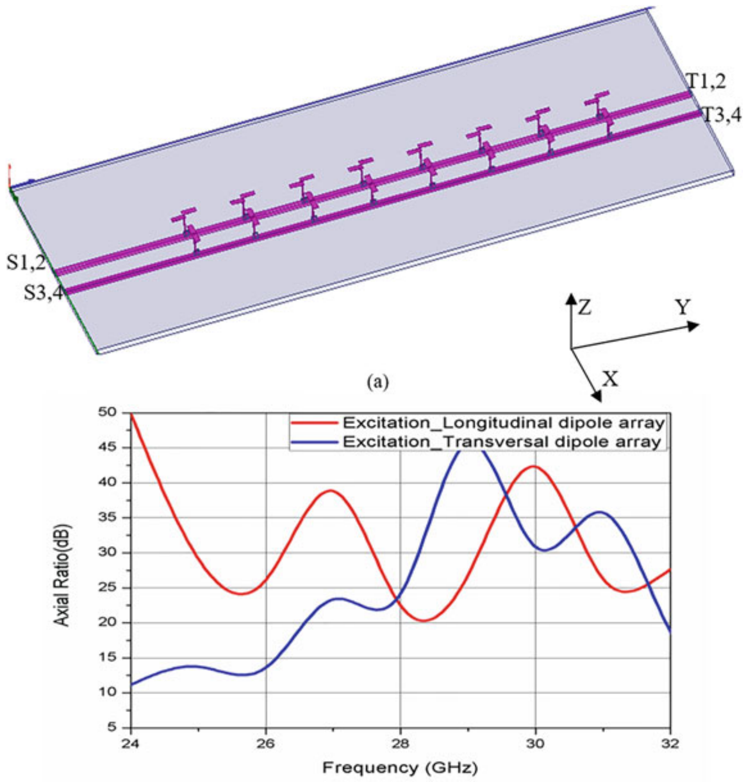

Fig. 6.57 8 × 2 dipole array antenna: (**a**) excitation scenario and (**b**) axial ratio vs. frequency

6.3.3 Circular Polarization

For several applications [44, 45] such as satellite communication, it is desirable to have an antenna that radiates circular polarization. We can realize a CP antenna array by simultaneously exciting the transversal and longitudinal dipole arrays as shown in Fig. 6.57a. Here, the combination dipole array is excited with differential phase which is equal to 180° between the coupled lines, i.e., between S_1 and S_2, as well as S_3 and $S_{4,}$ as shown in the inset in Fig. 6.58. Additionally, differential phase shifts of 90° is used between the feed lines of the two arrays to realize the CP. Figure 6.58 shows that this design generates a circular polarization with a narrow bandwidth of 8.38%.

Various numerical studies have been carried out in an attempt to improve the CP bandwidth of the array. Figure 6.59 shows one such configuration, with the feed excitations similar to the previous example. The simulated 3 dB axial ratio (see Fig. 6.60) bandwidth was found to increase from 8.38% to 10.2%, but it is still relatively narrow. This lets us to further investigate the possibility of enhancing the CP bandwidth by using the configuration shown in Fig. 6.61a.

Figure 6.61 shows that the axial bandwidth can be increased from 10.2% to 25.88% by varying the differential phases in the excitation ports, as shown in Table (Fig. 6.61a).

Before closing this section, we mention that an alternative to the LPAA array, presented in Sect. 6.2.1, is to add longitudinal slots to the existing transverse slots,

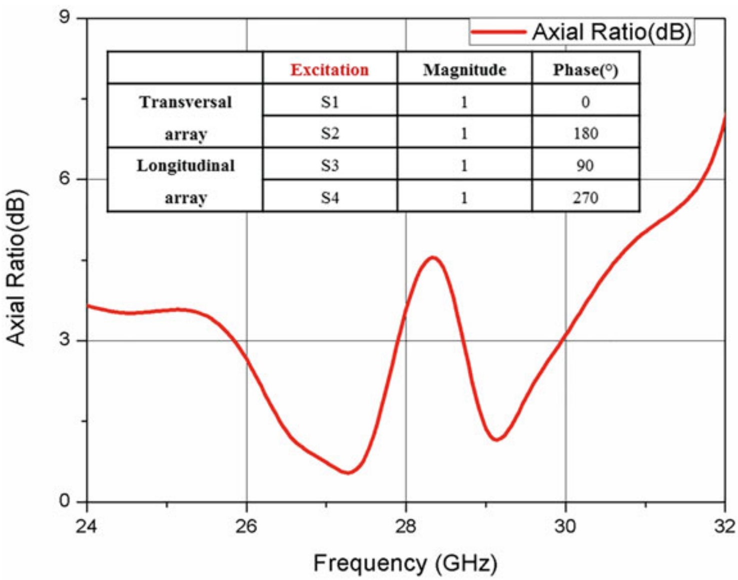

Fig. 6.58 Axial ratio of the 8 × 2 Combination dipole antenna array versus frequency

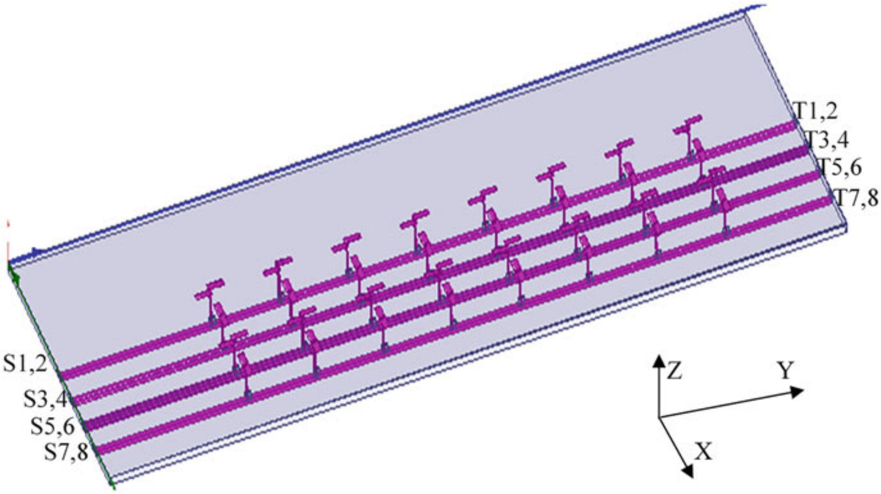

Fig. 6.59 8 × 4 combination dipole antenna arrays

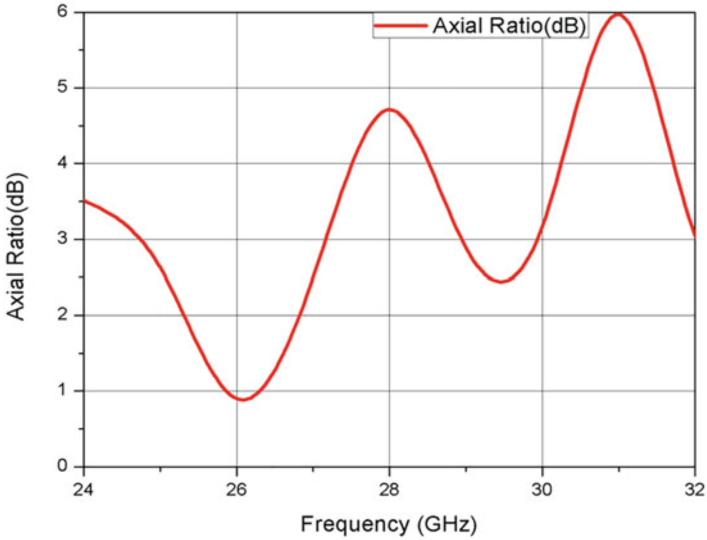

Fig. 6.60 Axial ratio versus frequency

at appropriate locations. In this way, it is possible to realize circular polarization without compromising the array performance, delineated in Sect. 6.2.1. While it is relatively straightforward to achieve the desired circular polarization characteristic we seek by using this strategy, the challenging part is to reduce the grating lobes in the transverse plane and to maintain the beam scanning ability (see Sect. 6.2) over

	Excitation	Phase(°)
Transversal array	S1 and S5	0
	S2 and S6	180
Longitudinal array	S3 and S7	106
	S4 and S8	286

(a)

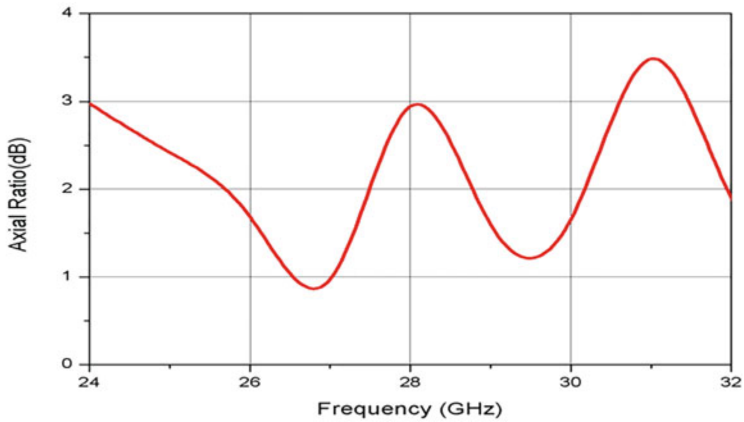

(b)

Fig. 6.61 (**a**) Excitation array feeding sources phases and (**b**) the axial ratio versus frequency

a wide range, with a stable array gain, together with a sidelobe level better than −10 dB.

Both the LPAA structure, shown in Fig. 6.15, as well as alternative LPAA array designs given in [46], are linearly polarized. The microstrip antenna array utilizes a magneto-electric dipole antenna for the radiating element. This array, described in Sect. 6.2.2.1 and [46] has a wide operating bandwidth and stable radiation patterns over the entire frequency band centered at 26 GHz.

Figure 6.62 presents a modified LPAA design based on the slotted waveguide configuration. This design achieves the CP over a wide bandwidth of 4.2 GHz, which is almost 50% of the operating frequency band (see Fig. 6.63a). This is achieved by combining the radiation from longitudinal and transverse radiating elements with appropriate phase excitations. Figure 6.63b shows that the modified LPAA array maintains the wideband behavior in the mm-wave range. The proposed design is work in progress, and it is just one of the several and it is currently being considered for various millimeter-wave applications.

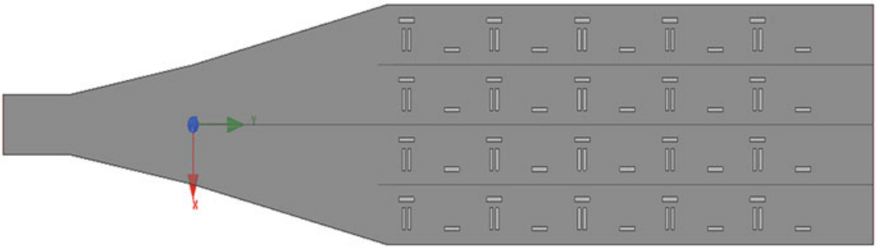

(a)

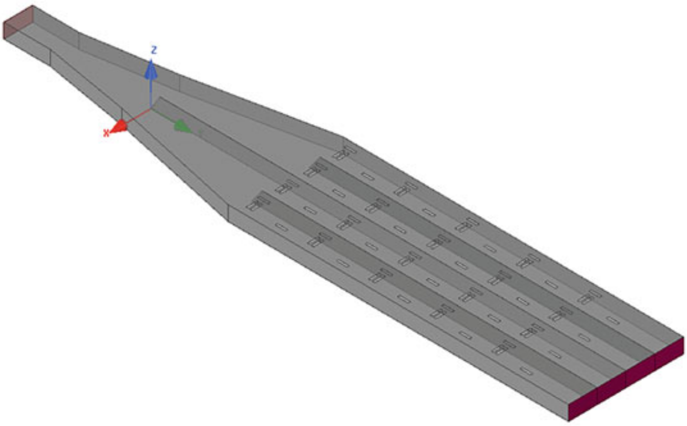

(b)

Fig. 6.62 Top (**a**) and Isotropic (**b**) views of mm-wave circular polarized LPAA

6.4 MIMO Antenna Arrays

It is well known that 5G applications require a high channel capacity (data rate) and that the channel capacity of an existing system can be enhanced by utilizing multiple input multiple output (MIMO) technology while maintaining the level of power consumption. There are several metrics that are used to test the performance of a MIMO system. Correlation coefficient (CC) is perhaps the most important parameter, which measures the effect on the communication channels when all the MIMO antenna elements are operated simultaneously [47, 48]. MIMO antennas are being used in 4G systems (mobile phones and base stations), and they are also being considered in 5G systems to provide higher bandwidths [49, 50]. We note also that aperture antennas are likely to be used at millimeter-waves for high gain. Given this background, in this section we describe a four-element collocated SIW slot antenna designed for a MIMO application. We point out that the individual elements of a MIMO system may themselves be an array used to point a beam in a

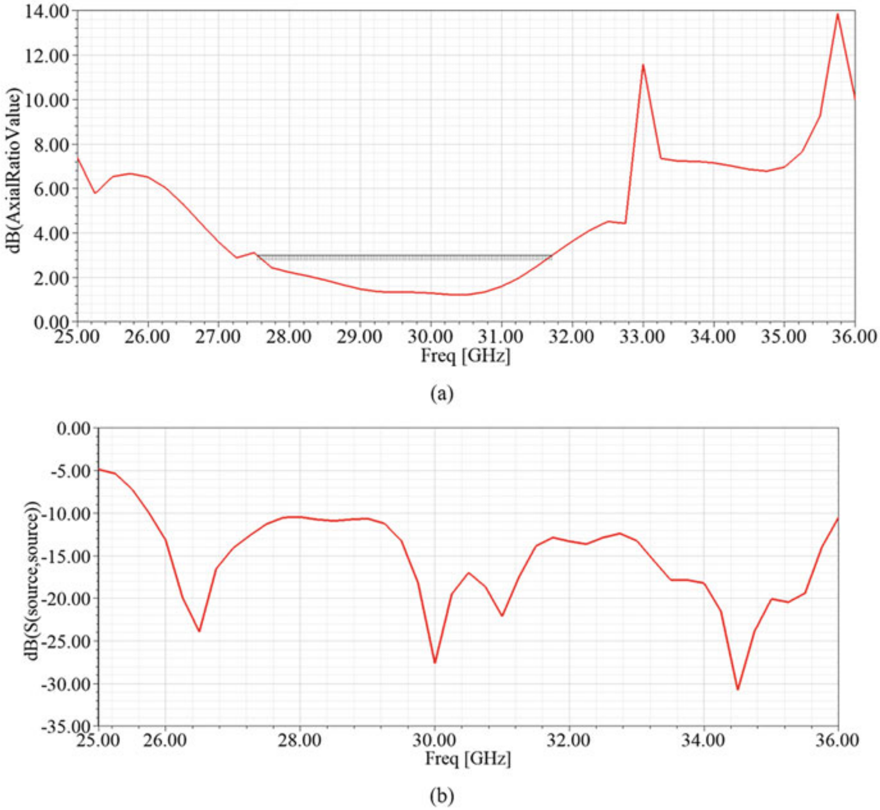

Fig. 6.63 Simulated (**a**) return loss and (**b**) axial radio vs. frequency

specific direction. Although the antennas are collocated, highly uncorrelated beams are generated by this system, by virtue of the design procedure proposed herein.

6.4.1 Single Element Design

The location and the offset position of the slots in an array determine the orientation of the beam. Genetic algorithm can be used to optimize the location of the slots, to point the beam in a desired direction [51, 52]. Since, we propose a four-element MIMO design, the beam directions of the antenna elements are pointed to -30°, $+\ 10^{\circ}$, $-\ 10^{\circ}$ and $+\ 30^{\circ}$, with respect to broadside. Pointing the beams in different directions helps to isolate the beams of the individual antennas and to reduce the correlation between the beams. In the design phase, we also need to take care of the sidelobe level, which increases significantly when the beam is tilted. For this reason, the maximum tilt of the beam in our design was limited to $\pm 30^{\circ}$.

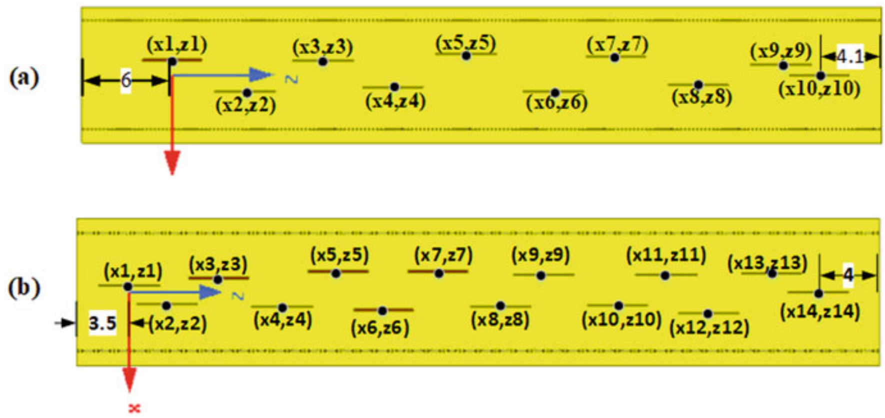

Fig. 6.64 SIW-based slot array: (**a**) 10 slots producing tilt of 10°; and (**b**) 14 slots producing tilt of 30°

Table 6.8 Location of the slots on the surface of SIW. The position is measured with respect to the first slot and the offset is measured with respect to the center line of SIW. All values are in mm

Slot	10° tilt		30° tilt	
	X (offset)	*Z* (Position)	*X* (offset)	*Z* (Position)
1	0.985197	0	0.389826	0
2	−1.07025	4.829121	−0.73713	2.496656
3	0.949758	10.03008	0.857617	5.889113
4	−0.81509	14.62258	−0.88597	10.07596
5	1.396286	19.4348	1.254531	13.77265
6	−1.11278	25.26113	−1.10569	16.77637
7	1.204917	29.41418	1.261619	20.37165
8	−0.6946	34.86867	−0.88597	24.49089
9	0.666248	40.35697	1.034811	27.35939
10	0	42.88743	−0.78674	32.22231
11	–	–	1.063162	35.44575
12	–	–	−1.28288	38.26354
13	–	–	1.119864	42.38278
14	–	–	−0.00709	45.4541

SIW-based slot arrays generating beams tilt at 10° and 30° are shown in Fig. 6.64. Ten slots were used to tilt the beam by 10° with respect to broadside, while 14 slots were used to generate a beam tilt of 30°. The array was built on a Rohacell 51 IG-F substrate of thickness 0.5 mm and was terminated by a matched load.

Table 6.8 shows the offsets and positions of the slots on the surface of the SIW. The reflection coefficients of the antennas are plotted in Fig. 6.65. The antennas provide a wide bandwidth (BW) of 5 GHz (27.5–32.5 GHz). The radiation patterns of the antennas are shown in Fig. 6.66. We observe that the main beams of the MIMO elements are tilted in the desired directions. Moreover, the beam maximum of the MIMO antenna tilts as we change the frequency. To tilt the beam in the

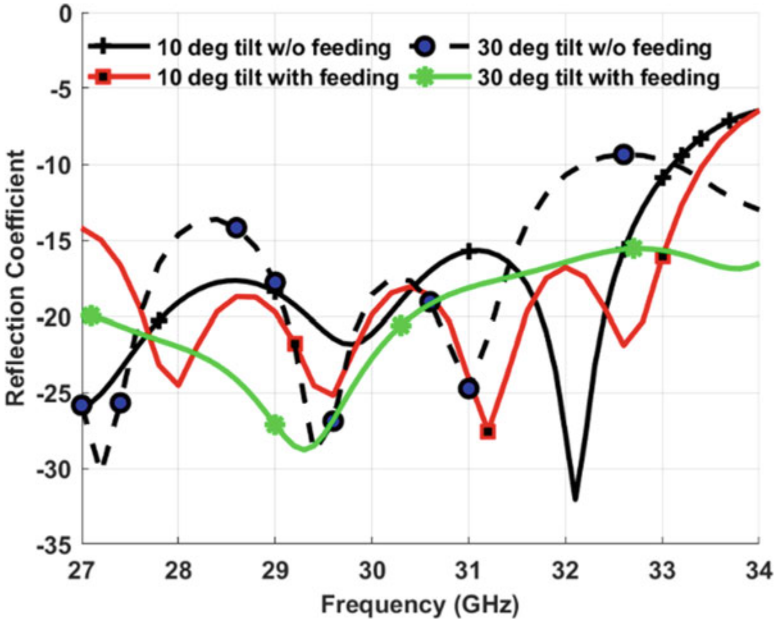

Fig. 6.65 Reflection coefficient plot of the SIW-based slot array

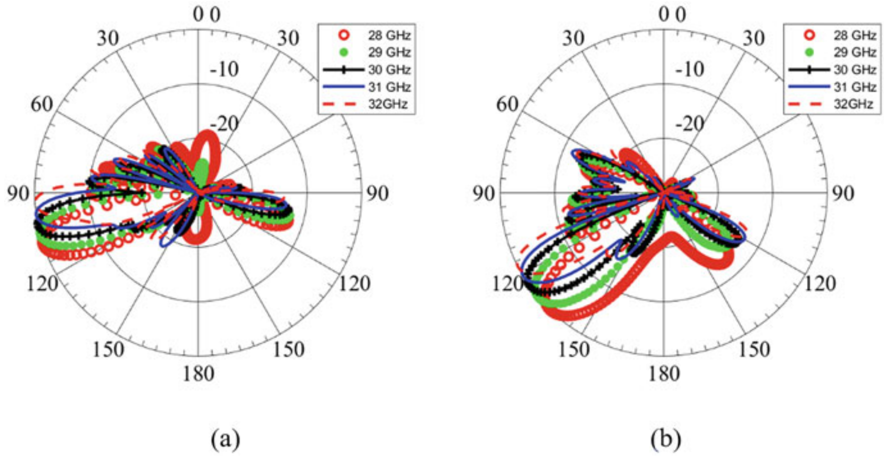

Fig. 6.66 2D normalized radiation patterns with a 10° and 30° tilt for $\phi = 90^{\circ}$ cut: (**a**) 10° tilt produce by 10-element slot array; and (**b**) 30° tilt produce by 14-element slot array

negative direction, for instance along -10° and -30°, we need to feed the array from the opposite end. The radiation patterns of the antennas are shown in Fig. 6.67.

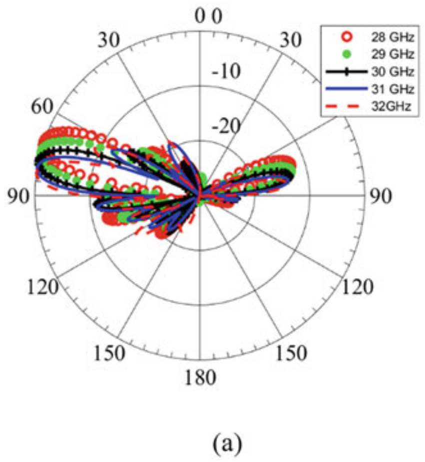

Fig. 6.67 2D Normalized radiation pattern at $\phi = 90^{\circ}$ cut: (**a**) $-10°$ tilt produce by 10-element slot array; and (**b**) -30° tilt produce by 14-element slot array

A microstrip-to-SIW transition was designed at the feed end to excite the array and was terminated by an SIW-to-microstrip transition, as shown in Fig. 6.68. The reflection coefficients of the antennas with transition are shown in Fig. 6.64. Figure 6.69 shows the effect of optimized transition on the SLL.

6.4.2 Four-Element MIMO Design

The design of four-element collocated MIMO antenna system is shown in Fig. 6.70. The adjacent antenna elements share the via walls. To separate the antennas spatially, the MIMO antenna elements (from left to right) were designed to produce tilts of -30°, $+ 10^{\circ}$, $- 10^{\circ}$ and $+ 30^{\circ}$, with respect to broadside. The reflection and the coupling plots of the MIMO antenna systems are shown in Fig. 6.71. All the antenna elements are designed to resonate in accordance with the VSWR <2.0 criterion. Although the antennas share a via wall, they are still sufficiently isolated at the feed ports, as shown in Fig. 6.71b.

The radiation patterns of the four-element collocated MIMO antennas are shown in Fig. 6.72. A slight deterioration in the SLL of the MIMO antenna elements located in the middle of the MIMO system is shown in Figs. 6.72b and 6.72c, although the main beam still points in the desired direction. The correlation coefficients between the MIMO antenna elements are presented in Table 6.9. The values obtained for the correlation are very low, and the design meets the criterion we desire, thanks to the beam tilt. The simulated gain and efficiency of the MIMO antenna elements are shown in Fig. 6.73. The MIMO antenna elements provide a maximum gain of 16.5 dB.

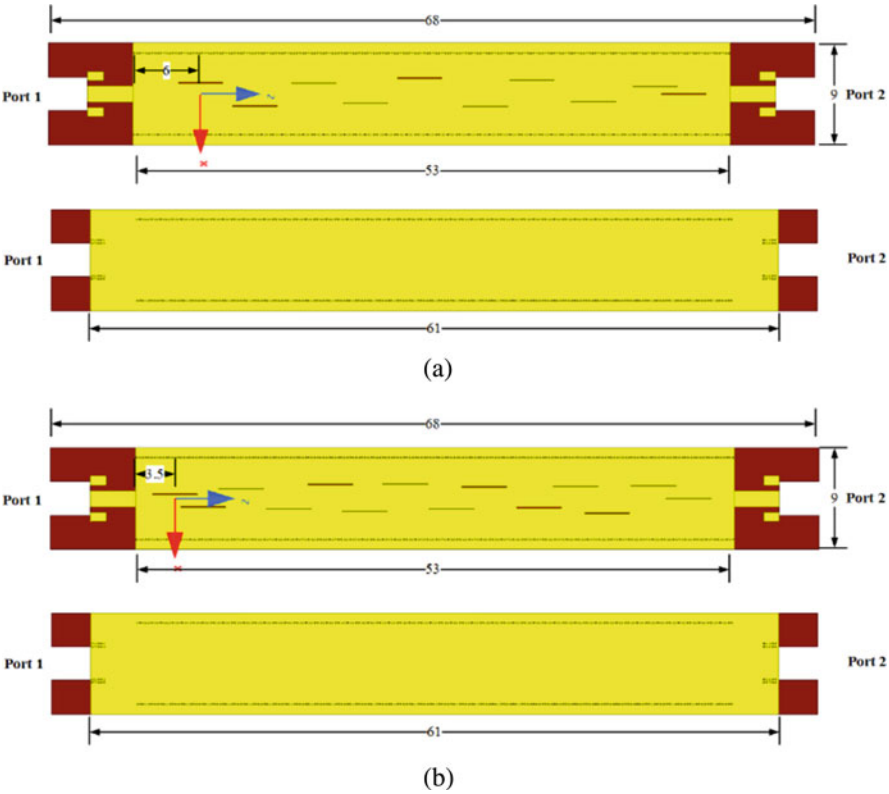

Fig. 6.68 Top and bottom view of SIW-based slot array with microstrip-to-SIW transition: (**a**) 10 slots produce tilt of 10°; and (**b**) 14 slots produce tilt of 30°

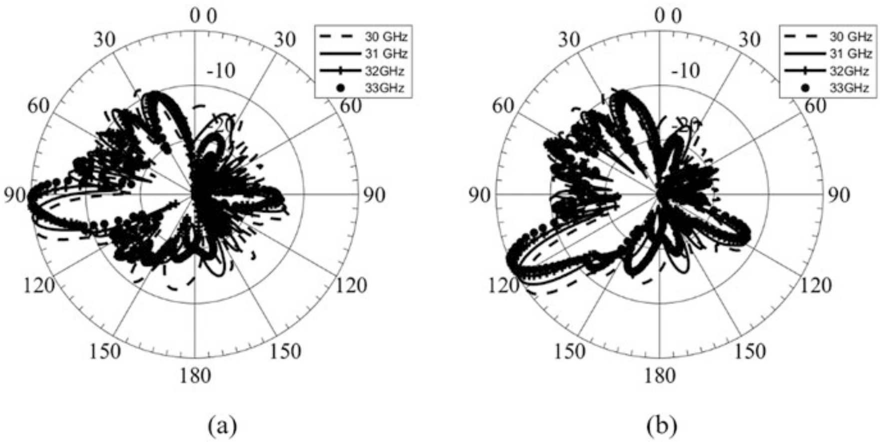

Fig. 6.69 2D Normalized radiation pattern at $\phi = 90^{\circ}$ cut in the presence of microstrip-to-SIW transition: (**a**) 10° tilt produce by 10-element slot array; and (**b**) 30° tilt produce by 14-element slot array

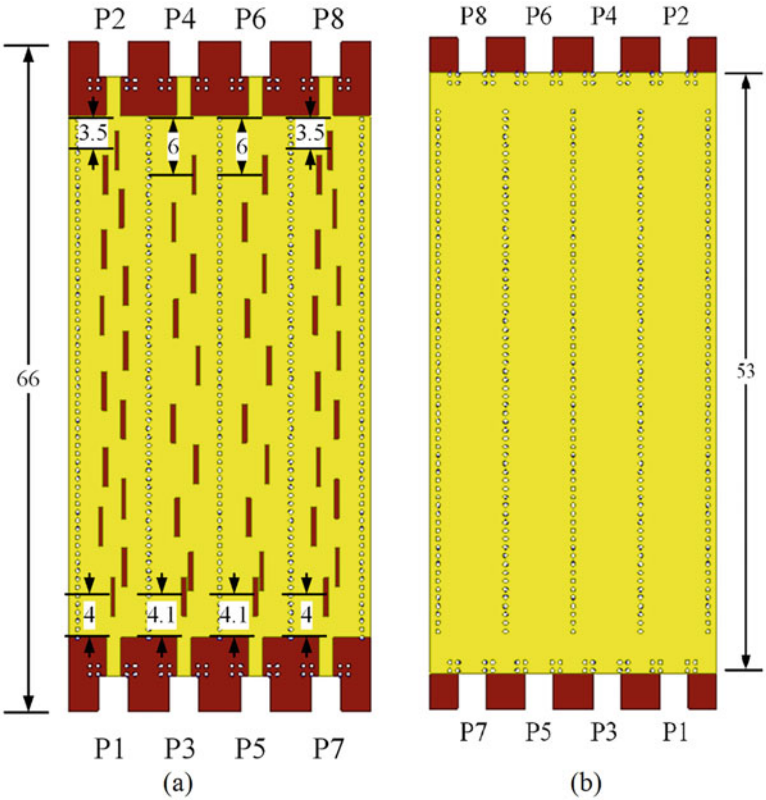

Fig. 6.70 Four-element collocated MIMO antenna design: (**a**) top view; and (**b**) bottom view. All dimensions are in mm

The fabrication of the proposed design is a challenging task. The substrate (Rohacell foam 51-IG-F) cannot withstand the level of heat required to insert a large number of vias; consequently, a copper wall was used instead of vias. The wall was fabricated by using the Rogers 5880 board and then plating copper strips on both sides. Similarly, slots were introduced on the top surface of SIW by using 0.5 mm Rohacell, and polyimide was attached to the copper sheet by using an adhesive material. The layered view of the design is shown in Fig. 6.74, while the fabricated prototype is displayed in Fig. 6.75. The port parameters of the fabricated prototype were measured by using a vector network analyzer and are presented in Fig. 6.76. The radiation patterns of the fabricated prototype were analyzed in an anechoic chamber and are plotted in Fig. 6.77. A slight difference in the measured and simulated results can be attributed to fabrication tolerances.

In this section, a four-element, collocated, SIW MIMO antenna design operating at mm-waves was presented. Correlation coefficient between the adjacent MIMO antenna elements was improved by tilting the beams of arrays in different directions.

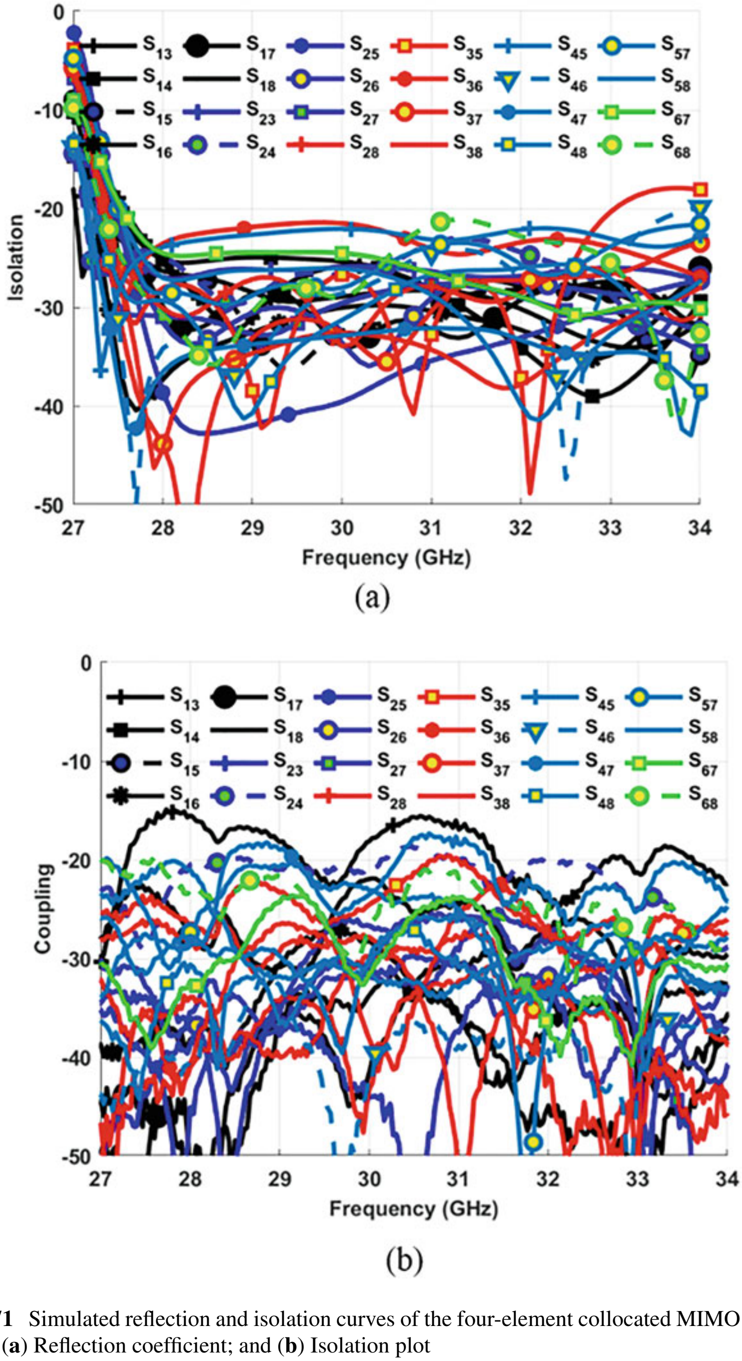

Fig. 6.71 Simulated reflection and isolation curves of the four-element collocated MIMO antenna design: (**a**) Reflection coefficient; and (**b**) Isolation plot

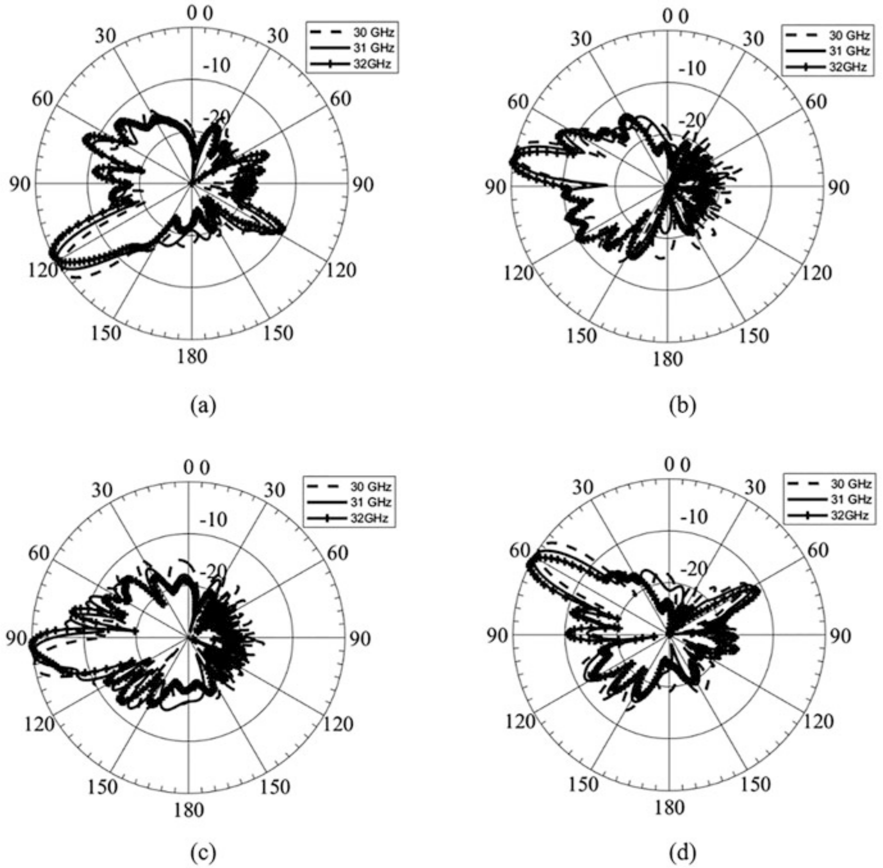

Fig. 6.72 Simulated 2D normalized radiation pattern of the four-element collocated MIMO antenna system at $\phi = 90^{\circ}$ cut: (**a**) Antenna-1 (Port-1 excited); (**b**) Antenna-2 (Port-4 excited); (**c**) Antenna-3 (Port-5 excited); and (**d**) Antenna-4 (Port-8 excited)

Table 6.9 Correlation coefficient between MIMO antenna elements at different frequencies

Frequency	CC_{12}	CC_{13}	CC_{14}	CC_{23}
29.5	0.013612	0.010105	0.002383	0.007699
30	0.003373	0.020323	0.000729	0.001414
31	0.000816	0.033474	0.010409	0.014979
32	0.000347	0.011153	0.007682	0.017815
32.5	0.003818	0.00084	0.004542	0.00189

The MIMO antenna elements provide a BW of 3 GHz with a measured maximum gain of 15 dB. Port isolation between the adjacent MIMO elements was better than 20 dB in the presented design. MIMO is expected to play a significant role in 5G applications, both in sub-6 and mm-wave versions of 5G, and this was the motivation for including this topic in this chapter on arrays.

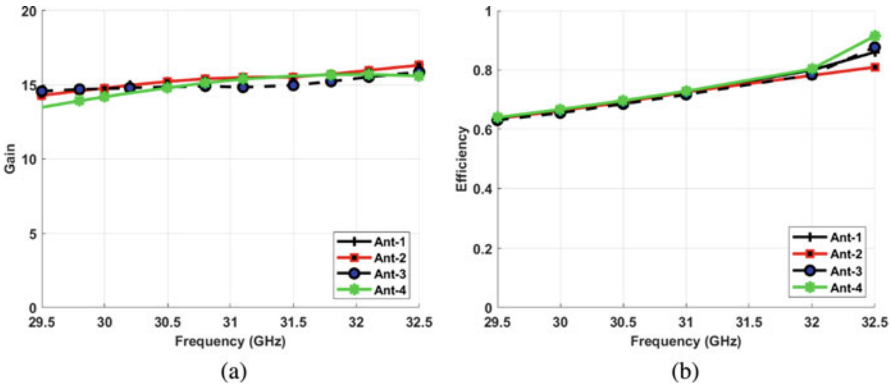

Fig. 6.73 Simulated gain and efficiency of the four-element collocated MIMO antenna design: (**a**) gain of the MIMO antennas; and (**b**) efficiency of the MIMO antennas

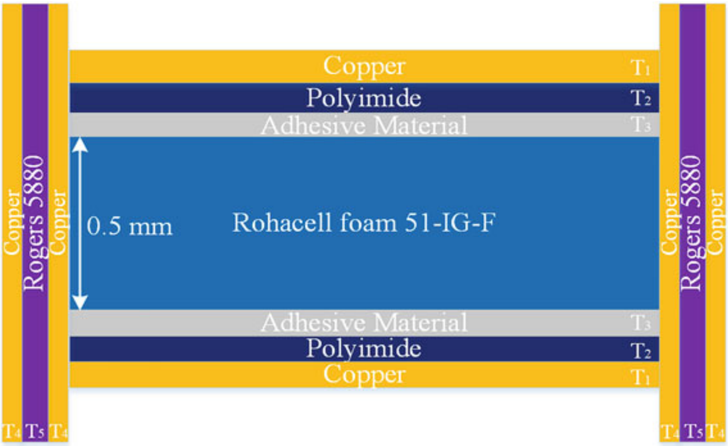

Fig. 6.74 Layered view of the fabricated geometry. The thickness T1 to T5 are 0.035 mm, 0.05 mm, 0.025 mm, 0.017 mm, and 0.381 mm, respectively

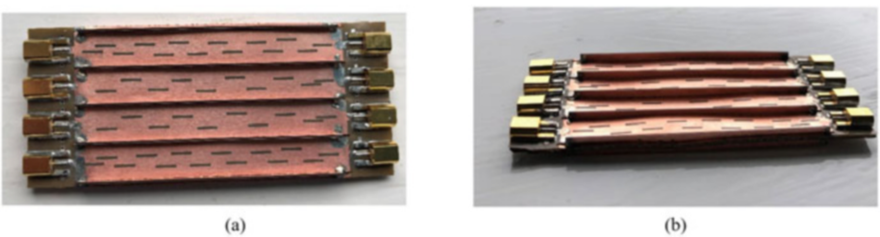

Fig. 6.75 Fabricated geometry: (**a**) Top view; and (**b**) side view

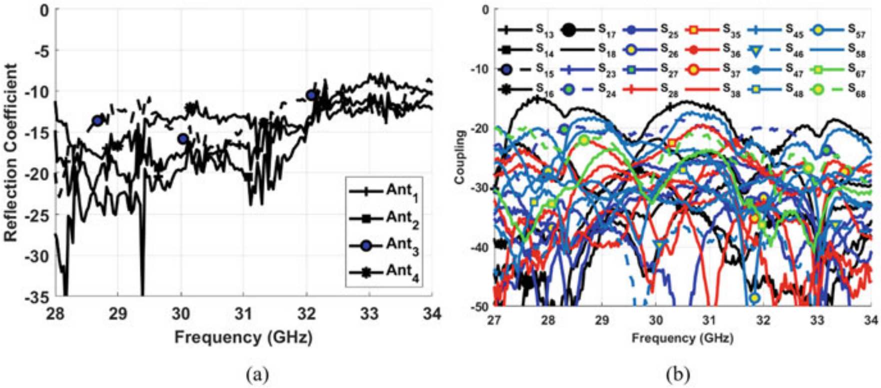

Fig. 6.76 Measured reflection and isolation curves of the four-element collocated MIMO antenna design: (**a**) Reflection coefficient; and (**b**) Isolation plot

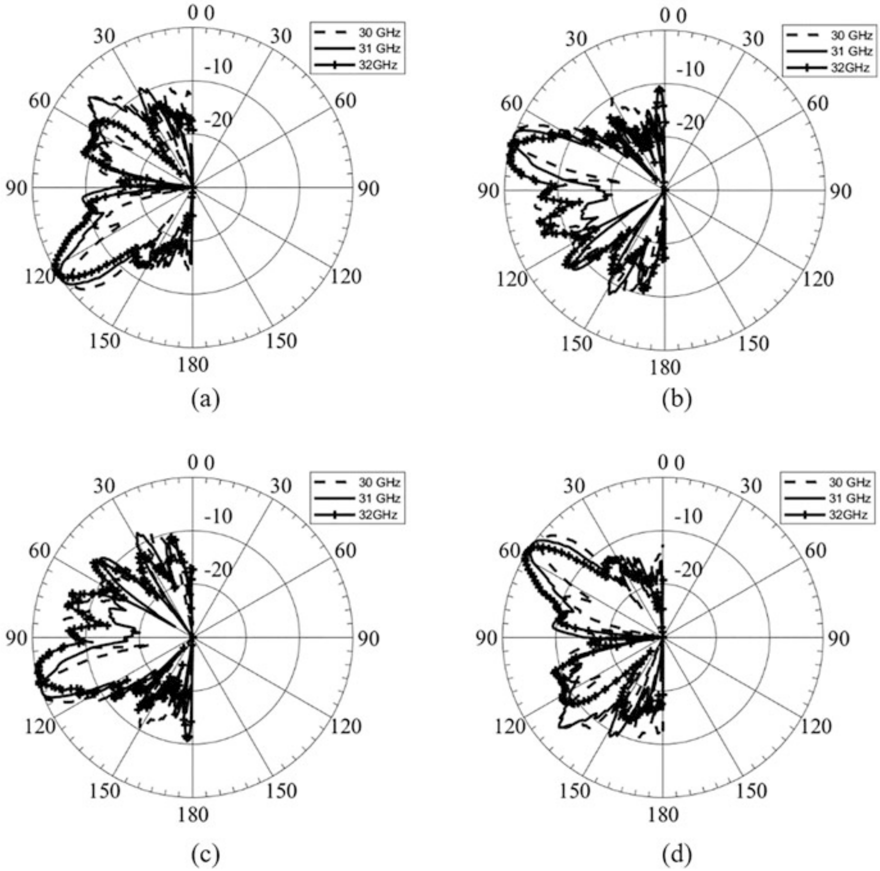

Fig. 6.77 Measured 2D normalized radiation patterns of the four-element collocated MIMO antenna system at $\phi = 90^{\circ}$ cut: (**a**) Antenna-1 (Port-1 excited); (**b**) Antenna-2 (Port-4 excited); (**c**) Antenna-3 (Port-5 excited); and (**d**) Antenna-4 (Port-8 excited)

6.5 Conclusion

In this chapter, we have presented a variety of low-profile and high gain antenna array designs, both for fixed-beam as well as scan applications. For fixed-beam antennas, we have presented some legacy designs in which the feed is integrated with the array to achieve profiles that are lower than other high gain aperture antennas such as reflectors, reflect arrays, and lenses. Next, we have introduced some novel design concepts for low-profile arrays that have certain desirable features over existing designs for high gain low-profile antennas, such as relatively wide bandwidth and potential for beam scanning. Following this, we have presented some approaches for beam scanning over a limited range, either by using switchable vias, or nonconventional phase shifters, which replace ferrite type phase shifters that are known to be lossy and costly devices at millimeter-waves. For wide-angle scanning, with little or no scan loss, we have presented a Luneburg lens design, with an array feed comprising of microstrip patch antennas, which outperforms existing phased array designs, insofar as their scan performance is concerned.

For the sake of completeness, we have included two other topics, namely arrays with polarization diversity and MIMO antennas. We have discussed dual linear as well as circular polarization type of arrays, both of which can be important for certain applications.

Finally, we have briefly touched on the topic of MIMO array design, which is expected to play an important role in enhancing the throughput of 5G systems. We have discussed the issue of lowering the correlation coefficient between the array elements in a MIMO system, which is key to enhancing its performance by increasing its throughput.

As a concluding remark, we mention that the design of high gain, low-profile, polarization-diverse, fixed-beam, and scanning antennas for 5G applications is a very active area of research and development, and it is our hope that both students and researchers, as well as development engineers interested in these areas, would find the subject matter of this chapter both interesting and useful.

References

1. L. Tan, J. Zhang, W. Wang, J. Xu, Design of a W-band one-dimensional beam scanning slotted waveguide antenna with narrow beam and low side lobe, in *2017 Progress in Electromagnetics Research Symposium - Spring (PIERS), St. Petersburg*, (2017), pp. 3625–3628
2. P. Kumar, A. Kedar, A.K. Singh, Design and development of low-cost low sidelobe level slotted waveguide antenna array in X-band. IEEE Trans. Antennas Propag. **63**(11), 4723–4731 (2015)
3. D.J. Bisharat, S. Liao, Q. Xue, High gain and low cost differentially fed circularly polarized planar aperture antenna for broadband millimeter-wave applications. IEEE Trans. Antennas Propag. **64**(1), 33–42 (2016)
4. B. Raaf et al., Vision for beyond 4G broadband radio systems, in *Proc. IEEE 22nd Int. Symp. Pers. Indoor Mobile Radio Commun. (PIMRC)*, (2011), pp. 2369–2373

5. D. Oueslati, R. Mittra, H. Rmili, Wideband low-profile aperture antenna for 5G-applications comprising of a slotted waveguide array and an integrated corporate feed, in *13th European Conference on Antennas and Propagation (EuCAP), Krakow, Poland*, (2019), pp. 1–5
6. S. Mehri, D. Oueslati, R. Mittra, H. Rmili, Gain enhancement of a substrate integrated waveguide slot array for millimeter waves, in *2019 13th European Conference on Antennas and Propagation (EUCAP), Karkow, Poland*, (2019)
7. M. Peng, A. Zhao, High performance 5G millimeter-wave antenna array for 37–40 GHz mobile application, in *2018 International Workshop on Antenna Technology (iWAT), Nanjing*, (2018), pp. 1–4
8. N.O. Parchin, M. Shen, G.F. Pedersen, End-fire phased array 5G antenna design using leaf-shaped bow-tie elements for 28/38 GHz MIMO applications, in *2016 IEEE International Conference on Ubiquitous Wireless Broadband (ICUWB), Nanjing*, (2016), pp. 1–4
9. N.O. Parchin, M. Shen, G.F. Pedersen, UWB MM-Wave antenna array with quasi omnidirectional beams for 5G handheld devices, in *2016 IEEE International Conference on Ubiquitous Wireless Broadband (ICUWB), Nanjing*, (2016), pp. 1–4
10. Z. Pi, J. Choi, R. Heath, Millimeter-wave gigabit broadband evolution toward 5G: Fixed access and backhaul. IEEE Commun. Mag. **54**(4), 138–144 (2016)
11. M. Hashemi, C.E. Koksal, N.B. Shroff, Out-of-band millimeter wave beamforming and communications to achieve low latency and high energy efficiency in 5G systems. IEEE Trans. Commun. **66**(2), 875–888 (2018)
12. M.U. Afzal, A. Lalbakhsh, K.P. Esselle, Electromagnetic-wave beam scanning antenna using near-field rotatable graded-dielectric plates. J. Appl. Phys. **124**(23), 1–11 (2018)
13. M. Faenzi, G. Minatti, D. González-Ovejero, F. Caminita, E. Martini, C.D. Giovampaola, S. Maci, Metasurface antennas: New models, applications and realizations. Sci. Rep. **9**, SP.10178 (2019)
14. G. Minatti, M. Faenzi, M. Sabbadini, S. Maci, Bandwidth of gain in metasurface antennas. IEEE Trans. Antennas Propag. **65**(6), 2836–2842 (2017)
15. J.A. Gonzalez Marin, A.A. Baba, D. Lopez Cuenca, J. Hesselbarth, R.M. Hashmi, K. Esselle, High-gain low-profile chip-fed resonant cavity antennas for millimeter-wave bands. IEEE Antennas Wirel. Propag. Lett. **18**(11), 2394–2398 (2019)
16. A.A. Baba, R.M. Hashmi, K.P. Esselle, Achieving a large gain-bandwidth product from a compact antenna. IEEE Trans. Antennas Propag. **65**(7), 3437–3446 (2017)
17. Y. Li, K.M. Luk, A multibeam end-fire magnetoelectric dipole antenna array for millimeter-wave applications. IEEE Trans. Antennas Propag. **64**(7), 2894–2904 (2016)
18. Y.J. Cheng, W. Hong, K. Wu, Millimeter-wave multibeam antenna based on eight-port hybrid. IEEE Microw. Wirel. Compon. Lett. **19**(4), 212–214 (2009)
19. M.M.M. Ali, S.I. Shams, A.R. Sebak, Printed ridge gap waveguide 3-dB coupler: Analysis and design procedure. IEEE Access **6**, 8501–8509 (2018)
20. M.M.M. Ali, A. Sebak, 2-D scanning magnetoelectric dipole antenna array fed by RGW Butler matrix. IEEE Trans. Antennas Propag. **66**(11), 6313–6321 (2018)
21. S. Park, Y. Tsunemitsu, M. Ando, Center feed single layer slotted waveguide array. IEEE Trans. Antennas Propag. **54**(5), 1474–1480 (2006)
22. J.C. Coetzee, J. Joubert, D.A. McNamara, Off-center-frequency analysis of a complete planar slotted-waveguide array consisting of subarrays. IEEE Trans. Antennas Propag. **48**(11), 1746–1755 (2000)
23. K.J. Nicholson, W.S.T. Rowe, K. Ghorbani, Split-ring resonator loading for the slotted waveguide antenna stiffened structure. IEEE Antennas Wirel. Propag. Lett. **10**, 1524–1527 (2011)
24. Y. Tyagi, P. Mevada, S. Chakrabarty, R. Jyoti, High-efficiency broadband slotted waveguide array antenna. IET Microw. Antennas Propag. **11**(10), 1401–1408 (2017)
25. W.L. Stutzman, G.A. Thiele, *Antenna Theory and Design*, 3rd edn. (Wiley, Hoboken, NJ, 2012)

26. S. Liao, P. Wu, K.M. Shum, Q. Xue, Differentially fed planar aperture antenna with high gain and wide bandwidth for millimeter-wave application. IEEE Trans. Antennas Propag. **63**(3), 966–977 (2015)
27. Y.J. Cheng, W. Hong, K. Wu, Millimeter-wave half mode substrate integrated waveguide frequency scanning antenna with quadri-polarization. IEEE Trans. Antennas Propag. **58**(6), 1848–1855 (2010)
28. P. Kumar, S. Dwari, S. Singh, N.K. Agrawa, Design investigation of a laminated waveguide fed multi-band DRA for military applications. J. RF-Eng. Telecommun. **72**(12), 1–8 (2016)
29. HFSS: High Frequency Structure Simulator, V.15, Ansoft Corp
30. Z.N. Chen, T. Li, Wideband substrate integrated waveguide (SIW)-fed end-fire metasurface antenna array. IEEE Trans. Antennas Propag. **66**, 7032–7040 (2018)
31. B. Yang, Z. Yu, Y. Dong, J. Zhou, W. Hong, Compact tapered slot antenna array for 5G millimeter-wave massive MIMO systems. IEEE Trans. Antennas Propag. **65**(12), 6721–6727 (2017)
32. O. Dinçer, A. Ünal, K_band substrate integrated waveguide slot array antenna with high efficiency, in *Presented at IEEE International Symposium on Antennas and Propagation*, (2015)
33. D.E.N. Davies, Application of electronic sector scanning techniques to height-finding radar systems. Proc. Inst. Electr. Eng. **110**(11), 1941–1948 (1963)
34. A. Parsa, Fast moving target detection in sea clutter using non-coherent X-band radar, in *2014 IEEE Radar Conference, Cincinnati, OH*, (2014), pp. 1155–1158
35. N. Vahabisani, S. Khan, M. Daneshmand, Microfluidically reconfigurable rectangular waveguide filter using liquid metal posts. IEEE Microw. Wirel. Compon. Lett. **26**(10), 801–803 (2016)
36. S.N. McClung, S. Saeedi, H.H. Sigmarsson, Band-reconfigurable filter with liquid metal actuation. IEEE Trans. Microw. Theory Tech. **66**(6), 3073–3080 (2018)
37. Z. Chen, H. Wong, J. Kelly, A polarization-reconfigurable glass dielectric resonator antenna using liquid metal. IEEE Trans. Antennas Propag. **67**(5), 3427–3432 (2019)
38. K. Alqurashi, J.R. Kelly, Z. Wang, C. Crean, R. Mittra, M. Khalily, Y. Gao, Liquid metal bandwidth reconfigurable antenna. IEEE Antennas Wirel. Propag. Lett. **19**(1), 218–222 (2020)
39. S. Jain, R. Mittra, S. Pandey, Flat-base broadband multibeam Luneburg lens for wide-angle scan. J. Electromagn. Waves Appl. **29**(10), 1329–1341 (2015)
40. J. Bor, O. Lafond, H. Merlet, P. Le Bars, M. Himdi, Foam based Luneburg lens antenna at 60 GHz. Prog. Electromagn. Res. Lett. PIER **44**, 1–7 (2014)
41. B. Fuchs, L. Le Coq, O. Lafond, S. Rondineau, M. Himdi, Design optimization of multishell Luneburg lenses. IEEE Trans. Antennas Propag. **55**(2), 283–289 (2007)
42. R.K. Arya, S. Zhang, S. Pandey, A. Kumar, Y. Vardaxoglou, W. Whittow, R. Mittra, Meta-atoms and artificially engineered materials for antenna applications, Chap. 10, in *Electromagnetic Waves*, Developments in Antenna Analysis and Design, vol. 1, (2018), pp. 351–405
43. V.T. Bharambe, J.J. Adams, Planar 2D beam steering antenna using liquid metal parasitics. IEEE Trans. Antennas Propag. **68**, 7320–7327 (2019)
44. F. Ferrero, C. Luxey, G. Jacquemod, R. Staraj, Dual-band circularly polarized microstrip antenna for satellite applications. IEEE Antennas Wirel. Propag. Lett. **4**, 13–15 (2005)
45. H. Legay, L. Shafai, A new stacked microstrip antenna with large bandwidth and high gain, in *IEEE AP-S Int. Symp. Digest*, (1993), pp. 948–951
46. O. Donia, A. Ghalib, R.K. Arya, H. Rmilli, R. Mittra, Microstrip-fed scanning dipole antenna array for 5G applications, in *2019 IEEE International Symposium on Antennas and Propagation and USNC-URSI Radio Science Meeting (APS/URSI), Atlanta, Georgia, USA*, (2019)
47. M.S. Sharawi, Printed multi-band MIMO antenna systems and their performance metrics [wireless corner]. IEEE Antennas Propag. Mag. **55**, 218–232 (2013)
48. M.S. Sharawi, *Printed MIMO Antenna Engineering* (Artech House, Norwood, MA, 2014)

49. M. Ikram, Y. Wang, M.S. Sharawi, A. Abbosh, A novel connected PIFA array with MIMO configuration for 5G mobile applications, in *Chez Australian Microwave Symposium (AMS), Brisbane*, (2018)
50. M.S. Sharawi, M. Ikram, A. Shamim, A two concentric slot loop based connected array MIMO antenna system for 4G/5G terminals. IEEE Trans. Antennas Propag. **65**(112), 6679–6686 (2017)
51. S. Clauzier, S.M. Mikki, A. Shamim, Y.M.M. Antar, A new method for the design of slot antenna arrays: Theory and experiment, in *Chez 10th European Conference on Antennas and Propagation (EuCAP), Switzerland*, (2016)
52. A. Ghalib, *Current Engineering Methods Applied to the Design of MIMO Antenna Systems* (King Fahd University of Petroleum and Minerals, Saudi Arabia, 2018)

Chapter 7
Co-design of 4G LTE and Millimeter-Wave 5G Antennas for Future Mobile Devices

M. Idrees Magray, G. S. Karthikeya, J. H. Tarng, and Shiban K. Koul

7.1 Introduction

Antennas are one of the most cortical components of design in a mobile device. There are a few instances when companies had to recall smartphone models due to design flaws in the antenna placement and integration with the mobile device [1]. Table 7.1 gives a glimpse of antenna evolution over various generations of cellular technology spread over four decades, which illustrates the evolution of the carrier frequency requirements and the expected gains for the respective antennas. Historically, antennas were designed exterior to the mobile device as evident in the first generation of cellular phones. These antennas would be telescopic element with poor radiation efficiency and gain. The form factor of antennas of cellular devices of previous generations was compromised as well. Free space power loss [2] of the first generation cellular service at 200 m is 76.5 dB, which meant that the base stations could be located as far as 2 km from each other for reasonable coverage in certain geography even with hundreds of subscribers. As the cellular devices evolved to advanced generations, the carrier frequency and the number of subscribers to the cellular service also grew. The same trend is observed with the current cellular technologies as well and the trend might continue in the future. It is important to note that as carrier frequency increased, free space power loss also increased which had to be considered in the link budget design and its respective deployment. Printed circuit board (PCB) based passive antennas became the norm during the second generation of cellular devices. As higher number of bands had to

M. I. Magray · J. H. Tarng
Department of Electrical and Computer Engineering, Centre for mmWave Smart Radar Systems and Technologies, National Chiao Tung University, Hsinchu City, Taiwan
e-mail: idreesmagray.eecs08g@nctu.edu.tw; j4t@mail.nctu.edu.tw

G. S. Karthikeya (✉) · S. K. Koul
Centre for Applied Research in Electronics, IIT Delhi, Delhi, India

M. A. Matin (ed.), *Wideband, Multiband, and Smart Antenna Systems*, Signals and Communication Technology, https://doi.org/10.1007/978-3-030-74311-6_7

Table 7.1 Cellular technologies and its antennas

Gen	C.F.	PL	Type of antenna	G
1G	800 MHz	76.5	Helical/telescopic	−10 to 0
2G	900 MHz1800 MHz	77.583.5	Printed dual band	−10 to 0
3G	2100 MHz	84.9	Printed multiband	−10 to 0
4G	850 MHz1800 MHz	7783.5	Printed multibandWith MIMO	−10 to 0
5G	Sub-6 GHz28 GHz	94107	Phased arrayMIMO	−10 to 08–10

Gen generation, *C.F.* carrier frequency, *PL* free space power loss at 200 m (dB), *G* gain of the antenna (dBi)

be accommodated, multiband designs with small form factors became the industry standard for mobile devices beyond 2G. The currently deployed commercial 4G mobile devices have multiband antennas integrated near the panel of the device [3, 4]. Extension of the multiband design logic might not be a feasible solution to attain mmWave frequencies, which shall be illustrated in Sect. 7.3. With the upcoming 5G, experts believe that mmWave and sub-6 GHz bands would be allotted for cellular communications. Design of antennas for the sub-6 GHz bands is well known and commercially viable [5] but antennas to be designed for 28 GHz band compatible with modern smartphones needs more investigation, as the design requirements of sub-6 GHz and mmWave would be incompatible. Co-design of antennas of previous generations with the current ones is essential as most of the commercial smartphones would offer backward compatibility in spite of the projected explosive growth of 5G subscribers. The co-design of 2G–3G–4G antennas is not very challenging as the carrier frequencies are in the 0.8–3 GHz frequency range with narrow bandwidth requirements. Electrically small radiators with modified parasitics would lead to the necessary multiband effects [3], wherein the additional parasitics would be specific to a particular band. Most of these parasitics would be strongly resonant, leading to narrowband for the corresponding carrier frequencies. But, co-design of 4G-mmWave 5G offers a unique challenge as the 5G's carrier frequency is tenth harmonic of 4G's highest carrier frequency, assuming the 28 GHz band for 5G operations. The simplest solution for this problem is to integrate an electrically small super wideband antenna covering all the bands from 2G to 5G [6]. The problem with this design logic is that the antennas would fail to have a unidirectional beam with hemispherical coverage at the higher frequencies, as these super wideband antennas have more or less omnidirectional patterns throughout the bandwidth. The design requirements for mmWave 5G is different from that of the previous generations, and hence co-design with 4G antennas is an important topic to be investigated.

The problem associated with free space power loss and penetration losses is of primary concern when designing antenna systems for mmWave 5G mobile devices. Free space power loss at 200 m for sub-6 GHz carrier frequencies is in the range of 80–95 dB. Penetration losses of common building materials would be in the range 1–10 dB for sub-6 GHz bands, this aspect proved to be a boon for commercial deployment of cellular technologies built around sub-6 GHz carrier frequencies. On the other hand, 28 GHz band has free space power loss in the range 105–110 dB at

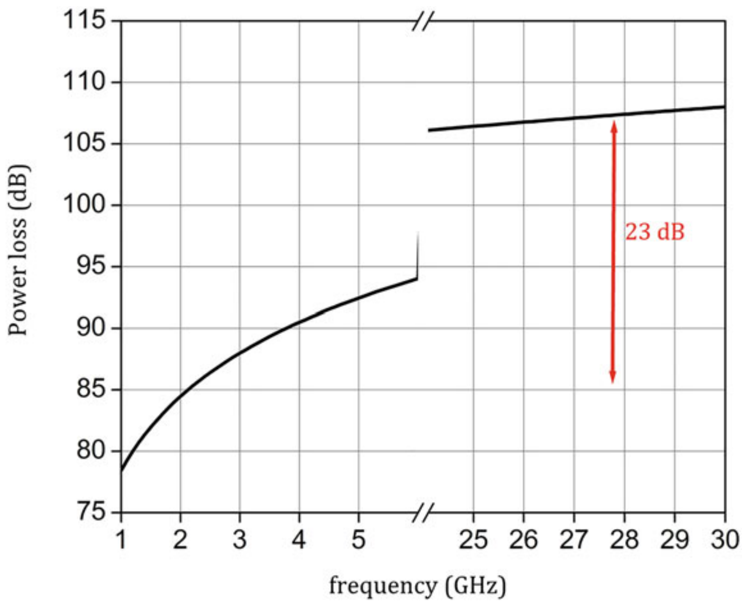

Fig. 7.1 Free space power loss comparison of Sub-6 GHz and 28 GHz bands

200 m as observed in Fig. 7.1. Penetration loss for this band is around 30–40 dB as reported in the testing campaigns [7]. This means that mmWave 5G has additional losses of at least 20–25 dB compared to a commercial 4G system. These additional losses have to be cleverly compensated by using high gain antennas in the mobile device as well as the base stations and access points [8]. The antenna requirements for 4G and 5G are different and hence need careful examination for co-design of both the antenna systems intended for modern mobile devices. This chapter delves into the desired specifications for co-design of 4G and 5G antenna modules along with state-of-the-art design examples.

7.2 Desired Characteristics of Co-designed Antennas

This section gives an insight into desired characteristics for 4G LTE (Long Term Evolution) antennas, mmWave 5G antennas, and co-design of both antennas. The following characteristics are the key factors to be considered for mobile antenna design. These characteristics are essential to comprehend the expected performance metrics of the co-designed antennas.

7.2.1 Form Factor

From antenna perspective, form factor indicates the shape, size, and physical configuration of antennas integrated inside the mobile terminal. The real estate available for antennas on modern smartphones is very much limited due to large display, battery, and other essential electronics. Antennas that would be designed for 4G–5G mobile devices must be compliant with the physical form factor to be useful for deployment. An exploded view of a typical commercial smartphone is illustrated in Fig. 7.2. The available space for integration of 4G LTE and 5G antennas is separately demonstrated in Fig. 7.2. The length of the smartphone is typically in the range 7–10 cm [9]. Width of the smartphone is in the range 4–7 cm with a panel height of 6–8 mm. Recent trends suggest that ultra-thin phones have much slimmer panel height making antenna designs even more challenging. Antennas for various wireless services of future mobile devices such as 2G, 3G, 4G, 5G, WLAN (Wireless local Area Network), GPS (Global Positioning System), and Bluetooth have to be integrated into the available space inside a mobile device. Designers must make sure that antennas offer minimal interference to other coexistent antennas in the cramped space. The electrical lengths for 4G and 5G antennas have been mentioned in Fig. 7.2. It is evident that the available space is only a fraction of wavelength for 4G LTE antennas, which means that electrically small, low gain antennas could be realized in the device. In contrast, 5G antennas have electrically larger space wherein high gain antennas with unidirectional hemispherical beam could be accommodated. Panel height seems to be the critical factor for the design of 5G antennas as it is only about 0.6 λ at 28 GHz. System ground plane also must be considered when integrating 4G and 5G antennas. Typically, a ground plane is part of the design for 4G antennas [3] and 5G antennas [10, 11] independently. But the challenge is to have a shared ground design for both the wireless services without significant deterioration of the characteristics of the respective antennas. Design examples in Sect. 7.4 illustrate this concept. One of the design philosophies for coexistence of 4G and 5G antennas is to mount 4G antennas along the longer edge and the 5G antennas on the shorter edge of the smartphone.

The interaction of the antenna systems for various wireless services has to be minimal with the back-end electronics and various metallic parts of an actual mobile device. Metal rim also seems to be another parameter to be considered for some of the smartphone modes, but the design examples dealt in this chapter do not consider this aspect.

7.2.2 Radiation Pattern

The term radiation pattern refers to the power radiated by the antenna at different angles. Typically, this would be a polar plot with a normalized power pattern on the radial axis. The actual amount of power radiated by the antenna post-integration

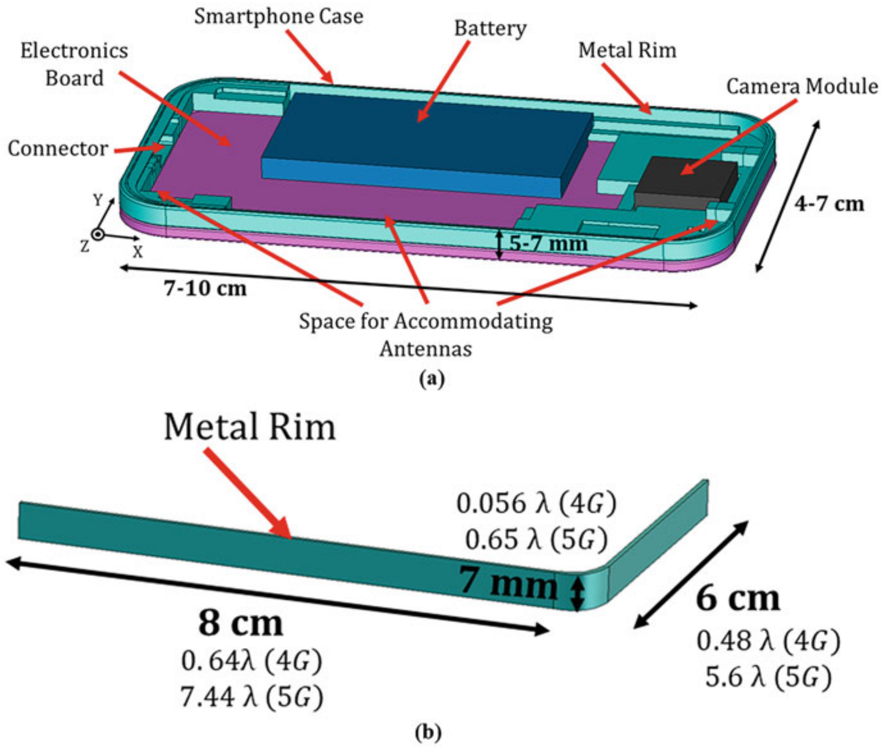

Fig. 7.2 (**a**) Break-up of typical smartphone and (**b**) Space for antennas in a typical smartphone

with the mobile device depends on the insertion loss of the feeding lines and the power pumped into the antenna by the battery via the RF switch and other electronics. Radiation patterns are an important aspect of consideration for future smartphones, as the patterns of the antennas must offer a legitimate data link when in data mode engaged by the user. Most of the experts opine that 5G would be designated for data-oriented services and 4G for the low data rate applications. Maintaining a decent link budget with electrically small low gain, omnidirectional antennas would be readily feasible with 4G systems. However, 5G antenna systems need to offer high gain even at the mobile device to maintain a reliable link budget at 28 GHz. The antenna location and desired radiation patterns for 5G and 4G LTE are shown in Fig. 7.3, respectively. The antenna location for 5G would be along the shorter edge of the mobile device, this is a design choice depending on the form factor and actual available space for 5G antennas.

Most of the power must be radiated away from the user for optimal link budget at higher frequencies. Conventional planar broadside antennas would fail to be operational for the 5G antenna application hence innovative solutions are required for high gain antenna designs with a small form factor. In contrast to 5G antennas, 4G LTE antennas have simpler radiation pattern specifications. 4G LTE antennas

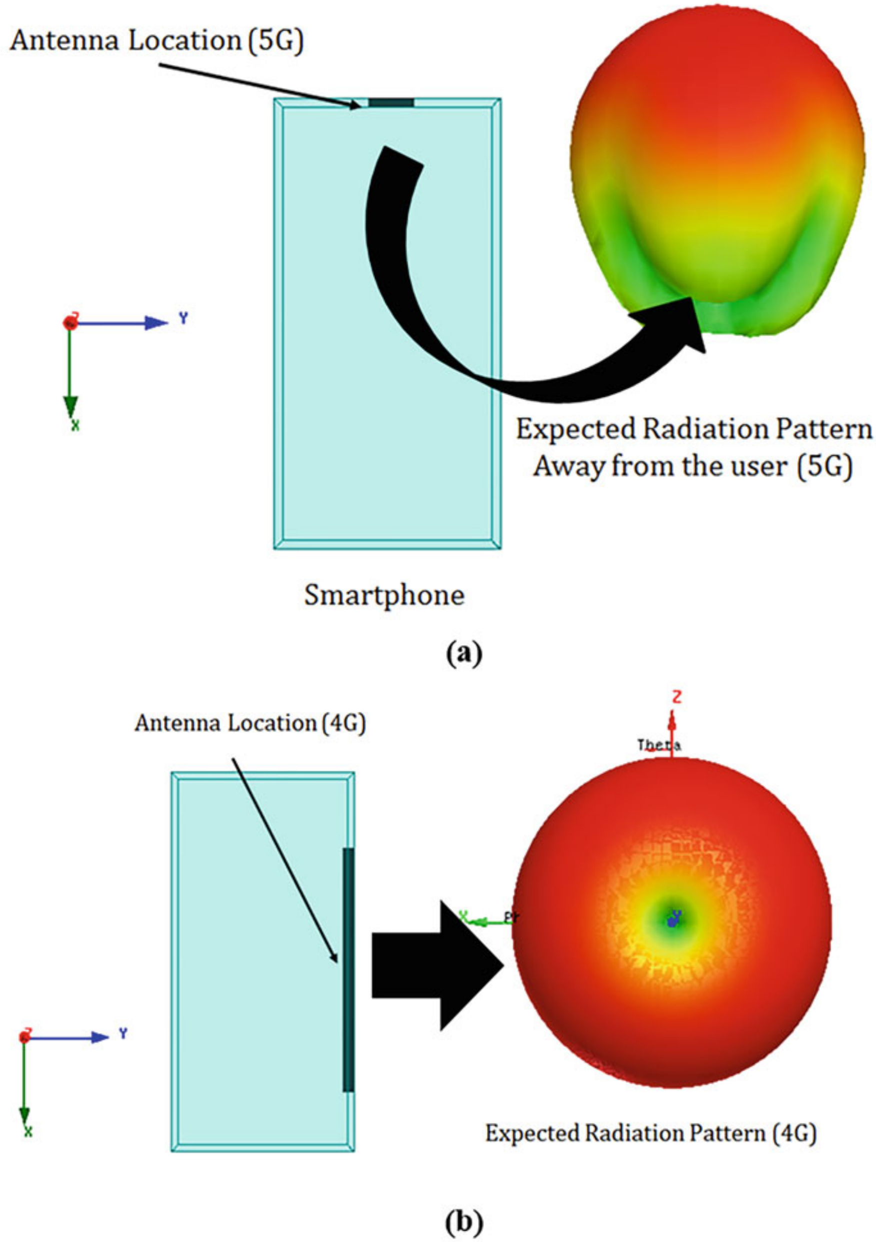

Fig. 7.3 Antenna location and desired radiation patterns (**a**) mmWave 5G and (**b**) 4G

must offer omnidirectional coverage. Multiple antenna elements might be integrated for higher throughput but the pattern requirement would be omnidirectional for each element. A simple printed monopole would serve this purpose. With the 4G–5G co-designed antenna module the radiation patterns of 5G must not be deteriorated by the metallic portions of the 4G radiating system.

7.2.3 Beamwidth

Beamwidth refers to the angular widths for 3 dB half-power points in the normalized radiation patterns. The concept of beamwidth is not of much importance when the pattern is omnidirectional but would be critical for patterns which have a unidirectional beam, such as the pattern from a phased array of four or more elements. Millimeter-wave-based 5G would be exclusively meant for data hungry applications. Users would hold the mobile device similar to the sketch shown in Fig. 7.4. Antennas operating in the 28 GHz band must radiate away from the user's hands and torso to avoid signal attenuation. This issue is not a problem in the sub-6 GHz bands, as the signal attenuation is not significant in those bands. End-fire antennas like planar dipoles and Vivaldi antennas would be an ideal candidate for the aforementioned purpose [10, 11]. Beamwidth for 5G antennas could be in the range of 80°–120°. Beamwidth is also decided by the desired gain and the radiating aperture of the antenna mounted in the mobile device. Co-designed 4G–5G antennas must have beam integrity.

7.2.4 Data Modes

The user engages with the smartphone in different orientations, which is termed as data modes. One of the unique challenges in designing antennas for 5G frequencies is the data modes of the user. The user might engage with the smartphone either in single hand or dual hand modes as illustrated in Fig. 7.5. The beam integrity must be maintained irrespective of the orientation of the smartphone. In other words, the antenna system designed for 5G must support orthogonal beams which will not be possible by the most popularly advertised approach of phased arrays [10–12]. The attenuation suffered by the user's hands is negligible for 4G frequencies and hence an irrelevant problem for designing 4G antennas.

7.2.5 Gain

Gain tells the antenna designer the amount of power boost due to the antenna at a given direction. For instance, a 5 dBi gain at 25° indicates that the power level at 25° of the antenna would be 5 dB higher compared to the power radiated by an isotropic antenna mounted at the same location. Gain is a far-field phenomenon

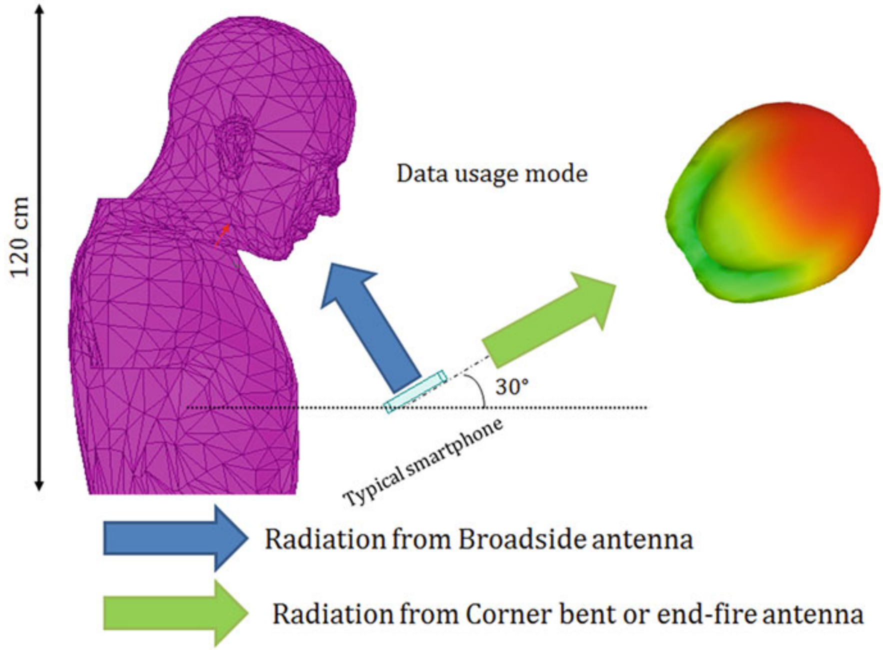

Fig. 7.4 Typical human interaction with smartphone in data mode (5G)

and is measured in the far-field, and hence the pattern measurement performed in the far-field is essential for gain estimation or calculation. Gain of the antennas for 5G systems is the most discussed and debated parameter. A gain of 8–15 dBi seems to be a reasonable choice for 5G systems given the available form factor and the corresponding electrical length at 28 GHz. Gain enhancement would shrink the beamwidth, leading to a decreased angular coverage. Hence, gain corresponding to a predetermined angular coverage would be a clever choice for 5G systems. Gain for 4G antennas systems is not an important design aspect to be considered, primarily due to the implementation of electrically small antennas within a small form factor. A gain of 0 dBi would be recommended for 4G systems, but the feasibility of this requirement depends on a lot of parameters post-integration of the antennas with the mobile unit's electronics.

7.2.6 Radiation Efficiency

Radiation efficiency indicates the ratio of radiated power to that of the input power pumped from the source. A higher radiation efficiency would mean that low-power systems could be realized both at the mobile device and base station side. Radiation efficiency is another cortical factor for designing mmWave 5G systems primarily

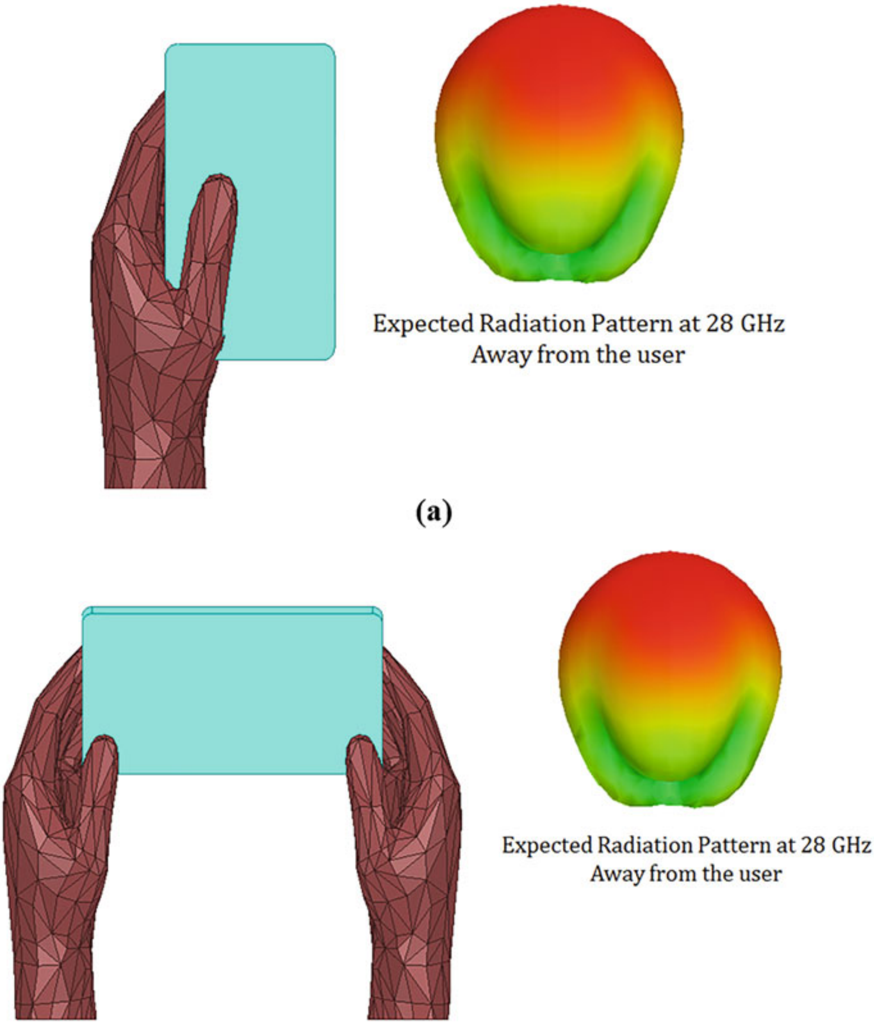

Fig. 7.5 Data modes in 5G (**a**) Single hand mode and (**b**) Dual hand mode

due to the link budget constraints. Radiation efficiency of above 75% would be feasible with the 28 GHz antenna systems. This is evident from the numerous reported articles in the literature. As the physical form factor supports an electrically large radiating element, high radiation efficiencies can be easily obtained. The same logic cannot be extrapolated to 4G antenna systems due to the form factor, leading to efficiencies in the range of 20–40%. Signal interference between 4G and 5G antenna systems also determines the radiation efficiency.

7.2.7 Impedance Bandwidth

The 10-dB impedance bandwidth is the portion of the frequency spectrum wherein at least 90% of the power is radiated by the antenna. This definition seems to be a norm among the antenna engineering community. 10-dB bandwidth seems to be norm for 28 GHz-based 5G antennas. On the other hand, 6-dB impedance bandwidth is the benchmark for 4G antennas. The specifics of bands available for the specific carrier and the mobile device manufacturer is geography-dependent. The effects of user's hands might detune the antennas of both 4G and 5G systems. Rigorous analysis and design iterations are necessary to minimize the effects from user's hands. The lower harmonics of the 5G antennas must not coincide with that of the 4G bands. Also, higher order harmonics of 4G antennas must not coincide with that of 5G bands. Mutual coupling between the two antenna systems must be less than 10 dB at the lower bands and 20 dB at the higher bands of the utilized spectrum.

7.2.8 Specific Absorption Rate

SAR tells the amount of energy penetration into the human tissue. A higher SAR value from the mobile device indicates higher power penetration into the human head, which could be potentially dangerous. SAR is primarily a sub-6 GHz design parameter since 5G wireless service is intended for data-oriented applications, wherein the user engagement with the mobile device is similar to Fig. 7.4. The mmWave signal penetration into human head is minimal, in addition to this argument, 28 GHz band is not as critical as the sub-6 GHz bands. Also, deployment of end-fire or corner bent antenna systems for 5G would automatically ensure minimal signal penetration into human head. The desired radiation pattern for 4G antennas for minimal SAR for voice mode is depicted in Fig. 7.6.

The expected radiation must be away from the user's head when the user is engaged in a voice call. As evident from patterns of Figs. 7.3b and 7.6, the patterns for angular coverage and minimal SAR are contradicting to each other. A hemispherical unidirectional pattern is preferred for minimal SAR as against an omnidirectional pattern of electrically small printed monopoles. This design aspect forces designers to find a middle-ground in the 4G antenna design and its placement with respect to user's orientation. It is important to note the feasibility to achieve a unidirectional beam is very challenging given the form factor of future smartphones.

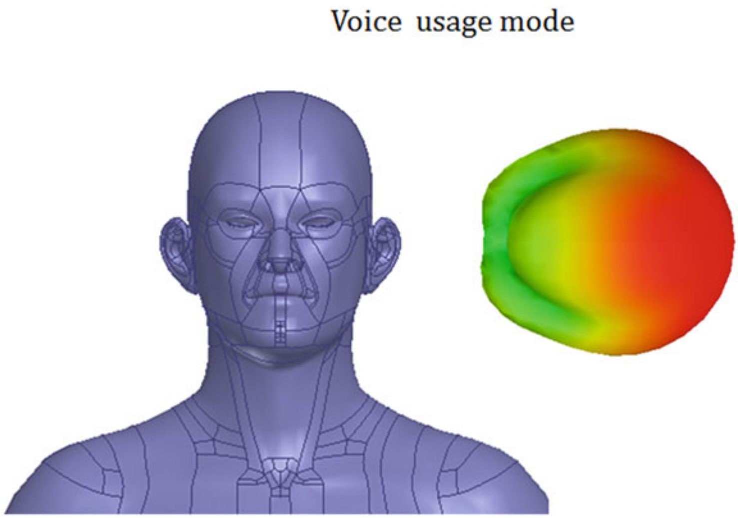

Fig. 7.6 Typical human interaction with smartphone in voice mode (4G)

7.3 Design Logic for 4G and 5G Antennas

This section explains the rationale behind co-design of 4G–5G antennas. The straightforward approach for co-design would be to design multiband antennas and the reason for the failure of this design strategy is explained in this section. Consider an inset-fed patch antenna designed on Neltec NY9220 with a dielectric constant of 2.2 and a loss tangent of 0.0009 as illustrated in Fig. 7.7. The thickness of the substrate is 20 mil. Patch A is designed for resonance at 2.4 GHz as evident from the input reflection coefficient curve of Fig. 7.8a. A conventional patch at 2.4 GHz has dimensions which would exceed the form factor of a mobile device. The same Patch A is simulated for its response at 28 GHz to study the feasibility of patch A working for both bands. As the schematics of Fig. 7.7 illustrates the radiating portion of the antenna is 4.7 $\lambda \times 3.6 \lambda$ at 28 GHz. Even though the antenna meets the 10 dB specification for input reflection coefficient at 28 GHz, the pattern seems to be unusable due to the multimoding effects of the primary radiator. A harmonic filter could be integrated for improving the impedance characteristics of the antenna but would not have much effect on the radiation patterns of the higher band of the 4G antenna. This example proves that up-scaling the resonant type of antennas for 5G operation might be ineffective. Also, commercial 4G printed monopoles and their variants would have poor beam integrity at 5G frequencies.

Inset-fed patch antenna B is designed to resonate at 28 GHz, schematics for the antenna is illustrated in Fig. 7.9. The purpose of this example is to investigate the impedance and radiation characteristics of the 5G antenna at 4G bands. As the input reflection curves of Fig. 7.10a prove a strong impedance mismatch happens at the lower frequency band, due to the electrically small size of the radiator for 4G. The

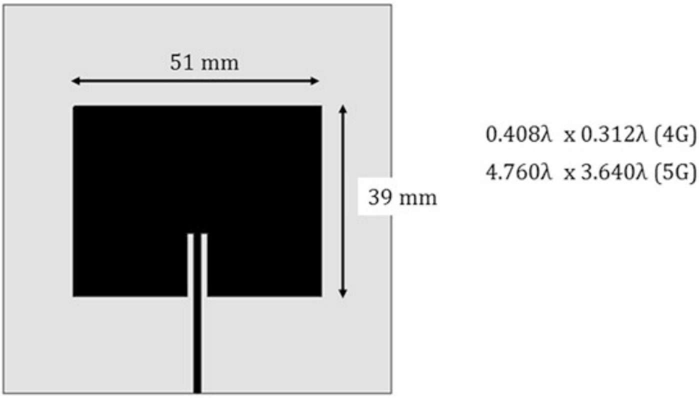

Fig. 7.7 Schematics of an inset-fed patch antenna A operating at 2.4 GHz

3D patterns of Fig. 7.10b also prove that the 28 GHz antenna has poor radiation characteristics at 2.4 GHz.

Hence, co-design would be a suitable choice for 4G–5G antenna system design. Wherein 4G LTE antennas and mmWave 5G antennas would be designed independently and integrated together. Design examples in the following section prove this idea.

7.4 Integrated 4G LTE and Millimeter-Wave 5G Antenna Design Examples

The earlier sections discussed in detail the frequency requirements for 4G LTE and mmWave 5G antennas, motivation behind co-design, and various design constraints for 4G LTE and mmWave 5G antennas. This section explores various published integrated 4G LTE and mmWave 5G antenna designs. The investigated 4G/5G antennas are compared with each other and some insights are given about the candidate integrated 4G LTE and mmWave 5G antennas applicable for mobile devices.

7.4.1 Design-I (Co-designed mmWave and LTE Handset Antennas)

This integrated 4G LTE and mmWave 5G antenna design is proposed by J. Kurvinen et al. [13] for future mobile handsets. The design uses plastic-filled metal rim for mmWave 5G antenna and the same metal rim as capacitive coupling element (CCE)

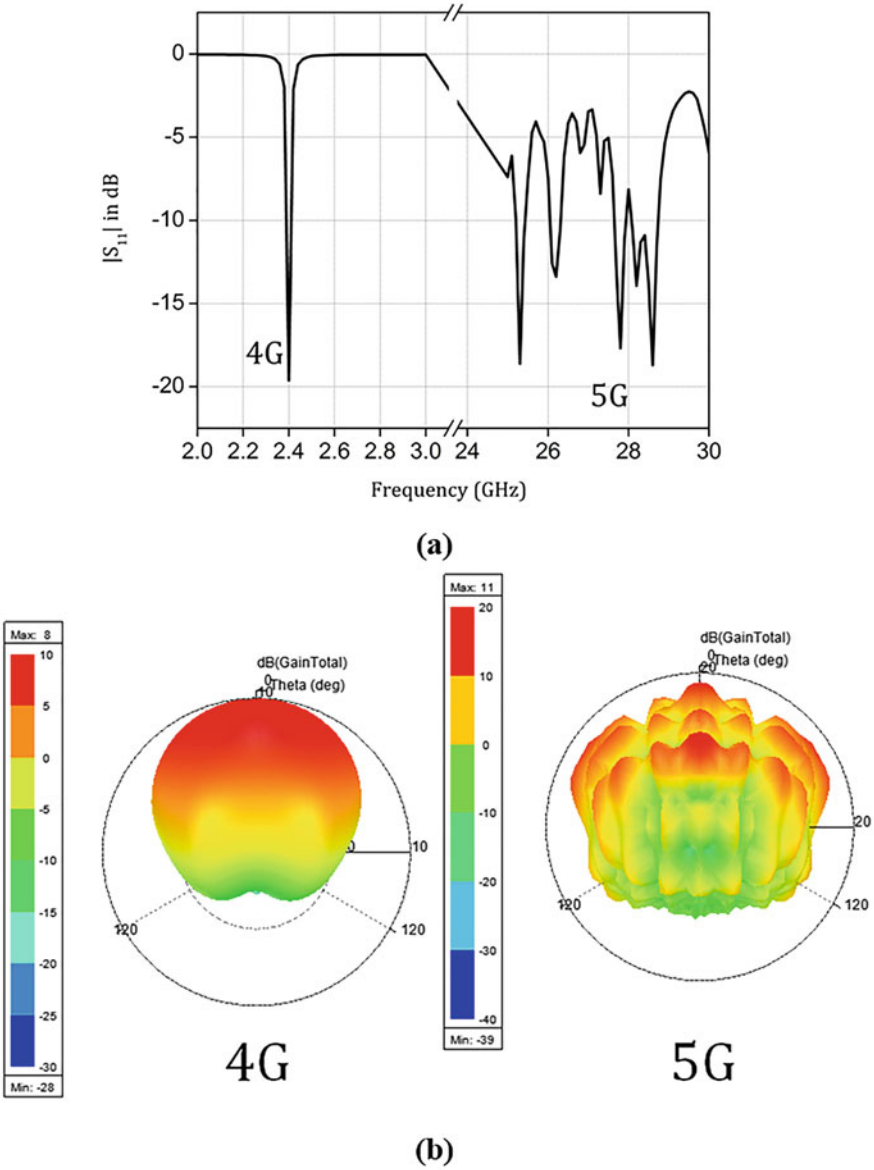

Fig. 7.8 (**a**) $|S_{11}|$ of the patch antenna A and (**b**) 3D Radiation patterns at 2.4 and 28 GHz

for 4G LTE antenna. This co-design claims a novel plastic-filled window in metal rim for mmWave 5G antenna which serves the purpose of proper visualization and sealing of smartphone as the solid metal rim would block the radiation from the

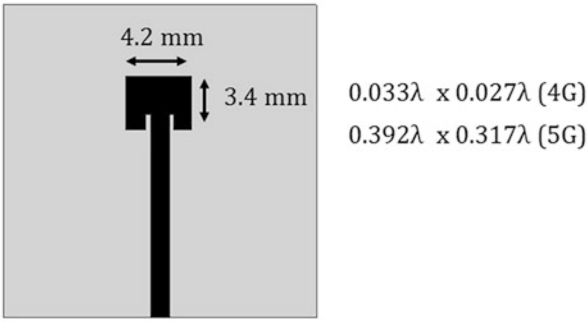

Fig. 7.9 Schematics of an inset-fed patch antenna B operating at 28 GHz

antenna. The 4G LTE antenna would not require any window in metal rim as the latter itself acts as a radiator for covering LTE frequencies.

The proposed co-designed 4G LTE and mmWave 5G antenna module is integrated into the 5G smartphone which utilizes the dimensions as $150 \times 75 \times 7\ mm^3$. Two different substrates are used for the realization of 4G LTE and mmWave 5G antennas, FR4 substrate with dielectric constant, ε_r of 4.3 and loss tangent, tanδ of 0.025 for 4G case and Rogers RO4350B substrate with ε_r of 3.48 and tanδ of 0.0037 for mmWave 5G case. The additional PREPERM L450 plastic with ε_r of 4.5 and tanδ of 0.0005 is used for filling the window in metal rim which holds the mmWave 5G antenna. Since gain is not a major concern at LTE frequencies, therefore the low-cost substrate bearing high loss tangent is used. In contrast, for mmWave 5G antenna, low loss tangent bearing substrate is used for attaining high gain to mitigate path and penetration losses. The 4G LTE antenna design will be discussed at first followed by co-designed mmWave 5G antenna design.

7.4.1.1 4G LTE Antenna Design

The 4G LTE antenna should be designed taken into consideration the geometry and location of mmWave 5G antenna so that both of the antennas will work independently without interfering with each other.

In this proposed work, metal rim which acts as a capacitive coupling element (CCE) is designed and optimized for covering LTE low and high frequency bands. The LTE LB, 700–960 GHz and LTE HB, 1710–2690 GHz are covered by the proposed 4G antenna topology. The antenna is accommodated at the lower left end of 5G handset which is the common location for insertion of 4G LTE antennas. The main FR4 substrate-based PCB acts as a RF-ground for the LTE antenna module. Various types of 4G antennas can be designed to serve the purpose in this scenario but CCE was chosen for its simple design and ability to attain wide impedance bandwidth.

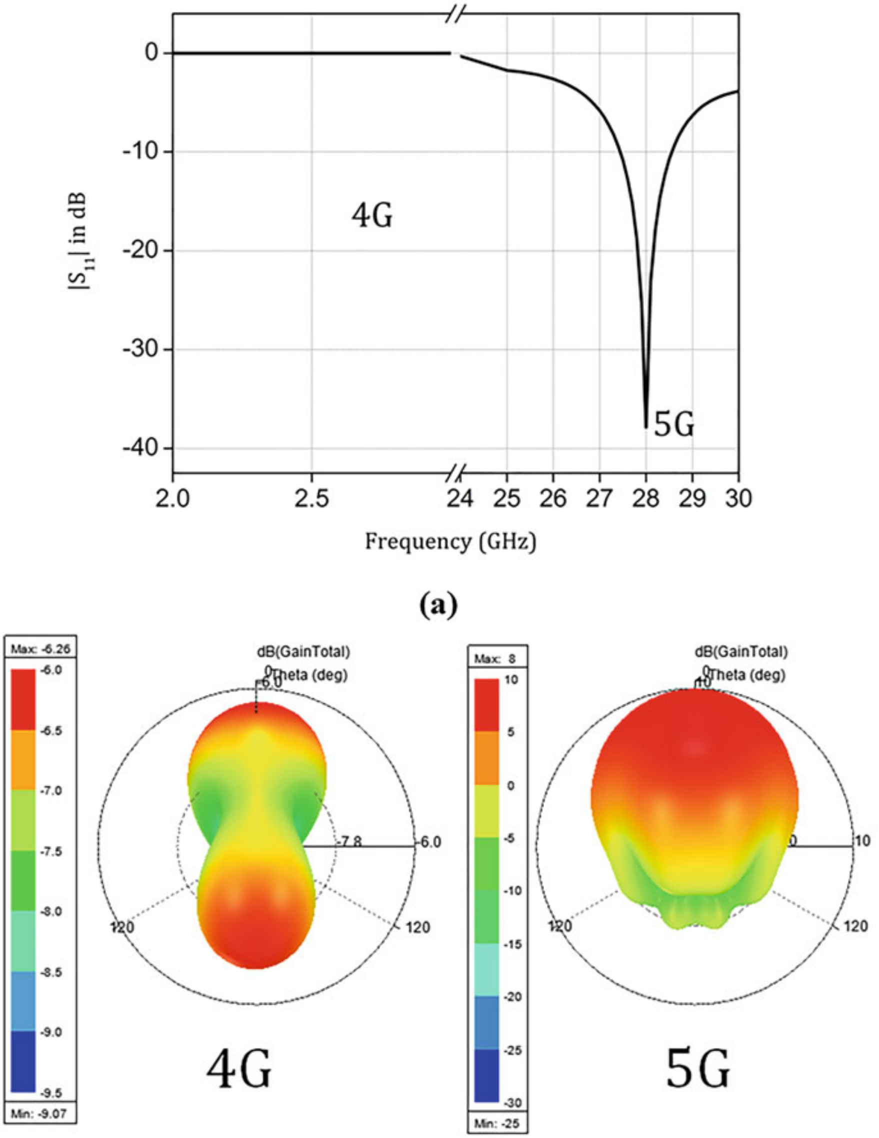

Fig. 7.10 (**a**) $|S_{11}|$ of the patch antenna B and (**b**) 3D Radiation patterns at 2.4 and 28 GHz

Schematic of the proposed integrated 4G–5G antenna module is depicted in Fig. 7.11. Separate feed lines are used in 4G LTE antenna for LB and HB coverage and this is mainly done for obtaining better performance without any matching deterioration in the respective bands. Port 1 is excited for covering the LB frequencies and Port 2 is excited for covering the HB frequencies supporting a

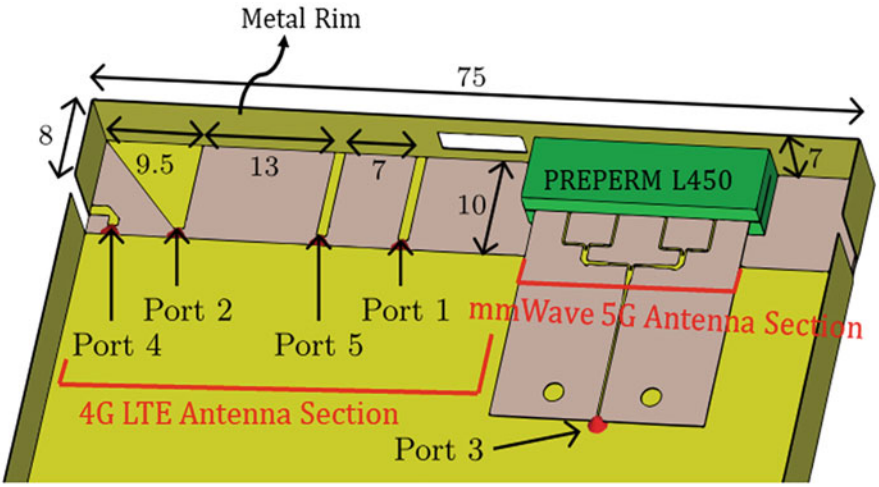

Fig. 7.11 Schematic of co-designed 4G LTE and mmWave 5G antenna module integrated inside mobile terminal (All dimensions are in mm). (Adapted from [13])

triangular feed line. Ports 4 and 5 are used for attaining aperture matching. Multiple LTE bands are obtained for making carrier aggregation possible.

Simulated and measured input reflection coefficient of the proposed CCE-based LTE antenna is depicted in Fig. 7.12. The 4G LTE antennas are designed conventionally for the −6 dB matching level and therefore the antenna is covering LB and HB frequencies when excited by Port 1 and Port 2, respectively. Isolation between the two ports is greater than 15 dB which is significant for preventing any sort of deterioration in individual antenna parameters. The total efficiency of the antenna varies between 60% and 90% in both low and high LTE frequency bands. High radiation efficiency is attained which is due to low losses offered by metal rim since there is no dielectric substrate in the radiator per se. Only the RF-ground plane is based on FR4-based substrate which attributes to low losses. Omnidirectional radiation patterns are achieved in *H*-plane and bidirectional in *E*-plane as illustrated in Fig. 7.13.

7.4.1.2 Co-designed mmWave 5G Antenna

An array of Vivaldi antennas is designed for coverage of mmWave 5G frequencies due to its wide impedance bandwidth and beam steering property over a wideband. The aperture width of Vivaldi antennas is chosen to be small around half-wavelength which is mainly in order to decrease the overall size of array module for its easier integration into 5G handset. The half-wavelength aperture width of single Vivaldi antenna is the optimal size for the design of Vivaldi antenna array.

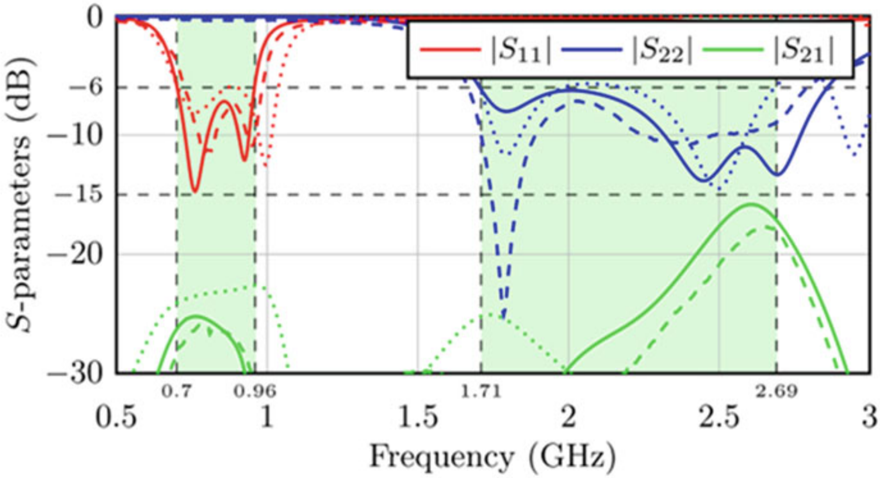

Fig. 7.12 Input reflection coefficient of presented 4G LTE antenna. Solid lines: measurement, dashed lines: Simulated, and dotted lines: simulated results without mmWave antenna module. (Adapted from [13])

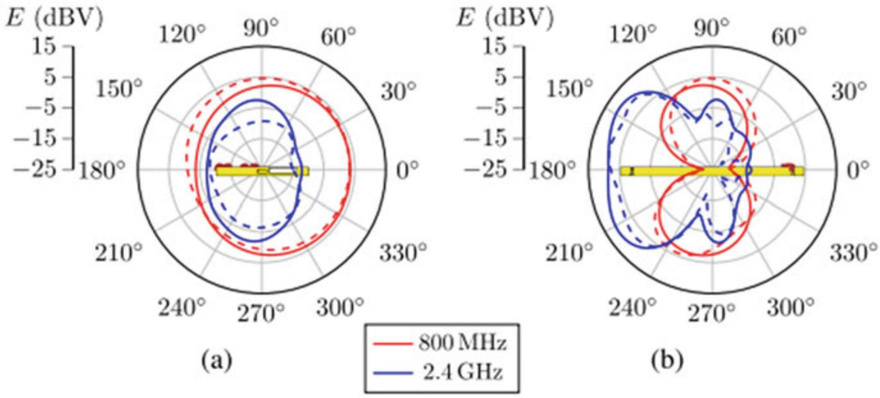

Fig. 7.13 Radiation patterns in (**a**) azimuth and (**b**) elevation planes. (Adapted from [13])

The Vivaldi antenna array is enclosed inside a PREPERM L450 plastic which is integrated into a window cut through a metal rim. The end-fire beam will be easily radiated through a plastic covering fitted in a metal rim. Schematics of the mmWave antenna module are shown in Fig. 7.14. The material for enclosing Vivaldi antenna array should be chosen properly due to its influence on antenna parameters. There is some detuning in impedance matching due to insertion of plastic material and enhancement of radiation characteristics due to its low loss. The high value of relative permittivity of plastic material aids in the miniaturization of electrical size of Vivaldi antenna.

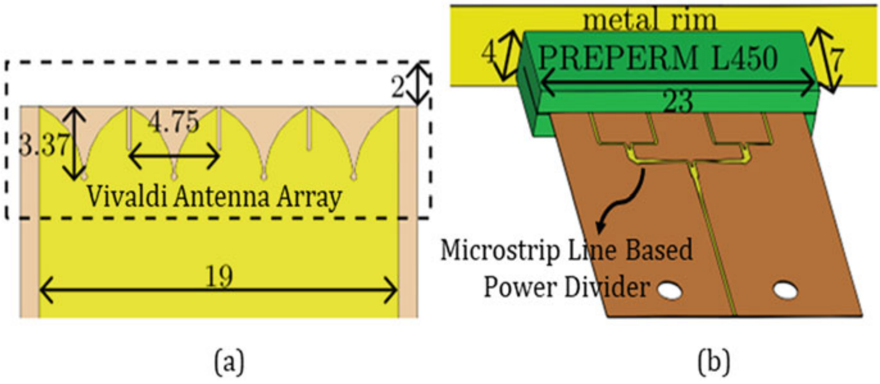

Fig. 7.14 (**a**) Schematics of the mmWave 5G antenna module and (**b**) Vivaldi antenna array enclosed inside PREPERM L450 plastic structure (All dimensions are in mm). (Adapted from [13])

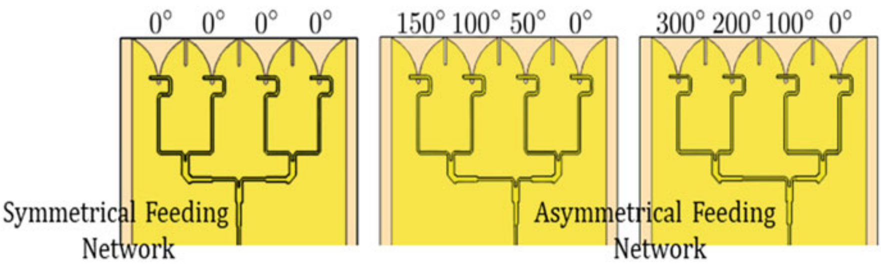

Fig. 7.15 Microstrip line-based feeding network for achieving progressive phase shift between Vivaldi antenna elements. (Adapted from [13])

Different phase shifts between various Vivaldi antenna elements are used for scanning the end-fire radiation beam. Three different PCB-based power dividers are employed for attaining phase shifts having a constant phase difference in each topology as illustrated in Fig. 7.15. For practical application, phase shifters or butler matrix-based beamforming network can be employed to perform electric beam scanning.

The −10-dB impedance bandwidth of the proposed antenna varies from 25 to 30 GHz as depicted in $|S_{11}|$ plot in Fig. 7.16. The three different graphs are plotted for different phase shifters. Beam steering at 0°, +20°, and +40° at 28 GHz is realized by introducing three separate phase shifting Vivaldi antenna array modules as illustrated in Fig. 7.17. Peak gain of 7 dBi is attained across the operational frequency band.

The mmWave 5G antenna module is integrated along the bottom right side of the smartphone. The interaction between mmWave 5G and 4G LTE antenna is minimal since both the antennas are realized on different dielectric substrates and the mmWave 5G antenna is realized while enclosed in plastic material which

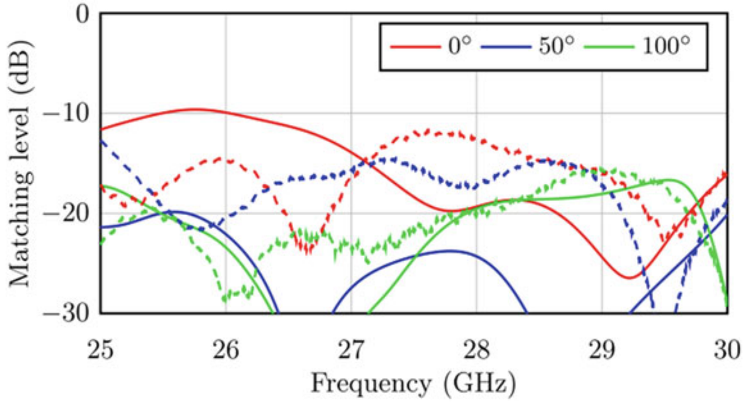

Fig. 7.16 $|S_{11}|$ plot for mmWave 5G antenna array for three realized phase shifters. (Adapted from [13])

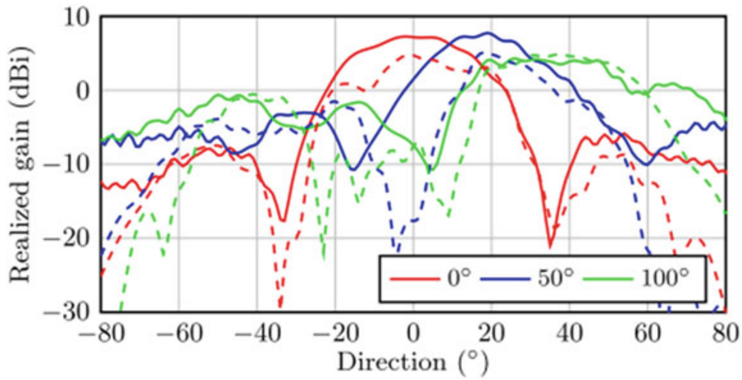

Fig. 7.17 Realized gain patterns in azimuth plane at 28 GHz with beam steered at 0°, +20°, and +40°. (Adapted from [13])

has negligible interaction with metal rim, radiator for 4G LTE antenna. The USB and metal rim windows can act as slot antennas which would not be desirable in this configuration since the main radiators are clearly CCEs and Vivaldi antenna array. Since the electrical size of these windows are very small at LTE frequencies, the impact on the main radiator of 4G antenna is very minimal. Furthermore, the mmWave 5G antenna is enclosed in plastic material and therefore the coupling between metal rim window and Vivaldi array is almost negligible.

7.4.2 Design-II (Corner Bent Integrated Design of 4G LTE and mmWave 5G Antennas for Mobile Terminals)

This co-designed 4G LTE and mmWave 5G antenna includes a corner bent topology proposed by M. Idrees Magray et al. [14]. The proposed antenna module utilizes a single substrate for 4G–5G antenna design unlike antenna design proposed by Kurvinen et al. [13] which employs separate substrates for 4G and 5G antennas. Also, the 4G–5G radiators are designed in shared topology which decreases the overall size of the antenna module. In addition to this, Multiple-Input Multiple-Output (MIMO) technique is also implemented for attaining higher data rates. In this research work, orthogonal pattern diversity is achieved for high gain mmWave 5G antennas which helps in the usage of smartphone in portrait as well as landscape mode as illustrated in Fig. 7.18.

The presented antenna module is designed on 10-mil thick Rogers 5870 substrate with relative permittivity of 2.33 and loss tangent of 0.0012. In order to keep cross-polarization at a minimum level, substrate of low thickness is chosen. Also, for achieving corner bending, thin substrate would be optimal. Low dielectric constant-based substrate was chosen to keep various surface wave modes to minimum. Schematics of the proposed co-designed 4G LTE and mmWave 5G antenna module is depicted in Fig. 7.19.

The proposed antenna module is designed in the shared topology for decreasing the overall size of antenna. The overall electrical size of 4G LTE antenna is determined by taking the whole size of antenna module into consideration. The 4G LTE section of antenna module consists of rectangular shaped slot antenna fed by 50 Ω microstrip line. The impedance matching of slot antenna depends on length of feed, width of the rectangular slot, and position of feed line with respect to radiator.

The simulated and measured $|S_{11}|$ plot of 4G LTE antenna is depicted in Fig. 7.20. Proposed antenna occupies 55% fractional bandwidth covering multiple LTE frequency bands, LTE1700 (1710–2170 MHz), LTE2300 (2300–2400 MHz), and

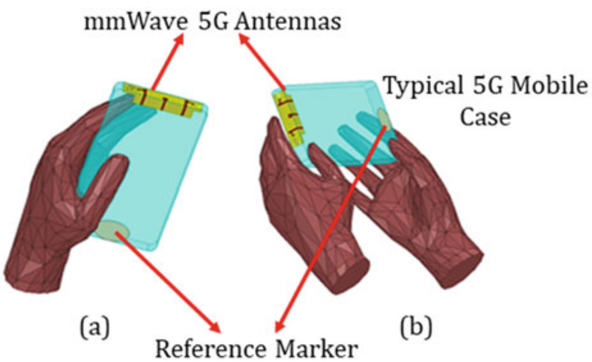

Fig. 7.18 Topology of the smartphone (**a**) portrait mode and (**b**) landscape mode

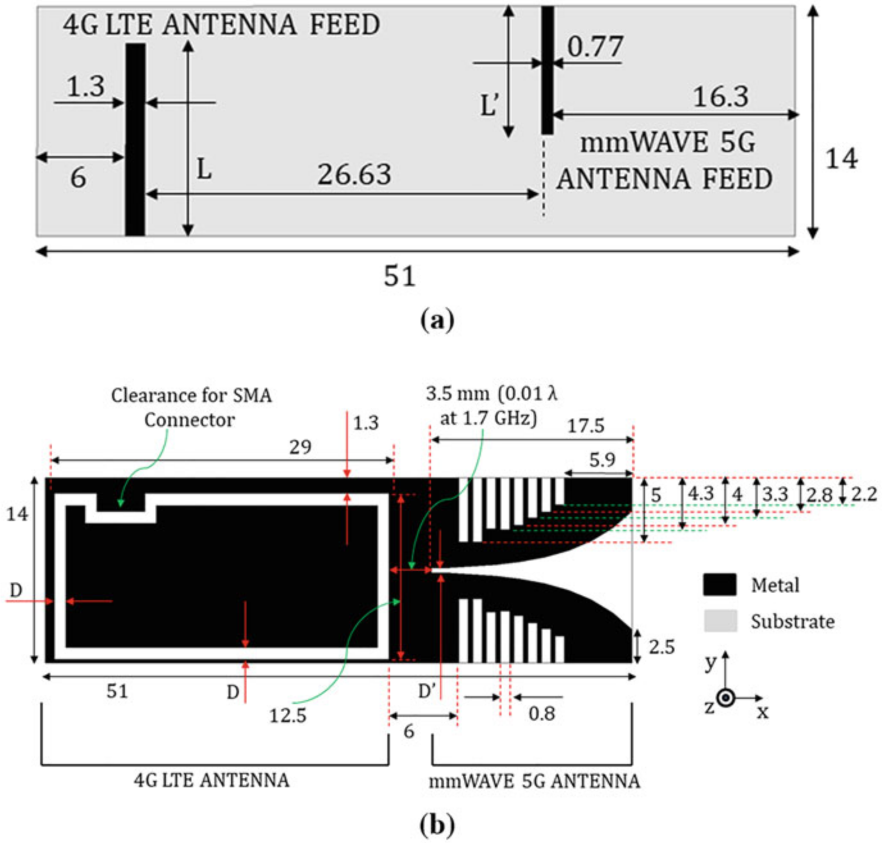

Fig. 7.19 Schematics of the 4G–5G antenna module (**a**) top plane and (**b**) bottom plane (All dimensions are in mm). (Adapted from [14])

LTE2500 (2500–2690 MHz). Multiple low frequency bands are covered for making carrier aggregation possible. Gain of the 4G LTE antenna varies between 1.7 and 2.1 dBi across the entire operating frequency band. Radiation efficiency varies between 60% and 80% which is high due to usage of thin substrate with low loss tangent. Moreover, dipole-like radiation patterns are achieved in the *E*-plane (*YZ*-plane) of antenna as shown in Fig. 7.21.

The mmWave 5G section of proposed antenna module comprises of microstrip fed Vivaldi antenna which is chosen for its simple structure and wide bandwidth. The 5G antenna is designed in the vicinity of 4G antenna and the 4G LTE slot radiator does not interfere with Vivaldi antenna as the slot radiator of 4G LTE antenna is not blocking any radiating aperture of mmWave 5G taper slot antenna. Dimensions of the proposed mmWave 5G antenna are 1.75 λ × 1.4 λ × 0.0254 λ at 28 GHz. The impedance matching is obtained by optimizing the microstrip to slot line transition of Vivaldi antenna. Varying length horizontal corrugations are

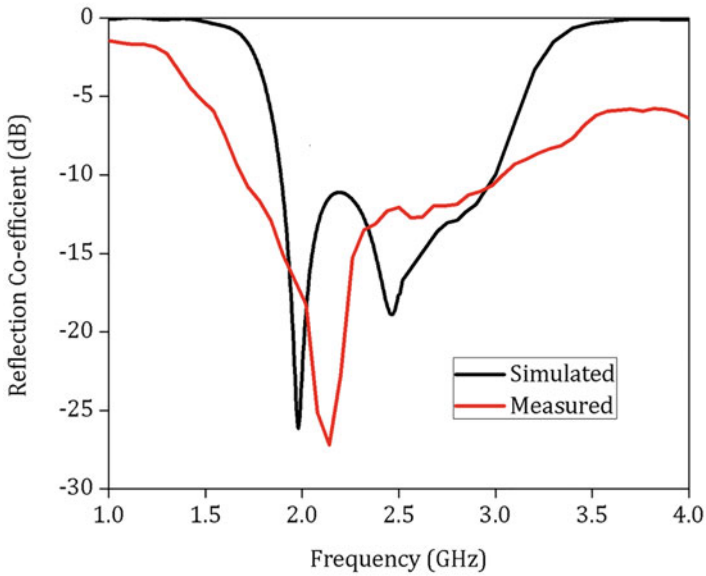

Fig. 7.20 $|S_{11}|$ plot of presented ground shared 4G LTE slot antenna. (Adapted from [14])

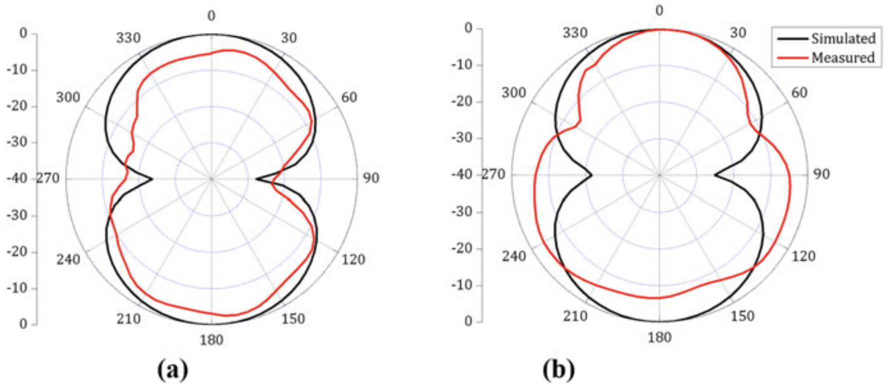

Fig. 7.21 Simulated and measured radiation patterns in *E*-plane at (**a**) 1.8 GHz and (**b**) 2.6 GHz. (Adapted from [14])

introduced in the metallic taper arms of Vivaldi antenna for concentrating E-field towards the main radiating aperture thereby reducing side and back lobe levels.

The input reflection coefficient of the proposed antenna is depicted in Fig. 7.22. Proposed mmWave 5G antenna is wideband covering frequency band from 25 to 38 GHz with fractional bandwidth of 41%. Both the candidate mmWave 5G bands, 28 and 38 GHz are covered by the proposed corrugated Vivaldi antenna. High end-fire gain ranging between 9 and 10.5 dBi is attained with 1-dB gain bandwidth of around 28%. The high 1-dB gain bandwidth demonstrates high pattern integrity

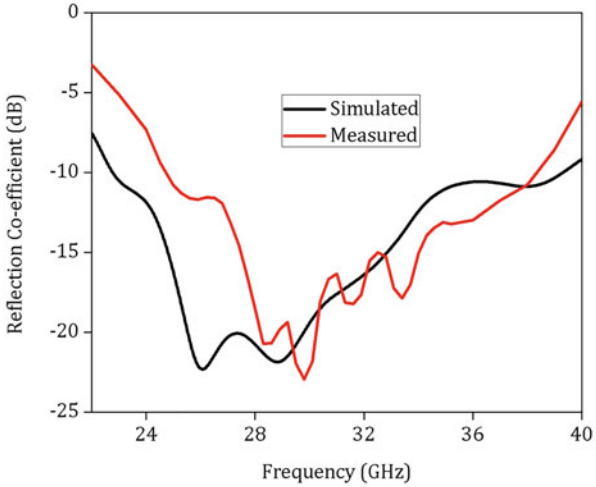

Fig. 7.22 Input reflection coefficient of the presented horizontally corrugated Vivaldi antenna. (Adapted from [14])

across the operational frequency band. End-fire radiation patterns are achieved in the *E*-plane (*XY*-plane). Front-to-back ratio of more than 15 dB is attained for the proposed mmWave 5G antenna topology.

The 4G LTE and mmWave 5G radiators are separated by a distance of 3.5 mm from each other for realizing corner bending. Corner bending is carried out for decreasing the overall effective radiating volume of antenna. The isolation between 4G and 5G antennas is greater than 30 dB in the operating bands of 4G LTE and mmWave 5G. Orthogonal pattern diversity is attained by inserting another corner bent 4G–5G antenna module around the opposite bottom corner of the smartphone as illustrated in Fig. 7.23. The radiation beams of antenna modules are oriented orthogonally so that mobile phones can be used in portrait as well as landscape mode.

7.4.3 Design-III (Compact Co-design of Conformal 4G LTE and mmWave 5G Antennas for Mobile Terminals)

This integrated 4G–5G antenna design proposed by M. Idrees Magray et al. [15] incorporates conformal 4G LTE and mmWave 5G antennas for mobile devices. This co-designed 4G–5G antenna module is designed for achieving compact topology which involves composite right/left-handed (CRLH)-based miniaturization technique for the design of 4G LTE antenna since the electrical size of LTE antennas are much larger than mmWave 5G antennas. The proposed 4G–5G antenna module also investigates MIMO technique for obtaining higher data rates. Moreover, proposed

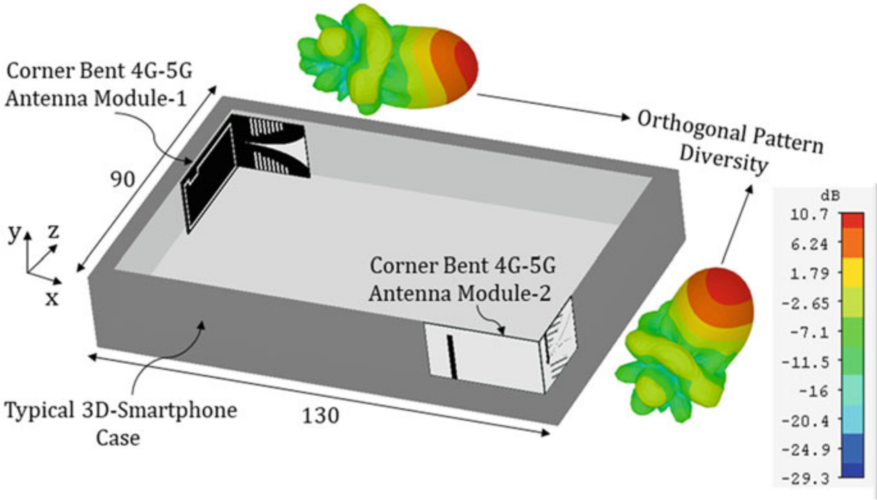

Fig. 7.23 Integration of co-designed 4G LTE and mmWave 5G antenna modules demonstrating orthogonal pattern diversity. (Adapted from [14])

antenna module achieves orthogonal pattern diversity for orthogonal data usage modes of smartphone.

The 4G LTE antennas are designed separately and then integrated with mmWave 5G antennas with significant isolation of less than 40 dB. Separate substrates are used for 4G LTE and mmWave 5G antennas. The 4G LTE MIMO antennas are designed on 10-mil thick Rogers 5870 substrate with relative permittivity of 2.33 and dielectric loss tangent of 0.0012. The 10-mil thick substrate is used for achieving easier antenna conformity. Schematics of the proposed 4G LTE antenna are depicted in Fig. 7.24.

The 4G LTE antenna consists of three asymmetric CRLH-based metamaterial unit cells which resonate at a specific frequency determined by phase constant, β_n. The zeroth-order resonating (ZOR) mode is excited in which the operating frequency of radiator is independent of its physical size. The physical size of proposed planar CRLH-based 4G LTE antenna is small having dimensions of $20 \times 20 \times 0.254$ mm^3. The physical footprint is further decreased by conforming the antenna at 90° as illustrated in Fig. 7.24. The CRLH-based 4G LTE antenna topology comprises of various series and shunt parameters, namely series capacitance (C_L), series inductance (L_R), shunt inductance (L_L), shunt capacitance (C_R), series resistance (R), and shunt conductance (G). The ZOR frequency depends only on shunt parameters. Since the increase in shunt capacitance, C_R results in decrease of operational bandwidth, therefore only shunt inductance (L_L) is increased which results in effective miniaturization of antenna.

Coplanar waveguide (CPW) feeding is chosen for its feasible nature to achieve impedance matching in electrically small antennas by a decrease in capacitive reac-

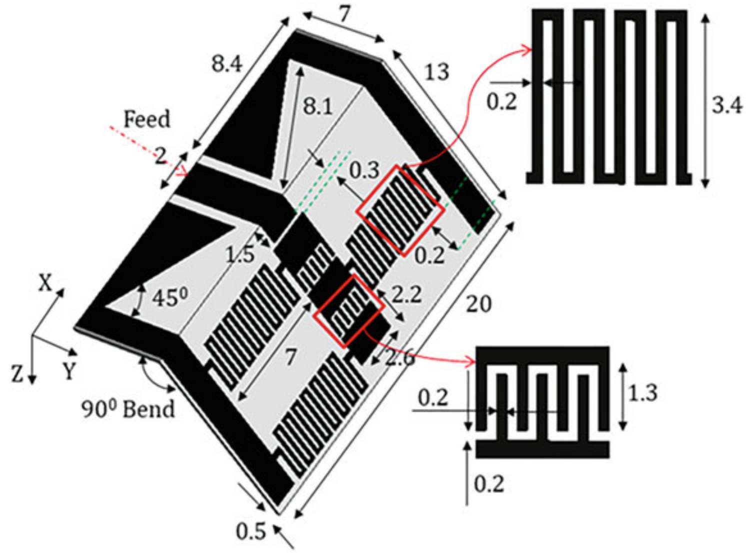

(a)

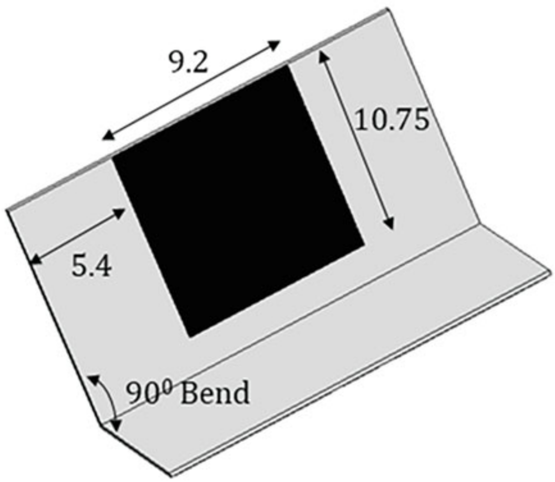

(b)

Fig. 7.24 The conformal CRLH-based 4G LTE topology (**a**) top plane and (**b**) bottom plane (All dimensions are in mm). (Adapted from [15])

tance. Moreover, the number of asymmetric meander lines can be easily increased by introducing CPW feeding. Also, the conformity will create less discontinuities

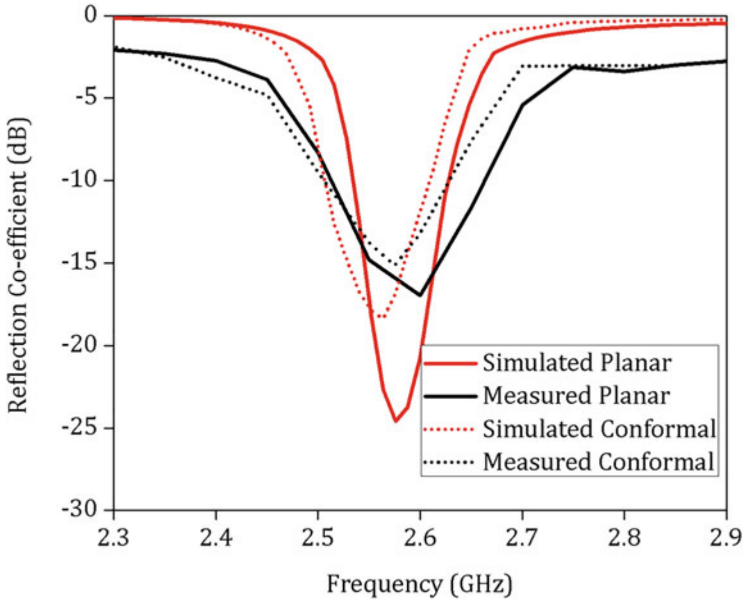

Fig. 7.25 $|S_{11}|$ plot of investigated conformal 4G LTE antenna. (Adapted from [15])

when CPW feeding is considered. The 50 Ω CPW feed line comprises of tapered triangular shaped ground for enhancing impedance bandwidth.

The simulated and measured $|S_{11}|$ plot of proposed CRLH-based 4G LTE antenna is shown in Fig. 7.25. Proposed antenna covers class 7 4G LTE band with impedance bandwidth from 2.5 to 2.65 GHz. The conformal antenna topology covers less bandwidth than planar topology which is mainly due to discontinuities occurring while performing corner bending. Proposed antenna achieves omnidirectional radiation patterns both in *E*-plane as well as in *H*-plane as presented in Fig. 7.26. The gain of proposed 4G LTE antenna varies from 1.6 to 2.2 dBi which is significant enough for the available electrical size of antenna.

The mmWave 5G antenna is designed on 10-mil thick Nelco NY9220 with dielectric constant of 2.2 and loss tangent of 0.0009. A standard inset-fed microstrip patch antenna is designed for mmWave 5G mobile terminals. Conformity is introduced for directing radiation beam away from user and to decrease the overall radiating volume of antenna. A localized ground is placed behind the patch radiator to focus the broadside beam in a single direction away from user with high gain. Schematic of the proposed mmWave 5G antenna is depicted in Fig. 7.27.

Input reflection coefficient of the inset-fed microstrip patch antenna is shown in Fig. 7.28. The proposed antenna covers the 28 GHz mmWave 5G frequency band which is one of the candidate frequency bands of mmWave 5G communication. Peak gain of 9 dBi is attained across the operating frequency band with front-to-back ratio of more than 15 dB. Broadside unidirectional radiation patterns are attained in

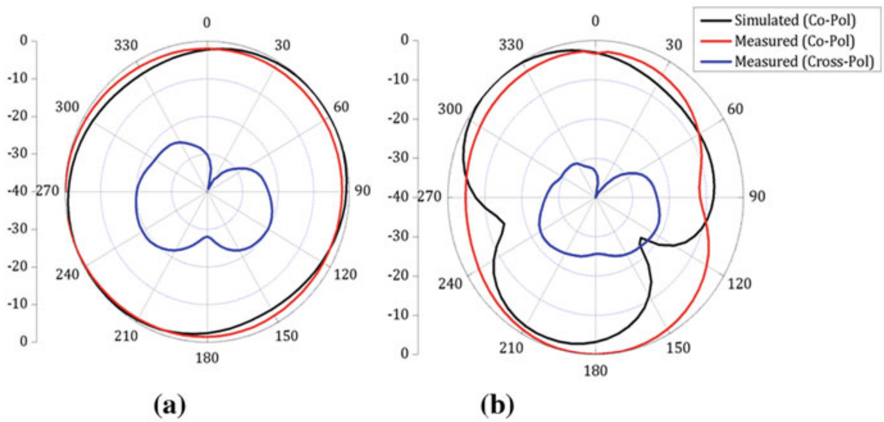

Fig. 7.26 Radiation patterns in (**a**) *H*-plane and (**b**) *E*-plane at 2.6 GHz. (Adapted from [15])

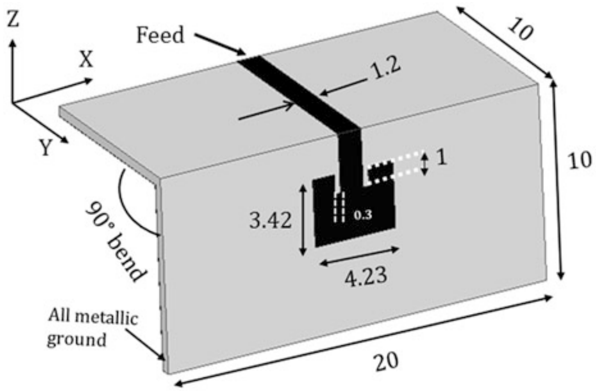

Fig. 7.27 Schematic of conformal inset-fed patch mmWave 5G antenna. (Adapted from [15])

both the principal planes directing away from user as shown in Fig. 7.29. Cross-polarization of less than −35 dB is attained over the entire operating frequency band.

A separate MIMO antenna module is introduced for both 4G LTE and mmWave 5G antennas and then integrated with each other for obtaining a compact co-designed 4G–5G antenna module as illustrated in Fig. 7.30. The 4G LTE MIMO antenna module consists of electrically close two CRLH-based conformal antennas with a 0.3 λ_0 distance between them. Isolation of more than 15 dB is achieved over the entire operating frequencies. The mmWave 5G MIMO antenna module consists of two orthogonally placed inset-fed microstrip patch antennas designed on the same substrate. The broadside radiation beams are directed away from user at 0° and 90° angles which makes the usage of smartphone possible for both portrait

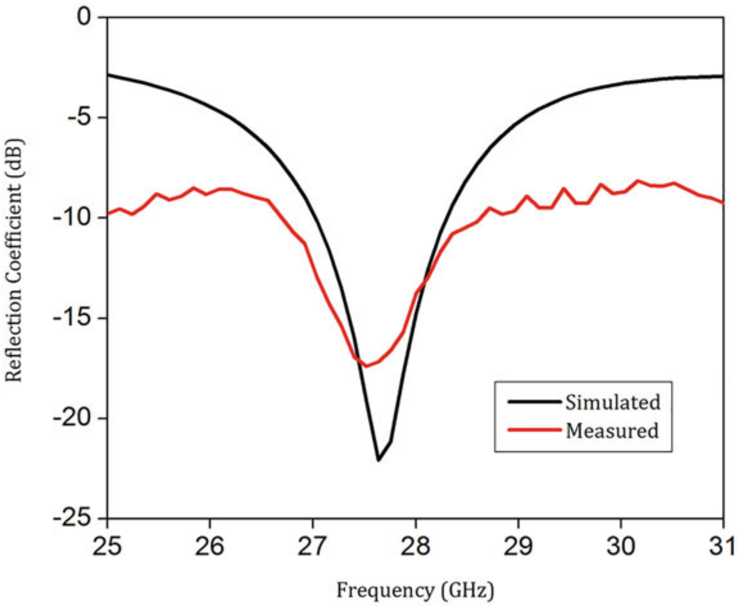

Fig. 7.28 Input reflection coefficient of inset-fed microstrip conformal patch antenna. (Adapted from [15])

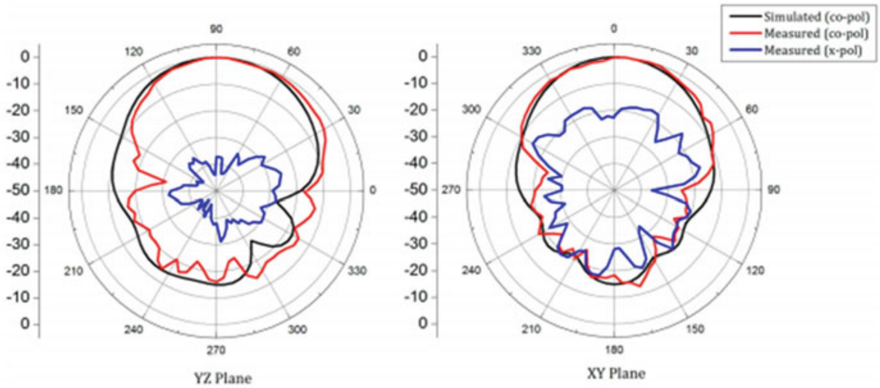

Fig. 7.29 Simulated and measured radiation patterns at 28 GHz for conformal mmWave 5G antenna. (Adapted from [15])

and landscape modes. The antenna characteristics almost remain invariant after 4G and 5G MIMO antenna module integration.

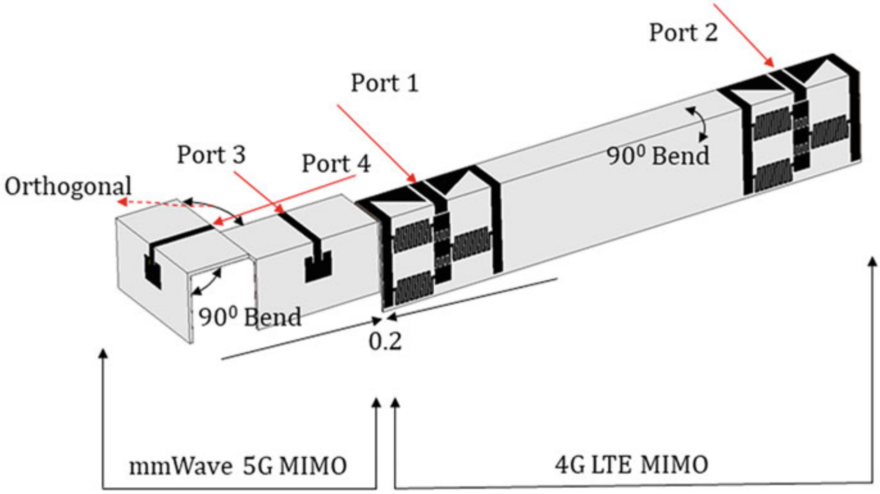

Fig. 7.30 Co-designed 4G LTE and mmWave 5G MIMO antenna module. (Adapted from [15])

7.4.4 Design-IV (Realization of a Tapered Slot Array as both Decoupling and Radiating Structure for 4G/5G Wireless Devices)

This integrated 4G–5G MIMO antenna design proposed by M. Ikram et al. [16] utilizes a single substrate with mmWave 5G antenna array acting as a decoupling structure as well as radiating structure. A co-designed 4G–5G antenna module with 4G LTE and sub-6 GHz 5G monopole radiators on one side and mmWave 5G end-fire antenna on the other side of substrate is investigated. Unlike the other 4G–5G antenna designs discussed in earlier sections which are accommodated along the edge panel of smartphones, this antenna module is suitable to be integrated inside the corner end lying parallel to the screen of 5G handset.

Schematic of the proposed 4G–5G antenna module is depicted in Fig. 7.31. The dimensions of co-designed 4G–5G antenna module are 70 × 50 × 0.51 mm^3. The 4G LTE and sub-6 GHz antenna section comprise of two meandered microstrip-fed monopole MIMO antennas. A defected shared ground structure based on taper slot antenna array is investigated for wideband isolation between monopole radiators. The monopole radiators are designed on top layer of Rogers 5880 substrate with dissipation factor of 0.0009 and relative permittivity of 2.2. The arms of monopole radiators are meandered for achieving compact size and optimized for dual-band operation.

The simulated and measured $|S_{11}|$ plot of proposed meandered monopole antennas is shown in Fig. 7.32a. The proposed monopole antennas cover 2.6 GHz 4G LTE frequency band and 3.5 GHz sub-6 GHz frequency band. Since the spacing between two monopole radiators is less than $\lambda_0/2$ at 2.6 GHz and the radiators

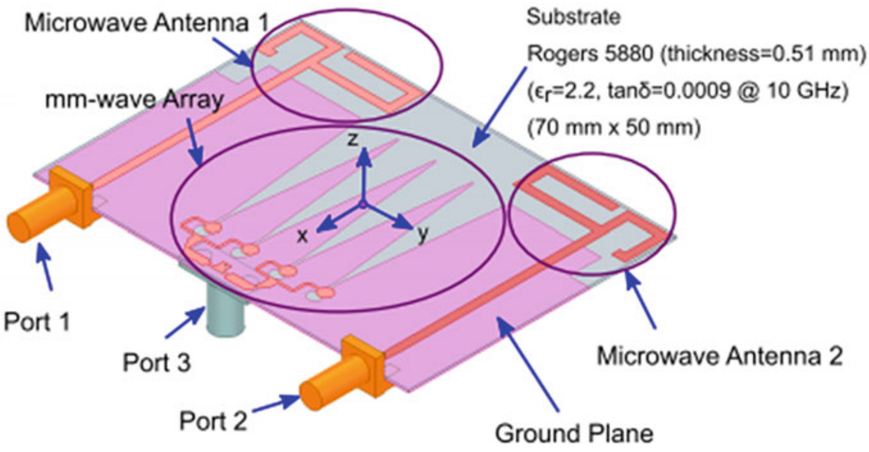

Fig. 7.31 Co-designed 4G LTE and mmWave 5G MIMO antenna module. (Adapted from [16])

share a common ground plane, therefore isolation is around 9 dB which is low. Thus, a decoupling structure in the form of taper slot antenna array is inserted which decreases the mutual coupling between monopole radiators and isolation increases by more than 25 dB as shown in Fig. 7.32b. The monopole radiators achieve omnidirectional radiation patterns in both the principal planes at 2.6 and 3.5 GHz as illustrated by 3D plots in Fig. 7.33. Average gain of 4 dBi and radiation efficiency of more than 85% is achieved for both the monopole antennas in both microwave operating frequency bands.

Taper slot antenna array (TSAA) is designed on the bottom plane of same substrate on which low frequency radiators are designed as illustrated in Fig. 7.31. TSAA serves dual function in this topology, an end-fire high gain antenna array at mmWave 5G frequency band, and decoupling structure at low frequency bands. The TSAA is fed by a microstrip-based power divider which is terminated with a circular stub for enhanced impedance matching. The radiating aperture of taper slot antenna is around $\lambda_0/2$ at 25 GHz, lower operating frequency of mmWave 5G frequency band. The mutual coupling between individual ports of TSAA is less than −16 dB.

Input reflection coefficient of proposed TSAA is represented in Fig. 7.34. Proposed antenna operates over a wideband from 25 to 30 GHz with fractional bandwidth of 18.18%. The proposed taper slot antenna covers one of the candidate bands of mmWave 5G communication, i.e., 28 GHz frequency band. Moreover, the isolation between low frequency and high frequency ports is greater than 30 dB as shown in Fig. 7.34. Proposed antenna array attains end-fire radiation patterns with high peak gain of around 15 dBi as depicted in Fig. 7.35.

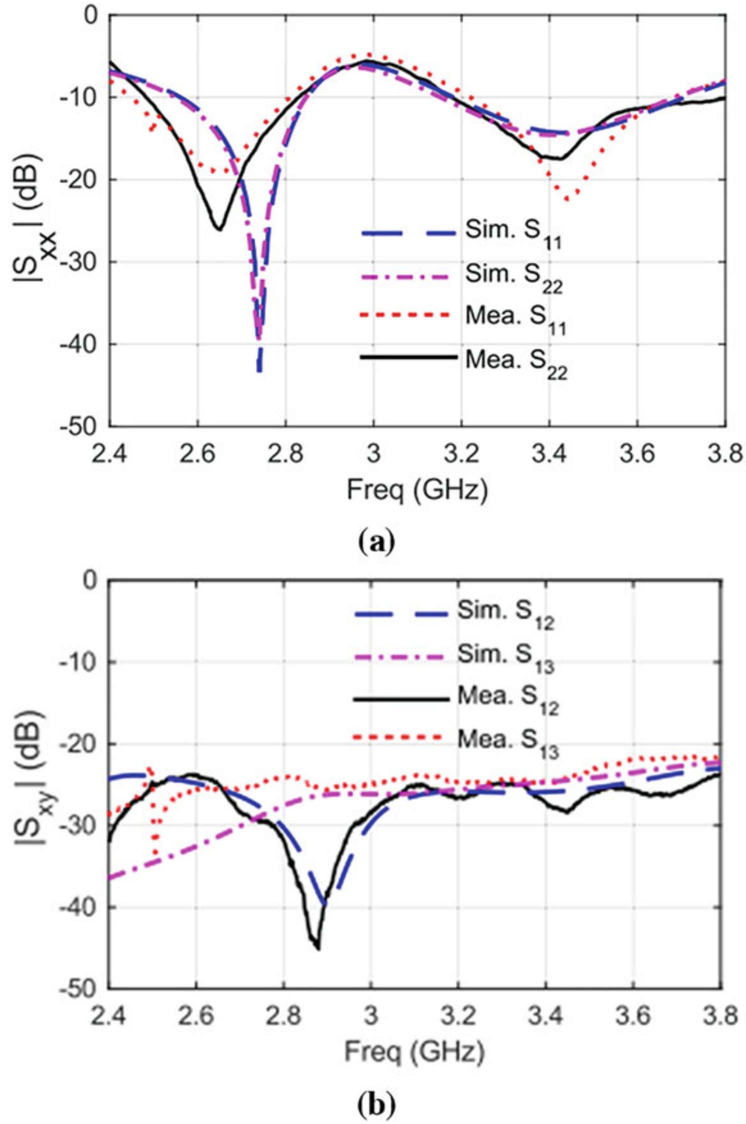

Fig. 7.32 $|S_{11}|$ plot of presented meandered monopole antennas. (Adapted from [16])

7.4.5 Design-V (Low Cost Substrate-Based Compact Antennas for 4G/5G Side-Edge Panel Smartphone Applications)

This low cost substrate-based co-designed 4G–5G antenna module proposed by I. S. Masoodi et al. [17] consumes antenna width of only 6 mm which will be compatible

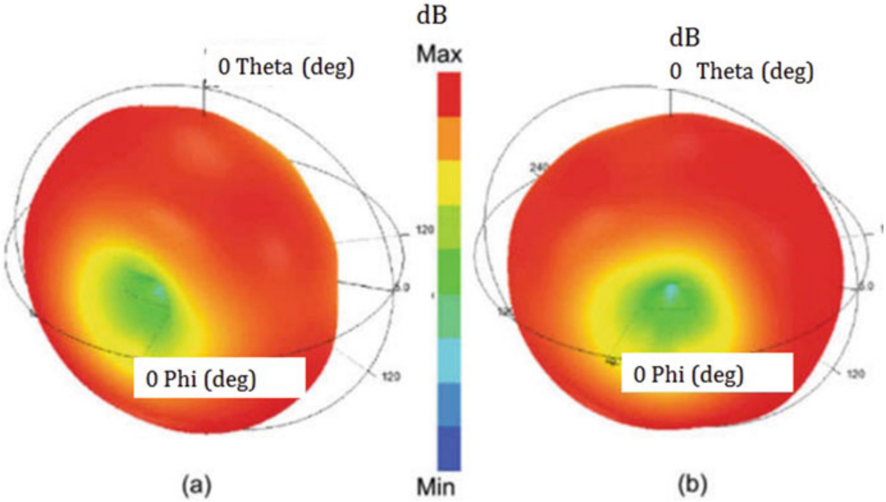

Fig. 7.33 3D-radiation patterns at 2.6 GHz for (**a**) microwave antenna 1 and (**b**) microwave antenna 2. (Adapted from [16])

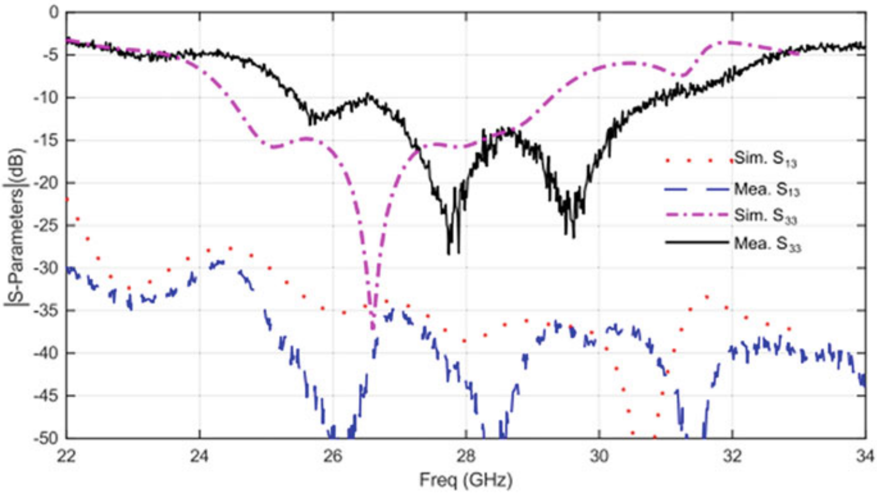

Fig. 7.34 Reflection coefficient of TSAA. (Adapted from [16])

for the integration along the side panel of future 5G handsets. This co-designed antenna module also investigates MIMO technique in utilizes corner bending in one module so that it will be accommodated along the smaller edge of the smartphone. Moreover, orthogonal pattern diversity is also explored for mmWave 5G antenna topology so that 5G handset can be used in both the orthogonal modes, landscape as well as portrait mode.

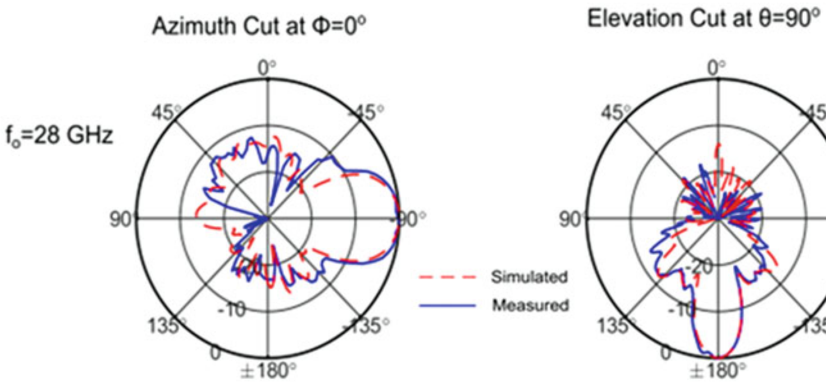

Fig. 7.35 Normalized end-fire radiation patterns for mmWave 5G antenna array. (Adapted from [16])

Schematics of the presented integrated 4G LTE and mmWave 5G antenna module is illustrated in Fig. 7.36. The presented antenna module is designed on polycarbonate substrate bearing dielectric loss tangent of 0.01 and dielectric constant of 2.9. Polycarbonate substrate is utilized for its low cost and flexibility to attain corner bending easily. The overall antenna module is compact feasible for integration along the side-edge panel of future smartphones. Since the conventional SMA connector used for measurement at low frequencies would not be suitable to be soldered properly on polycarbonate substrate, therefore 2.92 mm end-launch connector is used for measurement purposes both at microwave and mmWave frequencies. The substrate is extended along the sides at the feed lines of 4G LTE and mmWave 5G antennas for accommodating bulky end-launch connectors for measurement purposes.

The 4G LTE section of antenna module consists of asymmetric coplanar stripline (ACS)-fed antenna with stepped radiator for achieving wide impedance bandwidth. The ACS feeding is chosen for its compact topology with respect to the conventional CPW feeding technique. The 50 Ω ACS feed line consists of signal trace of width 1.5 mm and gap of 0.3 mm between signal trace and asymmetric ground plane. The overall 4G LTE antenna topology is electrically compact with dimensions of 0.03 λ × 0.26 λ × 0.003 λ at 1.8 GHz. The stepped radiator is optimized by varying number and lengths of steps for covering LTE frequencies.

Input reflection coefficient of the presented ACS-fed 4G LTE antenna is shown in Fig. 7.37. The 4G antenna covers multiple high frequency LTE bands, LTE 1900, LTE 2300, and LTE 2500 thereby making carrier aggregation possible. The presented LTE antenna achieves dipole-like radiation patterns in *E*-plane and omnidirectional radiation patterns in *H*-plane as shown in Fig. 7.38. Broadside high peak gain of around 2.9 dBi is achieved which is significant for the available electrical size.

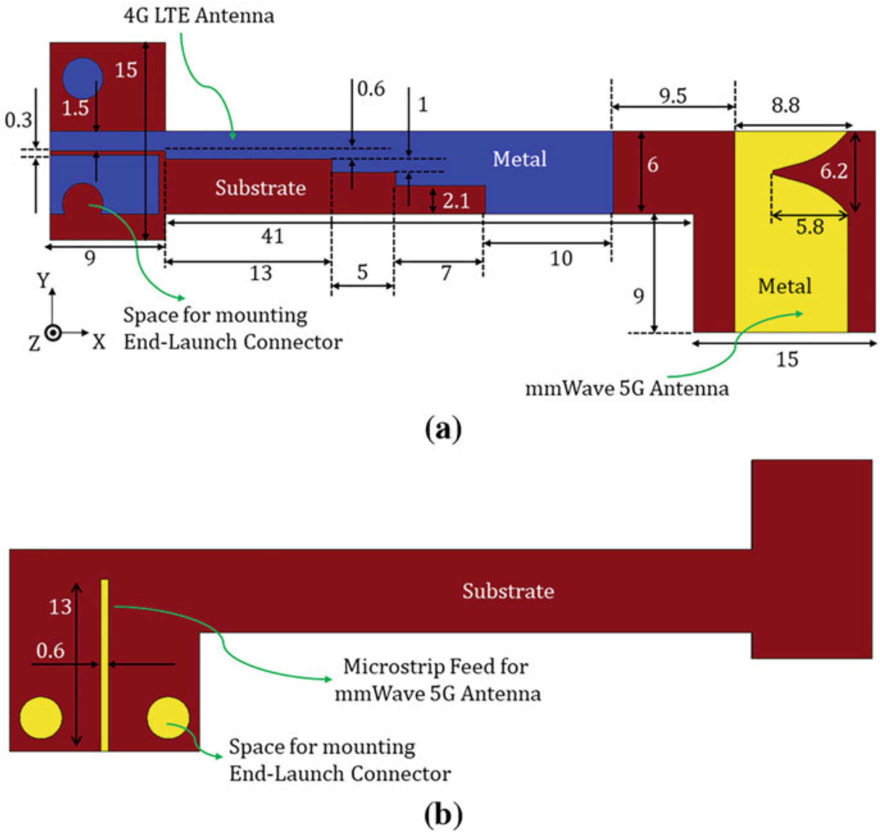

Fig. 7.36 Polycarbonate-based 4G LTE and mmWave 5G antenna module. (Adapted from [17])

An electrically compact Vivaldi antenna is designed for mmWave 5G frequencies on the same polycarbonate substrate on which 4G LTE ACS-fed antenna is designed as illustrated in Fig. 7.36. The electrical size of presented Vivaldi antenna is small with dimensions of 0.56 $\lambda \times$ 0.82 $\lambda \times$ 0.046 λ at 28 GHz which is compatible for side-edge panel integration into future 5G handsets. A 50 Ω microstrip feed line excites the balun of slot line which is optimized for better impedance matching.

The simulated and measured $|S_{11}|$ plot of the presented mmWave 5G antenna is shown in Fig. 7.39. The presented mmWave 5G antenna is wideband covering frequencies from 23 to 39 GHz with fractional bandwidth of 51.6%. High peak gain of 7.2 dBi is attained across the operating frequency band. The radiating aperture is limited by the side-edge panel height, and therefore limited gain can be obtained. However, gain can be enhanced by various gain enhancement techniques which are feasible in this topology by integrating metamaterial unit cells in the radiating aperture of antenna [18] or by employing dielectric loading [19]. End-fire radiation patterns are attained in the *E*-plane (*XY*-plane) with high pattern integrity.

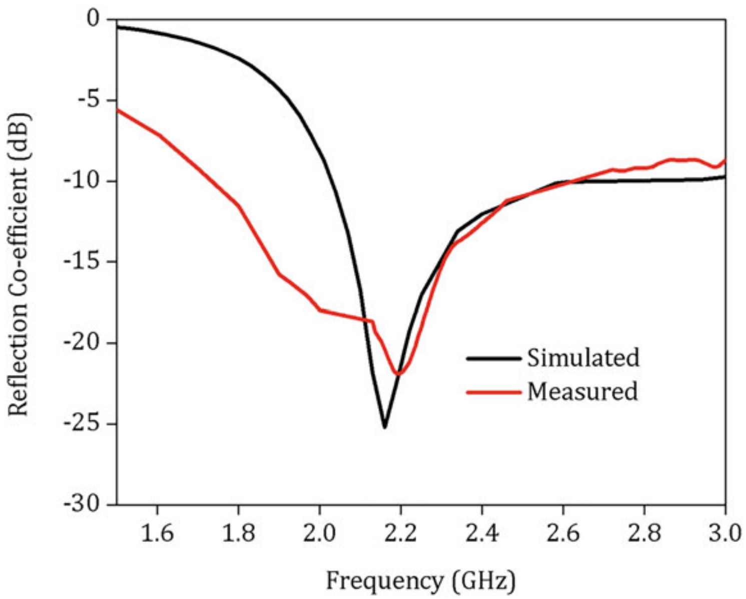

Fig. 7.37 Input reflection coefficient of ACS-fed 4G LTE antenna. (Adapted from [17])

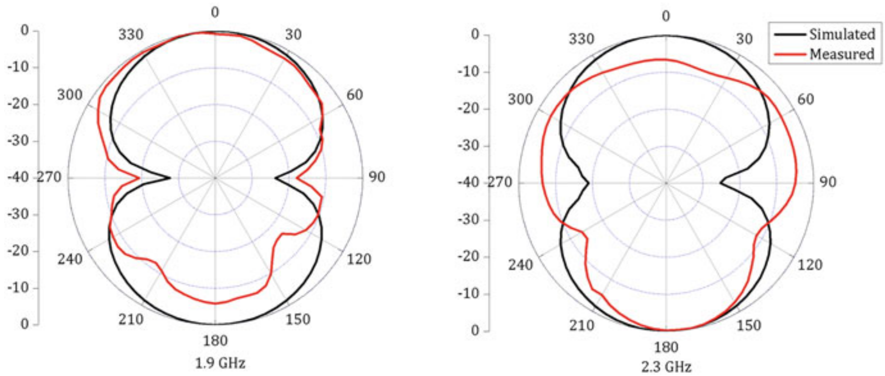

Fig. 7.38 Simulated and measured radiation patterns in *XZ*-plane. (Adapted from [17])

Since the substrate is extended at the feed line which makes the metallic tapers of presented Vivaldi antenna asymmetrical, thereby producing a beam tilt in the end-fire direction.

The integrated 4G LTE and mmWave 5G MIMO antennas are inserted inside the typical smartphone along the side-edge panel as illustrated in Fig. 7.40. Orthogonal pattern diversity is achieved for mmWave 5G Vivaldi antennas. Since the overall dimensions of 4G–5G antenna module are $6 \times 64.5 \times 0.5$ mm^3, which is minimal thereby can be easily integrated inside the handset. The antenna characteristics remain almost invariant since 4G–5G antenna modules are electrically far from each other.

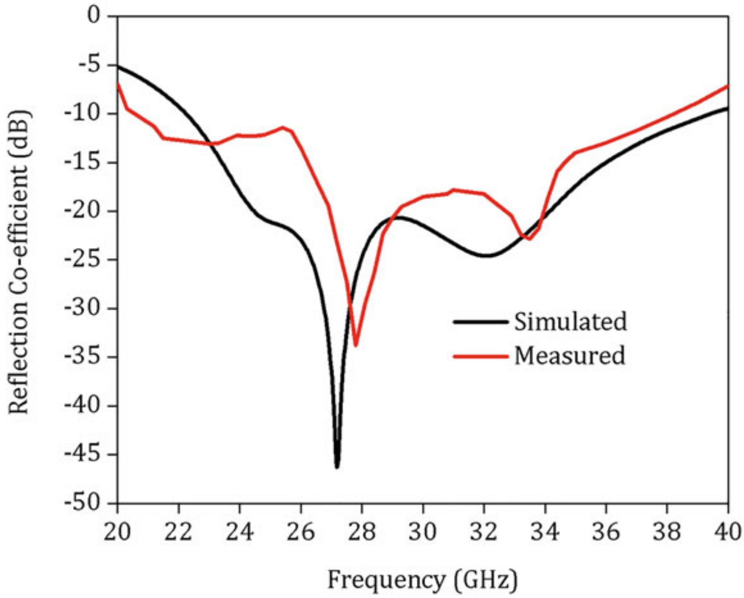

Fig. 7.39 $|S_{11}|$ of presented electrically compact mmWave 5G Vivaldi antenna. (Adapted from [17])

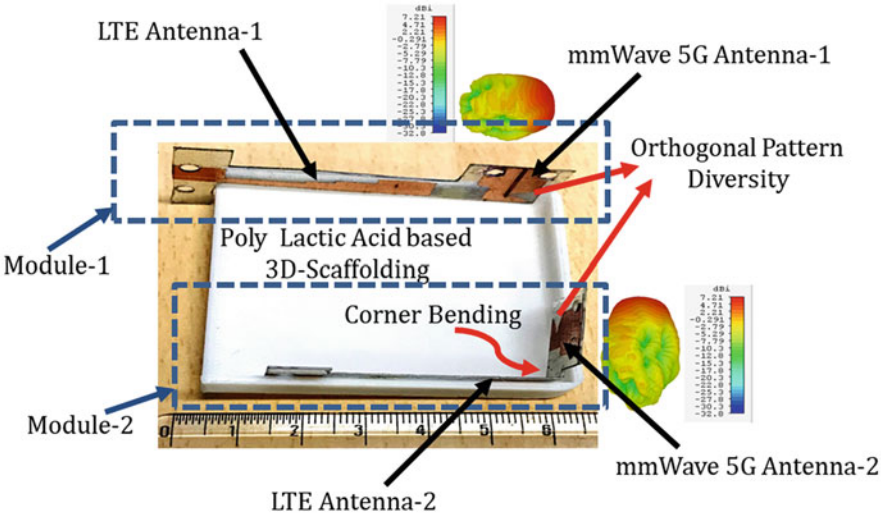

Fig. 7.40 Co-designed low-cost substrate-based 4G–5G antenna module accommodated inside a typical 3D-5G mobile case. (Adapted from [17])

The co-designed 4G–5G antenna modules presented above investigated different design topologies applicable for 5G handsets. Different techniques were implemented for coverage of 4G LTE and mmWave 5G frequencies. For mmWave 5G frequencies, antennas either exhibit beam steering or orthogonal pattern diversity for wider beam coverage and orthogonal mode operation, respectively. For 4G LTE frequencies, MIMO technique is implemented for increasing the data rates. Table 7.2 illustrates the comparison of various performance characteristics of presented integrated 4G–5G antenna modules.

Although the antenna modules explored above displays promising results about their applicability for typical 5G smartphones, however the performance needs further improvement which makes them more suitable for 5G smartphone applications. The integration of presented co-designed 4G–5G antenna modules inside 5G smartphone are limited by various factors like large physical footprint, low gain at mmWave frequencies, large antenna physical width which would be inappropriate for panel integration into future 5G handsets.

The antenna design-I [13] implements 4G–5G co-design on different substrates which makes them almost independent and therefore occupies large physical footprint which limits their applicability into 5G handsets. Moreover, the mmWave Vivaldi array attains a peak gain of only 7 dBi when the beam is radiated in the end-fire direction at 0°, the gain is further reduced when beam is steered at higher angles which further limits their suitability for 5G mobile terminals. The 4G–5G co-design-II investigated the shared 4G–5G radiator integrated along the panel edge of smartphone; however, the width of antenna is 14 mm which is huge and may be not feasible for current smartphones whose panel height is less than 7 mm. The antenna design-III also proposed highly miniaturized 4G LTE antenna integrated with mmWave 5G conformal patch antenna inserted along the panel of 5G handset, but the 4G LTE antenna covers only single LTE frequency band thereby limits carrier aggregation. Also, the width of antenna is 13 mm which limits the integration capability into future smartphones. The co-designed 4G–5G antenna module-IV achieves better performance but it covers large physical footprint which would hinder its integration into future 5G smartphones. Moreover, nowadays mmWave 5G antennas, in particular, are designed along the side-edge panel so that enough space in the smartphone will be available for other circuitry to be accommodated with ease. Therefore, this antenna module may not be suitable for future 5G handsets. Similarly, the integrated 4G LTE and mmWave 5G antenna module-V presents low-cost design with orthogonal pattern diversity for 5G mobile terminals. Although the antenna module bears a width of only 6 mm which would be suitable for easier integration into future mobile terminals, however the gain of mmWave 5G antennas still has many rooms to be improved. Also, the radiation patterns attained for mmWave 5G antenna are not so uniform across the entire operating band.

For future smartphones, the design and integration of 4G–5G antennas is going to be critical. The co-designed 4G LTE and mmWave 5G antenna module need to be designed on a single substrate with a small form factor so that the whole module can be easily accommodated inside the 5G mobile terminal. The 4G LTE and mmWave 5G antennas should be designed very close to each other or should be designed with shared topology so that the physical footprint of entire antenna module is going to be minimal, provided the microwave and mmWave antennas

Table 7.2 Comparison of various performance characteristics among presented co-designed 4G–5G antennas

Figures of merit	[13]	[14]	[15]	[16]	[17]
4G Antenna					
Physical footprint	Relatively high	Relatively small	Highly miniaturized	Relatively high	Relatively small
Fractional bandwidth (BW)	Very high (both LB and HB covered)	High (only HB covered)	Very low (only single class 7 band covered)	Low (only single class 7 band covered)	High (only HB covered)
Operating LTE bands	LTE 700/1900/2300/2500	LTE 1900/2300/2500	LTE 2500	LTE 2500	LTE 1900/2300/2500
Antenna type	Multiband	Wideband	Narrowband	Dual band	Wideband
MIMO implementation	No	Yes	Yes	Yes	Yes
Corner bent/conformal	No	Yes	Yes	No	Yes
Radiator topology	Disconnected from mmWave 5G radiator	Shared with mmWave 5G radiator	Disconnected from mmWave 5G radiator	Shared with mmWave 5G radiator	Disconnected from mmWave 5G radiator
Integration inside mobile terminal	Side-edge panel integration	Side-edge panel integration	Side-edge panel integration	Integrated at the bottom plane lying parallel to screen	Side-edge panel integration
5G Antenna					
Single element physical footprint	Relatively small	Relatively high	Relatively high	Relatively high	Relatively small
Impedance bandwidth performance	Wideband (18%)	Ultra-wideband (41%)	Narrowband (7%)	Wideband (18%)	Ultra-wideband (51%)
Peak realized gain	Relatively low	Relatively high	Relatively low	Very high	Relatively low
Orthogonal pattern diversity	No	Yes	Yes	No	Yes
Array implementation	Yes	No	No	Yes	No
Cost	Relatively high	Relatively high	Relatively high	Relatively high	Low
Radiation pattern type	End-fire	End-fire	Broadside	End-fire	End-fire

should operate independently. The mmWave 5G antennas should radiate away from user possessing pattern diversity or beam steering.

In order to save space inside a smartphone, antennas are integrated along the panel edge. Moreover, the decrease in bezel area of the mobile device from year to year prompted antenna designers to implement either Antenna-on-Display (AoD) [20] or to design antennas along the panel edge for better radiation characteristics. Since the design and implementation of AoDs are very intricate, antennas designed along the panel edge of smartphone are comparatively easier to implement. However, the effect of smartphone panel/metal rim on the radiation properties of integrated antennas should be properly analyzed. It will be challenging to design compact co-designed 4G–5G antennas with uniform radiation patterns and without any frequency detuning in presence of metal-based panel edge of smartphone. The low panel height of smartphone will also be a design constraint for 4G–5G integrated antennas.

From the last few years, mobile antennas are designed using multilayered substrate topology inside a package along with radio frequency integrated circuits (RFICs) which are termed as Antenna-in-Package (AiP) [21]. The purpose of antenna-in-package (AiP) technology is to reduce the overall size of transceiver systems and to decrease the transmission losses which are higher in discrete antenna systems in which RFICs and antennas are designed separately. Therefore, the integrated 4G–5G antennas designed and integrated inside a package with RFICs might be more suitable for 5G smartphones.

7.5 Summary

Evolution of antennas for different mobile generation networks is presented in detail with their characteristics. Design constraints for 4G LTE and mmWave 5G antennas are investigated along with their coexistence. Various specifications are explored for integrated 4G–5G antenna design and its integration inside the typical 5G handset. The rationale behind co-designing of 4G–5G antennas is also analyzed. Various 4G–5G co-designed antenna examples are surveyed along with their applicability for modern thin-panel-based smartphones. Some insights for future 4G–5G co-designed antennas are presented with various design complications.

References

1. J. Retartha, B. Riordan, J. Tingey, K. Vega, J.S. O'Rourke, *Antennagate: Apple's Loss of Signal (a)* (The Eugene D. Fanning Center for Business Communication, Mendoza College of Business, University of Notre Dame, Notre Dame, 2010)
2. H.T. Friis, A note on a simple transmission formula. Proc. IRE **34**(5), 254–256 (1946)
3. G.-H. Zhao, A.-G. Wang, W. Leng, B. Chen, H. Chen, Wideband internal antenna with coupled feeding for 4G mobile phone. Microw. Opt. Technol. Lett. **55**(3), 513–516 (2013)

4. A. Affandi, R. Azim, M.M. Alam, M.T. Islam, A low-profile wideband antenna for WWAN/LTE applications. Electronics **9**(3), 393 (2020)
5. D. Serghiou, M. Khalily, V. Singh, A. Araghi, R. Tafazolli, Sub-6 GHz dual-band 8x8 MIMO antenna for 5G smartphones. IEEE Antennas Wirel. Propag. Lett. **19**(9), 1546–1550 (2020)
6. N. Agnihotri, G.S. Karthikeya, K. Veeramalai, A. Prasanna, S.S. Siddiq, Super wideband conformal antenna array on cylindrical surface, in *2016 21st International Conference on Microwave, Radar and Wireless Communications (MIKON), Krakow*, (2016), pp. 1–4
7. T.S. Rappaport et al., Millimeter wave mobile communications for 5G cellular: It will work! IEEE Access **1**, 335–349 (2013)
8. W. Roh et al., Millimeter-wave beamforming as an enabling technology for 5G cellular communications: Theoretical feasibility and prototype results. IEEE Commun. Mag. **52**(2), 106–113 (2014)
9. Y. Huo, X. Dong, W. Xu, 5G Cellular user equipment: From theory to practical hardware design. IEEE Access **5**, 13992–14010 (2017)
10. S.X. Ta, H. Choo, I. Park, Broadband printed-dipole antenna and its arrays for 5G applications. IEEE Antennas Wirel. Propag. Lett. **16**, 2183–2186 (2017)
11. J. Shim, J. Go, J. Chung, A 1-D tightly coupled dipole array for broadband mmWave communication. IEEE Access **7**, 8258–8265 (2019)
12. I. Hwang, B. Ahn, S. Chae, J. Yu, W. Lee, Quasi-Yagi antenna array with modified folded dipole driver for mmWave 5G cellular devices. IEEE Antennas Wirel. Propag. Lett. **18**(5), 971–975 (2019)
13. J. Kurvinen, H. Kähkönen, A. Lehtovuori, J. Ala-Laurinaho, V. Viikari, Co-designed mmwave and LTE handset antennas. IEEE Trans. Antennas Propag. **67**(3), 1545–1553 (2019)
14. M. Idrees Magray, G.S. Karthikeya, K. Muzaffar, S.K. Koul, Corner bent integrated design of 4G LTE and mmWave 5G antennas for mobile terminals. Prog. Electromagn. Res. M **84**, 167–175 (2019)
15. M. Idrees Magray, G.S. Karthikeya, K. Muzaffar, S.K. Koul, Compact co-design of conformal 4G LTE and mmWave 5G antennas for mobile terminals. IETE J. Res. (2019). https://doi.org/10.1080/03772063.2019.1690593
16. M. Ikram, N. Nguyen-Trong, A.M. Abbosh, Realization of a tapered slot array as both decoupling and radiating structure for 4G/5G wireless devices. IEEE Access **7**, 159112–159118 (2019)
17. I.S. Masoodi, I. Ishteyaq, K. Muzaffar, M. Idrees Magray, Low cost substrate based compact antennas for 4G/5G side-edge panel smartphone applications. Prog. Electromagn. Res. Lett. **91**, 145–152 (2020)
18. K. Muzaffar, M.I. Magray, G.S. Karthikeya, S.K. Koul, High gain broadband Vivaldi antenna for 5G applications, in *2019 International Conference on Electromagnetics in Advanced Applications (ICEAA), Granada, Spain*, (2019), pp. 496–497
19. K. Kota, L. Shafai, Gain and radiation pattern enhancement of balanced antipodal Vivaldi antenna. Electron. Lett. **47**(5), 303–304 (2011)
20. J. Park, S.Y. Lee, J. Kim, D. Park, W. Choi, W. Hong, An optically invisible antenna-on-display concept for millimeter-wave 5G cellular devices. IEEE Trans. Antennas Propag. **67**(5), 2942–2952 (2019)
21. D. Liu, X. Gu, C.W. Baks, A. Valdes-Garcia, Antenna-in-package design considerations for Ka-band 5G communication applications. IEEE Trans. Antennas Propag. **65**(12), 6372–6379 (2017)

M. Idrees Magray (Graduate Student Member, IEEE) received the B.Tech degree in electronics and communication engineering from Islamic University of Science and Technology (IUST), Awantipora in 2018. He is currently pursuing his Master's degree with National Chiao Tung University (NCTU), Taiwan, where he is working as research assistant (RA) under the supervision of Prof. Jenn-Hwan Tarng. He received INAE fellowship for 2 months and during that tenure, he worked under the supervision of Prof. S. K. Koul. He worked on various projects at CARE, IIT Delhi, under the guidance of Prof. S. K. Koul. He has authored or coauthored several articles in peer-reviewed journals and conference proceedings. His research interests include co-designed 4G/5G antennas for smartphones, mmWave antennas for mobile terminals and base stations, and antenna in packaging (AiP). He received the Best Project Competition Award in InCAP 2019.

G. S. Karthikeya (Member, IEEE) received his undergraduate degree in electronics and communication engineering in the year 2010 from Visvesvaraya Technological University, Belgaum. He received Master's degree in Microwave Engineering from the University of Kerala in 2012. He worked as an assistant professor at Visvesvaraya technological university from 2013 to 2016. He received his PhD degree at CARE, IIT Delhi in 2019. Currently, he is working as a Project Scientist at CARE, IIT Delhi in collaboration with Synergy Microwave Corporation, USA. He has authored or coauthored more than 55 articles in peer-reviewed journals and international conference proceedings. He has also filed four Indian patents and two US patents. He is also coauthor of the book, "Millimeter Wave Antennas for 5G Mobile Terminals and Base Stations" published by CRC Press. His research interests include mmWave antennas for mobile terminals and base stations.

J. H. Tarng (Senior Member, IEEE) is a Professor in the Department of Electrical Engineering and Dean of College of Electrical and Computer Engineering, National Chiao Tung University. Prof. Tarng research interests include Antennas, RFIC Design, Radio Channel Modeling, and Measurement and RFID/IoT (Internet of Things). He has published more than 100 referred journal papers and conference papers. He was on leave to ITRI (Industrial Technology Research Institute, the largest government founded research) as the general director of ISTC (2007–2011), and Service Systems Technology Center (2011–2016, merging two other centers). Now he is the Co-PI of the Center for mmWave Smart Radar Systems and Technologies (a flag-ship project). In the center, he is also the PI of the subproject entitled large and scalable mmWave digital phased antenna array.

Shiban K. Koul (Life Fellow, IEEE) received the B.E. degree in Electrical Engineering from the Regional Engineering College, Srinagar, India, in 1977 and the M.Tech. and Ph.D. degrees in Microwave Engineering from the Indian Institute of Technology Delhi, New Delhi, India, in 1979 and 1983, respectively. He is currently an Emeritus Professor at the Indian Institute of Technology, Delhi. He served as Deputy Director (Strategy and Planning) at IIT Delhi from 2012 to 2016 and Mentor Deputy Director (Strategy and Planning, International affairs) at IIT Jammu from 2018 to 2020. He also served as the Chairman of Astra Microwave Products Limited, Hyderabad from 2009 to 2019 and Dr. R.P. Shenoy Astra Microwave Chair Professor at IIT Delhi from 2014 to 2019. His research interests include RF MEMS, High Frequency Wireless Communication, Microwave Engineering, Microwave Passive and Active Circuits, Device modeling, Millimeter wave IC Design, and Reconfigurable Microwave Circuits including Antennas. He has successfully completed 38 major sponsored projects, 52 consultancy projects, and 60 technology development projects. He has authored/coauthored 450 Papers, 11 state-of-the art Books, and 3 Book Chapters. He holds 13 patents and 6 copyrights. Prof. Koul is a Life Fellow of the IEEE, USA, Fellow of the Indian National Academy of Engineering, India, and Institution of Electronics and Telecommunication Engineers (IETE), India. He is the Chief Editor of IETE Journal of Research and Associate Editor of the International Journal of Microwave and Wireless Technologies, Cambridge University Press. He served as a Distinguished Microwave Lecturer of IEEE MTT-S for the period 2012–2014. He also served as an AdCom member of the IEEE MTT-S from 2010 to 2018 and is presently a member of the Awards, Nomination and Appointments, MGA, M&S, and Education committees of the IEEE MTT-S.

Dr. Koul is recipient of numerous awards including IEEE MTT Society Distinguished Educator Award (2014); Teaching Excellence Award (2012) from IIT Delhi; Indian National Science Academy (INSA) Young Scientist Award (1986); Top Invention Award (1991) of the National Research Development Council for his contributions to the indigenous development of ferrite phase shifter technology; VASVIK Award (1994) for the development of Ka-band components and phase shifters; Ram Lal Wadhwa Gold Medal (1995) from the Institution of Electronics and Communication Engineers (IETE); Academic Excellence Award (1998) from Indian Government for his pioneering contributions to phase control modules for Rajendra Radar, Shri Om Prakash Bhasin Award (2009) in the field of Electronics and Information Technology, VASVIK Award (2012) for the contributions made to the area of Information, Communication Technology (ICT), and M N Saha Memorial Award (2013) from IETE.

Chapter 8
Application of the Whale Optimization Algorithm to Antenna Design for mm-Wave 5G Communications Systems

Sotirios K. Goudos

8.1 Introduction

The 5G New Radio (NR) proposed frequency bands by 3GPP include two distinct frequency ranges [1, 2]. It is a well-known fact that the new emerging 5G technology will use both frequency ranges (FR 1 and FR 2) above and below 6 GHz. Frequency Range 2 (FR2) [2] includes frequency bands in milliliter wavelengths from 24.25 to 52.6 GHz. Hence, the antenna engineer is faced with new challenges regarding the antenna design for the new 5G devices. This is more evident with respect to antenna design in the millimeter-wave band [21, 22]. Among others, the desired characteristics of these antennas in 5G cellular communications require circular polarization (CP) and wide bandwidth. CP is considered as a key factor that can reduce the delay spread in a multi-path environment [18].

Patch antennas constitute an attractive solution for 5G antenna design. This is due to their advantages like low profile, ease of fabrication, and relatively low cost. Several researchers in the literature have designed and fabricated antennas with acceptable performance in millimeter-wave frequency bands [4, 17]. The E-shaped patch antenna is a popular shape found in the literature [10, 14, 30]. The motivation for adopting this design is to increase the original rectangular patch functionality and bandwidth by integrating slots in the patch. The main features of this antenna are wide-band operation and linear polarization. The authors in [16] present a modification to E-shaped antenna design that is a half-shaped patch with an additional shorting bar. The modified E-shaped antenna is circularly polarized in the frequency of interest. The authors in [16] present a two layered, probe fed, half E-shaped antenna for operation at 2.4 GHz. The authors in [11, 12] present designs

S. K. Goudos (✉)
ELEDIA@AUTH, Department of Physics, Aristotle University of Thessaloniki, Thessaloniki, Greece
e-mail: sgoudo@physics.auth.gr

M. A. Matin (ed.), *Wideband, Multiband, and Smart Antenna Systems*, Signals and Communication Technology, https://doi.org/10.1007/978-3-030-74311-6_8

of half E-shaped patch antennas for operation at two different 5G frequencies (3.7 and 26 GHz). The antenna designs are accomplished using a hybrid GWO-Jaya algorithm.

Antenna design requires the simultaneous optimization of several different geometrical parameters. An optimization algorithm or technique is a suitable approach for solving this problem. In the literature, there are several examples of patch antenna design and optimization using different evolutionary algorithms (EAs). These approaches include Genetic Algorithms (GA) [13, 26] Particle Swarm Optimization (PSO) [14], Differential Evolution (DE) [25, 30], and Teaching-Learning-Optimization (TLBO) [10].

The WOA is a nature-inspired Swarm Intelligence (SI) algorithm that is introduced in [19]. The WOA is based on the social and the hunting behavior of humpback whales. In this chapter, we apply WOA for half-E-shaped patch antenna design. We present a design case of half E-shaped patch antenna for operation at 39 GHz, which covers the n260 band defined by 3GPP [2]. This antenna is fabricated on a Taconic substrate with 2.2 dielectric constant. We apply a single microstrip feed that provides additional design simplicity. The proposed antenna is circularly polarized in an acceptable bandwidth of the operating frequency. Moreover, the derived antenna presents an ultra wide-band behavior that covers a large part of the FR2 band.

8.2 Related Work

There are several examples in the literature that use evolutionary algorithms for 5G antenna design. The authors in [9] design three different antenna types: a pixelated patch, a patch with shorting pins and a monopole antenna using a GA. The GA is also used in [24] for designing an electromagnetic bandgap (EBG) structure for two planar antennas operating at 28 GHz. Moreover, the authors in [28] design a 77 GHz series-fed patch array antenna using a binary GA. A multi-objective approach is applied by the authors in [27] where they design pixelated patch antenna using the non-dominated sorting genetic algorithm (NSGA-II). The proposed antenna works in three bands 18.4, 25, and 28 GHz.

Additionally, the authors in [7] use a new emerging algorithm the Salp Swarm Algorithm [20] for designing a MIMO bow tie antenna at 28 GHz. The authors in [3] use another emerging algorithm the Social Spider Algorithm [29] for designing a reconfigurable antenna for operation at 26 GHz.

Moreover, a comparative study on patch antenna design for 5G systems is performed in [15] using three different algorithms the PSO, the cross-entropy (CE), and covariance matrix adaptation evolutionary strategy (CMA-ES) for operation in the frequency range of 12–18 GHz. The authors in [10] optimize an E-shaped patch antenna for operation in 25 GHz using the TLBO algorithm. Finally, a hybrid Grey Wolf Optimizer-Jaya (GWO-Jaya) is applied in [12] for two different half-E-shaped antennas operating at 3.7 and 26 GHz.

Table 8.1 Comparison of different antenna designs using evolutionary algorithms for 5G applications

Antenna type	Algorithm	Design frequency	Reference
Pixelated patch	GA	2.4, 5.8 GHz	[9]
Planar EBG	GA	28 GHz	[24]
Series-fed patch array	GA	77 GHz	[28]
Pixelated patch	NSGA-II	18.4, 25, 28 GHz	[27]
MIMO	SSA	28 GHz	[7]
Reconfigurable	Social Spider	26 GHz	[3]
Patch antenna	PSO, CE, CMA-ES	12–18 GHz	[15]
Half-E-shaped	Hybrid GWO-Jaya	3.7 and 26 GHz	[12]

The above details are summarized in Table 8.1.

8.3 Whale Optimization Algorithm

The WOA is a nature-inspired SI algorithm that is proposed in [19]. WOA basic concept is the social and the hunting behavior of humpback whales. In their natural environment, the whales after they identify the prey location, they perform specific movements to encircle them. In WOA terminology, the prey denotes the best solution vector obtained in each iteration. The population members (whales) are trying to come close to that best solution, and they are updating their positions accordingly. This type of whale behavior (prey encirclement) is in WOA expressed mathematically by

$$D_k = \left| C_k \times x_{k,G}^{best} - x_{k,G}^{m} \right| \tag{8.1}$$

$$x_{k,G+1}^{i} = x_{k,G}^{best} - A_k D_k \tag{8.2}$$

where G denotes the current iteration, $x_{k,G}^{m}$ is the m-th population member in the k-th dimension, $x_{k,G}^{best}$ is the best solution found in the k-th dimension, D_k denotes the distance vector of the current whale to the prey, and C_k, A_k are the k-th dimension coefficient vectors. These latter coefficient vectors are derived as

$$A_k = 2a_k rnd_k - a_k \tag{8.3}$$

$$C_k = 2 \times rnd_k \tag{8.4}$$

where a_k denotes a number $\in$ [2, 0], that is linearly decreased during the iteration process, and rnd_k is a uniformly distributed random number $\in$ [0, 1].

Moreover, the exploitation phase of the optimization algorithm corresponds to the bubble-net behavior of humpback whales. This phase is modeled mathematically by WOA. WOA accomplishes this modeling using the combination of two different movement mechanisms: the encircling mechanism with a shrinking radius and the updating position mechanism with a spiral trajectory. The latter is expressed mathematically as

$$x_{k,G+1}^{m} = B_k e^{ps} cos(2\pi s) + x_{k,G}^{best} \tag{8.5}$$

where B_k is the k-th coordinate of the distance vector of the m-th solution to the best solution, p is a constant number that defines the shape of the logarithmic spiral, and s is a uniformly distributed random number $\in [-1, 1]$.

Simultaneously, the whales make two types of movements; they swim toward the prey in a circle with a shrinking radius and along a spiral-shaped trajectory. This fact is modeled by authors in [19] using a 50% probability, that can be written as

$$x_{k,G+1}^{m} = \begin{cases} x_{k,G}^{best} - A_k D_k, & if \;\; b < 0.5 \\ B_k e^{ps} cos(2\pi s) + x_{k,G}^{best}, & otherwise \end{cases} \tag{8.6}$$

where b is a uniform random number $\in [0, 1]$. Additionally, the exploration phase of WOA corresponds to the humpback whales random search for prey. This can be modeled mathematically as

$$D_k = \left| C_k \times x_{k,G}^{r} - x_{k,G}^{i} \right| \tag{8.7}$$

$$x_{k,G+1}^{i} = x_{k,G}^{r} - A_k D_k \tag{8.8}$$

where r, with $r \neq i$ is a randomly selected member of the population that the i-th member will follow.

The pseudo-code of WOA is given in Algorithm 1. WOA was utilized for wearable Wi-Fi antenna design in [8].

8.4 Half E-shaped Patch Antenna

The E-shaped patch antennas are wideband and linearly polarized (LP). One of the many possible applications of patch antennas is high-speed short distance communication. Moreover, such communication systems have usually a key requirement to operate using circular polarization (CP). The main benefit of CP is the fact that it disengages the receiver from the dependency of the direction of arrival in an incident electromagnetic wave. CP eliminates the mismatch between the transmitter and the receiver due to misalignment and thus has the potential to improve the efficiency of the antenna. Therefore, it is sometimes important for some applications to design CP

Algorithm 1 WOA algorithm

```
Initialize randomly a population of whales (m = 1, 2, ··· , NP)
Compute the objective function values for each population member x^m
Find the best solution vector x^best
while (i < G_max) do
    for (k = 1 : D) do
        Calculate a_k, rand_k, A_k, C_k
        for (m = 1 : NP) do
            if (b < 0.5) then
                if (|A_k| ≥ 1) then
                    Calculate distance vector D_k using (8.7)
                    Calculate position vector x^m_{k,i+1} using (8.8)
                else
                    Calculate distance vector D_k using (8.1)
                    Calculate position vector x^m_{k,i+1} using (8.2)
                end if
            else
                Calculate position vector x^m_{k,i+1} using (8.5)
            end if
        end for
    end for
    Set: i = i + 1
end while
```

antennas. In order to design a CP antenna based on the E-shaped patch, the authors in [16] design a half E-shaped antenna that operates at 2.4 GHz. The proposed design in [16] consists of two layers and it is probe fed. The half E-shaped CP antenna can be derived from the E-shaped. This is depicted in Fig. 8.1, where the shape evolution is shown.

From these figures we may observe that the half E-shaped CP antenna requires the addition of a shorting bar of width W_b. This shorting bar induces currents in the y-direction. Thus, it allows the CP operation of the antenna. We may notice that one important factor that affects the Axial Ratio (AR) bandwidth is the shorting bar position. Thus, the suitable shorting bar position is another unknown variable.

8.4.1 Antenna Design Procedure

The geometry of a modified half E-shaped patch antenna is illustrated in Fig. 8.2. One may notice that the antenna geometry is quite complex. It consists of 12 different geometrical design parameters. Hence, it will be very difficult or even impossible to estimate the effect of each design parameter in order to achieve the desired antenna performance. Thus, an optimization technique is the obvious solution to this design problem. If there is a need for a circular polarized antenna, the design should take into account the antenna axial ratio (AR).

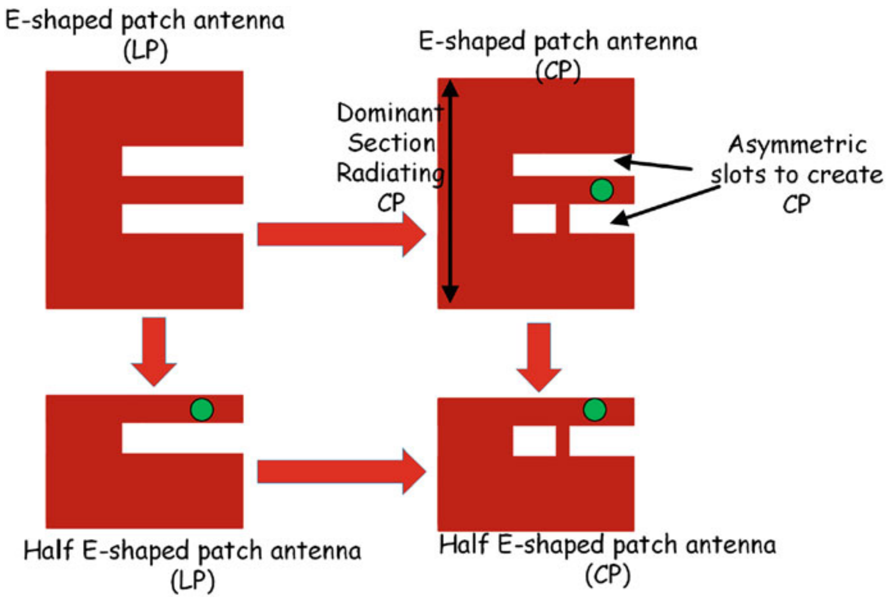

Fig. 8.1 The evolution of shape from the LP E-shaped antenna to CP Half E-shaped antenna [16]

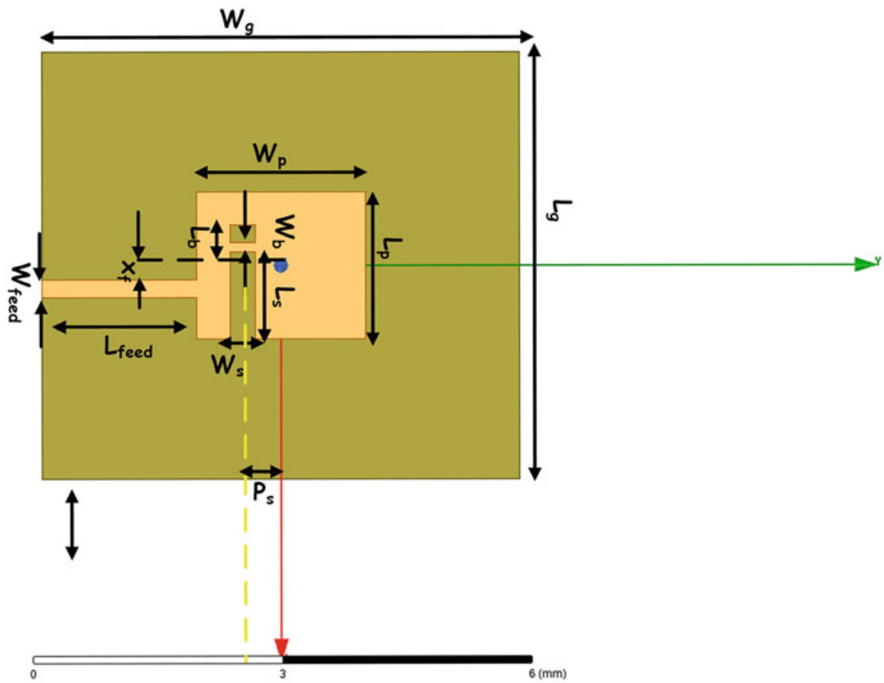

Fig. 8.2 Antenna geometry top view

In this case there are two design objectives, the first is to minimize the S_{11} magnitude at the operating frequency below -10 dB and the second objective is to reduce the AR below 3 dB. We formulate the design problem using the following expression [12]:

$$F(\bar{u}) = S_{11}(\bar{u}) + \xi \times \left| |S_{11}(\bar{u})| - |L_{dB}| \right| + \\ + \xi \times \left| AR(\bar{u}) - L_{AR} \right| \tag{8.9}$$

where $\bar{u}$ is the vector of the antenna geometry design variables, S_{11} is the S_{11} magnitude, and AR is the Axial Ratio at the design frequency, respectively, L_{dB} is the S_{11} dB limit, L_{AR} is the AR dB limit, and ξ is a penalty factor. For both design cases, we select $L_{dB} = -10$ dB and $L_{AR} = 3$ dB.

The computation of such an objective function like (8.9) requires the use of a full-wave numerical method. The half E-shaped patch antenna can be modeled in a commercial full-wave electromagnetic (EM) software. A possible software to use suitable for this task is ANSYS HFSS [5]. Moreover, the integration of the in-house source code of an evolutionary algorithm with such EM solver requires the use of a wrapper program. The implementation of a separate optimizer that calls external software to do the simulations for the evaluation of the objective function can also be found in [6]. In order to integrate the source code of an evolutionary algorithm written in Matlab with ANSYS HFSS, the wrapper program can use the HFFS Matlab API [23]. Thus, in our case the WOA algorithm can be integrated with the wrapper program and call the EM solver. The whole process can be described in Algorithm 2.

Algorithm 2 Antenna design procedure

1: For each new geometry vector $\bar{u}$
2: Generate a HFSS Visual Basic script file from Matlab
3: Run HFSS with the newly created script and generate antenna geometry
4: Calculate the metrics of interest (e.g S_{11}, AR) at desired operating frequency
5: Output a text file with the results from the EM software
6: Read the results from the output file and calculate objective function value
7: Return objective function value to Whale Optimization Algorithm

In the previous example, we need to set the upper and lower limits for every antenna geometrical parameter. This is quite complex and it is frequency dependent. If set the limits of the geometrical parameters, then these are valid only for the specific design for the design frequencies. The question that arises is how to optimize another antenna with the same shape that would operate at different frequencies. One would have to find the appropriate limits again for every geometrical parameter. This procedure requires a lot of computational resources, and it takes more time because one has to perform several tests to find the most suitable limits.

Hence, a more generic frequency independent design procedure can be followed. The basic idea is to set the first two initial parameters, i.e. the patch width W_p

and the patch length L_p, with appropriate limits for specific frequency and then set the other parameters as a perchance of these two. Then the limits for the other unknowns will be within the range of [0, 1]. For example, the twelve optimization variables $(u_1, u_2, \ldots, u_{12})$ in the above-described problem can be expressed as

$$\begin{aligned}
L_p &= u_1 \\
W_p &= u_2 \\
L_g &= (1 + u_3) \times L_p \\
W_g &= (1 + u_4) \times W_p \\
L_s &= u_5 \times L_p \\
W_s &= u_6 \times W_p \\
P_s &= u_7 \times W \\
L_b &= u_8 \times L_p \\
W_b &= u_9 \times W_p \\
L_{feed} &= u_{10} \times (L_p/2) \\
W_{feed} &= u_{11} \times (W_p/2) \\
x_f &= u_{12} \times (L_p/2)
\end{aligned} \tag{8.10}$$

That way if we need to make another design only the limits of the first two optimization variables will have to be determined for the new frequencies. By setting the limits of an optimization variable within [0, 1] decreases the search space and its easier for an evolutionary algorithm to obtain results.

8.5 Numerical Results

In this section, we design the antenna for 5G communication systems. This antenna is designed for operation at 39 GHz. This is the center frequency of the n260 band set by 3GPP for 5G operation between 37–40 GHz. A similar design case was presented in [12] using hybrid Jaya-GWO for operation at 26 GHz.

The antenna geometry for this case is depicted in Figs. 8.2 and 8.3. The antenna is fabricated on a single layer of dielectric, and the feeding is accomplished using 50 Ohm feed line. The dielectric material selected is Taconic material ($\epsilon_r = 2.21$) with 1.58 mm thickness. This type of antenna requires the setting of twelve (12) geometrical parameters. In this case, we optimize the antenna using the WOA algorithm. The population size was set small to 20, while we set the maximum

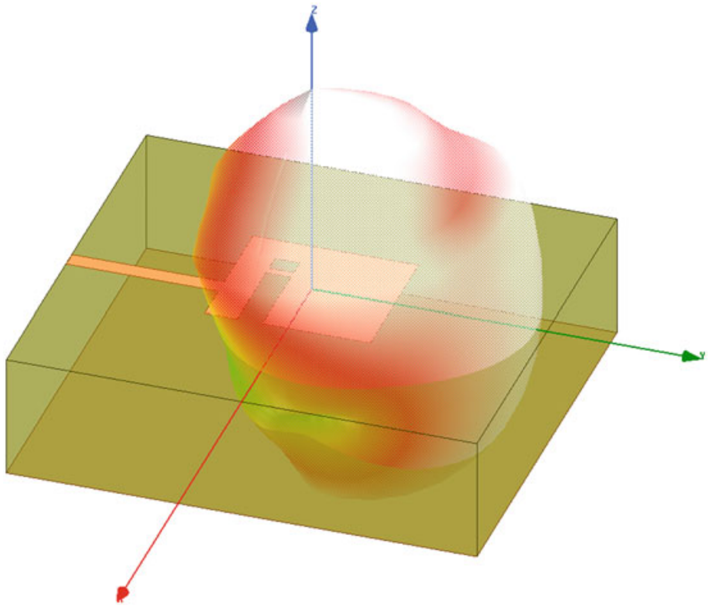

Fig. 8.3 Antenna geometry in 3D view

Table 8.2 WOA statistical results for antenna design

Best	Worst	Mean	Median	St. dev	SR(%)
−17.72	−15.17	−16.34	−16.27	0.87	90

Table 8.3 Parameter values of the best achieved antenna design at 39 GHz

Parameter	Value (mm)	Parameter	Value (mm)
W_p	2.97	W_{feed}	0.25
L_p	1.80	L_{feed}	2.77
W_g	8.52	P_s	0.67
L_g	5.17	W_s	0.44
L_b	0.29	L_s	1.44
W_b	0.06	x_f	0.40

number of objective function evaluations to 2000. We run the WOA for ten independent runs. The SR column in Table 8.2 is for the success rate percentage. If the success rate is less than 100, then the algorithm did not succeed in all runs to find a solution. We notice that WOA failed to obtain a feasible solution in one case so the success rate is 90%. However, we notice the WOA obtained results with small standard deviation. This means the WOA was quite efficient in obtaining the results.

Table 8.3 holds the geometrical parameters of the best design obtained by WOA. Figures 8.4 and 8.5 show the 3D radiation patterns for two different frequencies at

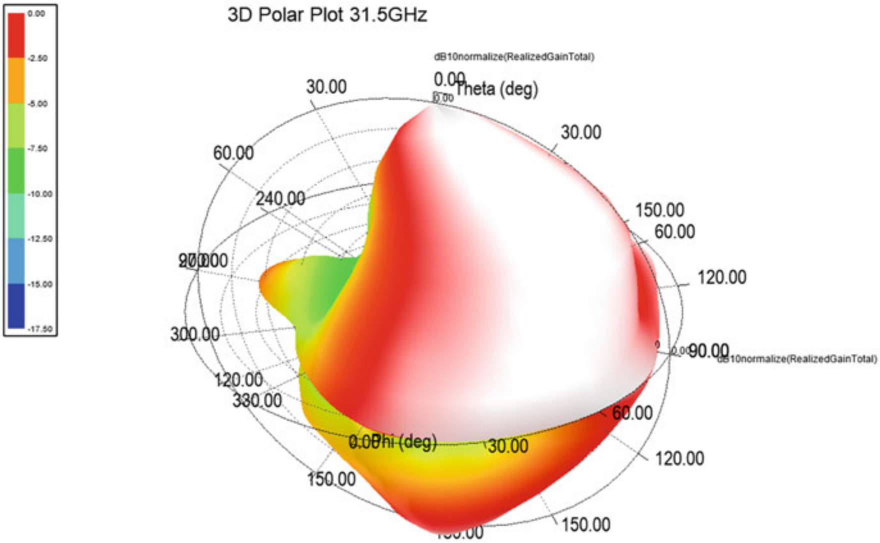

Fig. 8.4 3D gain pattern of the best design found by WOA at 31.5 GHz for 5G operation

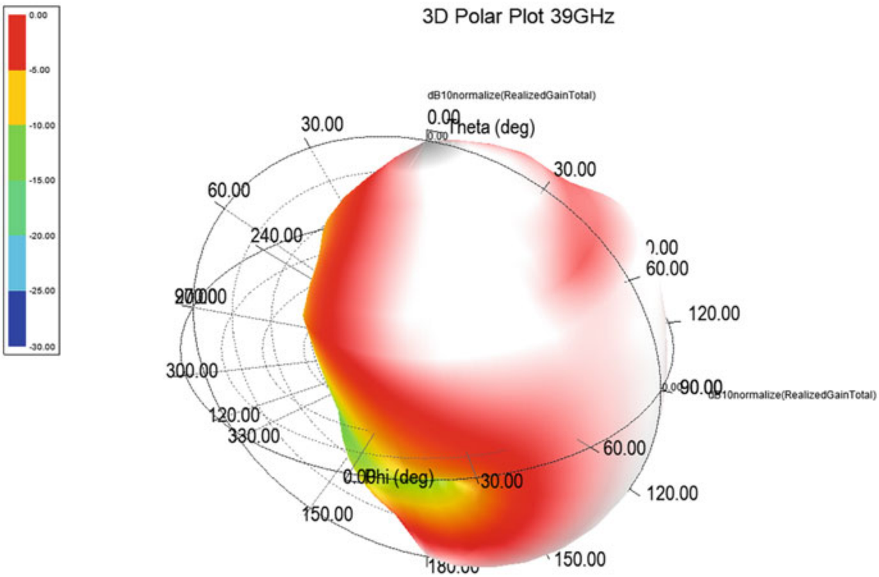

Fig. 8.5 3D gain pattern of the best design found by WOA at 39 GHz for 5G operation

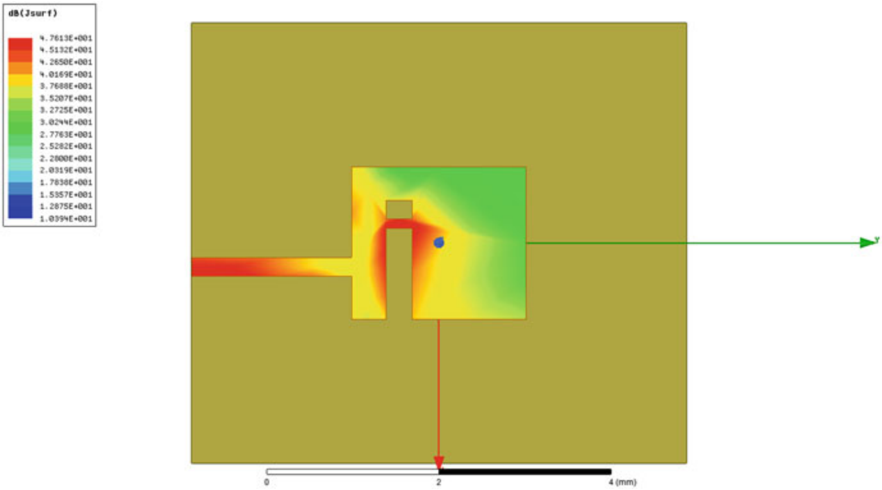

Fig. 8.6 Simulated surface current distribution of the best design at 31.5 GHz for 5G operation

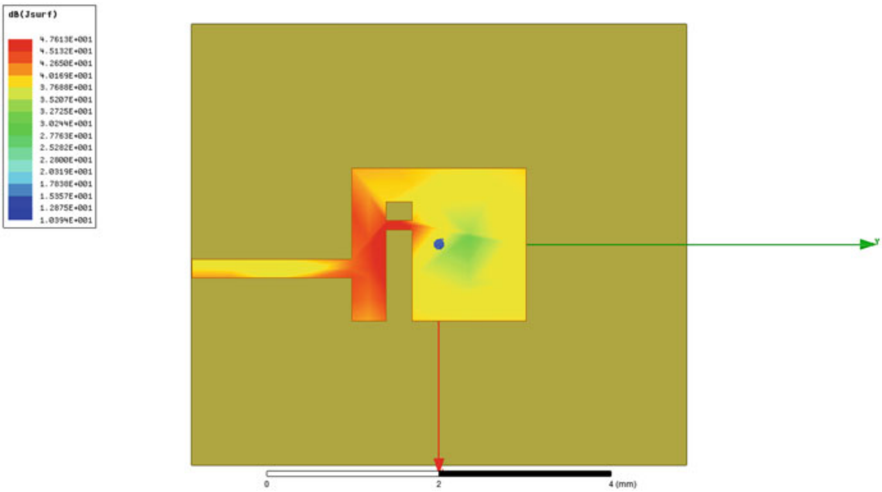

Fig. 8.7 Simulated surface current distribution of the best design at 39 GHz for 5G operation

31.5 and 39 GHz. We notice that the pattern is very close to omni-directional in space for both frequencies. Moreover, Figs. 8.6 and 8.7 depict the corresponding surface current distribution for both same frequencies. One may observe that the surface current for 31.5 GHz shows higher values in the feed line and in the area

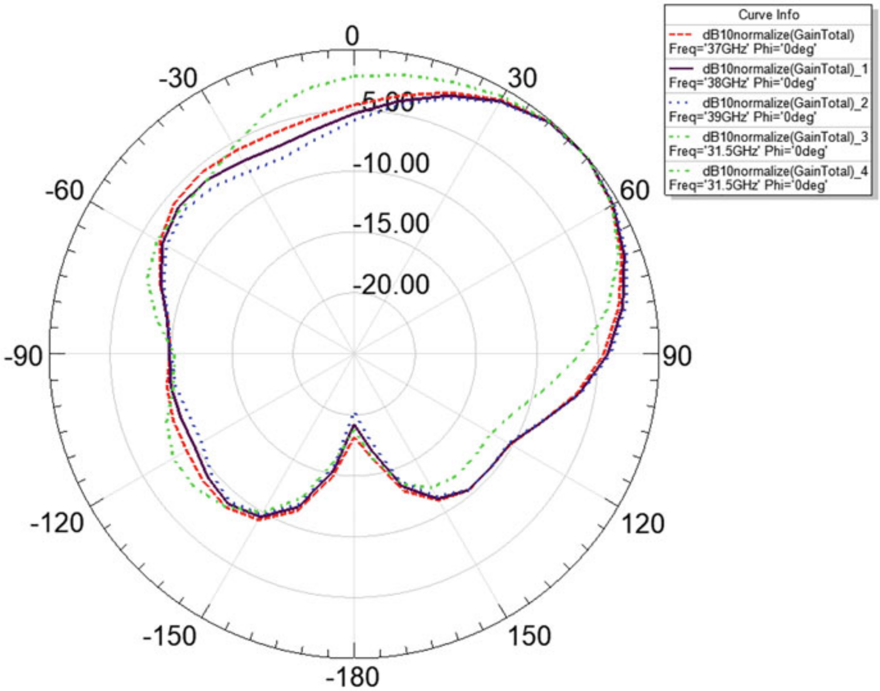

Fig. 8.8 Radiation pattern of the best obtained design by WOA at 31.5, 37, 38, 39 GHz for 5G operation. $\phi = 0^0$

near the shorting bar. Additionally, we notice that the surface current for 39 GHz is higher near the shorting bar and in a small area near the feed line. Figures 8.8, 8.9, and 8.10 present the radiation patterns for three plane cuts for different frequencies at 31.5, 37, 38, 39 GHz. The radiation patterns in the 5G n260 band are quite similar. Radiation patterns for the 31.5 GHz case are close to being uniform in space. Hence, the distribution of the radiated power is judged satisfactory as the gain holds values near the maximum, inside wide areas in space, making the antenna capable of transmitting and receiving, effectively, signals toward and from a large number of various directions. This performance is desirable in case of mobile communications.

Figure 8.11 presents the frequency response for both S_{11} and AR magnitudes. We notice that the obtained antenna shows an ultra wide-band behavior starting from 17 to 40 GHz. At the design frequency of 39 GHz the S_{11} value is -12.16 dB, while the AR magnitude is 1.65. We notice that the antenna is circularly polarized within two frequency zones. The first one, which is smaller, is from 30 GHz to about 30.5 GHz. The second one and larger is from 37.5 to 39.2 GHz. Thus, the $S_{11} - AR$ bandwidth covers a large part of the n260 5G band.

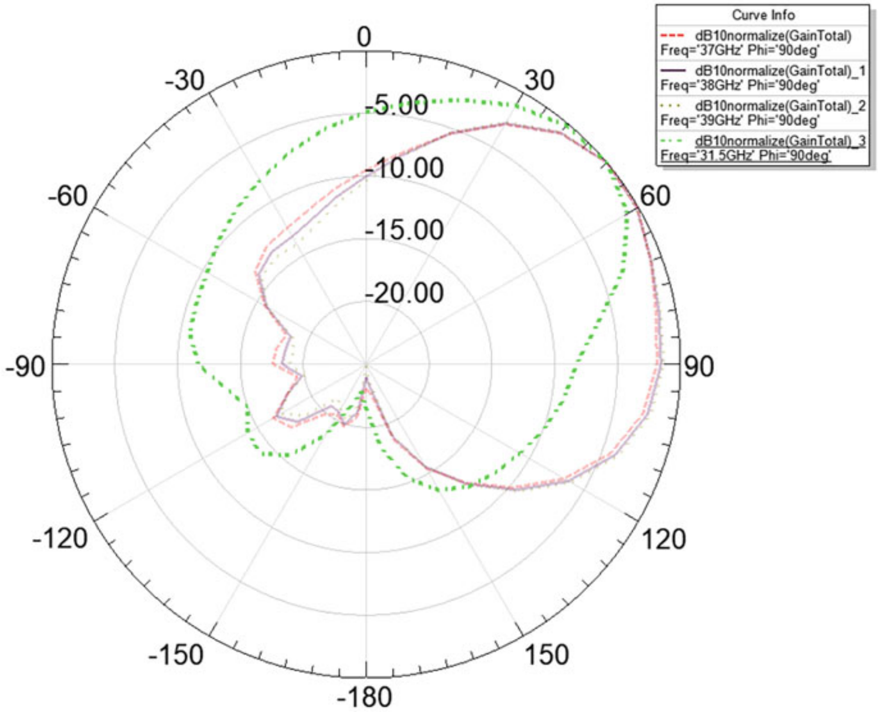

Fig. 8.9 Radiation pattern of the best obtained design by WOA at 31.5, 37, 38, 39 GHz for 5G operation. $\phi = 90^0$

Figure 8.12 shows the VSWR versus frequency plot. One may observe that this is very similar to the previous graph that shows a ultra wide-band behavior. Overall, WOA managed to find an antenna design that covers the strict design requirements for 5G operation and circular polarization.

8.6 Conclusion

We have introduced the application of WOA to 5G antenna design. The antenna is designed for operation in 39 GHz, which is in the n260 FR2 band defined by 3GPP. The antenna gain at the design frequency is about 7.5 dBi. The $S_{11} - AR$ bandwidth in this case is about 1.7 GHz. It is interesting to notice that in this case the antenna is ultra wide band with S_{11} bandwidth larger than 20 GHz. Overall, WOA has proven to be efficient for application in this kind of problem.

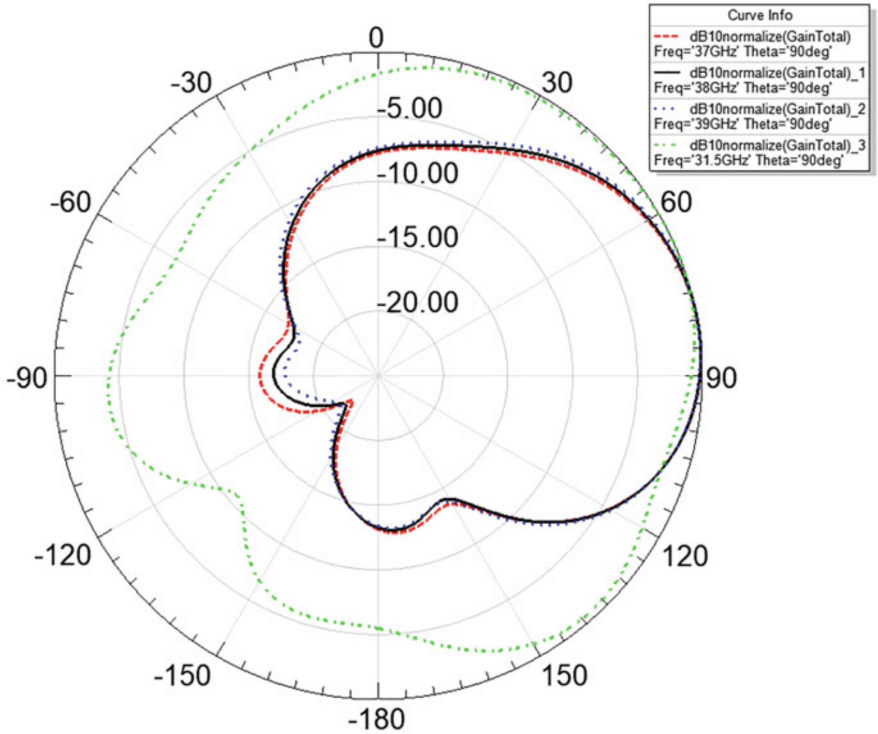

Fig. 8.10 Radiation pattern of the best obtained design by WOA at 31.5, 37, 38, 39 GHz for 5G operation. $\theta = 90^0$

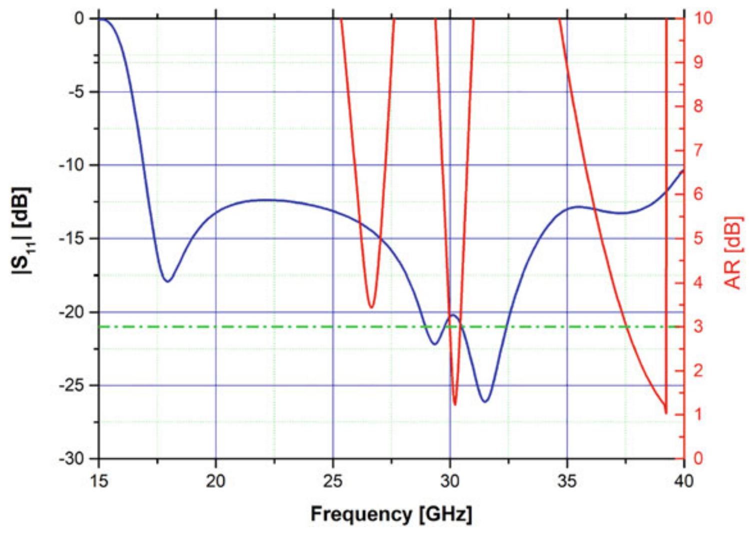

Fig. 8.11 $S_{11} - AR$ plot of the best antenna best design found for 5G operation

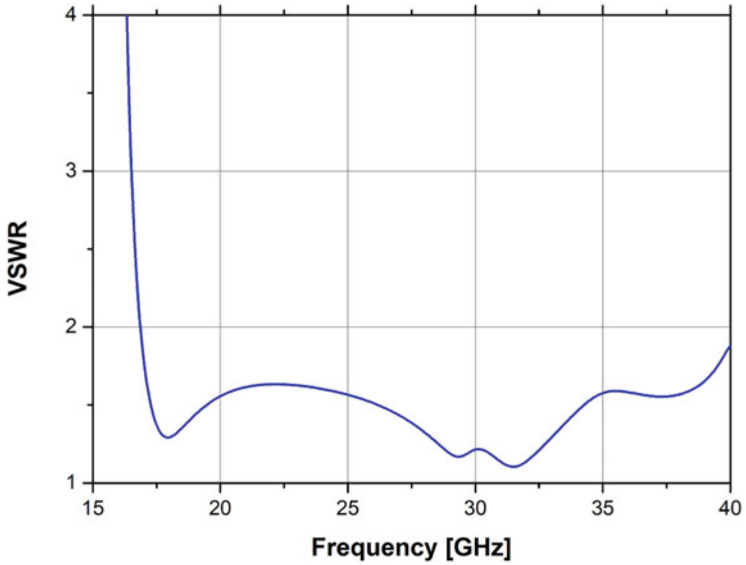

Fig. 8.12 VSWR plot of the best design found by WOA for 5G operation

References

1. 3GPP: TS 38.101-1, nr; user equipment (UE) radio transmission and reception; part 1: Range 1 standalone (release 16.5). Tech. Rep. (2020)
2. 3GPP: TS 38.101-2, nr; user equipment (UE) radio transmission and reception; part 2: Range 2 standalone (release 16.5). Tech. Rep. (2020)
3. M. Abraham, H. Shekhar, Social spider optimized design configuration of multiband reconfigurable antenna for 5G applications. Wireless Pers. Commun. **115**(2), 1161–1175 (2020). https://doi.org/10.1007/s11277-020-07616-4
4. H. Aliakbari, A. Abdipour, R. Mirzavand, A. Costanzo, P. Mousavi, A single feed dual-band circularly polarized millimeter-wave antenna for 5G communication, in *2016 10th European Conference on Antennas and Propagation, EuCAP 2016* (2016)
5. ANSYS: Electomagnetics Suite, ANSYS: User's Guide, Version 16.1 (2015)
6. D.J. Bekers, S. Monni, S.M. van den Berg, A.M. van de Water, B.J. Morsink, C. Alboin, V. Ducros, M. Celikbas, J. Blanche, N. Fiscante, G. Gerini, J.P. Martinaud, M. Rochette, G.H.C. van Werkhoven, Optimization of phased arrays integrated with FSS and feeding elements based on parametric models, in *The Second European Conference on Antennas and Propagation, EuCAP 2007* (2007), pp. 1–7
7. A.D. Boursianis, S.K. Goudos, T.V. Yioultsis, K. Siakavara, P. Rocca, MIMO antenna design for 5G communication systems using salp swarm algorithm, in *2020 International Workshop on Antenna Technology (iWAT)* (2020), pp. 1–3. https://doi.org/10.1109/iWAT48004.2020.1570618331
8. A.D. Boursianis, S. Koulouridis, D. Georgoulas, S.K. Goudos, Wearable 5-gigahertz Wi-Fi antenna design using whale optimization algorithm, in *2020 14th European Conference on Antennas and Propagation (EuCAP)* (2020), pp. 1–4. https://doi.org/10.23919/EuCAP48036.2020.9135735

9. V. Gjokaj, J. Doroshewitz, J. Nanzer, P. Chahal, A design study of 5G antennas optimized using genetic algorithms, in *2017 IEEE 67th Electronic Components and Technology Conference (ECTC)* (2017), pp. 2086–2091. https://doi.org/10.1109/ECTC.2017.286
10. S.K. Goudos, A. Tsiflikiotis, D. Babas, K. Siakavara, C. Kalialakis, G.K. Karagiannidis, Evolutionary design of a dual band e-shaped patch antenna for 5G mobile communications, in *2017 6th International Conference on Modern Circuits and Systems Technologies (MOCAST)* (2017), pp. 1–4
11. S. Goudos, T. Yioultsis, K. Dalidou, K. Siakavara, A low cost wide band and circularly polarized modified half e-shaped patch antenna for 5G mobile communications, in *IET Conference Publications, EuCAP 2018*, vol. 2018 (2018)
12. S.K. Goudos, T.V. Yioultsis, A.D. Boursianis, K.E. Psannis, K. Siakavara, Application of new hybrid jaya grey wolf optimizer to antenna design for 5G communications systems. IEEE Access **7**, 71061–71071 (2019)
13. R.L. Haupt, Antenna design with a mixed integer genetic algorithm. IEEE Trans. Antennas Propag. **55**(3 I), 577–582 (2007)
14. N. Jin, Y. Rahmat-Samii, Parallel particle swarm optimization and finite-difference time-domain (PSO/FDTD) algorithm for multiband and wide-band patch antenna designs. IEEE Trans. Antennas Propag. **53**(11), 3459–3468 (2005)
15. M. Kovaleva, D. Bulger, K.P. Esselle, Comparative study of optimization algorithms on the design of broadband antennas. IEEE J. Multiscale Multiphys. Comput. Tech. **5**, 89–98 (2020). https://doi.org/10.1109/JMMCT.2020.3000563
16. J.M. Kovitz, H. Rajagopalan, Y. Rahmat-Samii, Circularly polarised half e-shaped patch antenna: a compact and fabrication-friendly design. IET Microwaves Antennas Propag. **10**(9), 932–938 (2016)
17. K. Mak, H. Lai, K. Luk, C. Chan, Circularly polarized patch antenna for future 5G mobile phones. IEEE Access **2**, 1521–1529 (2014)
18. T. Manabe, Y. Miura, T. Ihara, Effects of antenna directivity and polarization on indoor multipath propagation characteristics at 60 GHz. IEEE J. Sel. Areas Commun. **14**(3), 441–447 (1996)
19. S. Mirjalili, A. Lewis, The whale optimization algorithm. Adv. Eng. Softw. **95**, 51–67 (2016). https://doi.org/10.1016/j.advengsoft.2016.01.008
20. S. Mirjalili, A.H. Gandomi, S.Z. Mirjalili, S. Saremi, H. Faris, S.M. Mirjalili, Salp swarm algorithm: a bio-inspired optimizer for engineering design problems. Adv. Eng. Softw. **114**, 163–191 (2017). https://doi.org/10.1016/j.advengsoft.2017.07.002
21. G. Oliveri, F. Robol, A. Polo, R. Lombardi, M. Chuan, M. Mattivi, C. Massagrande, P. Vinetti, C. Mazzucco, A. Massa, Design of compact printed antennas for 5G base stations, in *2017 11th European Conference on Antennas and Propagation, EUCAP 2017* (2017), pp. 3090–3093. https://doi.org/10.23919/EuCAP.2017.7928417
22. G. Oliveri, P. Rocca, L. Poli, G. Gottardi, N. Anselmi, M. Salucci, R. Lombardi, M. Chuan, M. Mattivi, P. Vinetti, F. Morgia, A. Massa, Innovative array architectures for 5G communications, in *2017 IEEE Antennas and Propagation Society International Symposium, Proceedings*, vol. 2017 (2017), pp. 1801–1802
23. V. A. Ramasami, HFSS API to Control HFSS from Matlab (2020). https://github.com/yuip/hfss-api
24. A. Rehman, C. Lee, H. Park, G. Namgung, J. Kwon, S. Kahng, A nature-inspired optimization technique for metasurfaces to improve the isolation between 5G MIMO antennas, in *2018 International Symposium on Antennas and Propagation (ISAP)* (2018)
25. P. Rocca, G. Oliveri, A. Massa, Differential evolution as applied to electromagnetics. IEEE Antennas Propag. Mag. **53**(1), 38–49 (2011). https://doi.org/10.1109/MAP.2011.5773566
26. F.J. Villegas, T. Cwik, Y. Rahmat-Samii, M. Manteghi, A parallel electromagnetic genetic-algorithm optimization (ego) application for patch antenna design. IEEE Trans. Antennas Propag. **52**(9), 2424–2435 (2004)

27. S.C. Wang, Y.J. Mao, M.J. Li, H.K. Yang, M.S. Tong, A novel design of multiband antenna based on non-dominated sorting genetic algorithm, in *2019 IEEE International Symposium on Antennas and Propagation and USNC-URSI Radio Science Meeting* (2019), pp. 1129–1130. https://doi.org/10.1109/APUSNCURSINRSM.2019.8888918
28. S. Yang, L. Zhang, J. Fu, Z. Zheng, X. Zhang, A. Liao, Design and optimization for 77 Ghz series-fed patch array antenna based on genetic algorithm. Sensors **20**(11) (2020). https://doi.org/10.3390/s20113066
29. J.J. Yu, V.O. Li, A social spider algorithm for global optimization. Appl. Soft Comput. **30**, 614–627 (2015). https://doi.org/10.1016/j.asoc.2015.02.014
30. L. Zhang, Z. Cui, Y.C. Jiao, F.S. Zhang, Broadband patch antenna design using differential evolution algorithm. Microwave Opt. Technol. Lett. **51**(7), 1692–1695 (2009)

Chapter 9
Reconfigurable Antenna: Analysis and Applications

Adnan Ghaffar, Xue Jun Li, Wahaj Abbas Awan, and Niamat Hussain

9.1 Background and History of Reconfigurable Antenna

The idea and concept of reconfigurable antennas have been investigated since the last few decades, and recently it gained much attention in industry and research due to advancement in modern wireless communication systems. In the early 1920s, some antennas with reconfigurable properties were designed for tuning the frequency and beam-steering purpose. However, the shifting between the frequencies and their characteristics parameters was controlled by external parameters.

The initial work related to the frequency reconfigurability was related to a patent by Norton in 1926 [1], and the frequency shifting was achieved by using variable inductive loading. In the early 1930s, another reconfigurable antenna consists of the nulls in the form of the two-element array was explained in [2], and it was steered by using a calibrated variable phase changer to determine the direction of arrival of a signal. The radiation pattern reconfigurable antenna was presented in [3] as shown in Fig. 9.1. It is rhombic-wire antenna, and the authors used motor with counterweights to change the dimension and angles of the proposed antenna. The Multiple-Unit Steerable Antenna (MUSA) was a six-element array of rhombic antennas with phase shifters at five of the elements [4], and the beams were steered in the elevation plane. The development of antennas with radiation pattern agility took place towards the

A. Ghaffar (✉) · X. J. Li
Auckland University of Technology, Auckland, New Zealand
e-mail: aghaffar@aut.ac.nz; xuejun.li@aut.ac.nz

W. A. Awan
Seoul National University of Science and Technology, Seoul, South Korea
e-mail: wahajabbasawan@seoutech.ac.kr

N. Hussain
Chungbuk National University, Chungbuk-do, South Korea
e-mail: hussain@chungbuk.ac.kr

M. A. Matin (ed.), *Wideband, Multiband, and Smart Antenna Systems*, Signals and Communication Technology, https://doi.org/10.1007/978-3-030-74311-6_9

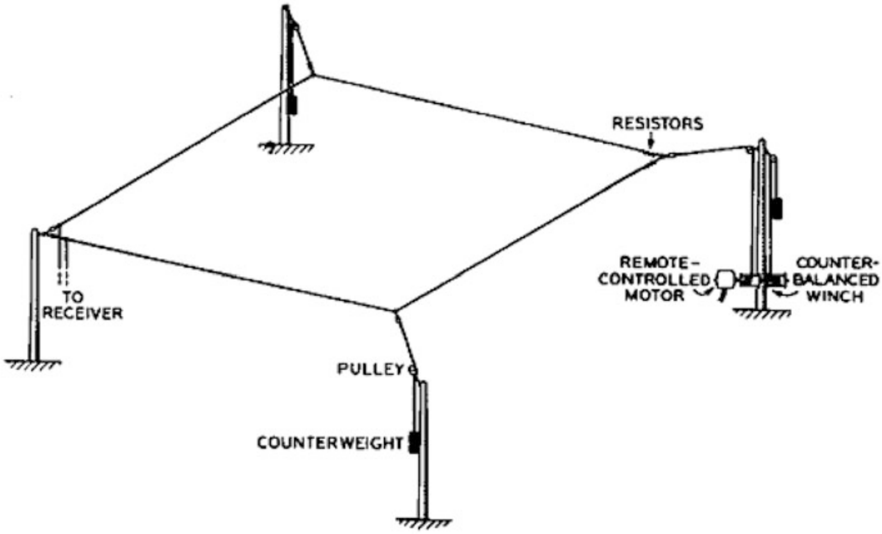

Fig. 9.1 Beam steerable rhombic antenna

1940s, basically driven by World War II when beam-scanning antennas played a key role in radar applications. The main techniques to achieve beam scanning were movable and multi-feed reactors and phased arrays. However, one can argue that strictly speaking, these designs are not reconfigurable antennas since there is not a clear interaction between the reconfiguration and the radiation mechanisms. Another example of a frequency tunable antenna was found in a patent by E. Werndl in 1942 where it is proposed to adjust the length of the dipole antenna by using a liquid metal [5]. This array had 13 rotary phase changers for beam steering [6].

In 1960, Rotman and Maestri reported one of the first few reconfigurable antennas that were realized by direct interaction between the reconfiguration and the radiation mechanisms [7]. This antenna is basically a radiating waveguide whose leaky modes were tuned electromechanically (mechanical movement by an electric motor) to produce multiple scanning beams. Some years after the first frequency tunable antennas, the first design of antennas with steerable radiation pattern appeared. In 1979, “reconfigurability” was defined as “the ability to adjust beam shapes upon the command” [8]. The authors used a six-beam antenna to dynamically change the coverage area for a communications satellite. Several additional papers reported other reconfigurable space-based arrays. On the other hand, the first hybrid patented reconfigurable antenna was claimed by Schaubert in [9], which demonstrates the concept of frequency agility and polarization reconfigurability. Even though most of the early stage designs involved bulky mechanical controls and limited functions, these pioneering works paved the way for furthering research and development on numerous reconfigurable antenna concepts. Inspired by the early RA concepts, researchers continued their investigations on this kind of controllable antenna and dealt with the implementation aspects for different practical applications.

In the 1990s, the advancement in the cellular networks, vast development of wireless sensor network, and telecommunication-based services open a new era of modern communication systems. To make the wireless system robust and portable was the priority at that time. Additionally, in the following years, other wireless standards (e.g. WiMAX, WLAN, Bluetooth, GPS, UMTS) were introduced in the market to fulfil the desire of modern communication systems. To support the different wireless standards and cover the wide area for quality service, a single wireless device must be multitasking to prove the high data rate, reliability, and high efficiency. To cover the problem, multiple fixed frequency antennas are a big challenge for compatible and small-size communication systems.

In the 2000s, there were vast researches conducted in the field of reconfigurable antennas on the different designs of frequency shifting, radiation pattern, and polarization switching applications [10, 11]. It is still a positive trend of research in the field of reconfigurable antennas in industry and academia. Due to recent development in the modern communication system, the pace is on the research of reconfigurable antenna to make controllable and adjustable according to the environment. Several designs have been explained in the past few years.

As mentioned, the physical modification technique is not always reliable, so electronic switching is a more promising technology, which is implemented in many of the latest designs. The changes in the smart materials were also incorporated in some designs [12–14]. Furthermore, other novel and robust designs investigated the printed antenna technology, which can be easily integrated with switching/tuning elements. Many antenna types like monopole, patch, Yagi-Uda, and dipole have been explored in the last few decades.

However, it remains a significant challenge to create a multi-mode, multi-functional integrated antenna to cope up with the latest wireless communication systems.

9.2 Introduction

Antenna development plays a key role in wireless technology with the rapidly increasing number of users in broadcasting, telecommunications, navigation, radar systems, military applications, and perhaps for future wireless communications, e.g., the cognitive radio. Passive antennas have reached a limit, and the use of a frequency reconfigurable antenna to extend operational bandwidth is a promising solution. The increasing number of users may lead to congestion of the existing spectrum allocation for wireless local area network (WLAN), wireless personal area network (WPAN), and cellular communications.

Since 2010, the reconfigurable antenna received a lot of attention due to its numerous applications and versatility in a wireless communication system such as radar system, cellular radio system, smart weapons protections, and wireless local area network system, as well as future applications, including the cognitive radio system. The reconfigurable antenna is capable of tunable adjustment on various parameters such as operating frequency, polarization, and radiation pattern.

9.3 Reconfigurable Techniques

The concept of reconfigurability, when is referred to as the antenna, means the capability to change the characteristic antenna electrical parameters through electric or mechanic mechanisms. Ideally, a reconfigurable antenna is designed to change the resonant frequency, input impedance, bandwidth, polarization, and radiation pattern as a function of the required systems. Broadly speaking, there are five different mechanisms to reconfigure the antenna characteristics, which are discussed as follows.

9.3.1 Physical Reconfigurable Antenna

Physical reconfiguration is one basic and classic technique that was used in the early designs. In this scenario, the antenna characteristics can be modified by changing the antenna structure by mechanical systems. Over time, some novel and innovative ideas were developed by implementing the actuation methods, and this helps to change the antenna structure and shifting radiation parts to get the reconfigurable antenna parameters. For example, some devices like a stepper motor and linear actuators were implemented to fully and partially change the antenna dimension physically. The motor-control-based [15] and rotatable antennas [16] were presented successfully. Moreover, reconfigurable antennas based on electrostatic/magnetic actuator were also presented in [17], and they achieved satisfactory results. A frequency reconfigurable antenna consisting of parasitic elements was presented in [18] as shown in Fig. 9.2a, and frequency is tuned with the help of piezoelectric actuator. In another example, as shown in Fig. 9.2b, where frequency reconfiguration is obtained by adjusting the inclination angle, it was controlled magnetically to get the required resonant frequency [17]. Besides these, physical adjustment by using the liquid metals can also be used to attain the reconfigurability in the form of the stretchable antenna [19] as shown in Fig. 9.2c and metal parasitic beam-steering antenna.

Although physical modification has been presented successfully in many designs, it has some drawbacks like slow speed, less life cycle, and dependence on the antenna physical dimensions. Despite these, it is still a promising technology for higher frequency band application where other technologies are limited due to some electrical characteristics.

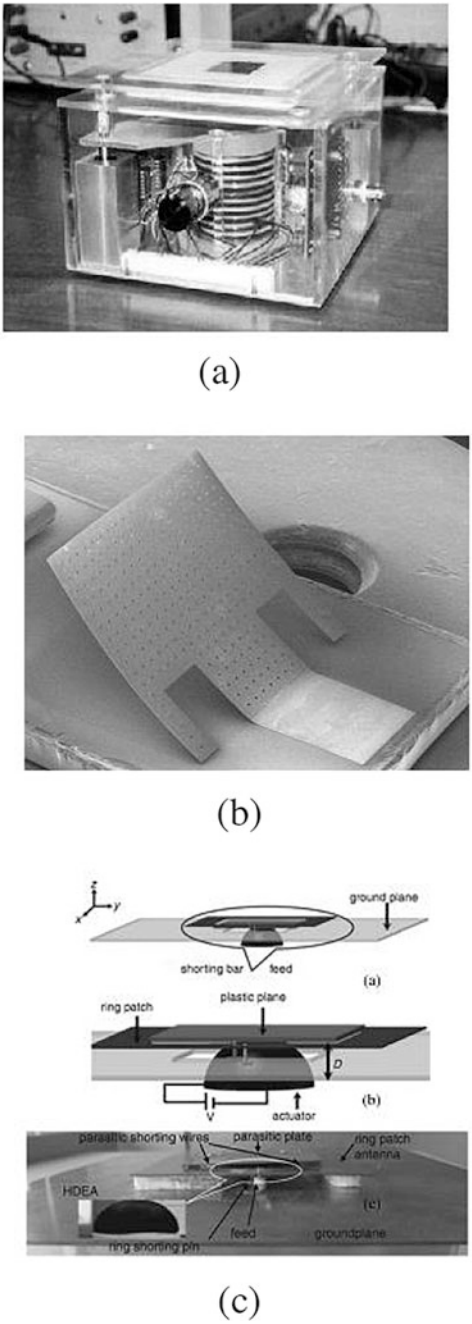

Fig. 9.2 (**a**) Peizoelectric actuator, (**b**) magnetic actuator, (**c**) electromechanical system

9.3.2 Electrical Switching Reconfigurable Antenna

The antenna reconfiguration by using the electrical mechanism is the most promising technology, as it is easily integrable and very compatible with low-profile antenna technology. In this technique, no physical adjustment technology is required to change the antenna parameter to get the required frequency/radiation pattern/polarization. Some lumped elements are inserted at the specific position of an antenna for the reconfiguration purpose. There are two types of electrical reconfiguration technology-RF switch like PIN diode, RF MEMS, and GaAs FET [20], and the other one is tunable capacitors called varactor diodes. These switching elements can produce the change in impedance matching, surface current distribution, and electrical behaviour of an antenna [21].

PIN diode consists of heavily doped p-type and n-type regions that are separated by lightly doped intrinsic region. PIN diodes behave good RF switch by shifting between forward and reverse biasing states. It has a very low resistance at high frequencies in forward biasing and behaves as an open circuit in the reverse-biased state. PIN diodes are current-controlled, so they take very few milliwatts power to turn on the diodes. PIN diodes are widely used in practical application due to their properties like robustness, low insertion losses, ability to control large RF signal power, and fast switching speed.

The alternative elements for the semiconductor technology are the RF-MEMSs that are considered as tiny mechanical switch. The RF-MEMS uses low-power consumption, low insertion loss, high isolation, and better linearly properties. The polarization reconfigurable antennas using RF-MEMS switches were explained in [22]. The antenna consists of the ring slot and feeds with coupled ring slot aperture. A stub is added to generate the CP, and RF-MEMS switches are inserted between them to switch the polarization between linear and circular as shown in Fig. 9.3. The measurement results show that antenna impedance bandwidth of 22.90% and 3 dB axial ratio bandwidth is 13.07%. These are not a good candidate for microwave and mm-wave frequencies due to bad power handling capabilities and expensive packing process to protect it against the environment.

Despite the numerous advantages, they have some issues due to the non-linearity of the switches, signal loss, and interference due to biasing circuit and these disturb the impedance matching and reduce the antenna efficiency. The coupling between the biasing circuit and antenna radiation elements can damage the antenna performance parameters as well. Some techniques to reduce the coupling are to minimize the length of biasing line and, if possible, use the available biasing circuit and put biasing lines on the less intense near field for example on the ground plane. Another method is to load the biasing line inductively or on high resistive material.

Fig. 9.3 (**a**) Antenna prototype with intergration of RF-MEMS. (**b**) Setup for radiation pattern measurement

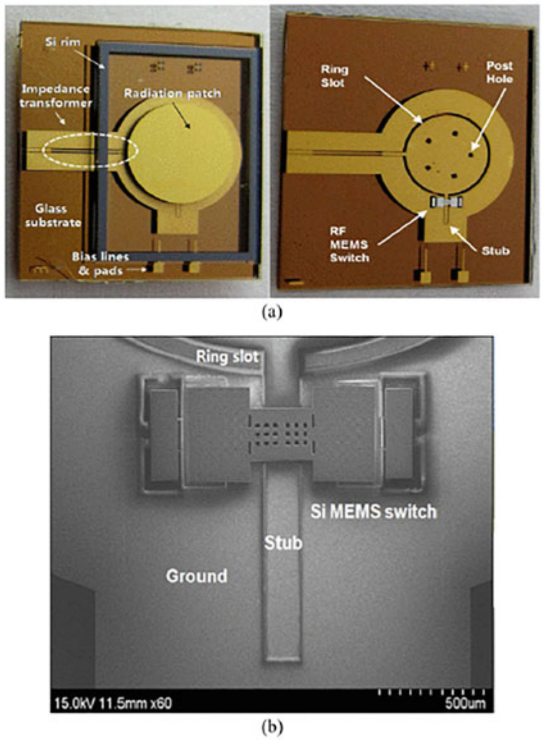

(a)

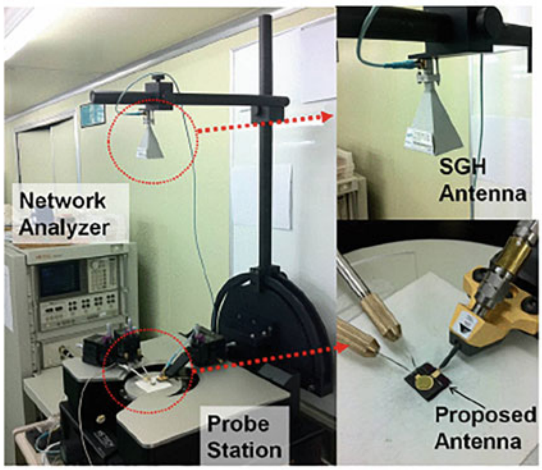

(b)

9.3.3 Material-Based Reconfigurable Antenna

The smart material with tunable properties is another prominent technology for antenna reconfiguration. The changes in the material characteristics are used to design the reconfigurable antenna design, and it is achieved by changing the material permittivity which modify the electrical length of an antenna. The electromagnetic characteristic (permittivity, r and permeability, r) of the material has a great impact on the properties of the antenna and RF microwave devices [11, 23, 24]. A static electric field is used to change the permittivity of a ferroelectric material, while the permeability of ferrite material is changed by applying the magnetic field [25, 26]. These materials have been used in many novel research works to obtain the antenna reconfigurability [27]. The frequency reconfigurable microstrip patch based on the ferrite material was presented in [25]. The required tuning frequency is obtained by changing the DC magnetic field. The reconfigurable microstrip antennas [24, 26] based on ferrite material show nonuniformity in the biasing and multi-field distribution, which limits their practical use.

Beam-steering antenna has been exclusively explored by the industry and academia. A leaky-wave antenna with stub array was explained in [28], and the phase shift can be tuned by changing the material properties. Another leaky-wave slot array antenna was designed in [29]. The ferroelectric base was used for this design. The permittivity of the material can be changed by applying the applied voltage between the top conducting layer and the bottom ground substrate. While changing the bias voltage, the permittivity of the ferromaterial changed and hence changes the beam direction.

Liquid crystal (LC) is another type of reconfigurable smart material, whose properties are affected by the molecular direction of the liquid and characteristics are also changed by applying the electric or magnetic field [30]. The beam-switchable reflection array antenna based on LC substrate was explained in [31]. By applying the voltage, the beam of the antenna can be tuned. Recently, some work has been done on this technology [32, 33]. Another material called vanadium dioxide (V_{O2}) by applying the thermal induction was also used for antenna reconfiguration [34] as shown in Fig. 9.4.

These smart materials provide the continuous reconfigurability; however, these are lossy and only provide solutions for short-range radios.

Tunable materials can achieve continuous reconfigurability with a simple control system; however, they are lossy and can provide reconfigurability for a limited range only. Additionally, proper modelling in the design process and reliability, sensitivity in the antenna operation, etc. are still notable, challenging issues. By overcoming these limitations and utilizing its potential, this technology could offer a great possibility for antenna reconfiguration soon, both at lower and higher frequency bands.

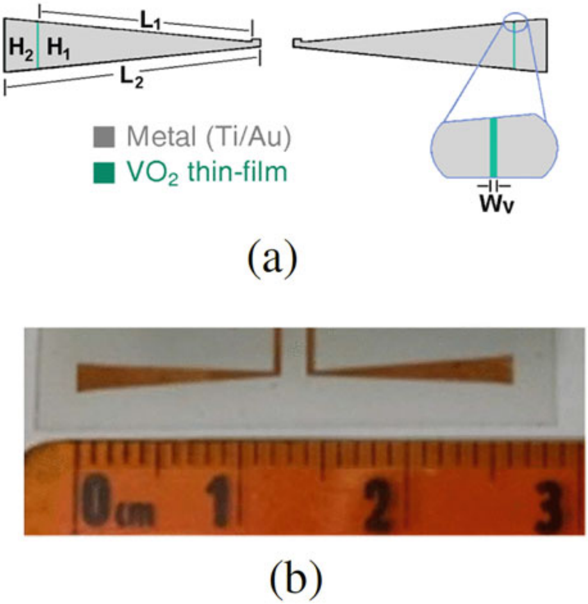

Fig. 9.4 (**a**) Layout of the reconfigurable bowtie antenna with (V_{O2}) and (**b**) fabricated bowtie antenna

9.3.4 Optical Switching Reconfigurable Antenna

Except for the techniques, optical reconfiguration has also gained much attention in recent years [35–37]. It deals with the photoconductive switches and does not need any complex biasing circuit and physical modification. Optical fibres are used for this purpose, and they need light for photo-switching [38]. When the laser is used to put the light, the charge density increased in the material, which also increases the conductivity of the semiconductor devices. This optical switching technique has a complex structure and needs some extra fibre that is costly. Although they have low distortion, they have lossy behaviour and slow switching speed as compared to lumped element switching technology. This technique has been implemented successfully in many designs.

As shown in Fig. 9.5, the frequency reconfigurable annual ring circular patch antenna by using the photoconductive switches was designed in [39], and these switches were activated by using the laser light and frequency is tuned between two application bands.

The frequency and beam reconfigurable antennas based on CPW to CPS (coplanar stripline) feed were explained in [40]. Two silicon switches are used in this printed dipole antenna as shown in Fig. 9.6. The antenna prototype shows good agreement, and there is a frequency shift of 40%. There are also 50 shifts in beam nulls of the bore-sight gain.

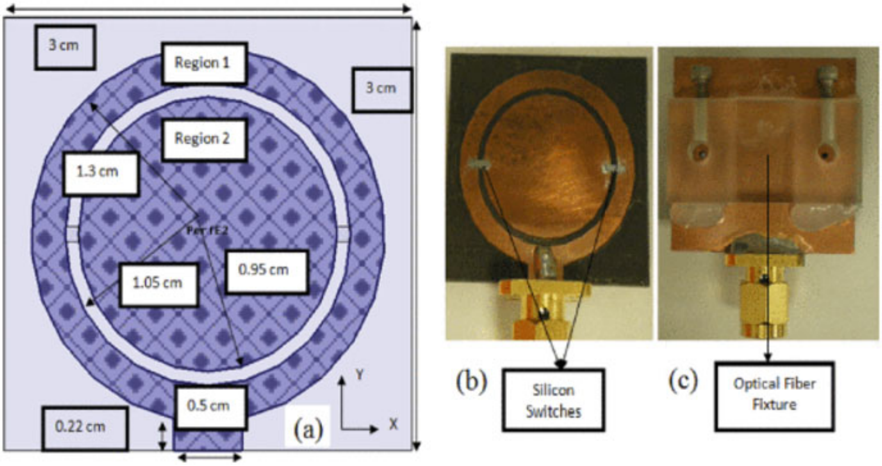

Fig. 9.5 (**a**) Antenna dimensions. (**b**) Antenna top layer. (**c**) Bottom view

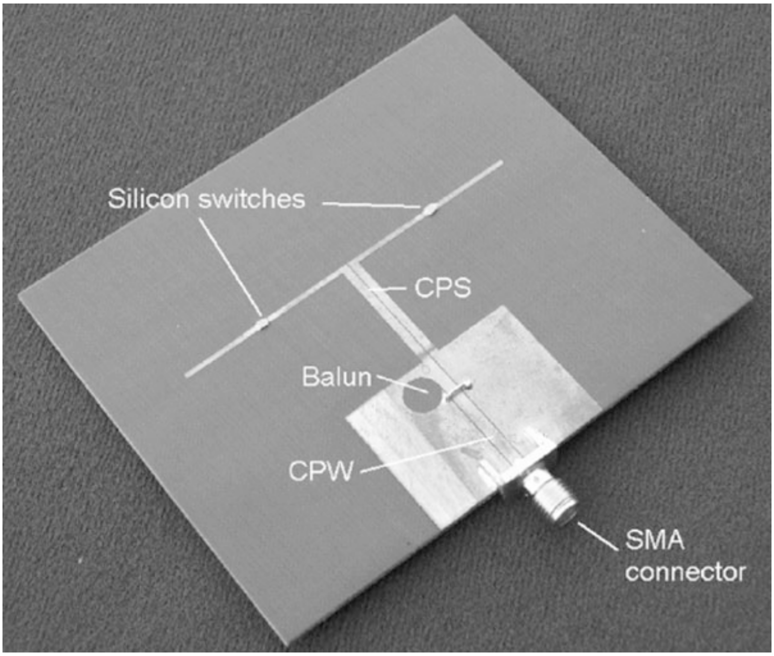

Fig. 9.6 The switched dipole antenna

The extensive research on this technology was not studied, but some attempts are made to further investigate technology in the form of frequency reconfigurable patch antenna [37] and notch-band UWB antenna [35] by using optical switching.

9.3.5 Software-Based Reconfigurable Antenna

Controlling a reconfigurable antenna with software can be done using many platforms such as Field Programmable Gate Arrays (FPGAs), Microcontroller, or Arduino Boards [69]. The frequency reconfigurable antenna based on FPGA was explained in [41]. In this work as shown in Fig. 9.7, the FPGA is used to on/off the

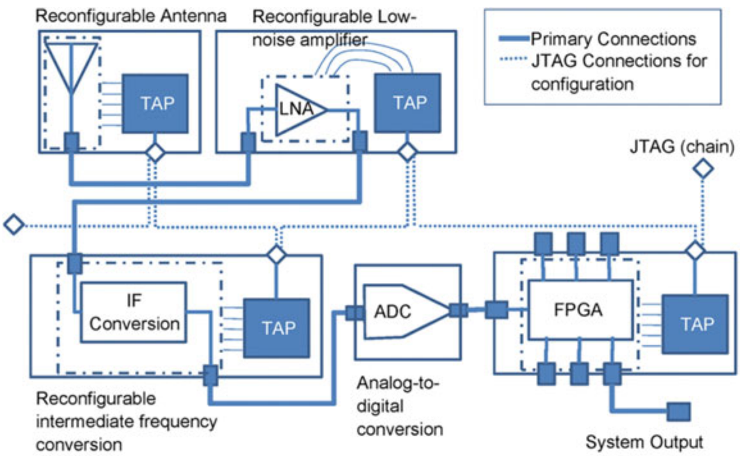

(a)

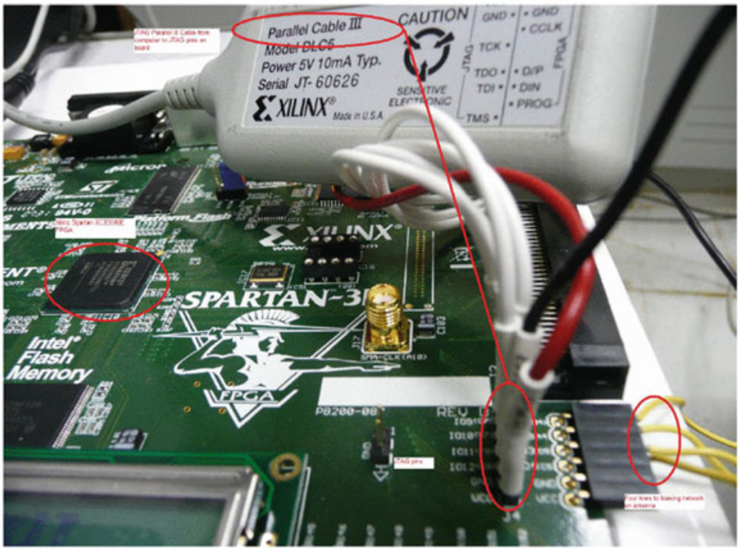

(b)

Fig. 9.7 (**a**) Reconfigurable antenna system (**b**). The paralleled III cable with FPGA board

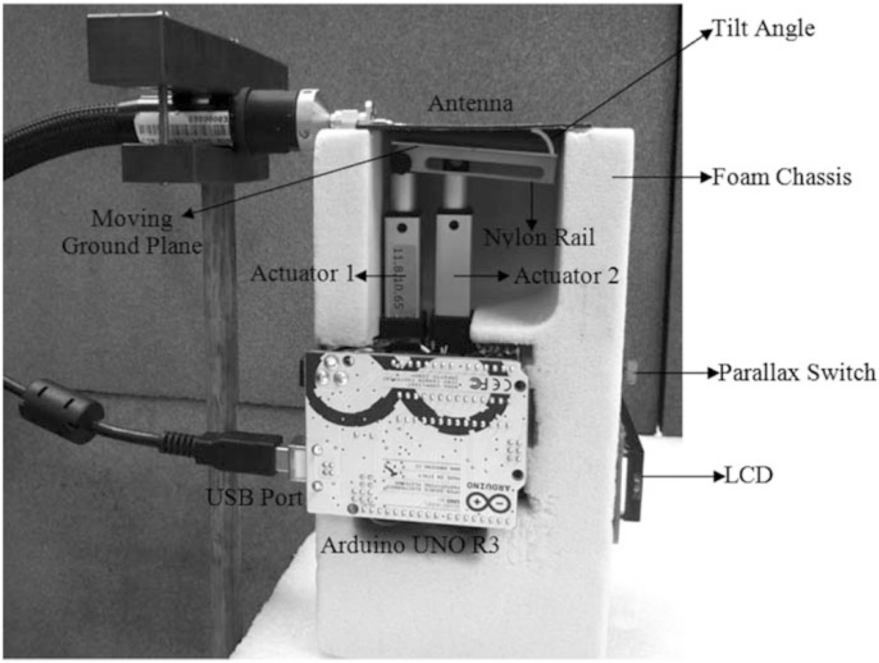

Fig. 9.8 Antenna prototype with controlling circuit

PIN diodes, which further connect and disconnect the different parts of an antenna to get the required frequency.

In another work [16], the LabVIEW is used to control the rotation of the stepper motor that is used for antenna reconfiguration purpose. The software control using LabVIEW and FPGA is a simple approach, and there is no need for complicated programming skills for antenna designer. Arduino boards are also used for antenna reconfigurability. In this scenario [42], the user can control the antenna movement and device when and how to change the antenna parts as per the requirement as shown in Fig. 9.8.

The surrounding activities also affect the antenna's operation. Such an example is explained in [43], where temperature sensors activate the thermal switches on the antenna structure. Motion detection is another technique, which also behaves as an active part for the biasing of the antenna reconfiguration. An infrared motion detector sensor [44] is used in the biasing circuit of varactor diode as shown in Fig. 9.9. It detects the motion and changes the voltage level of varactor diode to get the different frequency tunings.

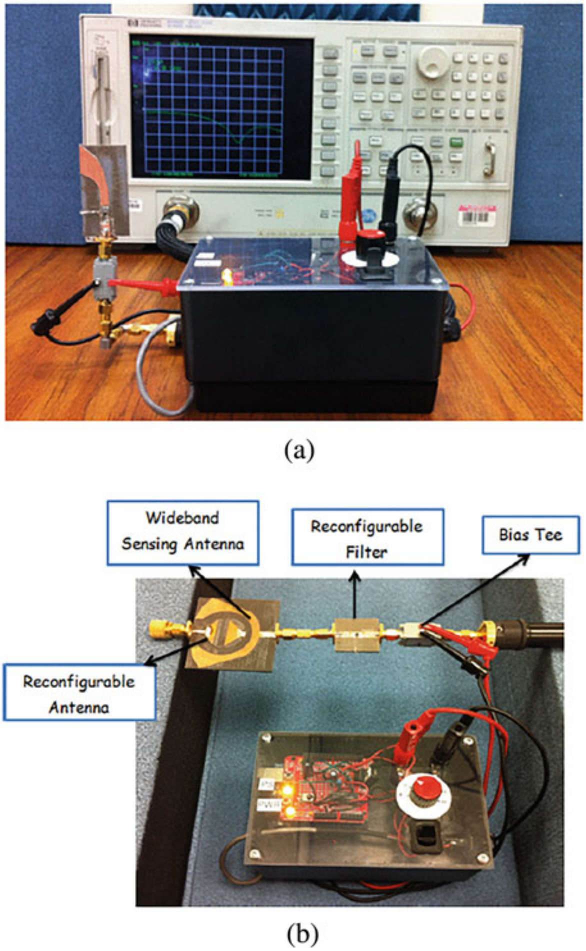

Fig. 9.9 (**a**) Measurement setup of the filtenna with surrounding (**b**). Reconfigurable filter with the wideband antenna awareness

9.4 Reconfigurable Antenna Properties

Reconfigurable antennas can be classified into four different categories.

9.4.1 Frequency Reconfigurable Antenna

Frequency reconfigurable antenna can adjust dynamically their frequency of operation. It can be achieved by changing the effective length and by connecting/disconnecting the different parts of an antenna to get the required resonant frequency. The successful application by changing length variation has been found in dipole [40, 45, 46], monopole/patch [47, 48], and slot antenna [49–51]. Moreover, the length of an antenna can adjust by changing the material property of the antenna without any physical alteration. The resonant frequency changes by changing the dielectric constant of the material. One can receive lower or higher resonant frequency with higher or lower permittivity, respectively. The printed antenna with dielectric variation was designed in [52, 53].

In the reactive method, the input impedance of the antenna changed by connecting the reactive parts then gets the required impedance matching to resonate at normal frequency. To get the continuous tuning of frequency, varactor diode is used with required impedance matching in a certain frequency range. The reconfigurable antenna with varactor tunability for the notched band was proposed in [54–56].

To better understand the working principle of frequency reconfigurability, an antenna was proposed in [57] as can be seen in Fig. 9.10. In this chapter, a new technique substrate integrated waveguide (SIW) has been introduced for low cost, easy fabrication, and more convenient for high-speed communication applications. The proposed antenna consists of right/left-handed transmission line that is the combination of capacitance, inductance, and shunt capacitance. The operation frequency can be modified by changing the capacitance of varactor diode embedded on the meander line. The resonance frequency is changed from 4.13 to 4.50 GHz by varying the biasing voltage from 0 to 36 V. The proposed antenna showed the good agreement between the simulated and measured results and promising candidate for the front end of the RF component and CR applications.

Similarly, another frequency reconfigurable antenna with miniaturized wideband and multi-band properties was presented in [58]. The antenna shape consists of a triangle patch connected with the microstrip transmission line. The main radiating patch relates to two serpentine-shape stubs at the edges with the help of two PIN diodes. The biasing circuit is designed on the backside to avoid the radiation pattern and connected with serpentine stubs with the help of shorting vias. The biasing circuit is the combination of the resistors to provide reasonable voltage and inductors. The antenna dimension is shown in Fig. 9.11. The proposed antenna resonates at eight different frequencies by changing the different states of the PIN diodes. The antenna prototype is shown in Fig. 9.12. When D1 is forward biased and D2 is reverse biased, the proposed antenna has three resonance frequencies at 3.05, 4.1, and 6 GHz. The values of the gain at resonance frequencies is 0.5, 1.62, and 1.74 dB, respectively, as can be seen in Fig. 9.13b–d. In another case, when D1 is forward biased and D2 is reverse biased, the resonance frequency and radiation pattern can be seen in Fig. 9.14. When both diodes are forward biased, the antenna has triple band at 3.3, 5, and 6 GHz. The gain as well as return loss can be seen at Fig. 9.15. The slight difference between the measured and simulated results is due to the imperfection fabrication.

They are particularly useful in situations where several communication systems converge because the multiple antennas can be replaced with a single reconfigurable antenna. Frequency reconfiguration is generally achieved by modifying antenna's dimensions physically, electrically using RF switches, impedance loading, or tunable materials.

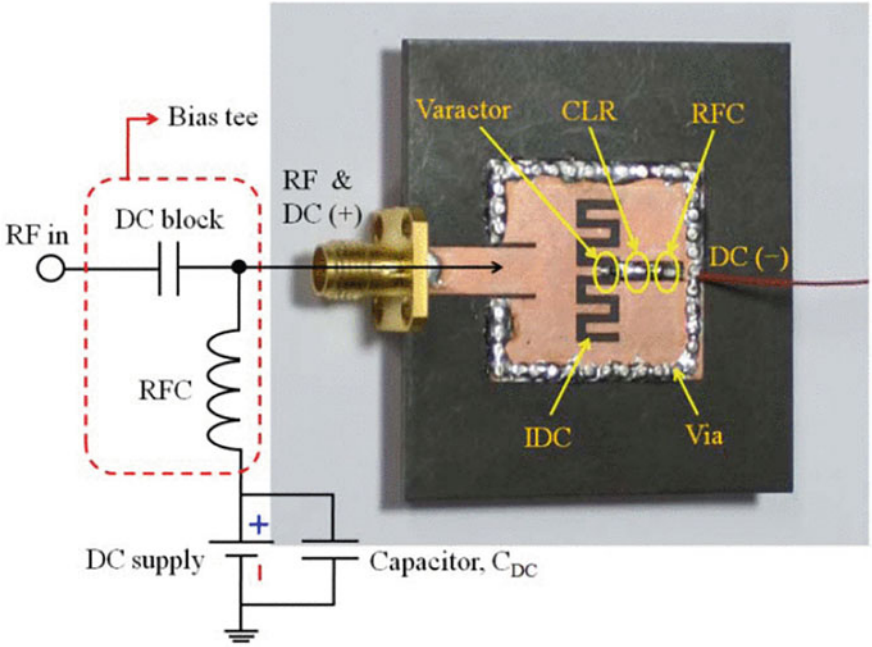

(a)

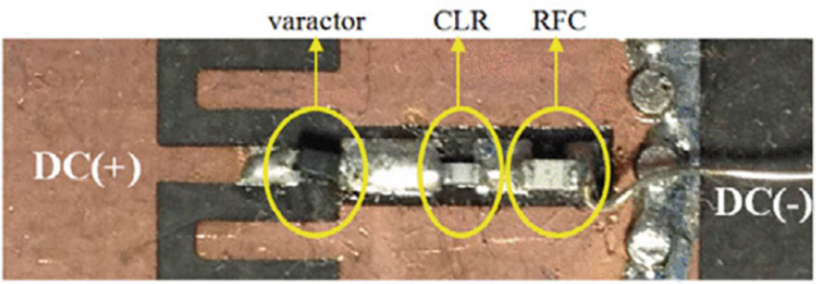

(b)

Fig. 9.10 (**a**) SIW–IDC antenna prototype. (**b**) Bias network section

Such antenna is widely used in wireless communications that require a change in operating frequency and to switch from one channel to another. Cognitive radio is an exemplar application for this antenna.

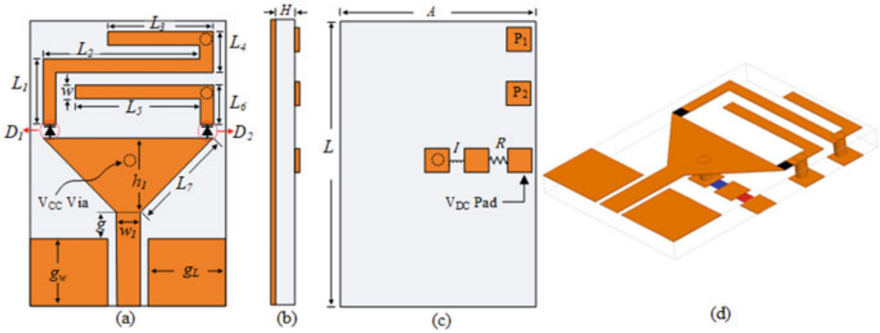

Fig. 9.11 Antenna schematic. (**a**) Top side. (**b**) Side view. (**c**) Bottom side. (**d**) Perspective view

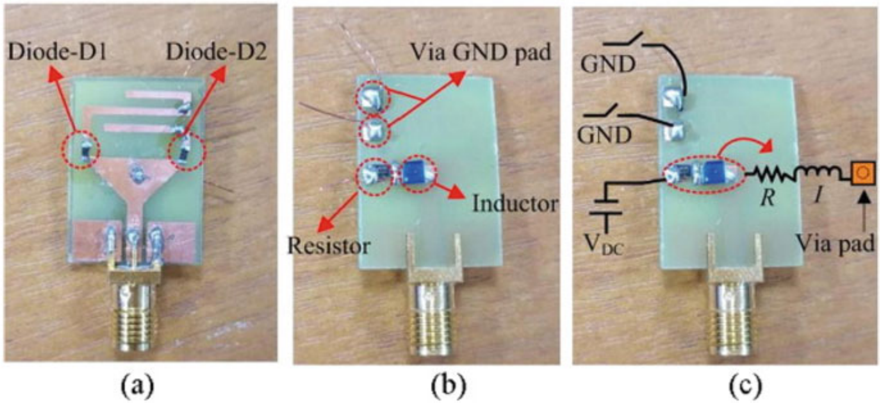

Fig. 9.12 Antenna prototype. (**a**) Top view. (**b**) Bottom view. (**c**) Bottom view with biasing circuit

9.4.2 Polarization Reconfigurable Antenna

Polarization reconfigurable antennas can switch between different polarization modes. The capability of switching between horizontal, vertical, and circular polarization can be used to reduce polarization mismatch losses, strong signal strength, and multipath fading in portable devices. In this case, the antenna can change, for example from vertical to left-hand circular polarization [59]. Different design techniques like slits, slots, cross on the ground plane, truncated corner of main radiation patch parasitic, and addition of electrical switches are employed to get the polarization reconfigurability [60, 61]. Additionally, reconfigurability in impedance matching network [62] also helps to switch between linear (vertical/horizontal) and circular (RHCP/LHCP) polarization at resonate frequency.

A novel wideband tri-polarization reconfigurable dipole antenna based on magneto-electric (ME) for WLAN application was designed in [63] The proposed

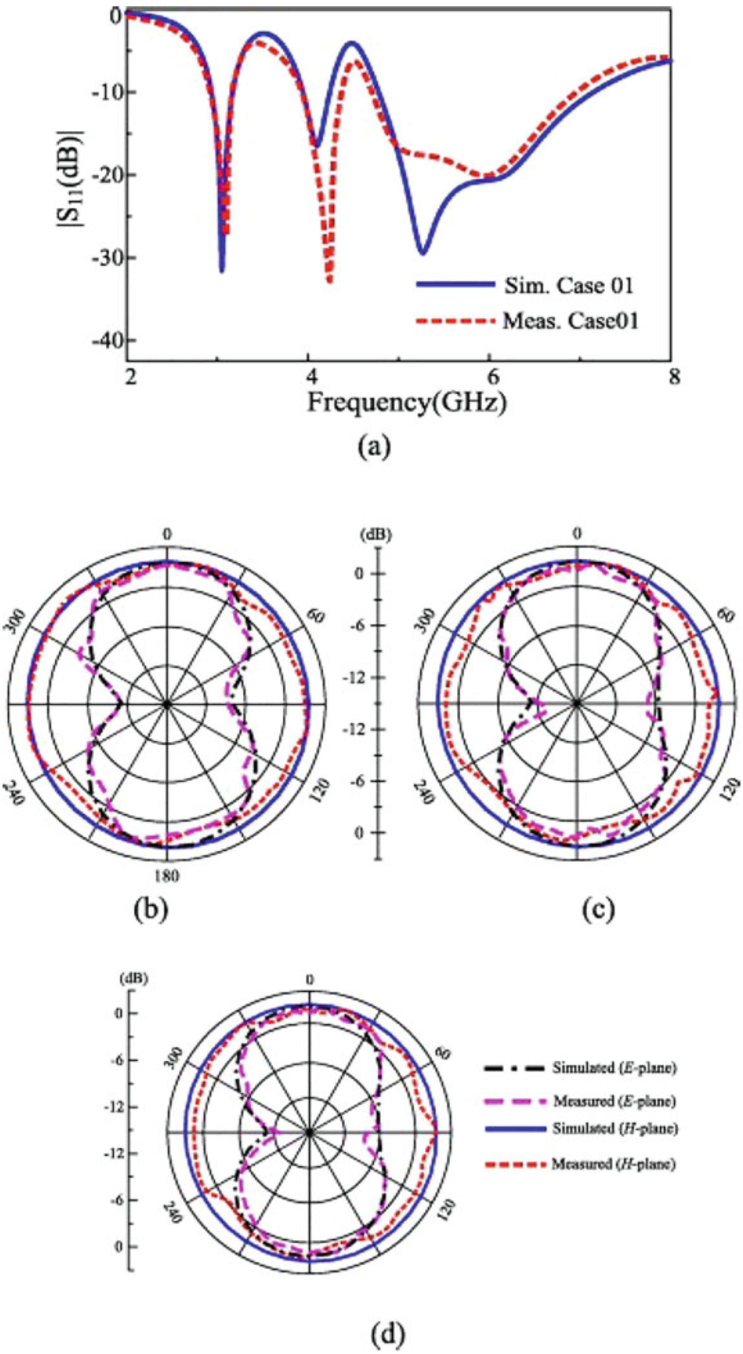

Fig. 9.13 Comparison among simulated and measured results of (**a**) S-parameters and radiation pattern at (**b**) 3.05 GHz (**c**) 4.1 GHz (**d**) 6 GHz, for D1 is reverse and D2 is forward biased

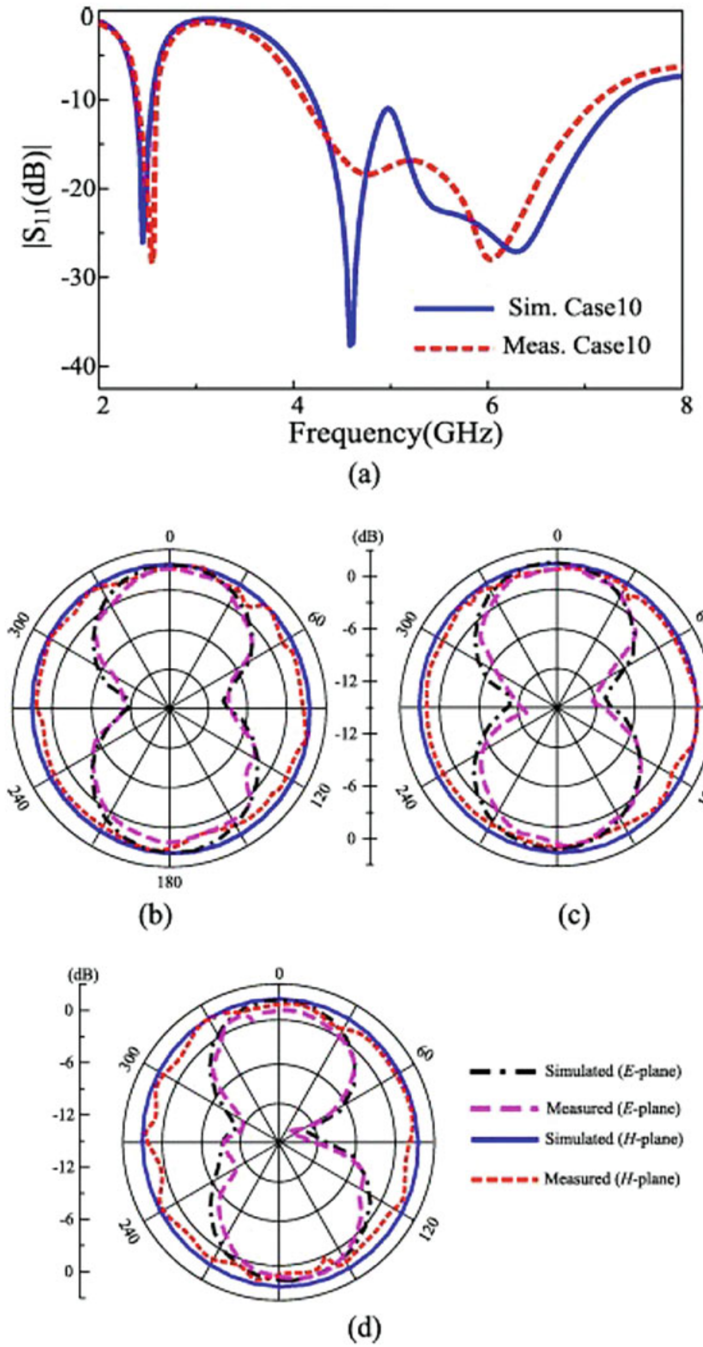

Fig. 9.14 Comparison between the simulated and measured results of (**a**) S-parameters and radiation pattern at (**b**) 2.45 GHz, (**c**) 4.6 GHz, (**d**) 6.2 GHz, for D1 is forward and D2 is reverse biased

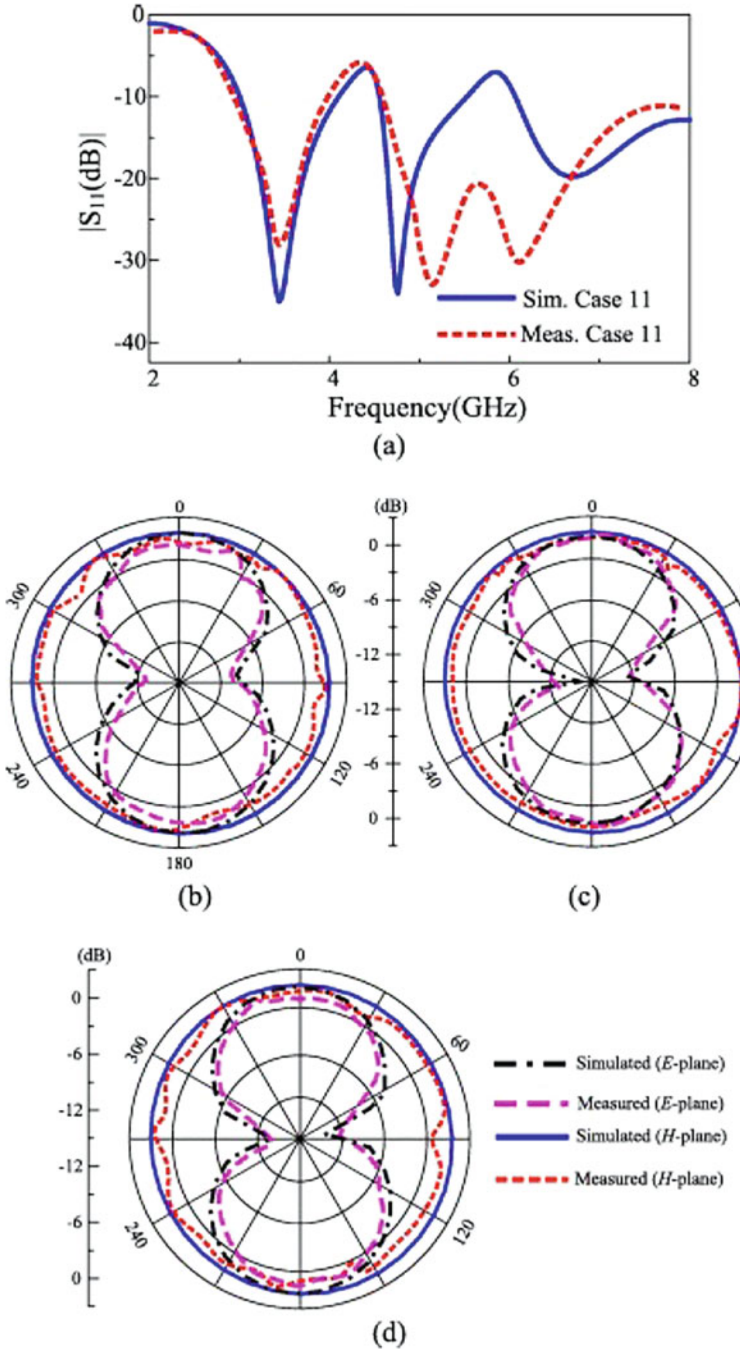

Fig. 9.15 Comparison between the simulated and measured results of (**a**) S-parameters and radiation pattern at (**b**) 3.3 GHz, (**c**) 5 GHz, (**d**) 6 GHz, for D1 and D2 are forward biased

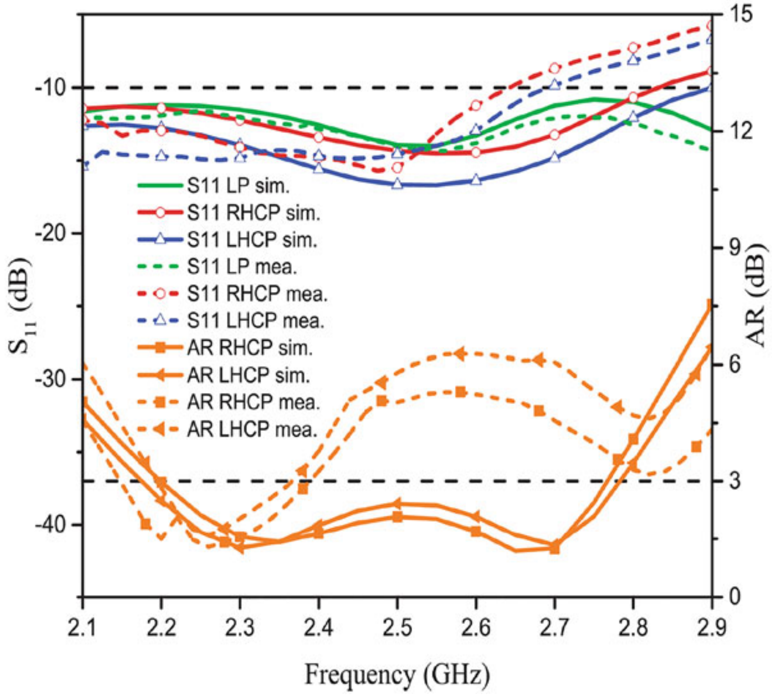

Fig. 9.16 Simulated and measured reflection coefficients under three polarization states and AR under two CP states, respectively

antenna operates in one linear polarization and two circular polarizations, and it is achieved by using four PIN diodes. The linear polarization is obtained by using T-probe fed on dipole antenna having four-sectional structure. The antenna prototype shows an impedance bandwidth of 31%, an axial ration BW of 7.9%, and an high efficiency of 80–90% for all polarizations. The simulated and measured reflection coefficients and AR can be seen in Fig. 9.16. The radiation pattern of the proposed antenna at different polarizations is shown in Fig. 9.17. It can be seen that the radiation pattern is the same for all three operation modes. The measured 3-dB bandwidth for LP, RHCP, and LHCP are 60, 62, and 66°, respectively. Another tri-polarization antenna was investigated in [64] and can be seen in Fig. 9.18. The antenna design is multi-layer PCB and consists of the radiation patch, ground plane, and cross-probe fed that is incorporated with pin diodes. On the bottom side of the radiation patch, there are horizontal and vertical metallic posts that form the L-shaped coupled fed, and it helps to increase the bandwidth of the proposed antenna design. Pin diodes and biasing circuit are designed on the ground plane, and the different states of pin diodes are to shift the polarization between linear and circular (RHCP/LHCP) polarizations. The measurement results of the proposed antenna

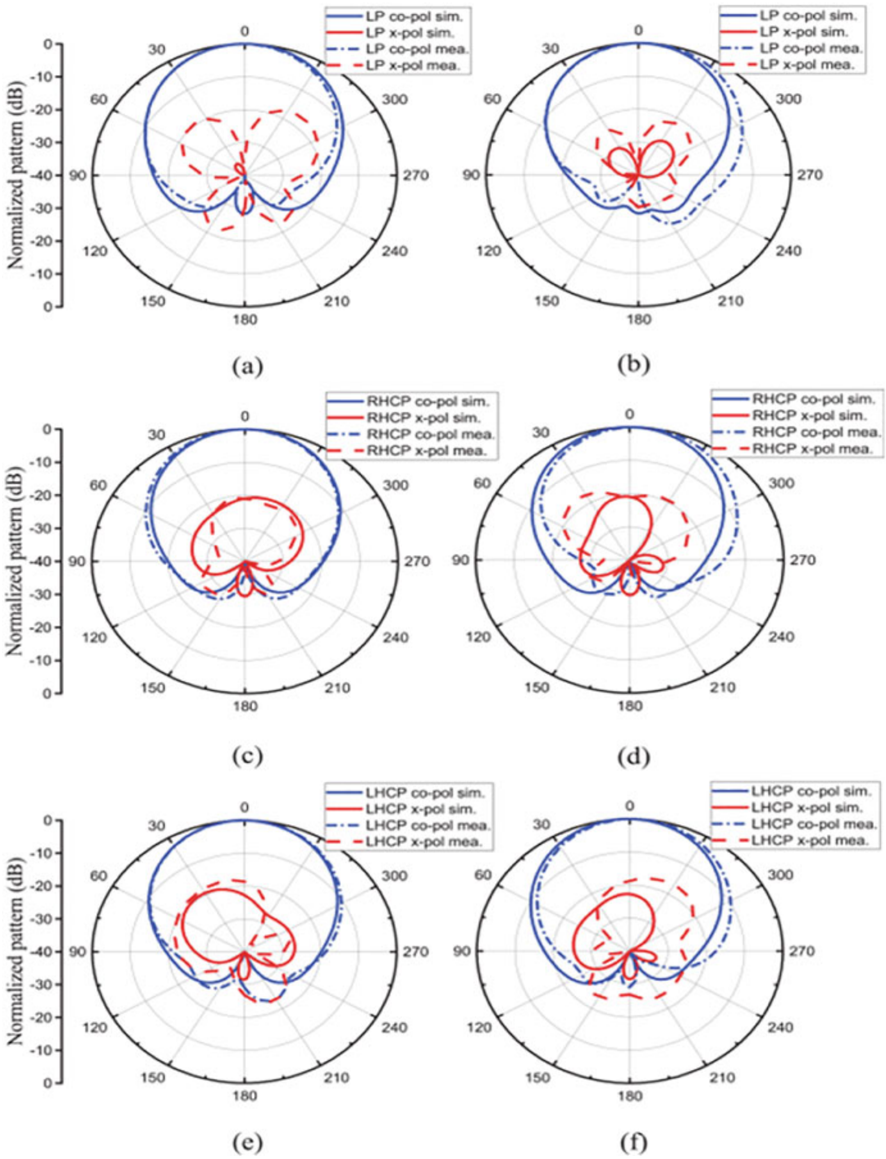

Fig. 9.17 Simulated and measured radiation patterns under different polarization states at 2.3 GHz. (**a**) LP mode, xoz plane. (**b**) LP mode, yoz plane. (**c**) RHCP mode, xoz plane. (**d**) RHCP mode, yoz plane. (**e**) LHCP mode, xoz plane. (**f**) LHCP mode, yoz plane

show good agreement with the simulated results, and it is a promising candidate for the WLAN and satellite communication applications.

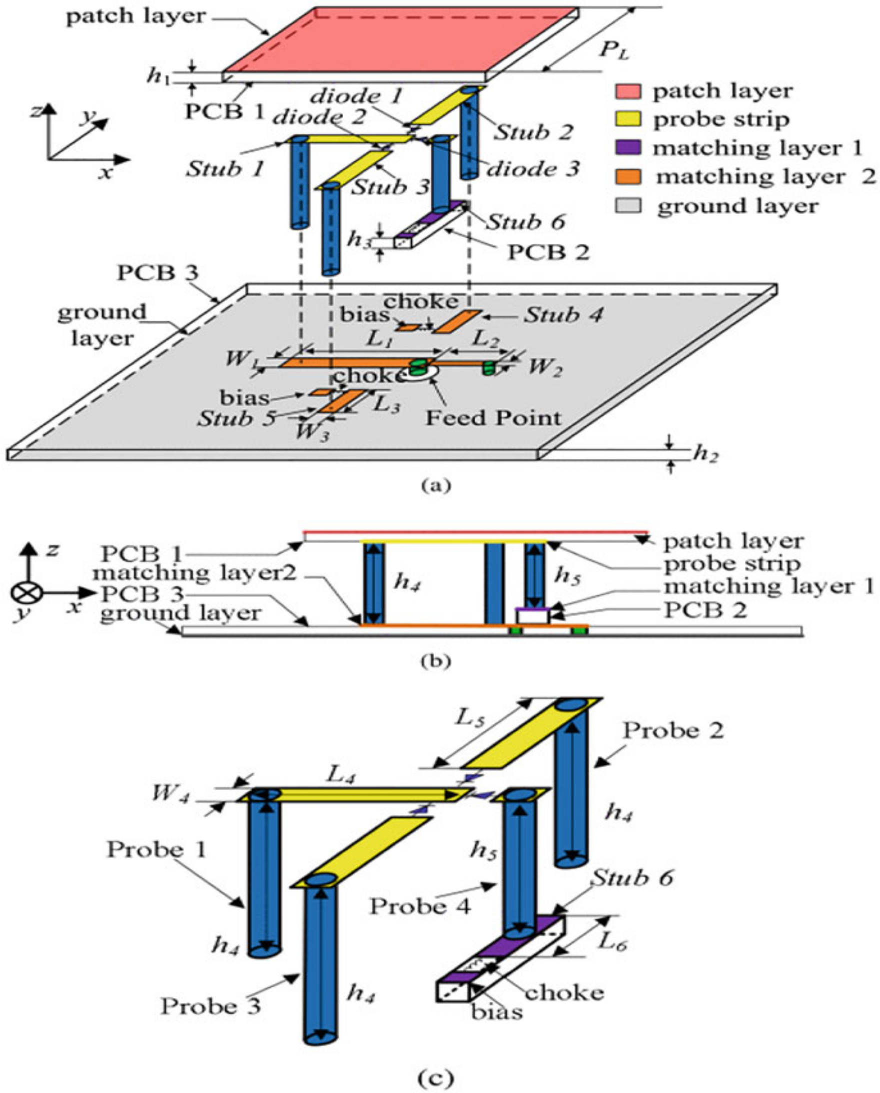

Fig. 9.18 Geometry of the proposed antenna

The compact-size, low-profile, wideband omnidirectional patch antenna with polarization reconfigurability for wireless communication was explained in [60]. The antenna geometry is the combination of circular patch and ground plane. The radiation patch and ground plane are connected via nine shoring pins. The annular slot and six radial slots are etched on the bottom side.

9.4.3 Radiation Pattern Reconfigurable Antenna

Radiation pattern reconfigurability is based on the intentional modification of the spherical distribution of radiation patterns. Beam steering is the most extended application and consists of steering the direction of maximum radiation to maximize the antenna gain in a link with mobile devices. In this technique, impedance matching is kept constant while changing the current distribution, which is challenging. Some conventional methods to get tunable radiation patterns are rotating the arms of a dipole or rotating the antenna itself in the orthogonal plane [65, 66]. One of the most frequently used methods is using tunable elements as parasitic with other main radiators. They behave as the coupled current and do not disturb the impedance matching as they do not have any electrical connection. This technique was implemented in designs with dipole/Yagi dipole [67, 68], monopole antenna [69], slot antenna [70–72], patch antenna [73–75], and Yagi antenna [76, 77].

Another method of pattern reconfiguration is multi-mode excitation that is obtained by activating the mode of an antenna [78, 79], though it has very limited applications. The electronics reconfiguration method was applied in many designs using SIW configuration, water grating, and periodic structure to control the mode and phase properties [80–83]. Leaky-wave antennas are famous for larger beam steering, but it is still challenging to increase the beam-scanning range.

The most attractive application of the pattern reconfigurable antenna is surveillance and tracking because they provide different directions with the same resonate frequency [84]. Mobile antenna systems are the example of this type.

9.4.4 Compound Reconfigurable Antenna

Antenna under this group can simultaneously change multiple characteristics in their operation. These antennas can, for example, change their operating frequency as well as their polarization scheme for each frequency of interest. They can also reshape their radiation pattern while changing their operating frequencies or polarizations. The most common application of hybrid reconfiguration is the combination of frequency agility and beam scanning to provide improved spectral efficiencies.

9.4.4.1 Frequency and Radiation Pattern Reconfigurable Antenna

In this property, the frequency and the radiation pattern of the antenna can be changed simultaneously. One can switch the radiation pattern between omnidirectional, broad-side, and end-fire modes. A dual-band frequency and radiation pattern reconfigurable antenna was explained in [85]. The antenna has a simple patch shape with a row of shorting vias in the centre. The antenna shows monopolar and

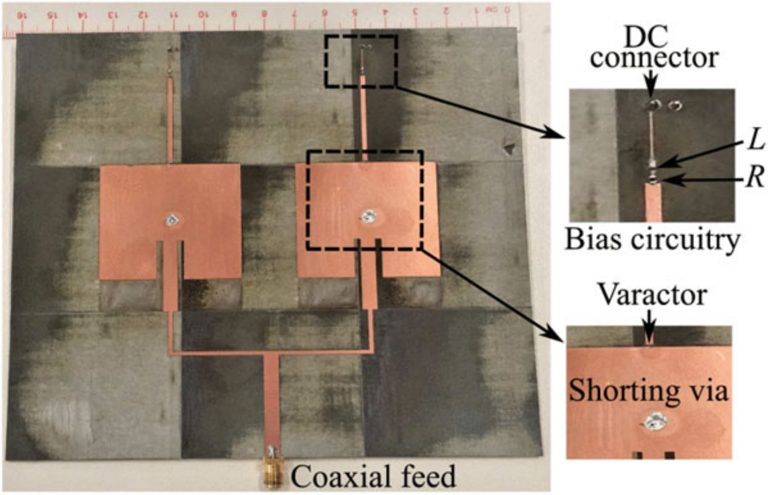

Fig. 9.19 Antenna prototype with biasing circuit

broad-side radiation patterns for its lower and upper frequencies, respectively. The presence of the shoring vias does not disturb the conventional mode of the microstrip patch antenna but helps to create another mode for radiation reconfigurability. Two separate biasing voltages and four varactor diodes are used for the independent switching of the resonant frequency. An antenna array for frequency and radiation patterns was designed in [86]. The proposed antenna is the combination of two patches, open stubs, and varactor diode with independent biasing voltage. The T-junction power divider is used to connect and feed the two-patch antenna array as shown in Fig. 9.19. The resonant frequency tuning range is from 2.15 to 2.38 GHz and beams steering across ±23 across the broadside. The reflection coefficient of the proposed antenna design for different combinations of biasing voltages is shown in Fig. 9.20. There is good agreement between the measured and simulated results. In this antenna, the frequency tuning range is 10% due to the difficulty of impedance matching. The gain pattern at three selected frequencies tuning is shown in Fig. 9.21. The antenna can be switched between the right and left directions by changing the values of capacitors.

The combination of monopole and patch antennas was studied in [87] to get the radiation pattern and frequency reconfigurable antennas. It consists of patch etched on the front side and monopole on the bottom side with the defected ground plane as shown in Fig. 9.22. The monopole and patch antennas are used to get lower and higher resonate frequencies, respectively. To get the omnidirectional radiation pattern, the substrate is truncated at the far end from the feed. By changing the states of two diode groups, the proposed antenna behaves as omnidirectional pattern mode at 2.21–2.79 GHz resonant frequency, unidirectional pattern mode of higher frequency at 5.27–5.56 GHz, and both working simultaneously. To cover the S and

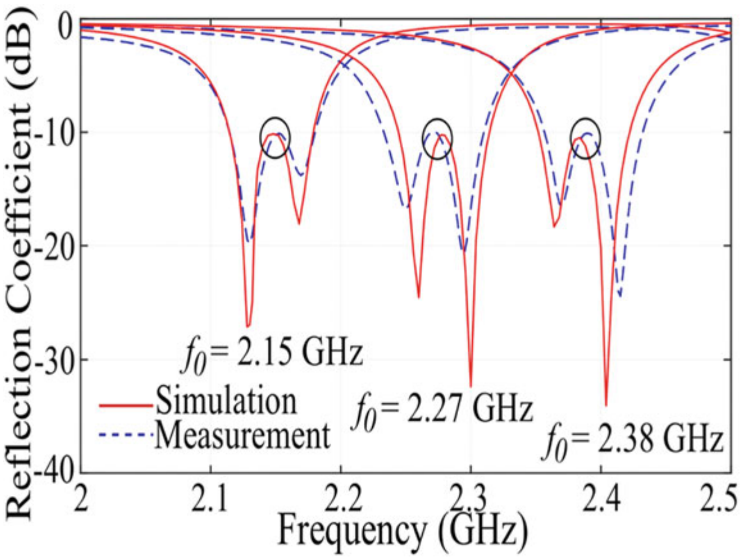

Fig. 9.20 Comparison between the simulated and measured reflection coefficients for different combinations of bias voltages

C, a microstrip antenna was presented in [88]. The reconfigurable antenna has a patch with inset feed on the front side, while it has two rectangular-shaped slots on the ground plane. The six PIN diodes are inserted into the slots on the ground plane. The different states of the PIN diodes resonate antenna at 3 frequencies of the S-band and 8 different frequencies of the C-band.

A wideband slot antenna for LTE and C-band applications was investigated in [89]. The substrate has a sickle-shaped slot with a ground plane on one side and fork-shaped microstrip line on the other side. Two PIN diodes are inserted into sickle-shaped slot for frequency reconfigurability, while two diodes are used for the connection of vertical and horizontal arms of the fork-shaped feed line for pattern reconfigurability. There is good agreement between the simulated and measurements results, and antenna shows 25 and 20 beam steering at 3.4–3.8 and 3.7–4.2 GHz, respectively. Another slot antenna to switch between three different frequencies (1.8, 1.9, 2.1 GHz) and beam steering for three angles (0, ±15) were presented in [90]. The proposed antenna consists of the main radiator slot on the front side and upper and lower slits on the ground plane. Two switches are placed on the main radiator, while three switches in each slit. To produce the directional radiation pattern, an aluminium reflector was placed behind the antenna as slot normally behaves as bidirectional radiation pattern.

The frequency and radiation pattern reconfigurable antennas consist of the centre-fed patch, and four identical BTFB (back-to-back F) elements were explained in [91].

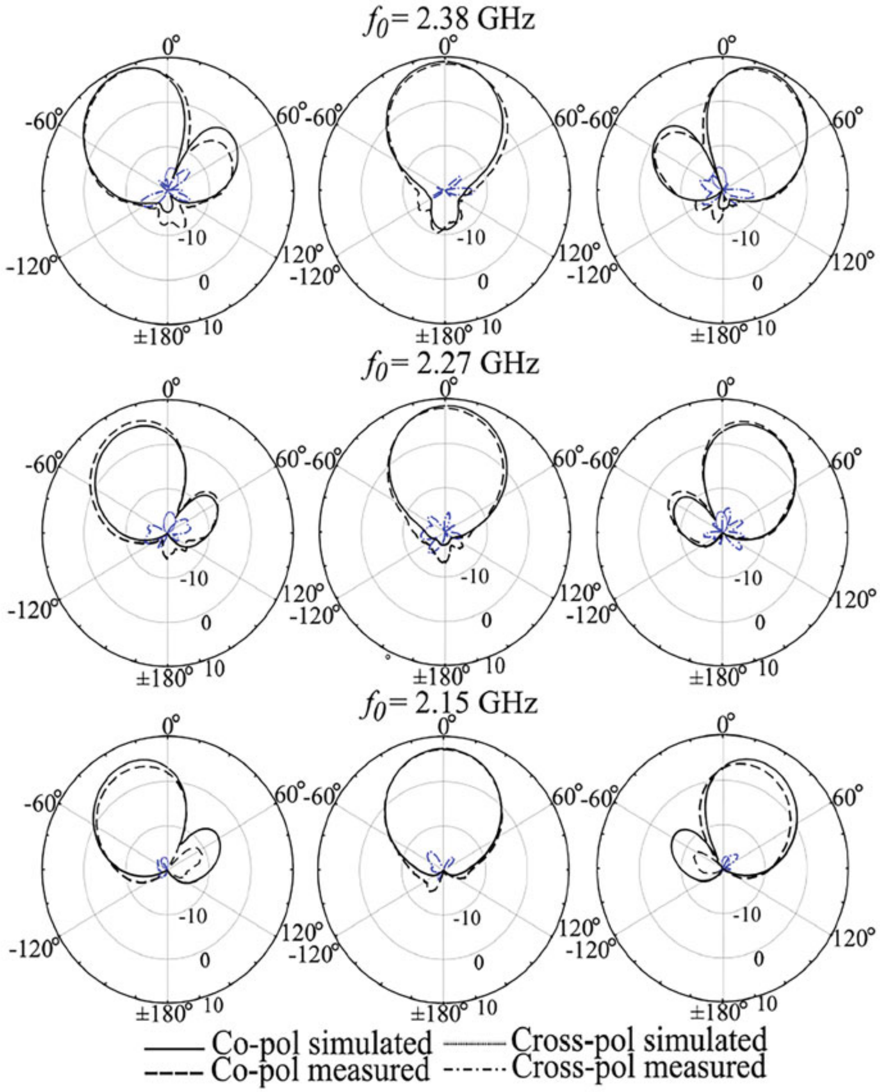

Fig. 9.21 Realized gain patterns at f_0 = 2.38, 2.27, and 2.15 GHz from top to bottom

9.4.4.2 Frequency and Polarization Reconfigurable Antenna

In this technique, the frequency can be tuned for the available band, and polarization switching helps to reduce the multipath effect and increase the channel capacity. Recently, it has gained much attention due to its useful applications like tracking, sensing, and radar, etc., and some design examples are explained below. A novel frequency and polarization reconfigurable antenna based on electromagnetic bandgap

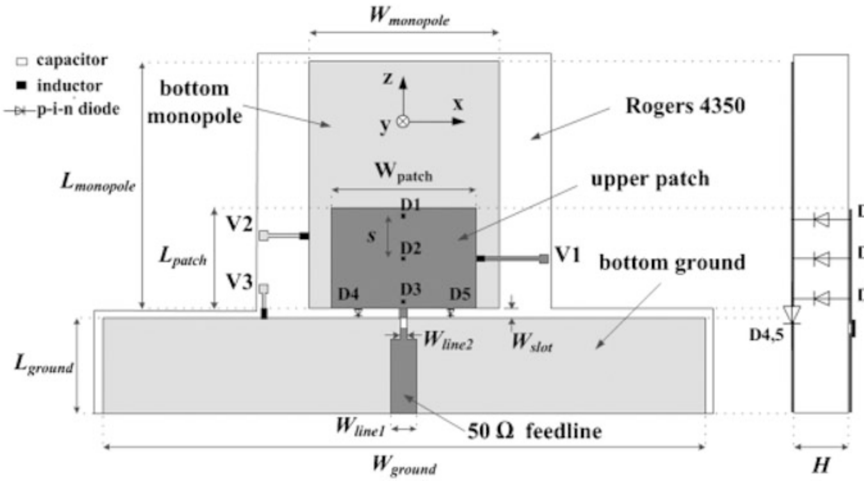

Fig. 9.22 Dimension of the proposed antenna

(EBG) for satellite navigation was explained in [92]. The proposed antenna consists of EBS surface that has the same metallic rectangular patches array on both sides of the thin substrate, and it has active biasing circuit on each surface that helps to rotate the reflection phase orthogonally concerning the incident waves. A CPW fed is used for the proposed antenna design and provides good impedance matching for the frequency tuning and switching the circular polarization (RHCP/LHCP). Measurement results show the good agreement with simulated and mathematical analysis, and antenna prototype shows the measured 3 dB AR bandwidth to 40%.

Another low-profile antenna based on EBG structure was presented in [93] for frequency tuning and shifting between linear and circular polarizations. The proposed antenna has a three-layer structure. The EBG pattern is on the top layer, which has 12 × 12-unit cells square patch at the centre and four strips at the edges. The central patch has a gap that was used for loading PIN diodes. By controlling the biasing voltage of pin diodes, the proposed antenna resonates at the required frequency with polarization switching.

A high-gain antenna with the combination of the metasurface, a planar slot, and the metallic reflector was investigated in [94] as shown in Fig. 9.23. The metasurface consists of 64 identical patches, and due to symmetry of the structure, the equivalent circuit of MS is considered as symmetry RLC circuit because the diagonal corner of the unit cell is not cut in a zigzag shape. Figure 9.24 shows the simulated and measured return losses with different rotating angles. Figure 9.24a shows the results when h_1=9.3 and h_o=19 mm, while Fig. 9.24b represents the results when h_1=7.2 and h_o=16 mm. It can be seen that the operating frequency range is from 8 to 11.2 GHz having return loss values less than −10 dB during the entire bandwidth. The AR of the proposed antenna with angles of $\theta°$=0 and 90° is shown in Fig. 9.25. The 3-dB AR bandwidth is obtained by adjusting the size of h_o and h_1.

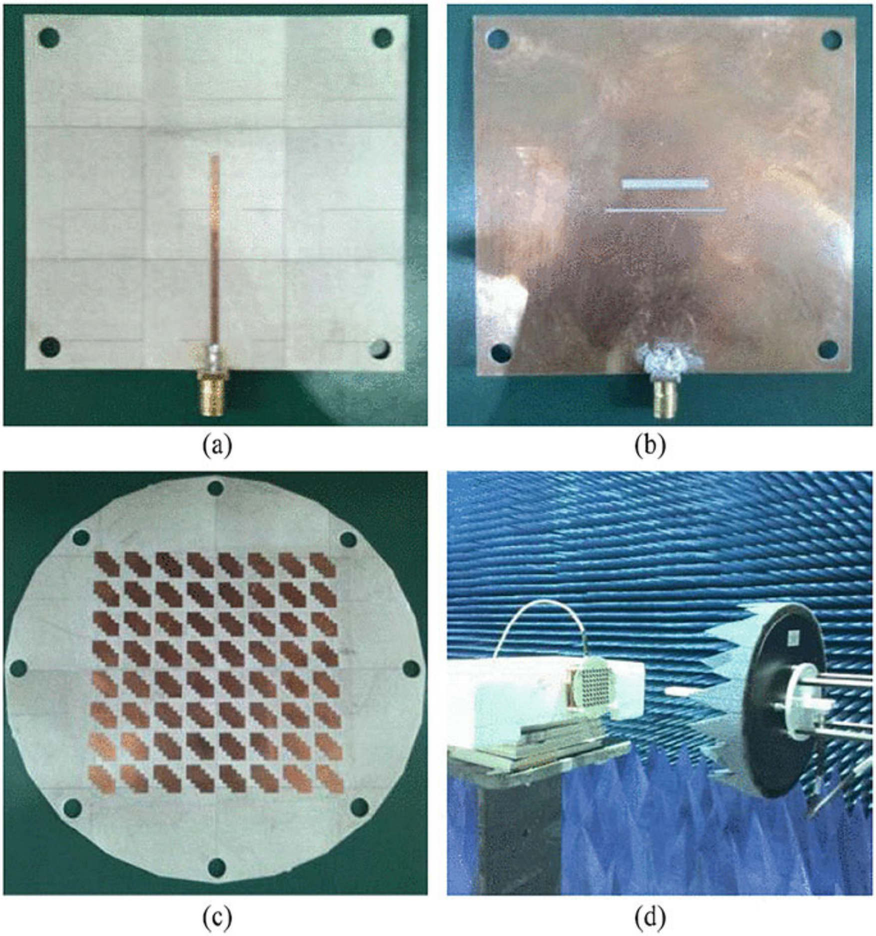

Fig. 9.23 (**a**) Feed line of the proposed antenna. (**b**) Surface of slot antenna. (**c**) MS. (**d**) Measurement setup

For the extension of the bandwidth, the slot antenna is converted into the double-slot structure. The polarization of the proposed antenna can be achieved by rotating the metasurfaces around the centre of the slot structure, and frequency can be tuned by the adjustment of the distance between slot, MS, and metallic reflector. The measured gain for the proposed antenna was 16.5 dBi with a fractional bandwidth of 33.33%.

A stub-loaded patch antenna microstrip patch antenna for smart communications was designed in [95]. The antenna consists of square microstrip patch and 12 identical stubs at the four edges of the patch. The varactor diodes are used for the connection between the stubs and the patch as shown in Fig. 9.26. The biasing circuit is at the other end of the stub and consists of a resistor and a choke inductor. The

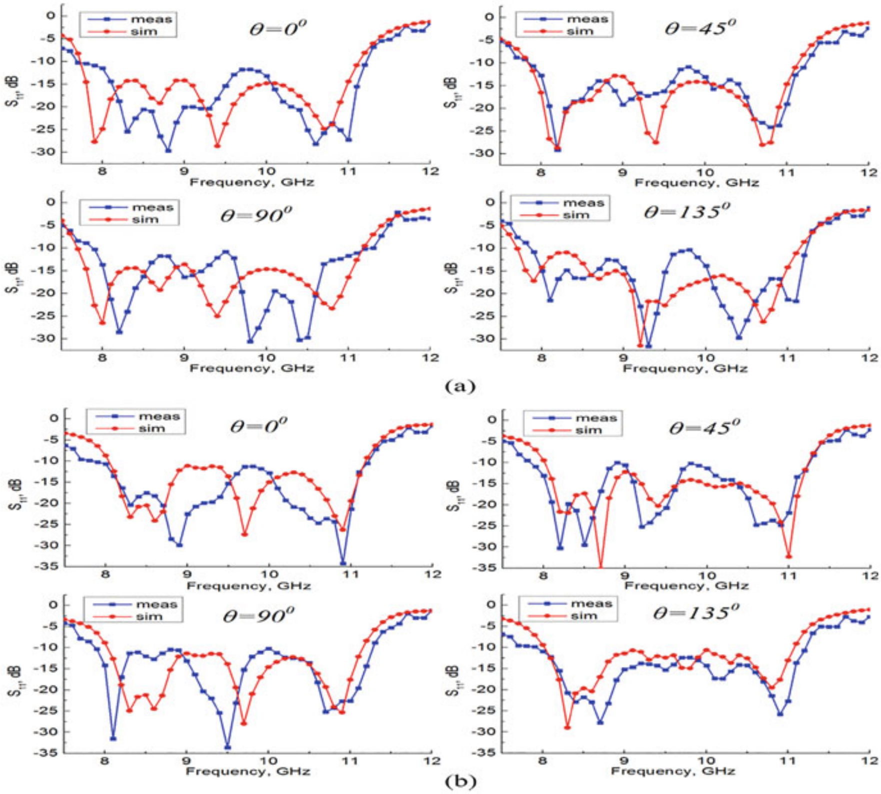

Fig. 9.24 Comparison between the measured and simulated reflection coefficients S_{11}; (**a**) $h_1 = 9.3$ mm, $h_0 = 19.8$ mm, and (**b**) $h_1 = 7.2$ mm, $h_0 = 16$ mm

12 varactors and stubs are divided into two groups and provide independent dc-bias voltage. The antenna prototype shows the wide tuning of frequency around 40%.

The reconfigurable antenna with frequency and polarization capability was presented in [96], and it consists of monopole structure, defected ground plane, and reflector. Two slots are etched, and pin diodes are inserted on the ground plane with the addition of metal vias along with the slots. The antenna shows four different behaviours by changing the different states of the pin diodes and shows linear polarization at states 1 and 2, while shows circular polarization at state 3 (LHCP) and state 4 (RHCP).

The frequency reconfigurability [97] can also be achieved by truncating the square patch at the corner as shown in Fig. 9.27. The truncated square patch is separated from the corner by a narrow slot, it behaves as radiation patch, and the diode is also inserted into the slot to change the circular polarization at different frequencies to make it suitable for modern communication systems.

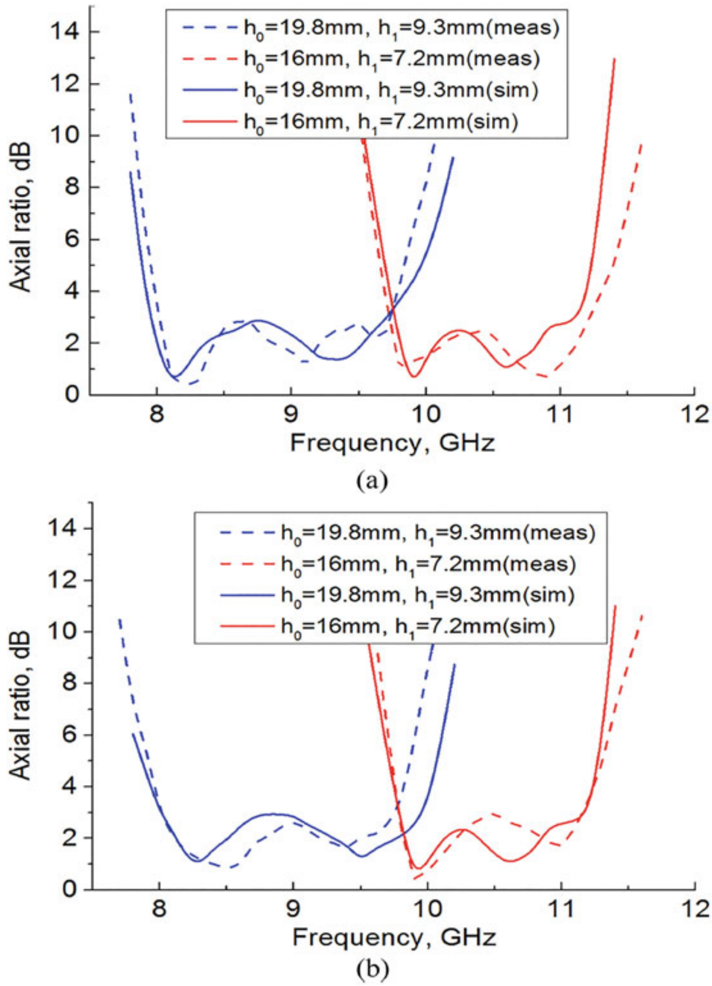

Fig. 9.25 Comparison between the measured and simulated axial ratios with different rotation angles. (**a**) $\theta = 0°$. (**b**) $\theta = 90°$

A dual-probe feed reconfigurable antenna was explained in [98]. The antenna consists of circular-shaped microstrip patch on the top layer and branch line coupler feed etched on ground plane at the bottom layer. The varactor diodes are inserted into the gaps of the circular patch at the top layer, and a reverse bias voltage is applied with the help of biasing pad that is at the side of the patch. An additional BLC feed network was used for simultaneously tuning of the frequency from 2.05 to 3.13 GHz along with circular polarization.

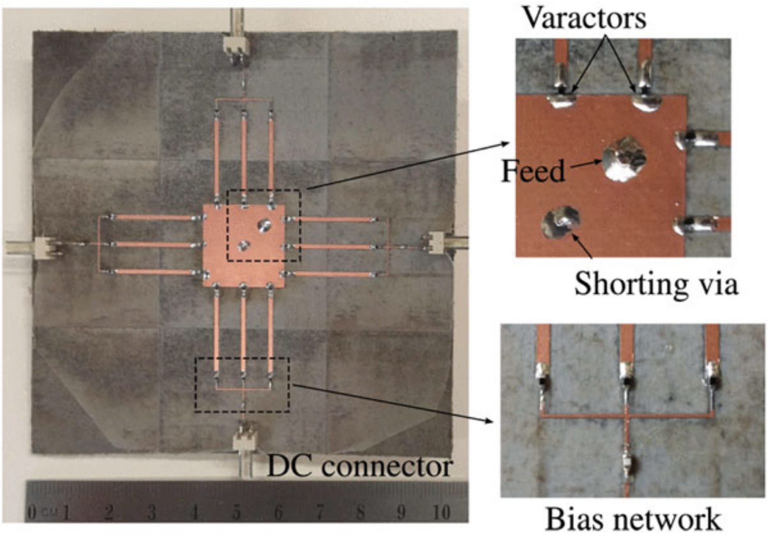

Fig. 9.26 Antenna prototype

9.4.4.3 Radiation Pattern and Polarization Reconfigurable Antenna

The reconfiguration in radiation pattern along with polarization supports beam steering and multiple polarization shifting on a single antenna radiator. They increase the capacity of modern communication systems and improve signal strength and radiation coverage. These types of examples are presented in recent years.

An omnidirectional patch that operates at two orthogonal ±45 linear polarizations and produces a dipole-like radiation pattern for convening both polarization and radiation pattern reconfigurability was explained in [99]. The proposed antenna consists of two back-to-back coupled patches with common ground. The antenna has four input ports, and polarization can be achieved by the port selection, while the phase difference between the ports is utilized for radiation pattern reconfigurability and promising candidate for the MIMO applications.

A compact-size, low-cost, and smart antenna for beam switching and polarization reconfiguration was designed in [100]. The antenna has dual-port inset fed patch, parasitic elements, and driven elements as shown in Fig. 9.28. The driven element is the combination of square patch antenna with simple feeding network, and parasitic element consists of the printed dipole with PIN diodes. The radiation pattern can be obtained by placing reconfigurable parasitic elements around the driven antenna over the three polarization states.

A simple, low-profile PIFA antenna for radiation pattern along with polarization reconfiguration for WLAN application was presented in [101]. The antenna consists of the printed inverted-F antenna on the top-left corner and another printed inverted F parasitic element for pattern reconfiguration on the bottom-right corner. The

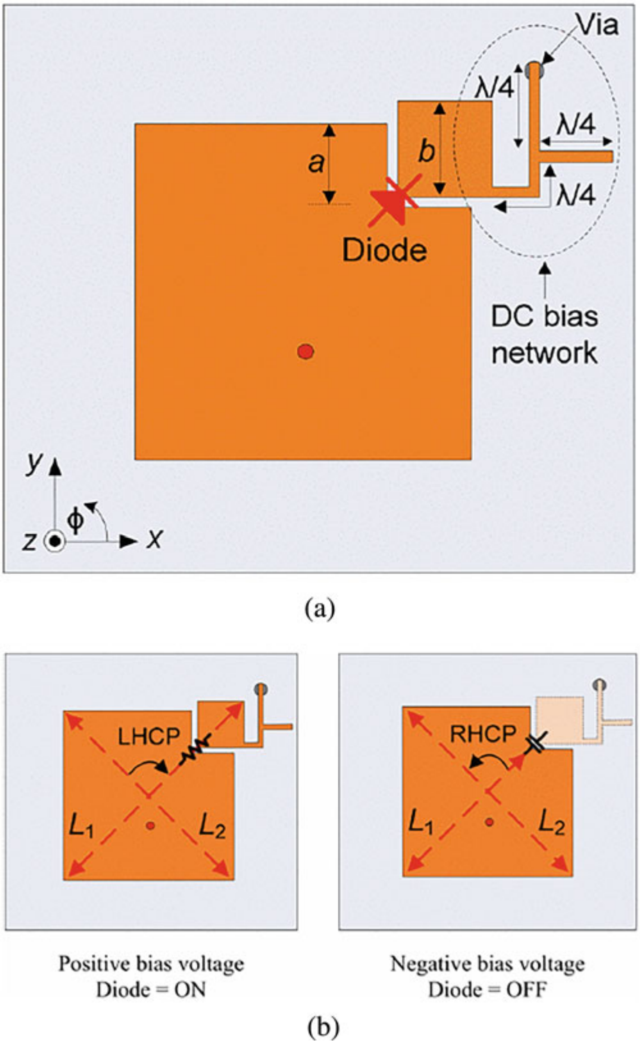

Fig. 9.27 (**a**) Schematic of the proposed antenna. (**b**) Biasing operation mechanism

antenna prototype shows a good gain of 1.2 and 4.2 dBi for ON and OFF states, respectively, and it can be used for wireless router applications. A circularly polarized switchable feed network antenna with reconfigurable beam pattern for the wireless system was expressed in [102] as shown in Fig. 9.29. A high-gain radiation pattern and polarization reconfigurable antenna using metasurface was explained in [103]. The antenna structure consists of three layers. The top layer consists of metasurface that is the combination of 4 × 4 nonuniform rectangular metal films. The pin diodes are inserted between these films and used to get the

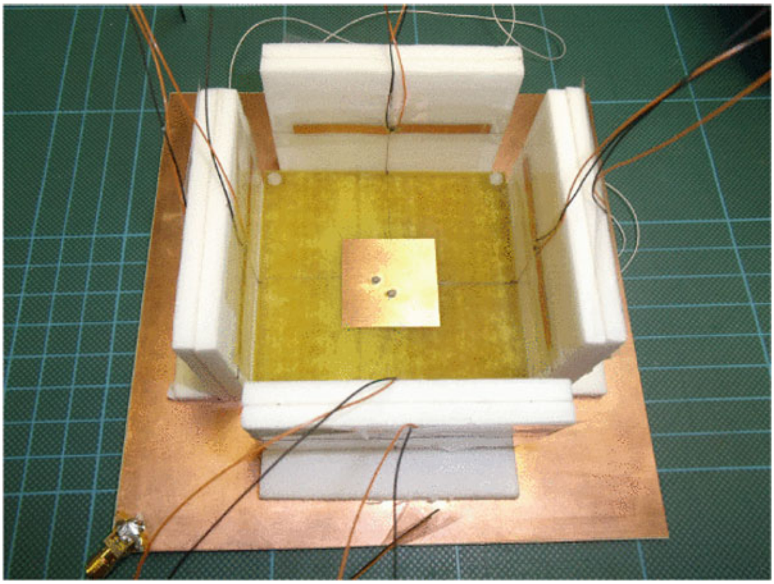

Fig. 9.28 Antenna prototype

pattern reconfiguration between ±20 in the direction of the Z-axis. The middle layer is the ground plane, and pin diodes are also used between the slots to get the polarization reconfiguration. The proposed antenna resonates between 4.95 and 5.05 GHz, and the gain of the main lobe is 7–8 dBi.

A compact-size cuboid quadrifilar helical antenna (QHA) to operate at 0.9 GHz with radiation pattern and polarization reconfigurability was explained in [104]. The proposed antenna is the combination of a reconfigurable radiator and switchable feeding network. The reconfigurable radiator consists of folding the thin substrate that behaves like a cuboid, and the radiation arms on the surface. The switchable feeding network consists of out-of-phase power divider and two reconfigurable couplers. The proposed antenna prototype resonates between two orthogonal CP and switch radiation pattern between broad-side and back-fire modes. The measured and simulated return losses are shown in Fig. 9.30. It shows the wide impedance bandwidth of 36.2% from 0.32 to 1.04 GHz for all resonating states. The measured and simulated ARs are shown in Fig. 9.31. The measured 3-dB AR bandwidth is 22% with frequency range (0.8–1 GHz). The slight difference between the simulated and measured results is due to the equivalent circuit of PIN diode model, which is not equal to the actual effect of the PIN diode. Another frequency and radiation pattern reconfigurable low-profile antenna was explained in [105]. The antenna consists of simple patch radiator and parasitic elements that relate to the help of pin diodes.

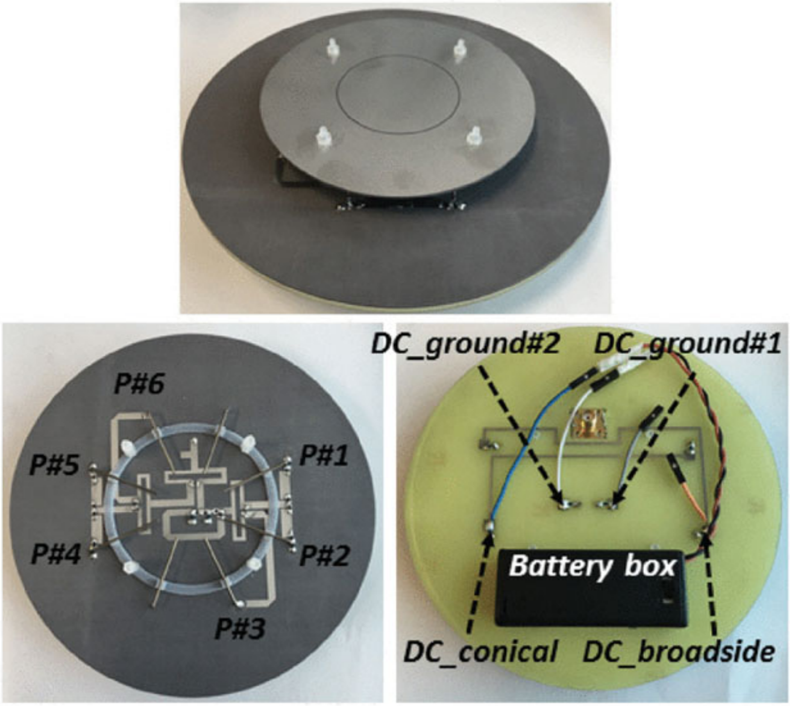

Fig. 9.29 Proposed antenna prototype

9.4.4.4 Frequency, Radiation Pattern, and Polarization Reconfigurable Antenna

Mostly designs explained in the above examples are either single or dual-characteristic reconfigurable antennas. In this technique, one can tune the antenna parameters (frequency, radiation pattern, polarization) simultaneously, and they help in multipath scenarios, fading, and shadowing effects. A little work has been done on this category. The first work on this technique was presented in [106]. This antenna consists of small metallic patches known as pixel surface, radiation patch, and 60 PIN diode switches as shown in Fig. 9.32. The antenna prototype shows the frequency tuning over 25% range, beam steering over ±30 in two principal planes and switching between four different polarizations (Fig. 9.33).

Another antenna of this type was explained in [107]. The antenna structure is the combination of a rhombus-shaped radiator, three excitation lines at different angles, and connected with common feed line. The required configuration can be obtained by changing the biasing states of three pairs of PIN diodes. The proposed antenna can tune frequency between 5.2/5.8 GHz, linear/circular/±45 polarizations with beam titled at 30 in right- and left-hand directions. The measured and simulated reflection coefficients, when D6 is off and on, can be seen in Fig. 9.34a, b,

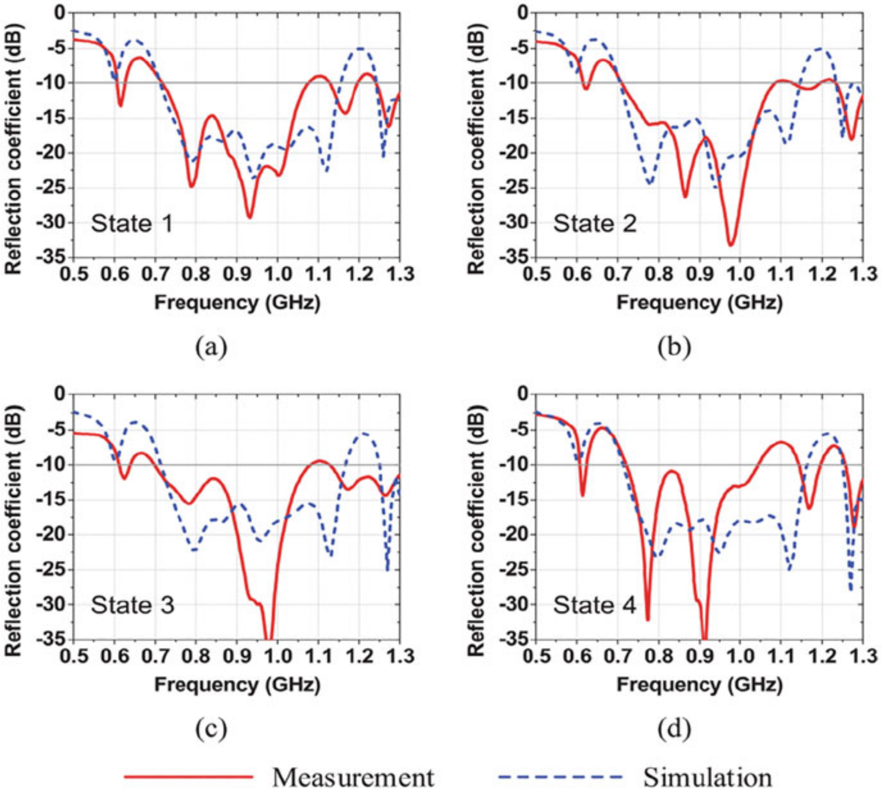

Fig. 9.30 Simulated and measured reflection coefficients of the proposed reconfigurable cuboid QHA. (**a**) State 1, (**b**) State 2, (**c**) State 3, and (**d**) State 4

respectively. The measured percentage bandwidths at 5.8 and 5.2 GHz frequency are 3.50 and 3.59%, respectively. A novel cavity-based slot antenna for frequency, radiation pattern, and polarization reconfiguration was investigated in [108] as shown in Fig. 9.33. The reconfigurability can be obtained controlling the states of the switches between the two cross slots etched on the surface of the SIW cavity.

9.5 Reconfigurable SIW Antenna

The invention of SIW provides low loss, good power handling capacity, and effective functionality with planar circuits [109]. The structure of SIW is similar to conventional cavity slot and provides a low profile, flexibility, and simple integration with planar circuits [110, 111]. The SIW is composed of fittingly divided vias with a similar distance between them engendering with least radiation loss. The dispersion

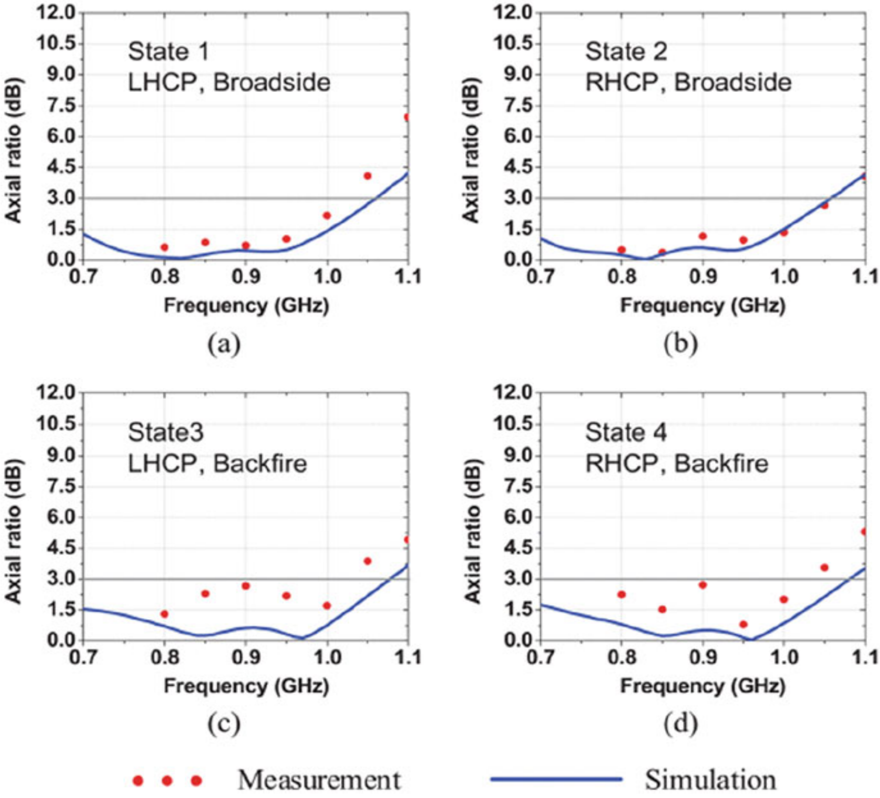

Fig. 9.31 Comparison between the simulated and measured ARs of the proposed reconfigurable antenna in different states; (**a**) State 1, (**b**) State 2, (**c**) State 3, and (**d**) State 4

between the vias controls the field spillage of the waveguide. The SIW waveguide shapes with rectangular waveguide shape along with two conveyor planes, which are separated by dielectric substrates with channel sidewalls by lines metalized through vias. The SIW technology is an elective strategy for the minimal effort of waveguide like the parts integrated with simple PCB standards [112, 113]. It is much better in comparison with existing technologies as for lightweight, ease of integration, and straightforward. A novel leaky-wave antenna with fixed frequency and switchable beam steering for 5G application was explained in [114]. In this chapter, the pin diodes are used to control the phase shift angle and position of the feeding slots as shown in Fig. 9.35. A new technique of central excitation based on four coupling plated through hole was introduced. The holes relate to the ground plane and top wall as well. The reconfigurable feeding method is applied by using the pin diodes. The measured and simulated return losses for the proposed antenna are shown in Fig. 9.36. The frequency range is from 26.2 to 27.3 GHz with reflection coefficient magnitude lower than −12 dB. The radiation efficiency varies between

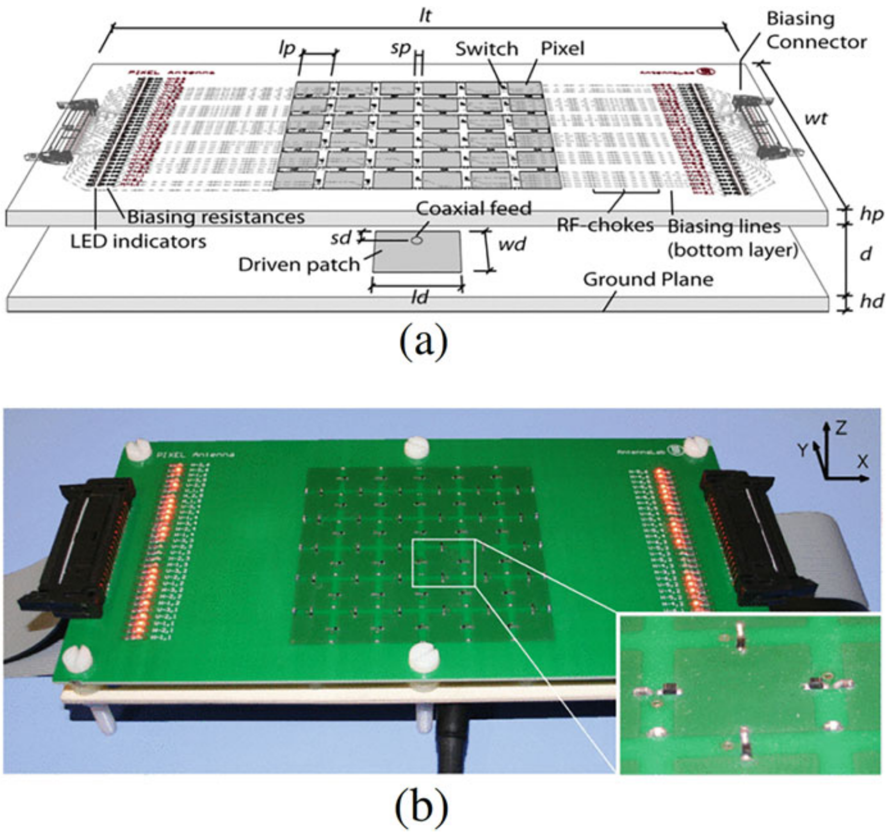

Fig. 9.32 (**a**) Schematic of the parasitic pixel layer. (**b**) Pixel antenna prototype

60 and 94% depending on the excitation configuration. The discrepancy between the measured and simulated results is due the construction of biasing circuit, which was not considered during the simulation.

9.6 Reconfigurable Band-Notch UWB Antenna

In the last few years, UWB technology gained much attention due to its advantages like low-power consumption, wide bandwidth, low cost, less complexity, and high data rate transmission [115, 116]. Due to these properties, UWB technology is widely used in many applications like indoor communication, cognitive radio, radar, localization, and automotive, etc. [117–119]. There are several other narrow band standards coexist within the UWB like IEEE 802.16 WiMAX (3.3–3.6 GHz; 5.25–5.825 GHz), IEEE 802.11a wide local area network (WLAN) (5.15–5.35 GHz;

Fig. 9.33 Proposed antenna prototype

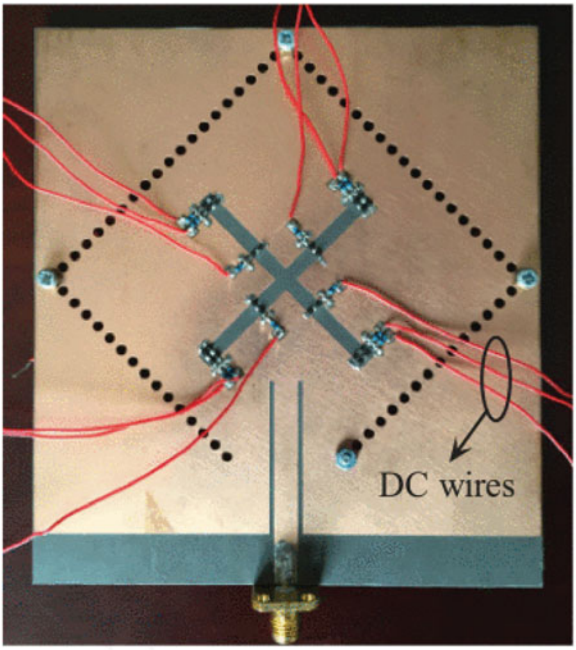

(a)

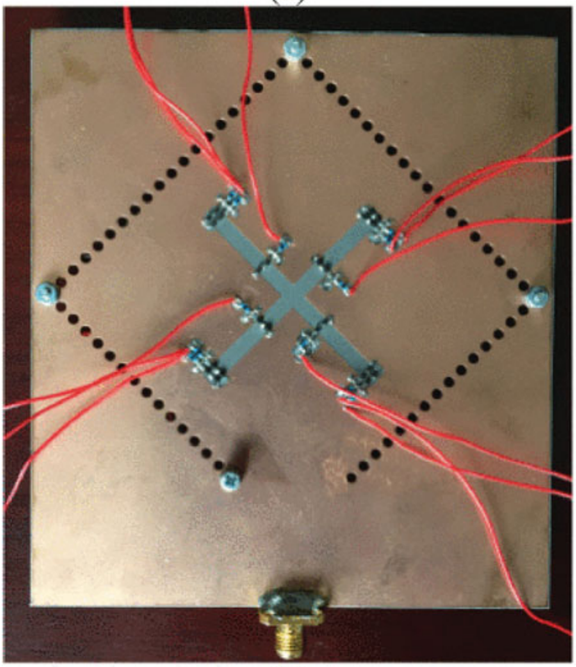

(b)

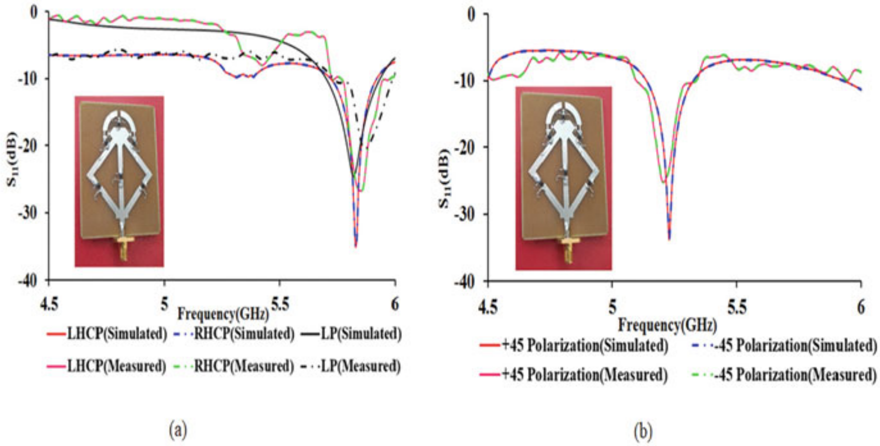

Fig. 9.34 (**a**) Comparison between the simulated and measured S-parameters, when PIN diode D6 is "OFF." (**b**) Comparison between the simulated and measured S-parameters, when PIN diode D6 is "ON"

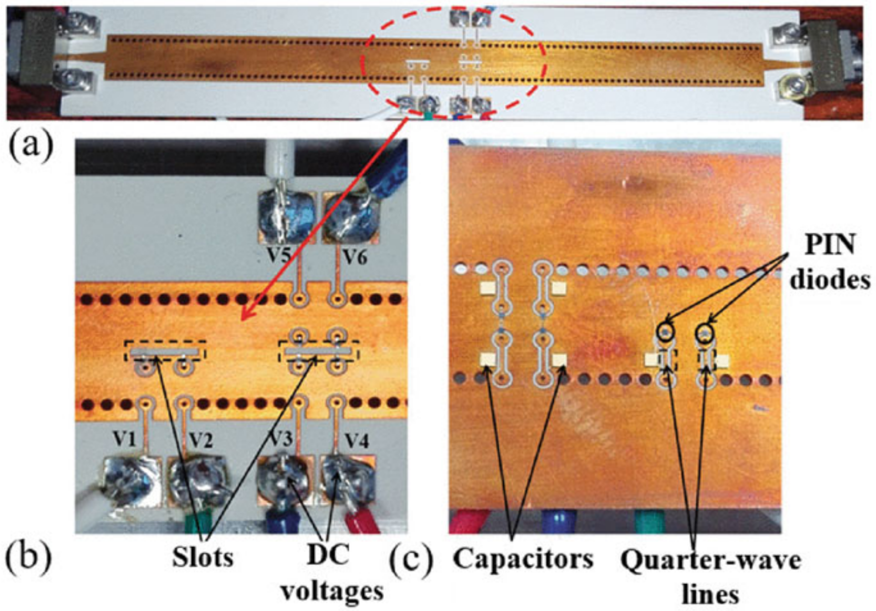

Fig. 9.35 (**a**) Prototype overview. (**b**) Front view. (**c**) Back view

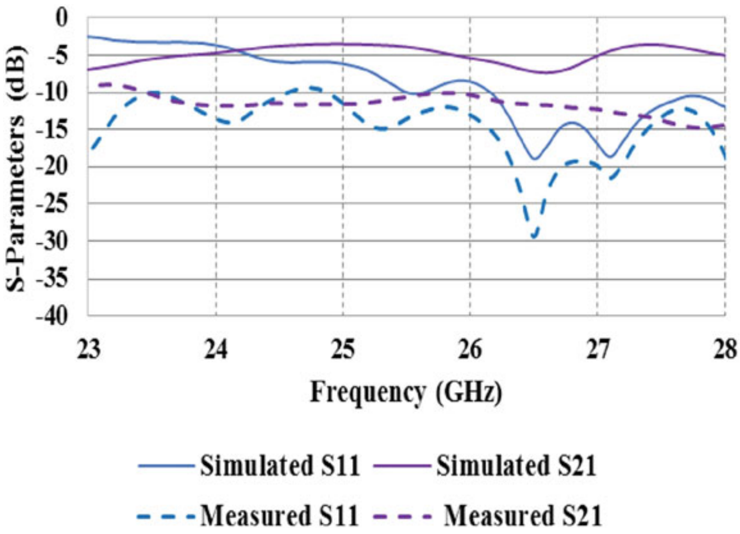

Fig. 9.36 Simulated and measured reflection coefficients of antenna array

5.725–5.825 GHz), and ETSI HiperLAN /2 (5.15–5.35 GHz, 5.47–5.725 GHz). This overlap band creates the electromagnetic interfaces with UWB technology when they are operating at the same time in other wireless devices [120–122]. Normally, filter is used to stop the unwanted band and increase the communication efficiency, but the addition of the filters in the latest compact communications systems increases the overall size, cost, makes more complex, and increases the insertion losses [123, 124]. So, much research is going on to design the UWB antenna with band-notch characteristics. The UWB antenna with band-notch characteristics was developed by using slot or slit [125–127], slots in the feeding network [128–130], slot in the ground plane [131–133], and parasitic patches [134, 135]. Hence, they are fixed band notched UWB antennas, and they are not applicable to utilize all frequency ranges of the UWB technology. By using the reconfigurable band-notching technique, one can use the required frequency band as per system requirement

The low-profile reconfigurable UWB antenna with single or dual-band rejection property was expressed in [136] as shown in Fig. 9.37. The proposed antenna is the combination of monopole structure, pin diode, biasing circuit, partial ground plane along with arc-shaped slot, and open-ended L-shaped stubs for band rejection. The antenna operates in four modes: full UWB (3.1–10.6 GHz), single-band rejection of WiMAX or WLAN, and dual-band (WiMAX, WLAN) band rejection. The dual-band reconfigurable notched slot-type split ring resonator (ST-SRR) antenna for WiMAX and WLAN applications was explained in [137]. The defected ground plane is used to for impedance matching, and ST-SRR is used in the feed to get the required band notch for UWB antenna. The measurement results show that antenna gains a fractional bandwidth of 138.63%. A novel compact triple band-

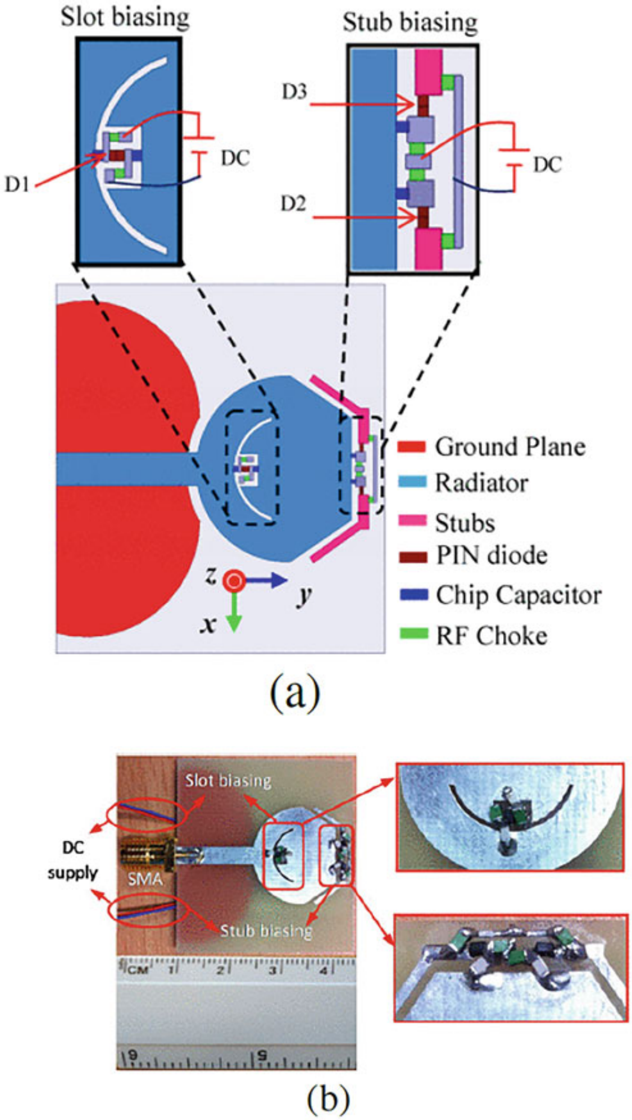

Fig. 9.37 (**a**) Antenna dimension. (**b**) Antenna prototype

notched reconfigurable fractal antenna was explained in [138]. By using the fractal technique, the overall size of the proposed antenna is reduced to 53% as shown in Fig. 9.38. The proposed antenna consists of circular patch, slots, pin diodes, and split ring resonator (SRR). The proposed antenna behaves as notched frequency at WiMAX, WLAN, and X bands.

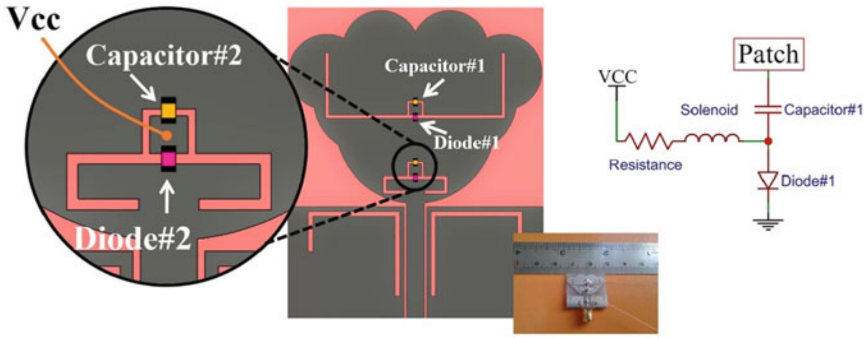

Fig. 9.38 Antenna structure with biasing circuit

9.7 Reconfigurable Metamaterial Antenna

The advancement in metamaterial and metasurface has brought more opportunities in the field of microwave devices. According to the definition, metamaterials have artificial and unusual characteristics such as negative permittivity and permeability that do not occur in natural materials [139]. Except for low profile, metamaterials also provide more flexibility in the design of microwave device and more functionality for the control. Metasurface (MS) is two-dimensional equivalent of metamaterials, and it helped to improve the return loss and gain along with the polarization of an antenna [140]. The frequency and polarization reconfigurable antenna using double-layer metasurface was explained in [141]. The polarization reconfigurable metasurface (PRMS) is in the uppermost layer on the side face to the middle layer, while frequency reconfigurable metasurface (FRMS) is on the opposite side of the patch antenna. The proposed antenna shows the frequency between 4 and 5 GHz and the polarization switching between LP, RHCP, and RHCP.

A wideband polarization reconfigurable antenna is presented in [142]. The metasurfaces in this chapter are the combination of 4 × 4 periodic metal plates. The proposed antenna consists of square patch radiation, metasurface, and four tunable switching feeding probes. The switchable feeding network is the combination of a 2-way power divider and SPDT switches that consist of pin diodes as shown in Fig. 9.39. By changing the biasing voltage, the proposed antenna is tuned between x and y direction linear polarization and RHCP/LHCP. The beam switching reconfigurable antenna was expressed in [143]. The reconfigurable metasurface is the combination of double-slit square ring and pin diodes.

9.8 Reconfigurable Antenna for Flexible Material

In recent years, wearable antenna technology has gained much attention in industry and academia due to its vast feathers like lightweight, flexible, low cost, and easily integrable with modern communication systems. In the medical field, wearable

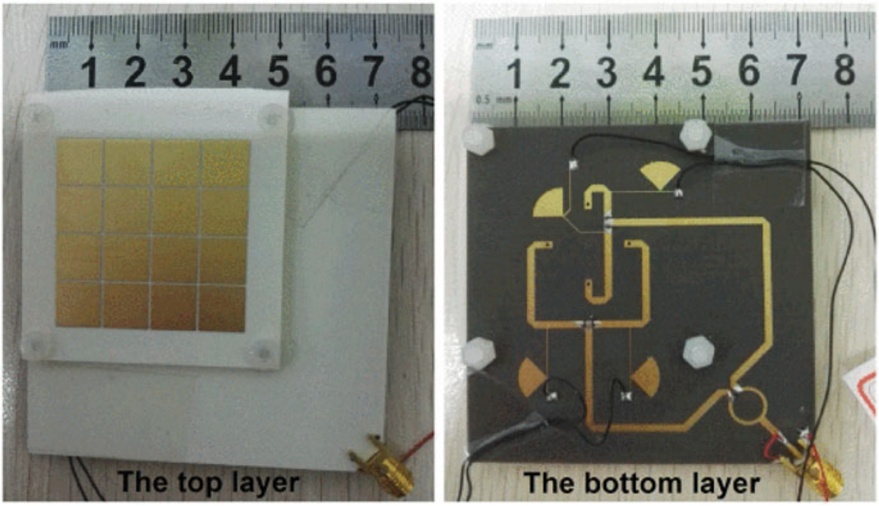

Fig. 9.39 Antenna prototype

antennas are used to monitor the critical health condition of the patient, check sugar level, and investigate the inner intestinal system, blood pressure, heartbeat, and temperature of the body. In the recreation side, they contribute in the way of augmented reality glasses, touchscreen computer, and smartwatches. The flexible antenna with reconfigurable technique provides the small-size and low-cost solution for modern electronics and advanced wireless communication systems. There are some challenges related to the integration of reconfigurable components such as switches, biasing circuits, and mechanical stability. Extensive research and antenna prototypes have been developed on the rigid and conventional substrate in the last few decades. The requirement of the flexible antenna with reconfigurable technique has been increased as they are the main component of the wearable technology and cope up with the advance wearable devices.

The CPW-fed-based quad-band and penta-band flexible reconfigurable antennas are presented in [144], [21], and [145], respectively. The copper tape is used in these antenna prototypes, making it difficult to predict the exact behaviour of PIN diodes for practical applications. The flexible reconfigurable antenna on PET film for WLAN/WiMAX wireless applications was presented in [146]. The antenna has folded slot and CPW-fed but with large antenna volume. The dual-band CPW-fed flexible reconfigurable antenna was explained in [147]. It is monopole antenna incorporated with U-shaped slot to get the required frequency. The frequency and polarization reconfigurable flexible antennas were investigated in [148]. The antenna consists of a folded slot, stub, and artificial magnetic conductor (AMC) surface to reduce the SAR value. The antenna prototype shows good agreement in a flat and curved situation, and measurement on the human body as well. A robust, flexible, and frequency reconfigurable antenna was presented in [149]. The antenna

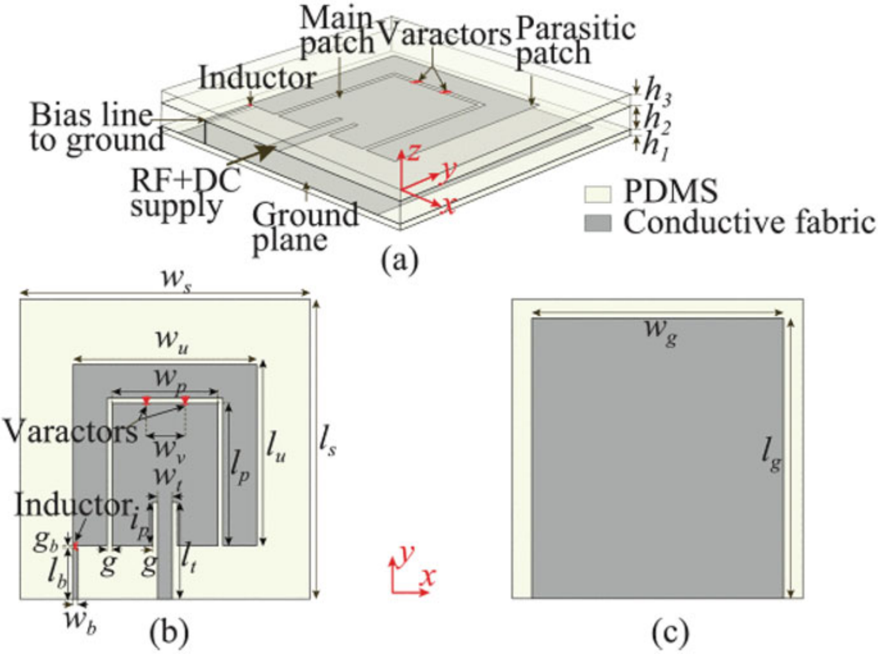

Fig. 9.40 Antenna configuration. (**a**) Cross-sectional view. (**b**) Patch layer. (**c**) Ground layer

consists of conductive fibre on polydimethylsiloxane (PDMS) substrate as shown in Fig. 9.40. The antenna prototype and other lumped components were encapsulated with an additional layer of PDMS. The antenna bending characteristics were investigated in free space, on body phantom, and in the household washing machine. These tests show that antenna working order is normal even in extreme bending (radius 28 mm) and after washing. An inkjet-printed frequency reconfigurable antenna on a paper substrate for wireless applications was explained in [150]. The antenna consists of a main radiator, L-shaped, U-shaped radiators, and the ground plane. With the help of a PIN diode, the proposed antenna can tune between 1.5 and 4 GHz.

9.9 Application of Reconfigurable Antenna

The new era of antenna design must generate an antenna that is cognitive and adjust to the environment and ever-changing conditions. Also, there is a need for antennas that can overcome failure and swiftly respond to new developments. Cognitive radio, massive multiple-input multiple-output (MIMO), wireless body area networks, satellite, and space communication platforms are all possible applications for the integration of highly, reliable, and efficient reconfigurable antenna.

9.9.1 Reconfigurable Antenna for MIMO Communication System

To fulfil the requirements of current and future modern communication systems, MIMO system plays a vital role to cover the high data rate and signal strength requirements within a defined bandwidth. The MIMO technology depends on the multiple antennas that are implemented on both sides of the communication systems. The implementation of MIMO reconfigurable antenna at the front end will improve the data capacity and directivity significantly.

A frequency reconfigurable antenna for MIMO applications was explained in [151]. The single element of an antenna is the combination of 4 × 4 MIMO antenna, and it is designed to operate 2.4 and 2.6 GHz frequency. The single element MIMO antenna is either two 2 × 2 MIMO antenna or a single 4 × 4 array as shown in Fig. 9.41. The proposed antenna is coaxially fed, and pin diodes are inserted on the backside. The different states of the pin diodes are controlled by microcontroller module. To get the high gain, an air gap is introduced between the radiation patch and the ground plane.

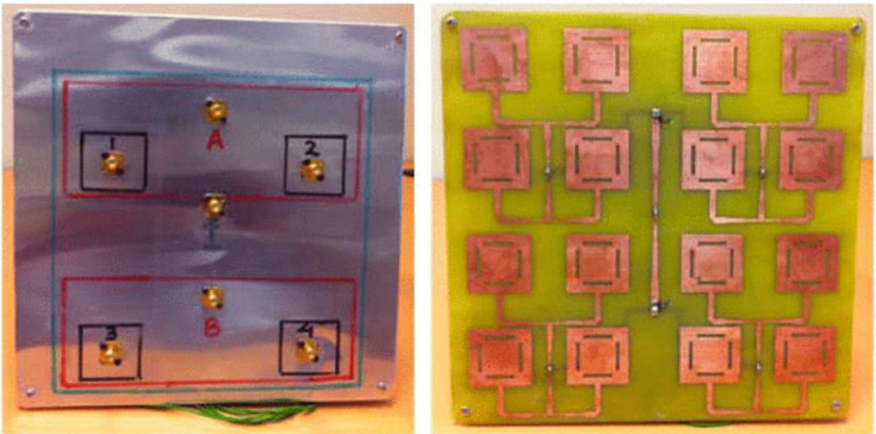

Fig. 9.41 Antenna prototype

9.9.2 *Reconfigurable Antenna for Cognitive Radio Applications*

With every passing day, the wireless subscribers are gradually increasing. It is a big challenge to provide a high data rate and fast browsing speed. Secondly, the distribution of the band spectrum is not uniform, which also badly affects the overall efficiency of the system. To overcome this limitation, a new technique named cognitive radio was introduced that uses the unoccupied/idle band spectrum for communication and increases the system efficiency. Wideband and reconfigurable antennas are a promising candidate for cognitive radio communication. Additionally, compact-size antennas are the requirements for portable mobile devices.

A compact novel broadband antenna was presented in [152]. In this chapter, both the discrete and continuous tuning was implemented to get a large frequency range. The antenna consists of UWB monopole antenna with reconfigurable impedance matching network as shown in Fig. 9.42. The proposed design has two independent paths to cover the 430 MHz and 5 GHz frequency. The first path is directly connected with a UWB antenna that covers the 1–5 GHz frequency range. The second path is controlled through a varactor-diode-based matching network. Two discrete switches are used to move between wideband and reconfigurable modes.

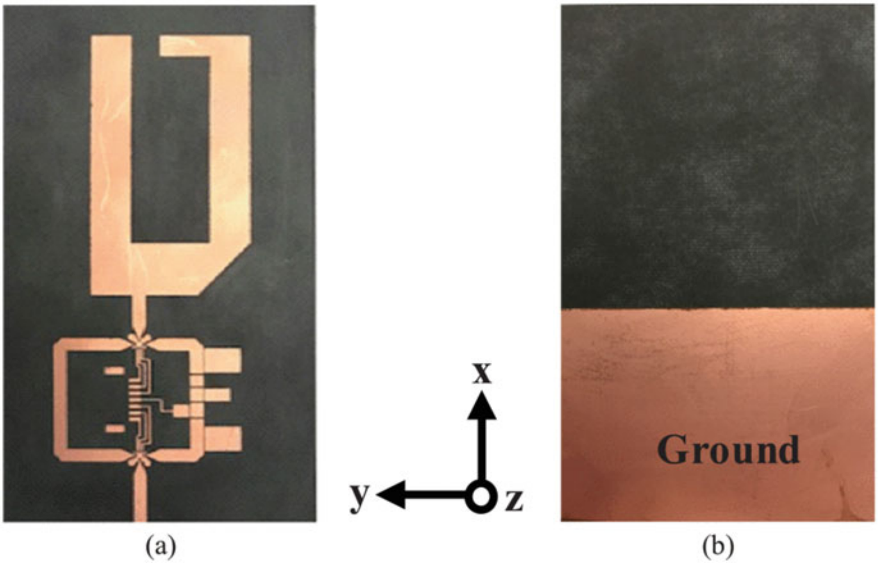

Fig. 9.42 Antenna prototype

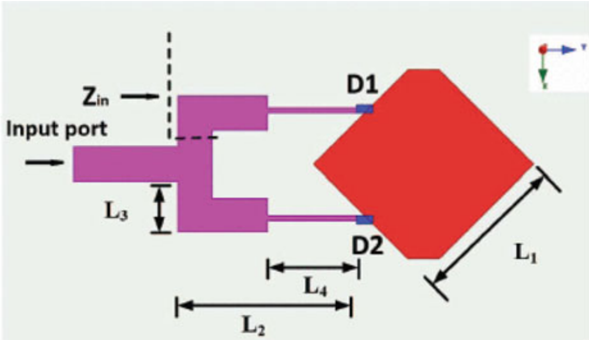

Fig. 9.43 Dimension of the proposed antenna

9.9.3 Reconfigurable Antenna for Millimetre-Wave Communication

5G is the promising solution to address the modern wireless network demands like higher data throughput and hence bandwidth. They also provide wide and unemployed bandwidth. The mm-wave band lies between 30 and 300 GHz frequency ranges. While using the higher frequency, the new challenges arise like an increase in patch loss and complexity of the system including antennas, filter, and amplifiers. The compact reconfigurable antenna with tunable radiation pattern is of great interest to maintain the user requirements in an atmosphere-dependent scenario.

Figure 9.43 shows a polarization reconfigurable antenna, consisting of square radiation patch, microstrip line, and two PIN diodes [153]. The proposed antenna can switch between RHCP and LHCP by changing the states of pin diodes. The antenna shows impedance bandwidth from 27.6 to 28.6 GHz. A good axial ration is also achieved between 27.65 and 28.35 GHz.

9.10 Future of Reconfigurable Antenna

The reconfigurable antennas have attractive features and provide flexibility in adjusting the functionality of the system, minimizing the overall system volume and circuit complexity. It is desired to use the reconfigurable antenna to increase the system capacity, spectrum, and energy efficiency. To make an antenna reconfigurable and change its three main properties (resonance frequency, radiation pattern, and polarization), different methods and novel design ideas have been proposed in the literature. However, there is still some imperfection, which adversely affects the performance of the reconfigurable antennas. These imperfections include large volume size, limited gain, and non-linear behaviour of RF switches, narrow bandwidth, complex impedance matching circuit, complicated biasing circuit, and finite overall performance.

Future research in this field will need to focus on the problem, which has a great impact on modern wireless communication systems. Since many antenna designs for advanced communication systems employ antenna array, including reconfigurable antenna array, metamaterial reconfigurable antenna array, and directional narrow beam antenna, hybrid (frequency, radiation pattern, and polarization) reconfigurable antenna will lead another important research direction for future endeavour.

9.11 Conclusion

This chapter starts with the brief history of reconfigurable antenna. The techniques and properties for the reconfiguration of an antenna were explained in detail. Some existing proposed reconfigurable antenna designs, methods, and their constraints are also discussed. In addition, the applications and the benefits of the reconfigurable antennas are highlighted.

References

1. G.A. Norton, Apparatus for wave changing in radio signaling, ed: Google Patents (1926)
2. H. Friis, C. Feldman, W. Sharpless, The determination of the direction of arrival of short radio waves. Proc. Inst. Radio Eng. **22**(1), 47–78 (1934)
3. E. Bruce, A. Beck, Experiments with directivity steering for fading reduction. Proc. Inst. Radio Eng. **23**(4), 357–371 (1935)
4. H.T. Friis, C.B. Feldman, A multiple unit steerable antenna for short-wave reception. Proc. Inst. Radio Eng. **25**(7), 841–917 (1937)
5. W. Ernst, Antenna tunable in its length. ed: Google Patents (1942)
6. R. Antennas, Bell Syst. Tech. J. **26**-317 (1947), p. 219
7. W. Rotman, A. Maestri, An electromechanically scannable trough waveguide array, in *1958 IRE International Convention Record*, vol. 8. (IEEE, Piscataway, 1966), pp. 67–83
8. E. Matthews, C. Cuccia, M. Rubin, Technology considerations for the use of multiple beam antenna systems in communication satellites. IEEE Trans. Microw. Theory Tech. **27**(12), 998–1004 (1979)
9. D.H. Schaubert, F.G. Farrar, S.T. Hayes, A.R. Sindoris, Frequency-agile, polarization diverse microstrip antennas and frequency scanned arrays, ed: Google Patents (1983)
10. J.T. Bernhard, Reconfigurable antennas. Synthesis Lect. Antennas **2**(1), 1–66 (2007)
11. R.L. Haupt, M. Lanagan, Reconfigurable antennas. IEEE Antennas Propag. Mag. **55**(1), 49–61 (2013)
12. D. Rodrigo, L. Jofre, B.A. Cetiner, Circular beam-steering reconfigurable antenna with liquid metal parasitics. IEEE Trans. Antennas Propag. **60**(4), 1796–1802 (2012)
13. X. Bai, M. Su, Y. Liu, Y. Wu, Wideband pattern-reconfigurable cone antenna employing liquid-metal reflectors. IEEE Antennas Wireless Propag. Lett. **17**(5), 916–919 (2018)

14. M. Alam, A. Abbosh, Beam-steerable planar antenna using circular disc and four PIN-controlled tapered stubs for WiMAX and WLAN applications. IEEE Antennas Wireless Propag. Lett. **15**, 980–983 (2015)
15. G. Ruvio, M.J. Ammann, Z.N. Chen, Wideband reconfigurable rolled planar monopole antenna. IEEE Trans. Antennas Propag. **55**(6), 1760–1767 (2007)
16. Y. Tawk, J. Costantine, K. Avery, C. Christodoulou, Implementation of a cognitive radio front-end using rotatable controlled reconfigurable antennas. IEEE Trans. Antennas Propag. **59**(5), 1773–1778 (2011)
17. J.-C. Langer, J. Zou, C. Liu, J. Bernhard, Micromachined reconfigurable out-of-plane microstrip patch antenna using plastic deformation magnetic actuation. IEEE Microw. Wireless Components Lett. **13**(3), 120–122 (2003)
18. J.T. Bernhard, E. Kiely, G. Washington, A smart mechanically actuated two-layer electromagnetically coupled microstrip antenna with variable frequency, bandwidth, and antenna gain. IEEE Trans. Antennas Propag. **49**(4), 597–601 (2001)
19. S. Cheng, Z. Wu, P. Hallbjorner, K. Hjort, A. Rydberg, Foldable and stretchable liquid metal planar inverted cone antenna. IEEE Trans. Antennas Propag. **57**(12), 3765–3771 (2009)
20. T. Aboufoul, A. Alomainy, C. Parini, Reconfiguring UWB monopole antenna for cognitive radio applications using GaAs FET switches. IEEE Antennas Wireless Propag. Lett. **11**, 392–394 (2012)
21. N. Haider, D. Caratelli, A. Yarovoy, Recent developments in reconfigurable and multiband antenna technology. Int. J. Antennas Propag. **2013**, 1–14 (2013)
22. T.J. Jung, I.J. Hyeon, C.W. Baek, S. Lim, Circular/linear polarization reconfigurable antenna on simplified RF-MEMS packaging platform in K-band. IEEE Trans. Antennas Propag. **60**(11), 5039–5045 (2012)
23. A. Tagantsev, V. Sherman, K. Astafiev, J. Venkatesh, N. Setter, Ferroelectric materials for microwave tunable applications. J. Electroceram. **11**(1–2), 5–66 (2003)
24. R. Mishra, S. Pattnaik, N. Das, Tuning of microstrip antenna on ferrite substrate. IEEE Trans. Antennas Propag. **41**(2), 230–233 (1993)
25. D. Pozar, V. Sanchez, Magnetic tuning of a microstrip antenna on a ferrite substrate. Electron. Lett. **24**(12), 729–731 (1988)
26. A.D. Brown, J.L. Volakis, L.C. Kempel, Y. Botros, Patch antennas on ferromagnetic substrates. IEEE Trans. Antennas Propag. **47**(1), 26–32 (1999)
27. Y. Yashchyshyn, J.W. Modelski, Rigorous analysis and investigations of the scan antennas on a ferroelectric substrate. IEEE Trans. Microw. Theory Tech. **53**(2), 427–438 (2005)
28. M.F. Iskander, Z. Yun, Z. Zhang, R. Jensen, S. Redd, Design of a low-cost 2-D beam-steering antenna using ferroelectric material and CTS technology. IEEE Trans. Microw. Theory Tech. **49**(5), 1000–1003 (2001)
29. G. Lovat, P. Burghignoli, S. Celozzi, A tunable ferroelectric antenna for fixed-frequency scanning applications. IEEE Antennas Wireless Propag. Lett. **5**, 353–356 (2006)
30. M. Rutschlin, V. Sokol, Reconfigurable antenna simulation: design of reconfigurable antennas with electromagnetic simulation. IEEE Microw. Mag. **14**(7), 92–101 (2013)
31. W. Hu et al., Liquid-crystal-based reflectarray antenna with electronically switchable monopulse patterns. Electron. Lett. **43**(14), 744–755 (2007)
32. W. Hu et al., Design and measurement of reconfigurable millimeter wave reflectarray cells with nematic liquid crystal. IEEE Trans. Antennas Propag. **56**(10), 3112–3117 (2008)
33. S. Bildik, S. Dieter, C. Fritzsch, W. Menzel, R. Jakoby, Reconfigurable folded reflectarray antenna based upon liquid crystal technology. IEEE Trans. Antennas Propag. **63**(1), 122–132 (2014)
34. T.S. Teeslink, D. Torres, J.L. Ebel, N. Sepulveda, D.E. Anagnostou, Reconfigurable bowtie antenna using metal-insulator transition in vanadium dioxide. IEEE Antennas Wireless Propag. Lett. **14**, 1381–1384 (2015)
35. D. Zhao, L. Lan, Y. Han, F. Liang, Q. Zhang, B.-Z. Wang, Optically controlled reconfigurable band-notched UWB antenna for cognitive radio applications. IEEE Photon. Technol. Lett. **26**(21), 2173–2176 (2014)

36. P. Alizadeh, C. Parini, K. Rajab, Optically reconfigurable unit cell for Ka-band reflectarray antennas. Electron. Lett. **53**(23), 1526–1528 (2017)
37. S. Pendharker, R. Shevgaonkar, A. Chandorkar, Optically controlled frequency-reconfigurable microstrip antenna with low photoconductivity. IEEE Antennas Wireless Propag. Lett. **13**, 99–102 (2014)
38. C.G. Christodoulou, Y. Tawk, S.A. Lane, S.R. Erwin, Reconfigurable antennas for wireless and space applications. Proc. IEEE **100**(7), 2250–2261 (2012)
39. Y. Tawk, A.R. Albrecht, S. Hemmady, G. Balakrishnan, C.G. Christodoulou, Optically pumped frequency reconfigurable antenna design. IEEE Antennas Wireless Propag. Lett. **9**, 280–283 (2010)
40. C.J. Panagamuwa, A. Chauraya, J. Vardaxoglou, Frequency and beam reconfigurable antenna using photoconducting switches. IEEE Trans. Antennas Propag. **54**(2), 449–454 (2006)
41. S. Shelley, J. Costantine, C.G. Christodoulou, D.E. Anagnostou, J.C. Lyke, FPGA-controlled switch-reconfigured antenna. IEEE Antennas Wireless Propag. Lett. **9**, 355–358 (2010)
42. J. Costantine, Y. Tawk, J. Woodland, N. Flaum, C.G. Christodoulou, Reconfigurable antenna system with a movable ground plane for cognitive radio. IET Microw. Antennas Propag. **8**(11), 858–863 (2014)
43. Z. Jiang, F. Yang, Reconfigurable sensing antennas integrated with thermal switches for wireless temperature monitoring. IEEE Antennas Wireless Propag. Lett. **12**, 914–917 (2013)
44. J. Costantine, Y. Tawk, C.G. Christodoulou, Motion-activated reconfigurable and cognitive radio antenna systems. IEEE Antennas Wireless Propag. Lett. **12**, 1114–1117 (2013)
45. Y. Cai, Y. J. Guo, T. Bird, A frequency reconfigurable printed Yagi-Uda dipole antenna for cognitive radio applications. IEEE Trans. Antennas Propag. **60**(6), 2905–2912 (2012)
46. D. Rodrigo, J. Romeu, L. Jofre, Interference rejection using frequency and pattern reconfigurable antennas, in *Proceedings of the 2012 IEEE International Symposium on Antennas and Propagation* (IEEE, Piscataway, 2012), pp. 1–2
47. L. Ge, K.-M. Luk, Frequency-reconfigurable low-profile circular monopolar patch antenna. IEEE Trans. Antennas Propag. **62**(7), 3443–3449 (2014)
48. C. Sun, H. Zheng, L. Zhang, Y. Liu, A compact frequency-reconfigurable patch antenna for BeiDou (COMPASS) navigation system. IEEE Antennas Wireless Propag. Lett. **13**, 967–970 (2014)
49. N. Behdad, K. Sarabandi, A varactor-tuned dual-band slot antenna. IEEE Trans. Antennas Propag. **54**(2), 401–408 (2006)
50. B.A. Cetiner, G.R. Crusats, L. Jofre, N. Biyikli, RF MEMS integrated frequency reconfigurable annular slot antenna. IEEE Trans. Antennas Propag. **58**(3), 626–632 (2009)
51. C.-Y. Chiu, J. Li, S. Song, R.D. Murch, Frequency-reconfigurable pixel slot antenna. IEEE Trans. Antennas Propag. **60**(10), 4921–4924 (2012)
52. G. Xu, H.L. Peng, C. Sun, J.G. Lu, Y. Zhang, W.Y. Yin, Differential probe fed liquid crystal-based frequency tunable circular ring patch antenna. IEEE Access **6**, 3051–3058 (2017)
53. L. Liu, R. Langley, Liquid crystal tunable microstrip patch antenna. Electron. Lett. **44**(20), 1179–1180 (2008)
54. S.A. Aghdam, A novel UWB monopole antenna with tunable notched behavior using varactor diode. IEEE Antennas Wireless Propag. Lett. **13**, 1243–1246 (2014)
55. A.K. Horestani, Z. Shaterian, J. Naqui, F. Martín, C. Fumeaux, Reconfigurable and tunable S-shaped split-ring resonators and application in band-notched UWB antennas. IEEE Trans. Antennas Propag. **64**(9), 3766–3776 (2016)
56. M.U. Memon, S. Lim, Frequency-tunable compact antenna using quarter-mode substrate integrated waveguide. IEEE Antennas Wireless Propag. Lett. **14**, 1606–1609 (2015)
57. S. Somarith, K. Hyunseong, L. Sungjoon, Frequency reconfigurable and miniaturized substrate integrated waveguide interdigital capacitor (SIW-IDC) antenna. IEEE Trans. Antennas Propag. **62**(3), 1039–1045 (2013)
58. W.A. Awan et al., A miniaturized wideband and multi-band on-demand reconfigurable antenna for compact and portable devices. AEU-Int. J. Electron. Commun. **22**, 153266 (2020)

59. W. Lin, S.L. Chen, R.W. Ziolkowski, Y.J. Guo, Reconfigurable, wideband, low-profile, circularly polarized antenna and array enabled by an artificial magnetic conductor ground. IEEE Trans. Antennas Propag. **66**(3), 1564–1569 (2018)
60. Y.M. Cai, S. Gao, Y. Yin, W. Li, Q. Luo, Compact-size low-profile wideband circularly polarized omnidirectional patch antenna with reconfigurable polarizations. IEEE Trans. Antennas Propag. **64**(5), 2016–2021 (2016)
61. B. Wu, M. Okoniewski, C. Hayden, A pneumatically controlled reconfigurable antenna with three states of polarization. IEEE Trans. Antennas Propag. **62**(11), 5474–5484 (2014)
62. H. Zhu, S. Cheung, X. Liu, T. Yuk, Design of polarization reconfigurable antenna using metasurface. IEEE Trans. Antennas Propag. **62**(6), 2891–2898 (2014)
63. F. Wu, K.M. Luk, Wideband tri-polarization reconfigurable magneto-electric dipole antenna. IEEE Trans. Antennas Propag. **65**(4), 1633–1641 (2017)
64. K.X. Wang, H. Wong, A reconfigurable CP/LP antenna with cross-probe feed. IEEE Antennas Wireless Propag. Lett. **16**, 669–672 (2016)
65. Y. Kim, N.G. Kim, J.M. Kim, S. H. Lee, Y. Kwon, Y.K. Kim, 60-GHz full MEMS antenna platform mechanically driven by magnetic actuator. IEEE Trans. Ind. Electron. **58**(10), 4830–4836 (2011)
66. D.R. López, Reconfigurable pixel antennas for communications. Universitat Politècnica de Catalunya (UPC) (2013)
67. Y.Y. Bai, S. Xiao, C. Liu, X. Shuai, B.Z. Wang, Design of pattern reconfigurable antennas based on a two-element dipole array model. IEEE Trans. Antennas Propag. **61**(9), 4867–4871 (2013)
68. P.Y. Qin, Y.J. Guo, C. Ding, A beam switching quasi-Yagi dipole antenna. IEEE Trans. Antennas Propag. **61**(10), 4891–4899 (2013)
69. T. Aboufoul, C. Parini, X. Chen, A. Alomainy, Pattern-reconfigurable planar circular ultra-wideband monopole antenna. IEEE Trans. Antennas Propag. **61**(10), 4973–4980 (2013)
70. S.S. Nair, M.J. Ammann, Reconfigurable antenna with elevation and azimuth beam switching. IEEE Antennas Wireless Propag. Lett. **9**, 367–370 (2010)
71. P.Y. Qin, Y.J. Guo, A.R. Weily, C.H. Liang, A pattern reconfigurable U-slot antenna and its applications in MIMO systems. IEEE Trans. Antennas Propag. **60**(2), 516–528 (2011)
72. S.J. Ha, C.W. Jung, Reconfigurable beam steering using a microstrip patch antenna with a U-slot for wearable fabric applications. IEEE Antennas Wireless Propag. Lett. **10**, 1228–1231 (2011)
73. M. Jusoh, T. Sabapathy, M.F. Jamlos, M.R. Kamarudin, Reconfigurable four-parasitic-elements patch antenna for high-gain beam switching application. IEEE Antennas Wireless Propag. Lett. **13**, 79–82 (2014)
74. M.H. Nemati, R. Kazemi, I. Tekin, Pattern reconfigurable patch array for 2.4 GHz WLAN systems. Microw. Opt. Technol. Lett. **56**(10), 2377–2381 (2014)
75. M. Nor, S. Rahim, M.I. Sabran, P.J. Soh, G. Vandenbosch, Dual-band, switched-beam, reconfigurable antenna for WLAN applications. IEEE Antennas Wireless Propag. Lett. **12**, 1500–1503 (2013)
76. S. Lim, H. Ling, Design of electrically small, pattern reconfigurable Yagi antenna. Electron. Lett. **43**(24), 1326–1327 (2007)
77. C. Kittiyanpunya, M. Krairiksh, A four-beam pattern reconfigurable Yagi-Uda antenna. IEEE Trans. Antennas Propag. **61**(12), 6210–6214 (2013)
78. I. Lim, S. Lim, Monopole-like and boresight pattern reconfigurable antenna. IEEE Trans. Antennas Propag. **61**(12), 5854–5859 (2013)
79. C. won Jung, M.J. Lee, G. Li, F. De Flaviis, Reconfigurable scan-beam single-arm spiral antenna integrated with RF-MEMS switches. IEEE Trans. Antennas Propag. **54**(2), 455–463 (2006)
80. R. Guzmán-Quirós, J.L. Gómez-Tornero, A.R. Weily, Y.J. Guo, Electronically steerable 1-D Fabry-Perot leaky-wave antenna employing a tunable high impedance surface. IEEE Trans. Antennas Propag. **60**(11), 5046–5055 (2012)

81. R.O. Ouedraogo, E.J. Rothwell, B.J. Greetis, A reconfigurable microstrip leaky-wave antenna with a broadly steerable beam. IEEE Trans. Antennas Propag. **59**(8), 3080–3083 (2011)
82. E. Ojefors, S. Cheng, K. From, I. Skarin, P. Hallbjorner, A. Rydberg, Electrically steerable single-layer microstrip traveling wave antenna with varactor diode based phase shifters. IEEE Trans. Antennas Propag. **55**(9), 2451–2460 (2007)
83. D.K. Karmokar, K.P. Esselle, S.G. Hay, Fixed-frequency beam steering of microstrip leaky-wave antennas using binary switches. IEEE Trans. Antennas Propag. **64**(6), 2146–2154 (2016)
84. Z.L. Lu, X.X. Yang, G.N. Tan, A wideband printed tapered-slot antenna with pattern reconfigurability. IEEE Antennas Wireless Propag. Lett. **13**, 1613–1616 (2014)
85. N. Nguyen-Trong, L. Hall, C. Fumeaux, A dual-band dual-pattern frequency-reconfigurable antenna. Microw. Opt. Technol. Lett. **59**(11), 2710–2715 (2017)
86. S.N.M. Zainarry, N. Nguyen-Trong, C. Fumeaux, A frequency- and pattern-reconfigurable two-element array antenna. IEEE Antennas Wireless Propag. Lett. **17**(4), 617–620 (2018)
87. P.K. Li, Z.H. Shao, Q. Wang, Y.J. Cheng, Frequency- and pattern-reconfigurable antenna for multistandard wireless applications. IEEE Antennas Wireless Propag. Lett. **14**, 333–336 (2014)
88. N.K. Sahu, A.K. Sharma, An investigation of pattern and frequency reconfigurable microstrip slot antenna using PIN diodes, in *2017 Progress in Electromagnetics Research Symposium-Spring (PIERS)* (IEEE, Piscataway, 2017), pp. 971–976
89. L. Han, C. Wang, W. Zhang, R. Ma, Q. Zeng, Design of frequency- and pattern-reconfigurable wideband slot antenna. Int. J. Antennas Propag. **2018**, 1–7 (2018)
90. H.A. Majid, M.K.A. Rahim, M.R. Hamid, M.F. Ismail, Frequency and pattern reconfigurable slot antenna. IEEE Trans. Antennas Propag. **62**(10), 5339–5343 (2014)
91. M. Ye, P. Gao, Back-to-back F semicircular antenna with frequency and pattern reconfigurability. Electron. Lett. **51**(25), 2073–2074 (2015)
92. B. Liang, B. Sanz-Izquierdo, E.A. Parker, J.C. Batchelor, A frequency and polarization reconfigurable circularly polarized antenna using active EBG structure for satellite navigation. IEEE Trans. Antennas Propag. **63**(1), 33–40 (2014)
93. G. Yi, C. Huang, X. Ma, W. Pan, X. Luo, A low profile polarization reconfigurable dipole antenna using tunable electromagnetic band-gap surface. Microw. Opt. Technol. Lett. **56**(6), 1281–1285 (2014)
94. C. Ni, M.S. Chen, Z.X. Zhang, X.L. Wu, Design of frequency- and polarization-reconfigurable antenna based on the polarization conversion metasurface. IEEE Antennas Wireless Propag. Lett. **17**(1), 78–81 (2017)
95. N. Nguyen-Trong, L. Hall, C. Fumeaux, A frequency- and polarization-reconfigurable stub-loaded microstrip patch antenna. IEEE Trans. Antennas Propag. **63**(11), 5235–5240 (2015)
96. J. Liu, J. Li, R. Xu, Design of very simple frequency and polarisation reconfigurable antenna with finite ground structure. Electron. Lett. **54**(4), 187–188 (2018)
97. M.A. Rahman, E. Nishiyama, I. Toyoda, A frequency diversity reconfigurable antenna with circular polarization switching capability, in *2017 IEEE International Symposium on Antennas and Propagation & USNC/URSI National Radio Science Meeting* (IEEE, Piscataway, 2017), pp. 1367–1368
98. M.S. Kumar, Y.K. Choukiker, Frequency and polarization reconfigurable antenna using BLC feed network, in *2017 IEEE International Conference on Antenna Innovations & Modern Technologies for Ground, Aircraft and Satellite Applications (iAIM)* (IEEE, Piscataway, 2017), pp. 1–4
99. A. Narbudowicz, X. Bao, M.J. Ammann, Omnidirectional microstrip patch antenna with reconfigurable pattern and polarisation. IET Microw. Antennas Propag. **8**(11), 872–877 (2014)
100. C. Gu, et al., Compact smart antenna with electronic beam-switching and reconfigurable polarizations. IEEE Trans. Antennas Propag. **63**(12), 5325–5333 (2015)

101. K. Yang, A. Loutridis, X. Bao, G. Ruvio, M. Ammann, Printed inverted-F antenna with reconfigurable pattern and polarization, in *2016 10th European Conference on Antennas and Propagation (EuCAP)* (IEEE, Piscataway, 2016), pp. 1–5
102. W. Lin, H. Wong, R.W. Ziolkowski, Circularly polarized antenna with reconfigurable broadside and conical beams facilitated by a mode switchable feed network. IEEE Trans. Antennas Propag. **66**(2), 996–1001 (2017)
103. A. Chen, X. Ning, L. Wang, Z. Zhang, A design of radiation pattern and polarization reconfigurable antenna using metasurface, in *2017 IEEE Asia Pacific Microwave Conference (APMC)* (IEEE, Piscataway, 2017), pp. 108–111
104. X. Yi, L. Huitema, H. Wong, Polarization and pattern reconfigurable cuboid quadrifilar helical antenna. IEEE Trans. Antennas Propag. **66**(6), 2707–2715 (2018)
105. N. Nguyen-Trong, A.T. Mobashsher, A.M. Abbosh, Reconfigurable shorted patch antenna with polarization and pattern diversity, in *2018 Australian Microwave Symposium (AMS)* (IEEE. Piscataway, 2018), pp. 27–28
106. D. Rodrigo, B.A. Cetiner, Frequency, radiation pattern and polarization reconfigurable antenna using a parasitic pixel layer. IEEE Trans. Antennas Propag. **62**(6), 3422–3427 (2014)
107. Y.P. Selvam, L. Elumalai, M.G.N. Alsath, M. Kanagasabai, S. Subbaraj, S. Kingsly, Novel frequency- and pattern-reconfigurable rhombic patch antenna with switchable polarization. IEEE Antennas Wireless Propag. Lett. **16**, 1639–1642 (2017)
108. L. Ge, Y. Li, J. Wang, A low-profile reconfigurable cavity-backed slot antenna with frequency, polarization, and radiation pattern agility. IEEE Trans. Antennas Propag. **65**(5), 2182–2189 (2017)
109. M. Hamid, P. Gardner, P.S. Hall, F. Ghanem, Vivaldi antenna with integrated switchable band pass resonator. IEEE Trans. Antennas Propag. **59**(11), 4008–4015 (2011)
110. N. Nguyen-Trong, C. Fumeaux, Reconfigurable half-mode substrate-integrated cavity antenna arrays, in *12th European Conference on Antennas and Propagation (EuCAP 2018)* (2018)
111. E.J. Rodrigues, H.W. Lins, A.G. D'Assunção, Reconfigurable circular ring patch antenna for UWB and cognitive radio applications, in *The 8th European Conference on Antennas and Propagation (EuCAP 2014)* (IEEE, Piscataway, 2014), pp. 2744–2748
112. W.Y. Sam, Z.B. Zakaria, Design of reconfigurable integrated substrate integrated waveguide (SIW) filter and antenna using multilayer approach. Int. J. RF Microw. Comput.-Aid. Eng. **28**(9), e21561 (2018)
113. K. Yan, P. Yang, F. Yang, X. Wang, J. Wang, Multi-band antenna design for full metal casing mobile handset, in *2017 Sixth Asia-Pacific Conference on Antennas and Propagation (APCAP)* (IEEE, Piscataway, 2017), pp. 1–3
114. I. Serhsouh, M. Himdi, H. Lebbar, H. Vettikalladi, Reconfigurable SIW antenna for fixed frequency beam scanning and 5G applications. IEEE Access **8**, 60084–60089 (2020)
115. G.P. Gao, B. Hu, J.S. Zhang, Design of a miniaturization printed circular-slot UWB antenna by the half-cutting method. IEEE Antennas Wireless Propag. Lett. **12**, 567–570 (2013)
116. R.J. Fontana, Recent system applications of short-pulse ultra-wideband (UWB) technology. IEEE Trans. Microw. Theory Techn. **52**(9), 2087–2104 (2004)
117. F. Fereidoony, S. Chamaani, S.A. Mirtaheri, UWB monopole antenna with stable radiation pattern and low transient distortion. IEEE Antennas Wireless Propag. Lett. **10**, 302–305 (2011)
118. K.G. Thomas, M. Sreenivasan, A simple ultrawideband planar rectangular printed antenna with band dispensation. IEEE Trans. Antennas Propa. **58**(1), 27–34 (2009)
119. M.G.N. Alsath, M. Kanagasabai, Compact UWB monopole antenna for automotive communications. IEEE Trans. Antennas Propag. **63**(9), 4204–4208 (2015)
120. T. Li, H. Zhai, L. Li, C. Liang, Y. Han, Compact UWB antenna with tunable band-notched characteristic based on microstrip open-loop resonator. IEEE Antennas Wireless Propag. Lett. **11**, 1584–1587 (2012)

121. D.E. Anagnostou, M.T. Chryssomallis, B.D. Braaten, J.L. Ebel, N. Sepúlveda, Reconfigurable UWB antenna with RF-MEMS for on-demand WLAN rejection. IEEE Trans. Antennas Propag. **62**(2), 602–608 (2013)
122. S. Nikolaou, N.D. Kingsley, G.E. Ponchak, J. Papapolymerou, M.M. Tentzeris, UWB elliptical monopoles with a reconfigurable band notch using MEMS switches actuated without bias lines. IEEE Trans. Antennas Propag. **57**(8), 2242–2251 (2009)
123. P. Kim, Y. Jeong, A coupled line impedance transformer for high termination impedance with a bandpass filtering response. J. Electromagnet. Eng. Sci. **18**(1), 41–45 (2018)
124. T.L. Wu, Y.M. Pan, P.F. Hu, S.Y. Zheng, Design of a low profile and compact omnidirectional filtering patch antenna. IEEE Access, **5**, 1083–1089 (2017)
125. K.S. Ryu, A.A. Kishk, UWB antenna with single or dual band-notches for lower WLAN band and upper WLAN band. IEEE Trans. Antennas Propag. **57**(12), 3942–3950 (2009)
126. M. Roozbahani, A. Kalteh, R. Fallahi, A novel UWB elliptical slot antenna with band notch characteristics. Progr. Electromagnet. Res. **82**, 127–136 (2008)
127. W. Choi, K. Chung, J. Jung, J. Choi, Compact ultra-wideband printed antenna with band-rejection characteristic. Electron. Lett. **41**(18), 990–991 (2005)
128. J.W. Jang, H.Y. Hwang, An improved band-rejection UWB antenna with resonant patches and a slot. IEEE Antennas Wireless Propag. Lett. **8**, 299–302 (2009)
129. C.R. Medeiros, J.R. Costa, C.A. Fernandes, Compact tapered slot UWB antenna with WLAN band rejection. IEEE Antennas Wireless Propag. Lett. **8**, 661–664 (2009)
130. J. Kim, C. Cho, J. Lee, 5.2 GHz notched ultra-wideband antenna using slot-type SRR. Electron. Lett. **42**(6), 315–316 (2006)
131. K. Bahadori, Y. Rahmat-Samii, A miniaturized elliptic-card UWB antenna with WLAN band rejection for wireless communications. IEEE Trans. Antennas Propag. **55**(11), 3326–3332 (2007)
132. F. Zhu, et al., Multiple band-notched UWB antenna with band-rejected elements integrated in the feed line. IEEE Trans. Antennas Propag. **61**(8), 3952–3960 (2013)
133. K.H. Kim, Y.J. Cho, S.H. Hwang, S.O. Park, Band-notched UWB planar monopole antenna with two parasitic patches. Electron. Lett. **41**(14), 783–785 (2005)
134. L. Peng, C.L. Ruan, UWB band-notched monopole antenna design using electromagnetic-bandgap structures. IEEE Trans. Microw. Theory Techn. **59**(4), 1074–1081 (2011)
135. W. Liu, Y.Z. Yin, Dual band-notched antenna with the parasitic strip for UWB. Progr. Electromagnet. Res. **25**, 21–30 (2011)
136. M.S. Alam, A. Abbosh, Reconfigurable band-rejection antenna for ultra-wideband applications. IET Microw. Antennas Propag. **12**(2), 195–202 (2017)
137. S. Lakrit, S. Das, A. El Alami, D. Barad, S. Mohapatra, A compact UWB monopole patch antenna with reconfigurable band-notched characteristics for Wi-MAX and WLAN applications. AEU-Int. J. Electron. Commun. **105**, 106–115 (2019)
138. A.H. Nazeri, A. Falahati, R. Edwards, A novel compact fractal UWB antenna with triple reconfigurable notch reject bands applications. AEU-Int. J. Electron. Commun. **101**, 1–8 (2019)
139. V.G. Veselago, The electrodynamics of substances with simultaneously negative values of img align= absmiddle Alt= ϵ Eps/Img and μ. Phys.-Uspekhi **10**(4), 509–514 (1968)
140. H. Zhu, K.L. Chung, X. Sun, S. Cheung, T.I. Yuk, CP metasurfaced antennas excited by LP sources, in *Proceedings of the 2012 IEEE International Symposium on Antennas and Propagation* (IEEE, Piscataway, 2012), pp. 1–2
141. X. Chen, Y. Zhao, Dual-band polarization and frequency reconfigurable antenna using double layer metasurface. AEU-Int. J. Electron. Commun. **95**, 82–87 (2018)
142. J. Hu, G.Q. Luo, Z.C. Hao, A wideband quad-polarization reconfigurable metasurface antenna. IEEE Access **6**, 6130–6137 (2017)
143. S. Chaimool, T. Hongnara, C. Rakluea, P. Akkaraekthalin, Y. Zhao, Design of a PIN diode-based reconfigurable metasurface antenna for beam switching applications. Int. J. Antennas Propag. **2019**, 1–7 (2019)

144. A. Ahmad, F. Arshad, S.I. Naqvi, Y. Amin, H. Tenhunen, J. Loo, Flexible and compact spiral-shaped frequency reconfigurable antenna for wireless applications. IETE J. Res. **66**(1), 22–29 (2020)
145. M.U. Hassan, F. Arshad, S.I. Naqvi, Y. Amin, H. Tenhunen, A compact flexible and frequency reconfigurable antenna for quintuple applications. Radioengineering **26**(3), 655–661 (2017)
146. S.M. Saeed, C.A. Balanis, C.R. Birtcher, Inkjet-printed flexible reconfigurable antenna for conformal WLAN/WiMAX wireless devices. IEEE Antennas Wireless Propag. Lett. **15**, 1979–1982 (2016)
147. K. Saraswat, A.R. Harish, Flexible dual-band dual-polarised CPW-fed monopole antenna with discrete-frequency reconfigurability. IET Microw. Antennas Propag. **13**(12), 2053–2060 (2019)
148. S.M. Saeed, C.A. Balanis, C.R. Birtcher, A.C. Durgun, H.N. Shaman, Wearable flexible reconfigurable antenna integrated with artificial magnetic conductor. IEEE Antennas Wireless Propag. Lett. **16**, 2396–2399 (2017)
149. R.B. Simorangkir, Y. Yang, K.P. Esselle, B.A. Zeb, A method to realize robust flexible electronically tunable antennas using polymer-embedded conductive fabric. IEEE Trans. Antennas Propag. **66**(1), 50–58 (2017)
150. H.F. Abutarboush, A. Shamim, A reconfigurable inkjet-printed antenna on paper substrate for wireless applications. IEEE Antennas Wireless Propag. Lett. **17**(9), 1648–1651 (2018)
151. E.A. Kadir, A reconfigurable MIMO antenna system for wireless communications, in *2017 4th International Conference on Electrical Engineering, Computer Science and Informatics (EECSI)* (IEEE, Piscataway, 2017), pp. 1–4
152. A. Kantemur, J. Tak, P. Siyari, A.H. Abdelrahman, M. Krunz, H. Xin, A novel compact reconfigurable broadband antenna for cognitive radio applications. IEEE Trans. Antennas Propag. **68**(9), 6538–6547 (2020)
153. E. Al Abbas, A.T. Mobashsher, A. Abbosh, Polarization reconfigurable antenna for 5G cellular networks operating at millimeter waves, in *2017 IEEE Asia Pacific Microwave Conference (APMC)* (IEEE, Piscataway, 2017), pp. 772–774

Chapter 10
Smart Antenna Design: Radiation Pattern Agility by Branch-Line Coupler

L. Sane, I. Dioum, K. Tall, and M. M. Khouma

10.1 Introduction

5G is a real technological paradigm shift. It is in full development [1] and is being implemented in some countries [2]. The major 5G services can be summed up in three basic business models which are enhanced Mobile Broadband Access (eMBB), Internet of Things connections (IoT), and Ultra-reliable low-latency communication (uRLLC) [3].

The variety of its services involves the real-time use of at least 100 billion devices [4]. These devices incorporate so-called smart, reconfigurable, or agile antennas [5]. A smart antenna consists of an antenna array and signal processing units with beamforming functionality as well as signal processing algorithms [6]. In other words, an antenna is reconfigurable if it can dynamically modify one of its fundamental characteristics (frequency, polarization, radiation pattern) by application of electric, mechanical, or optical control. Smart antennas offer many advantages over conventional antennas. Indeed, reconfigurable antennas offer the possibility of delegating to the antenna itself some of the functionalities generally reserved for the radio stage or for digital signal processing. The agile antennas in radiation pattern provide greater coverage, save energy, and avoid source noise. The adoption of smart antenna techniques in future wireless systems is expected to have a significant impact on the efficient use of spectrum, minimizing the costs of establishing new wireless networks, optimizing the quality of service, and the realization of a transparent multi-technology wireless operation [7, 8]. It is foreseen

L. Sane (✉) · K. Tall
Laboratoire Imagerie Médicale et BioInformatique, ESP/UCAD, Dakar, Senegal
e-mail: lamine.sane@esp.sn; khaly.tall@esp.sn

I. Dioum · M. M. Khouma
Laboratoire Informatique, Réseaux Télécom, ESP/UCAD, Dakar, Senegal
e-mail: ibra.dioum@esp.sn

M. A. Matin (ed.), *Wideband, Multiband, and Smart Antenna Systems*, Signals and Communication Technology, https://doi.org/10.1007/978-3-030-74311-6_10

that SAs will be widely implemented in the smart city, 5G and sixth-generation (6G) wireless communication systems, smart home, mobile satellite communication, IoT, space Internet, automobile, and other fields [9].

The techniques used to achieve antenna agility depend on the characteristic studied. For antennas that can be reconfigured in a radiation pattern, the techniques most used in practice are the use of active components such as PIN-diodes and Micro Electro Mechanical Systems (MEMS). However, although offering good performance, the use of these components increases the cost and complexity of manufacture but also induces the appearance of resistive effects which reduce the performance of the antenna.

To overcome these constraints, this work proposes a new approach of agility in radiation diagram by the use of components formed only from transmission lines: Branch-Line Couplers. The principle of this new approach is to modify the configuration of the antenna system radiation pattern by a single or a combination of port excitations.

This manuscript is organized as follows: in Sect. 10.2, we present the characteristics of a coupler and its principle of use for agility in radiation pattern. In Sect. 10.3, we apply this principle in the case of a single-band antenna system and the case of a dual-band antenna system. The last part of this chapter is devoted to the conclusion and perspectives of this work.

10.2 Principle of Agility in Radiation Pattern by Using a Branch-Line Coupler

10.2.1 What Is Branch-Line Coupler?

Couplers are widely used in electronic systems as combiners or power dividers and therefore constitute an essential element in electronic circuits [10]. In the antenna field, couplers are used in the design of beam splitters (phase shifters) [11, 12].

A main distinction is made between 3-dB 90° hybrid couplers and 3-dB 180° hybrid couplers. At half the power (−3 dB) a 3-dB coupler divides the power equally (within a certain tolerance) between the output ports [13]. A 3-dB quadrature hybrid coupler is a four-port system, consisting of quarter-wave (λ/4) transmission lines with impedance $Z_0 = 50\ \Omega$ and et $Z_0/\sqrt{2} = 35.5\ \Omega$ as shown in Fig. 3.1 [14, 15].

In the system shown in Fig. 10.1, ports 1 and 4 are input ports and ports 2 and 3 are output ports. A 3-dB coupler divides the input power evenly between the output ports and no power is passed to the isolated port. This is called a directional coupler. Ports 1 and 4, as well as ports 2 and 3 are decoupled and out of phase by 90°. This phase difference makes these couplers useful in the design of several electronic components such as modulators, microwave mixers, and particularly antenna feed circuits [13].

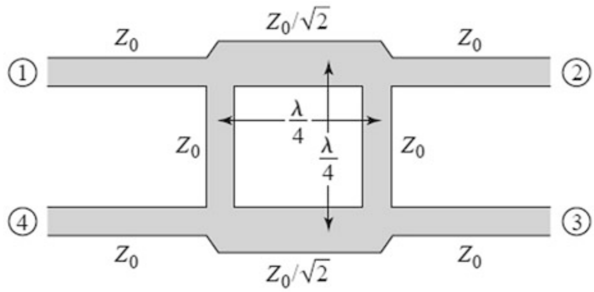

Fig. 10.1 Structure of standard hybrid BLC (3-dB, 90°)

A BLC has a high degree of symmetry such that each port can be used as an input port. The output ports will always be on the opposite side of the junction from the input port, and the isolated port will be the remaining port on the same side as the input port. This symmetry is reflected in the matrix [*S*]. Indeed, in the matrix [*S*] (Eq. 10.1) each row can be obtained by a transposition of the first row [14].

The matrix [*S*] is used to determine the fundamental parameters such as the adaptation, isolation, and coupling of the ports as well as the directivity of the coupler.

The dispersion matrix can be obtained by breaking down the voltage and current at the access ports of the junction into incident and reflected waves. Each access i, delimited by a reference plane Γ_i, is traversed by an incoming wave a_i propagating towards the junction and an outgoing wave b_i propagating in the opposite direction.

The operation of directional couplers is based on the principle of constructive and destructive interference of two waves. The incoming signal is divided into two waves which arrive at the isolated port in phase opposition and consequently cancel each other out. On the other hand, the two waves arrive in phase at the coupled port and consequently, they add up.

Figure 10.2 illustrates a quadrupole with wave decompositions at the inputs.

$$[S] = \begin{bmatrix} S_{11} & S_{12} & S_{13} & S_{13} \\ S_{21} & S_{22} & S_{23} & S_{24} \\ S_{31} & S_{32} & S_{33} & S_{34} \\ S_{41} & S_{42} & S_{43} & S_{44} \end{bmatrix} \tag{10.1}$$

Equation (10.1) gives the general structure of the matrix [*S*] of the quadrupole. The even-odd analysis allows to determine the different parameters S_{ii} and S_{ij} [15–17]. This procedure makes it possible to determine the matrix of branch coupler distribution parameters indicated in Eq. (10.2) below:

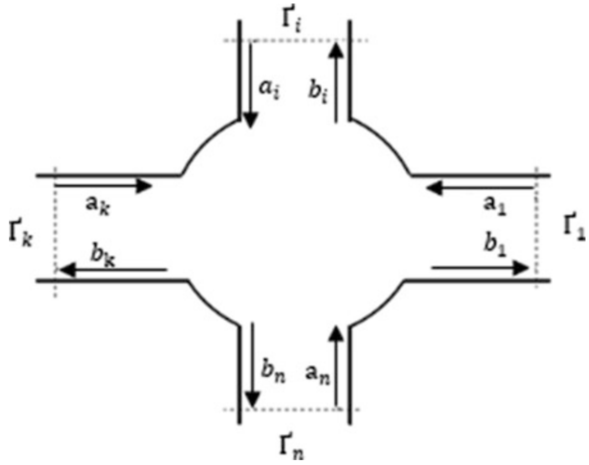

Fig. 10.2 Quadrupole model with wave decompositions at port entrances

$$[S] = \frac{-1}{\sqrt{2}} \begin{bmatrix} 0 & j & 1 & 0 \\ j & 0 & 0 & 1 \\ 1 & 0 & 0 & j \\ 0 & 1 & j & 0 \end{bmatrix} \tag{10.2}$$

The main parameters of a real directional coupler are coupling, isolation, and directivity. The equations of these parameters are given respectively by the following equations (10.3, 10.4, and 10.5):

- Coupling:

$$C\,(\mathrm{dB}) = 10 * \log\left[\frac{P_3}{P_1}\right] \tag{10.3}$$

- Isolation:

$$I\,(\mathrm{dB}) = 10 * \log\left[\frac{P_4}{P_1}\right] \tag{10.4}$$

- Directivity:

$$D\,(\mathrm{dB}) = 10 * \log\left[\frac{P_4}{P_3}\right] = 10 * \log\left[\frac{P_4}{P_1} * \frac{P_1}{P_3}\right]$$

$$D\,(\mathrm{dB}) = I\,(\mathrm{dB}) - C\,(\mathrm{dB}) \tag{10.5}$$

Directivity measures the quality of the coupler and plays a very important role in the accuracy of reflectometry measurements.

10.2.2 Agility Principle in Radiation Diagram by Branch-Line Coupler

The principle of agility in radiation pattern for small communicating objects is applicable for a system meeting the following three conditions:

- The system must consist of at least one pair of antennas
- The pair of antennas must be constituting of two identical antennas
- The pair of antennas must be arranged symmetrically

The excitation ports of the antennas that make up the pair are replaced by the output ports of the coupler. The input ports of the coupler then become the excitation ports of the antenna system. Radiation pattern agility is obtained in this case by simply exciting each port in the system and then combining the excitation of the ports.

The choice of the Branch-Line Coupler as an agility tool for the radiation pattern of our proposed antenna system is guided by the characteristics of the antenna radiation pattern. Indeed, its analysis shows that the excitation of port 1 makes it possible to cover the directions Y-negative and X-positive, the excitation of port 2, the directions X-negative and Y-positive. However, the antenna system is arranged in a small ground plane thus inducing a strong coupling between the two antennas.

When using the 3-dB BLC, we will replace the antenna excitation port 1 with the output port 2 of the BLC, respectively, and the antenna excitation port 2 with the output port 3 of the coupler. The fully decoupled ports 1 and 4 of the coupler become the excitation ports of antennas 1 and 2, respectively. Thus, a fully decoupled antenna system is obtained, the excitation of a port of the coupler makes it possible to cover two directions and the simultaneous excitation of the two ports makes it possible to cover the four directions as we will see in the study of the reconfigurability of the proposed antenna system.

10.3 Implementation of the Proposed Technique

The principle of agility in the radiation pattern is implemented in the case of a mono band antenna system then in the case of a dual-band antenna system.

10.3.1 Case of Single Band System

In this part, we present the design of an antenna system reconfigurable in the radiation pattern by Brach-Line Coupler. The proposed antenna system consists of two identical antennas and operates in the LTE2600 band (2.5–2.69 GHz). The single-band PIFA antenna which will be duplicated to form the antenna system is called the reference antenna. It is designed using the High-Frequency Simulator System (HFSS) electromagnetic simulator.

We will first present the justification for the choice of the type of antenna used in this work. Then the design procedure of the reference antenna will be presented before finishing with the design of the proposed antenna system.

10.3.1.1 Choice of the Reference Antenna Type

It should be noted that it is essential to make a judicious choice of the appropriate type of antenna to use for a given application. A suitable antenna can improve transmission and reception, reduce power consumption, and extend the life of the device. It also improves the marketability of the communication device [18].

In modern mobile terminals, such as smartphones, tablets, and connected objects, the most used types of antennas are monopole antennas [19–22] and PIFA (Planar Inverted-F Antenna) antennas [23–26]. These two types of antennas are quarter-wave and hold their popularity due to their compactness, ease of manufacture, ease of integration into mobile terminals, and low cost. Also, space constraints mean that the type of antenna that performs well while occupying the least space remains the best candidate for small communicating objects.

Depending on the objectives of each job, some antenna parameters are put forward over others. Our contribution concerning the reconfiguration in radiation diagram then the metric of this work will be the radiation diagram. However, requirements such as cover strips, minimum accepted efficiency for 5G are to be met. Thus, compared to monopolies, PIFA antennas take up less space and offer very high radiation efficiency and sufficient bandwidth while being compact. Also, the PIFA antennas present quasi-omnidirectional radiation with a fairly high level of cross-polarization [27].

A PIFA antenna is composed of a ground plane (PCB), a radiating element, a power line, and a short circuit which are connected between the ground plane and the top plate (radiating element). Figure 10.3 illustrates a typical PIFA configuration. The antenna is fed at the base by a feed line at the point where the line is connected to the ground plane. The addition of a short-circuit bar makes it possible to obtain a good measurement of input impedance with an upper plate generally less than $\lambda/4$ [29]. The dimensions of a PIFA antenna depend on the width of its short circuit. Its design is then done according to the equations given in the following part.

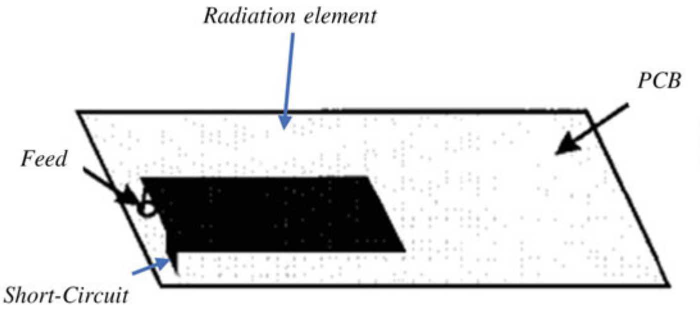

Fig. 10.3 Standard PIFA antenna structure [28]

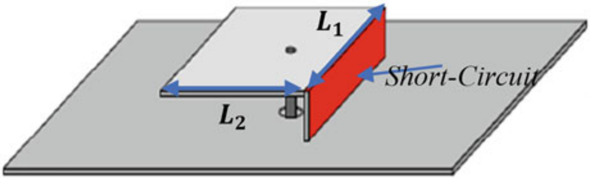

Fig. 10.4 Structure of a short-circuited PIFA antenna equal to the width of the radiation element [27]

10.3.1.2 PIFA Antenna Design Equations

The resonant frequency of a PIFA antenna depends on the width of the short circuit. Indeed, the expression of the resonant frequency of a PIFA changes according to the following cases:

- *The case where the width (W) of the short-circuit is equal to the width (L_1) of the radiating element* $W = L_1$ (Fig. 10.4)

  Under this condition, the dimensions of the quarter-wave PIFA at resonance are such as:

$$L_2 + H = \frac{\lambda}{4} \tag{10.6}$$

Or

$$\lambda = \frac{c}{f_r\sqrt{\varepsilon_r}} \tag{10.7}$$

where L_2 is the length of the radiating element, H its height relative to the substrate, and f_r the resonant frequency.

From where:

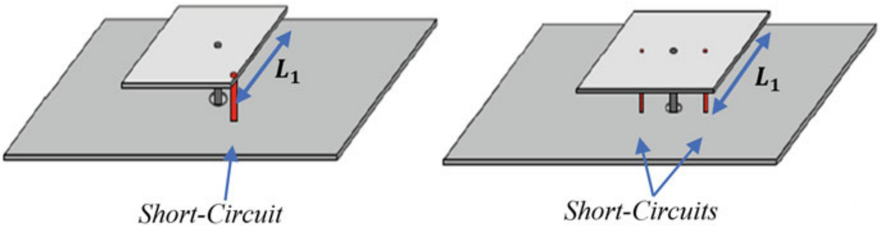

Fig. 10.5 Structure of an almost zero-width short-circuited PIFA antenna [27]

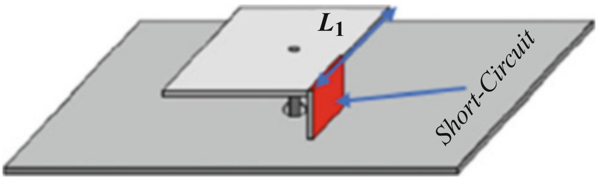

Fig. 10.6 Structure of a medium-width short-circuited PIFA antenna [27]

$$f_r = \frac{c}{4 * (L_2 + H) * \sqrt{\varepsilon_r}} \tag{10.8}$$

- *The case where the width (W) of the short-circuit is almost zero (W ≈ 0)* (Fig. 10.5)

  In this case, the short is similar to a wire. The effective length of the current is then $L_1 + L_2 + H$. In this case, the resonance condition is expressed by:

$$L_1 + L_2 + H = \frac{\lambda}{4} \tag{10.9}$$

  From where:

$$f_r = \frac{c}{4 * (L_1 + L_2 + H) * \sqrt{\varepsilon_r}} \tag{10.10}$$

- *The case where the width of the short-circuit is between the two ends* (Fig. 10.6)

  The resonance frequency is a linear combination of the resonance frequencies associated with the borderline cases and is given by:

$$f_r = \frac{c}{4 * (L_1 + L_2 + H - W) * \sqrt{\varepsilon_r}} \tag{10.11}$$

10.3.1.3 Design of the Mono Band Antenna System

In this part, we present the different stages of the design of the reference antenna and the multi-antenna system proposed in this work.

Design of the Reference Mono Band Antenna

The design variables of a PIFA antenna are the height, width, and length of the top plate, the width and location of the shorting plate, and the location of the feed line [28]. A difficult task in designing antennas with many different design variables is determining the dimensions to achieve a specified input impedance at the center design frequency. In their work entitled Analysis, Design, and Measurement of Small Low-Profile Antennas, *K. Hirasawa* and *M. Haneishi* describe some of the design parameters that affect the resonant frequency and bandwidth of PIFA and particularly its height as the dominant factor determining the bandwidth.

As part of our work, the reference antenna is designed to be used in a small communicating object compatible with 5G networks. This is why the standard dimensions of a smartphone are initially chosen. These dimensions are 120 mm long and 60 mm wide as shown in Fig. 10.7.

The initial model is a PIFA antenna with the radiating element folded back. Part of the folding is printed on an FR4-epoxy substrate with a relative permittivity $\varepsilon_r = 4.4$ and a thickness of 0.8 mm. On the underside of the substrate is printed a ground plane having the same width as the substrate. The length of the PCB is 113 mm and corresponds to the length of the substrate minus the dimension reserved for the antenna, namely 7 mm.

The antenna occupies a volume of $18 \times 6 \times 5$ mm^3 ($L_1 \times L_2 \times H$) and operates at the center frequency $f_r = 2.6$ GHz. The top plate material is nickel silver and the

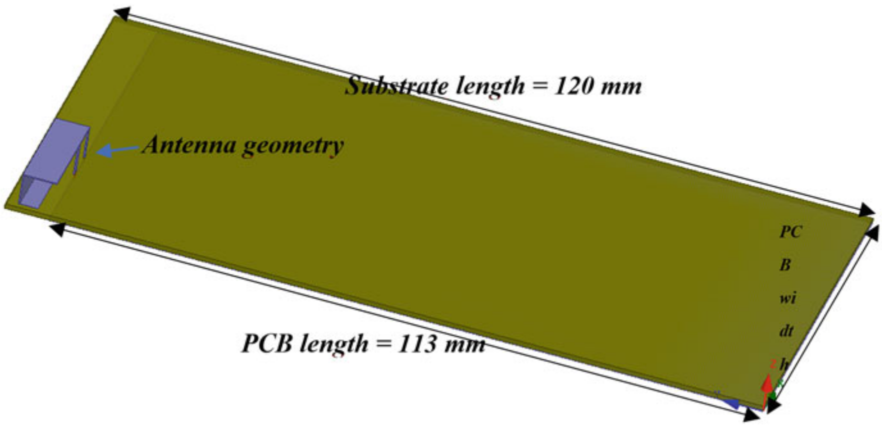

Fig. 10.7 Initial antenna configuration

printed part is 0.035 mm thick copper. The figure shows the initial model with the dimensions (Figs. 10.8 and 10.9).

The initial model that we presented in Fig. 10.7 is obtained after several steps that we describe according to the following three steps:

Step 1: Choice of the PIFA model and calculation of the initial dimensions

To reduce the design variables as much as possible, we have retained the second case of the design equations, namely the case where the width of the short-circuit resembles a wire. For this purpose, a minimum value of 0.5 mm width is assigned to the short circuit.

Using Eq. (10.2), the effective length of the quarter-wave equivalent antenna at the center frequency $f_r = 2.6$ GHz is 17.5 mm where $L_1 + L_2 + H = 17.5$ mm.To have a compact final structure, we have chosen a fixed width of 18 mm. The power line is placed in the center of the width L_1 to ensure an equitable

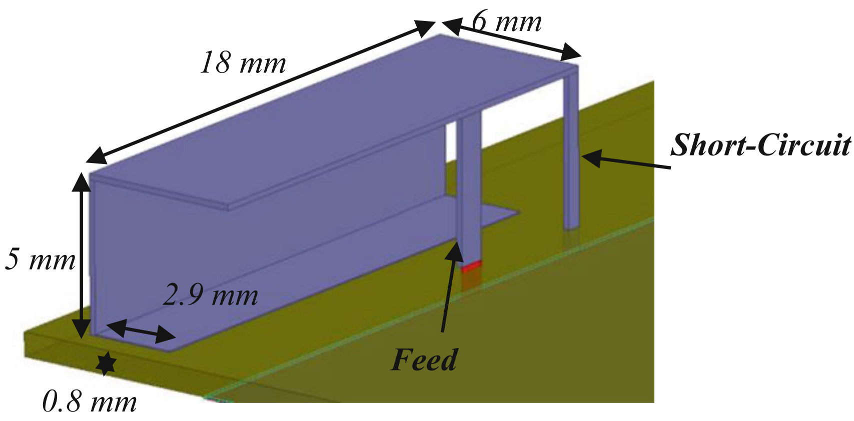

Fig. 10.8 The geometry of the initial model

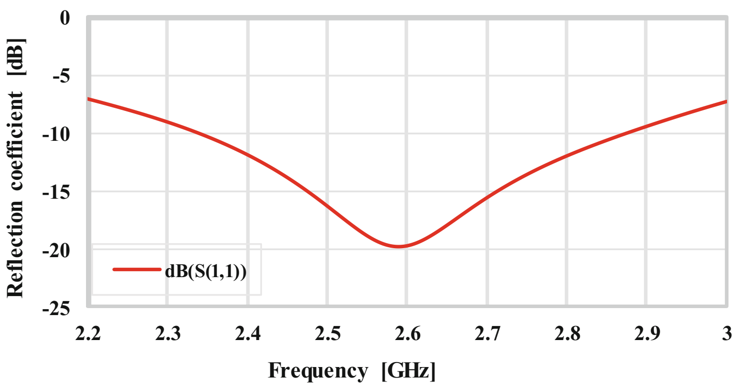

Fig. 10.9 The reflection coefficient of the initial model

Table 10.1 Initial values of the PIFA antenna and results (BP and f_r)

L_1	L_2	H	L_3	Feed position	BW at – 10 dB	f_r
18	6	6	3	9.5	2.28–2.89	2.56 GHz

distribution of the current. The radiating element is placed at a height $H = 6$ mm above the substrate. Table 10.1 gives all the initial values.

The first simulation with the values of Table 10.1 gives a reflection coefficient adapted to 3 GHz. This result means that the current distribution in the initial configuration does not allow to have an effective length equal to a quarter-wave of the central working frequency. To adapt the antenna to the desired frequency, a parametric study is made on the position of the supply line.

Step 2: Parametric study on the position of the supply line and the height

The parametric study is made on the position of the power line starting from the initial position (center of L_1) towards the short circuit. The simulations results presented in Fig. 10.10 show that the closer the power line approaches the short-circuit, the more the resonant frequency moves towards f_r. In other words, the reduction of the gap between the power line and the short circuit induces a decrease in the initial effective length which tends towards its 1/4 wave value at 2.6 GHz.

Of all the simulations, only the position Xalim = 13.5 mm allows us to have coverage of our entire working band (2.5–2.7 dB) at −10 dB. At this position, the antenna resonates at 2.56 GHz and covers a 510 MHz band ranging from 2.28 to 2.89 GHz.

Still, to adapt the antenna to the central frequency 2.6 GHz, a parametric study is carried out on the height H. The parametric study on the height is made by taking Xalim = 13.5 mm while fixing the initial values of the other parameters. It is noted in this case that the more the height of the antenna increases, the more the gain increases and reaches 5.9 dB with an adaptation of −14.9 dB at 2.6 GHz as shown in Fig. 10.11.

To obtain a better adaptation to the central frequency, a parametric study is carried out this time simultaneously on several variables at the same time. These variables are the position of the feed line Xalim, the height H, the length of the top plate L_2, and the length of the printed plate L_3.

Step 3: Parametric study on the variables Xalim, H, L_2, and L_3.

The parameters of the parametric study are given in Table 10.2.

This parametric study makes it possible to have a resonance at the working frequency with the following values of our parameters:

- Xalim = 13 mm
- $H = 5$ mm
- $L_2 = 5.4$ mm
- $L_3 = 2.9$ mm

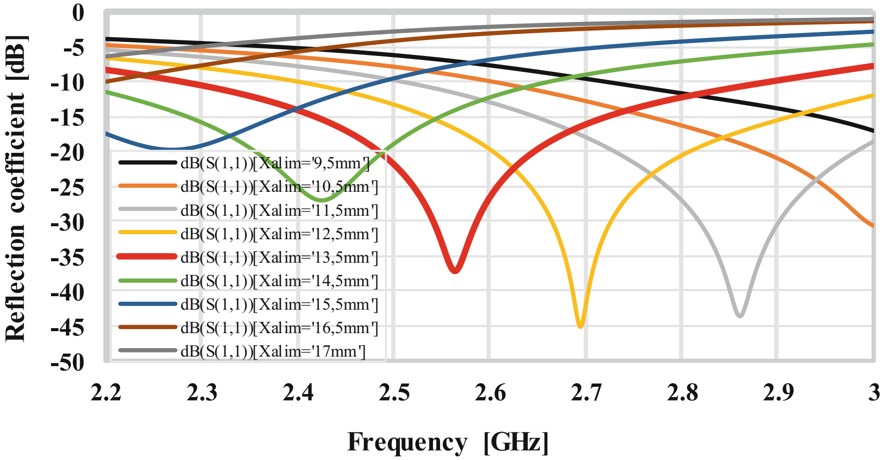

Fig. 10.10 Reflection coefficients of the parametric study on the position of the power line

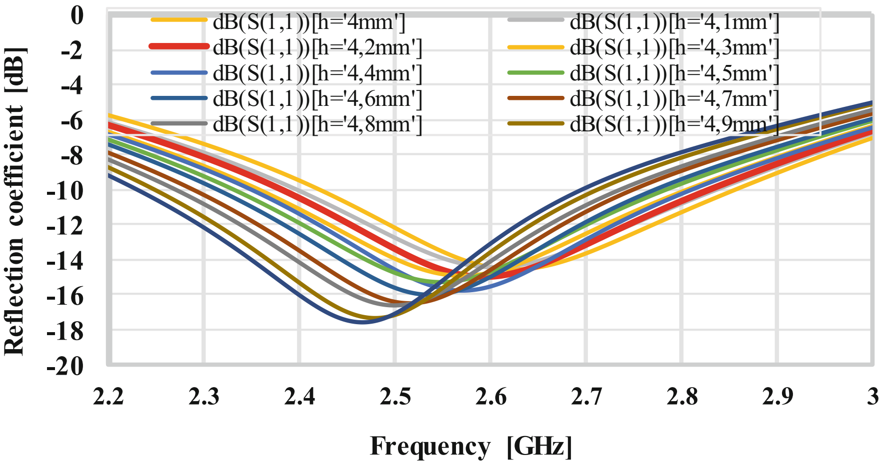

Fig. 10.11 Parametric study reflection coefficients on height

An adaptation of −22 dB is obtained in this state as well as a bandwidth of 580 MHz ranging from 2.34 to 2.92 GHz.

After having validated the impedance parameters, we study the radiation parameters of our antenna (Fig. 10.12).

Table 10.2 Parametric study parameters in HFSS

Variables	Condition on variables
Xalim	Linear variation from 13 to 14 mm in steps of 0.2 mm
H	Linear variation from 4 to 5 mm in steps of 0.2 mm
L_2	Linear variation from 5 to 6 mm in steps of 0.2 mm
L_3	Linear variation from 2.5 to 3.5 mm in steps of 0.2 mm

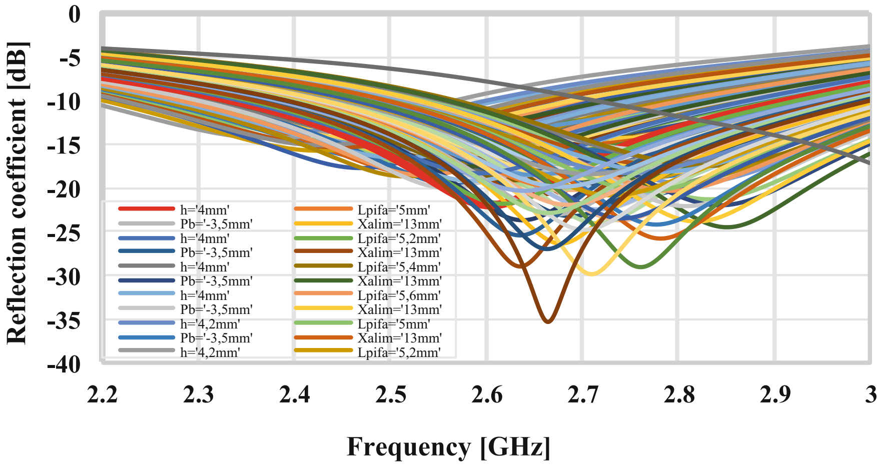

Fig. 10.12 Parametric study S-parameters on Xalim, H, L_2, and L_3

Analysis of the Initial Model Radiation Pattern

Figure 10.13 shows the three-dimensional (3D) and two-dimensional (2D) representations of the initial model radiation pattern.

To simplify the analysis of the radiation pattern and the various configurations thereof, we agree in what follows in this document on the following notations:

- $\varphi = 0°$ corresponds to the orientation along X-positive
- $\varphi = 90°$ corresponds to the orientation along Y-positive
- X-positive corresponds to the orientation in the increasing direction of the x-axis
- X-negative corresponds to the orientation in the decreasing direction of the x-axis
- Y-positive corresponds to the orientation in the increasing direction of the y-axis
- Y-negative corresponds to the orientation in the increasing direction of the y-axis

Analysis of the configuration of the radiation pattern shows that the antenna concentrates most of the radiated power along the opposite direction of the axis on which it is placed. Placed in the XY plane along Y-positive, the antenna radiates in the directions of the two planes which are perpendicular to it, namely X-positive and Y-negative. At $\varphi = 90°$, the antenna achieves a gain of 3.16 dB at $\theta = 270°$ or in the direction of Y-negative. And at $\varphi = 0°$, the antenna has a gain of -2.64 dB at

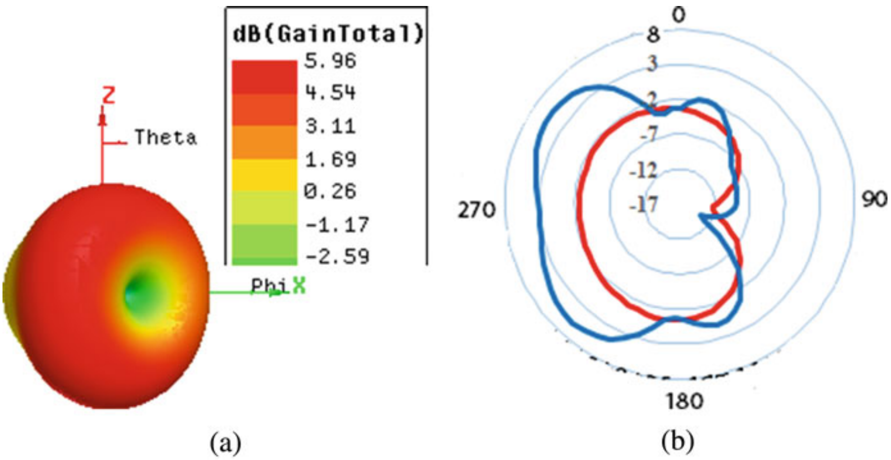

Fig. 10.13 3D (**a**) and 2D (**b**) radiation pattern of the initial model

$\theta = 270°$ either in the direction of X-positive. This configuration is explained by the position of the folded (vertical) part of the radiating element. Indeed, a visualization of the current distribution in the circuit shows that in this plane, this part of the radiating element acts as a reflector of the radiated energy. Thus, a parametric study is made on the length of the ground plane to determine the behavior of the radiation pattern.

The PCB, initially at 113 mm, is successively reduced in steps of 10 mm until a square configuration of 60×60 mm^2 is obtained. The different values of the gain at $\varphi = 0°$, $\varphi = 90°$, and the maximum gain are given in Table 10.3.

An analysis of the parametric study on the length of the PCB shows variations in the total gain both in the *Ox* direction and in the *Oy* direction.

At $\varphi = 0°$, we note a progressive increase in the total gain ranging from -2.64 dB (Lpcb = 113 mm) according to X-negative ($\theta = 270^{\circ}$) to 1.93 dB (Lpcb = 53 mm) according to X-positive ($\theta = 90^{\circ}$). In other words, by comparing the values of the total gain and the direction of orientation of the radiation pattern between the initial configuration and the final configuration, we note a considerable increase in the total gain (from -2.64 to 1.93 dB) and a change in the direction of the beam orientation (from X-negative to X-positive).

At $\varphi = 90°$, there is a clear decrease in the total gain which goes from 3.16 dB (Lpcb = 113 mm) to 2.97 dB (Lpcb = 53 mm) following the same Y-negative direction.

Likewise, there is a decrease in the total maximum gain between the initial configuration and the final configuration. This reduction is materialized by a change from the maximum total gain of 5.85 dB at $\varphi = 90°$ and $\theta = 225°$ with an almost unidirectional configuration to a total maximum gain with a bidirectional

Table 10.3 Values of the gains obtained on the parametric study on the PCB

Lenght PCB (mm)	Gain total (dB)		Gain total maximum (dB)
	$\varphi = 0°, \Theta = 270°$	$\varphi = 90°, \Theta = 270°$	
113	– 2.64	3.16	**5.85** ($\varphi = 90°$, **Θ = 225°**)
103	– 2.65	2.58	**5.58** ($\varphi = 90°$, **Θ = 225°**)
93	– 1.82	2.41	**5.19** ($\varphi = 90°$, **Θ = 220°**)
83	0.06	2.91	**4.89** ($\varphi = 90°$, **Θ = 220°**)
73	1.57	3.54	**4.57** ($\varphi = 90°$, **Θ = 225°**)
63	2.07 Et **1.93** à $\varphi = 0°, \Theta = 90°$	3.63	**4.29** ($\varphi = 90°$, **Θ = 225°**)
53	0.98 Et **3.11** à $\varphi = 0°, \Theta = 90°$	2.97	**3.89** ($\varphi = 90°$, **Θ = 220°**) Et **3.66** ($\varphi = 0°$, **Θ = 135°**)

configuration of 3.66 dB at $\varphi = 0°$ and $\theta = 135°$, and 3.89 dB at $\varphi = 90°$ and $\theta = 220°$.

Although there is a considerable decrease in the total maximum gain, we obtain a very interesting configuration of the radiation pattern, namely its bidirectional distribution. Indeed, the final configuration allows good coverage from two directions with the use of a single antenna. This bidirectional configuration allows in case of reproduction of the reference antenna to have coverage in all directions. Which is one of the objectives of our work.

The decrease in PCB naturally induces an increase in the resonant frequency. An optimization was then followed for an adaptation to the initial resonance frequency. Thus, the final values of the antenna parameters are given in Fig. 10.14.

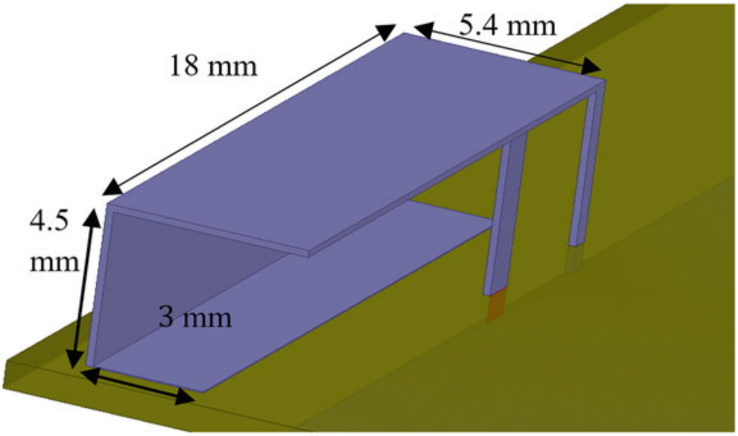

Fig. 10.14 Optimal values of the final model geometry

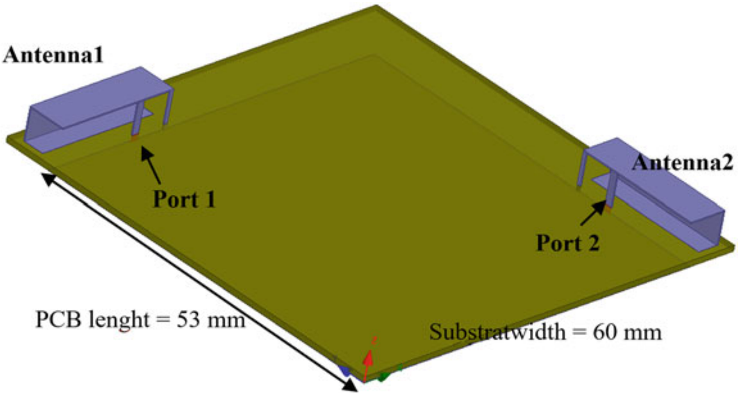

Fig. 10.15 Final antenna system without coupler

Multi-antenna System Design

The multi-antenna system illustrated in Fig. 10.15 is obtained by reproducing the same antenna symmetrically to the diagonal of the substrate. This configuration allows for complete coverage of the X-negative, Y-negative, X-positive, and Y-positive directions.

However, there is a strong coupling between the two excitation ports reflected by the transmission coefficients S_{12} and S_{21} such that $S_{12} = S_{21} = -11.03$ dB at the working frequency as shown in Fig. 10.16. Remember that in 5G wireless communication systems, it is necessary to obtain strong isolation between the excitation ports of the antennas of the system to optimize the radiation of each antenna.

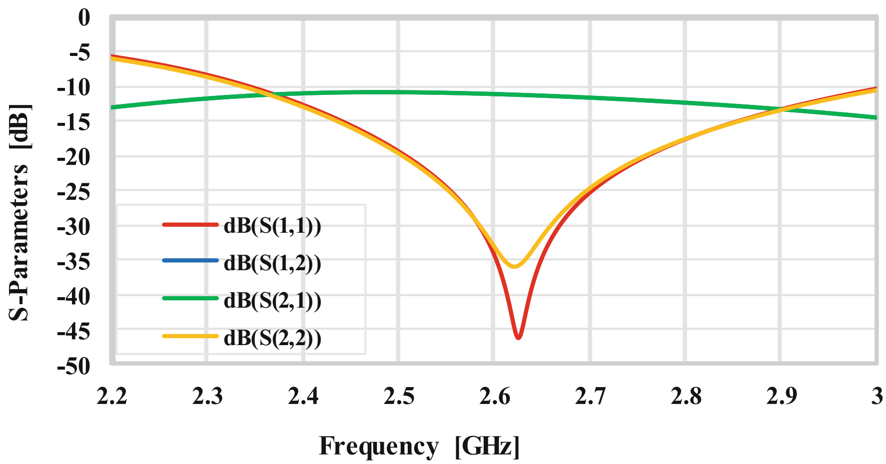

Fig. 10.16 Paramètres-*S* du système antennaire final sans coupleur

Also, it has been noted that if the ports are excited with a 90° phase shift, the gain increases from 3 to 5 dB with the same configurations.

The use of the 3 dB, 90° hybrid coupler then presents itself as an excellent solution not only to allow agility in the radiation pattern but also to achieve very good isolation between the ports of our antenna system.

Design of the 3-dB, 90° Single-Band Coupler

The Advanced Design System (ADS) simulator is primarily used for the design of the coupler. The dimensions of the coupler are obtained using Eqs. (10.12) and (10.13):

$$Z_0 = 50\ \Omega \tag{10.12}$$

$$\frac{Z_0}{\sqrt{2}} = 35.5\ \Omega \tag{10.13}$$

The length and width of each line of the coupler are calculated using ADS' LineCalc tool. Theoretical values obtained for the impedance lines $Z_0 = 50\ \Omega$ and $\frac{Z_0}{\sqrt{2}} = 35.5\ \Omega$ are given in Table 10.4.

The initial values are optimized to have isolation between ports 1 and 4 of the order of 40 dB. The configuration to achieve this high isolation under ADS is given in Fig. 10.17.

Table 10.4 Dimensions of the length and width of the coupler lines

Impedance	Length (mm)	Width (mm)
$Z_0 = 50\ \Omega$	15.86	1.48
$\frac{Z_0}{\sqrt{2}} = 35.5\ \Omega$	15.43	2.57

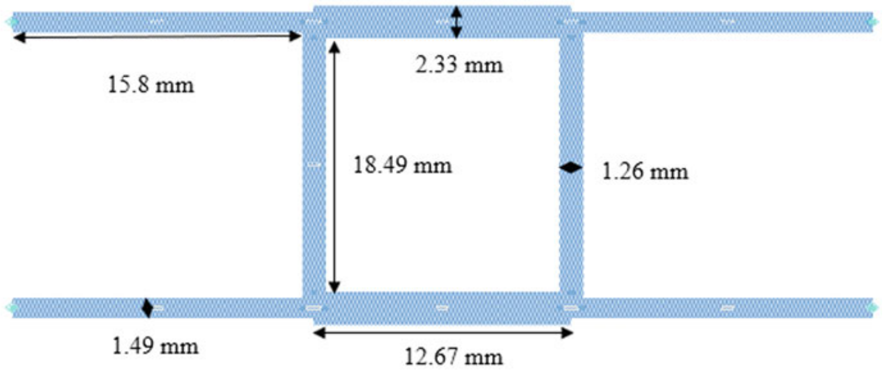

Fig. 10.17 Configuration of the BLC under ADS

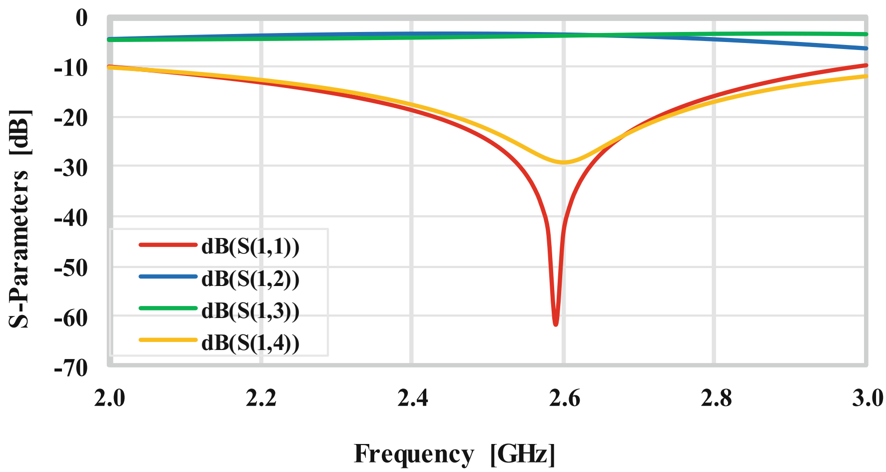

Fig. 10.18 *S*-parameters of the coupler under ADS

This configuration allows having an adaptation of 60 dB and an isolation of 40 dB between ports 1 and 4. It also has transmissions of −3.474 dB between port 1 and port 2 and −3.747 dB between port 1 and port 3 (Fig. 10.18). This neck also offers a 90° ± 2° phase shift throughout the working band as shown in Fig. 10.19.

The coupler designed with ADS is then exported and adapted to the antenna system in HFSS. The configuration under HFSS is shown in Fig. 10.20. The coupler is placed symmetrically to the diagonal so that the charging ports (port 2 and port 3) have the same electrical length (Table 10.5).

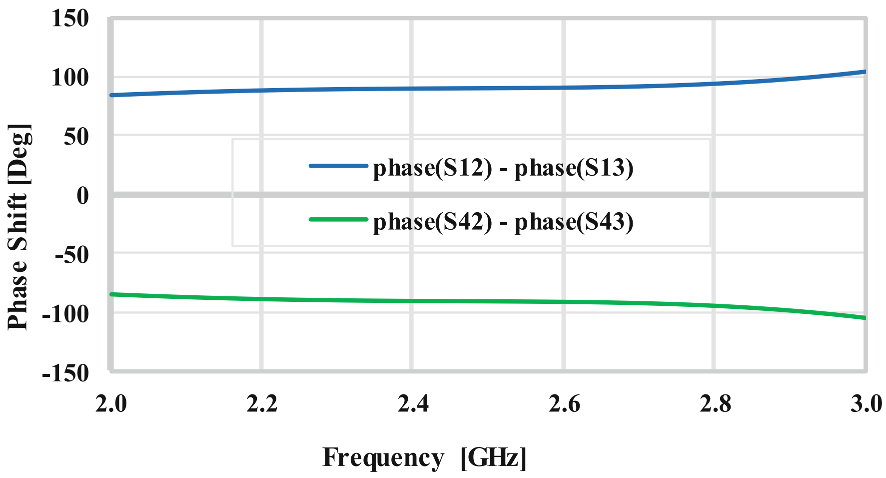

Fig. 10.19 Phase shifts between coupler ports

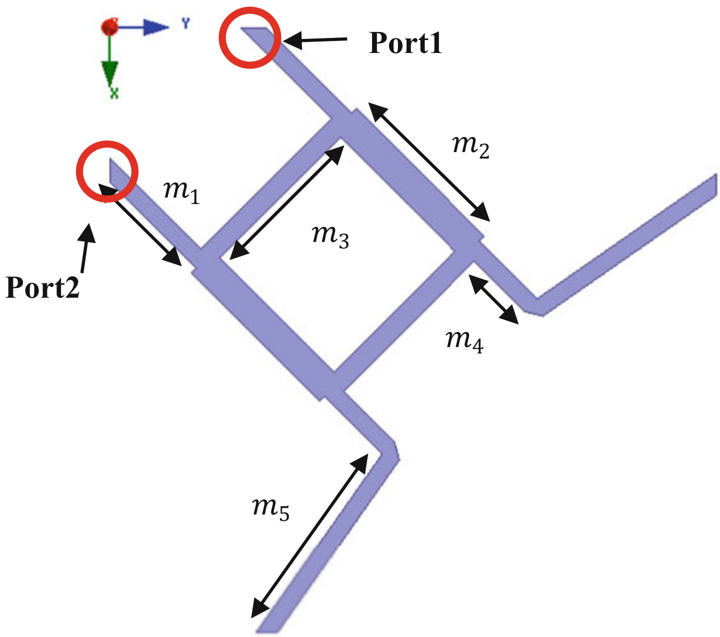

Fig. 10.20 Configuration of the coupler integrated into the antenna system

Figure 10.21 shows the configuration of the final system including the coupler.

The *S*-parameters of the antenna system with the coupler is shown in Fig. 10.22. These results show that the system with the coupler has an adaptation better than −10 dB over the entire working band. This adaptation is reflected by the reflection

Table 10.5 Coupler dimensions in HFSS

Variables	m_1	m_2	m_3	m_4
Values (mm)	11.26	15.8484	16.1358	7.3866
Variables	m_5	w_1	w_2	w_3
Values (mm)	19.1311	1.53	2.7326	1.7494

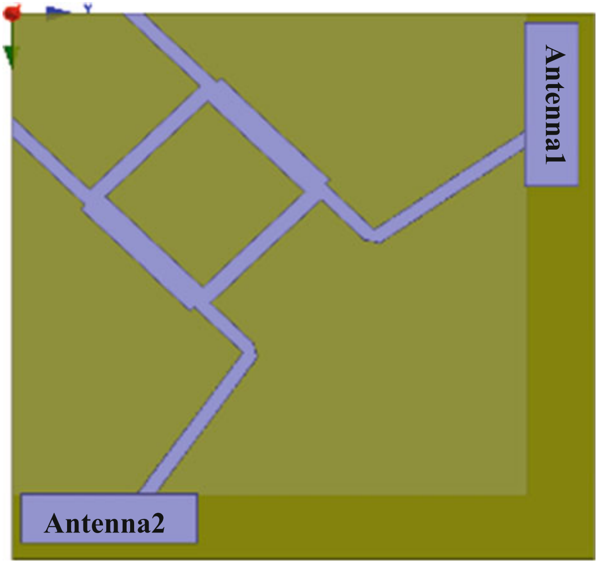

Fig. 10.21 Final antenna system with BLC

coefficients S_{11} and S_{22} (respectively red curve and orange curve) and correspond to the capacity of the system to supply more than 90% of its source power as accepted power. The coupling between the two antennas is reflected in the transmission coefficients S_{12} and S_{21} (respectively blue curve and green curve). This coupling corresponds respectively to the ratio of the wave transmitted to port 1 to the incident wave to port 2 and the ratio of the wave transmitted to port 2 to the incident wave to port 1. The use of the 3-dB coupler quadrature makes it possible to achieve isolation between the excitation ports of the two antennas of 60 dB and a bandwidth of 650 MHz to 2.6 GHz. These results are better than the results obtained in [30] and [31] which are respectively 41 dB and 57 dB.

10.3.1.4 Principle of the Use of the 3 dB, 90° Coupler for Agility in the Radiation Pattern

The choice of the coupler as an agility tool for the radiation pattern of our antenna system is guided by the characteristics presented in the previous paragraph. Indeed, the analysis of the radiation diagram of the final model shows that the excitation of

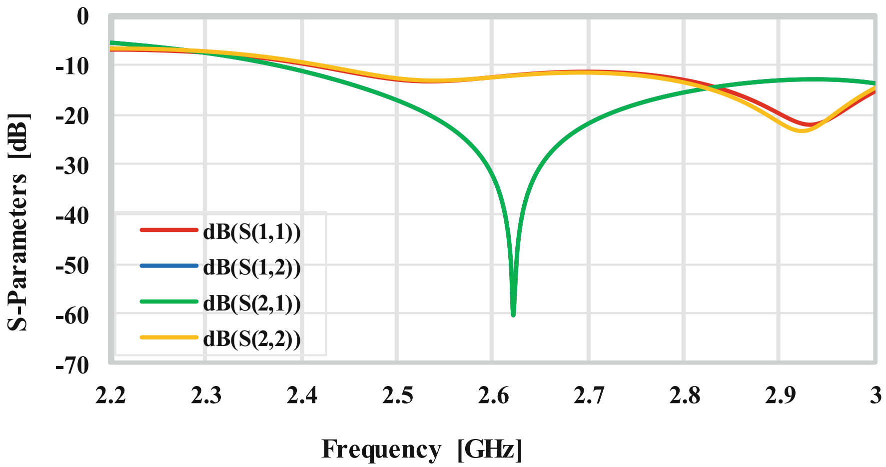

Fig. 10.22 S-parameters of the antenna system with the BLC

port 1 covers the Y-negative and X-positive directions, the excitation of port 2, the X-negative and Y-positive directions.

When using the 3-dB, 90° hybrid coupler, we will respectively replace the excitation port of antenna 1 by the output port 2 of the coupler, and the excitation port of antenna 2 by the port of output 3 of the coupler. Ports 1 and 4 of the coupler, fully decoupled, become the excitation ports of antennas 1 and 2. If port 1 is excited, both antennas are fed with 90° phase delay to antenna 2. Likewise, if port 2 is excited, both antenna 2 and antenna 1 are fed with a phase delay of 90° at antenna 1. Thus, we obtain a completely decoupled antenna system in which the excitation of one port of the coupler makes it possible to cover two directions and the simultaneous excitation of the two ports makes it possible to cover the four directions as we will see in the study of the reconfigurability of the final antenna system.

10.3.1.5 Study of the Antenna System Agility with the Coupler

The final antenna system being well adapted and fully decoupled, we present in this part the different reconfigurations offered by the antenna system proposed in this work. Figure 10.23 shows the different configurations obtained with our multi-antenna system.

State A is the state where only port 1 is excited. This state allows coverage of the Y-negative and X-positive directions. We note a total gain of 1.09 dB at $\varphi = 0°$, $\theta = 90°$ and a total gain of 2.72 dB at $\varphi = 90°$, $\theta = 270°$. The maximum gains of this state are respectively 2.09 dB obtained at $\varphi = 0°$, $\theta = 150°$ and 4.18 dB obtained at $\varphi = 90°$, $\theta = 220°$.

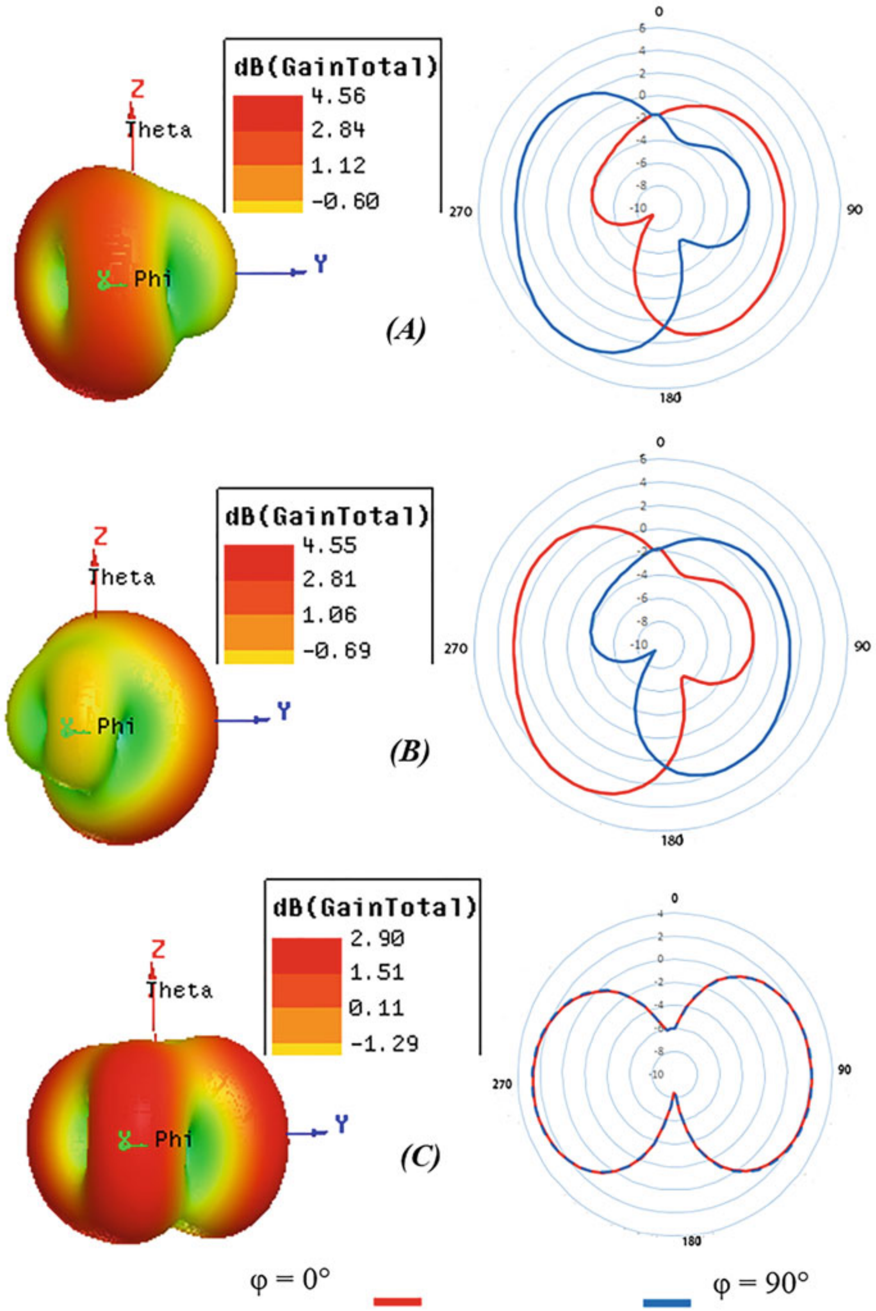

Fig. 10.23 The various reconfigurations of the antenna system radiation pattern

Configuration B represents the state where only port 2 is energized. In this state, we have coverage of the X-negative and Y-positive directions with respective gains of 2.63 dB at $\varphi = 0°$, $\theta = 270°$ and of 1.08 dB at $\varphi = 90°$, $\theta = 90°$. The maximum gains of the directions covered in this state are respectively 4.17 dB in the X-negative direction at $\theta = 270°$ and 2.15 dB in the Y-positive direction at $\theta = 150°$.

State C is obtained by simultaneously exciting ports 1 and 2. This state results in a configuration that covers the X-negative, Y-negative, X-positive, and Y-positive directions. The 2D diagram of this state shows a distribution of the perfectly symmetrical radiation pattern with gains of 2.31 dB at $\theta = 270°$ in the X-negative and Y-positive directions, and 2.82 dB at $\theta = 90°$ in the X directions-positive and Y-positive.

These different configurations obtained by excitation of the ports of the coupler show that the latter makes it possible to complete the reconfiguration of the proposed multi-antenna system while offering good at -10 dB and high isolation of the ports. The various reconfigurations of the antenna system radiation pattern.

10.3.2 Case of Dual-Band Antenna System

In this part, we apply the principle of agility in radiation pattern for a dual-band antenna system operating in the LTE2600 and LTE3600 bands and integrating a dual-band coupler operating in its same bands. Indeed, the need to use wireless communication systems operating on several standards is accelerating day by day due to the increased development of new technologies and the limited space reserved for the antenna system in the communicating object. However, the support of several communication standards by a single antenna can be achieved by a multiband antenna or by a wideband antenna [32]. Thus, it is important to make the most appropriate choice according to the design constraints.

10.3.3 Criteria of Appropriate Antenna Model to Cover Several Standards

Making a good choice between a multiband or a wideband antenna is a must for the antenna operator depending on the objective of covering several standards. An antenna is said to be multiband when it has several resonance frequencies and its performance is highly dependent on its frequencies. A wideband antenna is an antenna whose performance is independent or almost independent of frequency. It is characterized by a bandwidth of at least 500 MHz [33].

In his thesis, Sami Hebib [32] proposes a procedure which makes it possible to make the right choice according to the constraints imposed. This procedure is given by the flowchart below:

For a number n of frequency bands to be covered, three criteria (C_1, C_2, and C_3) apply in order of priority:

C_1: *the frequency difference between the first band (B1) and the last band (Bn)*
This difference is calculated by taking the difference between the minimum frequency of the last band and the maximum frequency of the first band. If the frequency difference is at least about 1 GHz, it is more convenient to use a multiband antenna model. Otherwise, the second criterion determines the choice of the model.

C_2: *the number n of bands to cover*
For a number of bands equal to two or three, the multiband model is suitable. Beyond three bands, the wideband model is therefore the most convenient.

C_3: *the gap between the successive bands*
In the case of covering many bands, the gap between successive bands becomes a determining factor if the first two are not met.

It should be noted that it is possible to have to design a multi-broadband antenna. When designing a dual-band antenna, all of the criteria boil down to the first criterion, namely the frequency difference between the first band and the last band. Therefore, the choice is easily deduced from the calculation of the frequency difference.

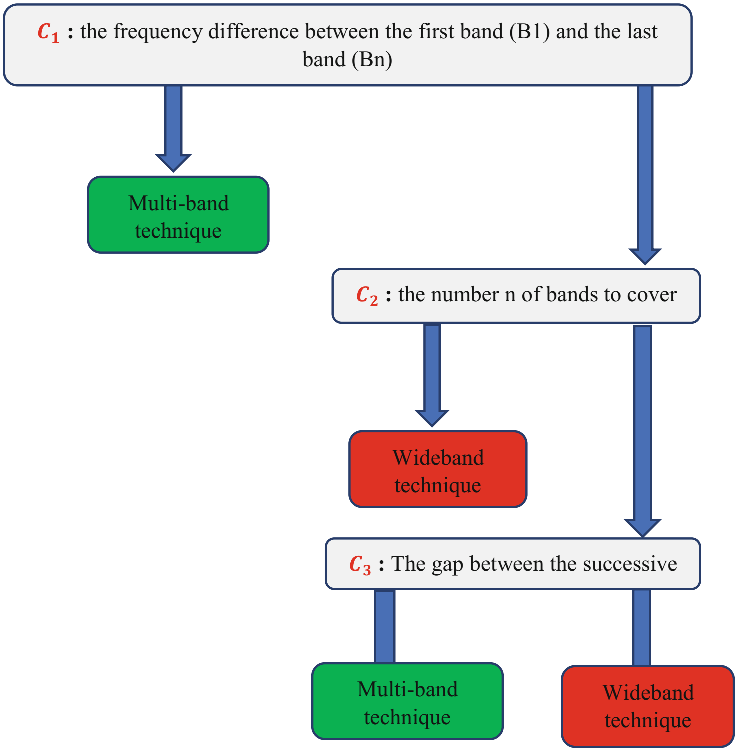

10.3.3.1 Dual-Band Antenna and Dual-Band Antenna System Design

Dual-Band Antenna Design

There are several methods of dual-band antenna design. We adapt the slit insertion method in this work. This technique consists of inserting a slit opening onto the antenna structure to create a new resonance in the upper band. This technique is applied to the reference antenna presented in the case of the single-band system. Thus, a slit of arbitrary values such as the length $L_{\mathrm{lit}} = 13$ mm and the width $W_{\mathrm{lit}} = 1.5$ mm is inserted on the printed part of the antenna as illustrated in Fig. 10.24a. We notice a second resonance with the insertion of the slit. However, the initial dimensions of the length and width of the slot do not allow us to cover our two working bands, namely the 2.5–2.69 GHz band and the 3.4–3.8 GHz band as shown in Fig. 10.24b.

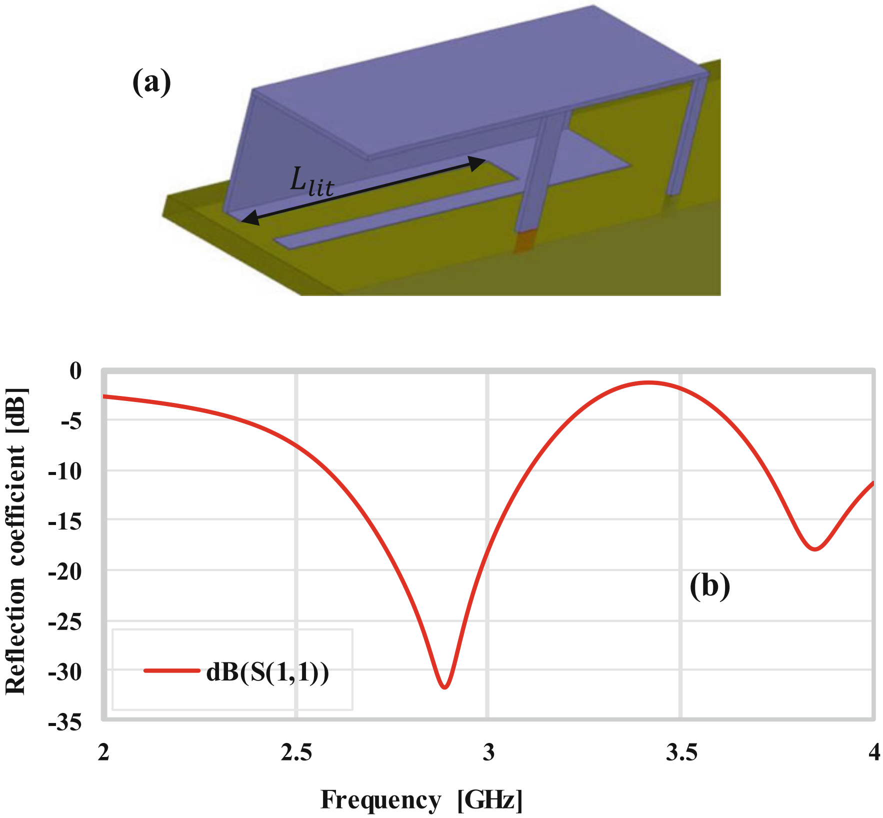

Fig. 10.24 Structure with slit (**a**), the reflection coefficient of the structure (**b**)

To define the influence respectively of the length and the width of the slot on the parameters of the antenna, a parametric study is made respectively on the length and the width of this slot.

The parametric study on the length of the slot (L_{lit}) shows that the more this length increases, the more the two resonances are adapted and tend towards the two central working frequencies. Indeed, this increase in (L_{lit}) causes an increase in the electrical length of the antenna and lowers the two resonant frequencies. This increase also affects the width of each band. Table 10.6 shows the variation of the bandwidth of the high band (HF BW) and the bandwidth of the low band (LF BW) as a function of L_{lit}.

It is noted for the high band that the passband increases successively de $L_{\mathrm{slot}} = 13$ mm to $L_{\mathrm{slot}} = 15$ mm, going from 280 to 520 MHz. It decreases from $L_{\mathrm{slot}} = 15.5$ mm to $L_{\mathrm{slot}} = 16.5$ mm passing from 500 to 490 MHz then increases again and gives a maximum value of 530 MHz at $L_{\mathrm{slot}} = 17$ mm. For the low band, there is a linear decrease in the passband going from 530 MHz for L_fente = 13 mm to 140 MHz for $L_{\mathrm{slot}} = 17$ mm. We note a dual-band operation completely covering the LTE2600 and LTE3600 tapes at a slot length $L_{\mathrm{slot}} = 15.5$ mm. At this length, we have a resonance at 2.59 GHz in the LTE2600 band with a bandwidth of 240 MHz and a resonance at 3.61 GHz of the LTE3600 band with a bandwidth of 500 MHz as shown in Fig. 10.25.

Table 10.6 Variations of the BW as a function of the length of the slot

L_{lit} (mm)	13	13.5	14	14.5	15	15.5	16	16.5	17
BW BH (MHz)	280	370	440	500	520	500	500	490	530
BW BB (MHz)	530	480	400	340	290	240	190	170	140

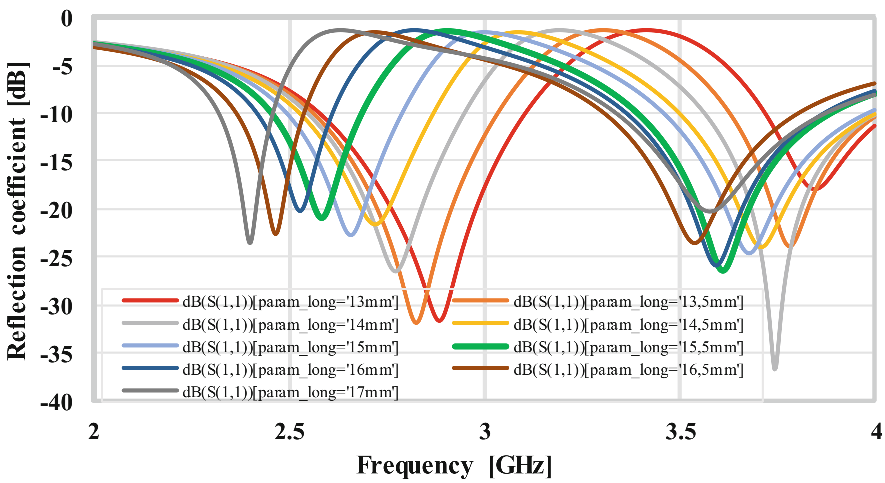

Fig. 10.25 *S*-parameters of the parametric study on L_{lit}

The parametric slit width study only influences the bandwidth widths of the two bands but only slightly.

Dual-Band Antenna System Design

The dual-band antenna system is obtained by reproducing the same antenna symmetrically to the diagonal of the substrate as shown in Fig. 10.32 (without the coupler). We notice with the first simulation a shift towards the increasing values of the resonance frequencies of the system. This shift is due to the inductive effect caused by the addition of antenna 2. The system is then optimized to operate in the working bands. The strong coupling between the two input ports is noted here only at low frequency as in the case of the single-band system presented in Chap. 3. In the 3.4–3.8 GHz band, we notice that the system presents a good decoupling of the order of −20 dB over the whole band as shown in Fig. 10.26.

Dual-Band Coupler Design

In the literature, several couplers suitable for multiband applications are presented and are proposed in particular in [34–40].

In [40] is presented the design of a new branch coupler able to operate at two arbitrary frequencies. This property of operation at two arbitrary frequencies guided our choice of reference for the design of the coupler adapted to our work.

In the proposed design, all transmission lines have a quarter-wavelength electrical length and are rated at the average frequency of the two operating bands.

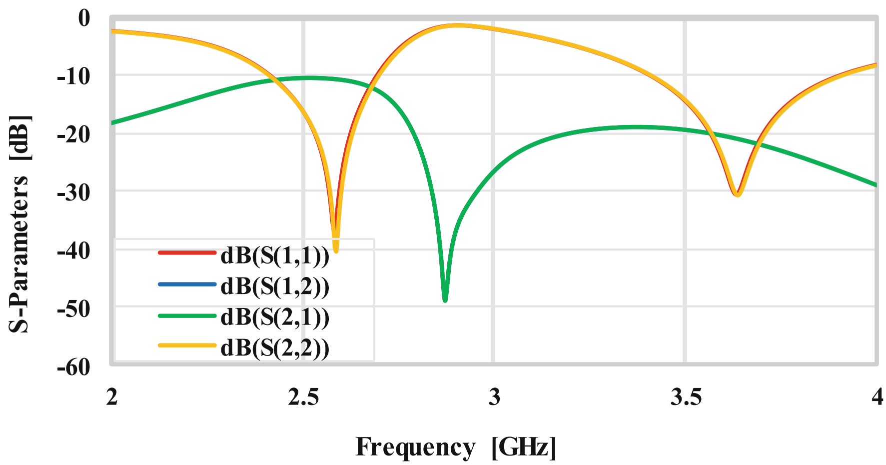

Fig. 10.26 Dual-band antenna system without coupler *S*-parameters

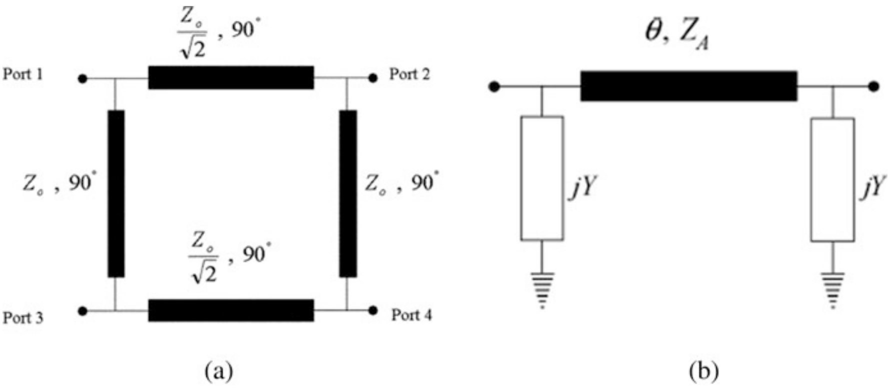

Fig. 10.27 The conventional structure of a BLC (**a**), Equivalent structure of a transmission line of the BLC (**b**)

The design procedure consisted of replacing each transmission line, conventional couplers of quarter-wavelength electrical length, and characteristic impedance Z (Fig. 10.27a) by an equivalent structure with more compact stubs (Fig. 10.27b). This structure consists of a transmission line of electrical length θ and characteristic impedance Z_A, connected to a pair of bypass elements (jY) called shunts. A shunt is a device of very low impedance relative to the load that allows current to pass from one point to another in an electrical circuit using very little energy. For analysis, the proposed structure is assumed to be lossless and reciprocal.

By applying a matrix formulation, the parameters—ABCD of the structure proposed by Fig. 10.27b can be written in the form of Eq. (10.14).

$$\begin{bmatrix} 1 & 0 \\ jY & 1 \end{bmatrix} \begin{bmatrix} \cos\theta & jZ_A \sin\theta \\ jY_A \sin\theta & \cos\theta \end{bmatrix} \begin{bmatrix} 1 & 0 \\ jY & 1 \end{bmatrix} \tag{10.14}$$

The development of Eq. (10.14) leads to Eq. (10.15):

$$\begin{bmatrix} \cos\theta - Z_A Y \sin\theta & jZ_A \sin\theta \\ jZ_A \sin\theta \left(1 - Z_A^2 Y^2 + 2Z_A Y \cot\theta\right) & \cos\theta - Z_A Y \sin\theta \end{bmatrix} \tag{10.15}$$

Simplified Eq. (10.15) gives Eq. (10.16):

$$\begin{bmatrix} 0 & jZ_A \sin\theta \\ j\frac{1}{Z_A \sin\theta} & 0 \end{bmatrix} = \begin{bmatrix} 0 & \pm jZ_T \\ \pm j\frac{1}{Z_T} & 0 \end{bmatrix} \tag{10.16}$$

With:

$$Z_A \sin\theta = \pm Z_T \tag{10.17}$$

$$Y = \frac{\cot\theta}{Z_A} \tag{10.18}$$

Equation (10.16) implies that the proposed structure is equivalent to a transmission line section with a characteristic impedance Z_T and an electrical length of $\pm 90°$.

Therefore, for dual-band operation, the necessary conditions can simply be stated as follows:

$$Z_A \sin\theta_1 = \pm Z_T \tag{10.19}$$

$$Z_A \sin\theta_2 = \pm Z_T \tag{10.20}$$

where

θ_1 corresponds to the electrical length of the transmission line evaluated at the central frequency f_1 of the lower band.

θ_2 corresponds to the electrical length of the transmission line evaluated at the central frequency f_2 of the upper band.

The general solutions of Eqs. (10.19) and (10.20) can then be expressed as follows:

$$\theta_2 = n\pi - \theta_1 \tag{10.21}$$

With $n = 1, 2, 3, \ldots$, Such that:

$$\frac{\theta_1}{\theta_2} = \frac{f_1}{f_2} \tag{10.22}$$

So we get:

$$\theta_1 = \frac{n\pi}{2}(1-\delta) \tag{10.23}$$

$$\theta_2 = \frac{n\pi}{2}(1+\delta) \tag{10.24}$$

$$\delta = \frac{f_2 - f_1}{f_2 + f_1} \tag{10.25}$$

Subsequently, the electrical length θ_0 of a transmission line evaluated at the average frequency of the center frequencies f_1 and f_2 can therefore be determined as follows:

$$\theta_0 = \frac{\theta_1 + \theta_2}{2} = \frac{n\pi}{2} \tag{10.26}$$

Moreover, by replacing Eqs. (10.23) and (10.24) by Eqs. (10.17) and (10.18), for any odd n, we have:

$$Z_A = \frac{Z_T}{\left|\cos\left(\frac{n\delta\pi}{2}\right)\right|} \tag{10.27}$$

$$Y = \begin{cases} \frac{\tan\left(\frac{n\delta\pi}{2}\right)}{Z_A}, & f = f_1 \\ -\frac{\tan\left(\frac{n\delta\pi}{2}\right)}{Z_A}, & f = f_2 \end{cases} \tag{10.28}$$

And for any even n we have:

$$Z_A = \frac{Z_T}{\left|\sin\left(\frac{n\delta\pi}{2}\right)\right|} \tag{10.29}$$

$$Y = \begin{cases} -\frac{\cot\left(\frac{n\delta\pi}{2}\right)}{Z_A}, & f = f_1 \\ \frac{\cot\left(\frac{n\delta\pi}{2}\right)}{Z_A}, & f = f_2 \end{cases} \tag{10.30}$$

The solutions of these equations give the analytical expressions for the design of the dual-band coupler. These solutions also include the choice of n and the different ways of making the shunt element with its input admittance Y, as defined by Eqs. (10.28) and (10.30). Several coupler topologies can be realized with these solutions. We present in this document only the open-circuit stub topology for $n = 1$. Using Eqs. (10.23) and (10.24), the input admittance Y_{CO} of the corresponding stub can thus be deduced as:

$$Y_{CO} = \begin{cases} \frac{\cot\left(\frac{\delta\pi}{2}\right)}{Z_B}, & f = f_1 \\ -\frac{\cot\left(\frac{\delta\pi}{2}\right)}{Z_B}, & f = f_2 \end{cases} \tag{10.31}$$

where Z_B is the characteristic impedance of the section. Therefore, by combining Eqs. (10.28) and (10.31), we obtain:

$$Z_{\mathrm{B}} = \frac{Z_{\mathrm{T}}}{\sin\left(\frac{\delta\pi}{2}\right)\tan\left(\frac{\delta\pi}{2}\right)} \tag{10.32}$$

Figure 10.28 shows the final structure of the dual-band coupler which is the result of the fusion of all the transformations of the transmission lines by their equivalent circuit. Thus, the values of Z_1, Z_2, and Z_3 can be determined using the following formulas:

$$Z_1 = \frac{Z_0}{\sqrt{2}} \cdot \frac{1}{\cos\left(\frac{\delta\pi}{2}\right)} \tag{10.33}$$

$$Z_2 = Z_0 \cdot \frac{1}{\cos\left(\frac{\delta\pi}{2}\right)} \tag{10.34}$$

$$Z_3 = \frac{Z_0}{1+\sqrt{2}} \cdot \frac{1}{\sin\left(\frac{\delta\pi}{2}\right) \bullet \tan\left(\frac{\delta\pi}{2}\right)} \tag{10.35}$$

In the end, Eqs. (10.25), (10.33–10.35) make it possible in theory to design a dual-band coupler of the open-circuit stub topology for any system operating at two arbitrary frequency bands. However, this technique is optimal in the fractional bandwidth range from 0.2 to 0.5 and in the impedance range from 30 to 90 Ω as shown in Fig. 10.29.

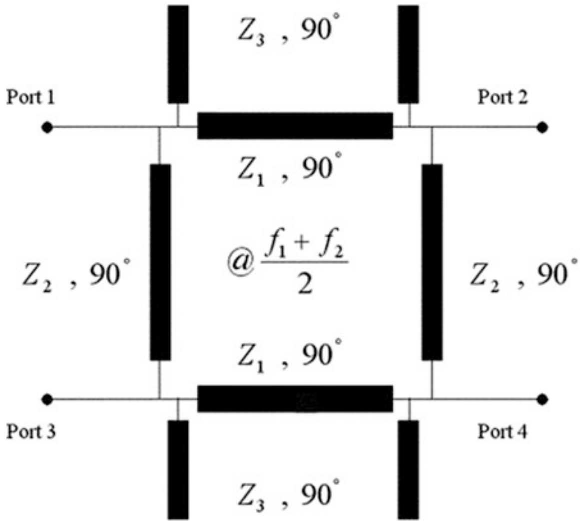

Fig. 10.28 Structure of the dual-band open-circuit stub coupler

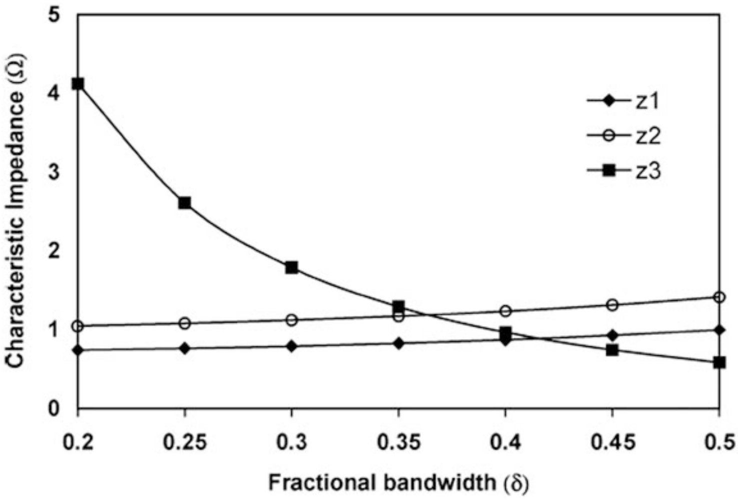

Fig. 10.29 Variations of normalized impedance versus fractional bandwidth

Table 10.7 Design parameters of the dual-band BLC operating at frequencies f_1 and f_2

Parameters	Values
f_1	2.6 GHz
f_2	3.6 GHz
f_0	3.1 GHz
δ	0.16
Z_0	50 Ω
Z_1	36.5 Ω
Z_2	51.6 Ω
Z_3	395.5 Ω

10.3.3.2 Design of the Dual-Band BLC Adapted to Our Antenna System

Based on the previously defined equations, we agree on the following notations:

- f_1 is the center frequency of the low band (2.5–2.69 GHz).
- f_2 is the center frequency of the high band (3.4–3.8 GHz).
- f_0 is the average frequency of the two center frequencies.

The design parameters are then given in Table 10.7.

Concerning the constraints on the fractional bandwidths and impedances required for an optimal design, we notice that our fractional bandwidth $\delta = 0.16$ does not respect the constraint cited in the previous paragraph and illustrated by Fig. 10.29. Likewise, the impedance $Z_3 = 395.5\ \Omega$ greatly exceeds the maximum value of the permissible impedance range. The calculation of the dimensions of the stub carried out with the impedance Z_3 gives stub width values of the order of 10^{-5} mm. These values are not achievable in practice. Therefore, we have solved this constraint by greatly increasing the length of the stub and setting a minimum value for the achievable stub width which is 0.2 mm. Figure 10.30 shows the dual-band Branch-Line Coupler integrated into the antenna system. The dimensions of the coupler are given in Table 10.8.

Figure 10.30 shows the *S*-parameters of the coupler produced under ADS. We note good adaptation both in the low band and in the high band but also full coverage of all the working bands. The transmissions from port 1 to port 2 (S_{12}) and from port 4 to port 3 (S_{43}) are perfectly combined. These transmissions are −2.8 dB at f_1 and −2.9 dB at f_2.

There is a strong decoupling between input ports 1 and 4 which is respectively −29 dB at f_1 and −21 dB at f_2.

It is also noted that the transmission curves (S_{12}) and (S_{43}) as well as the decoupling curve (S_{14}) all have their minimum value at the mean frequency f_0. Figure 10.31 shows the phase shifts between the ports of the dual-band coupler. We note a perfect symmetry of the phase shifts. The coupler has a phase shift between ports 2 and 3 such that que $\text{phase}(S(1,2)) - \text{phase}(S(1,3)) = 90.14^{\circ}$. Likewise, the phase shift between ports 3 and 2 is such that phase $\text{phase}(S(4,2)) - \text{phase}(S(4,3)) = 90.43^{\circ}$.

Figure 10.32 shows the antenna system realized integrating the dual-band coupler that we proposed in [41]. The *S*-parameters of this system is given in Fig. 10.33. The latter indicates a good agreement between the measured results and the simulated results.

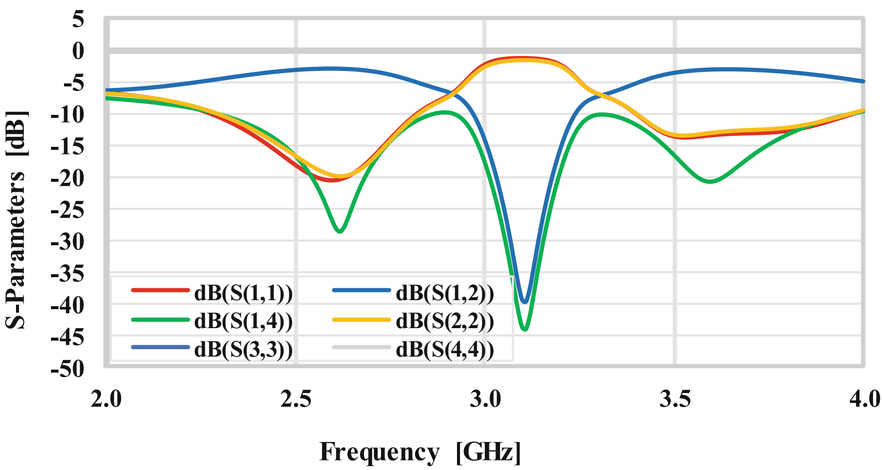

Fig. 10.30 *S*-parameters of the dual-band coupler

Table 10.8 Dimensions of the Dual-Band coupler

Variables	L_1	L_2	L_3	L_4	L_5	L_{stub}
Values	12.32	7.33	7.88	13.03	14.68	37.8
Variables	W_1	W_2	W_3	W_{stub}		
Values	1.5	1.13	2	0.22		

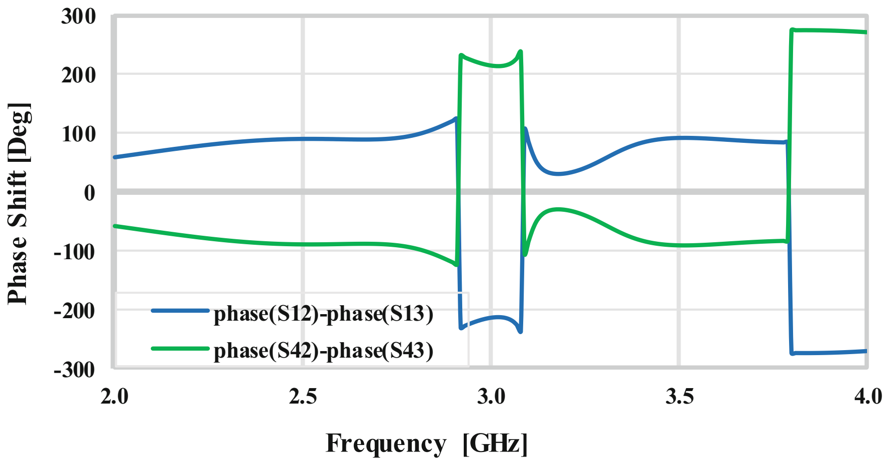

Fig. 10.31 Phase shifts of the dual-band coupler

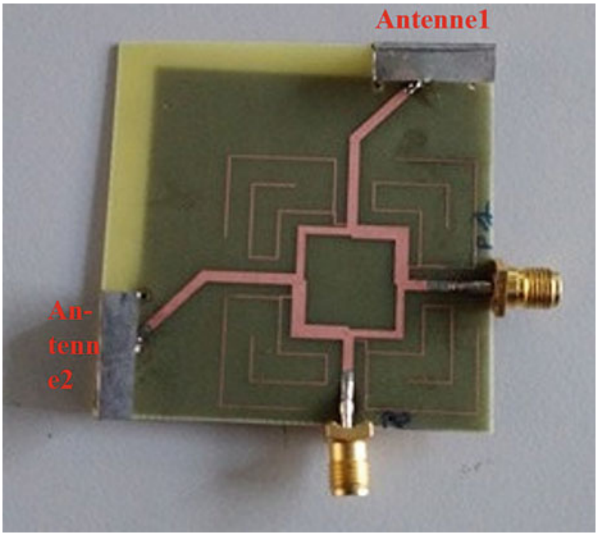

Fig. 10.32 Multi-antenna system manufactured with dual-band coupler

10.3.3.3 Study of Agility in the Two Bands

The antenna system with the dual-band coupler has the same reconfiguration states as those of the low-band system and those of the high-band system. The difference lies in the values obtained for each configuration. We summarize all of the configurations obtained in the two bands in Table 10.9.

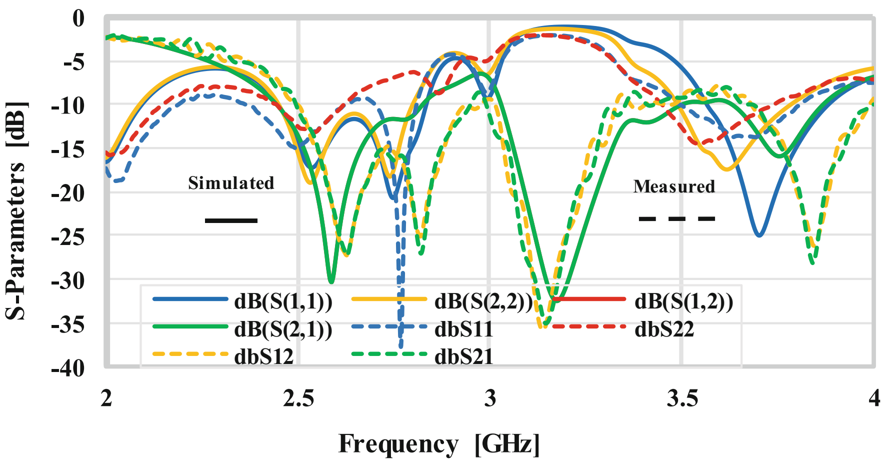

Fig. 10.33 Measured and simulated *S*-parameters of the system with dual-band BLC

Note that it would be even more interesting to present the results of radiation pattern measurements. However, for technical reasons linked to the availability of equipment and staff in our associated laboratory, these measurements have still not been able to be carried out.

10.4 Conclusion

In this chapter, we presented a new approach for agility in the radiation pattern of small communicating objects. The technique consists of using a Branch-Line Coupler to reconfigure the radiation pattern. The principle is easy to implement and corresponds to simple excitations of ports.

The proposed technique is first implemented in a single-band antenna system composed of two PIFA antennas integrating a coupler operating at the same 2.6 GHz central frequency. It has three configuration states and offers a maximum gain of 4.5 dB. Then the proposed technique is implemented in a dual-band system operating in the LTE2600 and LTE3600 bands. The dual-band system is obtained using the slot insertion technique. A dual-band coupler operating in the same bands is then integrated into the antenna system and manufactured. The *S*-parameters measurements carried out show good agreement with the simulations. This system has three configuration states in each band. It offers an efficiency of 64% in the low band and 44% in the high band.

The perspective of this work is to move away from the use of miniature BLC to save more space for the other electronic components integrated into small communicating objects. It is also envisaged to use the couplers in antenna systems having an infinite ground plane compared to standard couplers.

Table 10.9 Different reconfigurations of the radiation pattern in the two bands

Reconfigurations in 2.5-2.69 GHz band						
Excited Port(s)	***Couvered directions***				***Gain maximal (dB)***	***Efficiency (%)***
	+ X	+ Y	– X	– Y		
Only Port 1	***Yes***	*No*	*No*	***Yes***	**2.74** À $\varphi = 90°$ et $\theta = 215°$.	**64**
Only Port 2	*No*	***Yes***	***Yes***	*No*	**2.73** À $\varphi = 0°$ et $\theta = 225°$.	
Port1 and Port2 simultaneously	***Yes***	***Yes***	***Yes***	***Yes***	**2.42** À $\varphi = 0°$ et $\theta = 270°$ $\varphi = 90°$ et $\theta = 270°$	
Reconfigurations in 3.4–3.8 GHz band						
Excited Port(s)	***Covered directions***				***Gain maximal (dB)***	***Efficiency (%)***
	+ X	*+ Y*	*– X*	*– Y*		
Only Port 1	*No*	***Yes***	***Yes***	***Yes***	**1.95** À $\varphi = 0°$ et $\theta = 215°$.	**44**
Only Port 2	***Yes***	*No*	***Yes***	***Yes***	**1.51** À $\varphi = 90°$ et $\theta = 215°$.	
Port1 and Port2 simultaneously	*No*	*No*	***Yes***	***Yes***	**2.03** À $\varphi = 0°$ et $\theta = 235°$.	

References

1. UIT, R-ACT-WRC.14-2019-PDF-F.pdf, *Union Iternationale des Télécommunications*, https://www.itu.int/dms_pub/itu-r/opb/act/R-ACT-WRC.14-2019-PDF-F.pdf. Consulté le 13 Oct 2020
2. A. Kaloxylos, A. Gavras, R. De Peppe, Empowering Vertical Industries through 5G Networks - Current Status and Future Trends (2020), https://doi.org/10.5281/ZENODO.3698113.

3. V. Tikhvinskiy, V. Koval, Prospects of 5G satellite networks development, in *Moving Broadband Mobile Communications Forward - Intelligent Technologies for 5G and Beyond*, (2020). https://doi.org/10.5772/intechopen.90943
4. J.G. Andrews et al., What will 5G be? IEEE J. Selected Areas Commun. **32**(6), 1065–1082 (2014). https://doi.org/10.1109/JSAC.2014.2328098
5. NTT DOCOMO, DOCOMO 5G White Paper: 5G Radio Acces: Requirements, Concept and Technologies (2014), p. 13
6. Q. Luo, S. Gao, L. Zhang, Millimeter-wave smart antennas for advanced satellite communications, in *2015 IEEE MTT-S International Microwave Symposium, Phoenix, AZ, USA*, (2015), pp. 1–4. https://doi.org/10.1109/MWSYM.2015.7166770
7. A.P. Feresidis, P.S. Hall, T. Jackson, P. Gardner, Editorial - Emerging integrated reconfigurable antenna technologies. Antennas Propag. IET Microw. **8**(11), 809–810 (2014). https://doi.org/10.1049/iet-map.2014.0489
8. K. Moschner, NGMN Alliance Update on 5G Work Programme (2015), p. 15
9. S. Tian, L. Li, Z. Luo, Q. Cheng, T.J. Cui, Smart antenna designs, in *Wiley 5G Ref*, (American Cancer Society, Atlanta, 2020), pp. 1–37
10. T. Lin, C. Lin, K. Huang, J. Kuo, Compact branch-line coupler filter with transmission zeros, in *2015 Asia-Pacific Microwave Conference (APMC)*, vol. 3, (2015), pp. 1–3. https://doi.org/10.1109/APMC.2015.7413359
11. M. Koubeissi, Etude d'antennes multifaisceaux à base d'une nouvelle topologie de matrice de Butler: conception du dispositif de commande associé, Thesis, Limoges, 2007
12. A. Harck, Conception et validation de déphaseurs large bande intégrant des MEMS-RF dans un environnement hostile (2014). Consulté le 11 Mai 2019. [En ligne]. Disponible sur: https://tel.archives-ouvertes.fr/tel-01135972
13. MACOM an AMP Company, RF Directional Couplers and 3 dB Hybrids Overview, *s Asia*, p. 10.
14. D.M. Pozar, *Microwave Engineering*, 4th edn. (Wiley, Hoboken, NJ, 2019)., https://www.wiley.com/en-us/Microwave+Engineering%2C+4th+Edition-p-9781118298138. Consulté le 08 Mai 2019
15. J. Reed, G.J. Wheeler, A method of analysis of symmetrical four-port networks. IRE Trans. Microw. Theory Tech. **4**(4), 246–252 (1956). https://doi.org/10.1109/TMTT.1956.1125071
16. D.M. Pozar, Microstrip antennas. Proc. IEEE **80**(1), 79–91 (1992). https://doi.org/10.1109/5.119568
17. H. Boutayeb, Circuits et systèmes de communication micro-ondes (2006). Consulté le 11 Mai 2019. [En ligne]. Disponible sur: https://cel.archives-ouvertes.fr/cel-00156394
18. D.M. Khan, Design of Planar Inverted-F Antenna (2014)
19. I. Dioum, K. Diallo, M.M. Khouma, I. Diop, L. Sane, A. Ngom, Miniature MIMO antennas for 5G mobile terminals, in *2018 6th International Conference on Multimedia Computing and Systems (ICMCS)*, (2018), pp. 1–6. https://doi.org/10.1109/ICMCS.2018.8525870
20. M. Ikram, M.S. Sharawi, H. Attia, A compact dual standard MIMO antenna system for mobile applications, in *2017 IEEE 28th Annual International Symposium on Personal, Indoor, and Mobile Radio Communications (PIMRC)*, (2017), pp. 1–3. https://doi.org/10.1109/PIMRC.2017.8292652
21. L. Sun, H. Feng, Y. Li, Z. Zhang, Compact 5G MIMO mobile phone antennas with tightly arranged orthogonal-mode pairs. IEEE Trans. Antennas Propag. **66**(11), 6364–6369 (2018). https://doi.org/10.1109/TAP.2018.2864674
22. R. Hussain, A.T. Alreshaid, S.K. Podilchak, M.S. Sharawi, Compact 4G MIMO antenna integrated with a 5G array for current and future mobile handsets. Antennas Propag. IET Microw. **11**(2), 271–279 (2017). https://doi.org/10.1049/iet-map.2016.0738
23. A.A. Naser, K.H. Sayidmarie, J.S. Aziz, Design and implementation of a PIFA antenna for multi-band LTE handset applications, in *2016 Loughborough Antennas Propagation Conference (LAPC)*, (2016), pp. 1–5. https://doi.org/10.1109/LAPC.2016.7807548
24. K.M. Morshed, K.P. Esselle, M. Heimlich, D. Habibi, I. Ahmad, Wideband slotted planar inverted-F antenna for millimeter-wave 5G mobile devices, in *2016 IEEE Region 10 Symposium (TENSYMP)*, (2016), pp. 194–197. https://doi.org/10.1109/TENCONSpring.2016.7519403

25. O.M. Haraz, M. Ashraf, S. Alshebeili, Single-band PIFA MIMO antenna system design for future 5G wireless communication applications, in *2015 IEEE 11th International Conference on Wireless and Mobile Computing, Networking and Communications (WiMob)*, (2015), pp. 608–612. https://doi.org/10.1109/WiMOB.2015.7348018
26. W. Ahmad, W.T. Khan, Small form factor dual band (28/38 GHz) PIFA antenna for 5G applications, in *2017 IEEE MTT-S International Conference on Microwaves for Intelligent Mobility (ICMIM)*, (2017), pp. 21–24. https://doi.org/10.1109/ICMIM.2017.7918846
27. I. Dioum, Conception de systèmes multi-antennaires pour techniques de diversité et MIMO: application aux petits objets nomades communicants, PhD thesis, Université Nice Sophia Antipolis, 2013.
28. K.L. Virga, Y. Rahmat-Samii, Low-profile enhanced-bandwidth PIFA antennas for wireless communications packaging. IEEE Trans. Microw. Theory Tech. **45**(10), 1879–1888 (1997). https://doi.org/10.1109/22.641786
29. Y. Belhadef, N.B. Hacene, PIFAS antennas design for mobile communications, in *International Workshop on Systems, Signal Processing and their Applications, WOSSPA*, (2011), pp. 119–122. https://doi.org/10.1109/WOSSPA.2011.5931429
30. H. Gupta, A. Mehta, K. Shambavi, Miniaturization of a novel rat race coupler: A comparative analysis, in *2016 Thirteenth International Conference on Wireless and Optical Communications Networks (WOCN)*, (2016), pp. 1–3. https://doi.org/10.1109/WOCN.2016.7759031
31. A.L. Denis, Miniature microstrip rat-race couplers with artificial transmission lines, in *2017 40th International Conference on Telecommunications and Signal Processing (TSP)*, (2017), pp. 802–805. https://doi.org/10.1109/TSP.2017.8076099
32. S. Hebib, Nouvelle topologie d'antennes multi-bandes pour applications spatiales, PhD thesis, Université Paul Sabatier - Toulouse III, 2008.
33. D. Sanchez-Hernandez, I.D. Robertson, A survey of broadband microstrip patch antennas. Microw. J. (1996)., https://link.galegroup.com/apps/doc/A18779193/AONE?sid=lms. Consulté le 7 Sept 2019
34. M.-J. Park, B. Lee, Dual-band, cross coupled branch line coupler. IEEE Microw. Wirel. Compon. Lett. **15**(10), 655–657 (2005). https://doi.org/10.1109/LMWC.2005.856683
35. S. Amiri, M. Kamyab-Hesari, M. Dousti, A novel highly compact dual-band branch-line coupler utilizing left and right-handed technique, in *2011 Annual IEEE India Conference*, (2011), pp. 1–4. https://doi.org/10.1109/INDCON.2011.6139415
36. K.M. Cheng, S. Yeung, A novel dual-band 3-dB branch-line coupler design with controllable bandwidths. IEEE Trans. Microw. Theory Tech. **60**(10), 3055–3061 (2012). https://doi.org/10.1109/TMTT.2012.2210437
37. B.S. Elesela, Y. Chiang, Design of reconfigurable dual-band branch-line coupler, in *2016 IEEE International Workshop on Electromagnetics: Applications and Student Innovation Competition (iWEM)*, (2016), pp. 1–3. https://doi.org/10.1109/iWEM.2016.7504932
38. P. Liu, D. Yang, A dual-band compact branch line coupler based on Γ-shaped transformer, in *2016 17th International Conference on Electronic Packaging Technology (ICEPT)*, (2016), pp. 1476–1479. https://doi.org/10.1109/ICEPT.2016.7583402
39. M. Park, Comments on "Compact dual-band branch-line coupler with dual transmission lines". IEEE Microw. Wirel. Compon. Lett. **27**(1), 103–104 (2017). https://doi.org/10.1109/LMWC.2016.2629986
40. K.-M. Cheng, F.-L. Wong, A novel approach to the design and implementation of dual-band compact planar 90/spl deg/branch-line coupler. IEEE Trans. Microw. Theory Tech. **52**(11), 2458–2463 (2004). https://doi.org/10.1109/TMTT.2004.837151
41. L. Sane et al., Dual-band pattern reconfigurable 5G antenna using dual-band BLC, in *2018 IEEE Conference on Antenna Measurements Applications (CAMA)*, (2018), pp. 1–4. https://doi.org/10.1109/CAMA.2018.8530554

Chapter 11
Time-Domain Approach Towards Smart Antenna Design

Avishek Chakraborty, Gopi Ram, and Durbadal Mandal

11.1 Introduction

The demand for modern-age communication has encouraged the use of antenna arrays due to its larger gain and highly directional radiation characteristics compared to a single element antenna. Synthesis of different radiation patterns with amplitude and phase weightings suffer from high dynamic range ratio and quantization errors. The traditional methods of array synthesis also increase the complexity and cost of implementation. To overcome these problems, another control parameter "Time" is introduced as a fourth dimension [1]. Modulation of "Time" along with other control parameters adds an extra degree of freedom in array synthesis [2]. The simple idea behind "Time-modulation" is to control the high-speed RF switches connected with the elements of the array in a periodic manner [3]. By switching ON and OFF the elements for a certain period, equivalent amplitude and phase weightings can be generated for the desired pattern [4]. Time-modulated arrays (TMAs) are capable of steering the radiation pattern with appropriate switching sequence which implies a less complex array feeding network as no phase shifters are needed [5]. Moreover, the rapidly adjustable nature of "Time" parameter also enhances the adaptability and reconfigurability of the array [6].

The concept of the fourth dimension in antenna array synthesis was introduced by Shanks and Bickmore [7]. It has been emerged as a new way of electronic scanning by eliminating the need for mechanical movements of the array elements [8]. Earlier

A. Chakraborty · D. Mandal
Department of Electronics and Communication Engineering, National Institute of Technology, Durgapur, West Bengal, India

G. Ram (✉)
Department of Electronics and Communication Engineering, National Institute of Technology, Warangal, Telangana, India
e-mail: gopi.ram@nitw.ac.in

M. A. Matin (ed.), *Wideband, Multiband, and Smart Antenna Systems*, Signals and Communication Technology, https://doi.org/10.1007/978-3-030-74311-6_11

works with TMAs to reduce the sidelobe level (SLL) have opened up the possibilities of designing an efficient antenna system with interference rejection capability [9]. The emergence of evolutionary computation techniques and the availability of high-speed RF switches have accelerated the research on TMAs [10]. Evolutionary algorithms such as differential evolution (DE), particle swarm optimization (PSO), and genetic algorithms (GA) are extensively used for the desired pattern synthesis with reduced SLLs [10–13]. The simple way of controlling the radiation pattern with ON-OFF switching comes with a drawback of sideband radiations (SRs) generated at multiple harmonic frequencies due to periodic switching sequences [14]. These SRs are usually considered as a loss of power and reduce the efficiency of the array if not suppressed [15]. Several contributions have been made towards reducing the SRs with the help of optimization algorithms [16–20]. Different time schemes have been developed to reduce the power dissipation in unwanted sidebands [20–22]. To obtain the desired solution, switching sequences with shifted pulse [23] and subsectioned pulses [24] have been considered. Further advances have been reported with optimal pulse shifting of outer elements for the simultaneous reduction of SRs and SLL [25]. Apart from the reduction of SRs, some research works in recent times have also discussed the possibility of utilizing the sideband patterns for multichannel communication [26–28]. By exploiting the SRs with suitable switching sequence, steered beam patterns have been generated [29–31]. The idea is further extended with adaptive beamforming [32] and direction-finding applications [33]. This time-domain approach has also been used for shaped pattern synthesis [34, 35], sum and difference pattern generation [36, 37], adaptive nulling [38–40], and placement of broad nulls [41–43]. Cutting-edge applications like cognitive radio systems [44] and radar signal processing [45] have been addressed in several research works with appropriately designed switching schemes. The diversity and feasibility of TMAs have also been explored with different array geometries such as linear [24–32], planar [34, 35], circular [46–48], and concentric circular arrays [49, 50].

This chapter deals with the feasibility of time-modulated linear arrays (TMLAs) for different applications by optimizing several parameters of the array. Pattern synthesis with or without suppressing the SRs as well as exploiting the sidebands are briefly described with several examples. Towards this aim, this chapter is divided into separate sections. The theoretical insights of TMLA are presented in Sect. 11.2. In Sect. 11.3, evolutionary algorithms employed for optimizing the TMLA parameters are discussed. Section 11.4 deals with the numerical results and is divided into separate subsections. Section 11.4.1 describes the pattern synthesis of TMLA without suppressing the SRs. Separate examples are presented to discuss the overall reduction in SLL and reduction of SLL in a specific region for interference rejection. Section 11.4.2 is devoted to simultaneous reduction of SLL and suppression of SRs with suitably optimized TMLA parameters. Section 11.4.3 briefly describes the exploitation of SRs towards more advanced applications of TMLAs. In this regard, multipattern synthesis of TMLAs with simultaneous sum-difference pattern and multi-harmonic beam steering are addressed in separate subsections. Finally, some conclusive remarks are presented in Sect. 11.5. Throughout this discussion, 16-element TMLAs are considered and a wavelet mutation-based differential evolution

(DEWM) is used for optimal solution. Other well-known optimization techniques for electromagnetic problems such as PSO and real-coded GA (RGA) based results are also presented for comparison.

11.2 Theoretical Background

Consider a TMLA of N uniformly spaced isotropic elements aligned towards the positive z axis where each array element is connected with attenuators and high-speed RF switches, shown in Fig. 11.1. The array factor can be expressed as [6]

$$AF(\theta, t) = e^{j(2\pi f_0)t} \sum_{n=1}^{N} I_n U_n(t) e^{jk(n-1)d\cos\theta} \tag{11.1}$$

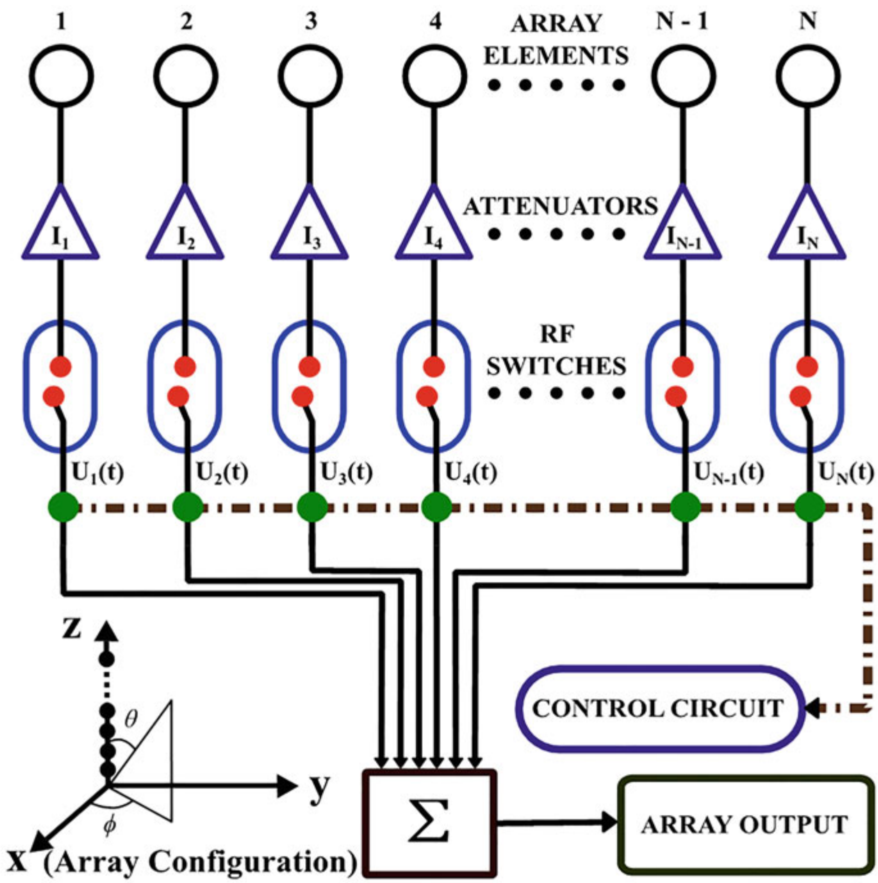

Fig. 11.1 Configuration of N-element TMLA with attenuators and RF switches

where I_n is the static amplitude coefficients of nth element, $U_n(t)$ denotes the time switching function, f_0 is the center frequency, k resembles the free space wavenumber, d is the separation between array elements, and θ is the angle of arrival measured from broadside direction. Due to the periodic nature of time-modulation, SRs are generated at the multiples of modulating frequency f_p ($f_0 \gg f_p$). The time switching function $U_n(t)$ can be expanded into frequency domain as [6]

$$U_n(t) = \sum_{m=-\infty}^{\infty} a_{mn} e^{jm(2\pi f_p)t} \tag{11.2}$$

where a_{mn} is the complex Fourier excitation of the nth element for mth order frequency (where, $m = 0, \pm 1, \pm 2, \ldots, \pm\infty$). The complex excitation coefficient a_{mn} can be decomposed into Fourier series as

$$a_{mn} = \frac{1}{T_p} \int_0^{T_p} U_n(t) e^{-jm(2\pi f_p)t} dt \tag{11.3}$$

where T_p is the modulation period and the array factor of Eq. (11.1) becomes

$$AF(\theta, t) = \sum_{m=-\infty}^{\infty} \sum_{n=1}^{N} I_n a_{mn} \left\{ e^{jk(n-1)d\cos\theta} \right\} e^{j2\pi(f_0 + mf_p)t} \tag{11.4}$$

The time-averaged response of the array factor for the mth order frequency can be simplified as

$$AF_m(\theta, \mathrm{t}) = e^{j2\pi(f_0 + mf_p)t} \sum_{n=1}^{N} I_n a_{mn} e^{jk(n-1)d\cos\theta} \tag{11.5}$$

The central frequency pattern can be obtained from Eq. (11.5) by putting $m = 0$ and the harmonic or sideband patterns can be generated with $m = \pm 1, \pm 2, \ldots, \pm\infty$. This also implies that some portion of the total radiated power is shifted from the central frequency to sidebands due to the periodic nature of time-modulation.

The power associated with the central pattern (P_0), the total radiated power due to all harmonic components including the central pattern (P_T), and the directivity of the N-element TMLA can be expressed as

$$P_0 = \int_0^{2\pi} \int_0^{\pi} |AF_0(\theta, \phi)|^2 \sin\theta d\theta d\phi \tag{11.6}$$

$$P_{\mathrm{T}} = \sum_{m=-\infty}^{\infty} \int_{0}^{2\pi} \int_{0}^{\pi} |AF_m(\theta, \phi)|^2 \sin\theta d\theta d\phi \tag{11.7}$$

$$D = \frac{4\pi |AF_0(\theta_0, \phi_0)|^2}{\sum_{m=-\infty}^{\infty} \int_{0}^{2\pi} \int_{0}^{\pi} |AF_m(\theta, \phi)|^2 \sin\theta d\theta d\phi} \tag{11.8}$$

where, the central pattern ($m = 0$) is directed along $\theta = \theta_0$, $\phi = \phi_0$, and $AF_m(\theta, \phi)$ represents the mth harmonic radiation pattern ($m \neq 0$).

11.2.1 Switching Configuration

The periodic time switching function $U_n(t)$ can be modified with different sequences for distinct applications. The general time scheme and the combination of various optimized time schemes are explored in this chapter to address the different TMLA applications. The simplest time scheme consisting of switching ON and OFF the elements of a TMLA is presented in Fig. 11.2a. Shifted time sequence within the stipulated modulation period is also shown in Fig. 11.2b which enables an additional control for desired pattern generation.

The normalized time scheme for the nth element is shown in Fig. 11.2a where the element is switched ON for a period of τ_n within the modulation period T_{p} ($0 \leq \tau_n \leq T_{\mathrm{p}}$). The switch ON and switch OFF instants are τ_n^1 and τ_n^2 respectively,

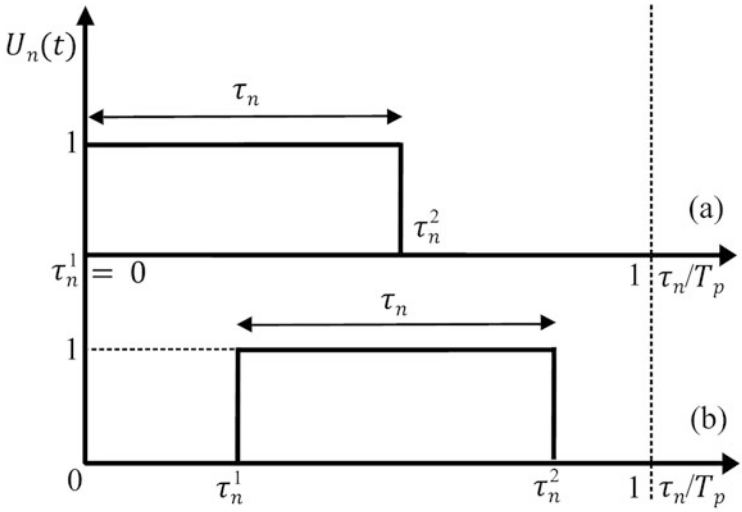

Fig. 11.2 (**a**) Generalized time sequence and (**b**) Pulse shifted time sequence for nth element

and the switching function $U_n(t)$ can be mathematically presented as

$$U_n(t) = \begin{cases} 1, & \tau_n^1 \le t \le \tau_n^2 \le T_\mathrm{p} \text{ where } \tau_n^1 = 0 \\ & 0, \quad \text{otherwise} \end{cases} \tag{11.9}$$

The ON-time duration of the nth element can be calculated as $\tau_n = \left(\tau_n^2 - \tau_n^1\right)$, and the complex excitation a_{mn} can be expressed as

$$a_{mn} = \frac{I_n \tau_n}{T_\mathrm{p}} \left\{\sin c\left(m\pi f_\mathrm{p}\tau_n\right)\right\} \mathrm{e}^{-jm\pi f_\mathrm{p}(\tau_n)} \tag{11.10}$$

The same time sequence is shifted within T_p and shown in Fig. 11.2b. The switching function $U_n(t)$ for the shifted time sequence can be mathematically described as

$$U_n(t) = \begin{cases} 1, & 0 < \tau_n^1 \le t \le \tau_n^2 \le T_\mathrm{p} \text{ where } \tau_n^1 \ne 0 \\ & 0, \quad \text{otherwise} \end{cases} \tag{11.11}$$

The expression of complex excitation a_{mn} for the shifted sequence can be given as

$$a_{mn} = \frac{I_n\left(\tau_n^2 - \tau_n^1\right)}{T_\mathrm{p}} \left[\sin c\left\{m\pi f_\mathrm{p}\left(\tau_n^2 - \tau_n^1\right)\right\}\right] \mathrm{e}^{-jm\pi f_\mathrm{p}\left(\tau_n^1 + \tau_n^2\right)} \tag{11.12}$$

The term $\mathrm{e}^{-jm\pi f_\mathrm{p}\left(\tau_n^1 + \tau_n^2\right)}$ is equivalent to the phase weightings of the conventional phased arrays, and the harmonic patterns ($m = \pm 1, \pm 2, \ldots, \pm\infty$) can be controlled by ON-OFF instants to generate the shifted or steered patterns which also eliminates the need of expensive phase shifters.

11.3 Evolutionary Optimization Employed

Evolutionary algorithms are population-based multidimensional search techniques inspired by natural phenomena. These meta-heuristics optimization processes have gained momentum in many fields of research due to the capability of finding global solutions by minimizing or maximizing the suitable objective functions.

Differential evolution (DE) algorithm is one of the most familiar stochastic optimization processes based on mutation, crossover, and natural selection to optimize the continuous variables in a multidimensional space. DE has been extensively used over the years for solving electromagnetic problems [51]. In this chapter, DE with wavelet mutation strategy (DEWM) is used for fine tuning the desired solution. In wavelet mutation (WM), certain seismic signals are modeled with a combination of translations and dilations of an oscillating function. The oscillating function has a finite duration, termed as a "wavelet." A continuous wavelet $\psi(x)$, also called as "mother wavelet," satisfies the following properties [52]:

1. The total positive momentum and the total negative momentum with respect to the center of the wavelet is equal.

$$\int_{-\infty}^{+\infty} \psi(x)dx = 0 \tag{11.13}$$

2. The energy of the continuous wavelet $\psi(x)$ is finite and bounded.

$$\int_{-\infty}^{+\infty} |\psi(x)|^2 dx < \infty \tag{11.14}$$

To control the magnitude and position of the continuous function $\psi(x)$, the dilation (scaling) and translation (shifting) properties of oscillating function is associated with wavelet as [52]

$$\psi_{a,b}(x) = \frac{1}{\sqrt{a}}\psi\left(\frac{x-b}{a}\right) \tag{11.15}$$

where a and b are the dilation and translation parameters, respectively. The dilation parameter a controls the scaling of the wavelet and the translation parameter b is used to control the positional shifting of the wavelet with respect to its center. The WM operation is associated with DE such that every particle element of the population will have a chance to mutate with a mutation probability $p_{\mathrm{m}} \in [0, 1]$. For each randomly selected particle element, if the mutation probability is less than or equal to p_{m}, the WM will take place. The selected pth particle and its jth element within the specified limits [$\mathrm{para}_{j\_\mathrm{min}}$, $\mathrm{para}_{j\_\mathrm{max}}$] will undergo the wavelet mutation process and the resulting particle for the ith iteration can be given as [52]

$$\overline{S}_j^p(i) = \begin{cases} S_j^p(i) + \sigma \times \left(\mathrm{para}_{j_{\max}} - S_j^p(i)\right), & \text{if } \sigma > 0 \\ S_j^p(i) + \sigma \times \left(S_j^p(i) - \mathrm{para}_{j_{\min}}\right), & \text{if } \sigma \le 0 \end{cases} \tag{11.16}$$

$$\text{where } \sigma = \psi_{a,0}(x) = \frac{1}{\sqrt{a}}\psi\left(\frac{x}{a}\right) \tag{11.17}$$

The mother wavelet is defined as [52]

$$\psi(x) = \mathrm{e}^{-x^2/2}\cos(5x) \tag{11.18}$$

$$\text{and, } \sigma = \frac{1}{\sqrt{a}} e^{-\left(\frac{x}{a}\right)^2/2} \cos\left(5\left(\frac{x}{a}\right)\right) \tag{11.19}$$

It is clear from Eq. (11.19) that if a increases, the wavelet will be scaled down and the value of σ will be smaller which also implies a smaller searching space with more fine tuning of a solution. This new mutation strategy is different from conventional mutation strategy of DM and a better global solution can be achieved with DEWM by controlling the dilation parameter a according to the following equation [52]

$$a = e^{-\ln(g)\times\left(1-\frac{i}{T}\right)^{\xi_{wm}}+\ln(g)} \tag{11.20}$$

where ξ_{wm} is a monotonically increasing function called shape parameter and g represents the upper limit of the dilation parameter a. The value of g is 10,000 and the dilation parameter a varies within 1 and 10,000. For the fine tuning of the solution, the dilation parameter also varies with i/T, where i is the current iteration, and T denotes the total number of iterations. It also ensures that as the number of iterations increase, the value of a also increases which eventually decreases the value of σ and the search space becomes smaller. In this way, finely tuned global solutions can be achieved with DEWM.

In this chapter, DEWM is used to optimize the various parameters of TMLA for different applications. Other familiar optimization techniques like PSO and RGA-based results are also presented along with DEWM-based results for comparison. A detailed discussion of PSO and RGA for solving electromagnetic problems can be found in [53, 54]. The best-proven values of control parameters for DEWM, PSO, and RGA are presented in Table 11.1.

Table 11.1 Best-proven control parameters of RGA, PSO, and DEWM obtained after several runs

Algorithms	Control parameters	Values
RGA	Size of population (n_p)	100
	Number of iterations (T)	300
	Rate of mutation (p_m)	0.01
	Rate of crossover (C_r)	0.8
	Probability of selection (p_s)	1/3
PSO	Size of population (n_p)	100
	Number of iterations (T)	300
	Weight of inertia (w_i)	0.5
	Acceleration constants (C_1, C_2)	2.05
DEWM	Size of population (n_p)	100
	Number of iterations (T)	300
	Rate of crossover (C_r)	0.25
	Shape parameter (ξ_{wm})	2.0
	Probability of mutation (p_m)	0.05

11.4 Results and Discussion

This section is devoted to the different applications of TMLA with distinct examples where the DEWM-based optimal numerical outcomes are presented and compared with PSO and RGA-based results. The adaptability of TMLA is explored by optimizing the parameters of the array. Sixteen-element TMLA structure is considered with a central frequency (f_0) of 3 GHz and a modulation frequency (f_p) of 1 GHz. The uniformly excited ($I_n = 1$) and evenly spaced ($d = 0.5\ \lambda$) array has the following properties: SLL = −13.15 dB, half power beamwidth (HPBW) = 6.48°, first null beamwidth (FNBW) = 14.4°, and directivity = 12.04 dB. All the numerical outcomes are obtained with MATLAB.

11.4.1 *Pattern Synthesis of TMLA Without SR Suppression*

Modulation of "Time" along with other control parameters such as amplitude, phase, and position of the array elements distinguishes the concept of "Time-modulation" from conventional methods of array synthesis. TMLAs can be implemented with periodical ON-OFF time sequences of array elements in a predefined manner. These time-domain antenna arrays are capable of achieving ultra-low sidelobe level (SLL), which is an important aspect of antenna design for modern-age applications. Two separate examples are presented in this section. The first example discusses the overall SLL reduction of a 16-element TMLA and the second one is concerned with the placement of broad nulls for a specific region.

11.4.1.1 SLL Reduction with Directivity Improvement

Suppression of SLL is an important issue in antenna array design. Low or ultra-low SLL is particularly important for point-to-point communication where a highly directed main beam or pencil beam is required. Ultra-low SLL with an improvement in directivity can be achieved by properly optimizing the switching sequences along with the spacing between array elements of TMLAs. To address this, a uniformly excited ($I_n = 1$) and evenly spaced 16-element TMLA is used. The total ON-time durations (τ_n) of each element and the spacing (d) between them are considered for optimization. The desired objective is cast into a minimization problem and the cost function (CF) is derived as

$$\mathrm{CF}_1 = w_1 * \left(\mathrm{SLL}_{\max}^{(i)}\right)\Big|_{f_0} + w_2 * (1/D_{\max}) \tag{11.21}$$

where the maximum level of sidelobe $\mathrm{SLL}_{\max}$ is calculated at central frequency f_0, i denotes the current iteration number, $D_{\max}$ is the maximum directivity of the central pattern, and w_1, w_2 are the equally weighted tuning parameters ($w_1 = w_2 = 1$). CF_1

is minimized with DEWM to get the optimal time sequence for the desired ultra-low SLL radiation pattern at the center frequency (f_0). The optimal switching sequence and the corresponding radiation patterns at f_0 and the first two positive harmonics ($f_0 + mf_{\mathrm{p}}$, $m = 1, 2$) with optimized element spacing of 0.8813 λ are shown in Figs. 11.3 and 11.4, respectively. The values obtained for SLL and directivity are improved to −43.29 and 12.4921 dB compared to −13.15 and 12.04 dB of uniform TMLA pattern. The HPBW and FNBW of the optimal pattern at f_0 are reported as 5.40° and 16.40°, respectively. PSO and RGA are also employed and the outcomes of these optimization techniques along with DEWM-based results are presented in Table 11.2 for a fair comparison. Although the sideband patterns ($f_0 + mf_{\mathrm{p}}$, $m = 1$, 2) are not considered for optimization in this example, the nature of first 20 positive sidebands are presented in Fig. 11.5. The nature of unoptimized SBLs will be helpful for comparative analysis in a later section where suppression of SRs is addressed. The percentage of total radiated power used in the desired pattern and the unwanted power wasted in higher sidebands are shown in Fig. 11.6. The convergence profiles are presented in Fig. 11.7 to show that the optimization processes of different algorithms are well converged.

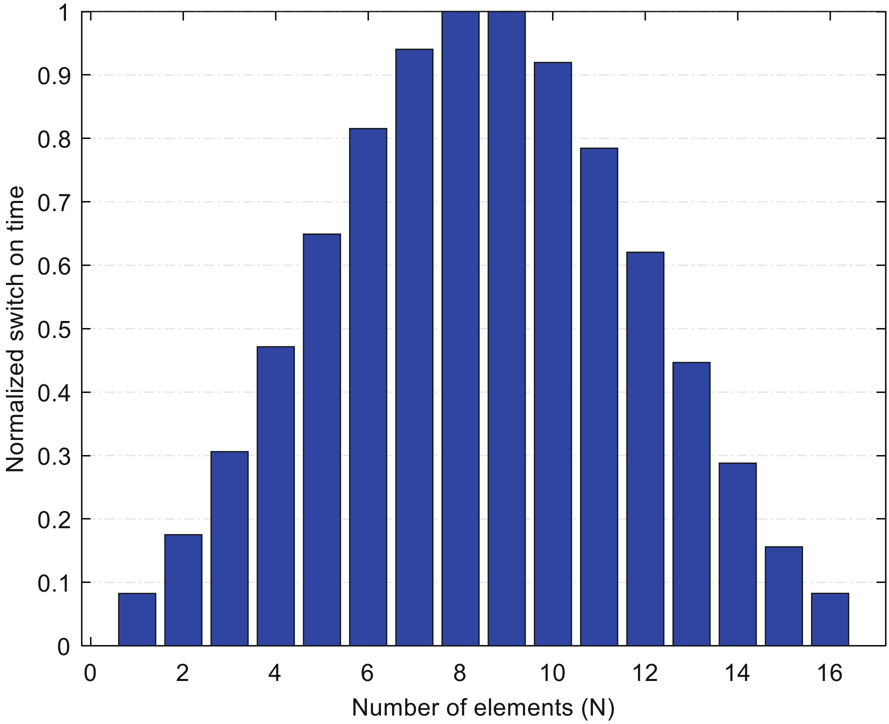

Fig. 11.3 Optimized ON-time sequence of 16-element TMLA for SLL reduction

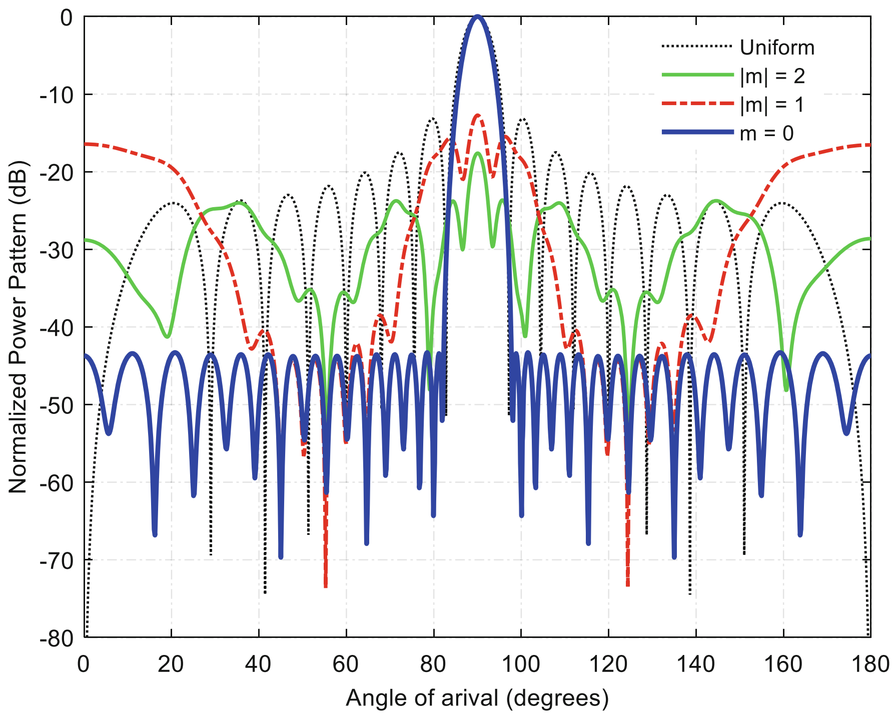

Fig. 11.4 Normalized power patterns for 16-element TMLA with optimal time sequence of Fig. 11.3

Table 11.2 Optimized results obtained with RGA, PSO, and DEWM for SLL reduction

Algorithms	SLL (dB)	SBL1 (dB)	SBL2 (dB)	FNBW (°)	Element spacing (λ)	Directivity (dB)
DEWM	−43.29	−12.72	−17.61	16.20	0.8813	12.4921
PSO	−38.43	−11.18	−15.72	14.76	0.8732	12.5608
RGA	−37.30	−12.46	−17.35	14.76	0.8682	12.6890

11.4.1.2 Broad Null Placement with SLL Reduction

This section discusses the possibility of placing broad nulls for a specific region as well as the reduction of SLL in all other regions of angle of arrival for a 16-element TMLA. Broad null placement is particularly useful in jamming environment where ultra-low SLLs are required for a particular region by rejecting all other interfering signals to establish a secure communication. The objectives of placing nulls for a specific region of 40°–70° and 110°–140° along with an overall reduction of the maximum SLL is cast into a minimization problem according to the following CF:

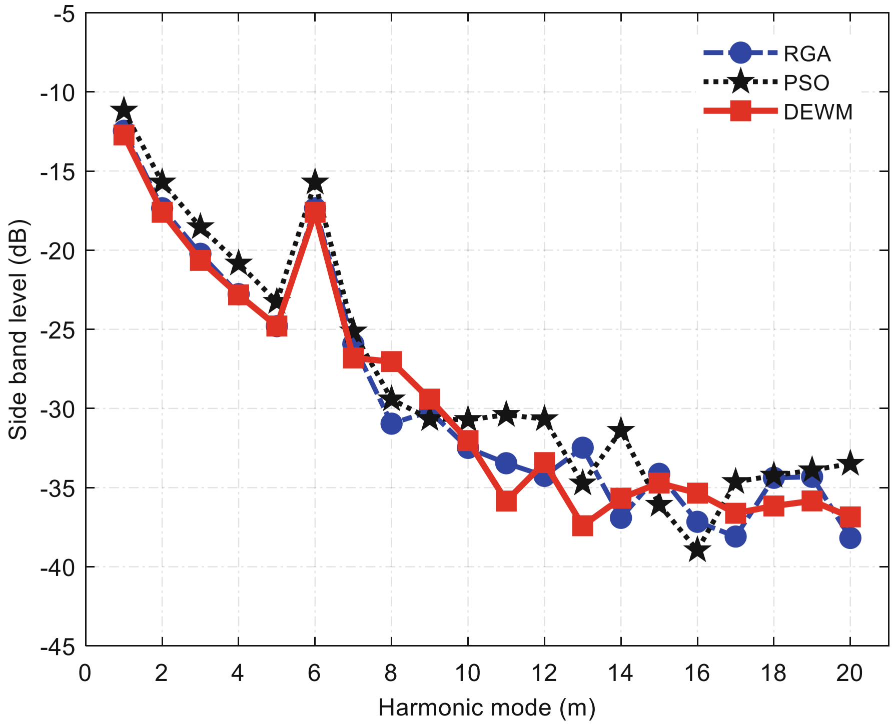

Fig. 11.5 Behavior of first 20 positive sideband patterns for 16-element TMLA

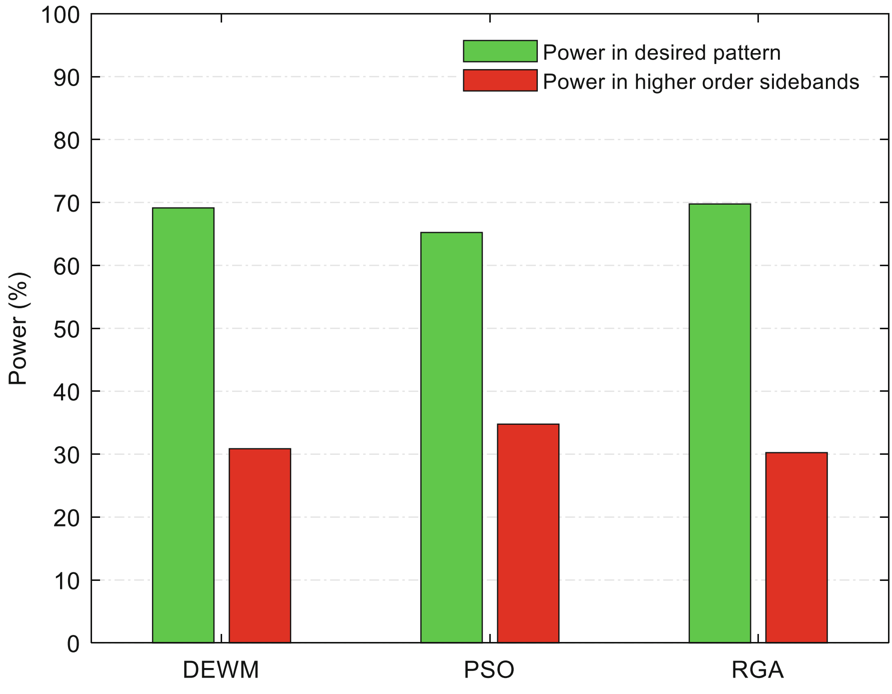

Fig. 11.6 Percentage of total radiated power for desired pattern and unwanted power at sidebands

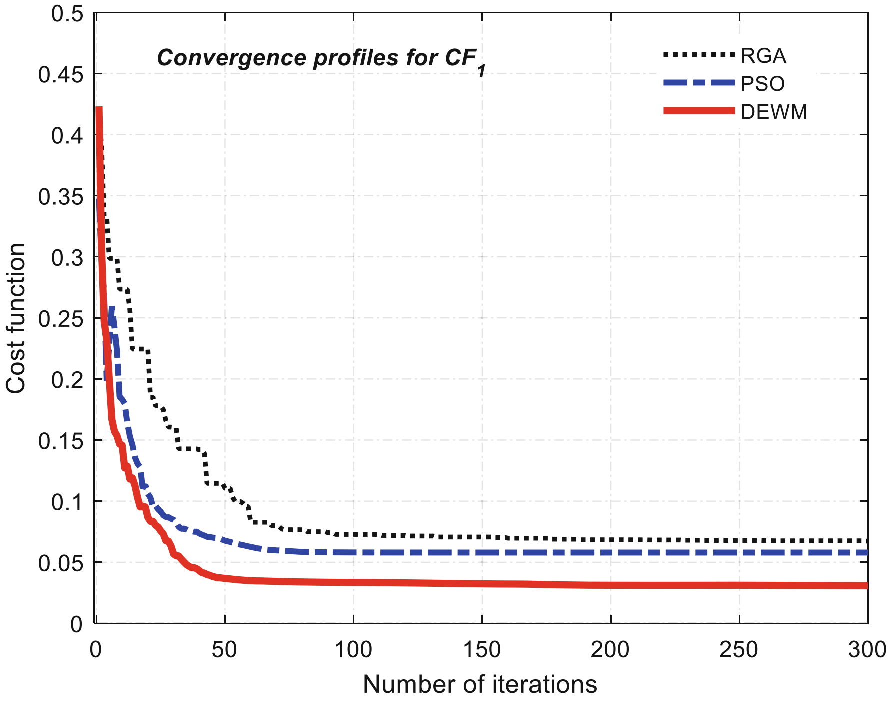

Fig. 11.7 Convergence profiles of RGA, PSO, and DEWM for CF_1

$$\mathrm{CF}_2 = w_1 * \left\{ \prod_{\theta=40^\circ}^{\theta=70^\circ} \left(\mathrm{SLL}^{(i)}_{\max\, l} \right) \right\} \Bigg|_{f_0} + w_2 * \left\{ \prod_{\theta=110^\circ}^{\theta=140^\circ} \left(\mathrm{SLL}^{(i)}_{\max\, r} \right) \right\} \Bigg|_{f_0} \tag{11.22}$$

The first term in CF_2 represents the maximum SLL for a specific region between 40° and 70° as well as the second term denotes the same for the region of 110°–140°. Tuning parameters of CF_2 are considered as equal ($w_1 = w_2 = 1$). DEWM-based optimized time sequence of each element and the normalized power patterns are shown in Figs. 11.8 and 11.9, respectively. Broad nulls are obtained for both the specified regions with a maximum SLL of −80.96 dB. An overall SLL of −25.72 dB as compared to the −13.15 dB SLL of the corresponding uniform pattern is achieved for the entire angle of arrival region apart from the specified regions. PSO and RGA-based results from an already published literature is compared with the DEWM-based results and the outcomes are summarized in Table 11.3. The convergence profile of DEWM for the minimization of CF_2 is presented in Fig. 11.10.

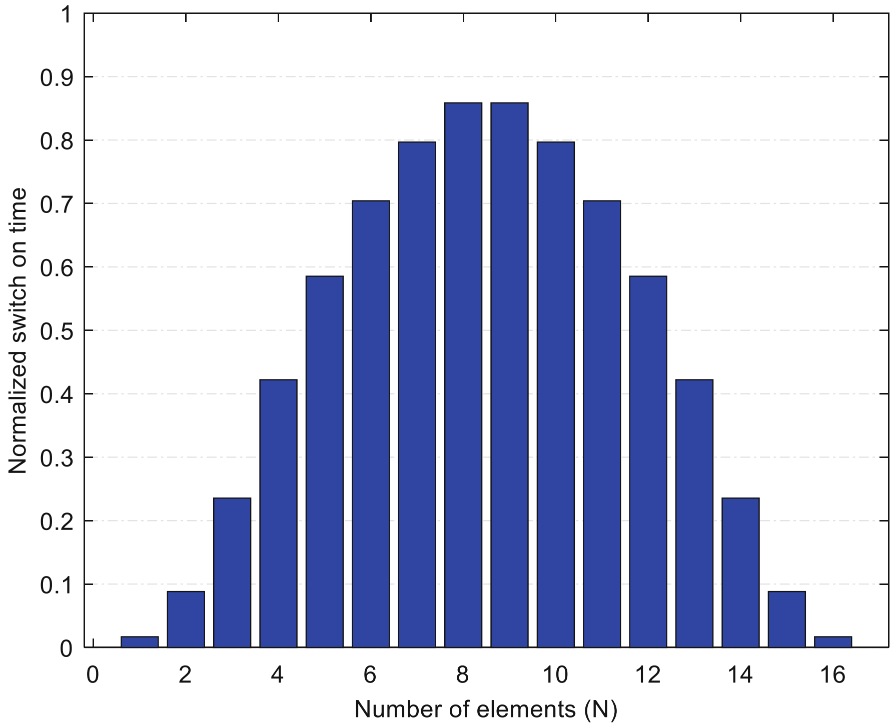

Fig. 11.8 Optimized ON-time sequence of 16-element TMLA for broad null placement

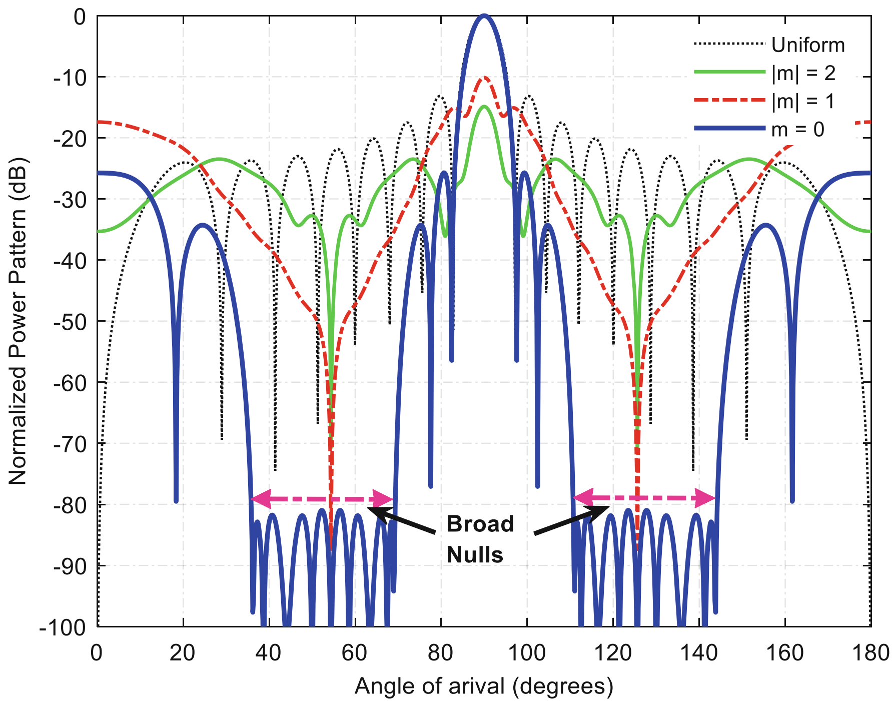

Fig. 11.9 Normalized power patterns of 16-element TMLA for broad nulls with reduced SLL

Table 11.3 Optimized results obtained with RGA, PSO, and DEWM for broad null placement

Algorithms	SLL in the region of 40°–70° and 110°–140° (dB)	SLL in the entire angle of arrival region (dB)	FNBW (°)	Element spacing (λ)	Directivity (dB)
DEWM	−80.96	−25.72	17.64	0.8588	11.9604
PSO [42]	−34.11	−15.89	NA	0.9252	11.5087
RGA [42]	−31.07	−14.06	NA	0.8595	10.0933

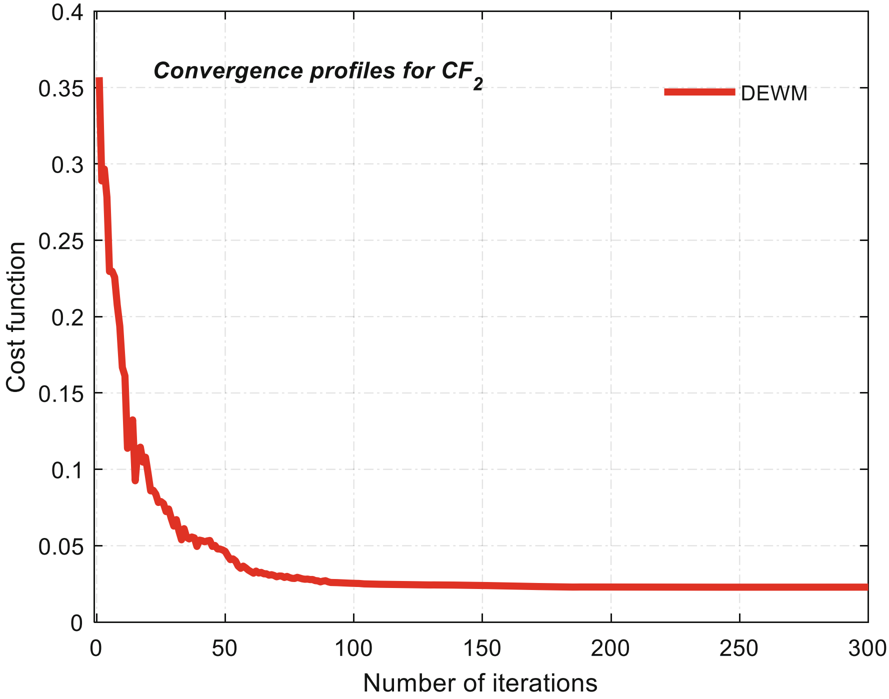

Fig. 11.10 Convergence profile of DEWM for CF_2

11.4.2 *Pattern Synthesis of TMLA with SR Suppression*

Sideband patterns are generated due to the periodic nature of switching sequences associated with "Time-modulation" and usually considered as a loss. Suppression of SRs can be achieved by lowering the SBLs of the harmonic patterns with pulse shifted switching sequences for efficient analysis of TMLAs. In this section, SRs and the SLL of a 16-element TMLA are suppressed along with enhanced directivity.

11.4.2.1 Simultaneous Suppression of SLL and SBLs

A simultaneous reduction of SLL and SBLs is performed by properly optimizing the excitations and the edge elements of the array. The desired radiation pattern can be generated by properly optimizing the ON-time instants and the total duration of ON-times of array elements. The ON-time durations of each element of TMLA are generally termed as pulses. Shifting of pulses within the modulation period gives additional control over the harmonic radiation patterns. The optimized excitation amplitudes along with pulse shifting of the edge elements are employed to achieve simultaneously suppressed SLL and SBLs with enhanced directivity. The CF to be minimized for this particular problem is designed as

$$\mathrm{CF}_3 = w_1 * \left(\mathrm{SLL}_{\max}^{(i)}\right)\Big|_{f_0} + w_2 * \left(\mathrm{SBL}_{\max}^{(i)}\right)\Big|_{f_0+mf_\mathrm{p}(m=1,2)} + w_3 * (1/D_{\max}) \tag{11.23}$$

where the maximum level of sidebands $\mathrm{SBL}_{\max}$ at first two harmonics are optimized along with equally weighted other parameters described in Eq. (11.21). DEWM is used to get the optimal solution for excitations, time sequences, and spacing between elements. The ON-time instants or the starting times of the pulse shifted sequence and the total ON-time durations of element number 1, 2, 15, and 16 (i.e., edge elements of the array) are considered for optimization. For the remaining elements (i.e., elements from 3 to 14), uniform time sequence is applied. The amplitude excitations for all the elements along with uniform spacing between them are also optimized to achieve the desired pattern. The optimized excitations, switching sequence, and the radiation patterns obtained are shown in Figs. 11.11, 11.12, and 11.13, respectively. A reduced SLL of −44.88 dB for the central pattern is achieved along with suppressed SBLs of −31.84 dB and −34.98 dB for the first two sidebands. The directivity is improved to 12.7945 dB from 12.04 dB of the corresponding uniform radiation pattern. The maximum level of sidebands for first 20 harmonic patterns are reported in Fig. 11.14, which shows that all the higher order SBLs are below the level of first SBL. A comparison between Figs. 11.5 and 11.13 can be drawn to show the improvements for SBL reduction. In Fig. 11.5, first two SBLs of −12.72 dB and −17.61 dB is reported as compared to the −31.84 dB and −34.98 dB SBLs of Fig. 11.13. PSO and RGA-based results along with the DEWM-based optimal results are summarized in Table 11.4. The convergence profiles are presented in Fig. 11.15.

11.4.3 Pattern Synthesis of TMLA with SR Exploitation

SR is generally considered an undesired aspect of TMLAs, but it can be exploited for specific applications as an advantage. Two separate examples are discussed in this section by exploiting the harmonic radiation patterns for advanced applications

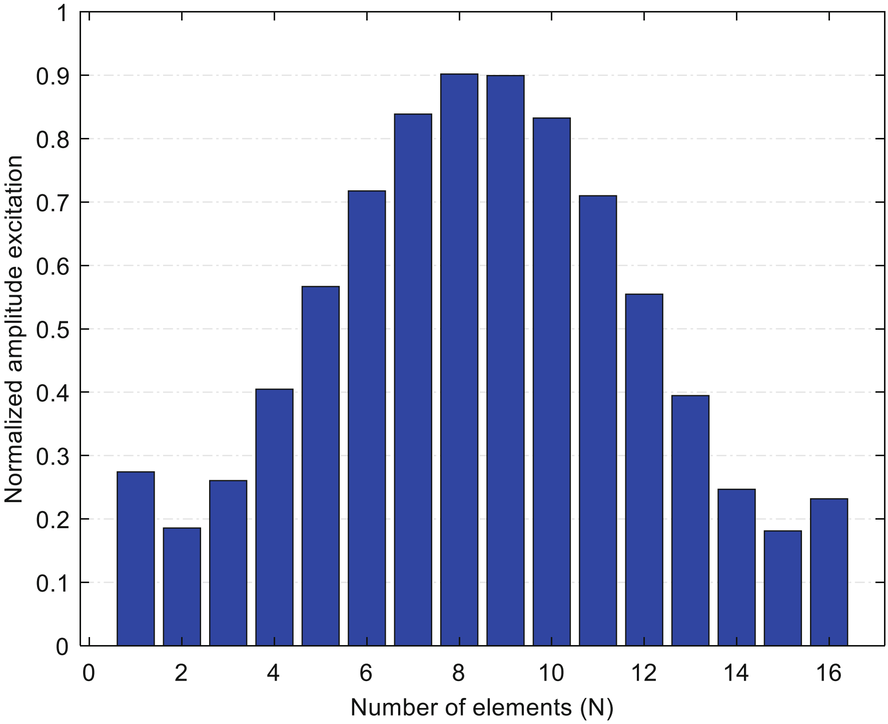

Fig. 11.11 Optimized excitations for the simultaneous suppression of SLL and SBLs

of TMLAs rather than suppressing it. The first example evaluates a simultaneous sum-difference pattern by profitably exploiting the first harmonic radiation pattern for monopulse antenna systems. The second example discusses the possibility of generating multiple steered patterns simultaneously by controlling the sideband patterns with optimized time sequences.

11.4.3.1 Simultaneous Sum and Difference Pattern Generation

Simultaneously generated sum and difference pattern at central frequency (f_0) and first sideband ($f_0 \pm f_p$) is discussed in this section. Simultaneous sum-difference patterns are useful for monopulse tracking systems [53] where a sum pattern and a squinted beam difference pattern are generated at the same time. By optimizing time sequences of each element, multiple patterns can be generated with TMLA. DEWM is used to optimize the switching sequence of 16-element TMLA in a way such that an equivalent in-phase and out-of-phase excitations for the first and the second half of the array elements can be generated. To achieve this, ON-time durations of the first half of the array is divided into two parts and shifted according to the optimized ON-time instants. For the rest half of the array, only pulse shifted

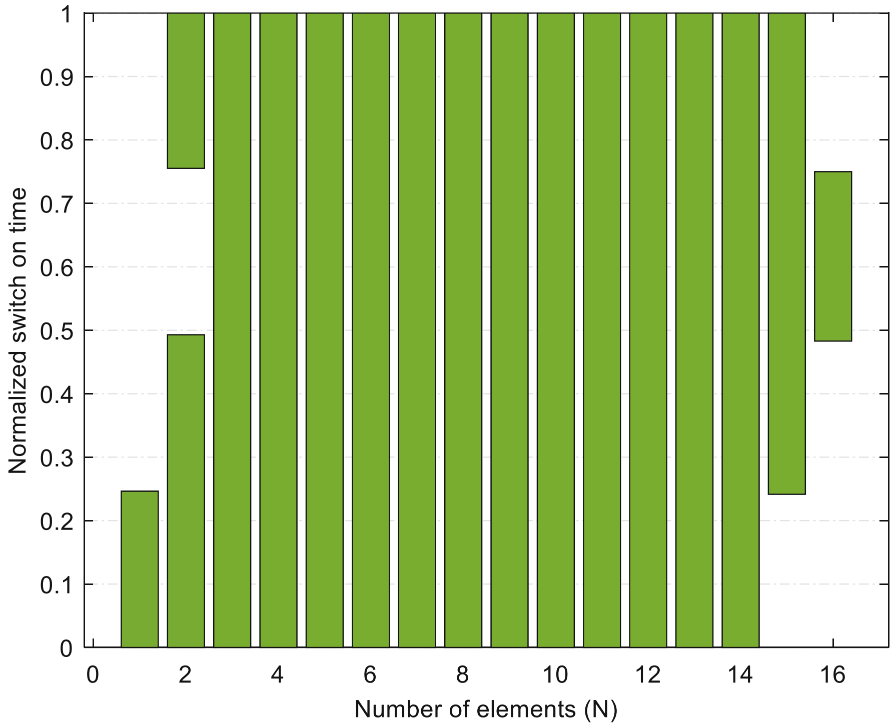

Fig. 11.12 Optimized pulse shifted ON-time sequence for SLL and SBL reduction

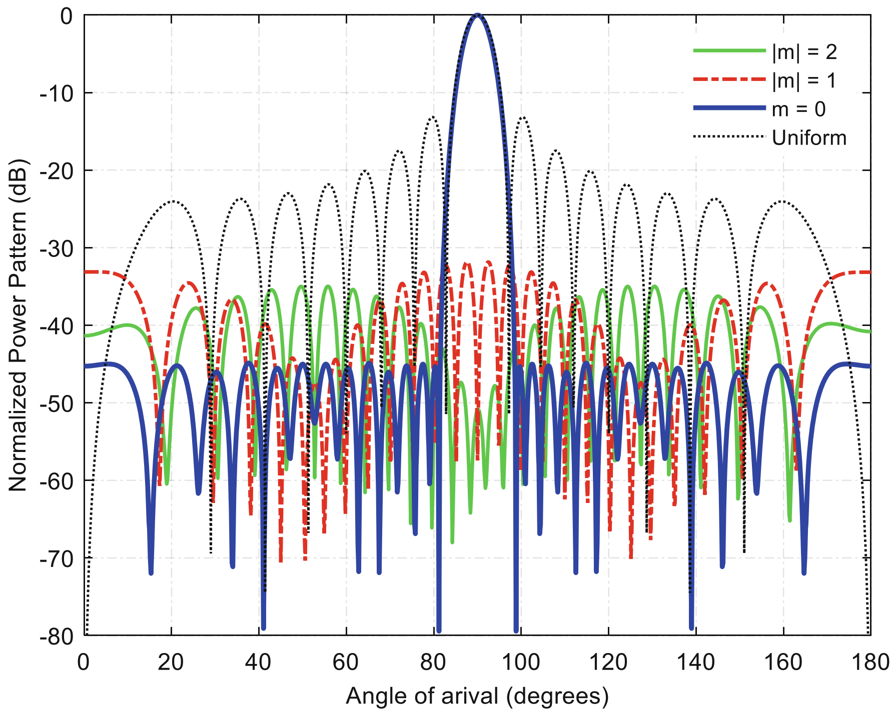

Fig. 11.13 Normalized power patterns of 16-element TMLA with reduced SLL and SBLs

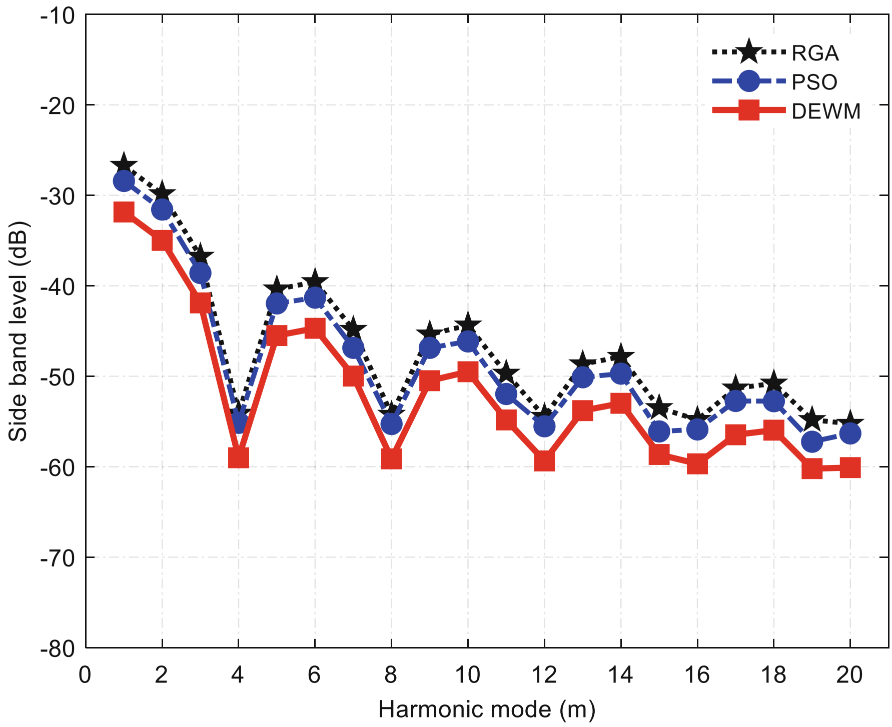

Fig. 11.14 Behavior of first 20 positive sideband patterns for 16-element TMLA

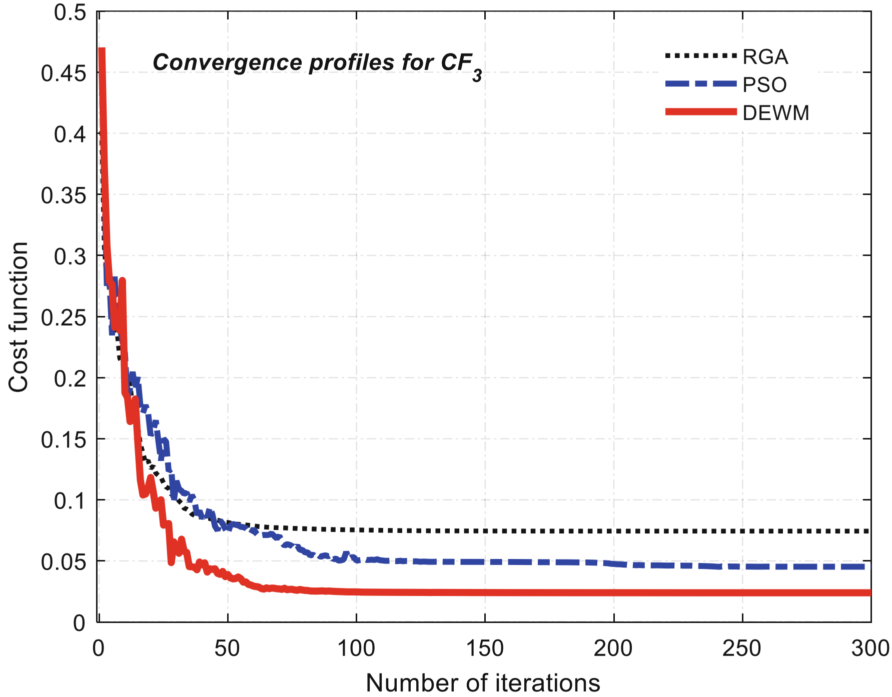

Fig. 11.15 Convergence profiles of RGA, PSO, and DEWM for CF_3

Table 11.4 Optimized results obtained with RGA, PSO, and DEWM for SLL and SBL reduction

Algorithms	SLL (dB)	SBL1 (dB)	SBL2 (dB)	FNBW (°)	Element spacing (λ)	Directivity (dB)
DEWM	−44.88	−31.84	−34.98	17.64	0.8253	12.7945
PSO	−38.45	−28.41	−31.57	15.48	0.8279	13.0722
RGA	−33.88	−26.72	−29.85	14.76	0.8153	13.1395

sequence is used. The array is considered to be uniformly excited ($I_n = 1$) and the spacing between elements is optimized. Reduction of SLLs for both the patterns are also considered as an important objective, and this multi-objective problem is addressed by designing a suitable CF as

$$\mathrm{CF}_4 = w_1 * \left(\mathrm{SLL}_{\max}^{(i)}\right)\Big|_{f_0} + w_2 * \left(\mathrm{SLL}_{\max}^{(i)}\right)\Big|_{f_0+mf_\mathrm{p}(|m|=1)} \tag{11.24}$$

In Eq. (11.24), SLLs at the central frequency as well as first sidebands are considered for minimization with equally weighted tuning parameters ($w_1 = w_2 = 1$).

The optimized time sequence and the normalized power patterns are shown in Figs. 11.16 and 11.17, respectively. An ultra-low SLL of −40.34 dB is achieved for the sum pattern (at f_0). The SBL (i.e., the peak level) of the difference pattern (at $f_0 \pm f_\mathrm{p}$) is obtained as −9.38 dB. The SLL of the difference pattern with respect to the peak level (SBL) is −21.84 dB. The HPBW and FNBW of the sum and difference patterns are 5.76°, 16.20°, and 4.14°, 9.18°, respectively. The behavior of first 20 SBLs are presented in Fig. 11.18. The percentage of power associated with central pattern, first sideband, and the unwanted power radiated at higher order sidebands are shown in Fig. 11.19. 77.9148% of the total radiated power is used for desired sum-difference pattern and 22.0852% power is radiated in higher order sidebands. PSO and RGA-based results along with optimal DEWM-based results are summarized in Table 11.5. The power associated with the desired pattern and the undesired power at higher order sidebands obtained with DEWM, PSO, and RGA are reported in Fig. 11.20. The convergence profiles are presented in Fig. 11.21.

11.4.3.2 Multi-harmonic Beam Steering

The potentialities of TMLAs are explored in this section with the exploitation of lower order harmonics for beam steering. The undesired SR at multiple harmonic frequencies can be exploited with suitably designed time schemes to get a steered beam pattern for multipoint communication [5]. Generally, progressive switching sequences are used to get a steered multi-harmonic pattern in TMLAs [55]. In this chapter, steered patterns at some prespecified direction are addressed. The desired objective is to generate steered patterns with ±30° shift from the broadside direction. The first negative ($f_0 - f_\mathrm{p}$) and the first positive ($f_0 + f_\mathrm{p}$) sidebands are optimized to get the desired steered patterns at 60° (−30° shift) and 120° (+30° shift) while the main beam at the center frequency (f_0) is pointed towards 90°. The

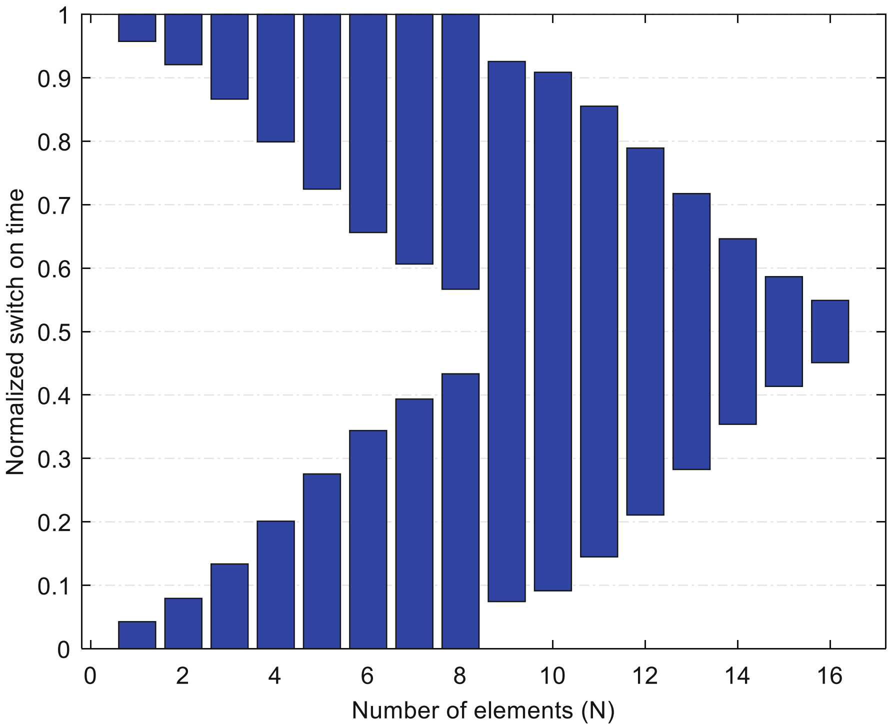

Fig. 11.16 Optimized ON-time durations for the simultaneous sum-difference pattern

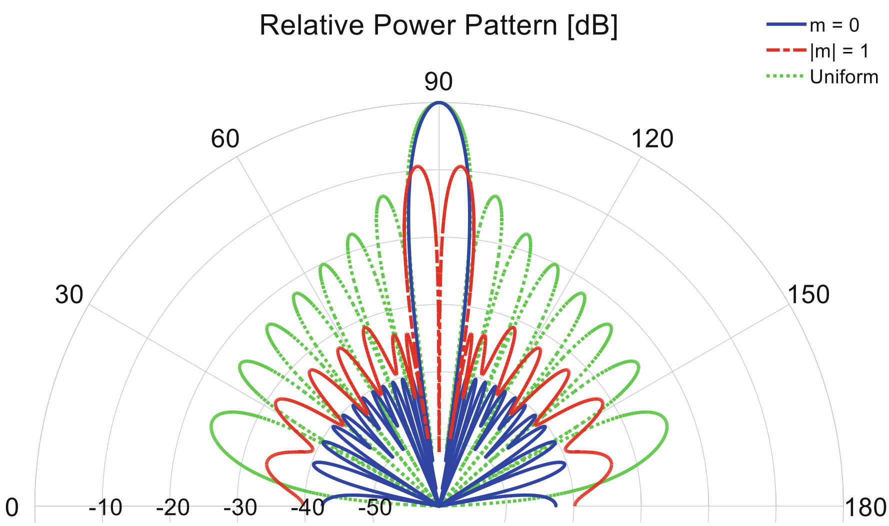

Fig. 11.17 Simultaneous sum-difference pattern using optimized time sequence of Fig. 11.16

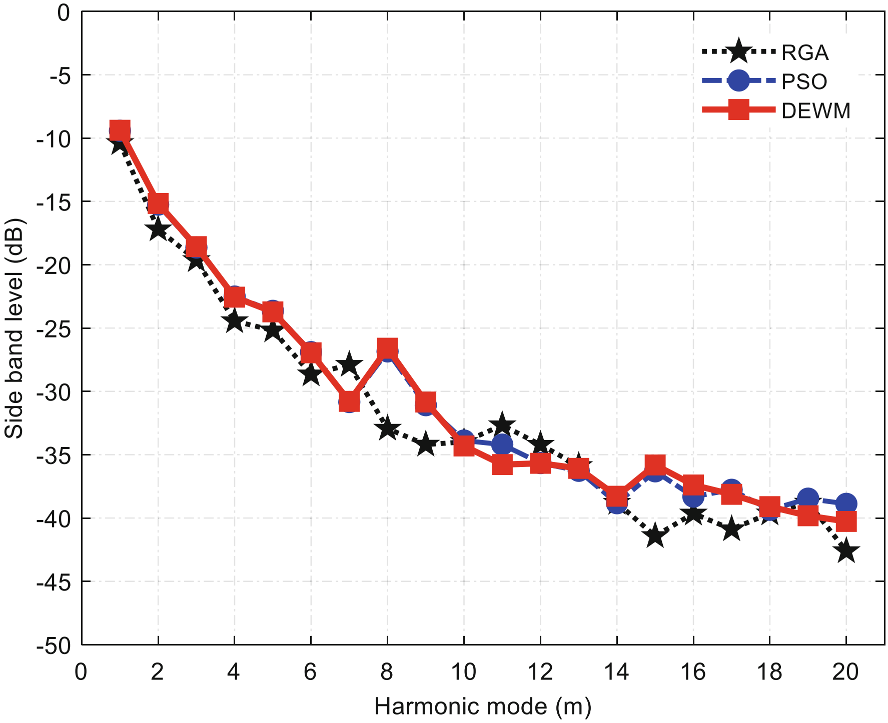

Fig. 11.18 Behavior of first 20 positive sideband patterns for 16-element TMLA

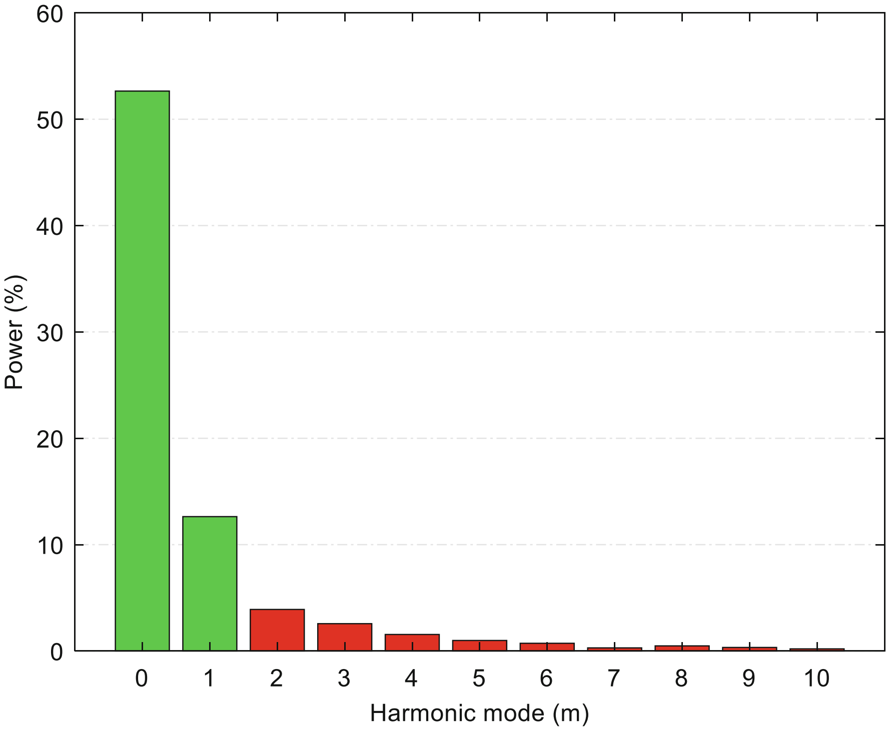

Fig. 11.19 Percentage of total radiated power for fundamental and harmonic patterns

pulse shifted sequence for beam steering at a specific direction can be calculated by combining Eqs. (11.5) and (11.12) as

$$\tau_n^1 = \left[\frac{(n-1)\,kd\cos\theta_0}{2\pi} - \frac{\tau_n}{2}\right] \bmod 1 \tag{11.25}$$

where τ_n^1 is the starting instants or the ON-time instants of each element, τ_n is the optimized ON-time durations, θ_0 is the predefined steering angle for sideband patterns, mod is the modulo operation to get the normalized starting instants of each pulse within the stipulated modulation period.

Multiple objectives such as reduction of SLLs for the central and the sideband patterns along with the steering of first sideband patterns are considered for optimization by designing the CF as

$$\mathrm{CF}_5 = w_1 * \left(\mathrm{SLL}_{\max}^{(i)}\right)\Big|_{f_0} + w_2 * \left(\mathrm{SLL}_{\max}^{(i)}\right)\Big|_{f_0 \pm f_\mathrm{p}} \tag{11.26}$$

Uniformly excited ($I_n = 1$) and evenly spaced ($d = 0.5\ \lambda$) 16-element TMLA is optimized with DEWM to get the optimal switching sequence for multi-harmonic steered patterns with reduced SLLs. The optimal time sequence and the normalized power patterns obtained are shown in Figs. 11.22 and 11.23, respectively. The pattern at the central frequency has achieved a low SLL of −39.86 dB. The SBLs for both the first sidebands ($|m| = 1$) are reported as −9.90 dB and the SLLs of −25.63 dB is achieved for the steered patterns with respect to the peak level of the corresponding pattern (i.e., SBL). 73.1592% of the total radiated power is used to generate the desired patterns and 26.8408% power is radiated in higher order sidebands. The power associated with the central pattern, first positive sideband, and first negative sideband are 31.0972%, 23.0310%, and 23.0310% of the total power, shown in Fig. 11.24. DEWM, PSO, and RGA-based results are summarized in Table 11.6. The power associated with the desired pattern and the power at higher order sidebands obtained with DEWM, PSO, and RGA are shown in Fig. 11.25. The convergence profiles for all optimization processes are presented in Fig. 11.26.

11.5 Conclusion

A "Time-domain" approach of antenna array design is addressed in this chapter. The applicability of time-modulated linear arrays (TMLAs) for advanced communication applications are discussed with several examples. A wavelet mutation-based differential evolution (DEWM) algorithm is used to optimize different parameters of 16-element TMLA for desired solutions. Towards this aim, distinct approaches are developed to address the multiple objectives by appropriately designed cost functions (CFs). Particle swarm optimization (PSO) and real-coded genetic algorithm (RGA) are also employed for all the problems, and the results are compared

Table 11.5 Optimized results obtained with RGA, PSO, and DEWM for sum-difference pattern

Algorithms	SLL_{f0} (dB)	$SBL_{f0 \pm fp}$ (dB)	$SLL_{f0 \pm fp}$ (dB)	$FNBW_{f0}$ (°)	Element spacing (λ)	$P_{desired}$ (%)	$P_{undesired}$ (%)
DEWM	−40.34	−9.38	−21.84	16.20	0.8169	77.9148	22.0852
PSO	−39.50	−9.42	−22.35	16.56	0.8135	78.2729	21.7271
RGA	−37.81	−10.39	−15.09	15.48	0.8263	81.2289	18.7711

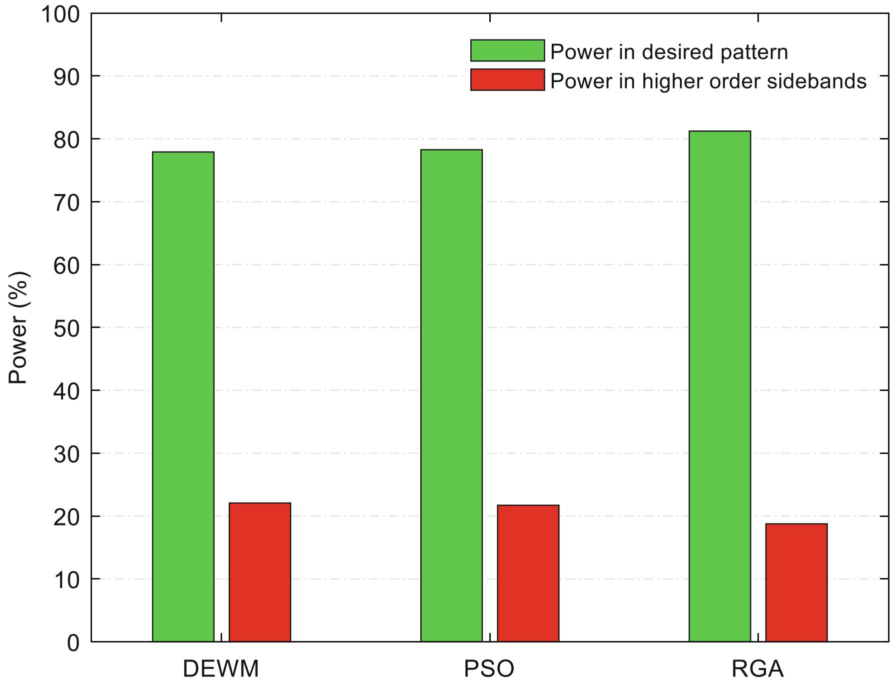

Fig. 11.20 Percentage of total radiated power for desired pattern and unwanted power at sidebands

Table 11.6 Optimized results obtained with RGA, PSO, and DEWM for harmonic beam steering

Algorithms	SLL_{f0} (dB)	$SBL_{f0 \pm fp}$ (dB)	$SLL_{f0 \pm fp}$ (dB)	P_{f0} (%)	$P_{f0 \pm fp}$ (%)	$P_{desired}$ (%)	$P_{undesired}$ (%)
DEWM	−39.86	−1.44	−25.63	31.0972	21.0310	73.1592	26.8408
PSO	−38.99	−1.45	−25.44	31.1263	21.0406	73.2075	26.7925
RGA	−37.31	−1.41	−25.17	30.7621	21.0107	72.7835	27.2165

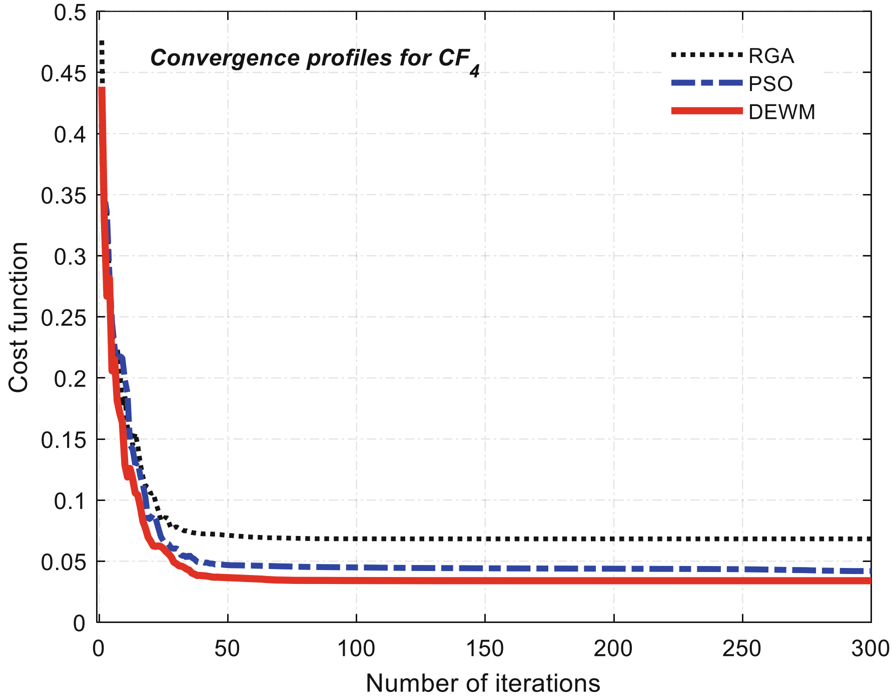

Fig. 11.21 Convergence profiles of RGA, PSO, and DEWM for CF_4

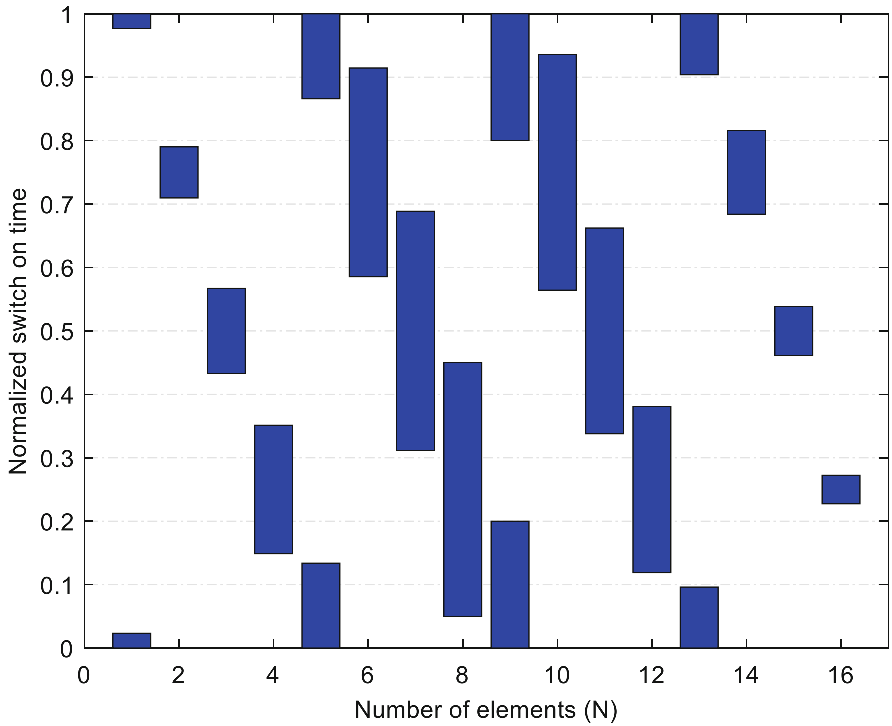

Fig. 11.22 Optimized ON-time durations for multi-harmonic beam steering

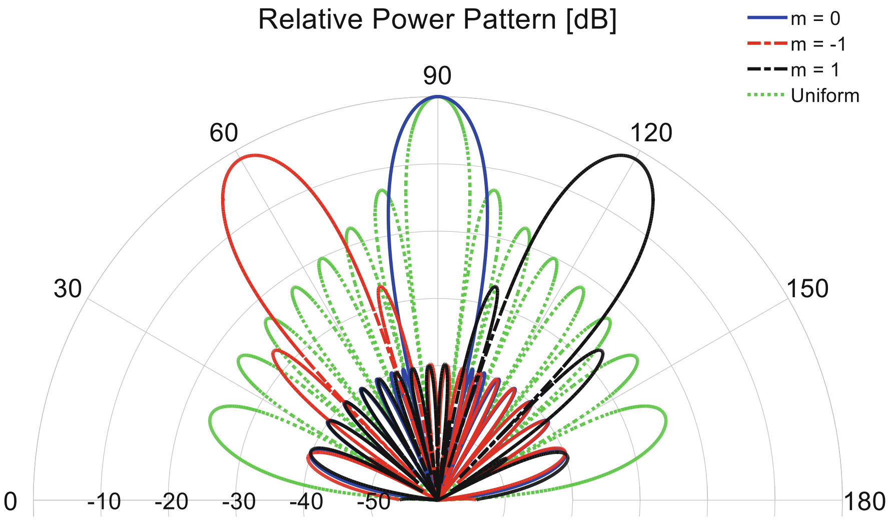

Fig. 11.23 Multi-harmonic beam steered patterns with optimized time sequence of Fig. 11.22

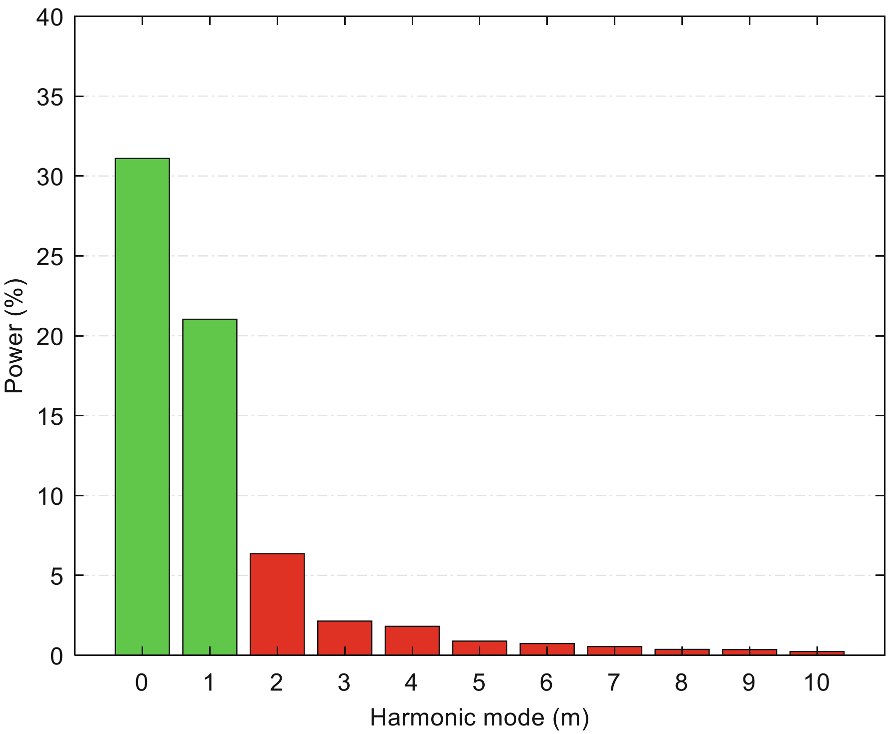

Fig. 11.24 Percentage of total radiated power for fundamental and harmonic patterns

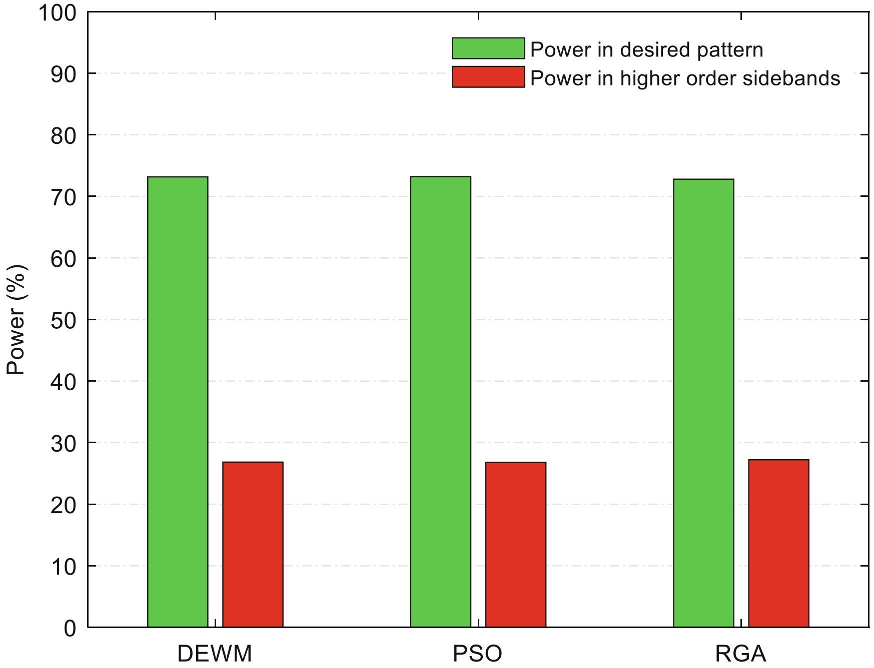

Fig. 11.25 Percentage of total radiated power for desired pattern and unwanted power at sidebands

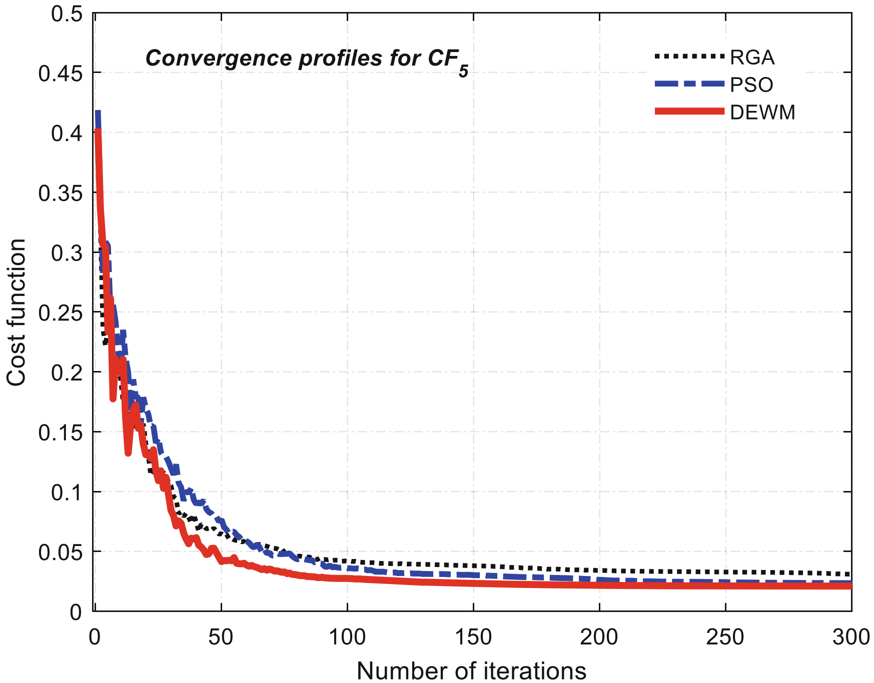

Fig. 11.26 Convergence profiles of RGA, PSO, and DEWM for CF_5

with DEWM-based results. Different examples like sidelobe level (SLL) reduction and placing broad nulls for interference rejection, efficient analysis of TMLAs with simultaneously suppressed SLL and sideband radiations (SRs) are briefly discussed with proposed methods to explore the potentialities of TMLAs. Simultaneously generated multiple beams such as the sum pattern and the difference pattern with reduced SLL is achieved which is beneficial for monopulse tracking radar systems. The feasibility of TMLAs is further enhanced with harmonic beamforming where lower order sidebands are steered to a predefined direction. Beam steering with low SLL and highly directed main beam is achieved which also implies that the TMLAs can be designed for multipoint communication systems. For all these examples, switching schemes of TMLAs along with other control parameters are optimized and multiple objectives are addressed with suitably designed CFs. In this way, the fourth dimension—"Time" is explored as an efficient control parameter for pattern synthesis of antenna arrays to make it more adaptable and reconfigurable with smart design approach.

Acknowledgments The research works carried out in this chapter was financially supported by the Science and Engineering Research Board (SERB), Department of Science and Technology (DST), Government of India (GoI), under grant no. EEQ/2017/000519 dated 23rd March 2018.

References

1. R.L. Haupt, Antenna arrays in the time domain: An introduction to timed arrays. IEEE Antennas Propag. Mag. (2017). https://doi.org/10.1109/MAP.2017.2686082
2. G. Franceschetti, J. Tatoian, G. Gibbs, Timed arrays in a nutshell. IEEE Trans. Antennas Propag. (2005). https://doi.org/10.1109/TAP.2005.859765
3. C. He, L. Wang, J. Chen, R. Jin, Time-modulated arrays: A four-dimensional antenna array controlled by switches. J. Commun. Inf. Netw. (2018). https://doi.org/10.1007/s41650-018-0004-7
4. P. Rocca, G. Oliveri, R.J. Mailloux, A. Massa, Unconventional phased array architectures and design methodologies—A review. Proc. IEEE (2016). https://doi.org/10.1109/JPROC.2015.2512389
5. R. Maneiro-Catoira, J. Brégains, J.A. García-Naya, L. Castedo, Time modulated arrays: From their origin to their utilization in wireless communication systems. Sensors (Switzerland) (2017). https://doi.org/10.3390/s17030590
6. P. Rocca, F. Yang, L. Poli, S. Yang, Time-modulated array antennas—Theory, techniques, and applications. J. Electromagn. Waves Appl. (2019). https://doi.org/10.1080/09205071.2019.1627251
7. H.E. Shanks, R.W. Bickmore, Four-dimensional electromagnetic radiators. Can. J. Phys. (1959). https://doi.org/10.1139/p59-031
8. H.E. Shanks, A new technique for electronic scanning. IRE Trans. Antennas Propag. (1961). https://doi.org/10.1109/TAP.1961.1144965
9. W.H. Kummer, A.T. Villeneuve, T.S. Fong, F.G. Terrio, Ultra-low sidelobes from time-modulated arrays. IEEE Trans. Antennas Propag. (1963). https://doi.org/10.1109/TAP.1963.1138102
10. S. Yang, Y.B. Gan, A. Qing, Sideband suppression in time-modulated linear arrays by the differential evolution algorithm. IEEE Antennas Wirel. Propag. Lett. (2002). https://doi.org/10.1109/LAWP.2002.807789

11. S. Yang, Y.B. Gan, P.K. Tan, A new technique for power-pattern synthesis in time-modulated linear arrays. IEEE Antennas Wirel. Propag. Lett. (2003). https://doi.org/10.1109/LAWP.2003.821556
12. S. Yang, Y.B. Gan, A. Qing, P.K. Tan, Design of a uniform amplitude time modulated linear array with optimized time sequences. IEEE Trans. Antennas Propag. (2005). https://doi.org/10.1109/TAP.2005.850765
13. L. Poli, P. Rocca, L. Manica, A. Massa, Handling sideband radiations in time-modulated arrays through particle swarm optimization. IEEE Trans. Antennas Propag. (2010). https://doi.org/10.1109/TAP.2010.2041165
14. S. Yang, Y.B. Gan, P.K. Tan, Evaluation of directivity and gain for time-modulated linear antenna arrays. Microw. Opt. Technol. Lett. (2004). https://doi.org/10.1002/mop.20241
15. J.C. Brégains, J. Fondevila-Gómez, G. Franceschetti, F. Ares, Signal radiation and power losses of time-modulated arrays. IEEE Trans. Antennas Propag. (2008). https://doi.org/10.1109/TAP.2008.923345
16. J. Fondevila, J.C. Brégains, F. Ares, E. Moreno, Optimizing uniformly excited linear arrays through time modulation. IEEE Antennas Wirel. Propag. Lett. (2004). https://doi.org/10.1109/LAWP.2004.838833
17. L. Poli, P. Rocca, L. Manica, A. Massa, Pattern synthesis in time-modulated linear arrays through pulse shifting. IET Microw. Antennas Propag. (2010). https://doi.org/10.1049/iet-map.2009.0042
18. L. Poli, P. Rocca, L. Manica, A. Massa, Time modulated planar arrays - Analysis and optimisation of the sideband radiations. IET Microw. Antennas Propag. (2010). https://doi.org/10.1049/iet-map.2009.0379
19. L. Poli, P. Rocca, A. Massa, Sideband radiation reduction exploiting pattern multiplication in directive time-modulated linear arrays. IET Microw. Antennas Propag. (2012). https://doi.org/10.1049/iet-map.2011.0159
20. E. Aksoy, E. Afacan, Thinned nonuniform amplitude time-modulated linear arrays. IEEE Antennas Wirel. Propag. Lett. (2010). https://doi.org/10.1109/LAWP.2010.2051312
21. S. Yang, Y.B. Can, P.K. Tan, Comparative study of low sidelobe time modulated linear arrays with different time schemes. J. Electromagn. Waves Appl. (2004). https://doi.org/10.1163/1569393042954910
22. S.W. Yang, Y.K. Chen, Z.P. Nie, Simulation of time modulated linear antenna arrays using the FDTD method. Prog. Electromagn. Res. (2009). https://doi.org/10.2528/PIER09092507
23. E. Aksoy, E. Afacan, Calculation of sideband power radiation in time-modulated arrays with asymmetrically positioned pulses. IEEE Antennas Wirel. Propag. Lett. (2012). https://doi.org/10.1109/LAWP.2012.2185916
24. Q. Zhu, S. Yang, L. Zheng, Z. Nie, Design of a low sidelobe time modulated linear array with uniform amplitude and sub-sectional optimized time steps. IEEE Trans. Antennas Propag. (2012). https://doi.org/10.1109/TAP.2012.2207082
25. A. Chakraborty, G. Ram, D. Mandal, Optimal pulse shifting in timed antenna array for simultaneous reduction of sidelobe and sideband level. IEEE Access (2020). https://doi.org/10.1109/ACCESS.2020.3010047
26. A. Tennant, B. Chambers, A two-element time-modulated array with direction-finding properties. IEEE Antennas Wirel. Propag. Lett. (2007). https://doi.org/10.1109/LAWP.2007.891953
27. J. Fondevila, J.C. Brégains, F. Ares, E. Moreno, Application of time modulation in the synthesis of sum and difference patterns by using linear arrays. Microw. Opt. Technol. Lett. (2006). https://doi.org/10.1002/mop.21489
28. S. Yang, Y. Chen, Z. Nie, Multiple patterns from time-modulated linear antenna arrays. Electromagnetics (2008). https://doi.org/10.1080/02726340802428671
29. G. Li, S. Yang, Y. Chen, Z. Nie, A novel electronic beam steering technique in time modulated antenna arrays. Prog. Electromagn. Res. (2009). https://doi.org/10.2528/PIER09072602
30. Y. Tong, A. Tennant, Simultaneous control of sidelobe level and harmonic beam steering in time-modulated linear arrays. Electron. Lett. (2010). https://doi.org/10.1049/el.2010.2629

31. L. Poli, P. Rocca, G. Oliveri, A. Massa, Harmonic beamforming in time-modulated linear arrays. IEEE Trans. Antennas Propag. (2011). https://doi.org/10.1109/TAP.2011.2152323
32. Y. Tong, A. Tennant, A two-channel time modulated linear array with adaptive beamforming. IEEE Trans. Antennas Propag. (2012). https://doi.org/10.1109/TAP.2011.2167936
33. C. He, X. Liang, Z. Li, J. Geng, R. Jin, Direction finding by time-modulated array with harmonic characteristic analysis. IEEE Antennas Wirel. Propag. Lett. (2015). https://doi.org/10.1109/LAWP.2014.2373432
34. D. Ni, S. Yang, Z. Nie, Efficient synthesis of irregularly shaped radiation patterns based on four-dimensional planar arrays and post-processing. Electromagnetics (2015). https://doi.org/10.1080/02726343.2015.1084570
35. A. Reyna, M.A. Panduro, Synthesis of timed antenna arrays for flat-top energy patterns. IETE Tech. Rev. (Institution Electron Telecommun Eng India) (2017). https://doi.org/10.1080/02564602.2016.1141666
36. P. Rocca, L. Manica, L. Poli, A. Massa, Synthesis of compromise sum-difference arrays through time-modulation. IET Radar Sonar Navig. (2009). https://doi.org/10.1049/iet-rsn.2009.0058
37. P. Rocca, L. Poli, G. Oliveri, A. Massa, Synthesis of sub-arrayed time modulated linear arrays through a multi-stage approach. IEEE Trans. Antennas Propag. (2011). https://doi.org/10.1109/TAP.2011.2161535
38. Y. Chen, S. Yang, G. Li, Z. Nie, Adaptive nulling with time-modulated antenna arrays using a hybrid differential evolution strategy. Electromagnetics (2010). https://doi.org/10.1080/02726343.2010.513931
39. L. Poli, P. Rocca, G. Oliveri, A. Massa, Adaptive nulling in time-modulated linear arrays with minimum power losses. IET Microw. Antennas Propag. (2011). https://doi.org/10.1049/iet-map.2010.0015
40. P. Rocca, L. Poli, G. Oliveri, A. Massa, Adaptive nulling in time-varying scenarios through time-modulated linear arrays. IEEE Antennas Wirel. Propag. Lett. (2012). https://doi.org/10.1109/LAWP.2012.2183849
41. L. Zheng, S. Yang, Z. Nie, Pattern synthesis with specified broad nulls in time-modulated circular antenna arrays. Electromagnetics (2011). https://doi.org/10.1080/02726343.2011.579770
42. G. Ram, M.A. Panduro, A. Reyna, R. Kar, D. Mandal, Pattern synthesis and broad nulling optimization of STMLAA with EM simulation. Int. J. Numer. Model Electron. Netw. Devices Fields (2018). https://doi.org/10.1002/jnm.2322
43. G. Ram, D. Mandal, M.A. Panduro, R. Kar, Z. Raida, Optimal design of timed antenna arrays for SLL reduction, dual and multiple broad nulls in the radiation pattern. IETE Tech. Rev. (Institution Electron Telecommun Eng India) (2020). https://doi.org/10.1080/02564602.2019.1699453
44. L. Poli, P. Rocca, G. Oliveri, et al., Advanced pulse sequence design in time-modulated arrays for cognitive radio. IEEE Antennas Wirel. Propag. Lett. (2018). https://doi.org/10.1109/LAWP.2018.2821715
45. G. Li, S. Yang, Z. Nie, A study on the application of time modulated antenna arrays to airborne pulsed Doppler radar. IEEE Trans. Antennas Propag. (2009). https://doi.org/10.1109/TAP.2009.2016788
46. G. Ram, D. Mandal, R. Kar, S.P. Ghoshal, Pencil beam pattern synthesis of time-modulated concentric circular antenna array using PSO with aging leader and challenger. J Electromagn. Waves Appl. (2015). https://doi.org/10.1080/09205071.2015.1054955
47. G. Ram, D. Mandal, S.P. Ghoshal, R. Kar, Optimization of radiation characteristic of time modulated circular geometry using DEWM. Sci. Iran (2018). https://doi.org/10.24200/sci.2017.4372
48. G. Ram, D. Mandal, R. Kar, S.P. Ghoshal, Radiation performance characteristic optimization of time-modulated circular antenna arrays. IETE Tech. Rev. (2017). https://doi.org/10.1080/02564602.2016.1271729
49. G. Ram, D. Mandal, R. Kar, S.P. Ghoshal, Cat swarm optimization as applied to time-modulated concentric circular antenna array: Analysis and comparison with other stochas-

tic optimization methods. IEEE Trans. Antennas Propag. (2015). https://doi.org/10.1109/TAP.2015.2444439
50. A. Das, D. Mandal, R. Kar, An optimal far-field radiation pattern synthesis of time-modulated linear and concentric circular antenna array. Int. J. Numer. Model Electron. Netw. Devices Fields (2019). https://doi.org/10.1002/jnm.2658
51. P. Rocca, G. Oliveri, A. Massa, Differential evolution as applied to electromagnetics. IEEE Antennas Propag. Mag. (2011). https://doi.org/10.1109/MAP.2011.5773566
52. S.H. Ling, H.H.C. Iu, F.H.F. Leung, K.Y. Chan, Improved hybrid particle swarm optimized wavelet neural network for modeling the development of fluid dispensing for electronic packaging. IEEE Trans. Ind. Electron. (2008). https://doi.org/10.1109/TIE.2008.922599
53. J. Robinson, Y. Rahmat-Samii, Particle swarm optimization in electromagnetics. IEEE Trans. Antennas Propag. (2004). https://doi.org/10.1109/TAP.2004.823969
54. D.S. Weile, E. Michielssen, Genetic algorithm optimization applied to electromagnetics: A review. IEEE Trans. Antennas Propag. (1997). https://doi.org/10.1109/8.558650
55. A. Chakraborty, D. Mandal, G. Ram, Beam steering in a time switched antenna array with reduced side lobe level using evolutionary optimization technique, in *2019 IEEE Indian Conference on Antennas and Propagation, InCAP 2019*, (2019). https://doi.org/10.1109/InCAP47789.2019.9134497

Avishek Chakrabortypassed his B. Tech degree in Electronics and Communication Engineering. He received his M. Tech degree in Radio Physics and Electronics with a specialization in Space Science and Microwaves from the University of Calcutta, West Bengal, India, in 2017. He is presently working as a project fellow in a DST-SERB-funded project at the National Institute of Technology, Durgapur, West Bengal, India. He is also pursuing Ph.D degree as a full-time Research Scholar in the Department of Electronics and Communication Engineering, National Institute of Technology, Durgapur. His current research interests include antenna array synthesis, application of soft computing in antenna array optimization, and radar signal processing.

Gopi Ram passed B.E. Degree in "Electronics and Telecommunication Engineering," from Government Engineering College, Jagdalpur, Chhattisgarh, India in the year 2007. He received M. Tech degree in "Telecommunication Engineering" from National Institute of Technology, Durgapur, West Bengal, India, in the year 2011. He joined as a full-time institute research scholar in the year 2012 at National Institute of Technology, Durgapur to carry out research for Ph.D degree. He received the scholarship from the Ministry of Human Resource and Development (MHRD), Government of India for the period 2009–2011 (M. Tech) and 2012–2015 (Ph.D). His research interest includes analysis and synthesis of antenna array via bio-inspired evolutionary Algorithm, antenna array optimization of various radiation characteristics. He has published more than 50 research papers in International Journals and Conferences.

Durbadal Mandal passed B.E. degree in Electronics and Communication Engineering, from Regional Engineering College, Durgapur, West Bengal, India, in the year 1996. He received the M.Tech and Ph.D degrees from National Institute of Technology, Durgapur, West Bengal, India, in the years 2008 and 2011, respectively. Presently, he is attached with National Institute of Technology, Durgapur, West Bengal, India, as Assistant Professor in the Department of Electronics and Communication Engineering. His research interest includes Array Antenna design; filter Optimization via Evolutionary Computing Techniques. He has published more than 300 research papers in International Journals and Conferences.

Chapter 12
Wireless Power Transfer for Implantable and Wearable Medical Devices

Mohammad Haerinia, Reem Shadid, and Sima Noghanian

12.1 Introduction

With the growth of biotechnology and materials, the biomedical implantable industry devices are improved. For instance, in the USA, 8–10% of people deal with implantable medical devices. Practically, there are two main ways to provide power for implantable medical devices. The common method is to provide the devices with implantable batteries to be used as a power supply. For implantable batteries, their lifetime, size, and toxic composition would lead to potential hazards to patients. WPT is an alternative way that overcomes the energy storage problem and supplies power for the implanted device through the skin and body tissues.

As rapid growth in wearable and implanted sensors, low power integrated circuits and wireless communications have enabled the use of biomedical electronic sensors. Typically, these sensors can be used to monitor and deliver the healthcare information of a human body. Accordingly, WPT is used to supply power for implantable and wearable medical devices. In addition to WPT, the system may be used to send/receive data communication between antenna/coil combination that is externally located outside the human body (EX) and may be called the transmitter (TX), and the implanted antenna/coil combination (IM) that may be called the receiver (RX).

M. Haerinia (✉)
University of Massachusetts Lowell, Lowell, MA, USA
e-mail: Mohammad_Haerinia@uml.edu

R. Shadid
Applied Science Private University, Amman, Jordan
e-mail: re_shadid@asu.edu.jo

S. Noghanian
Wafer LLC & American Public University System, Poway, CA, USA
e-mail: sima_noghanian@ieee.org

M. A. Matin (ed.), *Wideband, Multiband, and Smart Antenna Systems*, Signals and Communication Technology, https://doi.org/10.1007/978-3-030-74311-6_12

Although WPT is a promising technique to provide energy and communication for biomedical microsystems, it still suffers from some problems including unsatisfied power efficiency, transfer distance limitation, and unpredictable reliability due to mismatch and variable coupling. In this section, we will investigate more the challenges that face the WPT due to changes in the biological environment or body movement. This has an immediate effect on coil and antenna coupling between EX and IM devices part.

Ensuring a stable power transfer and data communication in implanted devices, under all conditions, is challenging. Figure 12.1 summarizes the two main factors that affect the efficiency of the WPT link due to mismatch coupling: the first challenge is the misalignment in the position of EX/IM and the second one is

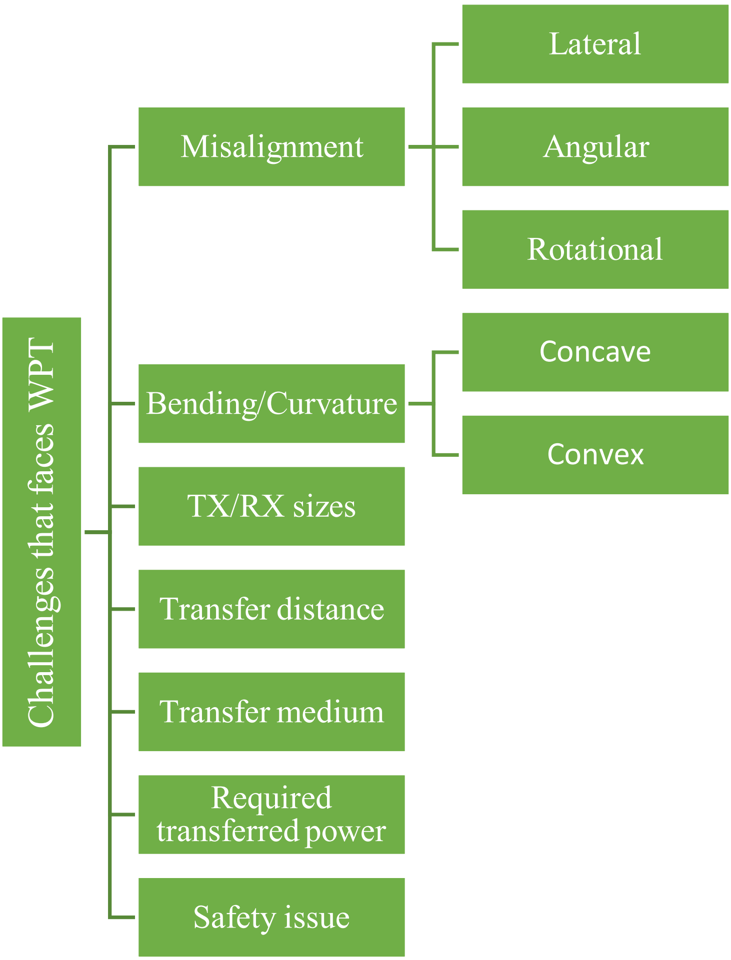

Fig. 12.1 Type of challenges that EX/IM coupling is facing

the curvature bending. Both challenges will be discussed in more detail in the subsequent sections.

12.2 Wireless Power Transfer Techniques for Medical Implants

Inductive coupling is a common and efficient way to transfer data and power into implantable medical instruments, including cardiac pacemakers, implantable cardioverter defibrillators, recording devices, neuromuscular stimulators, cochlear, and retinal implants. The development of an inductive link with a power amplifier is applied-based and can be adjusted with operating frequency, range, and form factor, and output power. The bandwidth to support data communication and reasonable efficacy for power transfer, insensitivity to misalignments, and biocompatibility are needed for a robust inductive link for medical implants [1]. In general, an inductive-based wireless power transfer system for IMDs has a pair of coils to inductively couple the power from a primary coil outside the body to a secondary implanted coil. Hundreds of kilohertz (kHz) to a few megahertz (MHz) is the operating frequency, and the size of the implanted coil is between several millimeters to a few centimeters. As the frequency increases, the electromagnetic wavelength gets more commensurate with the coil dimensions and the space between the coils. In this stance, the radiative and non-radiative components are part of the electromagnetic waves. Biological tissues also create significant problems for the propagation of electromagnetic fields and dilute the electrical field thus affecting the efficiency of the inductive link [2]. According to Faraday's induction law, increasing the size of coils and the number of turns boosts inductive link efficiency [2]. In case that the transmitting coil and the receiving coil have the same size, the maximum coupling is achievable. Although, in practice, the implanted coil is significantly smaller than the transmitting coil [3]. Moreover, implanted devices need a DC power source, while the power transmission is performed using AC signals. Therefore, there is a need for a rectifying unit to convert AC to DC [4]. Mainly, the inductive-based wireless power transfer system is used for medical devices such as brain and spinal cord stimulators. Lyu et al. [5] developed a stimulator, which occupies an area with the dimensions of 5 mm $\times$ 7.5 mm and operates at the resonant frequency of 198 MHz while having a 14 cm distance from the transmitter which is located outside of the body as shown in Fig. 12.2. The stimulator gets the energy that has already been stored by a switched capacitor and releases the energy as an output stimulus once the voltage reaches a threshold. The control unit utilizes positive feedback to trigger the circuit, so no stimulation control circuit block is needed. An in vivo experiment was performed to demonstrate the performance of the stimulator. Two electromyography (EMG) recording electrodes were implanted into the gastrocnemius muscle of a rat while the ground electrode was attached to the skin. A free-floating neural implant, which is insensitive to the location, is provided as an inductive link in [6] for

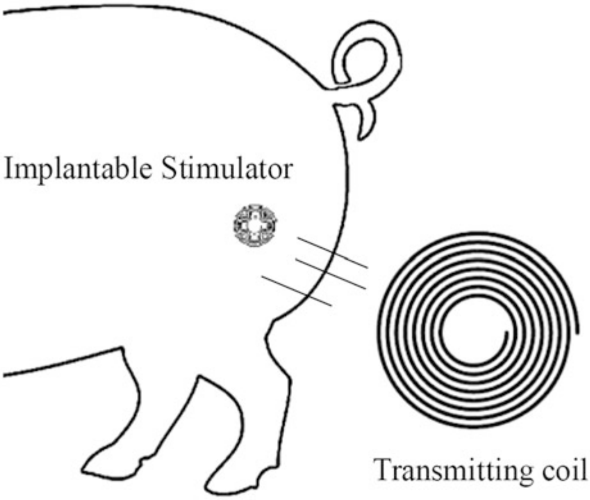

Fig. 12.2 A stimulator is implanted on the sciatic nerve of a pig

wireless energy transmission. The placement of a neurostimulator can be performed by a neurosurgical procedure called Deep Brain Stimulation (DBS) [7] as shown in Fig. 12.3.

The system works with a power transfer efficiency of 2.4% at 60 MHz and provides 1.3 mW power to the implant 14–18 mm away from the transmitter. Their coil link is stable against the lateral and angular misalignments of the floating implants if the coils continue to have the high-Q resonator. The extra heat produced by the resonator coil also does not exceed safety limits. The panel consists of printed and 3D coils. Printed coils maintain acceptable performance under lateral misalignment and are reliable for implants [8]. The shape of coils can affect overall wireless power transfer efficiency. The authors studied these effects in [9–11]. Another way to efficiently transmit power wirelessly over long distances in the order of meters to kilometers is microwave power transmission. The challenges for this technique in the present-day include the minimization of energy loss, protecting both humans and animals against exposure to excessive microwave radiation, and reconfiguring of a wireless transmission system in reaction to modifications such as a shift in a range between transmitter and receiver [12]. Pacemaker implantation is a popular method to cure people with cardiac insufficiency. Although, the lifetime of the pacemaker is restricted to the lifespan of the battery and the installation of a subcutaneous pocket [13]. Asif et al. [13] built a rectenna-based leadless pacemaker prototype as shown in Fig. 12.4. For energy transmission to the implanted unit, a wearable transmitting antenna range was fabricated. To evaluate the system's efficiency through Vivo ECG (Electrocardiogram) outcomes, an animal study is implemented.

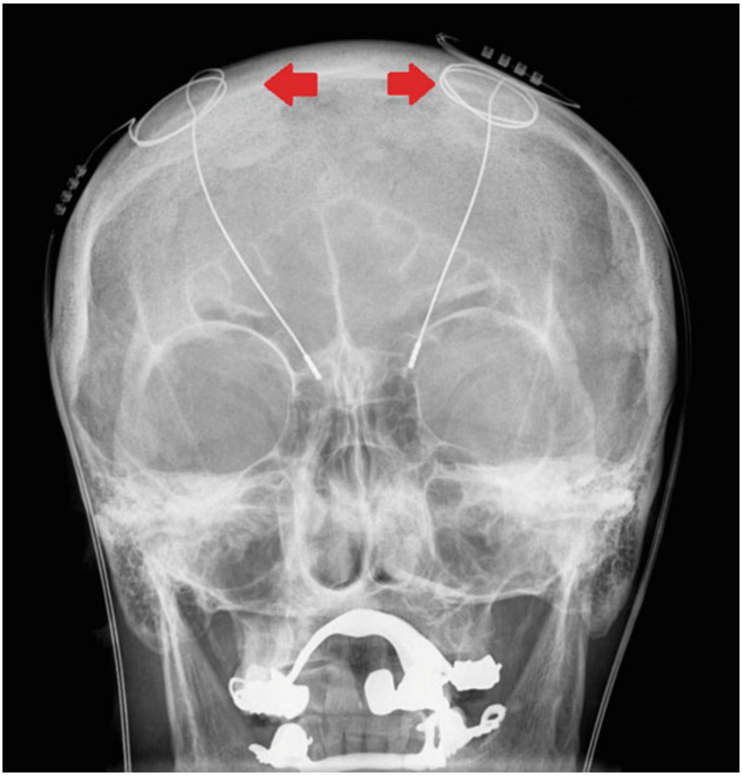

Fig. 12.3 Deep brain stimulation probes are shown in the X-ray of the skull [7]

Fig. 12.4 A rectenna-based leadless pacemaker and the wearable antenna were proposed by Asif et al. [13]

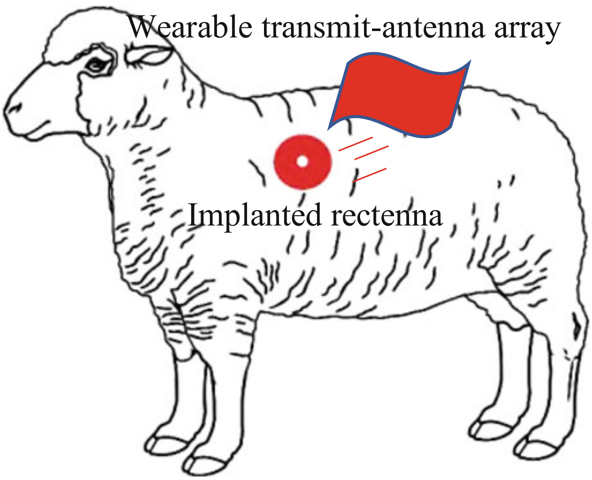

Ultrasound imaging is a well-known tool for evaluating patients' physiological and pathological conditions. In the passive ultrasonic recorder, the backscattered echo is derived from the reaction of biological tissue's acoustic properties to sound waves. Besides, the acoustic emission can be used for supplying energy wirelessly in the active biological environment [14]. The ultrasonic-based wireless power transfer system has a transmitter converting electrical energy to ultrasonic energy, and a receiver converting back the ultrasonic energy to electrical energy. The ultrasonic-based WPT system is an effective way for medical applications such as a cardiac defibrillator and a deep brain stimulator [15]. The advantage of ultrasound compared to magnetic resonance and induction coupling is that those methods are restricted to a short transfer distance, the misalignment issues [16], and magnetic field intensity should be under specified limitations for the safety of the body exposure. In the ultrasonic method, the operating frequency needs to be changed according to sound radiation and pressure distribution to obtain the optimum energy transition situation [15]. In the range of frequencies that individuals can hear, Kim et al. [16] have developed an implantable pressure sensing system driven by mechanical vibration. The pressure inductor has a planar coil with a ferrite core in which its distance differs from the involved stress. An implantable pressure sensor prototype is designed, as shown in Fig. 12.5, and examined in vitro and in vivo. The acoustic receiver is a piezoelectric cantilever and charges a capacitor by converting sound vibration harmonics to electrical energy. The stored electric charge will be discharged across an LC tank with an inductor sensitive to pressure during the period that the cantilever is not shaking.

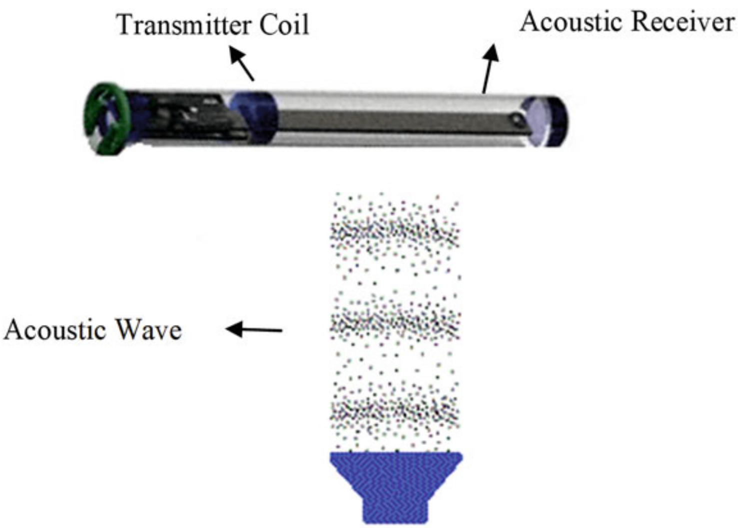

Fig. 12.5 An implantable pressure sensing system

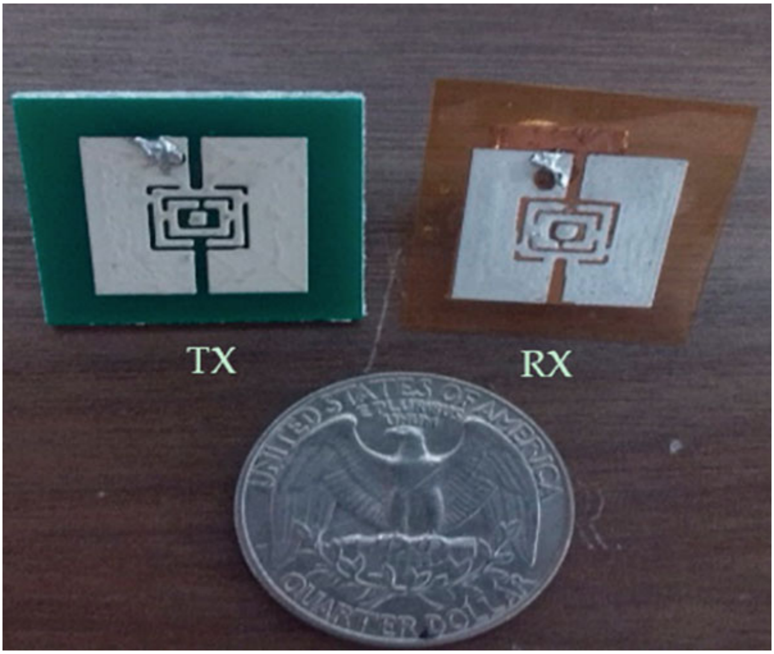

Fig. 12.6 Antennas printed on Kapton substrate [19]

WPT and communication both need bulky transmitters and receivers. Therefore, our major challenge is miniaturizing the communication and WPT systems. The unification and combination of the two systems provide the means of miniaturization of the overall system [17]. A hybrid inductive-based and microwave-based WPT system are presented in [18]. One of the current challenges for wireless transfer for small sensors is to minimize the system size. The authors decreased the size of the compact system, at the same time implementing multi-functionality. This goal is obtained by designing antennas having a 14 mm $\times$ 15 mm area and a 20 mm $\times$ 20 mm area for the hybrid system including antennas and coils. The coils' operating frequencies are 510 MHz and the antennas work at 2.48 and 4.66 GHz. In case the receiver dimension is larger than 40 mm, such a design can be printed on a flexible material substrate such as Kapton to facilitate the surgery procedures [19] as shown in Fig. 12.6. It is worth mentioning that rotational/lateral misalignment and bending are two conditions that may happen because of changes in the implanted antenna location or the person's movement [20]. Therefore, the bending of a flexible substrate and misalignment effect must be investigated precisely [21, 22].

12.3 Study of Misalignments

Implantable biomedical devices suffer from misalignment issues due to the curved surface of the anatomical system and body movement during daily life. Based on [23], there are three main types of patient movements that cause misalignments as follows:

(a) Slow irregular misalignment resulted from changes in the state of biological tissue at the location of implanted coils such as inflammation and implant migration.
(b) Rapid irregular misalignment due to the movement of the patient's position such as changing position from lying down to sitting.
(c) Rapid regular misalignment due to breathing.

Misalignments can also be classified according to their geometry into the three main types of misalignment: lateral, angular, and rotational between the TX and the RX or the EX and the IM. The definitions of the lateral and angle misalignments are as follows:

1. *Lateral Misalignment*
   In lateral misalignment, both the EX and IM are in parallel planes and separated by a certain depth, while the lateral distance between their centers is L as shown in Fig. 12.7a.
2. *Angular Misalignment*
   In angular misalignment, the plane of IM is tilted by an inclined angle $\varnothing$, while keeping the EX plane unchanged as shown in Fig. 12.7b.
3. *Rotational Misalignment*
   In rotational misalignment, the plane of IM is in parallel planes and separated by a certain depth, while the rotation angle is changed around itself (z-axis) as shown in Fig. 12.7c.

The three types of misalignments affect the coupling factor (k) between the TX and the RX and decrease its value. As a result, the transfer efficiency decreases. Therefore, ensuring a stable system design under certain misalignments is very important. A lot of research has been done regarding this topic. Moreover, for endoscopy capsule implantable devices that randomly rotate in the digestive tract, special coils/antennas, and circuits should be considered. Some of the techniques have been studied to improve the robustness due to misalignment and they are summarized in Table 12.1.

Since coil misalignment can result in an increase or decrease in the electrical power efficiency, the following section will explain in more detail the coupling calculation and presents some case studies. We will concentrate more on lateral and angular misalignments.

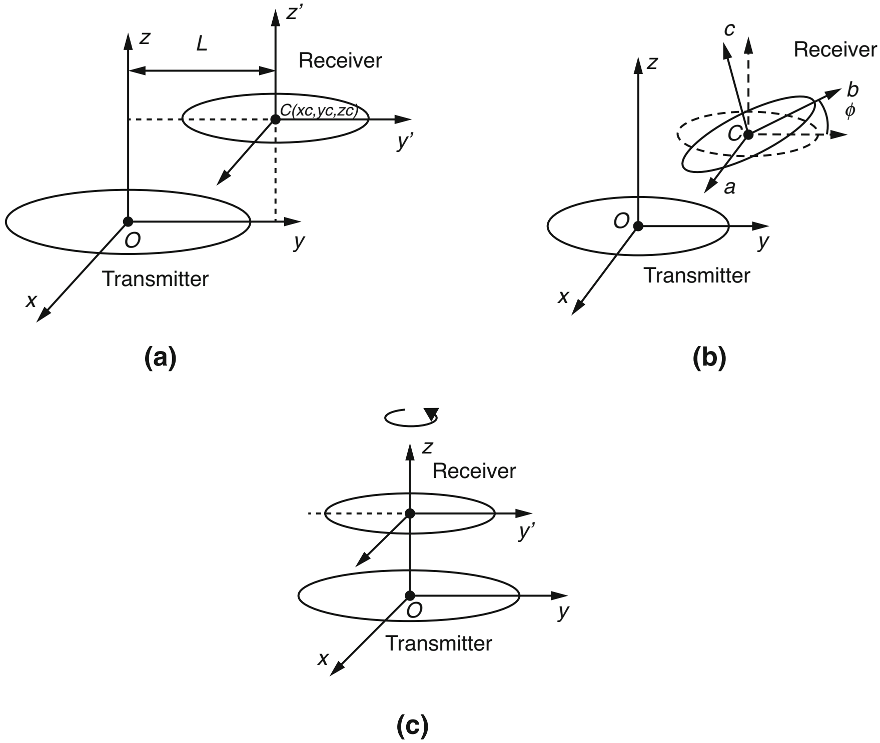

Fig. 12.7 Misalignment types (**a**) lateral, (**b**) angular, and (**c**) rotational [24]

12.4 Coupling Effects and Mutual Inductance Calculations

To calculate a mutual inductance (M) of A printed spiral coil (PSC) as shown in Fig. 12.8, PSC can be considered as a set of single-turn coils with a concentric diameter equal to ($d_\mathrm{i} + n(w + s)$), connected in series, where d_i is the inner coil diameter, n is the number of coil's turns, w is the width of conductor trace, and s is the space between each conductor turn. Accordingly, to study the effect of lateral and angular misalignment between the pair of single-turn coils to calculate M based on Fig. 12.4, the following parameters have been defined to calculate the mutual inductance between an inclined circular loop in any position:

- The outer diameter of the TX and RX loops, $d_{\mathrm{oTX}(i)}$, $d_{\mathrm{oRX}(i)}$.
- The parameters $\vec{a}$, $\vec{b}$, and $\vec{c}$ defining the normal vectors of the plane containing the RX coil.
- The center of the RX coil (x_c, y_c, z_c).

The partial mutual inductance M between every two turns of the PSC pair can be expressed as follows:

Table 12.1 Research studies on the misalignment between transmitter and receiver

Ref	Journal/conference	Pub. year	Type of studied misalignment	Distance between coils	The proposed solution to overcome the misalignment problems
[25]	Biosensors and Bioelectronics	2019	Lateral and angular	10 mm	The authors proposed a multi-coil solution. They used a 3-coil system having a circular-shaped external and miniaturized spherical shaped implantable coil at 13.56 MHz.
[26]	IEEE Transactions on Power Electronics	2017	Lateral and angular	The different distance starts from 120 mm	The authors proposed a Strongly Coupled Magnetic Resonance (SCMR) system. Specifically, they used two orthogonal coils 3D model instead of using planar coils for TX and RX to provide misalignment insensitivity.
[27]	Journal of Physics D: Applied Physics	2015	Lateral and angular	Mid-range	The authors applied a metamaterial to enhance the WPT efficiency.
[28]	IEEE Transactions on Power Electronics	2014	Lateral and angular	25 mm	The authors proposed a frequency control technique method by electronically turning a Class E inverter used as the primary coil.

$$M_{ij} = \frac{\mu d_{\mathrm{oRX}(j)}}{2\pi} \int_0^{2\pi} \frac{[p_1 \cos\varphi + p_2 \sin\varphi + p_3]\, \Psi\,(\nabla)}{k\sqrt{V_{\mathrm{o}}^3}} d\varphi \tag{12.1}$$

where M_{ij} is the mutual inductance between TX coil number i and RX coil number j, $\varphi \in [0, 2\pi]$ is a parameter angle and the following sequence of definitions should be calculated prior to evaluate (12.1) as follows:

Where $K(\nabla)$ and $E(\nabla)$ are the complete elliptic integrals of the first and second kind, respectively. Once the mutual inductance between a pair of single-turn coils have been calculated, the overall mutual inductance can be generated by the summation of the partial mutual inductances between every turn on one coil (TX i), and all the other turns of the other coil (RX j). By adding all the values of partial mutual inductance M is obtained as:

$$M = \sum_{i=1}^{n1} \sum_{j=1}^{n2} M_{ij} \left(d_{\mathrm{oTX}(i)}, d_{\mathrm{oRX}(j)} \right) \tag{12.2}$$

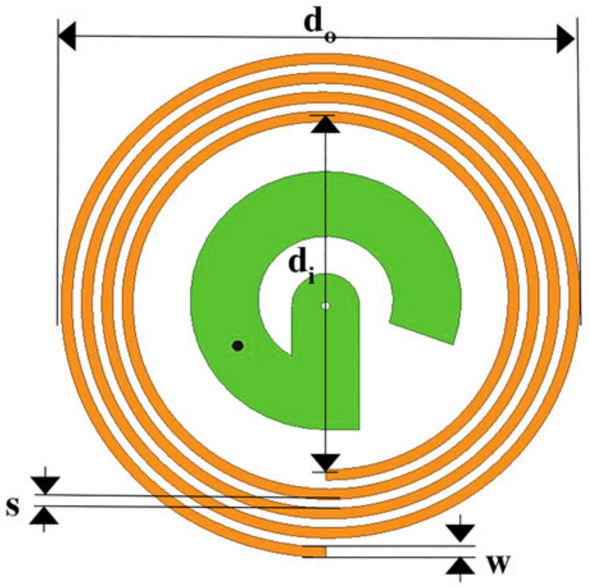

Fig. 12.8 Geometrical parameters of a circular planar spiral coil

Main parameter	Parameter to be evaluated first
$p_1 = \frac{\gamma c}{l}$	$\alpha = \frac{d_{\mathrm{oRX}(j)}}{d_{\mathrm{oTX}(i)}}$
$p_2 = -\frac{\beta l^2 + \gamma ab}{lL}$	$\beta = \frac{2x_{\mathrm{c}}}{d_{\mathrm{oTX}(i)}}$
$p_3 = \frac{\alpha c}{l}$	$\gamma = \frac{2y_{\mathrm{c}}}{d_{\mathrm{oTX}(i)}}$
$V_o^2 = \alpha^2 \left[\left(1 - \frac{b^2c^2}{l^2L^2}\right)\cos^2\varphi + \frac{c^2}{l^2}\sin^2\varphi + \frac{abc}{l^2L}\sin 2\varphi\right] + \beta^2 + \gamma^2 - 2\alpha\frac{\beta ab - \gamma l^2}{lL}\cos\varphi - \frac{2\alpha\beta c}{l}\sin\varphi$	$l = \sqrt{a^2 + c^2}$
$\Psi(\nabla) = \left(1 - \frac{\nabla^2}{2}\right) K(\nabla) - E(\nabla)$	$L = \sqrt{a^2 + b^2 + c^2}$
	$\tau = \frac{2z_{\mathrm{c}}}{d_{\mathrm{oTX}(i)}}$
	$p_4 = -\frac{\beta ab - \gamma l^2 + \tau bc}{lL}$
	$p_5 = -\frac{\beta c - \tau a}{l}$
	$A_{\mathrm{o}} = 1 + \alpha^2 + \beta^2 + \gamma^2 + \tau^2 + 2\alpha(p_4\cos\varphi + p_5\sin\varphi)$
	$\nabla = \sqrt{\frac{4V_{\mathrm{o}}}{A_{\mathrm{o}} + 2V_{\mathrm{o}}}}$

and

$$k = \frac{M}{\sqrt{L_1 L_2}} \tag{12.3}$$

where L_1 and L_2 are the inductance of the TX coil and RX coil, respectively, calculated as follows:

$$L_s = \mu\, n^2 d_{avg} \left[\ln\left(\frac{2.46}{u}\right) + 0.2u^2 \right] \tag{12.4}$$

$$d_{avg} = \frac{d_o - d_i}{d_o + d_i} \tag{12.5}$$

$$u = \frac{d_o + d_i}{2} \tag{12.6}$$

where μ is the permeability of the conductor and u is a parameter known as fill-factor, which takes values in the range of 0 (when all the turns concentrated on the perimeter) to 1 (when the first turn starts from the center of the spiral coil and d_i is equal to zero).

12.5 Case Studies: Calculating Coupling Coefficient Under Misalignment Conditions

12.5.1 Lateral Misalignments

In the first case study, we are calculating the value of coupling coefficient (k_{12}) generated from MATLAB software, under misalignment condition, the following model was used:

- The TX and RX coils are spiral shapes.
- The value of d_{oTX} is 40 mm and d_{oRX} is 20 mm.
- d_{iTX} and d_{iRX} values are specified relative to the total value of d_{oTX} and d_{oRX}. In this work, it is assumed that $d_i = 0.34d_o$ for both TX and RX.
- Twenty-one turns for the TX coil and 9 turns for the RX coil were considered.
- The distance between the TX and RX coils is 10 mm.

Both coils were simulated and the value of the coupling coefficient under lateral misalignments conditions along sweeping X- and Y-axes are recorded. Figure 12.9 shows the result. As seen that the maximum coupling happened at $L = 0$, as the L increased the value of M will decrease too.

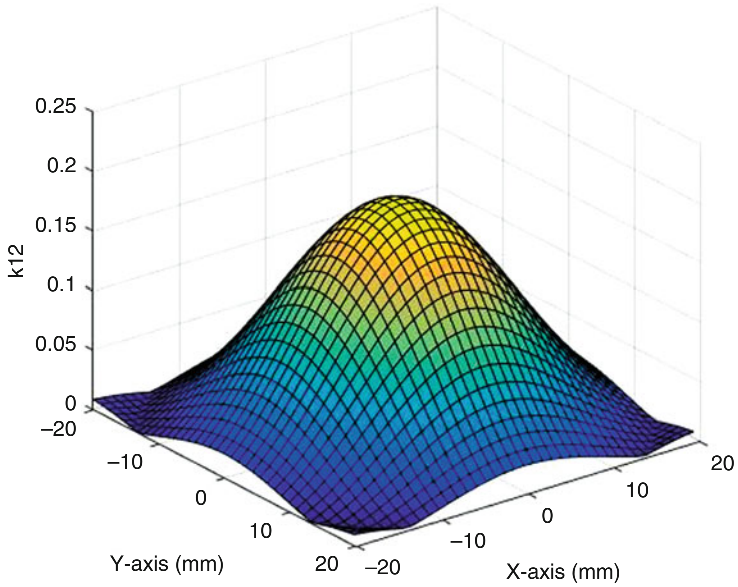

Fig. 12.9 Calculating the coupling coefficient for two spiral coils with lateral misalignments in *x*- and *y*-directions

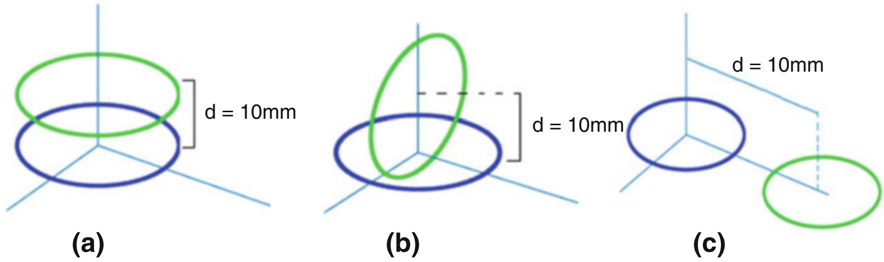

Fig. 12.10 Different positions of coils (**a**) Position A, (**b**) Position B, and (**c**) Position C

12.5.2 Angular Misalignment

For angular misalignment, the value of k_{12} is calculated between two identical single-turn circular coils and we assumed a 1.4 mm diameter in this example. The distance between the TX and RX is 10 mm, the same as the lateral case. The system was simulated to calculate the k_{12} for three positions as shown in Fig. 12.10:

- Position A: Coils are in parallel.
- Position B: Coils are perpendicular.
- Position C: Coils are on the same plane.

Table 12.2 provides the values of the coupling coefficient for single-turn identical circular coils of 1.4 mm diameter at three different position vector cases. It can be concluded that the maximum coupling occurred at Position A and the minimum coupling occurred at Position B.

12.5.3 Model of WPT Inside Body Tissue

In the following design and example, we will present a design model of TX and RX inside a body tissue model as presented in [29, 30]. As seen in Fig. 12.11, a system is a dual-band design consists of an EX antenna/coil combination placed directly at the upper surface of the skin, whereas the IM antenna/coil combination is embedded in the body tissue. We assumed that the layered body model consisting of three tissue layers: the skin layer (3 mm), the fat layer (7 mm), and the muscle layer (125 mm). Moreover, the geometry and dimensions of TX and RX coils and antennas are indicated in the same figure.

The EX and IM coils can transfer power at 13.56 MHz, and the pair of antennas is sending/receiving data at 905 MHz (please note that both TX and RX antennas have a shorting pin to determine their operating frequencies as shown in Fig. 12.11). Moreover, the electromagnetic properties of each layer at each frequency were obtained from the Institute of Applied Physics (IFAC) database [31] and are summarized in Table 12.3.

The impacts of coil/antenna misalignments between the EX and IM combinations are investigated to observe the changes in k, insertion loss (S_{21}), and η resulting from the following cases:

Table 12.2 Coupling coefficient between two single-turn identical circular coils of 1.4 mm diameter at three different position vector cases

Position	Center of the receiver (x_c, y_c, z_c) (mm)	Angular misalignment normal vector $(\vec{a}, \vec{b}, \vec{c})$	Coupling coefficient (k)
A (Parallel)	(0,0,10)	(0,0,1)	2.5×10^{-4}
B (Perpendicular)	(0,0,10)	(0,−1,0)	0
C (Coils in same plane)	(0,10,0)	(0,0,−1)	1.25×10^{-4}

Table 12.3 Electromagnetic properties for the body tissues in the layer tissue model at different frequencies

Frequency	13.56 MHz			905 MHz		
Parameter	Muscle	Fat	Skin	Muscle	Fat	Skin
ε_r	138.4	11.83	285.25	55	5.46	41.4
σ (S/m)	0.63	0.03	0.24	0.94	0.05	0.87

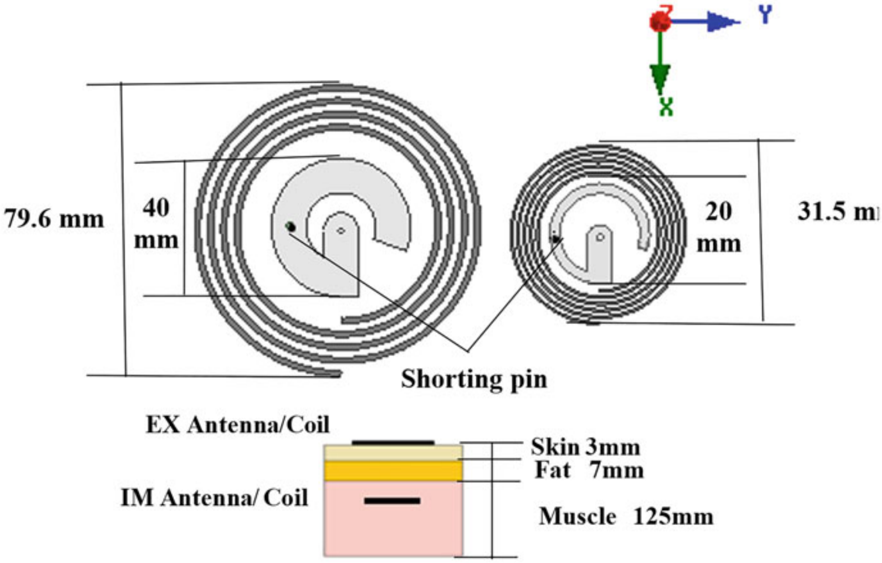

Fig. 12.11 The proposed WPT system and body tissue model

- A lateral misalignment by varying L in Fig. 12.4a from −60 to 60 mm in steps of 10 mm in direction of the y-axis. The distance between EX and IM combinations is 30 mm.
- An angular misalignment by varying ϕ in Fig. 12.4b from −60° to 60° in steps of 10° rotating around the z-axis at $L = 0$. The distance between EX and IM combinations is 30 mm.

After simulated the above two cases of alignment, Fig. 12.12 shows S_{21} and η versus L for both antenna and coil pairs. It can be noted that the lateral misalignment has a small effect on the values of S_{21} and η for the coil in the range of $L = [-20$ mm to 20 mm]. They reach their maximum of $S_{21} = -17.26$ dB and $\eta = 1.88\%$ at $L = 0$, then these values drop rapidly after L increases to more than 30 mm. Similarly, the value of S_{21} for the antenna is maximum at $L = 0$ ($S_{21} = -37.18$ to 37.18 dB).

Figure 12.13 shows S_{21} and η versus φ for both antenna and coil pairs. The maximum η occurred at $\varphi = 0°$ for the coil while it occurred at $\varphi = 40°$ for the antenna. Please note that while the angular misalignment moving counterclockwise around the z-axis, the antenna's performance is improved due to the distance between the TX and RX will be closer. In this study case, please pay attention to two important points. First, due to the shorting pin, the value of S_{21} for the antenna are not symmetrical around the y-axis, whereas it is symmetrical in the coil case. Second, since the antenna is used for data communication only, the required value of S_{21} and η for antennas pair is less than that required for coils pair.

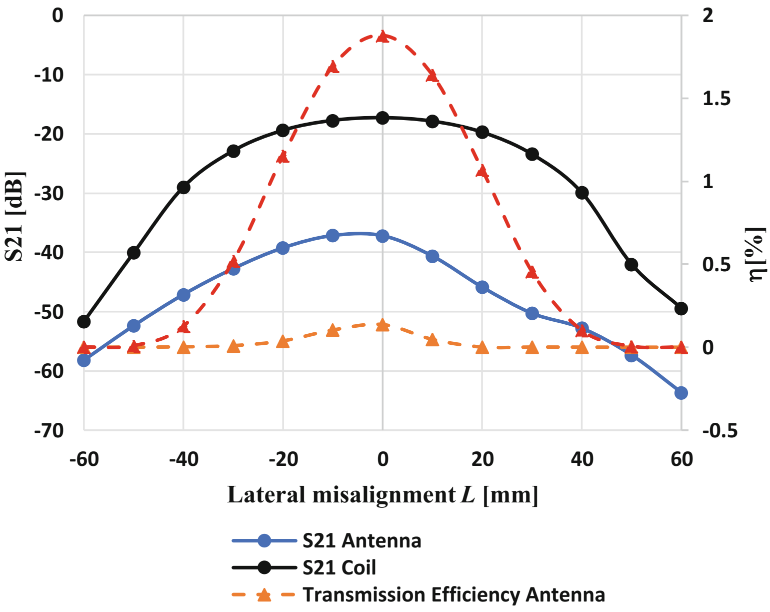

Fig. 12.12 η and S_{21} under lateral misalignment condition at 30 mm depth

12.6 Coil Geometry Optimizations Under Misalignment Condition

In the most biomedical applications, there is a very limited and available volume for the implanted part. For example, the capsule endoscopy maximum dimension is approximately 11–27 mm. Accordingly, optimization procedures should be applied to the RX and TX coils sizes to increase WPT efficiency for a limited coil size. Usually, the optimization methods include the following procedures:

1. The first step is to determine the maximum dimensions in the geometry of the RX and TX coils. RX size limitation depends on the location of the implanted part, whereas the TX limitation depends mainly on the fabrication method.
2. Then optimization of the TX coil geometry is applied. In this step, the coupling factor between the TX and the RX coils is calculated.
3. The third step is to conduct an estimated iterative experiment. The number of turns for the TX and RX coils and the quality factor could be determined.
4. The fourth step is to calculate the estimated efficiency transferred to the RX coil at a certain frequency.
5. The fifth step is to optimize the frequency in order to increase power efficiency.

In [32], optimization is done for both TX and RX to find the optimal PSC geometries under a well-aligned condition. In the same manner, the optimization

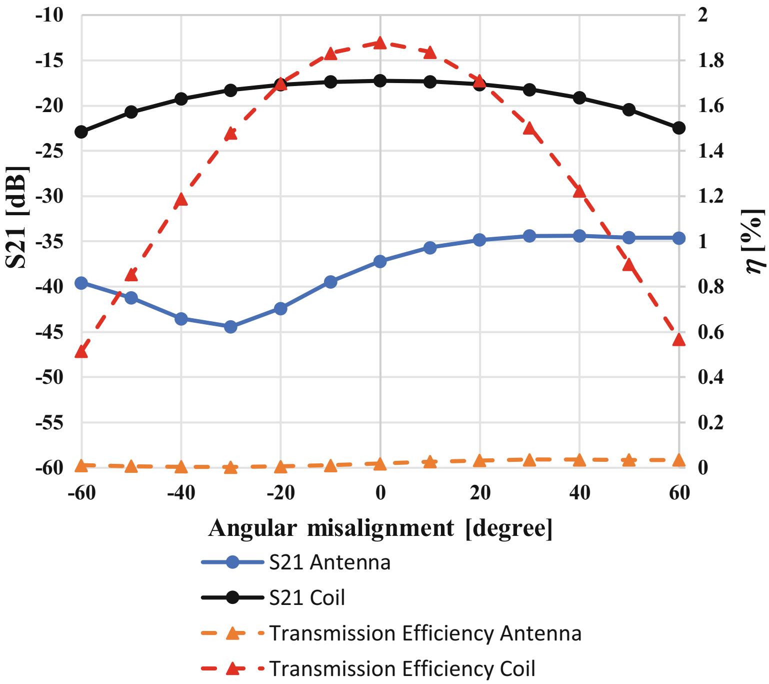

Fig. 12.13 η and S_{21} under angular misalignment condition at 30 mm depth

of TX and RX geometries could be done but under misalignment, conditions using iterative design procedures to perform the optimization process. Please refer to Fig. 12.14 which shows an example of an optimization flowchart. The flowchart procedure starts with a set of initial values, depending on design constraints and restrictions, taking into consideration the effects of the lateral and angular misalignment, and ends with the optimal PSC geometries for the TX and RX coils.

12.7 Bending

Due to the advancement of medical technologies, and the increasing demand for implants, advanced technologies are required to make the patient more comfortable by fabricating the implant devices on flexible substrates instead of rigid ones. Therefore, it can slightly vary its shape based on the patient's movement and ease surgical difficulties and mitigate injuries caused by rigid implants. Moreover, devices can be made smaller and implanted in a wider variety of locations. However, real-time flexion of the implant coils reduces transmission efficiency. There are two types of bending: concave and convex, other types of surfaces may be a combination

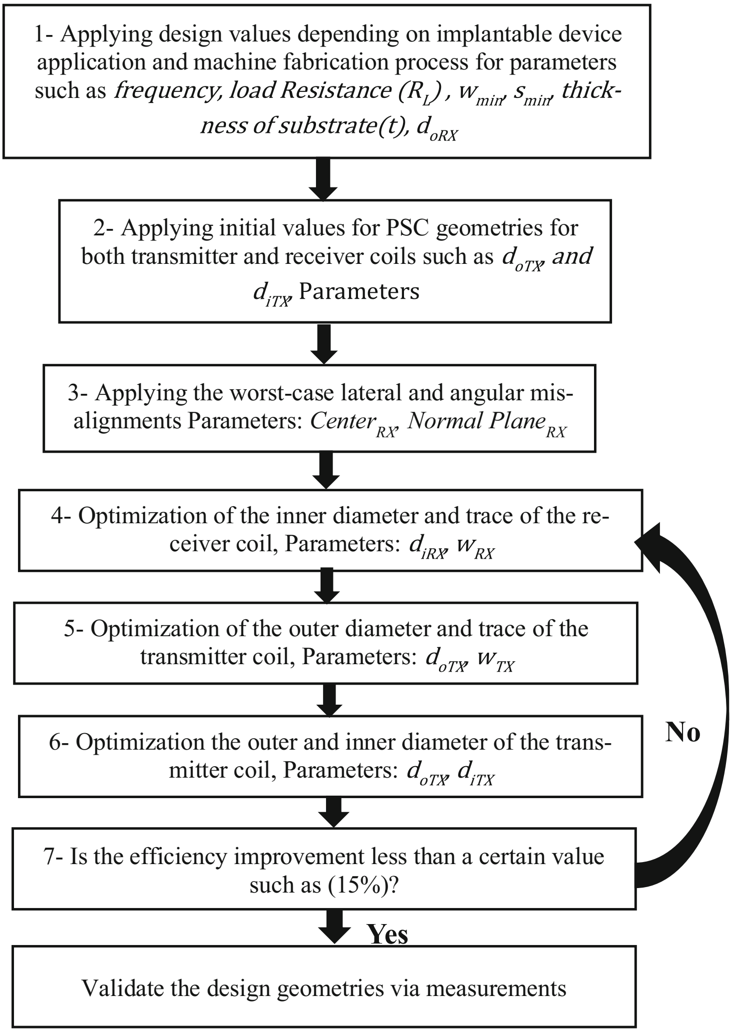

Fig. 12.14 Optimization method to determine PSC geometry flowchart

of the concave and convex surfaces. Efficiency, η, depends on the type of bending of the IM device since it will be closer or farther from the TX.

12.7.1 Bending Model

In this case study, we will present a design model of TX and RX inside a body tissue model [22]. The same EX and IM coil/antenna combinations and body tissue

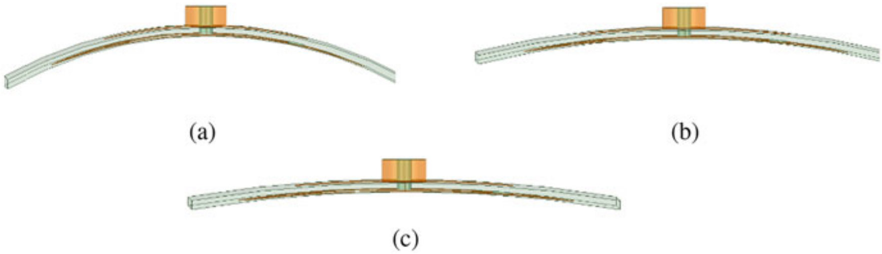

Fig. 12.15 The IM hybrid design under three bending conditions. (**a**) Rad = 40 mm, (**b**) Rad = 80 mm, and (**c**) Rad = 120 mm

Table 12.4 Coils coupling coefficient (k) under three bending conditions

Rad (mm)	Flat	40	80	120
k	0.057	0.054	0.052	0.054

models as seen in Fig. 12.9 have been used. But the substrate of the IM combination is changed to be flexible of Kapton type.

The impact of bending the IM coil/antenna on the performance was investigated under three bending conditions (Rad = 40, 80, and 120 mm, where Rad is the radius of bending), as shown in Fig. 12.15.

Figure 12.16 shows the simulation results of S_{22} versus frequency, where port 2 is assumed to be at the IM coil. Although the level of S_{22} matching is changing due to the bending, the center frequency is not showing a significant change. As the bending depth increases (for smaller Rad values) the −10 dB bandwidth is decreasing, as is expected. Figure 12.17 presents the result of S_{21} versus frequency (assuming port 2 is IM and port 1 is EX), under three bending conditions. It can be noted that the IM resonance frequency (f_{oIM}) varied as much as +15 MHz at Rad = 120 mm to −100 MHz at Rad = 80 mm, compared to its value at f_{oIM} for the flat case. It is also noted that the larger the Rad value, the closer the coil was to the flat case, while S_{21} did not vary more than 1.57 dB, and it is almost the same over a frequency range.

Table 12.4 shows k values under all three bending conditions for the coils pair at 13.56 MHz. It can be noted that bending had a very small and negligible effect on the performance of the inductive coils link.

12.8 Multi-coils

To overcome the problem of misalignment and bending challenges, using multiple transmitters is a promising technology to increase the transfer efficiencies over a SISO (Single-Input, Single-Output) WPT system. Multiple transmitters provide

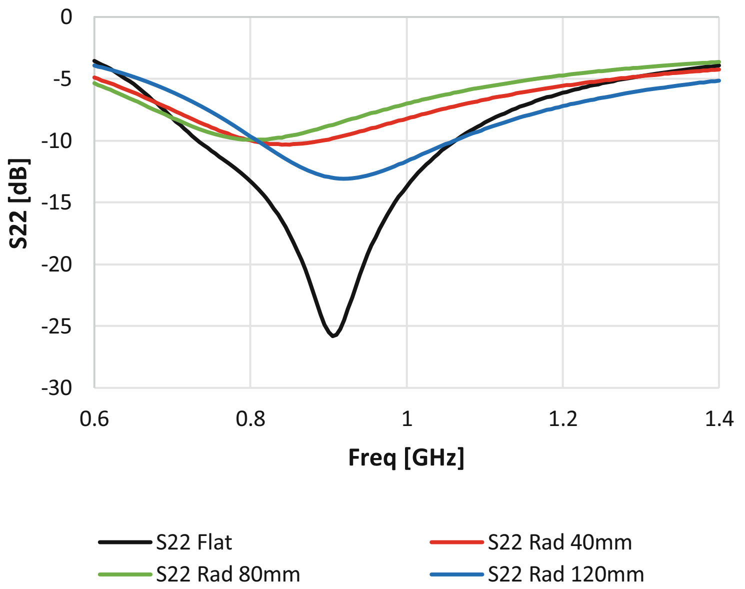

Fig. 12.16 Simulated S_{22} for the IM under three bending cases of Kapton substrate

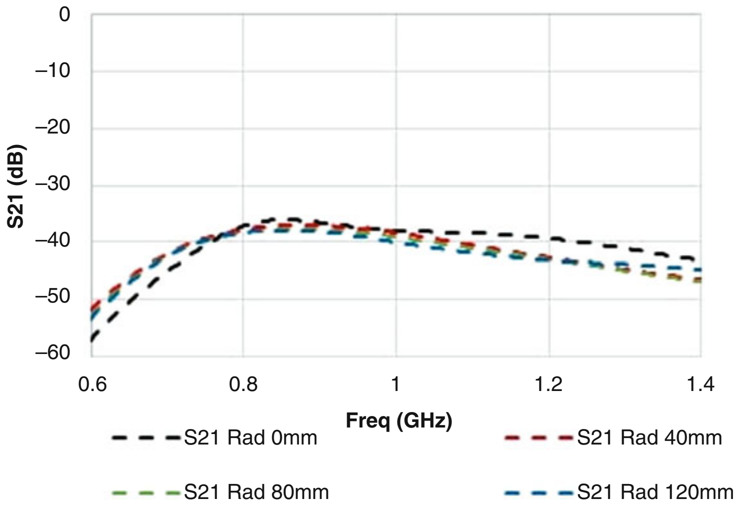

Fig. 12.17 Simulated S_{21} for the IM under three bending cases of Kapton substrate

more degrees of freedom of the primary field or current distribution, and, therefore, the performance of this system will be enhanced.

Recently, many techniques proposed to use multiple transmit coils to focus the energy of the magnetic field towards the receiver. This idea is similar to beamforming from phased array antennas which will be discussed more in Sect. 12.9. However, it is important to note that the scientific theory principles of radiative electromagnetic fields from antennas are different from that of magnetic near-fields [33]. There are many types of multi-coils that the research focuses on as follows (shown in Fig. 12.18):

1. *Multiple-input/single-output (MISO) WPT systems that deal with multiple transmitters and one receiver:* MISO configuration can minimize the magnetic flux leakage and orientate the magnetic field to the RX coil by powering the neighbor coils of the active ones in opposite directions. Moreover, the MISO system replaces the large sending coil with small ones occupying the same size of the surface.
2. *Single-input/multiple-output (SIMO) WPT systems that deal with one transmitter and multiple receivers*: For many WPT applications, it is practical to use multiple RXs and the power could be transferred to all RX devices simultaneously.
3. *Multiple-input/multiple-output (MISO) WPT systems that deal with multiple transmitters and receivers*: The MIMO system is used as a solution for achieving high power efficiency and data rates. Moreover, MIMO is a promising method to increase a channel capacity that can work on multi-operating frequency. Indeed, the MIMO system is a more complicated system than MISO or SIMO systems (Table 12.5).

12.8.1 A Case Study: SIMO Model

In this case study, we will present a SIMO design model that consists of one TX placed directly on the outer surface of the skin layer. The system is enhanced by adding three RX embedded in the muscle tissue [34]. The same EX and IM coil/antenna combinations and body tissue model as shown in Fig. 12.9 have been used but the diameter of the TX coil has been increased to 93.5 mm. Figure 12.19 illustrates the system model.

To investigate the enhancement impacts for adding multiple IM coils/antennas on system stability, a lateral misalignment is applied by varying L from −60 to 60 mm in steps of 10 mm in direction of the y-axis if Fig. 12.7a at a distance of 30 mm between the EX and IM combinations.

Simulations are conducted to observe the changes in S_{21} resulting in both antenna and coil pair. Figure 12.20 shows S_{21} vs. L of antenna pair for both the single and multiple IM combination under lateral misalignment conditions. It can be noted that for SIMO multiple IM designs, the values of S_{21} varied between −33.19 dB at $L = 0$ to −46.05 dB at $L = 60$ mm; whereas, for the SISO case, it varied between −37.18 dB at $L = 0$ to –63.3 dB at $L = 60$ mm. Therefore, it can be noted that the stability of system design has been increased by using SIMO multiple IM comparing to SISO one. For all the values of L, the S_{21} is better for the SIMO multiple IM case than the SISO system.

Table 12.5 Some references on wireless power transfer for implantable devices using multiple coils

Ref.	Journal	Pub. year	Freq	Single transmitter dimension	Number of transmitters	Single receiver dimension	Number of receivers	Efficiency (%)
[34]	2019 USNC-URSI	2019	13.56 MHz	Circular shape with d_{oTX}=93.5 mm	1	Circular shape with d_{oRX}=31.5 mm	3	Measured as transmission efficiency (TE)
[35]	IEEE Transactions on Power Electronics	2018	6.78 MHz	Rectangular shape 200 mm × 100 mm	1	Rectangular shape 100 mm × 60 mm	3	66.6
[36]	IEEE Transactions on Industrial Electronics	2016	22.5 MHz	Circular shape with d_{oTX}=56 mm	1	Circular shape with d_{oTX}=12 mm	3	0.24–0.29
[37]	IEEE Transactions on Industrial Electronics	2014	13.56 MHz	Rectangular shape 30 cm × 30 cm	1	Circular shape with d_{oTX}=4.2 cm	4	76 53
			200 kHz	1	Circular shape with d_{oTX}=5.4 cm	3	83.3	
[38]	IEEE Transactions on Industrial Electronics	2009	240 kHz	Rectangular shape of 16 cm × 18 cm	1	Rectangular shape of 4 cm × 5 cm	2	75
					1		3	74
					2		2	75
					2		3	74
					1	Rectangular shape of 7 cm × 8 cm	2	82
					2		2	88

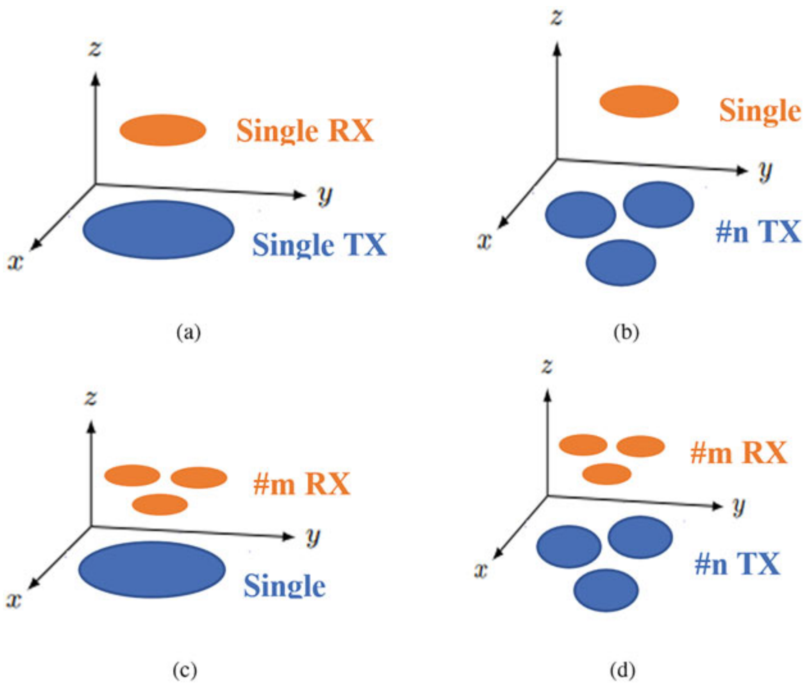

Fig. 12.18 Fundamental elements of a WPT network topology (**a**) SISO system, (**b**) MISO system, (**c**) SIMO system, and (**d**) MIMO system

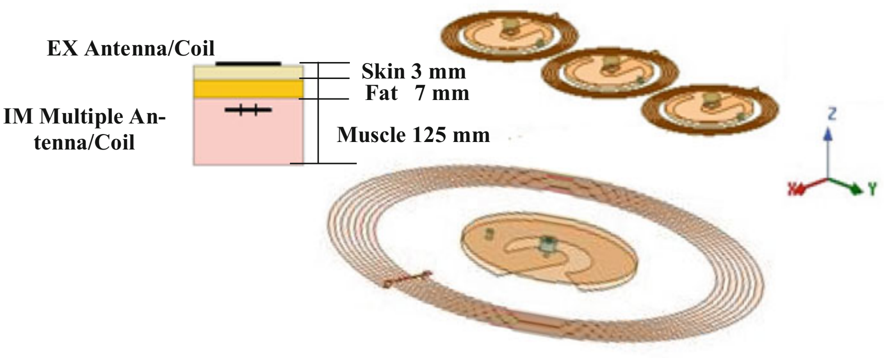

Fig. 12.19 SIMO hybrid system with body tissue

We noted that the values of S_{21} for the antenna are not symmetrical around the y-axis for both cases due to the existence of the shorting pin. The transmission efficiency is still acceptable for antenna pair since it is used for data communication only.

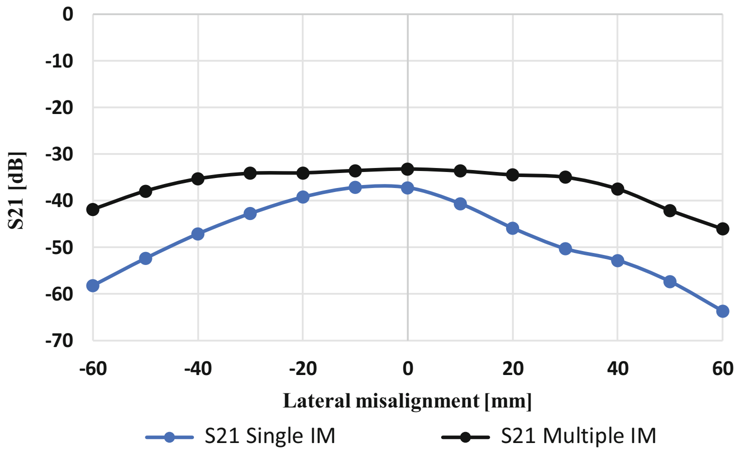

Fig. 12.20 S_{21} under lateral misalignment condition for the antenna pair

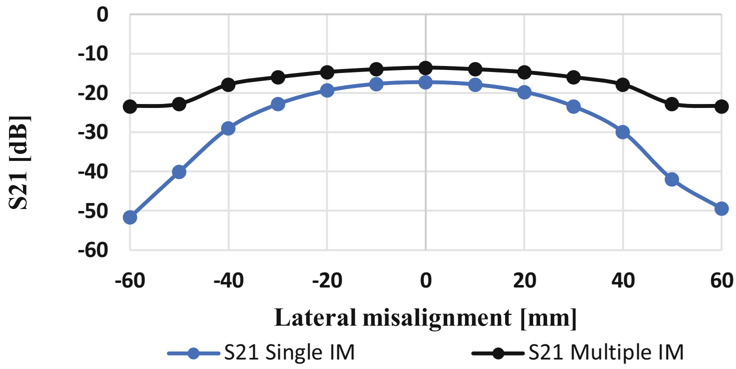

Fig. 12.21 S_{21} under lateral misalignment condition for coil pair

Figure 12.21 shows S_{21} 1 versus L for both SIMO and SISO systems under lateral misalignment for coil pair. It can be noted that at SIMO design, the values of S_{21} varied between -13.65 dB at $L = 0$ to -23.36 dB at $L = 60$ mm, and between -17.26 dB at $L = 0$ to -49.41 dB at $L = 60$ mm. Similarly, as in the antenna pair, in this case, the stability of the SISO system has been increased by using multiple IM combinations. Moreover, the system model for coils is symmetrical. From both Figs. 12.21 and 12.22, it can be concluded that the stability of WPT systems is improved using multi-coils.

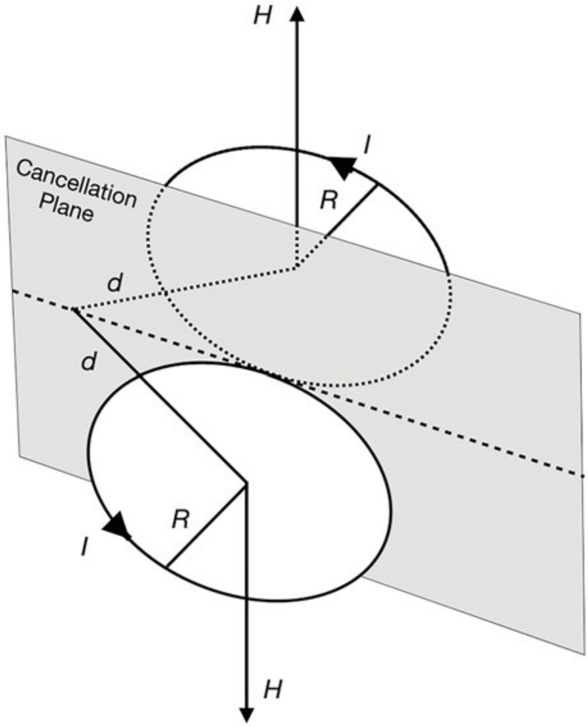

Fig. 12.22 The quadrupole loop creates a cancelation plane

12.9 MIMO Beamforming

To increase the charging distance in wireless power transfer for medical applications, various signal processing and beamforming methods have been proposed. The beamforming increases the power transfer efficiency and the range of transmission. Some of these methods are based on communication methods. In communication the concept of multiple-input multiple-output (MIMO) is well-known. In [39] the authors introduced the concept of Magnetic MIMO (MagMIMO). MagMIMO uses a magnetic charging method, but instead of one coil, it uses multiple transmitting coils. In a communication MIMO system, a channel (the propagation patch between the transmitter and receiver) needs to be known or estimated. Therefore, a lot of time a pilot signal is sent from the transmitter and sent back to the user to estimate the channel. In MagMIMO however, having the information about the loading effect of the coils the channel can be estimated without sending and receiving signals. Let us consider two transmitters and one receiver.

$$I_\mathrm{r}\left(R_\mathrm{r} + j\omega L_\mathrm{r} + \frac{1}{j\omega C_\mathrm{r}} + z_\mathrm{L}\right) = j\omega\left(M_1 + M_2\right) I_\mathrm{t} \tag{12.7}$$

where I_{r} and I_{t} are the receiver and transmitter currents, respectively. R_{r}, L_{r}, and C_{r} are the resistance, inductance, and capacitance of the receiver and z_{L} is the load impedance. In the situation that the receiver is tuned, the inductive and capacitive terms will cancel each other out. The two terms M_1 and M_2 are the mutual inductances between the receiver coil and the two transmitter coils. In a maximum ratio combining (MRC) the coefficients for the transmitter currents are defined as $\frac{m_i^*}{\sum_{i=1}^{2}|m_i|^2}$, where m_i^* is the complex conjugate of m_i. To do this optimization an estimate of mutual inductances is needed. This chapter presents a method of channel measurement by keeping one source active at each given time and leave the other transmitters open. Measuring the active transmitter impedance will provide the mutual inductance term. In [40] the authors extended the MagMIMO to multiple receivers and used the term MultiSpot for this system. In a MultiSpot system, multiple transmitters and multiple receivers will interact with each other. Despite the wireless communication beamforming that the users do not interact with each other, in MultiSpot the receiver coils have effects on each other as well as on the transmitters. In this system, the equations will be in a matrix format where the vector representing the receiver currents will be given by multiplication of the channel matrix by the transmitting current vector $\boldsymbol{I}_{\mathrm{r}} = \left(j\omega \boldsymbol{Z}_{\mathrm{r}}^{-1}\right)\boldsymbol{M}\boldsymbol{I}_{\mathrm{t}}$. Because of the interaction between the receivers and transmitters the channel matrix is written as $\boldsymbol{H} = \boldsymbol{H}_{\mathrm{r}-\mathrm{r}}\boldsymbol{H}_{\mathrm{r}-\mathrm{t}}$, where $=\boldsymbol{H}_{\mathrm{r}-\mathrm{r}}$ contains the receiver coupling and $\boldsymbol{H}_{\mathrm{r}-\mathrm{t}}$ contains the transmitter coupling. This chapter proves that the solution to maximizing the power is to maximizing the eigenvector of $\boldsymbol{H}^*\boldsymbol{R}_{\mathbf{r}}\boldsymbol{H}$ where $\boldsymbol{R}_{\mathbf{r}}$ is a diagonal matrix with diagonal entries that are the resistances of each receiver. This chapter also provides a method of channel estimation.

The method presented in [40, 41] is increasing the range of power transfer significantly, but it is complex due to the interaction of transmitter coils with each other. In [42] the authors introduce the concept of near-field magnetic induction MIMO (NFMI MIMO). In [42] NFMI MIMO is introduced as a means of data transfer however the concept can be used in power transfer as well. To reduce the interaction between transmitter coils a multipole loop is introduced. A multipole loop can generate a magnetic field in multiple directions. A quadrupole loop looks like number 8, where equal and opposite direction current are on each side of the loop. The opposite direction currents create opposite direction magnetic fields at the points that have the same distance from the center of each loop. Both loops have the same radius and number of turns. This will create a cancelation (or decoupling) plane (Fig. 12.22). Using an unbalanced quadrupole loop with one loop having a different radius than the other a curved cancelation surface can be created.

This concept was used in [42] to remove the coupling and therefore the impedance is a real number and the input current and voltage are in phase. In [42] the authors compared the cross talk of a 2×2 conventional MIMO arrangement of the coils with a heterogeneous multipole loop antenna array that included quadrupole coils. Also, they showed in an experimental example that signal to noise ratio increased as much as 30 dB in comparison with the conventional MIMO.

In [43] an iterative beamforming approach is taken. In the proposed system on the transmitter is using a 3D coil, that consists of three orthogonally deployed coils. Multiple receivers are placed around the transmitter. In the proposed system three receivers are considered. The resonance frequency of the coils is adjusted by a capacitor C and each receiver has a real impedance of z_{L}.

$$\begin{bmatrix} \boldsymbol{Z}_{\mathrm{Tx}} & \boldsymbol{Z}_{\mathrm{ch}} \\ \boldsymbol{Z}_{\mathrm{ch}}^{T} & \boldsymbol{Z}_{\mathrm{Rx}} \end{bmatrix} \begin{bmatrix} \boldsymbol{I}_{\mathrm{Tx}}^{C} \\ \boldsymbol{I}_{\mathrm{Rx}}^{C} \end{bmatrix} = \begin{bmatrix} \boldsymbol{U}_{\mathrm{Tx}} \\ \boldsymbol{0} \end{bmatrix} \tag{12.8}$$

where $\boldsymbol{U}_{\mathrm{Tx}}$ is the complex input voltage vector at the transmitter that needs to be optimized. $\boldsymbol{I}_{\mathrm{Tx}}^{C}$ and $\boldsymbol{I}_{\mathrm{Rx}}^{C}$ are the current vectors at the transmitter and receiver coils, respectively. The matrices $\boldsymbol{Z}_{\mathrm{Tx}}$ and $\boldsymbol{Z}_{\mathrm{Rx}}$ are the complex impedances corresponding to the transmitter and the receiver. At the transmitter since we have a 3-orthogonal coil combination, $\boldsymbol{Z}_{\mathrm{Tx}}$ is a diagonal matrix with the self impedance of each coil on the diagonal entries. $\boldsymbol{Z}_{\mathrm{Rx}}$ is not necessarily diagonal since the receiver coils might have mutual inductances. Finally, $\boldsymbol{Z}_{\mathrm{ch}}$ is a matrix that shows the mutual inductances between each receiver and each transmitter.

Equation (12.8) can be used to solve for $\boldsymbol{I}_{\mathrm{Tx}}^{C}$ and $\boldsymbol{I}_{\mathrm{Rx}}^{C}$

$$\boldsymbol{I}_{\mathrm{Tx}}^{C} = \left(\boldsymbol{Z}_{\mathrm{Tx}} - \boldsymbol{Z}_{\mathrm{ch}} \boldsymbol{Z}_{\mathrm{Rx}}^{-1} \boldsymbol{Z}_{\mathrm{ch}}^{T} \right)^{-1} \boldsymbol{U}_{\mathrm{Tx}} = \boldsymbol{A} \boldsymbol{U}_{\mathrm{Tx}} \tag{12.9}$$

$$\boldsymbol{I}_{\mathrm{Rx}}^{C} = -\boldsymbol{Z}_{\mathrm{Rx}}^{-1} \boldsymbol{Z}_{\mathrm{ch}}^{T} \boldsymbol{A} \boldsymbol{U}_{\mathrm{Tx}} = \boldsymbol{C} \boldsymbol{U}_{\mathrm{Tx}} \tag{12.10}$$

The total transmit power is given by

$$P_{t,\mathrm{total}} = \sum_{k=1}^{3} P_{t,k} = |\boldsymbol{U}_{\mathrm{Tx}}|^{\mathrm{T}} \, |\boldsymbol{A} \boldsymbol{U}_{\mathrm{Tx}}| \tag{12.11}$$

And the received power by the load $Z_{\mathrm{L},\,l}$ of the circuit l is:

$$P_{\mathrm{r},l} = |I_l|^2 \left| Z_{\mathrm{L},l} \right| \tag{12.12}$$

In the iterative method that is proposed, it is assumed that in the case of convergence $\boldsymbol{U}_{\mathrm{Tx}}$ at the nth iteration is almost the same as $\boldsymbol{U}_{\mathrm{Tx}}$ at the $n-1$th iteration. The algorithm that is explained in [42] explains how this becomes n eigenvalue problem in each iteration, and the maximum eigenvalue is picked as the solution at each nth iteration. During this process the total transmit power is approximated by the squared $L2$-norm and optimal beamforming is used to find a local optimum for the power efficiency.

12.10 Regulations Related to Medical Implants and Design Considerations

The development of wireless technology for medical devices is elevating the provision of healthcare with lower costs. Wireless telecommunications can be used for both wearable and implantable applications such as DBS, tracking of vital signs, measuring biological parameters, and cardiac rhythm control. The main advantage of wireless technology compared to landline networks is that the patient is not required to be linked to a certain location by cables [44]. Despite advances in biomedical implants such as a pacemaker, cochlear implant, and nerve stimulator these devices need to be improved in terms of miniaturization, the biocompatibility of materials, sources of electric charge, and wireless communication. To develop an effective implantable medical device, the doctor, the patient, and the technician must collaborate in collecting coherent initial information about different aspects of the device. In particular, the user's satisfaction, the doctor's technical priorities, and the workability of the model are necessary to be considered in the design process [45]. There are important factors for designing medical implants. Since an electric device is implanted inside the human body and the organs around the device may react to it. To avoid such an issue, the device should be made up or coated with biocompatible materials. Moreover, the medical implants should have appropriate packaging to isolate components of the device from body tissue.

Another factor is the structure of the design itself. Before the design, enough data should be collected from the patients, engineers, previous designs, and their advantages and drawbacks [45]. The United States' medical devices market is regulated by the three different organizations, Federal Medicines Authorities (FCC), the Food and Drug Administration (FDA), and the Centers for Medicare and Medicaid Services (CMS). Wireless medical instruments can be classified into two categories, short-range such as inductive implants, medical body area networks, and long-range such as wireless medical telemetry (WMTS). According to the FCC, short-range technology sends data to the local receivers and long-range technology sends user data to the remote spot [46]. The FDA's mission is to check if the proposed medical devices guarantee the factors of safeness and effectiveness for patient usage. The FDA divides medical devices into three classifications based on the risk factor. Class I includes the lowest risk devices and without FDA prior authorization, medical devices may be advertised in this class. The medical devices using wireless technologies are usually considered in Class II. The highest risk medical devices fall under Class III and clinical trials are mandatory to get FDA approval. The FCC and FDA must give permission before wireless medical devices can be marketed in the United States. It is worth mentioning that the FDA and FCC have distinct criteria, and one agency's authorization does not simply ensure the other's consent [44]. The designers of medical implants currently dealing with challenges in materials, output power, size miniaturization, the efficiency of the wireless link, and cybersecurity [45]. There are different types of cyber-attacks including theft of protected health information and execution of fraudulent device commands which require appropriate cybersecurity mechanisms [46].

12.11 Conclusion

This chapter provided a study concentrating on common wireless power transfer (WPT) techniques for implantable and wearable medical devices. WPT through Implantable antennas may suffer from misalignment issues due to the curved surface of the anatomical system and body movement during daily life. The main types of misalignments due to patient movements were analyzed with two case studies. Using multiple transmitters and beamforming as a potential solution to overcome the problem of misalignment and bending and increase power efficiency were discussed. A summary of current regulations related to medical implants and design considerations was provided.

References

1. H. Ali, T.J. Ahmad, S.A. Khan, Inductive link design for medical implants, in *IEEE Symp. Ind. Electron. Appl., Kuala Lumpur, Malaysia*, (2009)
2. H. Rahmani, A. Babakhani, A dual-mode RF power harvesting system with an on-chip coil in 180-nm SOI CMOS for millimeter-sized biomedical implants. IEEE Trans. Microw. Theory Tech. **67**(1), 414–428 (2019)
3. Z.N. Low, R.A. Chinga, R. Tseng, J. Lin, Design and test of a high power high-efficiency loosely coupled planar wireless power transfer system. IEEE Trans. Ind. Electron. **56**(5), 1801–1812 (2009)
4. M. Haerinia, E.S. Afjei, Design and analysis of class EF2 inverter for driving transmitting printed spiral coil. J. Electr. Eng. **18**, 1–5 (2018)
5. H. Lyu, J. Wang, J. La, J.M. Chung, A. Babakhani, An energy-efficient wirelessly powered millimeter-scale neurostimulator implant based on systematic codesign of an inductive loop antenna and a custom rectifier. IEEE Trans. Biomed. Circ. Syst. **12**(5), 1131–1143 (2018). https://doi.org/10.1109/TBCAS.2018.2852680
6. S.A. Mirbozorgi, P. Yeon, M. Ghovanloo, Robust wireless power transmission to mm-sized free-floating distributed implants. IEEE Trans. Biomed. Circ. Syst. **11**(3), 692–702 (2017). https://doi.org/10.1109/TBCAS.2017.2663358
7. Wikipedia [Online]. Available: www.wikipedia.org
8. S. Mutashar, M. Hannan, S. Samad, A. Hussain, Analysis and optimization of spiral circular inductive coupling link for bio-implanted applications on air and within human tissue. Sensors **14**(7), 11522–11541 (2014)
9. M. Haerinia, E.S. Afjei, Resonant inductive coupling as a potential means for wireless power transfer to printed spiral coil. J. Electr. Eng. **16**, 65–74 (2016)
10. M. Haerinia, Modeling and simulation of inductive-based wireless power transmission systems, in *Energy Harvesting for Wireless Sensor Networks: Technology, Components and System Design*, ed. by K. Olfa, 1st edn., (De Gruyter, Berlin, 2018), pp. 197–220
11. M. Haerinia, A. Mosallanejad, E.S. Afjei, Electromagnetic analysis of different geometry of transmitting coils for wireless power transmission applications. Prog. Electromagn. Res. M **50**, 161–168 (2016)

12. X. Wang, M. Lu, Microwave power transmission based on retro-reflective beamforming, in *Wireless Power Transfer—Fundamentals and Technologies*, ed. by E. Coca, (In Tech, London, 2016)
13. S.M. Asif, A. Iftikhar, J.W. Hansen, M.S. Khan, D.L. Ewert, B.D. Braaten, A novel RF-powered wireless pacing via a rectenna-based pacemaker and a wearable transmit-antenna array. IEEE Access **7**, 1139–1148 (2019). https://doi.org/10.1109/ACCESS.2018.2885620
14. B.M.G. Rosa, G.Z. Yang, Active implantable sensor powered by ultrasounds with application in the monitoring of physiological parameters for soft tissues, in *IEEE 13th Int. Conf. Wearable Implant. Body Sensor Netw. (BSN), San Francisco, CA, USA*, (2016)
15. S.Q. Lee, W. Youm, G. Hwang, Biocompatible wireless power transferring based on ultrasonic resonance devices. Proc. Meetings Acoust. **19**(1), 030030 (2013)
16. A. Kim, C.R. Powell, B. Ziaie, An implantable pressure sensing system with electromechanical interrogation scheme. IEEE Trans. Biomed. Eng. **61**(7), 2209–2217 (2014)
17. R. Shadid, M. Haerinia, R. Sayan, S. Noghanian, Hybrid inductive power transfer and wireless antenna system for biomedical implanted devices. Prog. Electromagn. Res. C **88**, 77–88 (2018)
18. M. Haerinia, S. Noghanian, Design of hybrid wireless power transfer and dual ultrahigh-frequency antenna system, in *Proceedings of the URSI EM Theory Symposium, EMTS 2019, San Diego, CA, USA, 27–31 May 2019*, (2019)
19. M. Haerinia, S. Noghanian, A printed wearable dual-band antenna for wireless power transfer. Sensors (Basel, Switzerland) **19**(7), 1732 (2019). https://doi.org/10.3390/s19071732
20. M. Haerinia, S. Noghanian, Analysis of misalignment effects on link budget of an implantable antenna, in *Proceedings of the URSI EM Theory Symposium, EMTS 2019, San Diego, CA, USA, 27–31 May 2019*. Accepted, (2019)
21. M. Haerinia, S. Noghanian, Study of bending effects on a dual-band implantable antenna, in *2019 IEEE International Symposium on Antennas and Propagation and USNC-URSI Radio Science Meeting, Atlanta, GA, USA*, (2019), pp. 753–754
22. R. Shadid, M. Haerinia, S. Noghanian, Study of rotation and bending effects on a flexible hybrid implanted power transfer and wireless antenna system. Sensors **20**, 1368 (2020). https://doi.org/10.3390/s20051368
23. A.A. Danilov, E.A. Mindubaev, S.V. Selishchev, Methods for compensation of coil misalignment in systems for inductive transcutaneous power transfer to implanted medical devices. Biomed. Eng. (NY) **51**, 56–60 (2017)
24. S. Babic, F. Sirois, C. Akyel, C. Girardi, Mutual inductance calculation between circular filaments arbitrarily positioned in space: Alternative to Grover's formula. IEEE Trans. Magn. **46**, 3591–3600 (2010)
25. Y. Palagani, K. Mohanarangam, J.H. Shim, J.R. Choi, Wireless power transfer analysis of circular and spherical coils under misalignment conditions for biomedical implants. Biosens. Bioelectron. **141**, 111283 (2019)
26. D. Liu, H. Hu, S.V. Georgakopoulos, Misalignment sensitivity of strongly coupled wireless power transfer systems. IEEE Trans. Power Electron. **32**(7), 5509–5519 (2017)
27. A.L.A.K. Ranaweera, C.A. Moscoso, J.W. Lee, Anisotropic metamaterial for efficiency enhancement of mid-range wireless power transfer under coil misalignment. J. Phys. D. Appl. Phys. **48**, 455104 (2015)
28. S. Aldhaher, P.C.K. Luk, J.F. Whidborne, Electronic tuning of misaligned coils in wireless power transfer systems. IEEE Trans. Power Electron. **29**(11), 5975–5982 (2014)
29. R. Shadid, S. Noghanian, Hybrid power transfer and wireless antenna system design for biomedical implanted devices, in *Proceedings of the ACES Conference in Denver*, (2018)
30. R. Shadid, S. Noghanian, Study of misalignment effects on hybrid power transfer and wireless antenna system for implanted devices, in *Proceedings of the 2018 IEEE AP-S Symposium on Antennas and Propagation and USNC-URSI Radio Science Meeting in Boston*, (2018)
31. Institute of Applied Physics (IFAC), http://niremf.ifac.cnr.it/tissprop/htmlclie/htmlclie.php
32. U. Jow, M. Ghovanloo, Design and optimization of printed spiral coils for efficient transcutaneous inductive power transmission. IEEE Trans. Biomed. Circ. Syst. **1**, 193–202 (2007)

33. H.D. Lang, A. Ludwig, C.D. Sarris, Convex optimization of wireless power transfer systems with multiple transmitters. IEEE Trans. Antennas Propag. **62**(9), 4623–4636 (2014)
34. R. Shadid, S. Noghanian, Performance comparison between single and multiple implanted receivers in a hybrid power/data transfer system, in *Proceedings of the 2019 IEEE International Symposium on Antennas and Propagation and USNC-URSI Radio Science Meeting, APSURSI 2019 - Proceedings*, (2019)
35. M. Fu, H. Yin, M. Liu, Y. Wang, C. Ma, A 6.78 MHz multiple-receiver wireless power transfer system with constant output voltage and optimum efficiency. IEEE Trans. Power Electron. **33**(6), 5330–5340 (2018)
36. Y.J. Kim, D. Ha, W.J. Chappell, P.P. Irazoqui, Selective wireless power transfer for smart power distribution in a miniature-sized multiple-receiver system. IEEE Trans. Ind. Electron. **63**(3), 1853–1862 (2016)
37. S. Abdollah Mirbozorgi, H. Bahrami, M. Sawan, B. Gosselin, A smart multicoil inductively coupled array for wireless power transmission. IEEE Trans. Ind. Electron. **61**(11), 6061–6070 (2014)
38. J.J. Casanova, Z.N. Low, J. Lin, A loosely coupled planar wireless power system for multiple receivers. IEEE Trans. Ind. Electron. **56**(8), 3060–3068 (2009)
39. J. Jadidian, D. Katabi, Magnetic MIMO: How to charge your phone in your pocket, in *Proceedings of the 20th Annual International Conference on Mobile Computing and Networking*, (2014), pp. 495–506
40. L. Shi, Z. Kabelac, D. Katabi, D. Perreault, Wireless power hotspot that charges all of your devices, in *Proceedings of the 21st Annual International Conference on Mobile Computing and Networking*, (2015), pp. 2–13
41. H. Kim, J. Park, K. Oh, J.P. Choi, J.E. Jang, J. Choi, Near-field magnetic induction MIMO communication using heterogeneous multipole loop antenna array for higher data rate transmission. IEEE Trans. Antennas Propag. **64**(5), 1952–1962 (2016). https://doi.org/10.1109/TAP.2016.2539371
42. K. Kim, H. Kim, J. Choi, Magnetic beamforming with non-coupling coil pattern for high efficiency and long distance wireless power transfer, in *2017 IEEE Wireless Power Transfer Conference (WPTC), Taipei*, (2017), pp. 1–4. https://doi.org/10.1109/WPT.2017.7953869
43. S. Kisseleff, I.F. Akyildiz, W. Gerstacker, Beamforming for magnetic induction based wireless power transfer systems with multiple receivers, in *Global Communications Conference (GLOBECOM), 2015*, (IEEE, New York, 2015), pp. 1–7
44. Fish & Richardson [Online], www.fr.com
45. Y.H. Joung, Development of implantable medical devices: From an engineering perspective. Int Neurourol. J. **17**(3), 98–106 (2013)
46. F. Badrouchi et al., Cybersecurity vulnerabilities in biomedical devices: A hierarchical layered framework, in *Internet of Things Use Cases for the Healthcare Industry*, ed. by P. Raj, J. Chatterjee, A. Kumar, B. Balamurugan, (Springer, Cham, 2020)

Mohammad Haerinia received a B.Sc. and a M.Sc. degree in Electrical Engineering, and a M.Sc. degree in Biomedical Engineering from Shahid Beheshti University, Tehran, Iran, and University of North Dakota, ND, USA, respectively. Currently, he is doing his Ph.D. at the University of Massachusetts Lowell, MA, USA in the field of Electrical Engineering. His research interests include wireless power transfer (WPT), WPT for medical devices, design of the implantable antenna, and applied electromagnetics. He is a member of IEEE-Eta Kappa Nu (IEEE-HKN), the honor society of IEEE and International Union of Radio Science URSI Commission B. He serves as a reviewer for IET Journals (Power Electronics, Electronics Letters and Microwaves, Antennas & Propagation), IEEE Journals (Antennas and Wireless Propagation Letters, Antennas and Propagation Magazine, Electromagnetics, RF, and Microwaves in Medicine and Biology).

Reem Shadid has earned her Bachelor's degree in Electrical Engineering from the University of Jordan in 2003. Also, she earned her Master's degree in Electrical Engineering from the same university in 2015. She earned her Ph.D. in Electrical Engineering from the University of North Dakota, USA in 2018. She was the head of transmission design section at National Electric Power Company in Jordan for 11 years. Currently, she is an assistant professor in the Department of Electrical Engineering of Applied Science Private University (ASU) in Jordan. Her research interests include wireless power transfer and power system and stability.

Sima Noghanian received B.Sc. degree in electrical engineering from the Sharif University of Technology, Tehran, Iran, and M.Sc. and Ph.D. degrees, both in electrical engineering, from the University of Manitoba, Winnipeg, Canada. In 2001, she was a researcher at YottaYotta Corporation, Edmonton, Canada. She received a Postdoctoral Fellowship from the Natural Sciences and Engineering Research Council of Canada in 2002, which she took at the University of Waterloo. She was an Assistant Professor in the Department of Electrical Engineering, Sharif University of Technology, Iran, during 2002–2003. From 2003 to 2008, she was an Assistant Professor in the Department of Electrical and Computer Engineering, University of Manitoba, Canada. She was an Assistant/Associate Professor and the Director of Applied Electromagnetic and Antenna Engineering Laboratory in the Department of Electrical Engineering, University of North Dakota, USA between 2008 and 2018. She also served as the Electrical Engineering Department Chair 2014–2016 at the University of North Dakota. In 2018–2019 she was a visiting professor with the Department of Electrical and Computer Engineering, San Diego State University, USA, where she is currently an Adjunct Professor. Currently, Dr. Noghanian is a Lead Antenna Engineer with Wafer LLC with a focus on designing and simulation of phased array planar antennas. Before joining Wafer LLC, she worked as an Electromagnetic Application Engineer with Phoenix Analysis and Design Technologies Inc. (PADT). Dr. Noghanian's research interests include antenna design and modeling, wearable and implanted antennas, 3D printed antennas, wireless power transfer, microwave imaging, and wireless channel modeling. Sima Noghanian is a member of ACES, a senior member of IEEE, a member of Eta Kappa Nu, and a member of International Union of Radio Science URSI Commission B. She was a member of the Board of Directors of ACES. Currently, she is an Associate Editor for IEEE Antennas and Propagation Magazine; IEEE Antennas and Wireless Propagation Letters; Applied Computational Electromagnetic Society Journal; IET Antennas, Microwave & Propagation; and AEU—International Journal of Electronics and Communications.

Chapter 13
Conclusion

Mohammad Abdul Matin

The world is undergoing a major wireless revolution both in terms of wireless and mobile technology that provides ubiquitous communication access to citizens [1]. In this modern era of wireless communication, the increasing demands for high data rate promote researchers to design wideband and multiband antennas with reasonable gain and good radiation characteristics. The designed antennas are compact in size, integrated into portable wireless devices and RF circuits with low fabrication cost. This book presents aforementioned recent findings and investigates the emerging research trends in the area of antenna engineering.

13.1 Emerging Research Trends

13.1.1 Mobile Handset Applications

The modern wireless handheld devices can enable cellular voice, video and data, Wi-Fi, and GPS services to the customers. These handheld wireless devices require antennas with compact size to integrate other electronic components to shrink the volume of devices as well as to make lightweight, low cost that can operate across multiple bands. All these desirable features impose research challenges in designing new broadband, multiband, and reconfigurable antennas for the new generation of mobile communication devices specially mobile phones, tablets, laptops, wearable computers, and so on. These have been addressed in this book with several design examples.

M. A. Matin (✉)
Department of Electrical and Computer Engineering (ECE), North South University, Dhaka, Bangladesh
e-mail: mohammad.matin@northsouth.edu

M. A. Matin (ed.), *Wideband, Multiband, and Smart Antenna Systems*, Signals and Communication Technology, https://doi.org/10.1007/978-3-030-74311-6_13

13.1.2 MIMO Applications

Massive MIMO is the extension of MIMO, which essentially groups together a huge number of antennas/antenna arrays at the transmitter and receiver to offer better throughput and higher spectral efficiency. However, the size has always been an important issue for designers in the context of accommodating huge number of antennas in physically small devices. On the other hand, it creates mutual interference which in turn degrades the performance of MIMO system. Therefore, the design of compact MIMO antennas with high gain, low loss; high isolation (low mutual coupling) for reliable communication remains a challenge for the researchers though significant research efforts have been found over the last few years to address the above issues. Our book has also attempted to deal with such issues.

13.1.3 IoT Applications

IoT (Internet of Things) allows communication among smart objects for transferring information without the interference of human beings [2]. The ever-growing number of smart devices creates opportunities in industrial and business fields along with improvement of human lifestyle. The antenna miniaturization allows its integration in IoT devices that enables these to participate in wireless communication. However, some considerations need to be focused on while designing antennas. High performing IoT demands for efficient low-profile antennas offering larger bandwidth and higher gain which can provide reliable communications. In addition, the requirements for ever-shrinking foot-print with reasonable performance under extreme interference condition pose additional design challenges of the antennas [3] explained in this book.

13.1.4 Medical Applications

The rapid growth of biomedical industry has gained a lot of attention in the development of wearable human biomedical systems that need to be comfortable and attractive for daily wear. In recent years, Ultra-Wideband (UWB) frequencies have been extensively used by researchers for Body Area Networks (BAN) applications. This requires low-profile, robust, lightweight, and compact antennas. It also requires QOS irrespective of the constraints such as movements of individuals or surrounding objects. The non-caustic and biocompatible material, such as titanium or platinum, can be used for implants resulting in the degradation of performance to compare with the antennas made of copper [4, 5]. Moreover, Organs and antenna positioning determines its shape and size which further controls the design.

.

13.1.5 Radar Applications

Radars have been extensively deployed in aircrafts, ships, and vehicles to avoid collisions and to save lives. The collision avoidance radar aims to provide advanced vehicle control and safety system in the Intelligent Transport System (ITS) which requires highly directional antennas that can distinguish targets in a predetermined field of view. The radar systems operated at millimeter wave band are robust against bad weather condition. Though there may be sufficient number of mm-wave antennas with reasonable performance, the radar system requires antennas or arrays with small size, ease of integration in structures which put some research challenges.

13.2 Concluding Remarks

The recent research effort in the area of wideband, multiband, and smart antennas for different applications are presented in this book. Instead of focusing on the 5G related applications only, this book fairly discusses the state-of-the-art antenna technologies for other wireless applications. The presented designs in this book show that the antenna structures are prudently selected to achieve compact size, lightweight, less power consumption, and ease of integration with other devices, gain and bandwidth requirements according to the specific applications. This will help to build a strong foundation for further investigations of wideband, multiband, and smart antennas to offer wide spectrum of applications in the future.

References

1. M.A. Matin (Ed.), *Developments in Wireless Network Prototyping, Design, and Deployment: Future Generations: Future Generations* (IGI Global, Pennsylvania, 2012)
2. M.R. Mahmood, M.A. Matin, Current research trends on cognitive radio based internet of things (IoT), in *Towards Cognitive IoT Networks* (Springer, Berlin, 2020), pp. 5–17
3. S. Ghosh, D. Sen, An inclusive survey on array antenna design for millimeter-wave communications. IEEE Access **7**, 83137–83161 (2019)
4. M. Patel, J. Wang, Applications, challenges, and prospective in emerging body area networking technologies. IEEE Wirel. Commun. **17**(1), 80–88 (2010)
5. S. Yan, P.J. Soh, G.A.E. Vandenbosch, Wearable ultrawideband technology-a review of ultrawideband antennas, propagation channels, and applications in wireless body area networks. IEEE Access **6**, 42177–42185 (2018)

Dr. Mohammad A Matin is a Professor of the Department of Electrical and Computer Engineering at North South University (NSU), where he has been since 2008. He was first appointed as Assistant Professor and then promoted to Associate Professor in 2011 and later on Professor at North South University. While in that post, he was also the coordinator of the EEE program. During 2012-2017, he was an Associate Professor at Universiti Teknologi Brunei (UTB), Brunei Darussalam. He received his B.Sc. degree in Electrical and Electronic Engineering from BUET (Bangladesh), M.Sc. degree in Digital Communication from Loughborough University, UK and PhD in Wireless Communication from Newcastle University, UK. Dr. Matin has been a visiting academic staff at the National University of Malaysia (UKM), University of Malaya (UM), etc. He has published over 100 peer-reviewed journal and conference papers. He is the author/editor of 16 (sixteen) academic books and 17 (seventeen) book chapters. Dr. Matin serves as a referee or member of the editorial board for several international journals including IEEE Communications Magazine. He is the Senior member of IEEE. He has received a number of Prizes and Scholarships including the Best Student Prize (Loughborough University), Commonwealth Scholarship, and Overseas Research Scholarship (ORS) conferred by the Committee of Vice Chancellors and Principals (CVCP) in the UK.

Index

M. A. Matin (ed.), *Wideband, Multiband, and Smart Antenna Systems*, Signals and Communication Technology, https://doi.org/10.1007/978-3-030-74311-6

C

D

N

O

P